PARTITIONING OF TRACE ELEMENTS BETWEEN PLAGIOCLASE, CLINOPYROXENE AND MELT

Louise Elizabeth Schoneveld

Initially Submitted October 2017

Revised and re-submitted June 2018

A thesis submitted for the degree of **Doctor of Philosophy**
from The Australian National University

Declaration

The work presented herein is an account of the research performed during the academic programme towards the degree of Doctor of Philosophy at the Australian National University.

I certify that this thesis does not contain any material previously submitted for a degree or diploma at a university, nor does it contain any material previously published or written by another person, except where due reference is made in text.

Louise Schoneveld

ACKNOWLEDGEMENTS

This thesis is the culmination of over 3 and a half years of study, though it could not have been completed without help from some wonderful people.

It is thanks to Carl Spandler; my honours supervisor at James Cook University, Townsville QLD, that I made my way to ANU and to Canberra to scope out the ANU for potential PhD supervisors.

RSES is full of wonderful earth scientist but I couldn't think of a supervisor more perfect for me than Hugh O'Neill. Hugh has been a wonderful supervisor over the past few years and it has been great to find someone who finds a singular row of the periodic table just as interesting as I do. I appreciate all the intellectual and financial assistance you have given me along with the freedom to shape my thesis to fit my interests.

To Richard Arculus and John Mavrogenes, thank you for being there for me when Hugh was absent. I appreciate your calm demeanours and confidence in me. To Joerg Hermann, thank you for your guidance in my first year of my PhD and for sitting with me in a park in Paris, talking science with me. I owe a huge debt to Greg Yaxley for reading my thesis with absolutely no context on what I am studying. His feedback was extremely valued and comforting in a time of great stress.

During my first few years here I needed lots of help to learn the black art of experimental petrology. For teaching me these skills I have to thank Dean Scott and Dave Clark, with whom the experimental petrology labs (and all the students contained therein) would fall apart without. Also, I must thank the analytical equipment operators for their tireless efforts in helping me collect the best data possible; Robert Rapp, Jeremy Wykes, Jung-Woo Park, Morgan Williams, Melanie Sieber, and the staff of the Centre for Advanced Microscopy at the ANU. Matt Kilburn, the nanoSIMS operator at UWA for collecting my nanoSIMS data when my time in Perth and a functioning nanoSIMS failed to coincide. Special thanks to all the LA-ICP-MS operators who helped be learn how to best use and operate the LA-ICP-MS system; Jung-Woo Park, Mike Jollands, Peter Tollan and James Tolley. Special thanks to Rick Skelton and Jo Stephenson who taught me how to use Python in the last few months of my PhD.

I am extremely grateful for all those who have lent me their prized samples for me to research. Thank you to Naotaka Tomioka, (Okayama University) who sent me some

anorthite crystals from his personal collection for me to run experiments on. To Kathrin Faak (Ruhr Universitaet Bochum) for lending me her experiments that I used practised my laser ablation skills on my second day at ANU. Also Peter Tollan (Universität Bern), Luca Ziberna (University of Bristol), Mike Jollands (Université de Lausanne), Tarun Whan, Richard Arculus and Joerg Herman for lending me their thin-sections and rock samples for me to study.

I also need to thank the ANUWFC and my soccer girls for giving me something to think about other than rocks and dragging me away from my desk to prevent me from fusing to it permanently.

I couldn't have gotten through these long years without the smiling faces of my fellow students here at RSES. Whether it is grabbing a coffee, walking around, late night study sessions or just sitting in a hallway, stretching and venting about our issues; I appreciate every second I have spent with you and glad to have you all in my life moving forward.

Most importantly I need to thank my family for caring for me and believing in me no matter what I choose to do.

This research is supported by an Australian Government Research Training Program (RTP) Scholarship.

This research is further supported by the Chappell-White Scholarship. I would like to thank the Chappell and White families for helping me live comfortably during this time studying.

I would also like to genuinely thank my 3 anonymous reviewers, whose detailed and helpful revisions vastly improved the quality of this thesis submission. I also would like to thank CSIRO and Steve Barnes, for allowing me the time to make these corrections.

ABSTRACT

This study focusses on the partitioning of trace elements between plagioclase, clinopyroxene and equilibrium melt. Such mineral/melt partition coefficients are widely used to model petrogenetic processes in igneous systems. However, theoretical considerations lead us to expect that the values of partition coefficients will change with many variables, including both mineral and melt compositions, as well as temperature and pressure. Plagioclase and clinopyroxene are two of the most common minerals in the Earth's crust and if we can understand what controls the partitioning of trace elements into common rock forming phases, we can more accurately model these processes.

To examine the major controls of partitioning in plagioclase and clinopyroxene, these two phases were grown experimentally at controlled pressure, temperature and oxygen fugacity. These minerals were grown from a wide range of simple, synthetic systems, mostly focussing on variations in CaO-MgO-Al_2O_3-SiO_2-Na_2O±Fe_2O_3 (CMASN±F) compositional space. 102 successful experiments are included in this thesis, 57 of these contain clinopyroxene and melt, 76 contain plagioclase and melt and 34 of these experiments contain both plagioclase and clinopyroxene and melt. This allows for the partitioning of each phase with their equilibrium melt to be well constrained before comparing the partitioning between the solid phases.

Melt composition is shown to play a significant role in the partitioning of trace elements in both phases, especially when the substituting trace element has a different charge to the element it replaces. Even-though melt composition plays a key role in the partitioning of trace elements in both phases, if the substitution and charge balancing mechanisms are the same in both minerals, the effect of melt composition will be cancelled out. Such is the case for the partitioning of the rare earth elements (REEs) between plagioclase and clinopyroxene. This is advantageous as in natural samples, the equilibrium melt is rarely preserved, so partitioning between the solid phases is much easier to measure than the mineral/melt partition coefficients.

The partitioning of the REEs between plagioclase and clinopyroxene has been used to calibrate a geothermometer. The geothermometer has been applied to a selection of natural coexisting plagioclase and clinopyroxene pairs, with ambiguous results.

TABLE OF CONTENTS

CHAPTER 1. INTRODUCTION

Plagioclase and clinopyroxene are common rock forming minerals in mafic to intermediate igneous rocks. It is generally assumed that post-magmatic re-equilibration of these phases is minimal, and so they are assumed to preserve their magmatic compositions. However, at present there is little empirical evidence to suggest that this assumption is universally applicable, and this uncertainty limits application of plagioclase and pyroxene chemistry to understanding how rocks such as gabbros, layered intrusions and basalts form. Understanding how partitioning of trace elements between these two phases is affected by temperature, pressure, oxygen fugacity, and possible sub-solidus re-equilibration, may create a new tool for determining the history of these mafic bodies.

Both plagioclase and clinopyroxene have a complete solid solution between end member minerals (Deer et al., 1992). Plagioclase has two end member compositions; albite ($NaAlSi_3O_8$) and anorthite ($CaAl_2Si_2O_8$). This solid solution is categorised by anorthite number into; albite (An_{0-10}), oligoclase (An_{10-30}), andesine (An_{30-50}), labradorite (An_{50-70}), bytownite (An_{70-90}) and anorthite (An_{90-100}) (Deer et al., 1992, 2001). Anorthite has a much higher melting point than albite at 1550 °C and 1100 °C respectively (Deer et al., 1992).

Pyroxene has a more complex solid solution and can have two behaviours, orthorhombic and monoclinic. Pyroxenes have a general formula of $(M2)(M1)(Si,Al)_2O_6$ and can be considered to have three different sub groups; magnesium-iron pyroxenes, calcic pyroxenes and sodium pyroxenes (Deer et al., 1992). The calcic pyroxenes will be the focus of this report; diopside ($CaMgSi_2O_6$), hedenbergite ($CaFeSi_2O_6$) and their intermediate composition; augite (Deer et al., 1992, 1997) as these phases commonly occur alongside plagioclase.

Minerals are made up of major elements, which are the major lattice forming elements and occur at concentrations >1 wt. % oxide. Additionally, to these elements, minerals can incorporate small amounts of other elements. Minor elements are defined as occurring in the mineral at concentrations between 0.1 – 1 wt. % oxide, while trace elements occur at concentrations less than 0.1 wt. % oxide (Winter, 2012). The amount of trace elements within a mineral are highly sensitive to igneous fractionation and other magma evolutionary processes. Trace elements within plagioclase and clinopyroxene is the focus of this thesis.

These two minerals occur together in a variety of different geological settings. Plagioclase and clinopyroxene are common phenocrysts in volcanic rocks. Also, rocks such as gabbros are formed almost entirely from these two minerals and make up a sizeable portion of the Earth's crust. As these two minerals are extremely common, if their trace element affinities are properly understood, they could become an extremely useful tool for modelling geological processes, if the mineral's equilibrium composition is preserved.

Equilibrium is a major problem in cumulate rocks. As they reside at high temperatures for long periods of time, the possibility of re-equilibration and quenching of un-equilibrated phases is high. Partition coefficients are calculated on the assumption that the melt and crystal remained at equilibrium (Bédard, 1994; Mollo et al., 2011) with the quenched melt. This is generally true for extrusive rocks, however, intrusive rocks have much longer cooling times, with processes such as assimilation, accumulation and expulsions changing the chemistry of the magma chamber. The slow cooling causes the partition coefficients to be quite distinct from volcanic rocks or experimental results (Blundy, 1997).

Furthermore, it has been shown that elements can move between crystals in solid state diffusion (Pun et al., 1997; Spandler et al., 2007; Van Orman et al., 2001). This would cause the concentrations of trace elements to vary from the equilibrium concentration and cause any models based on these trace elements to be highly uncertain.

1.1 Partition Coefficients

To assess the affinity for a certain element into a mineral we use partitioning coefficients. Partition coefficients are the ratio of a concentration of an element between a mineral and its equilibrium melt (Bédard, 2006) but can also refer to the ratio of concentrations of elements between two mineral phases:

Equation 1:
Partition Coefficients

$$\mathrm{D_i} = \frac{C_{i_{mineral}}}{C_{i_{melt}}}$$

Where C = concentration of an element (i), and D is the partition coefficient.

Therefore if the element have a partition coefficient of >1 it is said to be compatible, and therefore prefers to be in the crystals rather than the melt. Conversely, elements with a

partition coefficient of <1 are incompatible and prefer to exist in the melt, however small concentrations are still taken up in the crystal.

During crystallisation, elements are distributed unevenly between different mineral phases due to their unique affinity for certain elements. Partition coefficients are used to quantify this distribution. Partition coefficients are affected by the bulk composition of the melt, the minerals crystalizing, and formation conditions such as; temperature, pressure, oxygen fugacity and the water content (Aigner-Torres et al., 2007; Bédard, 2014; Bindeman and Davis, 2000; Blundy and Wood, 2003; Colson et al., 1988; Dohmen and Blundy, 2014; Evans et al., 2008; Gaetani and Grove, 1995; Gallahan and Nielsen, 1992; Wood and Blundy, 2014). It is important to note that the partitioning of trace element into crystals is not dependent on the total concentration of trace element in the melt (Miller et al., 2006).

Trace element mineral/melt partition coefficients are widely used to model petrogenetic processes in igneous systems (Dupuy et al., 1980; Krogh, 2000; Liang et al., 2013; Pirard et al., 2013; Sun and Liang, 2017; Witt-Eickschen and O'Neill, 2005).These partition coefficients are often used outside their scope of experimental calibrations in varied melt compositions. However, theoretical considerations lead us to expect that the values of partition coefficients will change with many variables, including both mineral and melt compositions, as well as temperature and pressure (Nielsen et al., 1988; Wood and Blundy, 2014).

If we can understand what controls the partitioning of trace elements into common rock forming phases, we can more accurately model petrogenetic processes. As partition coefficients have not been experimentally measured for every possible iteration of formation conditions and mineral chemistry, predictive models; such as the lattice strain model, are becoming widely accepted as a more accurate way to determine the correct partition coefficient for natural systems (Blundy and Wood, 2003; Wood and Blundy, 2014).

1.1.1 The lattice strain theory

The lattice strain theory for the prediction of trace element partition coefficients has reached peak popularity in the literature currently. It is widely used and the ‘lattice strain parameters’ have been calculated for almost every common mineral (Wood and Blundy, 2014). In this theory, the partitioning of the element of interest (i) is defined as:

Equation 2:
The lattice strain model

$$D_i = \mathrm{D_0} * \exp\left(\frac{-\Delta \mathrm{G}_{\mathrm{strain}}^{\mathrm{crystal}}}{\mathrm{RT}}\right)$$

D_0 colloquially defined as the partition coefficient of a cation the same charge as the cation of interest (D_i) that enters the site without strain i.e. minimising the Gibb's free energy of the crystal ($\Delta \mathrm{G}_{\mathrm{strain}}^{\mathrm{crystal}}$). This partitioning also has a predictable behaviour with temperature (T) in kelvin, and the gas constant (R).

To calculate the change in free energy when one mole of a trace element (X) is substituted into one mole of the mineral (Y), the strain caused to both the mineral and the melt phase must be considered:

Equation 3:
The change in free energy by the incorporation of strain

$$\Delta \mathrm{G}_{\mathrm{X}}^{0} = \Delta \mathrm{G}_{\mathrm{Y}}^{0} + \Delta \mathrm{G}_{\mathrm{strain}}^{\mathrm{melt}} - \Delta \mathrm{G}_{\mathrm{strain}}^{\mathrm{crystal}}$$

Where the melt strain component ($\Delta \mathrm{G}_{\mathrm{strain}}^{\mathrm{melt}}$) is almost zero can be omitted. Therefore, the major change in the partition coefficient will be due to the strain of incorporating the trace ion into the crystal lattice; hence "lattice strain" model

The strain energy was calculated by Brice (1975), given by the relationship with the radius of the cation that enters the site without strain (r_o) and the ionic radius of the trace element of interest (r_i):

Equation 4:
The extended lattice strain model

$$\mathrm{D_i} = \mathrm{D_o} * \exp\left(\frac{-4\pi \mathrm{E} \mathrm{N_A}\left(\frac{\mathrm{r_o}}{2}(\mathrm{r_o} - \mathrm{r_i})^2 + \frac{1}{3}(\mathrm{r_o} - \mathrm{r_i})^3\right)}{\mathrm{RT}}\right)$$

Where D_i is the partition coefficient of the element of interest that has a radius of r_i. D_o is the partition coefficient for a fictive element with a radius r_o that enters the crystal lattice without strain. E is the effective Young's modulus of the site, N_A is Avogadro's number, R is the gas constant, and T is temperature in kelvin.

The constants ($4\pi, N_{A,}R$) in this equation can be simplified to give:

Equation 5:
The simplified lattice strain equation

$$D_i = D_o * \exp\left(\frac{-910.17 * E * \left(\frac{r_o}{2}(r_o - r_i)^2 + \frac{1}{3}(r_o - r_i)^3\right)}{T}\right)$$

Where E is given in GPa, the ionic radii are given in angstroms (Å) and temperature is in kelvin.

The lattice strain model can also be used to predict the partitioning of isovalent cations from the partition coefficient of a measured cation. Rather than D_o, the lattice strain model is fixed to a nonfictive element, with partitioning of D_m and a radius of r_m:

Equation 6:
The simplified lattice strain model, calculated from a specific element

$$D_i = D_m * \exp\left[\frac{-910.17E\left(\frac{r_0}{2}(r_m^2 - r_i^2) + \frac{1}{3}(r_i^3 - r_m^3)\right)}{T}\right]$$

This lattice strain relationship, predicts that the partitioning of the trace elements will vary smoothly with respect to cation radius.

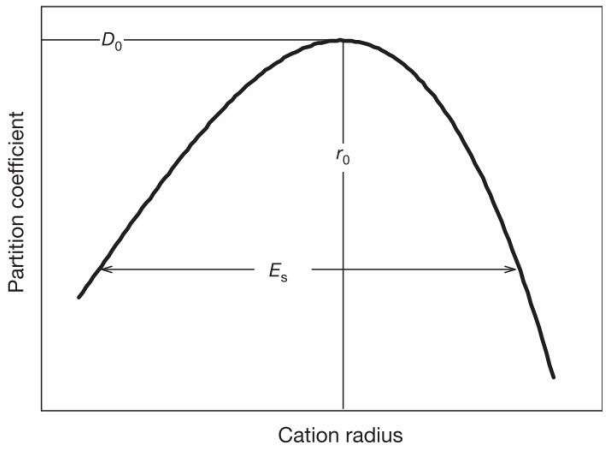

Figure 1: A schematic showing the relationship between cation radius on the parameters of the Brice equation. This diagram is often called an Onuma Diagram (Wood and Blundy, 2014)

Figure 1 shows this theory with respect to cation radius. The ion that will fit most readily in the mineral has a cation radius of r_o which correlates to the peak of the partitioning values (D_o). Any variation in the size from r_o causes more strain in the crystal lattice and therefore has a lower partition coefficient. The tightness of the parabola (E_s) is a

representation of the rigidity of the site, with the more rigid sites having a larger E_s values (Wood and Blundy, 2014).

This theory, though based in thermodynamics, makes one critical assumption; that melt composition does not play a (significant) role in the partitioning of trace elements in minerals ((Blundy and Wood, 2003)). Instead it assumes that all the changes to the free energy of the substitution are attributed to changes in mineral chemistry.

This thesis critically evaluated the use and effectiveness of this lattice strain model and aims to create a new thermodynamic based model for partitioning of trace elements into minerals.

1.1.2 Determining the stoichiometric control on partitioning

To determine the thermodynamic controls of the substitution of a trace element into a mineral, the stoichiometric chemical equation must be written out. Knowing where the trace element partitions into the mineral allows for any charge balancing mechanisms to be outlined. As plagioclase is one of the minerals centralised in this thesis, we will consider the creation of a strontium plagioclase as a simple example:

Equation 7:
The stoichiometric control for the substitution of Sr in anorthite

$$\underset{\text{anorthite}}{CaAl_2Si_2O_8} + \underset{\text{melt}}{SrO} = \underset{\text{plagioclase}}{SrAl_2Si_2O_8} + \underset{\text{melt}}{CaO}$$

The equilibrium constant (K) for strontium (Sr) in anorthite (An) reaction is:

Equation 8:
The equilibrium constant (K) for the substitution of Sr in anorthite

$$K_{Sr}^{An} = \frac{\alpha\, SrAl_2Si_2O_{8_{pl}} * \alpha CaO_{melt}}{\alpha\, SrO_{melt} * \alpha CaAl_2Si_2O_{8_{An}}}$$

Where α relates to the activity of the component in the melt and crystal phases. When in equilibrium, the free energy of this reaction must be zero:

Equation 9:
The free energy of an ideal mixture

$$\Delta G^0 + RT\ln K_{Sr}^{An} = 0$$

Then Equation 8 can be updated to include the relationship in Equation 9:

$$K_{Sr}^{An} = \exp\left(\frac{-\Delta G^0}{RT}\right) = \frac{\alpha\, SrAl_2Si_2O_{8_{plagioclase}} * \alpha CaO_{melt}}{\alpha\, SrO_{melt} * \alpha CaAl_2Si_2O_{8_{An}}}$$

The trace element components very rarely have reliable thermodynamic data available to calculate their activities. Instead, the activity of each of the components can be broken down to their relationship between their concentrations (given in mole fractions) multiplied by an activity coefficient (γ).

Equation 10:
The relationship between the activities of the trace components and their concentrations

$$K_{Sr}^{An} = \exp\left(\frac{-\Delta G^0}{RT}\right) = \frac{X_{SrAl_2Si_2O_8}^{plagioclase} * \gamma_{SrAl_2Si_2O_8}^{plagioclase}}{X_{SrO}^{melt} * \gamma_{SrO}^{melt}} * \frac{\alpha CaO_{melt}}{\alpha CaAl_2Si_2O_{8_{An}}}$$

The partition coefficients between minerals and melts are defined as the concentration of the trace element in the crystal ($X_{SrAl_2Si_2O_8}^{plagioclase}$) divided by the trace element in the melt (X_{SrO}^{melt}). Equation 10 can be rearranged to determine the main factors effecting the partitioning of strontium in anorthite:

Equation 11:
The partition coefficient of strontium and its stoichiometric control

$$D_{Sr}^{\frac{An}{melt}} = \frac{X_{SrAl_2Si_2O_8}^{plagioclase}}{X_{SrO}^{melt}} = \exp\left(\frac{-\Delta G^0}{RT}\right) * \left(\frac{\gamma_{SrO}^{melt}}{\gamma_{SrAl_2Si_2O_8}^{plagioclase}}\right) * \left(\frac{\alpha CaAl_2Si_2O_{8_{An}}}{\alpha CaO_{melt}}\right)$$

(1) (2) (3)

This equation outlines that the partitioning of Sr^{2+} for Ca^{2+} in anorthite (isovalent substitution) is controlled by three factors (1) the change in free energy in the solid due to the incorporation of the cation of interest (2) the ratio of the activity of the trace element component in the melt and crystal (3) the stoichiometric control. The latter refers to the position of the trace element within the mineral of interest, and the relevant couple substitutions that may occur to ensure neutrality of the crystal (e.g. Equation 7).

This stoichiometric control will change if the substitution is aliovalent, for example, the substitution of a trivalent rare earth element (REE^{3+}) for Ca^{2+} in anorthite:

Equation 12:
The stoichiometric control for the creation of REE in anorthite

$$\underset{melt}{[REE]O_{1.5}} + \underset{anorthite}{CaAl_2Si_2O_8} + \underset{melt}{AlO_{1.5}} = \underset{plagioclase}{[REE]Al_3SiO_8} + \underset{melt}{CaO} + \underset{melt}{SiO_2}$$

Therefore the equilibrium equation is:

Equation 13:
The equilibrium constant for the partitioning of REE in anorthite

$$K_{REE}^{An} = \frac{\alpha[REE]Al_3SiO_{8_{Pl}} * \alpha CaO_{melt} * \alpha SiO_{2_{melt}}}{\alpha[REE]O_{1.5_{melt}} * \alpha CaAl_2Si_2O_{8_{An}} * \alpha AlO_{1.5_{melt}}} = \exp\left(\frac{-\Delta G^0}{RT}\right)$$

Which is related to the partition coefficient in the same way as before, however there are extra melt components:

Equation 14:
The thermodynamics of REE partitioning in anorthite

$$D_{REE}^{An/melt} = \frac{X_{[REE]Al_3SiO_8}^{plagioclase}}{X_{[REE]O_{1.5}}^{melt}} = \exp\left(\frac{-\Delta G^0}{RT}\right) * \left(\frac{\gamma_{[REE]O_{1.5}}^{melt}}{\gamma_{[REE]Al_3SiO_8}^{plagioclase}}\right) * \left(\frac{\alpha AlO_{1.5_{melt}}}{\alpha SiO_{2_{melt}}}\right) * \left(\frac{\alpha CaAl_2Si_2O_{8_{An}}}{\alpha CaO_{melt}}\right)$$

(1) (2) (3) (3)

This aliovalent substitution is similar to Equation 11 however has an additional component in its stoichiometric control (3). Therefore, the partitioning of the REEs will be affected differently by melt composition than the partitioning of strontium in anorthite.

Although I have used substitution of the REEs and Sr in anorthite as examples, these same stoichiometric controls will be important for partitioning of trace elements in all minerals. Therefore partition coefficients calculated from different melt types cannot be compared unless the melt effect is well understood. Consequently, this is further evidence to suggest that partition coefficients cannot be interchanged between natural systems e.g. partition coefficients calculated in basaltic systems will be inherently different to granitic systems.

1.2 Partitioning between solid phases

So far we have considered the partitioning between a single mineral phase and an equilibrium melt. In natural samples, the equilibrium melt is rarely preserved and therefore it is more practical to compare the partitioning between two solid phases in equilibrium.

This thesis is focused on plagioclase (plag) and clinopyroxene (cpx). The partitioning between these two phases can be calculated either by a simple ratio of the concentration (C) of the element of interest (i) in each phase, or a ratio of the partition coefficients $D_{plag/melt}$ and $D_{cpx/melt}$.

Equation 15:
Partitioning between solid phases

$$\mathrm{D_i} = \frac{C_{i_{plagioclase}}}{C_{i_{clinopyroxene}}} \text{ OR } \mathrm{D_i} = \frac{D_{i_{plag/melt}}}{D_{i_{cpx/melt}}}$$

These two phases have grown from a shared equilibrium melt and as such, the melt composition will be equal for both phases. Consider the partitioning of the rare earth elements in both plagioclase and clinopyroxene:

Equation 16:
substitution to REE in anorthite

$$[\mathrm{REE}]\mathrm{O}_{1.5_{\mathrm{melt}}} + \mathrm{CaAl_2Si_2O_{8_{pl}}} + \mathrm{AlO}_{1.5_{\mathrm{melt}}} = [\mathrm{REE}]\mathrm{Al_3SiO_{8_{pl}}} + \mathrm{CaO}_{\ \mathrm{melt}} + \mathrm{SiO_{2_{melt}}}$$

Equation 17:

The thermodynamic equilibrium constant for the substitution of REE in anorthite

$$\mathrm{D}_{\mathrm{REE}}^{\mathrm{An/melt}} = \frac{\mathrm{X}_{[\mathrm{REE}]\mathrm{Al_3SiO_8}}^{\mathrm{plagioclase}}}{\mathrm{X}_{[\mathrm{REE}]\mathrm{O}_{1.5}}^{\mathrm{melt}}} = \exp\left(\frac{-\Delta \mathrm{G}^0}{\mathrm{RT}}\right) * \left(\frac{\gamma_{[\mathrm{REE}]\mathrm{O}_{1.5}}^{\mathrm{melt}}}{\gamma_{[\mathrm{REE}]\mathrm{Al_3SiO_8}}^{\mathrm{plagioclase}}}\right) * \left[\frac{\alpha\mathrm{AlO}_{1.5_{\mathrm{melt}}}}{\alpha\mathrm{SiO_{2_{melt}}}}\right] * \left(\frac{\alpha\mathrm{CaAl_2Si_2O_{8_{An}}}}{\alpha\mathrm{CaO_{melt}}}\right)$$

Equation 18:
substitution to REE in diopside

$$[\mathrm{REE}]\mathrm{O}_{1.5_{\mathrm{melt}}} + \mathrm{CaMgSi_2O_{6_{px}}} + \mathrm{AlO}_{1.5_{\mathrm{melt}}} = [\mathrm{REE}]\mathrm{MgAlSiO_{6_{px}}} + \mathrm{CaO_{melt}} + \mathrm{SiO_{2_{melt}}}$$

Equation 19:
The thermodynamic equilibrium constant for the substitution of REE in diopside

$$\mathrm{D}_{\mathrm{REE}}^{\mathrm{Di/melt}} = \frac{\mathrm{X}_{[\mathrm{REE}]\mathrm{MgAlSiO_6}}^{\mathrm{diopside}}}{\mathrm{X}_{[\mathrm{REE}]\mathrm{O}_{1.5}}^{\mathrm{melt}}} = \exp\left(\frac{-\Delta \mathrm{G}^0}{\mathrm{RT}}\right) * \left(\frac{\gamma_{[\mathrm{REE}]\mathrm{O}_{1.5}}^{\mathrm{melt}}}{\gamma_{[\mathrm{REE}]\mathrm{MgAlSiO_6}}^{\mathrm{diopside}}}\right) * \left[\frac{\alpha\mathrm{AlO}_{1.5_{\mathrm{melt}}}}{\alpha\mathrm{SiO_{2_{melt}}}}\right] * \left(\frac{\alpha\mathrm{CaMgSi_2O_{6_{Di}}}}{\alpha\mathrm{CaO_{melt}}}\right)$$

Writing the equations in the form above clearly outlines that the melt component (square brackets) is the same in both these substitutions.

When comparing the partitioning of the same element between solid phases the effect of melt composition is cancelled out if (1) the trace element partitions for the same element in both minerals, and (2) the trace element is charge balanced by the same mechanism.

1.2.1 The double lattice strain theory

The lattice strain theory can also be used to model the partitioning between two mineral phases. This model was used recently in Liang et al. (2013) and Sun and Liang (2017) for two mineral thermometry, the double lattice strain model and is a combination of the mineral/melt lattice strain models for each phase:

Equation 20:
The double lattice strain model

$$\ln D_i^{A/B} = \ln D_o^A + \left(-910.17 * \frac{E^A}{T} * \left[\frac{r_o^A}{2} * (r_i - r_o^A)^2 + \left(\frac{1}{3}\right) * (r_i - r_o^A)^3\right]\right) - \ln D_o^B - \left(-910.17 * \frac{E^B}{T} * \left[\frac{r_o^B}{2} * (r_i - r_o^B)^2 + \left(\frac{1}{3}\right) * (r_i - r_o^B)^3\right]\right)$$

Where the partitioning of the element of interest (D_i) between phase A and phase B is given by the ratio of the partitioning of the element of interest between each phase and their shared equilibrium melt.

The only caveat is; if the melt components were not factored in to the lattice strain model to calculate the lattice strain parameters, then the double lattice strain model will have propagated errors.

Using charge balanced equations to describe the partitioning of trace elements into minerals, it is suggested that melt composition will play a role. This thesis aims to determine how significant the effect of melt composition is between plagioclase/melt and diopside/melt and if this melt effect is completely cancelled out when comparing partitioning between these two phases.

1.3 Thesis Outline

Although many partitioning experiments have been done previously there is still some areas in which many assumptions are made. We assume that most trace elements partition into the large cation site of plagioclase and the M1 and M2 sites of clinopyroxene, although we do not have empirical evidence to support this. Another assumption is that the partitioning of trace elements is controlled almost entirely by the crystal chemistry and formation conditions (pressure and temperature) and that changes in melt components play an insignificant role. To solve these assumptions, the partitioning of many trace elements will be examined in very simple systems, which will allow for the variables to be disentangled and their individual effects on the partitioning to be studied. Once the

partitioning is defined for simple systems, more complex systems will be tested to determine which variables have the greatest influence on partitioning.

Plagioclase and clinopyroxene are some of the most commonly occurring minerals in the world. If the partitioning between these two minerals can be used to reverse engineer a thermometer, as suggested by (Sun and Liang, 2017) then it would be a widely applicable tool for many rock types.

This thesis aims to;

1) Define the controls of partitioning of trace elements in plagioclase
2) Define the controls of partitioning of trace elements in clinopyroxene
3) Determine if diffusion is an important variable for possible re-equilibration of these phases
4) Evaluate the partitioning between these two phases in equilibrium
5) Create a new geothermometer and asses the validity of it and the (Sun and Liang, 2017) REE-in-clinopyroxene-plagioclase thermometer

To complete these aims 102 individual experiments were conducted which successfully synthesise melt and plagioclase and/or clinopyroxene. Many of the experiments are used to calculate plagioclase / melt, clinopyroxene / melt and plagioclase / clinopyroxene partition coefficients. To avoid repetition, the experimental and analytical methods are detailed in a separate chapter; CHAPTER 2- Experimental and Analytical Methods .

The results of these experiments are laid out into four broad chapters.

CHAPTER 3 is separated into two sections. The first section is focussed on the effect of changing melt composition on the partitioning of trace element in anorthite. The second section expands on this study to determine the controlling factors of trace element partitioning in plagioclase of many compositions.

CHAPTER 4 investigates the diffusion of minor and trace elements in plagioclase through three experimental studies. This will allow for the determination of closure temperatures, diffusivities and possible re-equilibration times of trace elements in plagioclase.

CHAPTER 5 investigates the partitioning of trace elements between clinopyroxene and melt. This chapter is separated into two sections, determining the stoichiometric control of the REE partitioning in diopside and then is expanded to determine the main influences of trace element partitioning in clinopyroxene.

CHAPTER 6 compares the partition between plagioclase and clinopyroxene. The first section is the experimental section which compares the results from the previous two chapters and combines them to examine the partitioning between solid phases. A geothermometer is attempted using the rare earth element partitioning between plagioclase and clinopyroxene and is compared to the existing geothermometer outlined by Sun and Liang (2017).

This new thermometer and traditional thermometry methods are compared in the second section of this chapter in natural samples. The natural samples are plagioclase and clinopyroxene bearing rocks from both plutonic and volcanic environments. The locations are; Italy, New Caledonia, Lesser Antilles, Alaska and Vanuatu. Finally, the validity and useability of this thermometer will be assessed and summarised.

CHAPTER 2. EXPERIMENTAL AND ANALYTICAL METHODS

A number of plagioclase + clinopyroxene + melt experimental charges were synthesised for this study in which the results are distributed over 3 chapters. A short summary of the methods are included in each chapter but to avoid repetition a detailed experimental and analytical method is included here.

2.1 Experimental Apparatus

2.1.1 1 atm vertical tube gas mixing furnace

The gas mixing furnaces allow for experiments to be conducted at controlled oxygen fugacity at atmospheric pressure. The oxygen fugacity is controlled by pumping in a mixture of CO_2 and CO.

The furnace consists of a vertical tube with an alumina rod suspended from the top of the furnace. Within the furnace, there is a singular "hot spot" where the temperature is the highest (Figure 2a). This hot spot is calculated for each furnace and the alumina rod fashioned to ensure the samples will hang in this space.

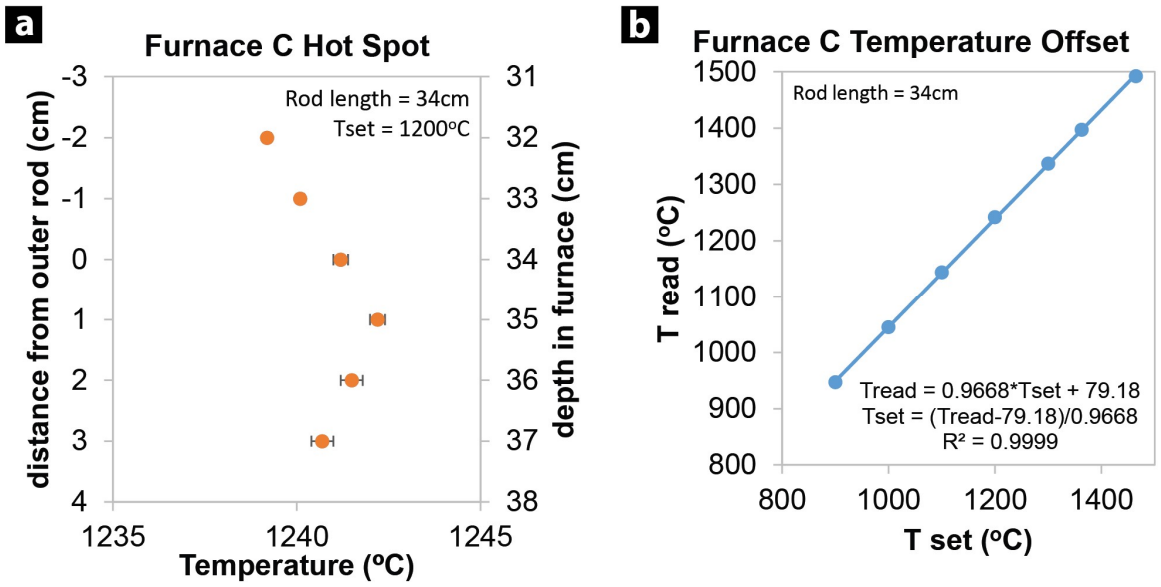

Figure 2: Temperature calibration for 1 atm gas mixing furnace "C" a) determination of the "hot spot" of the furnace as measured from the top of the furnace b) Temperature offset between programmed temperature and measured temperature at sample position

The temperature is controlled by a thermocouple located outside of the furnace so there is some offset between the programmed temperature and the temperature at which the samples are held. This temperature offset was calculated to allow for simple programming of the furnaces (Figure 2b); additionally the temperature of the sample for each run was recorded wherever possible.

Similarly, the offset between the calculated and measure fO_2 was investigated. This offset is close to zero, with the exception of the fO_2 of "air" (Figure 3). When "air" is used as the buffer, it means that no gasses are being pumped through the furnace, however the furnace tube remained sealed to ensure minimal heat loss.

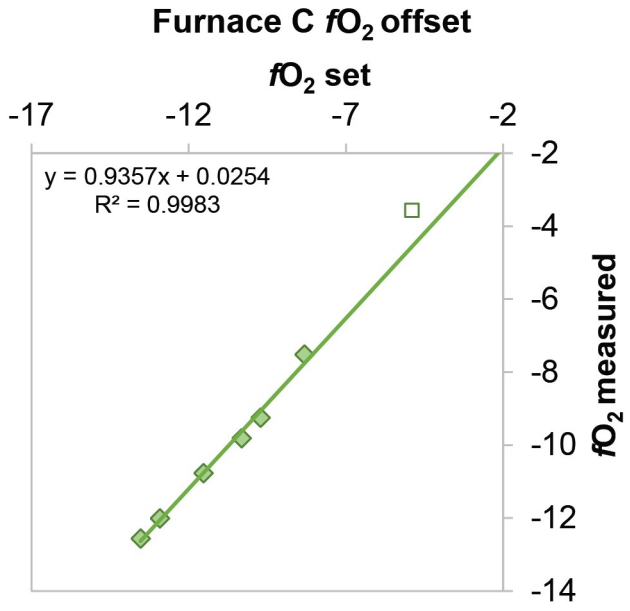

Figure 3: oxygen fugacity for furnace "C" difference between programmed flow rate and measured fO_2. Unfilled square is "air" which outlies from the general trend.

The 1 atm furnaces allow for multiple experimental charges to be run at the same temperature and fO_2, but to test effect of pressure, the minerals must be synthesised using the piston cylinder apparatus.

2.1.2 Piston Cylinder Apparatus

Pressurized experiments were conducted using a piston cylinder apparatus (Boyd and England, 1960). The sample was packed into a 3.5mm diameter platinum capsule and then placed inside a specifically crafted MgO tube, graphite, Pyrex and NaCl sleeves (Figure 4). The graphite acts as the heater while the NaCl acts as the compressible material to convert uniaxial pressure of the piston cylinder to a more hydrostatic type pressure. The dimensions of the final assembly are ½" diameter and 30mm length.

These assemblies are placed inside the piston cylinder apparatus which is driven to pressure using a hydraulic piston. Wherever possible, the experiments were carried out on the automated piston cylinder which are programmed to pump up any lost pressure.

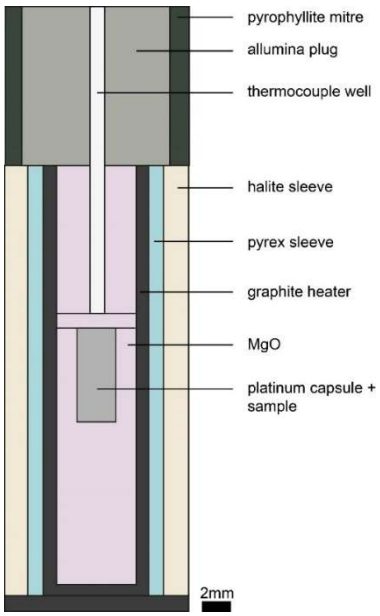

Figure 4: diagram of piston cylinder assembly to scale

2.2 The starting chemical mixes

The experiments in this thesis are broken up into three broad categories; plagioclase + melt, clinopyroxene + melt and plagioclase + clinopyroxene + melt experiments. These categories make up individual chapters in this thesis, however, the experimental method is shared.

There are two main types of experiments in this study, pressurized and unpressurized experiments, however both use common starting compositions.

The starting compositions were created by mixing dried, pure oxide powders. Oxides such as MgO, SiO_2 and Al_2O_3 were heated in a box furnace, ramped slowly to 900ºC and held for over 2 hours. Carbonates, such as $CaCO_3$ were heated at 300ºC for over 2 hours.

The trace elements were also measured from pure oxide powders. The trace elements were measured in large batches (0.05g each) and thoroughly mixed in acetone and allowed to dry. Small amounts of these mixed trace element batches were measured into each starting composition to obtain the desired amount of trace elements.

The major and trace element oxides were weighed and grinded in acetone for at least 45 minutes. After evaporating the acetone, the powder was pressed into pellets, which were then de-carbonated by heating in a box furnace, ramped over an hour to 900ºC and held for at least 2 hours. The pellets were then re-crushed and kept in labelled vials, ready for each experiment.

There are six broad categories for the starting compositions; CaO-Al_2O_3-SiO_2 (CAS), CaO-MgO-SiO_2 (CMS), CaO-MgO-Al_2O_3-SiO_2 (CMAS), CaO-MgO-Al_2O_3-SiO_2-Na_2O

(CMASN), CaO-MgO-Al_2O_3-SiO_2-Na_2O-FeO (CMASNF) and "natural". This combination of starting compositions allows for the transition for very simple experiments; with only a single mineral phase + melt, to more complicated system with many components; two solid phases and an equilibrium melt. The experimental starting compositions are outlined in (Figure 5) in relation to a diopside-anorthite-albite ternary. The major and trace elements of these mineral + melt pairs are included in the appendix in Table 43 to Table 45.

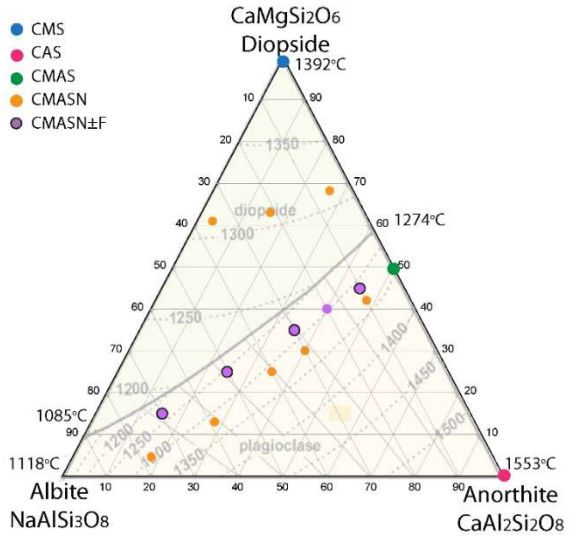

Figure 5: A summary of the starting compositions for all experiments. Black outlines represent duplicate experiments, one set containing iron and the other set iron free. CaO-Al_2O_3-SiO_2 (CAS), CaO-MgO-SiO_2 (CMS), CaO-MgO-Al_2O_3-SiO_2 (CMAS), CaO-MgO-Al_2O_3-SiO_2-Na_2O (CMASN), CaO-MgO-Al_2O_3-SiO_2-Na_2O-FeO (CMASNF). All experiments other than pure CMS and CAS are saturated in both plagioclase and clinopyroxene at the experimental conditions.

2.2.1 Anorthite and melt experiments in the CaO-Al_2O_3-SiO_2 (CAS) & CaO-MgO-Al_2O_3-SiO_2 (CMAS) systems

Five melt compositions were chosen from the CaO-Al_2O_3-SiO_2 system that synthesise anorthite at 1400°C (Levin et al., 1964). Four compositions based on the work of Miller et al. (2006) were chosen in the CMAS system in equilibrium with anorthite at 1332°C. The latter compositions deviate slightly in MgO content (8-14 wt. % MgO) and have proportional CaO-Al_2O_3-SiO_2,

This experimental series does not only vary in major elements but also trace elements to test the limits of Henry's Law; which states that the partitioning of trace elements is not dependant on the concentration of the trace element in the melt.

The total sum of all the trace elements are <1 wt. % O (~70 ppm per element), 1 wt. % O (~500 ppm per element), 3 wt. % O (~1300 ppm per element), and 8 wt. % O (~4000 ppm per element). The trace elements in this experimental series include; Sc, Fe, Sr, Nb, Ba, REE, Hf, Th, and U (Figure 6).

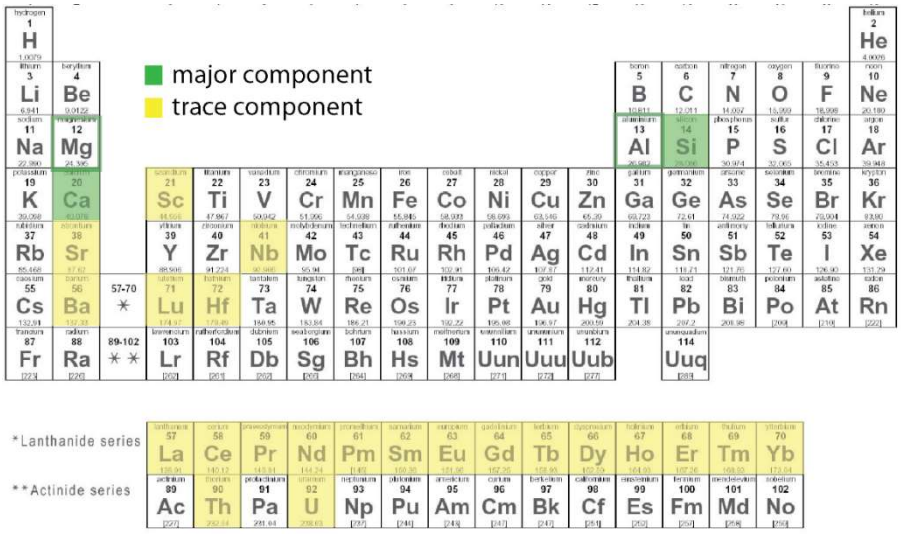

Figure 6: Trace element doping scheme 1: Trace and major elements chosen in CAS and CMS experimental series. Unfilled squares represent doping in certain experiments while solid shading represents contained in all experiments.

2.2.2 Diopside and melt experiments in the CaO-MgO-SiO_2 (CMS) & CaO-MgO-Al_2O_3-SiO_2 (CMAS) systems

Three compositions in the CaO-MgO-SiO_2 (CMS) ternary and three compositions in the CaO-MgO-Al_2O_3-SiO_2 (CMAS) space were chosen that synthesise diopside and melt (and occasionally olivine). This experimental series also varies in trace element concentration. The original starting compositions had an unintentionally high concentration of trace elements (20 wt. % total trace elements). These concentrations were diluted by mixing small portions with new major element mixes.

The trace elements doped in this experimental series are outlined in Figure 6.

2.2.3 Plagioclase + melt and diopside + melt in the CaO-MgO-Al_2O_3-SiO_2-Na_2O (CMASN) system

This experimental method was adapted from that published in Dohmen and Blundy (2014). Three compositions in the anorthite-albite-diopside ternary were chosen to synthesise diopside + melt at 1300 °C along with five compositions that synthesis plagioclase + melt at the same temperature (Figure 7a). The "P1" composition synthesised both plagioclase + diopside + melt.

Sodium is volatile at high temperatures and 1 atm, so there is potential for sodium to be volatilised from the melt into the atmosphere. Using the platinum loop method that was used for all other 1 atm experiments caused the sodium to be lost from the experiments (Figure 7b). To resolve this, these experiments were instead run in crimped platinum capsules. This contains the volatile elements and allows next to no sodium loss (Figure 7b).

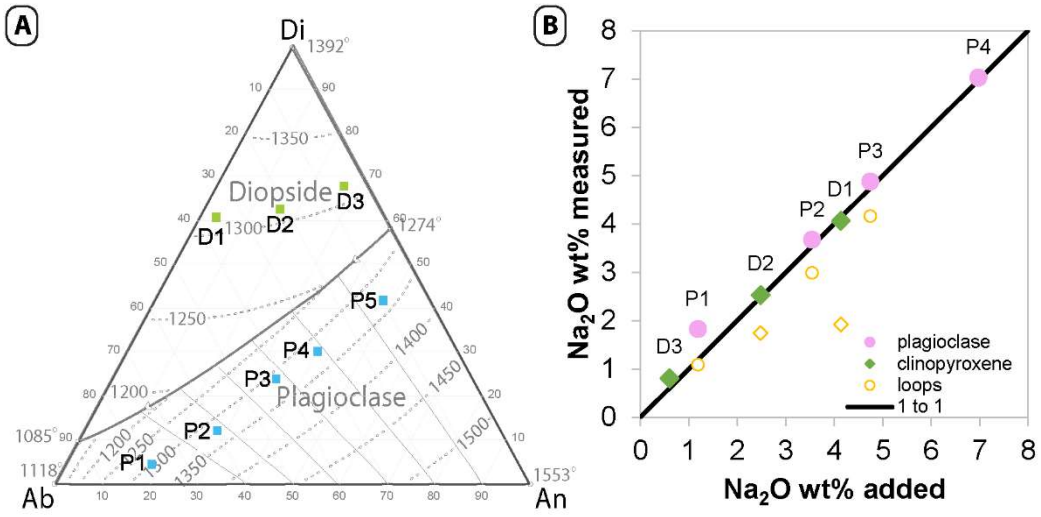

Figure 7: A) Plagioclase compositions in the An-Ab-Di space based on Dohmen and Blundy (2014) compositions B) Sodium loss; a comparison between crimped Pt capsules and open Pt loops

Each mineral powder was then doped with a total of 1 wt. % trace elements consisting of the following elements:

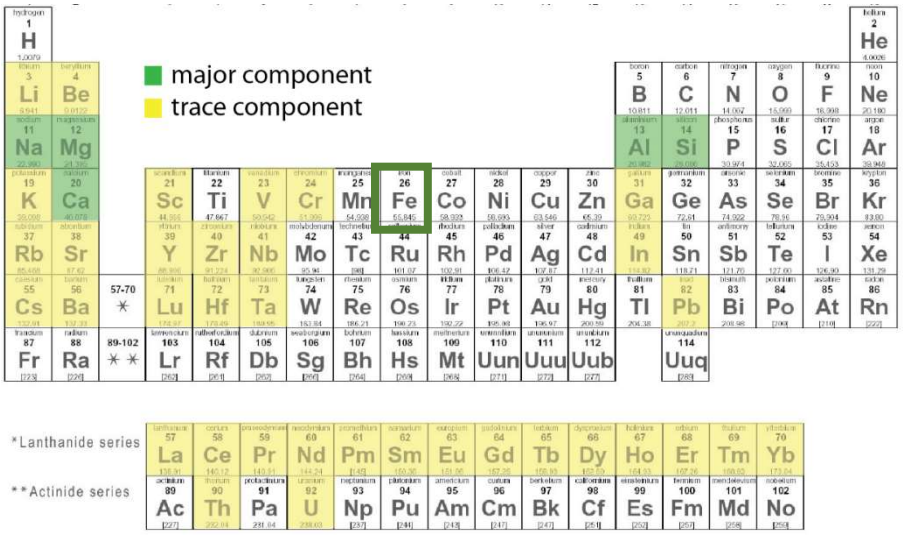

Figure 8: Trace element doping scheme 2: Trace and major elements chosen in CMASN experimental series. Most experiments are iron free except those in the CMASNF system, in which Fe is a major component.

2.2.4 Plagioclase + diopside + melt experiments in the CaO-MgO-Al_2O_3-SiO_2-Na_2O (CMASN) and CaO-MgO-Al_2O_3-SiO_2-Na_2O-FeO (CMASNF) systems

This starting composition makes up the majority of the pressurized samples, and the database as whole.

Five starting compositions were used. These compositions are made by combining a mix of pure albite component, with an anorthite + diopside component mix, the latter of which

was doped in trace elements. The trace elements follow doping scheme 2 (outlined in Figure 8) were doped at 1 wt. % total concentration in the anorthite-diopside mix. As the albite component is not doped in trace elements; as the melt compositions increase in Na_2O the total trace elements decreases. This allows for plagioclase of different compositions to grow at similar temperatures.

A second series of these experiments were run that were doped consistently at 1wt% trace elements to determine that Henry's law was followed. These experiments have labels ending in "x" (Table 3).

These five starting compositions were also used in the CMASNF system, with each composition being mixed with 1, 5, 10 or 15 wt. % Fe_2O_3.

2.2.5 "Natural" compositions

There are three compositions in more complex systems that are given the nomination "natural" compositions. This includes sample ALV-3352-7 which is a synthetic version of a Moai lava flow published in Aigner-Torres et al. (2007). This experiment is doped in trace elements according to doping scheme 2 (Figure 8) at a total of 1 wt. %.

Compositions BIR64 and BIR70 are roughly based on the USGS standard BIR-1 an Icelandic basalt. These compositions are used in the diffusion studies (the method is contained within the diffusion chapter) as well as in some partitioning studies. These experiments are doped in Be, Ga, Nb, Ba, the Rare Earth Elements (REE), Hf, Th and U.

2.3 The experimental method

2.3.1 Experiments in the 1atm gas mixing furnace

Approximately 0.05g of the sample powder was weighed and mixed with polyethylene oxide and adhered on a platinum wire. These experimental charges were hung from a circular platinum "chandelier" suspended from an alumina ring and placed in the hot spot of a vertical tube furnace equipped for gas mixing.

The chandelier was loaded into the furnace tube at 600°C. The temperature was ramped up at 6°C/min from 600°C to T_1; 100 °C above the target temperature then cooled at 0.1°C/min to the desired run temperature (T_2) and held for between 48 and 160 hours. The temperature was controlled using a type B thermocouple external to the furnace tube and was measured using a second type B thermocouple inside the alumina rod from which the chandelier is suspended.

To quench, the experimental charge was dropped from the furnace into a beaker of water. The beads were then cut from the chandelier and mounted in epoxy and polished with diamond paste of successively smaller grit size to 1μm for analysis.

2.3.2 High Pressure Experiments

For the pressurized experiments, 3.5mm diameter platinum tubing was cut to less than 8mm length and crimped, welded and flattened on one end to create a bucket. The bucket was weighed and packed with powder. Once the powder is 2mm from full, the bucket is crimped, welded and flattened to create a platinum capsule with the sample contained within. This sample is then weighed again and the weight of the power calculated. The capsule is placed in the piston cylinder assembly (Figure 4) and the assembly inserted into the large holder (Figure 9A).

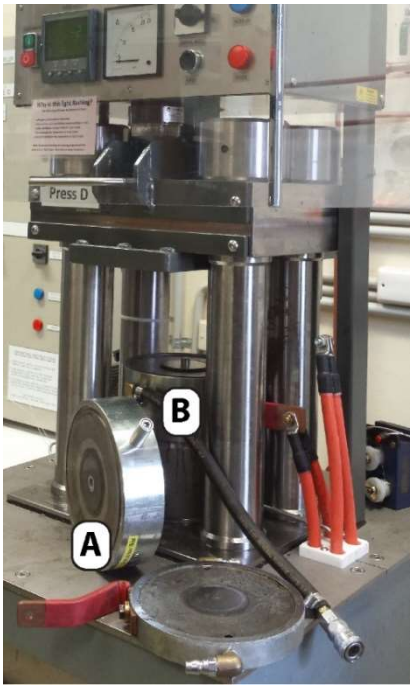

Figure 9: The piston cylinder apparatus. A) The holder of the sample B) the piston and ram

The piston (Figure 9B) is driven up into the sample and the resulting pressure measured in psi. The pressure has been calibrated to allow for simple conversion of psi to kbar. After at least 1000 psi of pressure is placed on the sample, the heating stage is started. This heating is controlled by a type B thermocouple, encased in a mullite sheath and with 5mm alumina at the end. This thermocouple is placed 1mm from the top of the platinum capsule.

The temperature is ramped up at 9000 °C/h to 100 °C above the target temperature and held for 2 hours. The pressure by this stage is at the target pressure and will remain for the entirety of the experiment. The temperature is cooled at 6 °C/h to the target

temperature (T_2) and held for 48 hours. During the cooling stage, the pressure relaxes. To ensure constant pressure during crystal growth, programmable piston cylinder apparatus was used whenever available, that automatically pumped up the pressure when lost. The automated piston cylinders usually maintain the pressure within 200 psi of the target.

At the end of the experiment, the current to the experiment was cut and the pressure released which will cause the experiment to quench. After decompression the capsule was broken out of its casing, mounted in epoxy and polished to 1 μm.

In the case of the Fe-containing runs at pressure; 10 wt. % (of the total powder weight) of Pt_2O was packed into the bottom of each capsule. This will create a finite buffer for the reaction $PtO_2 \rightarrow Pt_{(metal)} + O_2$ and creates a highly oxidising environment. This causes all the Fe to exist as Fe_2O_3 (Fe^{3+}). This creates an end member of Fe^{3+} partitioning that is not obscured by combination Fe^{2+} and Fe^{3+} partitioning.

2.3.3 Growing plagioclase and clinopyroxene

Attempts to grow crystals at a constant temperature were unsuccessful or too small for analysis by LA-ICP-MS. Similarly, heating the charge to 100°C above the target temperature and dropping to the target temperature as quickly as possible did not result in large minerals.

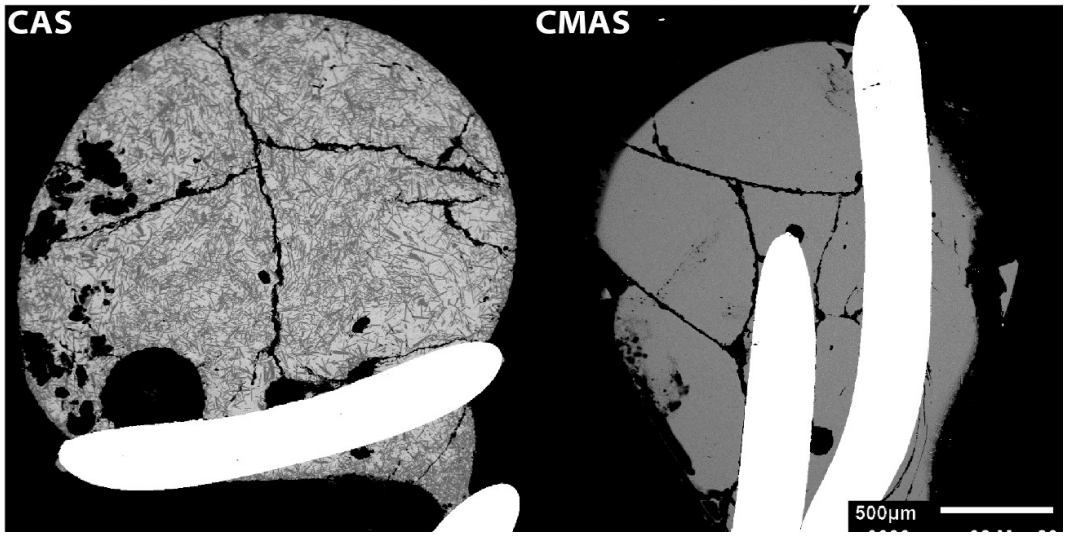

Figure 10: Experiments quenched after cooling from T_2 to T_1 with no dwell. Bright areas are platinum loops. CAS) microcrystalline plagioclase in a quenched glass. These microcrystal grew during the cooling stage between 11477-1374°C. CMAS) An experimental charge showing no crystal growth during the cooling stage from 1415-1333 °C.

The best method for growing large plagioclase was heating to T_1; roughly 100 degrees above the crystallisation temperature and cooling at 6°C/h to T_2; the final temperature and holding for more than 48h. This heating and cooling allows for all nucleation sites to be

homogenised and promote growth over nucleation, which results in large, homogeneous plagioclase (Tsuchiyama, 1983). Anorthite experiments quenched after the end of this cooling stage (no dwell) show either no crystal formation or thousands of microscopic plagioclase laths (Figure 10).

This proves that the plagioclase growth occurs during T_2 and not during the cooling stage.

Although this technique allows for the growth of large, homogenous plagioclase, the diopside can be highly zoned.

An investigation on rare earth element partitioning in anorthite grown during cooling

Crystals in most of these experiments are likely to have grown at their liquidus temperature (during the T_2 dwell stage), rather than during the T_1-T_2 cooling stage. As not every experiment was investigated to ensure no crystal growth at the end of T_2 the effect of cooling rate on the partitioning of the rare earth elements in anorthite is tested. This will allow for estimation of the error induced if minerals happened to grow during the cooling stage.

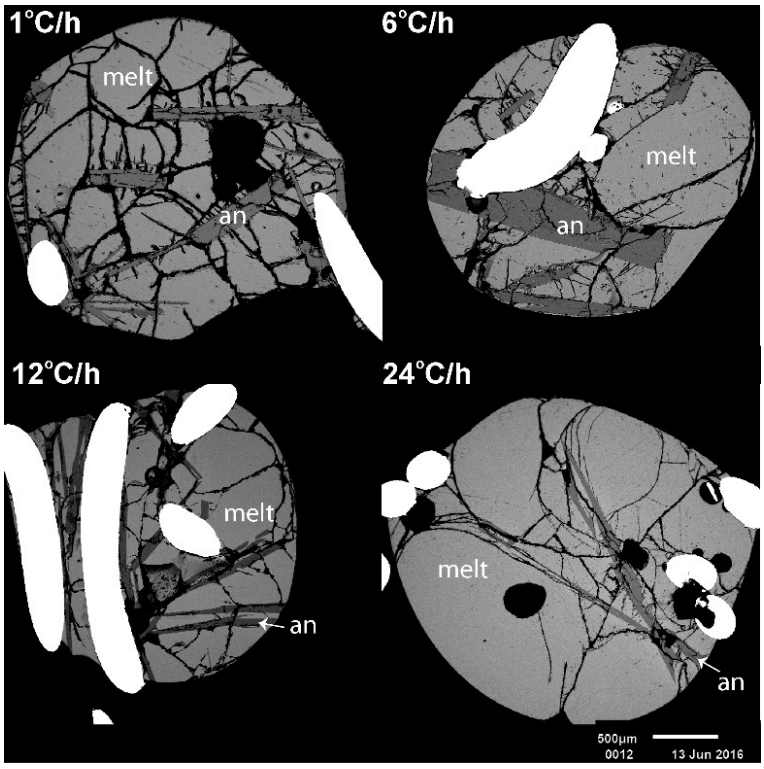

Figure 11: BSEI (Back scattered electron image) of anorthite + melt experimental charges; composition CMAS12. Samples cooled at different rates to 30 degrees past liquidus to ensure crystal growth during the cooling stage. Experiments cooled from 1415-1300 °C

The temperature was reduced past the liquidus (30°C cooler than the actual experimental temperature) between 1°C/h and 24°C/h to ensure plagioclase growth during the cooling stage.

Fast cooling rates cause the anorthite to grow as very thin laths, with the 24°C/h cooling rate too thin to analyse precisely (Figure 11). The cooling rates were compared to 6 °C/h (Figure 11b). There is an approximate 10% increase in partition coefficient with an increase in cooling rate.

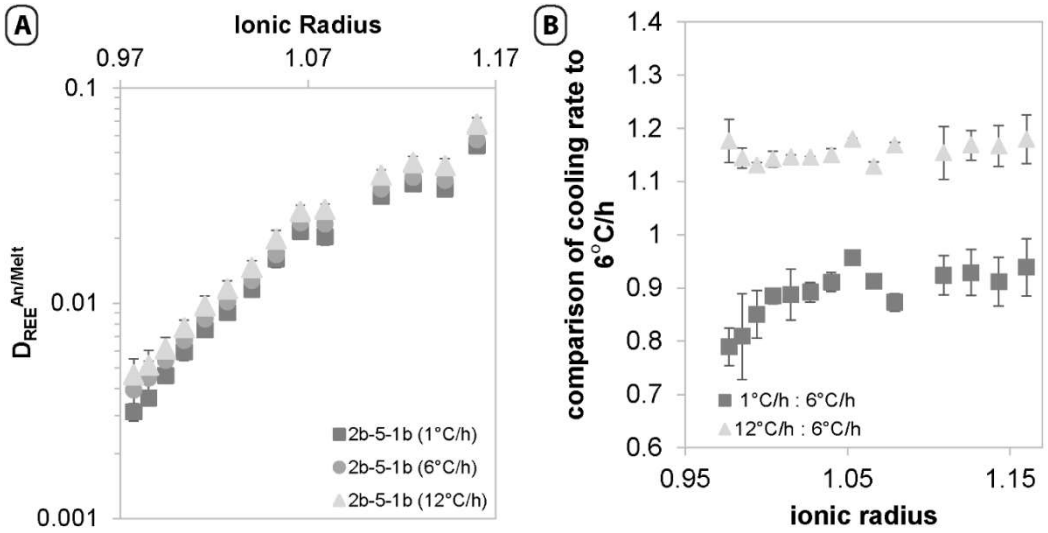

Figure 12: Partitioning of the rare earth elements in the CMAS system, cooled at different rates from 1415-1300 °C (i.e. 30°C past the liquids temperature). A) The partition coefficients of the rare earth elements against their ionic radius B) The difference between the partitioning coefficients in relation to 6 °C/h cooling rate.

This experimental test shows that the cooling rate of minerals can affect the partitioning of trace elements. This emphasises the importance of these experiments being carried out at the liquidus temperature of these minerals. If the minerals were grown during the cooling stage, the partition coefficients could be drastically changed.

Zoning in Clinopyroxene

Clinopyroxene is notoriously difficult to synthesise in as large, homogenous crystal. This is especially true when dealing with aluminium-bearing systems.

There is complex zoning of aluminium, iron and the rare earth elements in many of the clinopyroxene grains. This zonation can rarely be seen in the backscattered electron image, but is clearly evident in element maps (Figure 13).

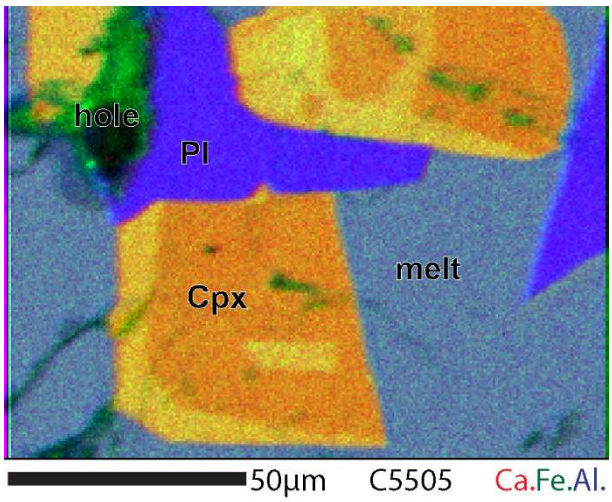

Figure 13: RGB combined image of zonation in cpx in sample C5505 in system CMASNF. Ca=red, Fe=green, Al=blue. Bright yellow corresponds to high aluminium and iron clinopyroxene. Image mapped by EPMA. cpx- clinopyroxene, Pl – plagioclase, melt – quenched glass

For each experiment that synthesises aluminous diopside, the relative standard deviation (RSD) for the Al_2O_3 analysis is calculated. This is an indication of the amount of zoning in the clinopyroxene grains.

2.4 A summary of all experiments

The following pages outline the conditions of formation of each of the experiments. They are separated into three sections; experiments that synthesised only plagioclase + melt (Table 1), experiments that synthesised only clinopyroxene + melt (Table 2) and those that formed plagioclase + diopside + melt (Table 3). The latter experiments are discussed in all three partitioning chapters; plagioclase / melt, clinopyroxene / melt and plagioclase / clinopyroxene.

Table 1: Summary of experimental runs that synthesise only plagioclase and melt. These experiments are discussed in the plagioclase + melt partitioning chapter. Ramp speed from T1 to T2 is 6°C/h and experiments are held at T2 for longer than 48 hours. Major element oxides and "trace" represent wt. % oxides of each component in the melt. "Label" is what each experiment is referred to in this thesis. Pl = plagioclase, An = anorthite

System	Run	Sample	Label	Pressure	fO2	T1	T2	Na_2O	MgO	Al_2O_3	SiO_2	CaO	FeO	Trace	Result
CAS	20140416	LS003	CAS45	1 atm	Air	1520	1453	0.08		24.38	41.06	25.94	0.24	8	An + Melt
	20140416	LS004	CAS64	1 atm	Air	1520	1453	0.47		23.39	53.05	14.07	0.26	8	An + Melt
	20140428	LS002	CAS30	1 atm	Air	1520	1399			32.63	30.66	26.27	0.12	8	An + Melt
	20140428	LS003	CAS45	1 atm	Air	1520	1399			20.88	40.47	27.88	0.11	8	An + Melt
	20140428	LS004	CAS64	1 atm	Air	1520	1399			20.21	54.47	12.83	0.19	8	An + Melt
	20140804	LS902	CAS30	1 atm	Air	1521	1408	0.06	0.11	35.55	32.33	28.69	0.36	2	An + Melt
	20140804	LS903	CAS45	1 atm	Air	1521	1408	0.08	0.11	22.44	43.96	30.23	0.39	2	An + Melt
	20140804	LS904	CAS64	1 atm	Air	1521	1408	0.37	0.16	20.89	60.59	12.47	1.14	2	An + Melt
	20141014	LS902	CAS30	1 atm	QFM	1517	1407			37	32.72	29.01		2	An + Melt
	20141014	LS903	CAS45	1 atm	QFM	1517	1407			22.88	44.56	30.7		2	An + Melt
	20150128	LS023	CAS45	1 atm	Air	1520	1414			22.34	45.43	12.62		1	An + Melt
	20150128	LS024	CAS64	1 atm	Air	1520	1414			21.37	64.23	32.12		1	An + Melt
	20150223	LS022	CAS30	1 atm	IW	1513	1403	0.03	0.07	37.13	33.17	12.62		1	An + Melt
	20150223	LS023	CAS45	1 atm	IW	1513	1403	0.1	0.07	22.84	47.11	29.77		1	An + Melt
	20150428	LS022.1	CAS37	1 atm	Air	1520	1400	0.28	0.18	28.2	37.58	30.4	0.17	1	An + Melt
	20150428	LS902	CAS30	1 atm	Air	1520	1400	0.29		36.02	31.58	27.71	0.11	2	An + Melt
	20150428	LS902.5	CAS37	1 atm	Air	1520	1400	0.3	0.05	28.53	36.75	29.8	0.13	2	An + Melt
	20150428	LS903.5	CAS52	1 atm	Air	1520	1400	1.3	0.05	20.95	51.46	22.05	0.14	2	An + Melt
	20150616	LS902	CAS30	1 atm	IW	1500	1385		0.05	36.46	31.43	29.07		2	An + Melt
	20150616	LS902.5	CAS37	1 atm	IW	1500	1385		0.05	27.98	36.97	30.89		2	An + Melt
	20150616	LS903	CAS45	1 atm	IW	1500	1385			21.44	44.31	30.96		2	An + Melt
	20150616	LS904	CAS64	1 atm	IW	1500	1385	0.29	0.06	19.81	63.13	12.01		2	An + Melt
	C4828	LS024	CAS64	10 kbar	none	1520	1400	0.17	0.32	25.73	58.86	14.46		3	An + Melt
	C4856	LS023	CAS45	10 kbar	none	1520	1400	0.18	1.83	25.47	43.69	27.15		3	An + Melt
	C4874	LS022.1	CAS37	10 kbar	none	1520	1400	0.25	0.54	31.75	38.15	29.38		3	An + Melt
	C4970	LS903.5	CAS52	10 kbar	none	1520	1400		4.63	24.6	49.67	21.1		3	An + Melt
CMAS	20151113	2b-4-1a	CMAS8	1 atm	Air	1412	1332	0.12	8.16	18.75	46.53	25.56		1	An + Melt
	20151113	2b-5-1a	CMAS10	1 atm	Air	1412	1332	0.12	9.88	19.47	46.14	23.59		1	An + Melt
	20151113	2b-6-1a	CMAS12	1 atm	Air	1412	1332	0.15	13.82	21.97	45.46	18.33		1	An + Melt
	20151113	2b-7-1a	CMAS14	1 atm	Air	1412	1332	0.13	11.75	20.11	45.64	21.16		1	An + Melt
CMASN	20160928	Plag1		1 atm	Air	1347	1248	1.89	9.58	16.3	51.99	20.25		1	Pl + Melt
	20160928	Plag2		1 atm	Air	1347	1248	4.13	6.9	18.05	55.03	16		1	Pl + Melt
	20161008	Plag3		1 atm	Air	1350	1250	5.1	5.48	18.56	57.61	13.25		1	Pl + Melt
	20161008	Plag4		1 atm	Air	1350	1250	7.55	3.14	20.14	61.29	7.9		1	Pl + Melt
	20161025	Plag2		1 atm	QFM	1340	1240	4.05	7.16	17.73	55.42	16.01		1	Pl + Melt

Table 1 continued: Summary of experimental runs that synthesise only plagioclase and melt. These experiments are discussed in the plagioclase + melt partitioning chapter. Ramp speed from T1 to T2 is 6°C/h and experiments are held at T2 for longer than 48 hours. Major element oxides and "trace" represent wt. % oxides of each component in the melt. "Label" is what each experiment is referred to in this thesis. Pl = plagioclase, An = anorthite

System	Run	Sample	Label	Pressure	dO2	T1	T2	Na_2O	MgO	Al_2O_3	SiO_2	CaO	FeO	Trace	Result
	20161025	Plag3		1 atm	QFM	1340	1240	5.29	5.86	18.6	57.36	13.51		1	Pl + Melt
CMASN	D2067	An35Di35Ab30	Ab30	5 kbar	none	1330	1230	3.34	7.32	17.76	55.42	16.15		0.7	Pl + Melt
	D2074	An15Di15Ab70	Ab70	8 kbar	none	1300	1200	7.87	2.82	19.06	63.04	6.87		0.3	Pl + Melt
CMASNF	C5470	Ab70-Fe1	Ab70-Fe1	11 kbar	Pt-PtO_2	1335	1235	7.8	2.84	19.83	64.46	6.28	1.07	1	Pl + Melt
"natural"	20160304	ALV-3352-7	ALV-3352-7	1 atm	QFM	1245	1190	2.74	9.09	15.45	55.02	12.66	4.06	1	Pl + Melt

Table 2: Summary of experimental runs that synthesise only diopside and melt. These experiments are discussed in the clinopyroxene + melt partitioning chapter. Ramp speed from T1 to T2 is 6°C/h and experiments are held at T2 for longer than 48 hours. Major element oxides and "trace" represent wt. % oxides of each component in the melt. "Label" is what each experiment is referred to in this thesis. The relative standard deviation (RSD) for each aluminium containing diopside to represent the amount of zoning.

System	Run	Sample	Label	Pressure	fO2	T1	T2	Na_2O	MgO	Al_2O_3	SiO_2	CaO	FeO	Trace	Result	Al RSD in cpx
	20140728	LS007	CMS-CaO	1 atm	Air	1389	1329		11		40.96	23.48		20	Di + Melt	
	20140811	LS906	CMS-MgO	1 atm	Air	1392	1349		16.73	0.67	45.63	27.19		9	Di + Melt	
	20140811	LS905	CMS-SiO2	1 atm	Air	1392	1349		10.79	0.79	58.15	22.17		9	Di + Melt	
	20140924	LS907	CMS-CaO	1 atm	Air	1397	1370		12.36	0.49	49.09	28.63		9	Di + Melt	
CMS	20140924	LS906	CMS-MgO	1 atm	Air	1397	1370		18.95	0.58	48.5	25.69		9	Di + Melt	
	20140925	LS906	CMS-MgO	1 atm	QFM	1393	1373		19.3	0.47	48.78	24.45		9	Di + Melt	
	20140925	LS905	CMS-SiO2	1 atm	QFM	1393	1373		14.49	0.37	55.89	21.78		9	Di + Melt	
	20150223	LS026	CMS-MgO	1 atm	Air	1399	1379		21.09	0.23	52.94	25.74		1	Di + Melt	
	20150318	LS026	CMS-MgO	1 atm	Air	1400	1366		20.41	0.3	50.94	28.28		1	Di + Melt	
	20150318	LS025	CMS-SiO2	1 atm	Air	1400	1366		13.65	0.32	63.64	22.15		1	Di + Melt	
	20140828	LS909		1 atm	Air	1351	1300		11.44	11.66	54.1	19.75		5	Di + Melt	15%
	20140828	LS910		1 atm	Air	1351	1300		14.62	12.73	52.88	19.76		5	Di + Melt	10%
CMAS	20141111	LS909		1 atm	Air	1350	1303		11.74	10.91	52.61	19.06		5	Di + Melt	20%
	20141111	LS910		1 atm	Air	1350	1303		13.94	11.63	50.78	19.04		5	Di + Melt	21%
	20150306	LS029		1 atm	Air	1353	1305		13.5	12.03	54.78	19.58		1	Di + Melt	32%
	20160928	Di1		1 atm	Air	1347	1248	7.11	6.16	13.53	61.49	11.88		1	Di + Melt	14%
CMASN	20161008	Di2		1 atm	Air	1347	1248	4.32	7.16	15.24	55.62	16.54	0.05	1	Di + Melt	13%
	20161008	Di3		1 atm	Air	1347	1248	1.55	8.18	16.77	50.59	21.53	0.05	1	Di + Melt	8%

Table 3: Summary of experimental runs that synthesise both plagioclase and diopside along with their equilibrium melt. These experiments are discussed in the plagioclase + melt, clinopyroxene + melt and plagioclase + clinopyroxene partitioning chapters. Ramp speed from T1 to T2 is 6°C/h and experiments are held at T2 for longer than 48 hours. Major element oxides and "trace" represent wt. % oxides of each component in the melt. The relative standard deviation (RSD) for each aluminium containing diopside to represent the amount of zoning.

System	Run	Sample	P kbar	fO2	T1	T2	Na_2O	MgO	Al_2O_3	SiO_2	CaO	FeO	Trace	Al RSD in cpx
CMAS	20150402	LS031	0	Air	1301	1265	0.24	11.64	16.21	51.25	20.82	0.04	1	8%
CMASN	20161025	Plag1	0	QFM	1340	1240	2.28	7.23	16.05	50.98	19.92		1	11%
	C5083	An45Di45Ab10	8	none	1350	1265	1.76	6.1	16.67	52.44	19.32		0.9	12%
	C5094	An40Di40Ab20	8	none	1330	1230	2.93	6.11	17.77	55.07	17.12		0.8	20%
	C5121	An35Di35Ab30	8	none	1330	1230	3.71	5.85	18.47	55.69	15.49		0.7	30%
	C5473	An15Di15Ab70x	11	none	1300	1200	8.83	2.55	17.82	68.29	4.36		1	14%
	C5480	An25Di25Ab50x	11	none	1300	1200	6.43	2.62	17.38	65.02	7.4		1	7%
	D2061	An25Di25Ab50	8	none	1330	1230	6.28	3.95	18.38	59.26	10.31		0.5	12%
	D2075	An35Di35Ab30	11	none	1360	1260	4.49	5.2	19.64	56.56	14.1		0.7	20%
	D2076	An35Di35Ab30	5	none	1300	1200	4.97	4.51	18.19	57.11	12.69		0.7	22%
	D2079	An35Di35Ab30	11	none	1330	1230	4.05	4.65	18.67	55.52	14.39		0.7	15%
	D2087	An25Di25Ab50	5	none	1270	1170	7.9	1.69	17.58	66.55	6.28		0.5	20%
	D2088	An35Di35Ab30	11	none	1330	1230	6.63	3.41	17.57	60.82	9.72		0.7	24%
	D2091	An45Di45Ab10	5	none	1300	1200	1.73	6.9	16.98	51.41	19.58		0.9	10%
	D2092	An45Di45Ab10	11	none	1330	1230	1.29	4.09	13.92	60.29	14.91		0.9	5%
	D2097	An15Di15Ab70	5	none	1270	1170	7.97	3.0	17.29	59.21	6.42		0.3	23%
	D2262	An15Di15Ab70	11	none	1345	1245	8.89	3.36	18.94	66.31	6.55		0.3	4%
	D2267	An15Di15Ab70	5	none	1255	1155	8.34	2.66	19.36	68.44	5.44		0.3	24%
	D2275	An25Di25Ab50	5	none	1285	1185	6.91	3.26	18.08	63.56	8.2		0.5	19%
	D2293	An15Di15Ab70x	8	none	1275	1175	8.71	2.63	18.5	68.74	4.58		1	15%
	D2479	An25Di25Ab50x	5	none	1235	1185	5.45	4.3	18.69	63.85	9.91		1	30%
CMASNF	C5430	Ab50-Fe10	11	Pt-PtO_2	1280	1180	6.26	3.42	17.9	60.31	7.78	5.49	1	9%
	C5442	Ab10-Fe10	11	Pt-PtO_2	1300	1200	2.08	5.67	17.81	50.28	14.01	6.99	1	7%
	C5443	Ab10-Fe1	11	Pt-PtO_2	1350	1250	2.21	4.32	16.75	54.82	17.1	1.03	1	18%
	C5469	Ab10-Fe5	11	Pt-PtO_2	1335	1225	2.29	6.37	16.29	51.2	15.08	4.79	1	9%
	C5485	Ab50-Fe1	11	Pt-PtO_2	1340	1240	6.17	4.2	19.2	58.13	10.11	0.59	1	33%
	C5505	Ab30-Fe1	11	Pt-PtO_2	1335	1235	4.4	5.47	18.3	54.15	13.92	1.1	1	27%
	C5507	Ab30-Fe10	11	Pt-PtO_2	1280	1180	5.66	4.64	16.27	59.35	8.3	5.81	1	9%
	D2488	Ab10-Fe15	11	Pt-PtO_2	1275	1175	2.03	5.25	18.29	49.79	12.89	6.95	1	8%
	D2489	Ab30-Fe1	11	Pt-PtO_2	1345	1245	3.93	5.39	18.59	53.85	14.23	1.01	1	15%
	D2504	Ab10-Fe1	5	Pt-PtO_2	1320	1220	2.18	6.36	16.54	50.61	17.79	1.08	1	33%
	D2495	Ab70-Fe10	11	Pt-PtO_2	1270	1170	7.86	3.63	16.18	62.37	5.04	6.08	1	40%
"natural"	20160315	BIR60	1	QFM	1245	1130	2.8	5.72	11.56	46.49	8.35	9.14	10	16%
	20160315	BIR64	1	QFM	1245	1130	3.11	5.98	12.43	49.9	8.81	9.82	10	14%

2.5 Major element Analysis

2.5.1 Electron Probe Micro Analyser (EPMA)

The major elements were collected by a Cameca SX100 EPMA at the Research School of Earth Sciences (RSES), the Australian National University (ANU). The beam conditions were set at a current of 20nA and voltage at 15kV. For melt and plagioclase analysis, the beam was defocussed to 10 μm to avoid sodium loss; for all other phases, the beam was focussed.

Secondary Standards

Secondary standards were also measured to ensure no beam or spectrometer drift over an analytical session and ensure precision between sessions.

Table 4: Secondary Standards for EPMA analysis. RSD stands for relative standard deviation

	Kakanui, NZ - USNM 122142						Gila Co, Arizona - USNM 111312/444					
	Augite						SanCarlos Olivine					
	average	σ	RSD	n	Ref.	%Diff	average	σ	RSD	n	Ref.	%Diff
Na_2O	1.24	0.07	5%	128	1.27	-2%						
MgO	16.48	0.32	2%	128	16.65	-1%	48.94	1.03	2%	92	49.42	-1%
Al_2O_3	8.48	0.21	3%	128	8.73	-3%	0.03	0.01	37%	92		
SiO_2	50.23	0.72	1%	128	50.73	-1%	40.58	0.64	2%	92	40.81	-1%
CaO	15.93	0.36	2%	128	15.82	1%	0.11	0.01	9%	92		
FeO	6.35	0.14	2%	128	6.34	0%	9.61	0.18	2%	81	9.55	1%
TiO_2	0.86	0.04	5%	53	0.74	16%						
Cr_2O_3	0.16	0.01	8%	81								
Total	99.26	1.05	1%	128	100.41		98.21	3.32	3%	92	100.25	

	Glass NBS K-412											
	K412 glass						Amelia Albite					
	average	σ	RSD	n	Ref.	%Diff	average	σ	RSD	n	Ref.	%Diff
Na_2O	0.06	0.01	20%	163			10.65	0.53	5%	25	11.74	-9%
MgO	19.46	0.31	2%	171	19.33	1%						
Al_2O_3	9.31	0.28	3%	179	9.27	0%	19.76	1.02	5%	25	19.5	1%
SiO_2	45.37	0.68	1%	179	45.35	0%	67.03	2.87	4%	25	68.67	-2%
CaO	15.16	0.35	2%	179	15.25	-1%						
FeO	9.93	0.18	2%	166	9.96	0%						
MnO	0.09	0.01	13%	19								
Total	97.70	6.92	7%	179	99.16		97.53					

Over 100 standard blocks were analysed over multiple analytical sessions. The standards have very low relative standard deviations which suggests that the major elements for the unknowns are accurate.

In addition to these published secondary standards, matrix matched phases; plagioclase, anorthite and Cr-Diopside were compared over analytical sessions (Table 5). The results are fairly consistent over all analytical sessions. A few elements have high relative standard deviations, however, these elements are of very low concentrations in the

crystals. When comparing these elements in minerals with higher concentrations, the relative standard deviations are very low.

Table 5: matrix matched secondary standards. RSD stands for relative standard deviation

	Natural, Miyake-jima											
	Anorthite				Plagioclase				Diopside			
	average	σ	RSD	n	average	σ	RSD	n	average	σ	RSD	n
Na_2O	0.42	0.05	11%	133	4.64	0.09	2%	40	0.32	0.02	5%	41
MgO									17.94	0.28	2%	41
Al_2O_3	35.97	0.75	2%	133	29.33	0.54	2%	40	0.23	0.02	8%	41
SiO_2	43.69	0.55	1%	133	53.79	0.64	1%	40	54.78	0.83	2%	41
K_2O					0.27	0.01	2%	11				
CaO	19.32	0.37	2%	133	11.50	0.24	2%	40	24.84	0.28	1%	41
FeO	0.47	0.04	9%	84	0.43	0.05	13%	37	1.09	0.05	5%	41
TiO_2					0.07	0.01	17%	11				
Cr_2O_3									0.67	0.02	3%	31
Total	99.75	1.08			99.81	0.96			99.70	1.07		

These minerals were measured for both trace and major elements during all session to allow consistency to be maintained.

2.5.2 Scanning Electron Microscope (SEM)

Qualitative major element analysis was measured by electron dispersive spectroscopy (EDS) on a JEOL JSM-6610A at the Research School of Earth Sciences (RSES), ANU. Operating conditions were set at 15 kV, a load current of between 70-76μA and a working distance of 10mm. All back-scattered electron imagery (BSEI) presented in this thesis were taken on this SEM.

2.6 Trace Element Analysis

2.6.1 Laser Ablation ICP-MS

Trace elements were collected by Laser Ablation Inductively Coupled Plasma Mass Spectrometry (LA-ICP-MS) at the Research School of Earth Sciences (RSES) at the Australian National University (ANU). This comprised of an ANU HelEX laser ablation cell with a pulsed 193 nm ArF Excimer laser feeding an Agilent 7700S ICP-MS with the laser conditions set to ~80 mJ fluence and 5 Hz repetition rate. Data acquisition involved 30s ablation of the crystal and 30s of recorded background between each analysis. The internal standard used was 43Ca. Standards were analysed before and after, at the most, 15 unknown analyses. The standards used were NIST610, NIST612 and BCR2g with the reference standard set as NIST610 (Jochum et al., 2011). The data was reduced using Iolite software (Paton et al., 2011).

The spot size was changed as required and bracketed by standards measured by the same spot size. Generally, experimental samples were measured by a 28 μm diameter spot. As the natural samples are much larger and have lower concentrations of trace elements, these samples were measured using a 105 μm spot.

The internal standard used was calcium as it has the same ablation properties as the rare earth elements (Jackson, 2008). Although there is an interference with $^{28}Si^{16}O^{+}$ for ^{44}Ca and an interference with $^{27}Al^{16}O^{+}$ for ^{43}Ca (May and Wiedmeyer, 1998), these interferences do not make a significant difference to the concentrations obtained.

Secondary Standards

The trace elements were normalised to published NIST610 values from Jochum et al. (2011). Secondary standards were also analysed to compare the consistency of individual sessions and compare the precision of the data collected overall. The precision of the individual isotopes from replica analysis are included in the appendix in Table 33 for BCR2g and Table 34 for NIST612.

The values for BCR2g are very consistent and closely represents the published data. NIST612 is very precise and accurate for most of the trace elements except for Fe^{57}. This is due to the very low counts for Fe in NIST610.

2.7 Mathematics and Calculations

2.7.1 Partition Coefficients

The partition coefficients (D) are simply calculated by dividing the average concentration of the element of interest in the mineral and melt (Equation 1). As both these values are averages they both have standard deviations. The standard deviation of the population must be calculated to obtain the correct standard deviation for the partition coefficient. The standard deviation for each partition coefficient is given by the formula:

$$\sigma_D = \frac{\sqrt{\bar{x}_m{}^2 * \sigma_X{}^2 + \bar{x}_X{}^2 * \sigma_m{}^2}}{\bar{x}_m{}^2}$$

Where; $\bar{x}$ is the average concentration of the element of interest and σ is the standard deviation in either crystal (X) or melt (m) analysis. The value σ_D is used as the error bar value for all partition coefficients in all figures.

The rare earth elements partition coefficients were also normalised to the partitioning of Gd as it is in the middle of the rare earth element pattern:

$$K_{\frac{D_{REE}}{D_{Gd}}} = \frac{D_{REE}}{D_{Gd}}$$

The standard deviation of this ratio is calculated by the propagation of errors:

$$\sigma_K = \sqrt{\left(\sigma_{D_{REE}}/D_{REE}\right)^2 + \left(\sigma_{D_{Gd}}/D_{Gd}\right)^2}$$

2.7.2 Error on Model Fits

This thesis aims to generate new models for predicting the partitioning of trace elements in plagioclase and clinopyroxene. To determine the accuracy of these, and published models (e.g. lattice strain model); the models are fit to the data using a least squares regression. The goodness of fit of these models is given by the chi squared (χ^2):

Equation 21:
Calculation of chi squared

$$\chi^2 = \Sigma\left(\frac{\ln D_{observed} - \ln D_{calculated}}{\sigma(D_{observed})/D_{observed}}\right)^2$$

Where the residuals between natural logs of the observed and calculated partition coefficients are weighted by the standard deviation of the partition coefficient. The natural logs of the partition coefficients are used to give equal weights to very small numbers (i.e. the highly incompatible elements).

This can be compared between models by calculating the reduced chi squared:

Equation 22:
Calculation of reduced chi squared

$$\chi^2_\nu = \frac{\chi^2}{\nu} \text{ Where } \nu = n_{points} - n_{parameters}$$

Which is the chi squared divided by the degrees of freedom (ν). The degrees of freedom is the number of points that the model is fit to less the number of parameters used to calculate the model. A perfect fit will have a $\chi^2_\nu = 1$.

2.7.3 Orthogonal polynomials

In addition to the widely used lattice strain model, the partitioning of the rare earth elements in this thesis will be fit to orthogonal polynomials as described by O'Neill (2016):

Equation 23:
Orthogonal polynomial

$$D_{REE} = \exp\begin{bmatrix}\lambda_0 + (r_i^{3+} - 1.055) * \lambda_1 + (r_i^{3+} - 1.005) * (r_i^{3+} - 1.128) * \lambda_2 \\ +(r_i^{3+} - 1.061) * (r_i^{3+} - 1.146) * (r_i^{3+} - 0.991) * \lambda_3\end{bmatrix}$$

Simplified λ_0 represents the magnitude of the rare earth element pattern (i.e. the value of a middle rare earth), λ_1 is the slope of the pattern, λ_2 represents the curve of the pattern and λ_3 represents the sigmoidal shape of the pattern.

CHAPTER 3. PLAGIOCLASE-MELT PARTITIONING

3.1 Introduction

Plagioclase is one of the most common minerals in the Earth's crust, and an essential phase in the crystallization of magma, from basaltic to granitic. Consequently, understanding its trace element partitioning is necessary for much geochemical modelling.

A large number of experimentally determined plagioclase/melt partition coefficients have been parameterized into the formalism of the lattice strain model by Wood and Blundy (2014). Ideally a holistic fit to the lattice strain model will be created to allow for the prediction of the trace element partitioning or, working backwards, calculation of the formation conditions of the rocks from trace element partitioning in the minerals. This has been attempted by a number of different sources, and here we will test their validity with 76 experiments of plagioclase melt pairs.

Three studies have attempted to model plagioclase / melt partitioning; Sun et al. (2017), Dohmen and Blundy (2014) and Wood and Blundy (2014) (which bases the models on the Bindeman et al. (1998) experiments). Variables considered most important in these are temperature and calcium content of the plagioclase. This thesis will provide evidence that melt composition can also be an important variable to consider.

3.1.1 Plagioclase crystal structure and substitution mechanisms

Plagioclase consists of two end members, albite ($NaAlSi_3O_8$) and anorthite ($CaAl_2Si_2O_8$) which have a complete solid solution. Plagioclase has two sites available for trace element partitioning and diffusion; the large cation "M" site which is VIII-fold coordinated and the tetrahedral site (Longhi et al., 1976; Miller et al., 2006). It is generally assumed that most of the trace element diffusion and partitioning occurs on the large cation site, however many plagioclase compositions have been synthesised and discovered in nature with substitutions of elements in the tetrahedral site (Table 6).

Table 6: Feldspar compositions that have been experimentally synthesised and found in nature.

	Name	Formula	Substitution	Reference
End member feldspars	Anorthite	$CaAl_2Si_2O_8$		
	Albite	$NaAlSi_3O_8$		
	Orthoclase	$KAlSi_3O_8$		
Large cation substitution	Celsian	$BaAl_2Si_2O_8$	$Ca^{2+} \rightarrow Ba^{2+}$	(Megaw et al., 1962)
	Magnesian plagioclase	$MgAl_2Si_2O_8$	$Ca^{2+} \rightarrow Mg^{2+}$	(Murakami et al., 1992)
Tetrahedral substitution	MacKenzie molecule	$CaMgSi_3O_8$	$2Al^{3+} \rightarrow Mg^{2+} + Si^{4+}$	(Longhi et al., 1976; Miller et al., 2006; Murakami et al., 1992)
	Fe-plagioclase	$CaFeSi_3O_8$	$2Al^{3+} \rightarrow Fe^{2+} + Si^{4+}$	(Sclar and Kastelic, 1979)
	Reedmergnerite	$NaBSi_3O_8$	$Al^{3+} \rightarrow B^{3+}$	(Megaw et al., 1962)
	Ga-albite	$NaGaSi_3O_8$	$Al^{3+} \rightarrow Ga^{3+}$	(Senderov et al., 1982)
	Zn-plagioclase	$CaZnSi_3O_8$	$2Al^{3+} \rightarrow Zn^{2+} + Si^{4+}$	(Fehr and Huber, 2001)
Excess components	Excess Aluminium	$AlAl_3SiO_8$	$Ca^{2+} + Si^{4+} \rightarrow 2Al^{3+}$	(Murakami et al., 1992)
	Megaw's Molecule (Vacancy)	$\square Si_4O_8$	$Ca^{2+} + 2Al^{3+} \rightarrow \square + 2Si^{4+}$	(Longhi and Hays, 1979; Murakami et al., 1992)

There are 3 substitution styles that have been discovered in plagioclase. The first is the simple large cation substitution. This involves the exchange of Ca^{2+} with a divalent cation such as Ba, or the exchange of Na^{1+} with other monovalent cations such as K^{1+} which gives the other feldspar end-member; orthoclase. The second type is the tetrahedral site substitution. The tetrahedral site is much smaller than the large cation site, however large cations can still substitute here. In the case of Ga-albite and Reedmergnerite, very small trivalent cations exchange for Al^{3+} in a straight substitution

Many divalent cations can also substitute onto the tetrahedral site (e.g. MacKenzie molecule), however this requires a charge balance. This allows the plagioclase to exist with two divalent cations, one in the tetrahedral site and one in the large cation site. This causes the plagioclase to take up a more albite-like structure to manage the triple silicon.

The third type is known as the excess component type which consists of plagioclase being made up of excess Si or Al with no large cations. This includes the Tschermak like substitution of $Ca^{2+} + Si^{4+} \rightarrow 2Al^{3+}$ where a relatively small Al cation is situated on the large cation site. Additionally, we can also have an excess silica component which includes a vacancy on the large cation site.

3.1.2 Models for the partitioning of the rare earth elements in plagioclase

There are currently 3 models for the partitioning of trace elements in plagioclase. These studies have modelled monovalent, divalent and trivalent cations. The trivalent cation partitioning models will be compared:

Sun et al. (2017)

This plagioclase lattice strain model was fit to 29 experiments from the published literature. The temperature range for this model is 1127-1410°C with pressures from 1 atm to 1.5 GPa. The anorthite number of these experiments ranges from An_{41-98}. Basaltic type melt experiments were the sole focus of this study.

Equation 24:
Sun et al. (2017) model for rare earth elements partitioning between plagioclase and basaltic melt

$$lnD_0^{3+} = 16.05(\pm 1.57) - \frac{19.45(\pm 1.78) + 1.17(\pm 0.14)P^2}{RT} * 10^4 - 5.17(\pm 0.37) * \left(X_{Ca}^{pl}\right)^2$$

$$r_0^{3+}(\text{Å}) = 1.179(\pm 0.027)$$

$$E^{3+}\ (GPa) = 196(\pm 51)$$

This model uses the amount of calcium per 8 oxygens in plagioclase, rather than the anorthite content and has a constant ideal cation radius (r_o^{3+}) and elasticity of the site (E^{3+}). This model also contains a pressure component, while all other studies have found pressure to have a negligible effect on the partitioning of trace elements in plagioclase.

Dohmen and Blundy (2014)

This model is fit to 17 experiments from variations of the simple system; diopside-anorthite-albite in 1 atm and over a temperature range of 204 °C (1086-1290 °C). This data was constrained using only 2 rare earth elements (La, Sm) and Y which is a total of 64 individual data points. Using this model; 26 of these 64 data points are constrained within a factor of 1.2 and 88% of the data can be constrained within a factor of 2.

Equation 25:
Dohmen and Blundy (2014) model for rare earth elements partitioning between plagioclase and basaltic melt

$$D_{La} = \exp\left(\frac{4.4_{kJ/mol} - 30.8_{J/mol/K} * T + RTln\left(\frac{{D_{Ca}}^2}{D_{Na}}\right)}{RT}\right)$$

$$r_o^{3+} = 1.331(\pm 0.043) - 0.068(\pm 0.061) * X_{An}$$

$$E = 152(\pm 29) - 31(\pm 41) * X_{An}$$

These components are used in the published equation:

$$D_i = D_{La} * exp * \left[\frac{-4\pi N_A E(\boldsymbol{X_{An}})\left(\frac{r_o^{3+}(\boldsymbol{X_{An}})}{2}({r_{La}}^2 - {r_i}^2) - \frac{1}{3}({r_{La}}^3 - {r_i}^3)\right)}{RT}\right]$$

However, this gives massive errors on the data presented here so we removed the addition dependence on the anorthite content (in bold above) on r_o and E. These components are already calculated by their relationship to X_{An} so instead we substitute the parameters into the modified lattice strain model (Equation 6) which gives much more reasonable results.

Wood and Blundy (2014)

This equation is based on the Bindeman et al. (1998) and the Bindeman and Davis (2000) studies of the Drake and Weill (1975) experiments. These experiments were grown from basaltic and andesitic melts between 1150-1343 °C. In this study only 9 of the rare earth elements were investigated. It has 89 individual rare earth element partitioning data points (omitting Y, Ce, and Eu) over 8 melt compositions.

Equation 26:
Wood and Blundy (2014) model for rare earth element partitioning between plagioclase and melt

$$D_{La} = exp * \left(\frac{-10.8(\pm 2.6) * X_{An} - 12.4(\pm 1.8)}{RT} \right)$$

$$r_0^{3+}(\text{Å}) = (1.258 - 0.057 * X_{An}) - 0.03$$

$$E^{3+}\ (GPa) = 210$$

These parameters are substituted into the modified lattice strain model (Equation 6) to give the partitioning for each of the rare earth elements.

3.1.3 This Study

This chapter presents a study on the partitioning of trace elements between plagioclase and melt. The melt composition, crystal composition, temperature, pressure and melt composition are varied to determine which combinations of the tested variable have the largest impact on the partitioning of each of the trace elements.

The first section is a very simple system, isolating the melt effect on the partitioning in anorthite. The second section expands on these data, with more complex melt systems and various plagioclase compositions to give a suite of 72 experiments (864 individual REE data points) ranging from An_{100}-An_{24}, over a temperature range of 320°C, 11kbar pressure and 4 four different relative oxygen fugacities.

3.2 The influence of melt composition on the partitioning of trace elements between anorthite and silicate melt

3.2.1 Preface

Section 3.2 was re-written in May of 2018 as a stand-alone manuscript with the intention of submitting it for publication in Chemical Geology.

3.2.2 Abstract

The effect of melt composition on the partitioning of trace elements between anorthite and silicate melts has been studied in five compositions in the system CaO-Al_2O_3-SiO_2 (CAS) at ~1400 °C and four compositions in the system CaO-MgO-Al_2O_3-SiO_2 (CMAS) at 1332 °C. Melt composition has a significant impact on the substitution of trace elements into anorthite, particularly if the trace element substitution is aliovalent and requires a charge balance for substitution. Melt composition strongly influences the partitioning of the trivalent rare earth element (REE) cations into the large cation site (M) of anorthite. Due to charge balance requirements, the activity of alumina in the melt is the most important compositional variable for the REE partitioning in anorthite. Scandium, another trivalent cation, is much more compatible than is predicted for trivalent cations partitioning on the M-site. Therefore, scandium is likely partitioning onto the tetrahedral site in place of an aluminium, which requires no charge balance and therefore is not affected strongly by melt composition. Similarly, the partitioning of the small divalent cations (Be and Mg) show a stronger relationship with changing melt composition than the large divalent cations (Ca, Sr, and Ba) and therefore are likely to partition on the tetrahedral site (T) of plagioclase rather than the large cation site (M). We have determined that melt composition plays an important role in the aliovalent substitution and should be a variable considered when examining the partitioning into all minerals.

3.2.3 Introduction

The partitioning of trace elements between minerals and silicate melts is sensitive to the composition of both the minerals and the melts, as well as pressure, temperature, and, for elements occurring in different oxidation states, oxygen fugacity. The effect of these variables is often inextricably entangled, presenting a challenge in assigning the observed effects to the appropriate variables in the descriptive models that are required to apply measured partition coefficients to geological systems. There has been a focus on the effect of the mineral composition due to the development of the lattice strain model, reviewed recently by Wood and Blundy (2014) but the major-element composition of the melt will

also have an influence. As well as determining mineral compositions, this variable operates on partition coefficients in two rather different ways (O'Neill and Eggins, 2002) Firstly, the melt composition determines the activities of the components required by the mineral's stoichiometry to balance the trace element substitution; this phenomenon has been called "the stoichiometric control". The stoichiometric control becomes particularly significant where the trace element has a different valence state to the major element for which it is substituting. Secondly, melt composition determines the activity coefficients of the trace element's oxide components in the melt.

Deconvoluting the effect of melt composition from that of mineral composition is often difficult because minerals of a given composition are only in equilibrium with a limited range of melt compositions at a given pressure and temperature. Therefore in complex systems the composition of the mineral will often change systematically with the composition of the melt (O'Neill and Eggins, 2002). This latter problem does not arise with trace-element partitioning into a phase of fixed, stoichiometric composition, allowing the effect of melt composition to be varied independently.

Here we report an experimental investigation of the trace element partitioning between anorthite (nominally $CaAl_2Si_2O_8$) and silicate melts with compositions in the simple systems CAS (CaO-Al_2O_3-SiO_2) and CMAS (CaO-MgO-Al_2O_3-SiO_2). Particular attention is given to the Rare Earth Elements (REEs), not only because of the importance of these quintessential trace elements in the geochemical modelling of igneous systems, but also because of their usefulness in testing hypotheses of trace element partitioning at a fundamental level. Accordingly, we present data for all 14 REEs, the first study to do this in feldspars. As anorthite consists of three oxide components (CaO, Al_2O_3 and SiO_2), the effect of the "stoichiometric control" on partition coefficients for trace elements that require charge-balance substitutions is more complex than with one- or two-component phases like SiO_2 or Mg_2SiO_4, allowing more scope for the exploration of this effect. The REEs substitute for Ca^{2+} in anorthite, so for the REEs in their usual 3+ oxidation state, the requirements of charge balance make the stoichiometric control particularly important.

3.2.4 Experimental Methods

Five melt compositions were chosen from the CAS phase diagram that are in equilibrium with anorthite at 1400 °C (Levin et al., 1964), which are named for their wt.% of SiO_2 in the melt (Figure 14). Four compositions were chosen in the CMAS system in equilibrium with anorthite at 1332°C based on the work of (Miller et al., 2006), with the sample labels

representing the MgO wt.% in the coexisting melt. To these compositions Sc, Sr, Nb, Ba, REE, Hf, Th, and U were added as trace elements, in varying amounts to test the limits of Henry's Law. For experiments in the CMAS system, Be was also studied. The total sum of all the trace elements are <1 wt. % O (~70 ppm per element), 1 wt. % O (~500 ppm per element), 3 wt. % O (~1300 ppm per element), and 8 wt. % O (~4000 ppm per element). To avoid erroneous and misleading results only elements known not to be significantly volatile under the conditions of the experiments were studied.

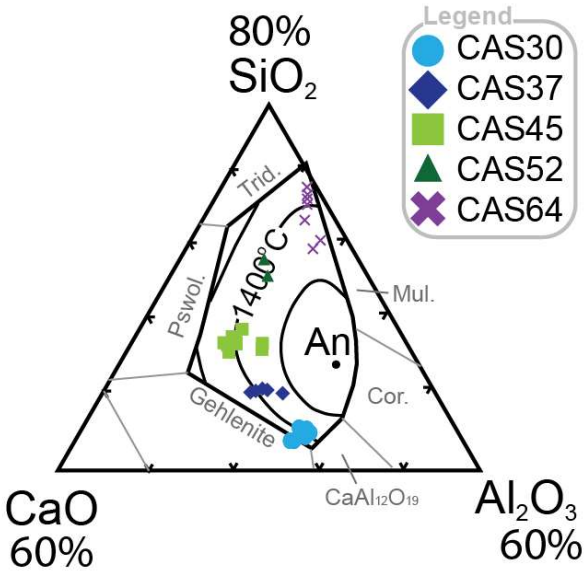

Figure 14: CaO-Al_2O_3-SiO_2 ternary modified from Levin et al. (1964). Plotted compositions are glass compositions measured by EPMA after completion of the experiments. Small variations in the melt compositions are due to various amounts of anorthite crystallisation. An - pure anorthite. Trid. – tridymite, Mul. – mullite, Cor. – corundum, Pswol – Pseudowollastonite.

For in-depth description of the experimental and anylitical methodology please refer to Chapter 2 (beginning page 19).

The five CaO-Al_2O_3-SiO_2 (CAS) and four CaO-MgO-Al_2O_3-SiO_2 (CMAS) starting compositions make up 30 individual experiments which vary in trace element concentrations, pressure and oxygen fugacity.

Table 7: List of 30 experiments that synthesised both anorthite and melt. Ramp rate from T1 to T2 is 6°C/h and experiments are held at T2 for (t) hours. Temperatures (T1 & T2) are in °C. “Air” represents no controlled gas flow throughout the furnace. IW is the iron-wüstite buffer and QFM is the quartz-fayalite-magnetite buffer. Pressurized runs had no solid buffering assemblage within the capsule

Run	Label	P (kbar)	fO_2	T1	T2	t (h)	Total Trace (wt. % O)
20140428	CAS30	0.001013	Air	1520	1399	168	8
20140804	CAS30	0.001013	Air	1521	1408	140	2
20141014	CAS30	0.001013	QFM	1517	1407	141	2
20150223	CAS30	0.001013	IW	1513	1403	148	1
20150428	CAS30	0.001013	Air	1520	1400	141	2
20150616	CAS30	0.001013	IW	1500	1385	62	2
20150428	CAS37	0.001013	Air	1520	1400	141	1
20150428	CAS37	0.001013	Air	1520	1400	141	2
20150616	CAS37	0.001013	IW	1500	1385	62	2
20140416	CAS45	0.001013	Air	1520	1453	156	8
20140428	CAS45	0.001013	Air	1520	1399	168	8
20140804	CAS45	0.001013	Air	1521	1408	140	2
20141014	CAS45	0.001013	QFM	1517	1407	141	2
20150128	CAS45	0.001013	Air	1520	1414	144	1
20150223	CAS45	0.001013	IW	1513	1403	148	1
20150616	CAS45	0.001013	IW	1500	1385	62	2
20150428	CAS52	0.001013	Air	1520	1400	141	2
20140416	CAS64	0.001013	Air	1520	1453	156	8
20140428	CAS64	0.001013	Air	1520	1399	168	8
20140804	CAS64	0.001013	Air	1521	1408	140	2
20150128	CAS64	0.001013	Air	1520	1414	144	1
20150616	CAS64	0.001013	IW	1500	1385	62	2
20151113	CMAS10	0.001013	Air	1412	1332	76	1
20151113	CMAS12	0.001013	Air	1412	1332	76	1
20151113	CMAS14	0.001013	Air	1412	1332	76	1
20151113	CMAS8	0.001013	Air	1412	1332	76	1
c4874	CAS37	10	none	1520	1400	48	2
c4856	CAS45	10	none	1520	1400	48	1
c4970	CAS52	10	none	1520	1400	48	2
c4828	CAS64	10	none	1520	1400	48	1

3.2.5 Results

Run products

A list of all experiments is given in Table 7. The experiments produced anorthite crystals with the co-existing melt quenched into glass. The anorthite shape varies systematically with changes in melt compositions (Figure 15), with the low silica compositions (CAS30) producing very thin anorthite (~1mm x 10 μm) and the highest silica composition producing anorthite with a lower aspect ratio. Generally, the standard deviations of the trace-element concentrations in the melts are less than 3%, whereas the crystals are considerably less homogeneous, as the rare earth elements in the anorthite have an

average relative standard deviation of 14%. The variations in the concentrations of trace elements in different crystals or parts of crystals within one experiment tend to be highly correlated, such that the standard deviations of element ratios such as La/Sm are considerably lower than the standard deviations of La or Sm by themselves. For example, in run 20151113 – sample CMAS 14, the highest MgO content in the CMAS system has one of the highest standard deviations of REE in the anorthite of a single sample. Both La and Sm have relative standard deviations of approximately 19%, while the La/Sm ratio has a relative standard deviation of 3%. The average measured concentrations of elements in both the anorthite and accompanying melt along with their standard are given in Appendix 2 in Table 37 to Table 39.

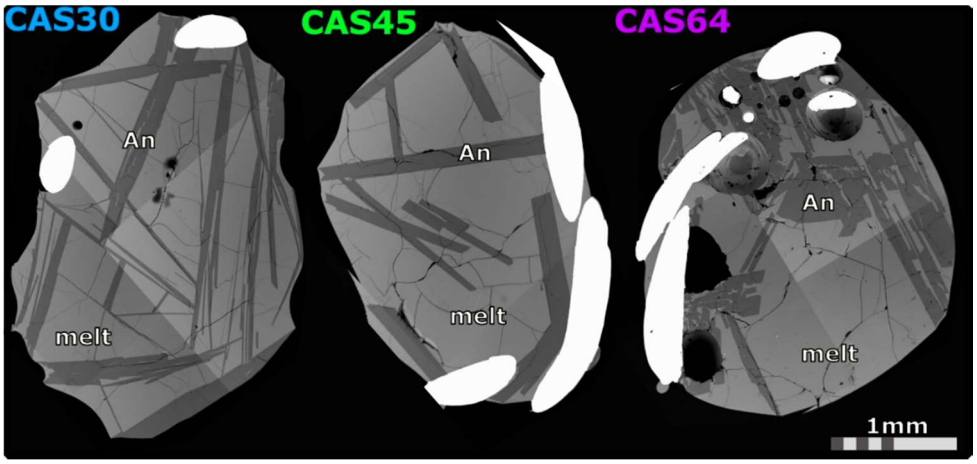

Figure 15: Back scattered electron images (BSEI) of experimental charges, bright is platinum wire, light grey is melt and dark is anorthite (An). Anorthite size and shape changes in different melt types. Images are a mosaic of multiple images. Experiments from run 20140428

Apart from melt composition, there are several other variables on which partition coefficients may depend. Temperature was not investigated in this study and pressure was found to have no effect on the partitioning (Figure 16). The concentrations (i.e., doping levels) of the trace elements have no effect on the partitioning (Figure 17a); i.e., the partition coefficient of an element does not change with the concentration of that element (Henry's law). Oxygen fugacity (fO_2) effects only two REEs which exist in more than one oxidation state in the range covered in the experiments, namely Ce and Eu. Therefore, the focus of this paper is melt composition.

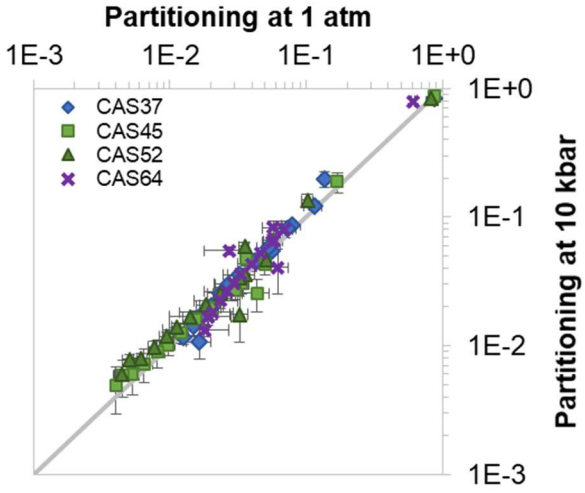

Figure 16: Partitioning of trace elements between anorthite and melt at 1 atm pressure at 10 kbar. Trace elements displayed are: Mg, Sc, Sr, Ba, La, Pr, Nd, Sm, Gd, Tb, Dy, Ho, Er, Tm, Yb and Lu.

All melts that are saturated in stoichiometric anorthite at a specified temperature will have the same activity of anorthite, given by the activity quotient $(\alpha CaO)(\alpha Al_2O_3)(\alpha SiO_2)^2$, or for brevity, (αAn), relative to the standard state of the pure oxide components at the temperature of interest and 1 bar. The activities of these oxide components were calculated from the analysed melt compositions using the model of Berman and Brown (1984), and values of (αAn) thus obtained are plotted against temperature in Figure 17b. These values correlate well with previous studies of Libourel et al. (1989) and Miller et al. (2006).

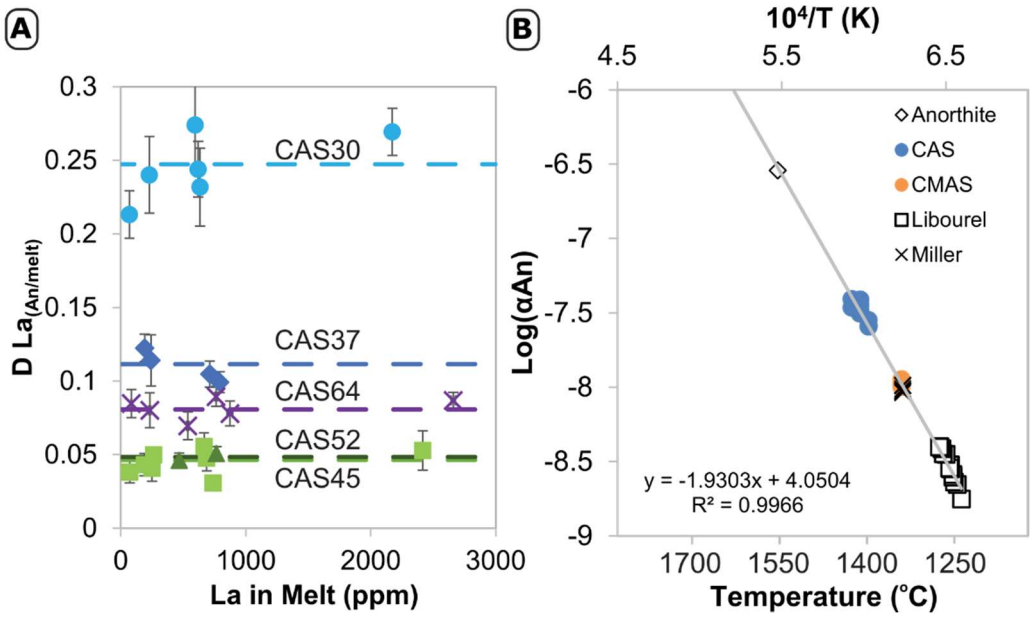

Figure 17: A) Henry's Law for all experiments. Showing that the partition coefficient does not vary significantly with increasing doping of trace elements. Lines represent the average value. B) Saturation of anorthite (An) with temperature. Includes data from Libourel et al. (1989) and Miller et al. (2006). αAn calculated from $(\alpha CaO)(\alpha Al_2O_3)(\alpha SiO_2)^2$ using the model from Berman and Brown (1984)

Anorthite stoichiometry

Although there was no sodium added to the starting compositions, the impurities in the starting materials and contamination from the furnaces causes some of the experimental anorthite to contain a measurable albite component. Four out of the five anorthite compositions in the system CAS have the ideal stoichiometry on the join $CaAl_2Si_2O_8$-$NaAlSi_3O_8$ within analytical uncertainty. The high silica composition (CAS64) has less than five cations to eight oxygens (Table 8), due to the incorporation of excess silica in the form of a vacancy ($\square Si_4O_8$), which has been documented in experimental, lunar and some natural plagioclase (Ito, 1976; Longhi and Hays, 1979). It has been suggested that plagioclase can form with excess aluminium, as Al_4SiO_8 (Williamson et al., 2016) with Al substituting for Ca on the large cation site, charge-balanced by Al for Si on the tetrahedral sublattice, but we find no evidence for this substitution in the experiment with the high activity of alumina, CAS30.

The anorthite in CMAS are all stoichiometric within uncertainty, allowing for minor Mg substitution as $CaMgSi_3O_8$ (Longhi et al., 1976; Miller et al., 2006; Murakami et al., 1992; Peters et al., 1995).

Table 8: Atoms per formula unit (APFU) for synthesised anorthite normalised to 8 oxygens. Where anorthite number (An#) is given by the APFU of Ca/ (Ca+Na+K).

system	**CAS30**	**CAS37**	**CAS45**	**CAS52**	**CAS64**	**CMAS**
APFU	***LS902***	***LS902.5***	***LS903***	***LS903.5***	***LS904***	
Na		0.008	0.007	0.057	0.020	0.015
Mg			0.006		0.006	0.016
Al	2.03	2.02	2.00	1.95	1.88	1.99
Si	1.97	1.98	2.00	2.05	2.12	2.00
Ca	1.01	1.00	0.99	0.94	0.92	0.98
Total	5.01	5.01	5.01	5.00	4.96	5.01
An #	100	99	99	94	98	98

Partitioning of Trace Elements in Anorthite

For a crystal in equilibrium with a silicate melt of a given composition, the partition coefficients of trace elements forming cations with a given charge (1+, 2+, 3+ etc.) vary more-or-less systematically with ionic radius, within the limitation that the cations of the given charge substitute onto the same crystallographic site. While this principle owes much to Goldschmidt's rules, its modern basis lies with lattice strain theory (e.g., Wood and Blundy 2014). Specifically, it is often found that when the partition coefficients of a set of homovalent cations, substituting onto a given crystallographic site are plotted against the ionic radius of the cation as given by Shannon (1976), the resulting curve is a slightly asymmetric parabola, whose vertex lies close to the ionic radius of the cation for

which they are substituting (Onuma et al., 1968) (Figure 1). Sets of mineral/melt partition coefficients of the REEs in their usual trivalent oxidation state provide many such examples.

In high-temperature plagioclases, including the nearly end-member anorthite of this study, there are two crystallographic sites: the tetrahedral framework site occupied by Si and Al, and the large M site that is interstitial to the framework, occupied by Ca^{2+}. This M site is commonly assumed to be VIII-fold coordinated, however, in anorthite the geometry of the site is irregular, and it has been described by some as closer to VII-fold and sometimes even VI-fold coordination (Megaw et al., 1962). Here we have continued with the approximation that the relevant ionic radii are VIII-fold coordinated, for which the ionic radii are much better known (Shannon, 1976). The ionic radius consideration suggests that most of the trace elements investigated in this study substitute for Ca^{2+} on the M site, but smaller cations (e.g., Be^{2+}) substitute onto the tetrahedral framework sites. Mg^{2+} has two substitution mechanisms, predominantly going onto the tetrahedral site as $CaMgSi_3O_8$ but with some on the M site as $MgAl_2Si_2O_8$ (e.g., Miller et al. 2006). These two substitution mechanisms have different stoichiometric controls, hence the ratio of Mg substituting for Ca on the M site to that substituting onto the Si-Al-framework must vary with melt composition.

The partition coefficients of cations of similar charge substituting onto the same site are not only expected to fall on the same lattice-strain parabolas but also have the same stoichiometric control, and will therefore vary with melt composition in the same way. Therefore the results of this study will be arranged in groups of elements according to the charge of their cations. The data are presented as Onuma curves. As the systems investigated here crystallize end-member anorthite, any variation in the partition coefficients should be due to melt composition effects, with the possible exception of the composition CAS64 with its non-negligible Si_4O_8 component.

Partitioning of the trivalent cations: REEs, Y and Sc

The rare earth elements (REEs) make up the lanthanide series of the periodic table; atomic numbers 57-71. These 14 elements (omitting promethium due to its scarcity in nature) are of similar size and behave chemically similar. All of these elements exists as trivalent cations except for europium (atomic number 63) and cerium (atomic number 58) which also exist as 2+ and 4+ cations respectively.

As these elements are chemically similar, varying only in atomic radius, they create easily interpreted patterns. It is common to measure only a handful of these 14 elements and extrapolate the missing elements, however much of the intricacies of the rare earth element patterns can only be discovered when all 14 are measured.

Yttrium (atomic number 39) has an ionic radius in VIII-fold coordination of 1.019 Å. It is often included as a pseudo-rare earth element as it has a comparable size to Ho (1.015 Å) and Dy (1.027 Å). Similarly, scandium (atomic number 21) is occasionally lumped into the pseudo-REEs as it is also a trivalent cation however it is much smaller at 0.87 Å.

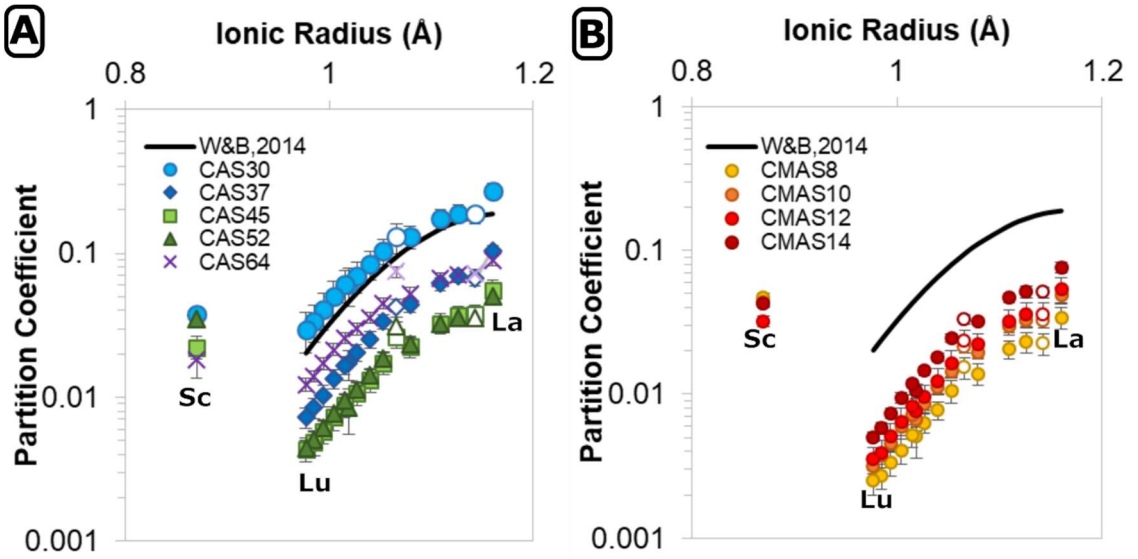

Figure 18: Partitioning of rare earth elements (REEs) and scandium (Sc) in anorthite in different melt compositions in A) CaO-Al_2O_3-SiO_2 system (CAS) and B) CaO-MgO-Al_2O_3-SiO_2 (CMAS) and comparing with the prediction of the REE partitioning using the Wood and Blundy, 2014; equation 62. All cations are trivalent except Eu, and Ce which have multiple valencies and represented by open symbols.

The effect of melt composition on the partition coefficients of the REEs is significant in both the CAS and CMAS systems (Figure 18). Overall, partition coefficients of the REEs increase by approximately a factor of four with decreasing silica content of the melt in the CAS system. The effect of melt composition in the CMAS system is less dramatic, with a 125% increase from low to high MgO content for the REEs + Y.

Sc is affected less by the changes in melt composition, increasing by 206% with decreasing silica content in the melt in the CAS system and increasing with by 110% with increasing magnesium in the CMAS system. The plots of partition coefficients versus the ionic radius of the rare earth elements (r_{REE}) fall on smooth curves with the exception of Ce and Eu, broadly consistent with lattice strain theory (Figure 18). The curves form the left-hand limbs of the expected parabolas, indicating that the heavy REEs are too small

for the M site, with La the least incompatible of the REEs. This behaviour contrasts with the partitioning of REEs into augite, where the REE^{3+} cations also replace Ca^{2+} in a distorted 8-coordinated site, but with the heavy REEs favoured over La.

Scandium however, does not fall on the REE parabola. Sc is much more compatible than is predicted by the REE partitioning into the M site in anorthite. This suggests that scandium is substituting into the only other site in the anorthite structure available for substitution – the tetrahedral site.

Yttrium does fit within the REE defined parabola but for consistency, only the true rare earth elements are used in the partitioning prediction calculations in the following sections.

With the exception of CAS64 which crystallizes the non-stoichiometric anorthite (CAS64), the shapes of the Onuma curves remain approximately constant (Figure 18), hence the effect of melt composition can be modelled by examining the controls on the most compatible of the REE in anorthite; Lanthanum.

Figure 19 shows that there is no trend between values of D_{La} and the universal melt descriptors; non-bridging oxygens over tetrahedrally coordinated oxygens (NBO/T), or the optical basicity (Duffy, 1993). Such simple descriptors do not capture the thermodynamic properties of silicate melts with sufficient resolution to be useful for parameterizing mineral/melt partition coefficients.

A thermodynamic approach starts with the activity of the components in the melt, which can be calculated using a thermodynamic model for CaO-MgO-Al_2O_3-SiO_2 silicate melts. Berman and Brown (1984) have developed such a model, which will be used here. Firstly, we need to determine which melt component controls the partitioning of the rare earth elements. To do this we need to determine the "stoichiometric control", which is the reaction that determines how a trace element partitions into a crystal of a given stoichiometry (O'Neill and Eggins, 2002).

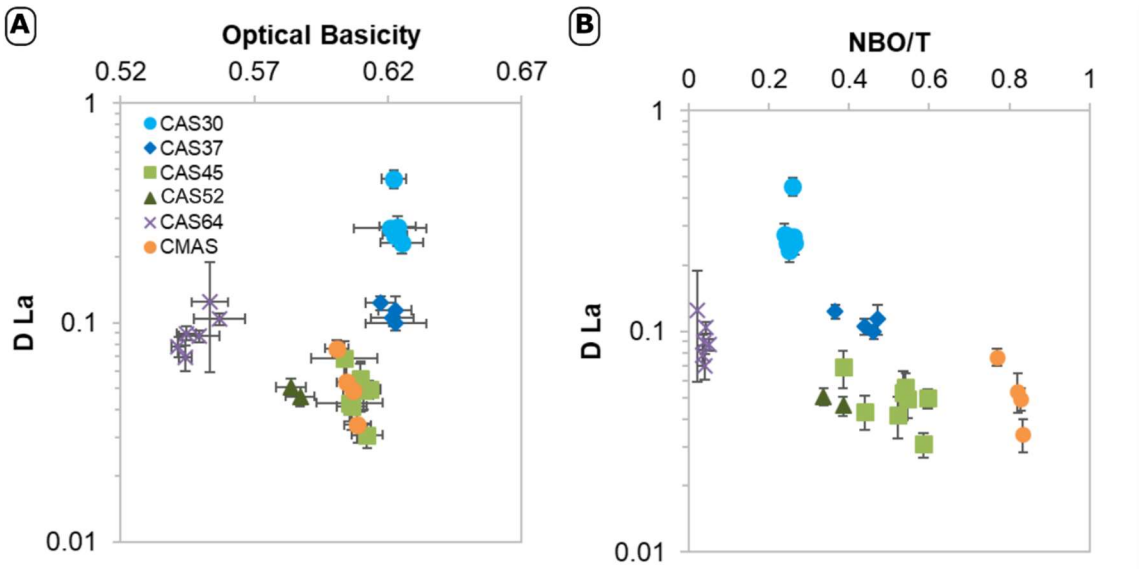

Figure 19: Partition coefficient for lanthanum in anorthite against "traditional" melt parameters A) Optical basicity B) Non-bridging oxygens over tetrahedra. Note the log scale for the y-axis

Scandium in anorthite substitutes onto the tetrahedral site in place of aluminium in the exchange outlined in Equation 27. This substitution does not require a charge balance substitution and therefore will not be affected by melt composition.

Equation 27:
The stoichiometric control for the partitioning of scandium onto the tetrahedral site of plagioclase

$$ScO_{1.5_{melt}} + CaAl_2Si_2O_{8_{pl}} = CaScAlSi_2O_{8_{pl}} + AlO_{1.5_{melt}}$$

The REEs and Y partition onto the large cation (M) site of anorthite as a REE-plagioclase component by an exchange with calcium (Dohmen and Blundy, 2014);

Equation 28:
The stoichiometric control for the partitioning of rare earth elements into plagioclase

$$REEO_{1.5_{melt}} + CaAl_2Si_2O_{8_{pl}} + AlO_{1.5_{melt}} = REEAl_3SiO_{8_{pl}} + CaO_{\ melt} + SiO_{2_{melt}}$$

When rearranged to consider the ratio of the REE-plagioclase over the REE oxide in the melt (i.e. the partition coefficient); it is suggested that the melt activity should be proportional to the partitioning of the REEs;

Equation 29

$$\frac{REEAl_3SiO_8}{REEO_{1.5}} \propto \frac{(\alpha Al_2O_3)^{1/2}}{(\alpha CaO)(\alpha SiO_2)}$$

The saturation of anorthite in the system should be a constant at constant temperature (Figure 17b). Therefore, the activity of the anorthite component (αAn) can be expressed as:

Equation 30

$$(\alpha An) = (\alpha CaO)(\alpha SiO_2)^2(\alpha Al_2O_3)$$

Rearrangement gives:

Equation 31

$$(\alpha CaO) = \frac{(\alpha An)}{(\alpha SiO_2)^2(\alpha Al_2O_3)}$$

Then, we can simplify the REE exchange by substituting the calcium activity (Equation 31) into Equation 29:

$$D_{REE} = \frac{REEAl_3SiO_8}{REEO_{1.5}} = \frac{(\alpha Al_2O_3)^{1.5}(\alpha SiO_2)}{(\alpha An)}$$

Where (αAn) is constant and can be omitted from the equation.

Equation 32
the activity of aluminium exchange

$$D_{REE} \propto (\alpha Al_2O_3)^{1.5}(\alpha SiO_2)$$

Although this activity quotient is positively correlated with the partitioning of lanthanum in the stoichiometric anorthite in the CAS system (Figure 20a), the slope of $ln D_{La}$ versus $ln[(\alpha Al_2O_3)^{1.5}(\alpha SiO_2)]$ differs significantly from unity, and the non-stoichiometric anorthite (CAS64) with its $\square Si_4O_8$ type substitution produced at high αSiO_2 falls off the trend. These deviations are qualitatively consistent with large negative deviations from ideality for $REEO_{1.5}$ in silicate melts due to the formation of $REEO_{1.5}$-SiO_2 complexes, as previously found by Evans et al. (2008) for REE partitioning between forsterite and silicate melts of various compositions in the CMAS system.

Empirically, there is a good linear correlation between the D_{La} and the activity of alumina in the melt (Figure 20b), which incorporates all melt composition types and includes the non-stoichiometric anorthite. Moreover, the slope of $ln D_{La}$ versus $ln(aAl_2O_3)$ is close to unity (Figure 20b). Comparing published data, it appears that the linear correlation between the activity of alumina in the melt and the partitioning of lanthanum continues for all plagioclase compositions (Figure 20d). However, this stoichiometry suggested by this correlation does not correspond to any substitution mechanism that is plausible on crystal-chemical grounds. Given also the independent evidence for the $REEO_{1.5}$-SiO_2 complexes from Evans et al. (2008), we conclude that, despite its simplicity, the correlation results from a fortuitous play-off between the two factors by which melt

composition influences partition coefficients, namely the stoichiometric control and the effect of melt composition on activity coefficients.

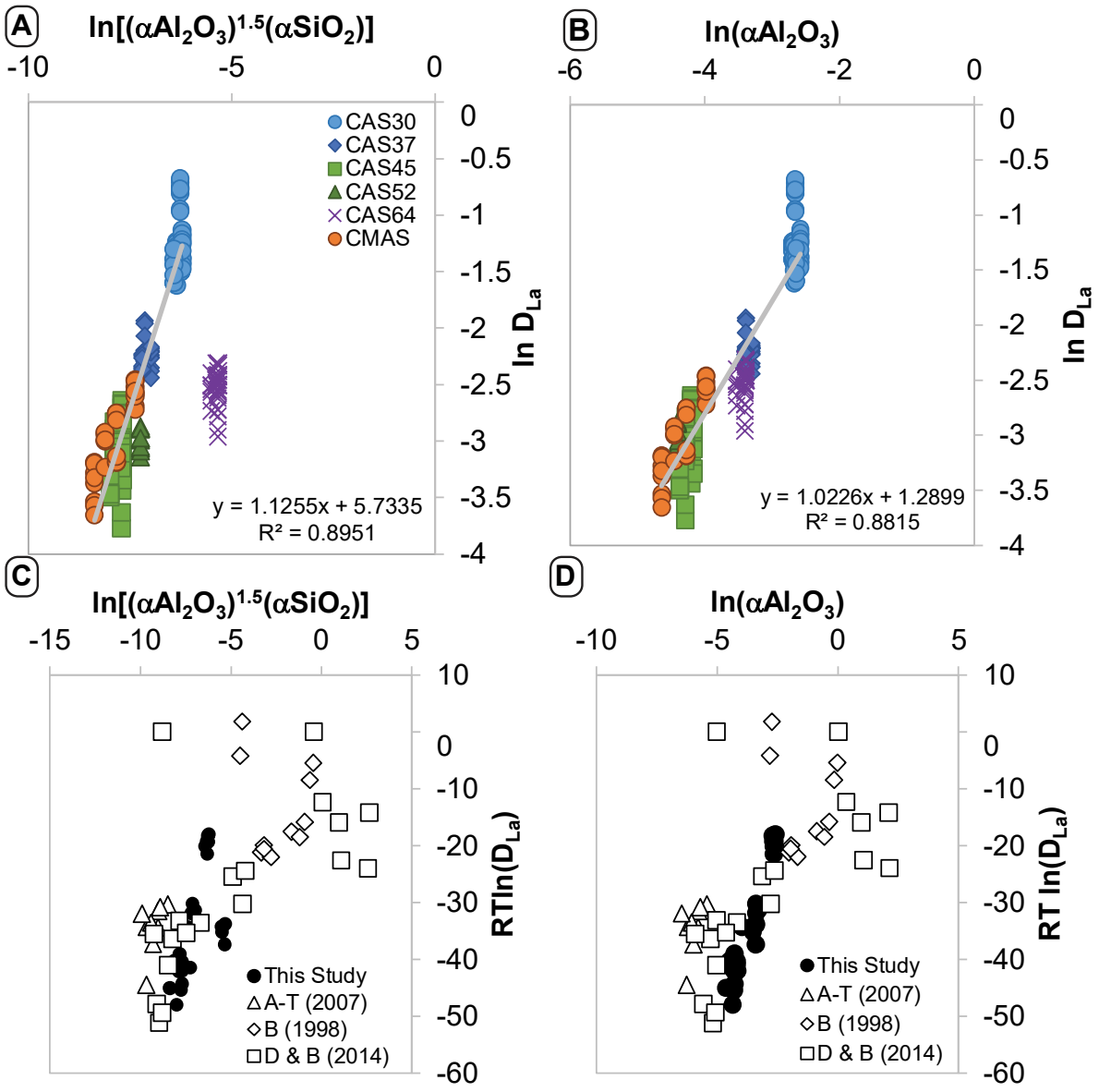

Figure 20: Relationship between partitioning of lanthanum and a) the activity of the alumina exchange, fit to stoichiometric anorthite only. Where the equation of the line is: $lnD_{La}=1.13*ln[(\alpha Al_2O_3)^{1.5}(\alpha SiO_2)]+5.73$ b) the activity of alumina in melt, fit includes non-stoichiometric anorthite. Where the equation of the line is: $lnD_{La}=1.03*ln(\alpha Al_2O_3) + 1.29$ c) activity of alumina exchange in published plagioclase/melt experiments and d) melt alumina activity in published plagioclase/melt experiments. Literature data includes (Aigner-Torres et al., 2007; Bindeman et al., 1998; Dohmen and Blundy, 2014)

Having established that the partitioning of lanthanum is highly dependent on the activity of alumina in the melt, we now use our experimental results to test how efficaciously the lattice strain model predicts the partition coefficients for the other rare earth elements.

Comparing the lattice strain model with simple polynomial functions

For a crystal and melt of a given composition, the lattice strain model relates the crystal/melt partition coefficients, (D_i), of a group of elements of the same charge to their

ionic radii (r_i) by an equation due to Brice (1975) describing an asymmetric parabola (Wood and Blundy 2014). This equation is outlined in Equation 5 on page 5. The vertex of the parabola is specified by D_o, the partition coefficient of a hypothetical element with radius r_o. Apart from the position of its maximum in $D_i - r_i$ space, and its width (through the value of E), the shape of the parabola is not a variable but is specified by the model. Parts of the effects of the stoichiometric control are incorporated into the value of D_o, as is the activity coefficient in the silicate melt of the hypothetical element defining D_o and r_o. However, the variations among the group of elements of neither the equilibrium constants of the partitioning reaction nor their activity coefficients are accounted for. Thus with reference to Equation 28, the equilibrium constant for the partitioning reaction is assumed to be the same for all REE, as are the values of $\gamma REEO_{1.5}$. There is also the problem of what is meant by r_i when applied to a crystallographic site such as one so greatly distorted from any regular polyhedron in shape as is the M site in anorthite. In practice, the ionic radii tabulated by Shannon (1976) are used, despite these being derived from room-temperature interatomic distances in highly symmetrical crystal structures. The present data provide an opportunity of determining to what extent these simplifications matter.

We have therefore also fitted the values of D_{REE} to a simple polynomial expression in r_{REE} using orthogonal polynomials, which allows the expression to be truncated at an arbitrary number of terms without affecting the values of the remaining terms (O'Neill, 2016). The orthogonal polynomial equation is outline in Equation 23 on page 31.

The lambda parameters for the representative experiments are given in Table 9.

Table 9: lambda parameters for representative experiments

		λ0		λ1		λ2		λ3		λ4	
		av.	σ	av.	σ	av.	σ	av.	σ	av.	σ
20151113	CMAS 8	-4.76	0.18	14.4	0.6	-38.8	7.2	75	114	3622	1144
20151113	CMAS 10	-4.42	0.11	14.7	0.2	-41.0	1.8	135	75	1737	1350
20151113	CMAS 12	-4.33	0.22	14.7	0.2	-46.8	3.4	173	29	2440	1241
20151113	CMAS 14	-3.94	0.07	14.6	0.4	-49.9	3.1	210	43	2725	1496
20150428	CAS30	-2.45	0.22	11.9	1.1	-38.1	4.5	277	37	1902	491
20150428	CAS37	-3.62	0.13	14.3	0.5	-46.2	4.0	244	38	2815	1509
20140804	CAS45	-4.25	0.18	13.8	0.3	-34.1	3.0	118	49	3191	844
20150428	CAS52	-4.21	0.11	13.1	0.3	-44.5	3.9	186	33	2939	687
20140804	CAS64	-3.35	0.09	10.5	0.2	-52.1	2.4	265	20	1679	604

The λ_0 term corresponds to a hypothetical partition coefficient near the middle off the REE series, and as such is comparable to the role of D_o^{3+} in the lattice strain model. The λ_0 term is highly correlated with the melt activity (Figure 21). λ_1 indicates the slope of the

rare earth element partitioning pattern and would be related to E and r_o^{3+} while λ_2 represents the curvature of the D_{REE} pattern. These two parameters are almost constant with the exception of the non-stoichiometric anorthite from composition CAS64.

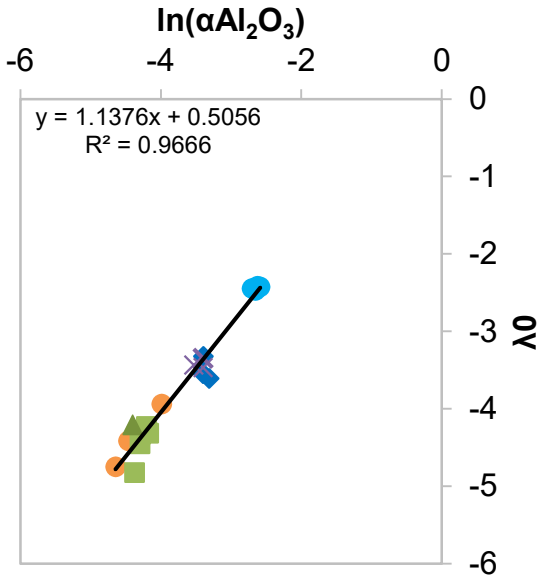

Figure 21: correlation of λ_0 (magnitude of the rare earth element partitioning) with alumina activity in the melt

The goodness-of-fit of the alternative models may be evaluated from the chi-squared (χ^2) statistic (Equation 21). Here the measured partition coefficient value (D_{obs}) are the mean values calculated from all the analyses within a given experiment, and $\sigma(D_{obs})$ are their standard deviations. The reduced chi squared (χ^2_ν) (Equation 22) is compared between these models. If values of $\sigma(D_{obs})$ were random, then χ^2_ν should approach 1 for a large number of data, if the model describes the data adequately. However, as pointed out earlier, there is a great deal of correlation between deviations from the mean in any given laser-ablation analysis of the anorthite crystals in most of the experiments, hence we must expect values of χ^2_ν rather less than 1. Nevertheless, relative values of χ^2_ν from different models are a valid means of comparison. Because of their variable oxidation states, Ce and Eu were not used in the fit.

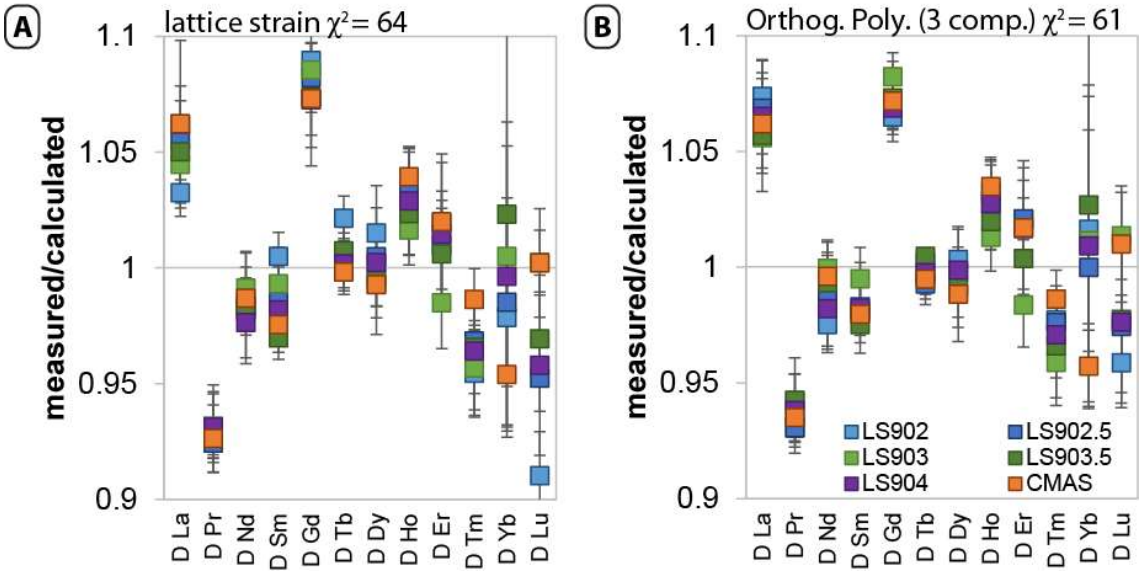

Figure 22: mismatch in measured and modelled REE partitioning values A) for the lattice strain model, with unique values for E, R_o and D_o for each experiment B) An orthogonal polynomial with 3 components, which are unique for each experiment.

Fitting the lattice strain model to each set of D_{REE} values gives a fit of $\chi_\nu^2 = 0.24$. By comparison, the orthogonal polynomial model with three parameters (λ_0, λ_1 and λ_2) gives no better a fit to the data, with a $\chi_\nu^2 = 0.23$. Adding an extra term (λ_3) decreases χ_ν^2 significantly to 0.12 but a fifth term with makes little difference ($\chi_\nu^2 = 0.10$). The residuals from the fits of the different models are shown in Figure 22. There may be need for an adjustment in the ionic radius for Gd as it is poorly fit in every model (Figure 22). Overall, however, our data provide an emphatic experimental validation of the Brice equation, despite the problematic nature of defining r_{REE} in the context of the anorthite M site.

As the fits of the lattice strain model and the three-term orthogonal polynomial fit the REE partitioning are very similar, both will employed in generating parameterizations for predicting the REEs in the following section.

Table 10: Model fit of the partitioning of the rare earth elements in anorthite

	χ^2	χ^2_ν	no. of data	parameters
Lattice strain model	64.39	0.24	360	90
Orthogonal polynomial – 3 parameters	60.61	0.23	360	90
Orthogonal polynomial – 4 parameters	29.51	0.12	360	120
Orthogonal polynomial – 5 parameters	20.53	0.10	360	150

Predicting the partitioning of the rare earth elements

An update on the lattice strain model for the partitioning of the rare earth elements into anorthite has been recently published as equation 62 in Wood and Blundy (2014) and is as follows:

Equation 33:
Predicting the partitioning of the rare earth elements in plagioclase, from the partition of lanthanum.
As published by Wood and Blundy (2014)

$$D_i = D_{La} \exp\left[\frac{-910.17E\left(\frac{r_0}{2}(r_{La}^2 - r_i^2) + \frac{1}{3}(r_i^3 - r_{La}^3)\right)}{T}\right]$$

Because the values of D_{REE} all fall on the left-hand side of the parabola, values of D_o and r_o are difficult to define, and instead Wood and Blundy (2014) relate the parabola to D_{La} and r_{La}, with the former based on the relationship given by Bindeman et al. (1998):

$$RTlnD_{La} = -10.8X_{An} - 12.4$$

From the ample amount of data published since that time, it is clear that this relationship is not very precise (Figure 23). Disregarding the evidence from plagioclase compositions in general, even for end-member anorthite, it fails to address the effects of melt composition, as discussed in the previous sections. Therefore, it is time to create a new model for the partitioning of rare earth elements into plagioclase.

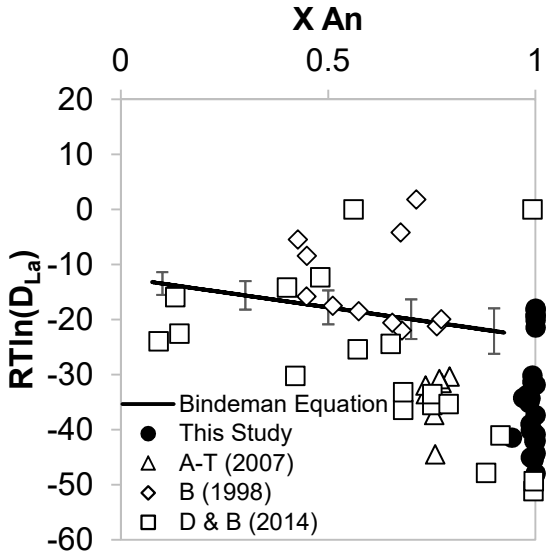

Figure 23: Linear correlation between D_{La} and X_{An} used to constrain the partitioning of rare earths into plagioclase in Wood and Blundy (2014). A-T = Aigner-Torres et al. (2007), B = Blundy et al. (1998) D & B = Dohmen and Blundy (2014)

We tested both the lattice strain equation and the 3-term orthogonal polynomial to determine which is most accurate for predicting the partitioning of all the rare earth elements.

As the r_0^{3+} and E values are related to the lattice strain in the mineral. As these experiments grow only anorthite, these two values should be constant. Similarly, for the polynomial equation, λ_1 and λ_2 are treated as constants.

The new parameters to be substituted into the lattice strain model (Equation 33) are:

Equation 34:
New parameters for the lattice strain model for predicting partitioning of rare earth elements in anorthite. These variable substitute into Equation 33.

$$D_{La}^{3+} = \exp(ln(\alpha Al_2O_3) * 0.92 + 0.77)$$

$$r_0^{3+} = 1.19$$

$$E_0^{3+} = 175$$

This equation predicts the partitioning of the rare earth elements in anorthite; including non-stoichiometric anorthite, with a $\chi_v^2 = 6.19$.

The polynomial expression was more accurate in modelling the rare earth elements partitioning between anorthite and melt. We have used the same method to arrive at a predictive equation for the partitioning of the rare earth elements into anorthite using the polynomial approach.

Equation 35:
New model for predicting partitioning of rare earth elements in anorthite using the activity of alumina in the melt. These variable substitute into Equation 23

$$\lambda_0 = \alpha Al_2O_3 * 30.34 - 4.67$$

$$\lambda_1 = 12.80$$

$$\lambda_2 = -47$$

where the activity of the alumina (αAl_2O_3) is calculated by the method given in Berman and Brown (1984) and these variables are substituted into Equation 23. This equation predicts the partitioning of the rare earth elements in anorthite with a $\chi_v^2 = 5.19$.

Although this is the most accurate way to model these experiments, it is impractical to calculate the activity of aluminium in a natural system. Rather than the activity, the mole fraction of Al_2O_3 in the CMAS system was used. The parameters for this equation are given in Equation 36. The error between the calculated and measured partition coefficients increases to χ_v^2 =14.1. Although this is a less accurate model, it is more practical in its application.

Equation 36:
New model for predicting partitioning of rare earth elements in anorthite using the mole fraction of alumina in the melt. These variable substitute into Equation 23

$$\lambda_0 = X[Al_2O_3]^{CMAS} * 12.49 - 5.69$$

$$\lambda_1 = 12.87$$

$$\lambda_2 = -55.2$$

Divalent cations

The divalent cations doped and measured in all experiments were Mg, Ca, Sr and Ba with the experiments in the CMAS system having an additional divalent element, Be. The partitioning of Ca was calculated from EPMA analysis, while the other elements are calculated from LA-ICP-MS. The partition coefficients in the CMAS system are in good agreement with the Miller et al. (2006) data.

The larger divalent cations (Sr^{2+} and Ba^{2+}) are thought to partition onto the calcium (M) site of the plagioclase e.g. as in the end-member feldspar celsian ($BaAl_2Si_2O_8$) (Megaw et al., 1962).

Equation 37:
The substitution of divalent cations into the large cation site (M) of plagioclase

$$CaAl_2Si_2O_{8\,plagioclase} + M^{2+}O_{melt} = M^{2+}Al_2Si_2O_{8\,Plagioclase} + CaO_{melt}$$

If this is the case, the stoichiometric control does not involve the activities of silica or alumina, and apart from any difference in the dependence of the activities of CaO from those of SrO or BaO as a function of melt composition, the values of $KD_{Sr\text{-}Ca}$ and $KD_{Ba\text{-}Ca}$ (i.e., D_{Sr}/D_{Ca} and D_{Ba}/D_{Ca} respectively) should be constant (Figure 25).

Intriguingly, D_{Sr} is higher than D_{Ca}, which suggests that Ca is larger than ideal for the M site (Figure 24). It has been noted previously that the Ca^{2+} cation is too small for the available site in anorthite (Megaw et al., 1962). In the CMAS experiments, the partitioning of these three cations increase slightly as the concentration of Mg in the melt increases.

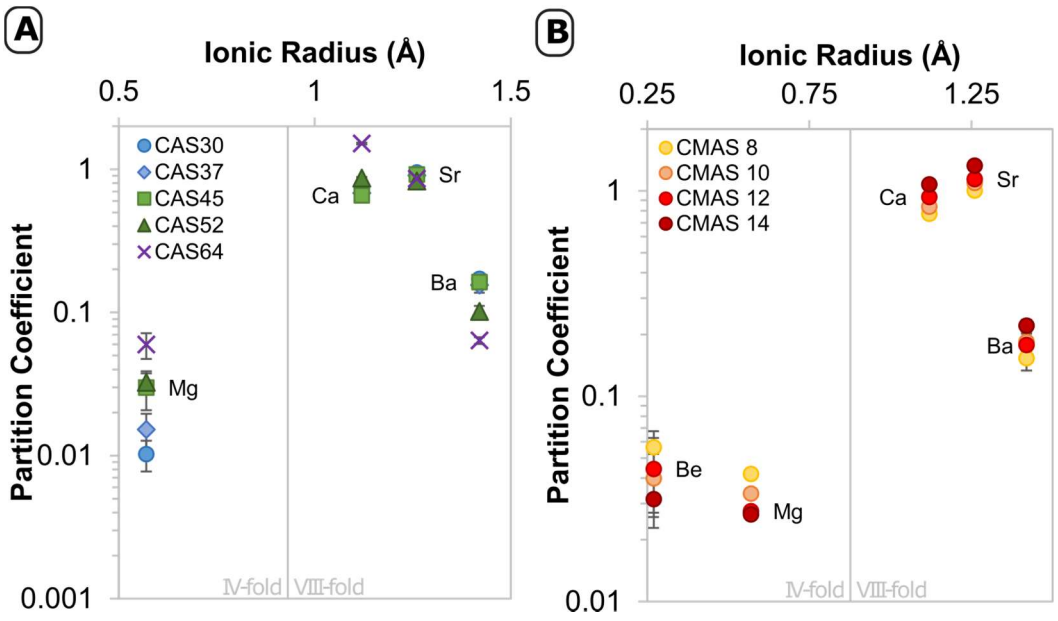

Figure 24: Partitioning of the divalent cations in anorthite in a) CAS system at 1400°C b) CMAS at 1332°C. Calcium partitioning in anorthite in CAS system is from EPMA analysis while all other data was obtained by LA-ICP-MS.

Be^{2+} is a very small cation, which is unlikely to exist in VIII-fold coordination (Shannon, 1976) and is expected to substitute onto the Si/Al framework positions in the anorthite crystal structure. It will therefore have a different stoichiometric control than the larger divalent cations, according to the reaction:

Equation 38:
The substitution of divalent cations on the tetrahedral site of plagioclase

$$CaAl_2Si_2O_{8\,plagioclase} + BeO_{melt} + SiO_{2\,melt} = CaBeSi_3O_{8\,plagioclase} + Al_2O_{3\,melt}$$

This reaction shows that D_{Be} will depend on activities of the melt components SiO_2 and Al_2O_3. As only 4 of the 30 experiments tested in this study contained Be, no significant conclusions can be made.

Magnesium has a cation radius between Be^{2+} and the larger divalent cations and is thought to partition onto both the large cation site and the tetrahedral site (e.g., Miller et al. 2006 and references therein). The two partitioning reactions mean that there are two different stoichiometric controls, and that the ratio of the $CaMgSi_3O_8$ to $MgAl_2Si_2O_8$ components vary with melt composition.

Due to the differences in stoichiometric control for the substitution of Mg (Equation 38) and Ba (Equation 38) these cations behave differently with changing melt composition (Figure 25). The partitioning of Mg is strongly correlated with the silica activity of the melt while the partitioning of Ba is not.

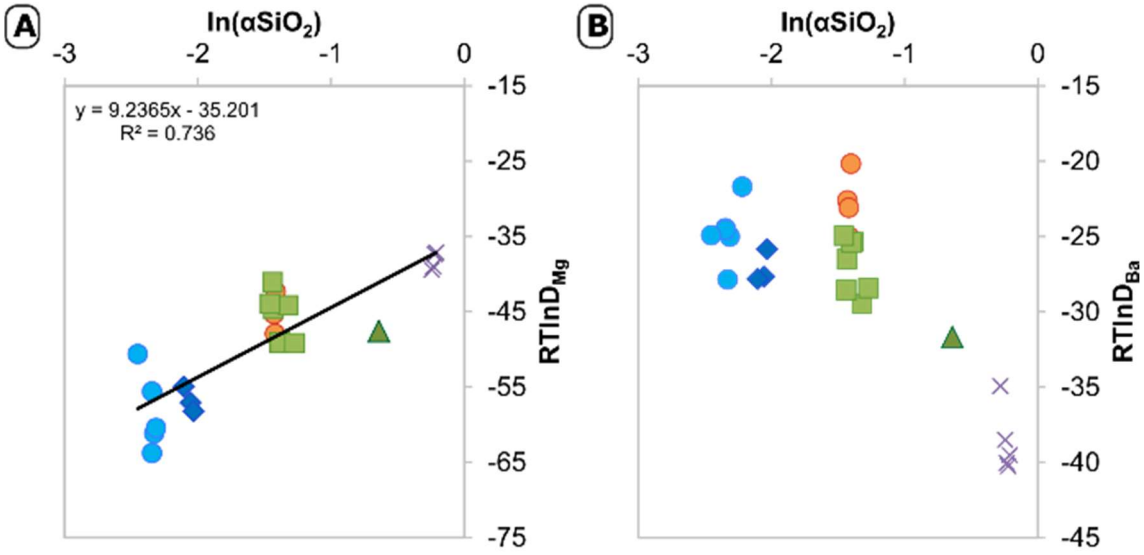

Figure 25: The effect of silica activity in the melt on the partitioning of the divalent cations A) silica activity compared with the partitioning of Mg in anorthite B) silica activity in the melt compared with the partitioning of Ba in anorthite.

4+ cations

The partitioning of Nb, Hf, Th and U were also measured in these experiments. These elements are extremely incompatible in anorthite, and have very low partition coefficients. The concentrations of these elements are near or below the limit of detection for this analytical method, which causes the relative standard deviations of these elements to be much higher than the other elements. Therefore, no significant conclusions can be made.

Multi-valent cations

Of the elements tested in this series, Nb, Eu, Ce, and U have multiple valence states. Oxygen fugacity was controlled at QFM (quartz-fayalite-magnetite) and IW (iron-wüstite), which have log fO_2 values of -6.21 and -9.71 respectively at 1400°C. Most experiments were carried out in air at 1 atmosphere which is given an $f\,O_2$ value of -0.7. This gives 3 valence states to test the partitioning of these multivalent cations.

The unique lattice strain fits were used to determine the partition coefficients of Ce^{3+} and Eu^{3+} partitioning onto the large cation site in plagioclase and given the notation D_{Ce*} and D_{Eu*}. The ratio between the measured values for the partitioning of Ce and Eu were compared with the oxygen fugacity to outline the anomalies in the rare earth element patterns. As oxygen fugacity increases, the cerium anomaly decreases and the europium anomaly increases (Figure 26).

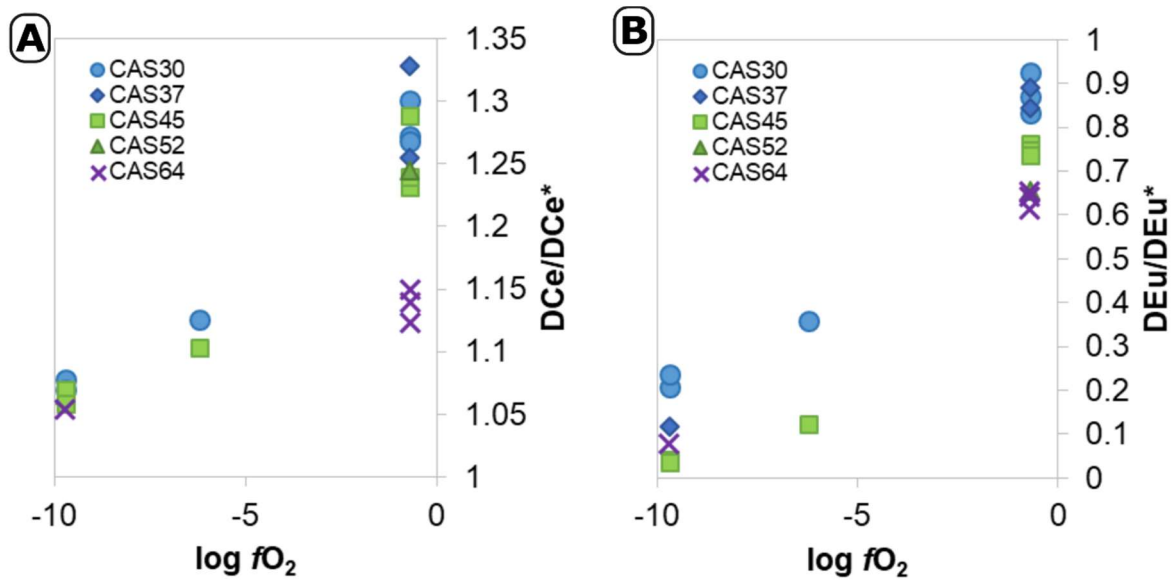

Figure 26: The change of the rare earth element partitioning anomalies with changes in oxygen fugacity. Y axis is the ratio of the measured partitioning value over that suggested by a lattice strain fit to all other rare earth elements. Includes oxygen fugacities of air (-0.7), quartz-fayalite-magnetite (-6.21) and iron-wüstite (-9.71). A) Cerium partitioning anomaly B) Europium partitioning anomaly

U and Nb are extremely incompatible in anorthite and very close to detection limits and much lower than the limit of quantification, which gives very high standard deviations. This makes conclusions from this data impossible.

3.2.6 Discussion and Conclusions

The partitioning in this study focuses on anorthite grown in isothermal conditions. The experiments tested variations in trace element concentrations and oxygen fugacity, however both were found to have no effect on the partitioning of elements which have only a single valence state. The changes in melt composition had a significant effect on the partitioning of the trivalent rare earth elements.

The partitioning of the rare earth elements are highly dependent on the activity of melt components and specifically the activity of aluminium in the melt. This is due to the requirement of a charge balance to substitute a trivalent rare earth element into the divalent large cation site. This charge balance takes the form of an additional aluminium in the tetrahedral site and therefore, the partitioning of the rare earth elements will depend on the availability on aluminium in the melt, given by the activity (αAl_2O_3).

This melt activity component is difficult to calculate in complex systems and therefore the dependence of the rare earth element partitioning on the molar proportion of Al_2O_3 in the melt is Equation 36, which can be used to accurately predict the partitioning of any of the trivalent rare earth elements in anorthite. Additionally, we found that the traditional

lattice strain model is slightly less accurate than a simple polynomial for model the relationship between the partitioning of the trivalent rare earth elements and their ionic radius.

Scandium is also a trivalent cation but behaves differently to the rare earth element suite, having a much more compatible nature than if it partitioned on the M-site. It is therefore assumed that scandium is partitioning into the tetrahedral site and is much more compatible in this site.

Similarly, Mg and Be were also found to deviate from the parabola outlining the partitioning of the divalent cations into the M-site, and these elements too partition onto the tetrahedral site.

The partitioning of the small divalent cations into the tetrahedral site of the anorthite also depends heavily on melt composition. As the partitioning of magnesium is strongly affected by the changing melt composition, we propose that the dominant substitution mechanism for Mg substitution into anorthite takes the form; $CaMgSi_3O_8$. The partitioning of the larger divalent cations (Sr and Ba) do not show a strong dependence on melt composition which suggests that they substitute for calcium on the large cation site, and therefore do not require a charge balanced substitution.

This study has shown that melt composition is an important variable to consider for aliovalent substitution of trace elements in anorthite and may be a very important variable for aliovalent substitution in all minerals.

3.3 Controls on the partitioning of trace elements in $CaAl_2Si_2O_8$-$NaAlSi_3O_8$ plagioclase solid solutions

3.3.1 Introduction

More complex systems allow for more complex substitute mechanisms for trace elements. Plagioclase itself has a coupled substitution of $Ca^{2+} + Al^{3+} \rightarrow Na^{1+} + Si^{4+}$.

It is widely believed that crystal composition is much more important than melt compositions when considering trace element partitioning. The effect of anorthite content on the partitioning of elements into plagioclase has been studied through experiments in simple systems (Dohmen and Blundy, 2014; Sugawara, 2001) and more natural systems (Aigner-Torres et al., 2007; Bindeman et al., 1998; Bindeman and Davis, 2000; Ching-oh et al., 1974; Drake and Weill, 1975; Dunn and Sen, 1994; Longhi et al., 1976; Mollo et al., 2011; Tepley et al., 2010) and also through measuring natural occurring plagioclase/melt pairs (Dudas et al., 1971; Ginibre et al., 2002; Longhi et al., 1976; Norman et al., 2005; Pun et al., 1997).

The previous chapter outlined the dramatic effect melt composition has on the partitioning of trace elements into anorthite. This chapter will compare the melt effect to crystal composition changes due to the addition of $NaAlSi_3O_8$. Note that the considerably lower melting temperature of albite (melting point of 1118ºC) compared to anorthite (1550ºC) means that this effect cannot be studied isothermally (Deer et al., 1992).

Here we investigate the partitioning of trace elements in different plagioclase compositions grown at different pressures, temperatures, melt compositions and oxygen fugacities in the simple systems CaO-MgO-Al_2O_3-SiO_2-Na_2O (CMASN) and CaO-MgO-Al_2O_3-SiO_2-Na_2O-Fe_2O_3 (CMASNF). Some compositions were also borrowed from and.

The five CaO-Al_2O_3-SiO_2 (CAS) and four CaO-MgO-Al_2O_3-SiO_2 (CMAS) (Miller et al., 2006) compositions from the previous section are added upon in this section. These nine major element compositions, make up 30 individual experiments which vary in trace element concentrations, pressure and oxygen fugacity. An additional composition in the CMAS system is added in this series which is a composition of 50% pure diopside and 50% pure anorthite. Nine major element compositions in CaO-Al_2O_3-SiO_2-Na_2O (CMASN) space, four of which were replicas of experiments published in Dohmen and Blundy (2014). An additional nine in CaO-Al_2O_3-SiO_2-Na_2O-FeO (CMASNF) were also tested. We also look at the partitioning of plagioclase in a more natural compositions, BIR60 and BIR70 as well as the ALV-3352-7 composition from Aigner-Torres et al. (2007).

This experimental series consists of 31 starting compositions and 76 individual experiments (864 individual REE data points) ranging from An_{100}-An_{24} (Figure 27), 1130-1453 °C and pressures of 1atm and 5, 8, 10 and 11 kbar. Oxygen fugacity's also change with the highly oxidising Pt-PtO_2 buffers and gas mixes equal to fayalite-magnetite-quartz (FMQ) and iron-wüstite (IW) which makes this the most comprehensive study of trace element partitioning in plagioclase.

For an in-depth method please refer the methods chapter beginning on page 19. The experiments included in this section are summarised in Table 1 and Table 3 and full major and trace elements are given in Appendix 2 in Table 37 to Table 48.

The following section will discuss what controls the partitioning of each of the trace elements.

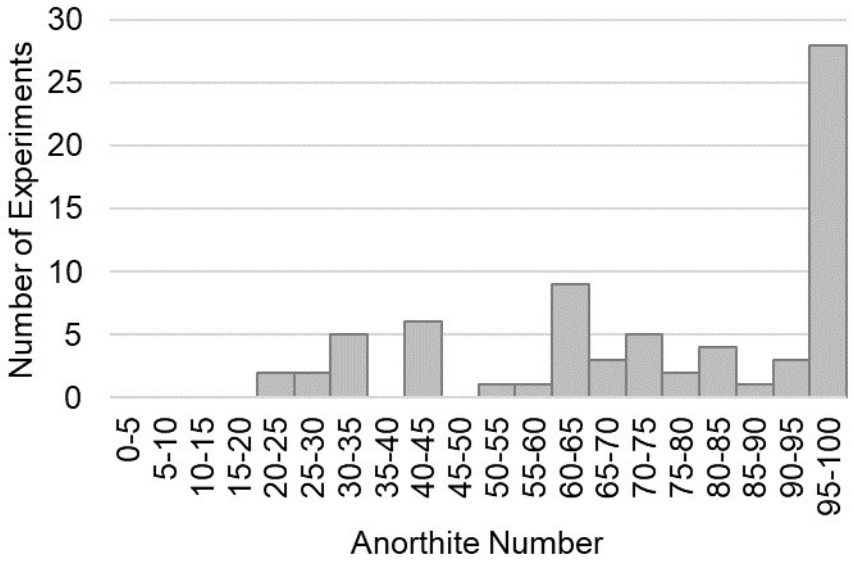

Figure 27: Frequency of experiments by An content

3.3.2 Monovalent cations

The partitioning of the monovalent cations into plagioclase requires no charge compensation (Equation 39)

Equation 39:
The stoichiometric control on the substitution of a monovalent cation into the large cation site of plagioclase

$$Li_2O_{\,melt} + NaAlSi_3O_{8\,Albite} = LiAlSi_3O_{8\,Li-plagioclas} + Na_2O_{\,melt}$$

This means that the partitioning of the monovalent cations should be heavily dependent on the anorthite content of the plagioclase.

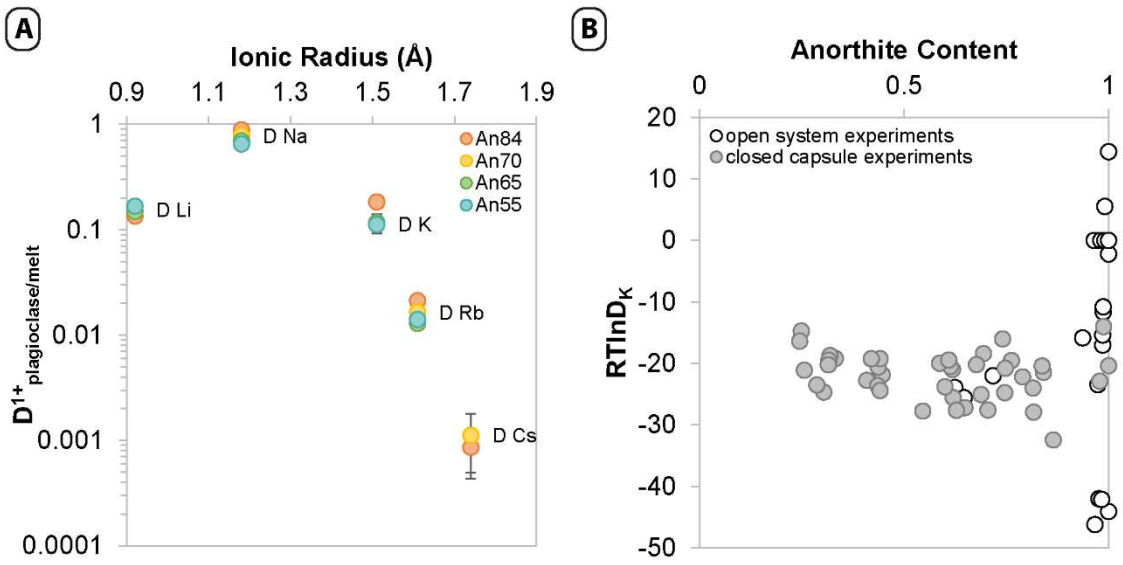

Figure 28: A) Partitioning of monovalent cations in experiment 20160928 at 1248 °C. Plagioclase compositions range from An_{84}-An_{55} where hotter colours represent higher anorthite contents. B) Partitioning of monovalent cations in open systems compared with closed systems

The alkali metal cations are known to be volatile at high temperatures and 1 atm pressure. Due to this, the experiments containing sodium were run in crimped or welded capsules, which effectively minimized volatile loss (Figure 28b). The anorthite-melt experiments that were run on wire loops were omitted from consideration in the following the alkali-metal cation partitioning results.

There is a linear correlation between the monovalent cation partitioning and the anorthite content of the plagioclase in the form:

$$RTlnD_i^{1+} = m * X_{An} + c$$

Table 11: linear fit for the monovalent cations partitioning into plagioclase

	m	X	c	χ^2	No. points	χ^2_v
$RTlnD_{Li}$	-1.91	X An	-20.18	411	39	11.11
$RTlnD_{Na}$	3.61	X An	-2.36	294	42	7.36
$RTlnD_K$	-6.42	X An	-17.83	210	41	5.39
$RTlnD_{Rb}$	-15.08	X An	-37.41	551	37	15.73
$RTlnD_{Cs}$	-50.01	X An	-54.64	359	32	11.98
linear method			total	1825	191	10.09

Using unique values for D_0^{1+}, r_0^{1+} and E^{1+}, the lattice strain model was fit to each experiment. This gives a good fit for all the data (χ^2_v=4.89) suggesting that all these elements are partitioning into the same site in the plagioclase. r_o^{1+} varies by less than 1% from 1.23 Å. The values for E, however are more variable (12%) with an average of 56 GPa. For this reason, r_o^{1+} was set a constant and E^{1+} was treated as a linear relationship with X_{An}:

Equation 40:
Lattice strain model for the partitioning of monovalent cations in plagioclase

$$\ln D_{Na} = \frac{5.08 - 3.04(X_{An})}{RT}$$

$$r_o^{1+} = 1.23$$

$$E^{1+} = 26.77 * X_{An} + 41.9$$

These parameters are substituted into the lattice strain model (Equation 6) which gives a fit of χ^2_v=11.08. The lattice strain model is less precise than individual linear fits.

Two recent models for the partitioning of monovalent cations in plagioclase are those of Wood and Blundy (2014) and Sun et al. (2017).

Equation 41:
Sun et al. 2017 monovalent lattice strain model

$$\ln D_o^{1+} = -9.99 + \frac{11.37 + 0.49 * P}{RT} * 10^4 + 1.7(X_{Ca})^2$$

$$r_o^{1+} = 1.213$$

$$E^{1+} = 47$$

The Sun et al. (2017) equation includes pressure in GPa and the atoms per formula unit of calcium in the plagioclase. Also the ideal radius and elastic moduli are set to constants. The Sun et al. (2017) model for the partitioning of monovalent cations in plagioclase (Equation 41) fits this data poorly, with an error of fit of χ^2_v=71.87. If each of the constants are treated as variables and minimised, the error between the calculated and observed partition coefficients improves the fit to χ^2_v =12.44.

Equation 42:
Wood and Blundy 2014 monovalent lattice strain model

$$\ln D_{Na} = \frac{2.1 - 9.4(X_{An})}{RT}$$

$$r_o^{1+} = \left(1.258 - 0.057(X_{An})\right) + 0.03$$

$$E^{1+} = 64$$

The Wood and Blundy (2014) model is similar, however calculates the partitioning of the monovalent cations from the partitioning of sodium. The only variable in this equation is the anorthite content of the plagioclase. The Wood and Blundy (2014) model (Equation

42) has an error of fit of χ^2_v =57.96 for the experiments presented here. Treating the constants as variables and minimising the error improves the fit to χ^2_v =12.45

The linear fits to each element are more accurate in predicting the partitioning of the monovalent cations than the models published by Sun et al. (2017) and Wood and Blundy (2014). The Wood and Blundy (2014) method, with the error minimised for this data set is the most accurate of the lattice strain models.

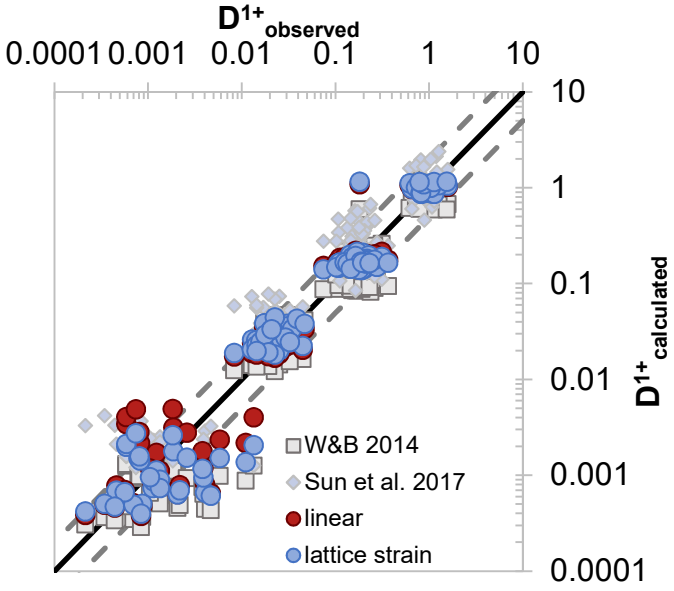

Figure 29: Comparison of the observed and calculated partition coefficients for the monovalent cations (Li, Na, K, Rb, Cs) using various models

Table 12: error of fit on the predictive models for the partitioning of monovalent cations in plagioclase. Less experiments as these experiments have 2 or less measured elements, and the lattice strain model cannot be fit precisely.

Equation	In text reference	Chi²	Red.Chi²	n exp	n point	n param.
individual fit		323	4.89	39*	186	120
Linear fit to each	Table 11	1825	10.09	42	191	10
Lattice strain	Equation 40	2060	11.08	42	191	5
Sun et al. 2017_minimised		2301	12.44	42	191	6
Wood and Blundy 2014_minimised		2316	12.45	42	191	5
Wood and Blundy 2014_published	Equation 42	10721	57.96	42	191	6
Sun et al. 2017_published	Equation 41	13295	71.87	42	191	6

3.3.3 Divalent cations

If the divalent cations are substituting onto the large cation site (M) of the plagioclase, the exchange should be a straight swap of Ca with the new divalent cation (M^{2+}).

Equation 43:
The stoichiometric control on the substitution of a divalent cation into the large cation site of plagioclase

$$CaAl_2Si_2O_{8\,plagioclase} + M^{2+}O_{melt} = M^{2+}Al_2Si_2O_{8\,Plagioclase} + CaO_{melt}$$

This exchange should depend on the calcium content of the melt as well as the An content of the plagioclase.

The partitioning of Sr (Figure 30) and Ba are highly correlated with the anorthite content of the plagioclase and have no correlation with the alumina and silica content of the melt

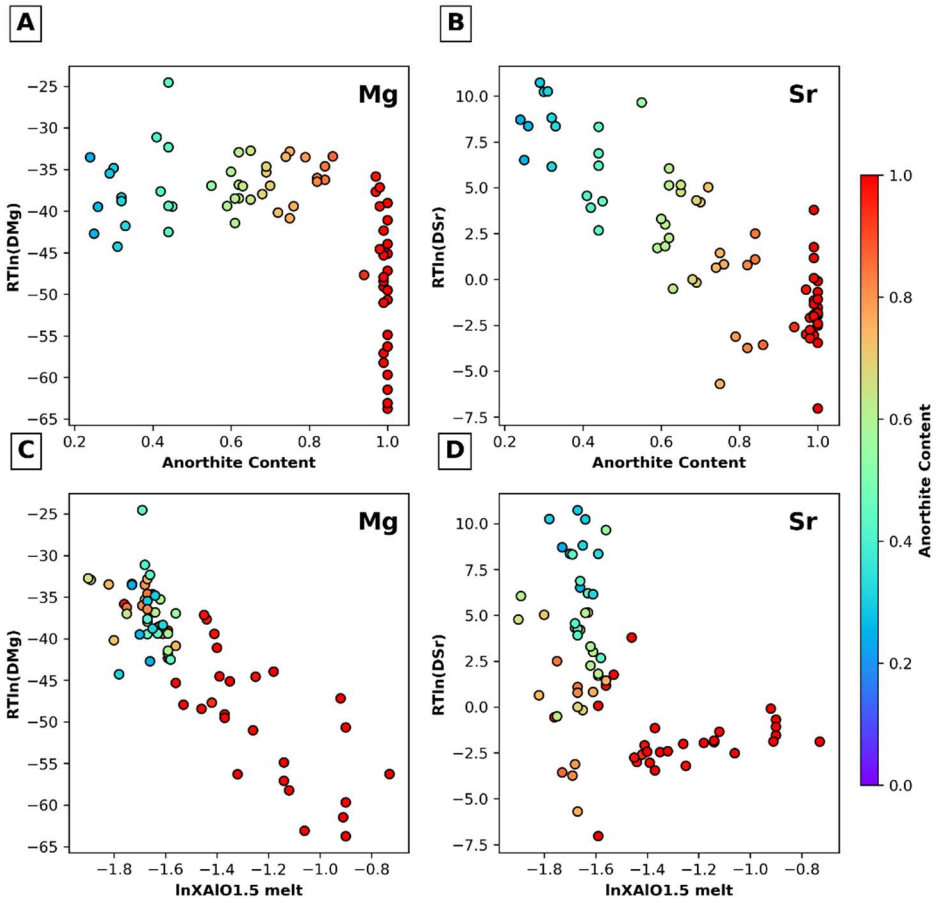

Figure 30: A comparison between the partitioning controls on Sr and Mg. The effect of anorthite content on the partitioning of A) Mg B) Sr. The effect of melt aluminium proportion on the partitioning of C) Mg and D) Sr.

As discussed previously, beryllium forms a very small 2+ cation, which is not known in VIII-coordination, which means it cannot substitute on the large cation (M) site. It is possible that Be exists in plagioclase in the tetrahedral (T) site which is IV coordinated. This means that the partitioning of beryllium should be dependent on melt composition.

Equation 44:
The stoichiometric control on the substitution of a divalent cation into the tetradhedral site of plagioclase

$$CaAl_2Si_2O_{8_{plagioclase}} + M^{2+}O_{melt} + SiO_{2_{melt}} = CaM^{2+}Si_3O_{8_{plagioclase}} + Al_2O_{3_{melt}}$$

It has been suggested that Mg also exists on the tetrahedral site (Fehr and Huber, 2001; Miller et al., 2006; Murakami et al., 1992; Sugawara, 2000). The partitioning of magnesium is highly correlated with the fraction of SiO_2 and $AlO_{1.5}$ in melt (Figure 30).

If all the Mg is assumed to be on the M site, the lattice strain fit becomes poor for Sr and Ca (Figure 31).

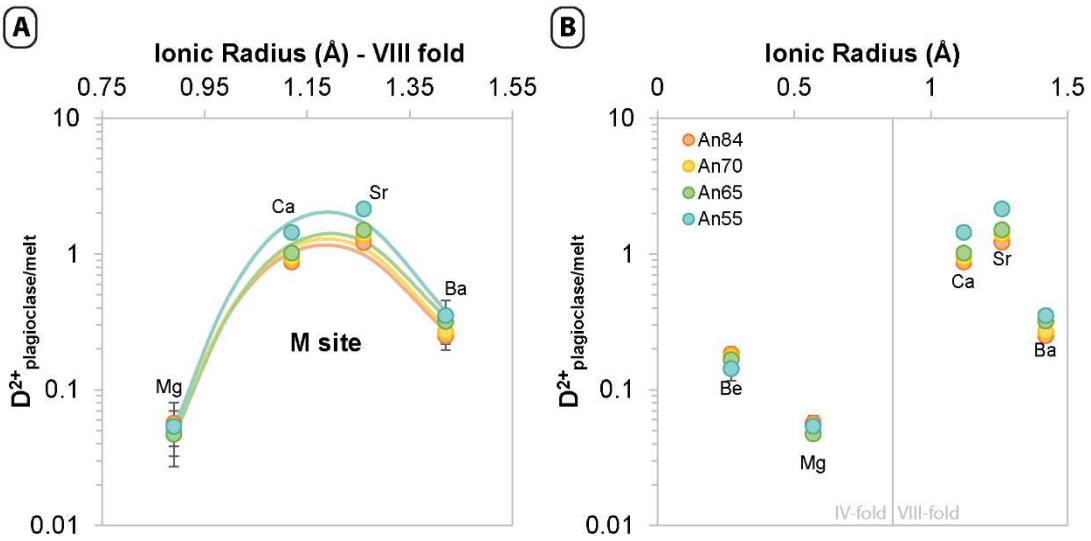

Figure 31: Possible sites for divalent cations in plagioclase a) Mg assumed to be entirely in M-site b) Mg assumed to be entirely in T-site. Experiment 20160928, 1248°C, 1 atm.

As there are only two divalent cations that could fit into the T-site, there are too many possibilities to fit the T-site lattice strain model accurately, however, the partitioning of Mg can be fairly accurately assumed by a linear regression of the melt fraction:

Equation 45:
A linear regression for the partitioning of Mg in plagioclase

$$RTlnD_{Mg} = -29.52 * \ln(XAlO_{1.5})_{melt} - 88.15$$

Where $XAlO_{1.5}$ is the mole fraction of $AlO_{1.5}$ in the melt. Similarly, the partitioning of Be into the T-site of plagioclase can be modelled by a similar linear relationship (Table 13).

Table 13: Linear method for estimating the partition coefficients for the divalent cations in plagioclase

	m	X	c	chi^2	n	reduced chi^2
RTlnD$_{Be}$	-9.08	lnX[AlO1.5]melt	-28.58	829	50	17.28
RTlnD$_{Mg}$	-29.52	lnX[AlO1.5]melt	-88.15	1410	70	20.73
RTlnD$_{Sr}$	-14.33	X An	12.75	1675	74	23.26
RTlnD$_{Ba}$	-24.99	X An	-3.03	1429	75	19.05
linear method			T site	229	120	19.30
			M site	3104	149	21.41
			Total	5343	269	20.47

Using the linear relationships of the small divalent cations with the proportion of alumina in the melt, the divalent partitioning in the T-site can be modelled with an accuracy of χ^2_v=19.30. The large divalent cation partitioning into the M-site can be modelled with their linear relationship with the anorthite content of the plagioclase, with an error of χ^2_v=21.41.

Fitting the three divalent cations that exist on the M site of plagioclase (Ca, Sr, Ba) to a unique lattice strain model gives a perfect fit ($\chi^2 = 3.26*10^{-10}$) which suggests that the lattice strain model can be used for these elements. Over the 76 experiments, r_0^{2+} have an average of 1.20 and varies by only 2%. This variation is visibly correlated with the anorthite content of the plagioclase. E^{2+} has a much larger variation of 138 GPa ± 12%.

Predicting the divalent cation partitioning into the M site using the lattice strain model and the relationship between the parameters, temperature and anorthite content we arrive at the equation:

Equation 46
A new lattice strain model for the divalent cations on the M site.

$$D_0^{(M)2+} = exp\left(\frac{10.6 - 8.5(X_{An})}{RT}\right)$$

$$r_o^{2+} = 1.26 - 0.08(X_{An})$$

$$E^{2+} = 138$$

This fits the data with a χ^2_v=21.8 which is less precise than the linear approach for Sr and Ba.

The lattice strain model suggested by Sun et al. (2017) fits this data very poorly. This model assumes the partitioning of Mg on the M site and gives an error of χ^2_v =731.6 including Mg and χ^2_v =644 omitting Mg.

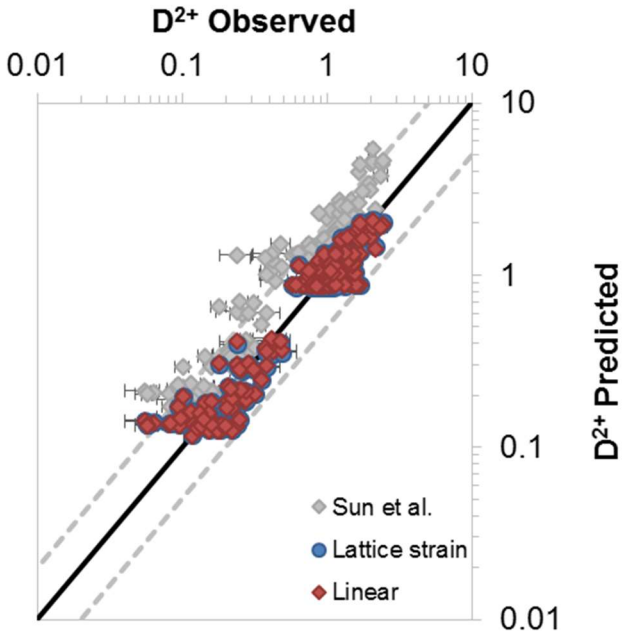

Figure 32: Error between observed and calculated partitioning of Ba in plagioclase

In the case of the divalent cations, the lattice strain model is very accurate therefore could be used to predict the partitioning of Ra, which is not measured in this study but will also partition on the M site.

Elements such as Zn are known to partition onto the T site in plagioclase (Fehr and Huber, 2001) and have a very similar ionic radius to Mg. This would be an ideal candidate to further constrain the partitioning of the divalent cations on the T site.

Cd is another divalent cation and it has an ionic radius larger than Mg. It is possible that due to its large size, Cd will partition onto the M site of plagioclase and allow for refinement of the lattice strain model for divalent cations on the M site in plagioclase.

3.3.4 Rare earth element lattice strain model

This data comprise 896 individual rare earth element partition coefficients (omitting Y, Ce and Eu) in 72 individual experiments which makes it the largest database of plagioclase/melt coefficients. Uniquely compared to previous work, all of the rare earth elements were measured. 34 of these experiments are CAS in composition and were discussed in the previous section.

The partitioning of the REEs in plagioclase defines only one limb of the Onuma curve (Figure 33) which suggests that the REEs are all smaller than the ideal radius for trivalent partitioning in plagioclase.

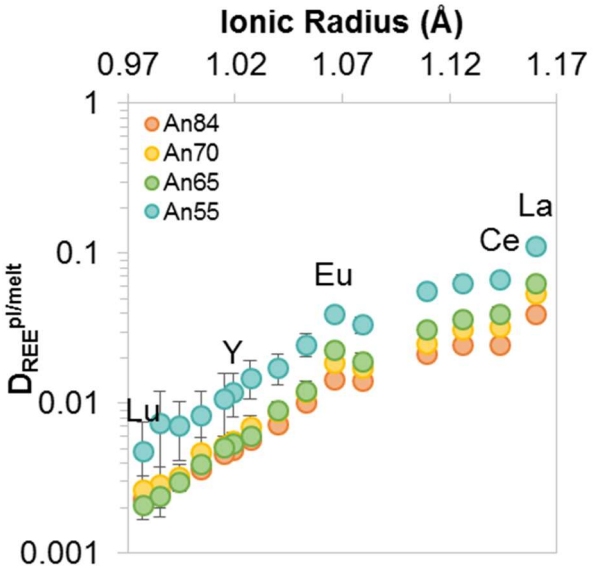

Figure 33: The partitioning of rare earth elements (REE) and yttrium into plagioclase of different compositions at 1248°C and 1 atm pressure in air.

The rare earth elements are assumed to partition on the M site of plagioclase, but as they are trivalent cations, their substitution requires a charge balance.

The most likely form this will take is the following exchange:

Equation 47
Stoichiometric control of the partitioning of rare earth elements into anorthite

$$[\mathrm{REE}]\mathrm{O}_{1.5_{melt}} + \mathrm{CaAl_2Si_2O_{8}}_{plagioclase} + \mathrm{AlO_{1.5}}_{melt} = [\mathrm{REE}]\mathrm{Al_3SiO_{8}}_{plagioclase} + \mathrm{CaO}_{melt} + \mathrm{SiO_2}_{melt}$$

Due to the requirement of a charge balance, the partitioning of the rare earth elements will be dependent on the activity of the melt components. The previous section outlined a new lattice strain model for the prediction of the rare earth elements in anorthite based on alumina activity in the melt and anorthite number (Equation 35). As the system becomes more complex, it becomes increasingly difficult to accurately calculate the activity of each component in the melt. Instead, the mole fraction of the single cation component (i.e. X $AlO_{1.5}$) is used as a proxy for the activity. The relationship between the partitioning of lanthanum and the aluminium content of the melt remains even when the system becomes more complex (Figure 34d).

The partition coefficients for each experiment were modelled by both the lattice strain model and an orthogonal polynomial equation (Equation 23). The reduced chi squared (χ^2_ν) for 72 individual pl/melt experiments is; 0.44 for the lattice strain model and 0.47

for the orthogonal polynomial equation with 5 parameters becomes less accurate with 3 parameters (χ_v^2=0.51).

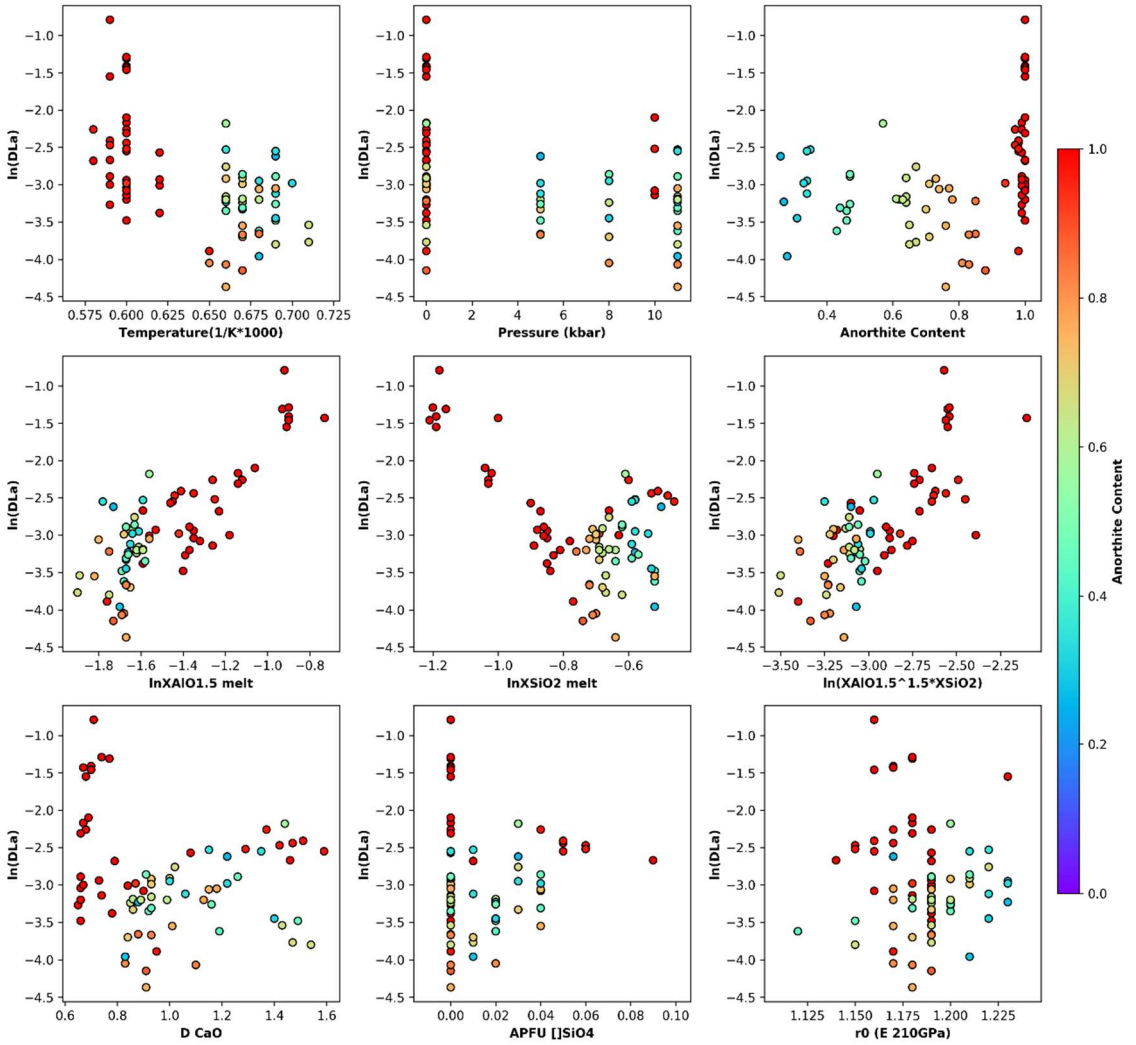

Figure 34: ln D_{La} (observed) plotted against some compositional variables. Top, left to right; inverse temperature, pressure (kbar) and anorthite content, middle row, left to right; natural log of the molar proportion of $AlO_{1.5}$ in the melt, natural log of the molar proportion of SiO_2, natural log of the melt exchange ($AlO_{1.5}^{1.5}$*SiO_2) from Equation 32. Bottom row; the partitioning of calcium, the atoms per formula unit of large cation vacancies, the ideal cation radius from the lattice strain model assuming E as a constant at 210 GPa

In the previous section, the relationship between the melt activity of alumina and partitioning of the rare earth elements was outlined (Equation 32). This equation is based in the CAS system and is expanded upon to include a total of 72 experiments. The least-squares fit for these new experiments gives the parameters:

Equation 48:
Parameters for the orthogonal polynomial for the partitioning of REE between plagioclase and melt.

$$\lambda 0 = \ln XAlO_{1.5_{melt}} * 2.19(\pm 0.08) + 0.84(\pm 0.13)$$

$$\lambda 1 = 14.86(\pm 0.31)$$

$$\lambda 2 = -64.68(\pm 5.58)$$

Predicting the rare earth element partitioning from the melt composition and anorthite content gives a very good fit (χ^2_v=37.83). The lattice strain model with E and r_o^{3+} as 221 and 1.17 respectively, and D_o^{3+} calculated from the aluminium content of the melt gives an almost identical fit (χ^2_v=37.40)

Equation 49:
A lattice strain model for the rare earth element partitioning in plagioclase

$$\ln D_{La}^{3+} = \ln XAlO_{1.5_{melt}} * 1.92(\pm 0.08) - 0.04(\pm 0.12)$$

$$r_o = 1.17(\pm 0.01)$$

$$E = -221(\pm 17)$$

Which substitutes into the lattice strain model Equation 6.

To improve the equation further we can investigate the stoichiometric control of rare earth elements partitioning in plagioclase (Equation 47). This stoichiometric control can be written out as a thermodynamic based equation:

Equation 50:
The thermodynamic equilibrium constant for the substitution of REE in anorthite

$$D_{REE}^{An/melt} = \frac{X_{[REE]Al_3SiO_8}^{plagioclase}}{X_{[REE]O_{1.5}}^{melt}} = \exp\left(\frac{-\Delta G^0}{RT}\right) * \left(\frac{\gamma_{[REE]O_{1.5}}^{melt}}{\gamma_{[REE]Al_3SiO_8}^{plagioclase}}\right) * \left[\frac{\alpha AlO_{1.5_{melt}}}{\alpha SiO_{2_{melt}}}\right] * \left(\frac{\alpha CaAl_2Si_2O_{8_{An}}}{\alpha CaO_{melt}}\right)$$

Where the change in free energy ($\exp\left(\frac{-\Delta G^0}{RT}\right)$) is calculated by the lattice strain theory. The last term in this equation is equivalent to the partition coefficient of calcium between plagioclase and melt. Therefore the new lattice strain model, incorporating the stoichiometric control takes the form:

Equation 51:
A stoichiometric control equation for the partitioning of REE in plagioclase

$$\ln D^{pl/melt}_{REE} = \ln D_0^{3+} + \left(\frac{-910.17\ E}{T}\right) * \left[\frac{1}{2} r_0 * (r_i - r_0)^2 + \frac{1}{3} * (r_i - r_0)^3\right] + \ln\left(\frac{XAlO_{1.5melt}}{XSiO_{2melt}}\right) + \ln D_{Ca}^{\frac{pl}{melt}}$$

Where:

$\ln D_0^{3+} = 7.89(\pm 0.40) - 1.66(\pm 0.07) * X_{An}$

$r_0 = 2.07(\pm 0.03) * (1 - 0.005(\pm 0.02) * X_{Ab})$ and

$E = 23(\pm 1)$.

This equation predicts all plagioclase experiments with a reduced chi squared of 24.40. These are unrealistic E and r_o values. R_o^{3+} are should be a similar radius to calcium (1.12 Å) or sodium (1.18 Å) because the rare earth elements are substituting into the M-site. These unrealistic values are caused by only one limb of the parabola being defined. To fix the parabola at more realistic values, the equation can be modified to determine the ideal radius compared to that of lanthanum in the equation:

Equation 52:
A stoichiometric control equation for the partitioning of REE in plagioclase, relative to lanthanum

$$\ln D^{pl/melt}_{REE} = \ln D_0^{3+} + \left(\frac{-910.17\ E}{T}\right) * \left[\frac{r_0}{2}(r_{La}^2 - r_i^2) + \frac{1}{3}(r_i^3 - r_{La}^3)\right] + \ln\left(\frac{XAlO_{1.5melt}}{XSiO_{2melt}}\right) + \ln D_{Ca}^{\frac{pl}{melt}}$$

Where:

$\ln D_0^{3+} = 1.38(\pm 0.32) - \frac{0.55(\pm 0.05)}{T} * 10^4$

$r_0 = 1.17(\pm 0.008) * (1 - 0.019(\pm 0.004) * X_{Ab})$ and

$E = 235(\pm 16)$.

This equation predicts all plagioclase experiments with a reduced chi squared of 34.25

There have been some indications that the mixing of the rare earth elements can be hindered by REE-SiO_2 relationships in the melt (Evans et al., 2008). Therefore, we

investigate the same stoichiometric control with the addition of a $[X_{SiO2}]_{melt}$ term that represents $\left(\frac{\gamma^{melt}_{[REE]O_{1.5}}}{\gamma^{plagioclase}_{[REE]Al_3SiO_8}}\right)$ in the thermodynamic relationship.

Equation 53:
A stoichiometric control equation for the partitioning of REE in plagioclase, relative to lanthanum. Including a REE-mixing component in the melt

$$\ln D^{pl/melt}_{REE} = \ln D_0^{3+} + \left(\frac{-910.17\ E}{T}\right) * \left[\frac{r_0}{2}(r_{La}^2 - r_i^2) + \frac{1}{3}(r_i^3 - r_{La}^3)\right] + \boldsymbol{\gamma_{REE}} + \ln\left(\frac{XAlO_{1.5melt}}{XSiO_{2melt}}\right) + \ln D^{\frac{pl}{melt}}_{Ca}$$

Where

$\ln D_0^{3+} = 2.60(\pm 0.37) - \frac{0.65(\pm 0.05)}{T} * 10^4$

$\boldsymbol{\gamma_{REE}} = 0.77(\pm 0.13) * \ln(XSiO_{2melt})$

$r_0 = 1.18(\pm 0.01) * (1 - 0.009(\pm 0.005) * X_{Ab})$ and

$E = 208(\pm 17)$.

This equation predicts all plagioclase experiments (864 data points) with a reduced chi squared of 32.99.

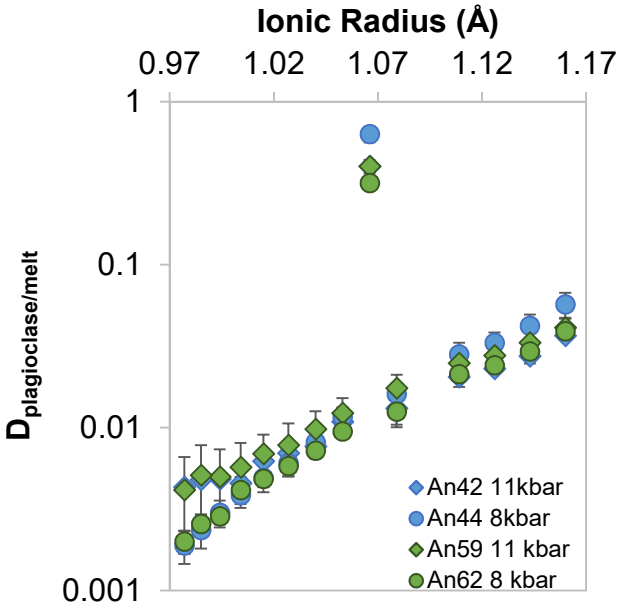

Figure 35: Effect of pressure on the partition of the rare earth elements. Two experiments of very similar composition and temperature but 2kbar different in pressure.

The heavy rare earth elements seem to increase in compatibility at high pressures (Figure 35), although the uncertainty on the heavy rare earth elements is quite large. Incorporating pressure into Equation 53 does not improve the fit.

Comparing this equation to the published models (Dohmen and Blundy, 2014; Sun et al., 2017; Wood and Blundy, 2014), the stoichiometric control equation (Equation 53) is by far the most accurate. Both the Wood and Blundy (2014) and Sun et al. (2017) equations use only crystal chemistry components, while the Dohmen and Blundy (2014) study uses the partition coefficients of calcium and sodium, which cannot be measured when no melt is present. All the published models fit the data presented here poorly. To test the robustness of the other studies' methods we also minimise the error by changing each of the constants in these equations to fit the data presented in this thesis.

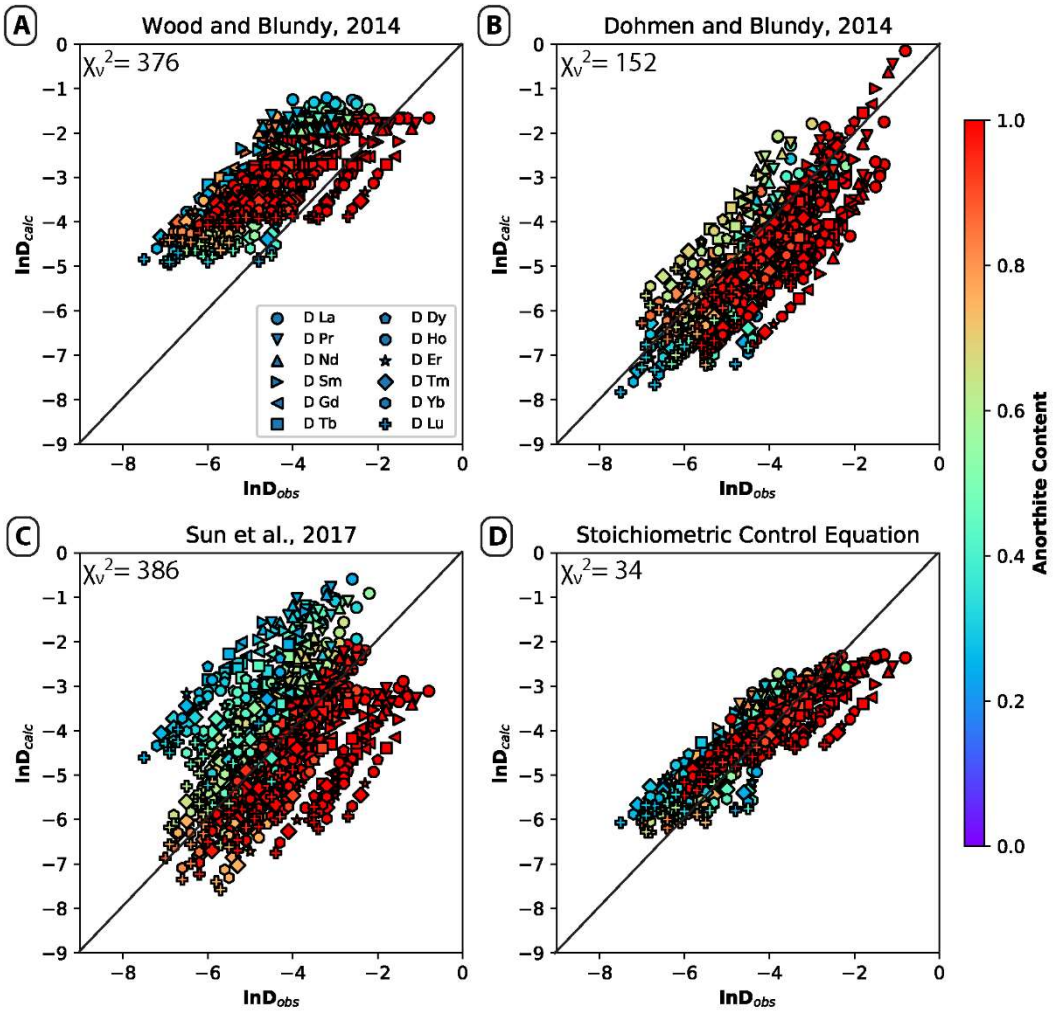

Figure 36: Mismatch between the natural log of the observed rare earth element partition coefficient against predictive models for rare earth element partitioning. Omitting cerium, europium and yttrium. A) Wood and Blundy (2014) (Equation 26) B) Dohmen and Blundy (2014), (Equation 25) C) Sun et al. (2017) (Equation 24) D) This study, the stoichiometric equation (Equation 52).

The Dohmen and Blundy (2014) and Wood and Blundy (2014) equations improve to reduced chi squared of χ^2_ν = 61 and 49 respectively. The Dohmen and Blundy (2014) equation was fit to 3 fewer experiments as sodium was not measured by LA-ICP-MS and was below detection on EPMA for these samples. Sun et al. (2017) is the most accurate of all the published equations when the model parameters are edited. This minimised equation takes the form:

Equation 54:
Modified Sun et al. (2017) equation for the partitioning of REEs in plagioclase using only crystal chemistry components

$$\ln D_0^{3+} = 8.76(\pm 0.53) + \frac{-13.55(\pm 0.64) - 0.33(\pm 0.05)P^2}{RT} * 10^4 - 1.14(\pm 0.09)(XCa_{Pl})^2$$

$$r_0^{3+}(\text{Å}) = 1.27(\pm 0.04)$$

$$E^{3+}\ (GPa) = 84(\pm 16)$$

Which substitutes into the simplified lattice strain model (Equation 5). This equation has pressure in GPa, temperature in kelvin and X_{Ca} represents the amount of calcium per 8 oxygens in plagioclase. This equation predicts the data with a precision of χ^2_ν=36.

Table 14: Predicting the rare earth element partitioning from melt and crystal compositions are associated error.

Equation	In text reference	χ^2_ν	n_{exp}	n_{param}
Stoichiometric control equation inc. REE mixing	Equation 53	32.99	72	6
Stoichiometric control equation	Equation 52	34.25	72	5
Sun et al. 2017 minimised	Equation 54	36.84	72	6
CAS method	Equation 49	37.40	72	4
Orthogonal polynomial 3 parameters	Equation 48	37.83	72	4
Wood & Blundy 2014 minimised		49.24	72	6
Dohmen and Blundy, 2014 minimised		61.17	69	6
Dohmen and Blundy, 2014 published	Equation 25	152.1	69	6
Wood & Blundy 2014_predicted published	Equation 26	376.9	72	6
Sun et al. 2017 published	Equation 24	385.6	72	6

Rare earth element ratios

The rare earth elements are highly dependent on melt composition due to the stoichiometric control, however as each of the rare earth elements are chemically similar, they will each be affected the melt composition equally. If the ratios of the rare earth elements are taken, this will cancel out the effect of the stoichiometric control, leaving only crystal chemistry and formation conditions to affect the rare earth element ratio partitioning patterns. Gd was chosen as the normalising rare earth element as it is in the

middle of the pattern. These partition coefficient ratios will be given the notation; $K_{REE/Gd}^{pl/melt}$.

These ratios are described by orthogonal polynomials. The λ0 and λ2 (magnitude and curvature) do not have strong relationships with any tested variables. The λ1 (slope of the pattern) is strongly dependant on anorthite content.

Equation 55:
A polynomial to describe rare earth element ratios

$$\lambda 0 = -0.20(\pm 0.01)$$

$$\lambda 1 = -9.96(\pm 2.8) - 2.49(\pm 0.73) * X_{An} + 4.19(\pm 0.36) * \frac{10^4}{T} - 0.21(\pm 0.02) * P$$

$$\lambda 2 = -35.19(\pm 2.07)$$

$$\lambda 3 = 154(\pm 37)$$

These equations fits the rare earth element ratios normalised to $D_{Gd}^{pl/melt}$ with an error of χ^2_v=1.13.

Trivalent cations

The trivalent cations that are not in the rare earth element suite are Sc, Fe (in Pt-PtO_2 buffered experiment), Ga, Y and In. Y is widely considered a pseudo rare earth element, with Sc also occasionally being included as a rare earth even though Sc is a much smaller cation.

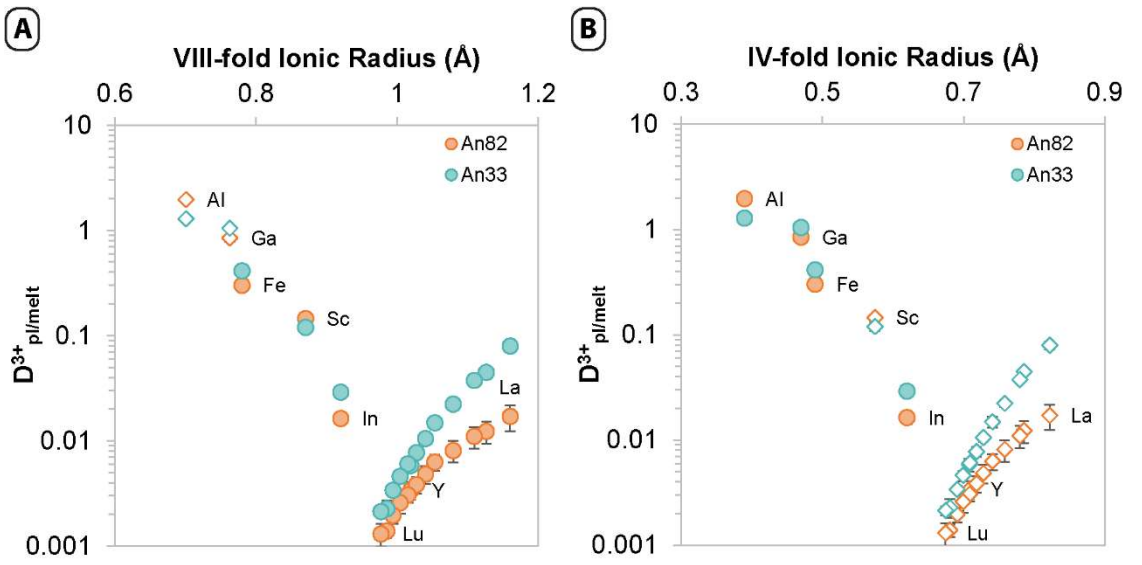

Figure 37: trivalent cation partitioning in Pt-PtO_2 buffered experiments at 11kbar and 1235°C in melt compositions Ab10-Fe5 (An_{82}) and Ab70-Fe1 (An_{33}). A) assuming all VIII-fold coordination B) assuming all IV fold coordination. Open diamonds are calculated ionic radius. Filled circles are published ionic radius from Shannon (1976)

In these experiments, Y behaves very similarly to the rare earth elements however Sc does not (Figure 37). This may indicate that Sc is partitioning onto the tetrahedral site rather than the large cation site, however the Shannon radius database does not include data for IV-fold coordinated Sc.

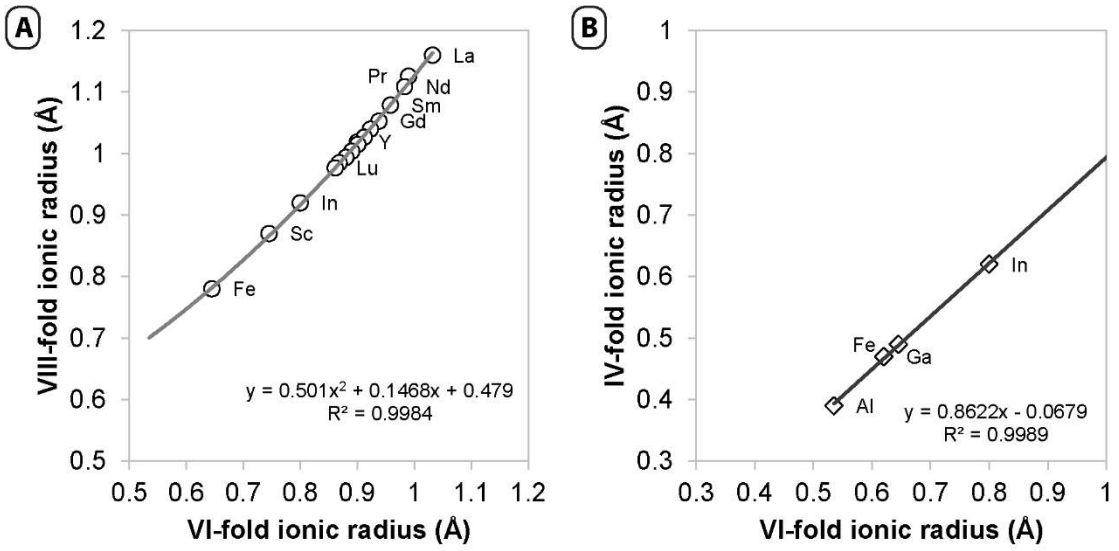

Figure 38: relationships between ionic radii of the trivalent cations in different coordination (Shannon, 1976). A) VI-fold and VIII-fold coordination b) VI-fold and IV-fold coordination.

The size of the ionic radius in different coordination have an intrinsic relationship (Figure 38) and using this relationship we can calculate likely sizes for the trivalent cations in both VIII and IV coordination.

If the lattice strain theory is correct, it is most likely that the rare earth elements and yttrium define the trivalent cations in the M site while Al, Ga, Fe^{3+}, Sc and In define the lattice strain of trivalent cations in the tetrahedral site.

If this is true and the relationship between the ionic radius of the VI-fold and IV-fold sites is also correct than the ionic radius for Sc in tetrahedral coordination is 0.57 Å.

If the smaller trivalent cations are partitioning onto the tetrahedral site, they will exchange for aluminium in the form:

Equation 56:
The partitioning of trivalent cations in the tetrahedral site of plagioclase

$$CaAl_2Si_2O_{8_{plagioclase}} + T^{3+}{}_2O_{3_{melt}} = CaT^{3+}{}_2Si_2O_{8_{plagioclase}} + Al_2O_{3_{melt}}$$

$$D_{REE}^{An/melt} = \frac{X_{Ca[Sc]AlSi_2O_8}^{plagioclase}}{X_{Sc\ 1.5}^{melt}} = \exp\left(\frac{-\Delta G^0}{RT}\right) * \left(\frac{\gamma_{[Sc]O_{1.5}}^{melt}}{\gamma_{Ca[Sc]AlSi_2O_8}^{plagioclase}}\right) * \left(\frac{\alpha CaAl_2Si_2O_{8_{An}}}{\alpha Al_2O_{3_{melt}}}\right)$$

If the trivalent cations partition on the M site, their partitioning will be correlated with the melt components and the partitioning of calcium in plagioclase (Equation 47). If the trivalent cations partition on the tetrahedral site, their partitioning should correlate with the partitioning of aluminium in plagioclase.

Comparing An_{82} and An_{33} at 1235°C and 11 kbar, it appears that the partitioning of Al and Sc increase with increasing anorthite content of plagioclase while Fe^{3+}, In and Ga show the inverse trend (Figure 37).

Comparing all experiments, aluminium and gallium are highly correlated with the aluminium content of the melt, with aluminium also highly correlated with anorthite content (Figure 39). Sc is not strongly correlated with melt composition or anorthite content but is correlated to the temperature of the system (Figure 40).

Indium was only measured in 42 of 76 experiments, and these measurements have high standard deviations (average >50% of D_{In}). There is no obvious relationship between indium and any of the tested variables.

Ga can be confidently assigned to the tetrahedral site of plagioclase and Y to the M-site of the plagioclase. Due to their size, Sc and In most likely also partition onto the tetrahedral site (Figure 37).

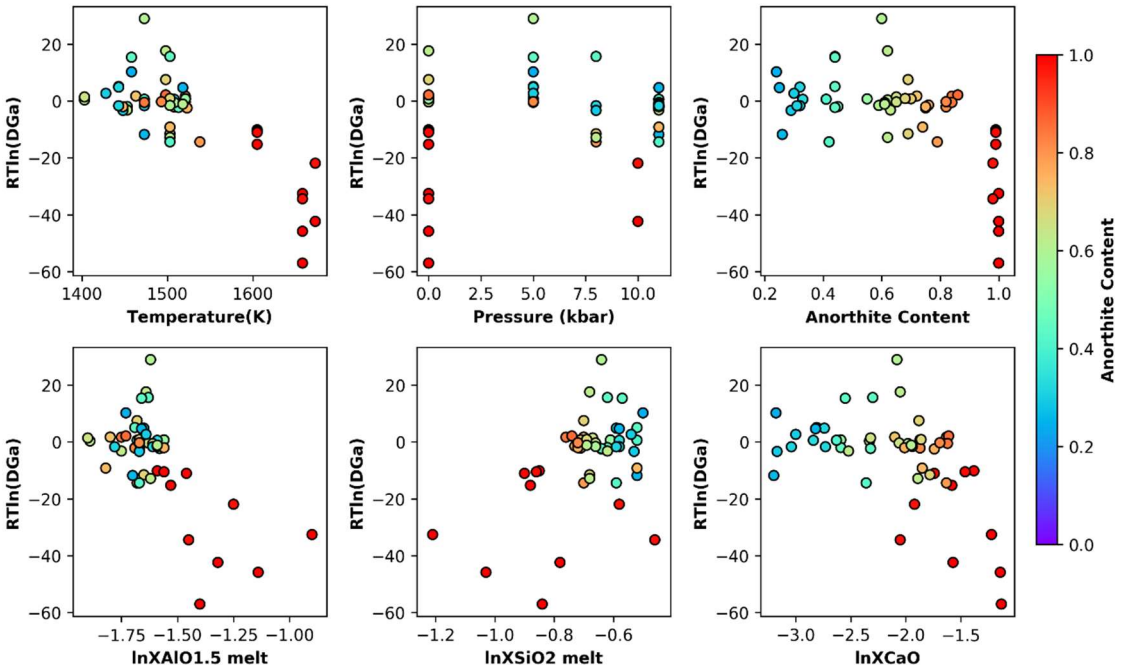

Figure 39: partitioning of Gallium against tested variables. The second row compares the melt components. Melt components are the natural logs of the mole proportion of single cation components in the melt.

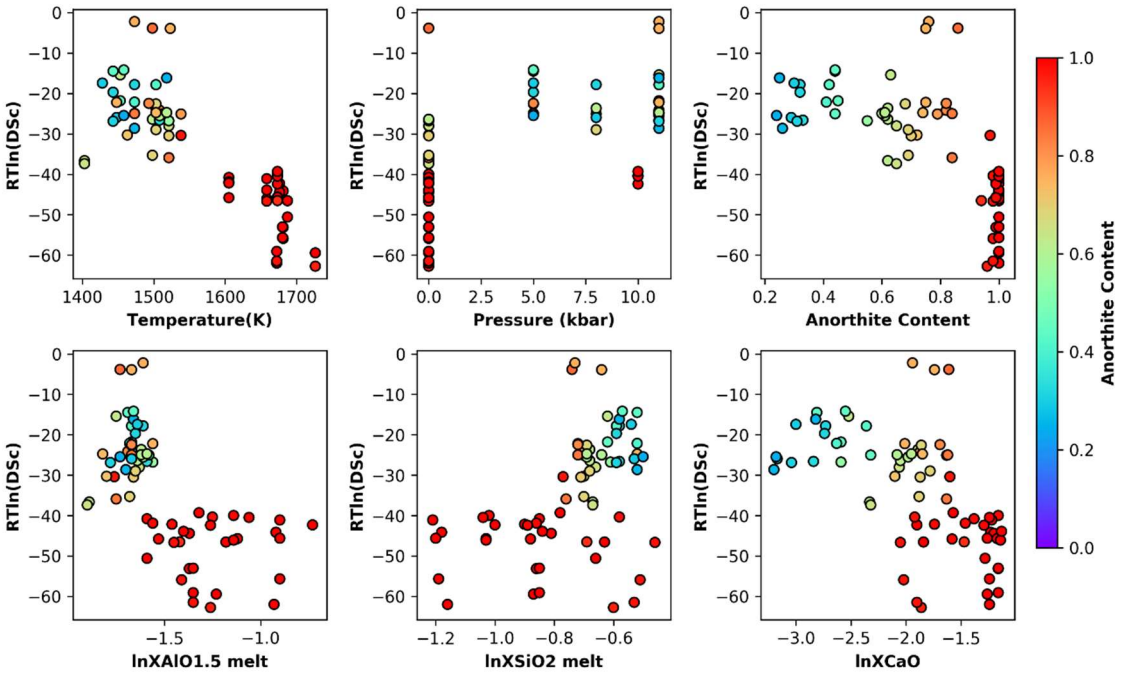

Figure 40: partitioning of scandium against tested variables. The second row compares the melt components. Melt components are the natural logs of the mole proportion of single cation components in the melt.

3.4 Discussion

This study covered a wide range of plagioclase compositions, however focusses on the pure anorthite compositions (Figure 27). This is to ensure the understanding of the partitioning of trace elements into plagioclase in the simplest of systems. This information can then be extrapolated to more complicated systems.

It has been shown in this chapter that melt composition plays an important role in the partitioning of trace elements in minerals; especially when the trace element substitutes into a site that usually holds a cation of a different charge, e.g. $REE^{3+} \rightarrow Ca^{2+}$ in plagioclase. Melt compositions vary in nature and rocks that produce plagioclase exist (usually) in the range of 45 wt. % SiO_2 and 70 wt. % SiO_2 in bulk rock composition. Pure anorthite has a liquidus temperature of 1550 °C while pure albite has a melting point of 1100 °C (Deer et al., 1992). This means that plagioclase can be formed at a very wide range of temperatures and melt compositions and therefore a wide range of temperatures and compositions were tested in this study.

This study covers a temperature range of 1130 °C and 1453 °C and melt silica values (post plagioclase growth) of between 31 and 69 wt. % SiO_2. For conversion to "bulk rock" silica values we need to account of the silica in plagioclase and the approximate proportion of plagioclase growth which works out to an additional ~3 wt. % SiO_2. Therefore this experimental range is between ~34 and ~72 wt. % SiO_2. This shows that the experimental series presented in this thesis represents the conditions under which most plagioclase forms.

Oxygen fugacity was also tested in this study at air, quartz-fayalite-magnetite (QFM) buffer and that extremely oxidising Pt-PtO_2 buffer. The QFM buffer is more relevant to natural systems as mid-ocean-ridge basalts have been measured to be 0.41 log units below this buffer (Bezos and Humler, 2005). The Pt-PtO_2 buffer is less relevant to natural systems, however as it is extremely oxidising, it should cause all the multivalent cations (e.g. Fe^{3+}, Eu^{3+}, Ce^{4+}) to exist in their most oxidised form. This allows for the assessment of the partitioning of these elements without the uncertainty of multiple valence states.

The pressures tested in this study range from 1 atm to 11 kbar. This upper range represents mid-crustal depths, approximately ~35km. This is relevant to natural systems as all rocks containing plagioclase are formed in crustal conditions.

Ideally, this study would continue and investigate compositions and conditions that replicate natural systems. Although the pressures, temperatures and bulk silica

components of the melt are relevant to natural systems, key components such as water, and complex melt compositions have not been covered in this experimental series.

The addition of more components will increase the complexity of the melt structure and potentially the formation conditions of plagioclase. For example, the addition of water is known to supress both the liquidus and the solidus at a given pressure (Winter, 2012). This means that that the effect of temperature could be tested for much lower temperatures, as well as the effect of water itself on the partitioning of trace elements in plagioclase. Water is suggested to reduce the partitioning of trace elements in minerals, such as in clinopyroxene (Wood and Blundy, 2014) however this may be due to water being implicitly tied to formation temperature for minerals i.e. as you add water you decrease the formation temperature and decrease the partition coefficient. Whether the effect of water itself can be disentangled from its ability to decrease formation temperatures would be an interesting avenue for future investigation.

This study however serves as a basis to expand upon and increase our understanding of partitioning of trace elements in plagioclase in a systematic way.

Other authors have also conducted plagioclase + melt experiments in a variety of conditions (Aigner-Torres et al., 2007; Bédard, 2006; Bindeman et al., 1998; Bindeman and Davis, 2000; Blundy and Wood, 1991; Ching-oh et al., 1974; Coogan, 2011; Dohmen and Blundy, 2014; Drake and Weill, 1975; Longhi et al., 1976; Namur et al., 2012; Nielsen et al., 2017; Severs et al., 2009; Sun et al., 2017; Tepley et al., 2010). These partition coefficients can be added to the models presented here, either to test this models validity and/or increase the efficacy.

3.5 Conclusions

This study is the collation of 72 experiments ranging from An_{100}-An_{24}, over a temperature range of 320°C, up to 11 kbar pressure and four different relative oxygen fugacities which makes this the most comprehensive study of trace element partitioning in plagioclase.

The partitioning of monovalent, divalent and trivalent cations has been thoroughly investigated, outlining the factors that have the most significant impact on partitioning. It has been shown conclusively that melt composition plays a very important role in the partitioning of trace elements into plagioclase. This is especially true when the substitution requires a charge balance.

The monovalent cations all substitute onto the M-site of plagioclase and can be accurately modelled using individual linear fits with their relationship with the anorthite content of

plagioclase. The monovalent cations are highly susceptible to volatile loss at high temperatures and low pressures which gives inaccurate partition coefficients. This volatile loss was minimised in this experimental series so allow for highly precision on partitioning on these elements.

For the divalent cations, Mg and Be favour the tetrahedral site while Ca, Sr and Ba prefer the M-site. The divalent cations are best described by individual linear regressions. The divalent cations on the M site is linearly correlated with anorthite content of the plagioclase. The divalent cations on the tetrahedral site are linearly correlated with aluminium content of the melt.

The rare earth elements are a group of trivalent cations that substitute into the large cation site. This requires a charge balance in the form of Equation 47; where an extra aluminium is incorporated into the plagioclase to balance the REE. The partitioning of the rare earth elements into plagioclase can be most accurately predicted by Equation 53, a stoichiometric control based equation using the melt components.

When the effect of melt composition is removed, in the case of the REE ratios, the partitioning of the rare earth elements depends mostly on anorthite content and is relatively insensitive to temperature. This has been noted before by Drake and Weill (1975).

The rare earth element partitioning in minerals is a potential candidate for a precise geothermometer (Liang et al., 2013; Sun and Liang, 2017) as they define easily interpretable patterns and generally, their partitioning changes with temperature. As the partitioning of the REE between plagioclase and melt is insensitive to temperature, it does not make a good candidate for geo-thermometry.

The other trivalent cations not in the rare earth element suite show much higher compatibilities and very little melt dependence. This suggests that they are partitioning onto the tetrahedral site rather than the M-site and if so, Sc^{3+} in tetrahedral coordination would have an ion radius of approximately 0.57 Å.

Even though plagioclase is a relatively simple mineral, the trace element partitioning into this mineral is very complicated. The sites and mechanisms of substitution have been assumed incorrectly for many of the trace elements which highlights the importance of rigorous experimental investigations of trace element partitioning in mineral phases.

CHAPTER 4. DIFFUSION IN PLAGIOCLASE

4.1 Introduction

The trace element partitioning of plagioclase in equilibrium system was described in the last chapter, however natural systems and experiments vary in a key aspect, their cooling rate. In partitioning experiments, it is ideal to quench the co-existing equilibrium melt into a glass so that the correct partition coefficient can be measured. In natural magma chambers, the system cools much more slowly, rarely preserving any equilibrium melt and remaining very hot for many years after becoming completely solid.

This heat gives energy to elements in crystal structures and allows them to move through the crystal structures across a concentration gradient. These concentrations gradients can be as simple as two touching minerals, one which has a much higher concentration of a given element than the other. For example, Mg is a major component in clinopyroxene but a trace element in plagioclase. Therefore it is probably that some Mg will jump from the high concentration into the low concentration lattice and give a measurable signal of Mg diffusion out of clinopyroxene and into plagioclase.

Diffusion in minerals can occur within the crystal structure (such as exchange or ring), within vacancies, within defect or even between the spaces in the crystal lattice (interstitial diffusion) (Figure 41; from Watson and Baxter (2007)).

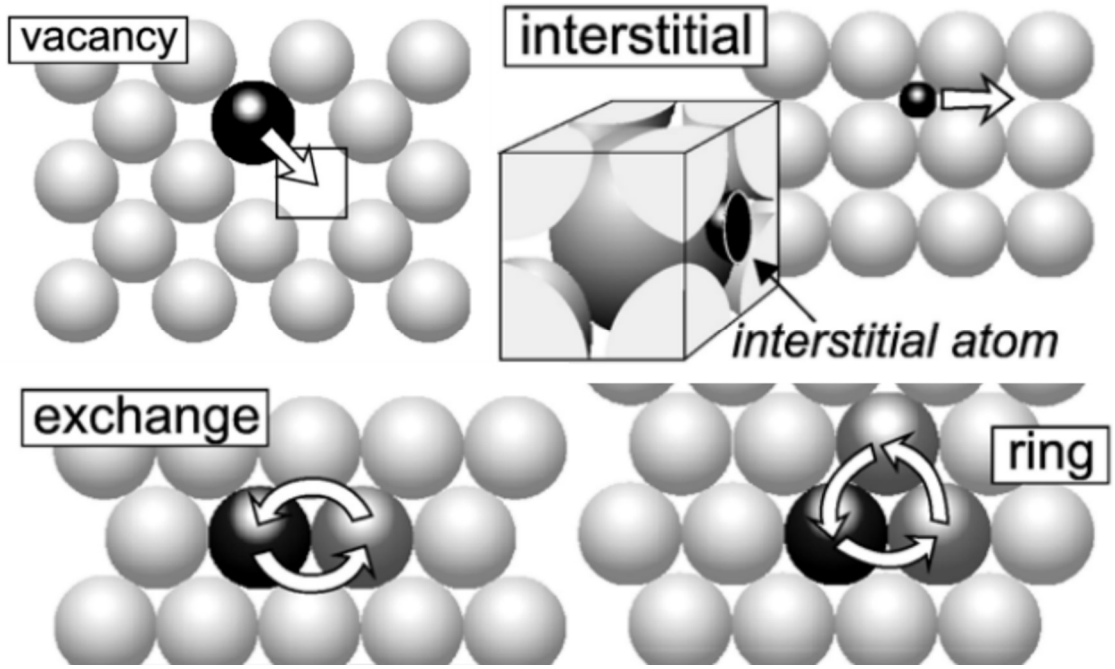

Figure 41: Various exchange mechanisms as illustrated by Watson and Baxter (2007)

Plagioclase is the mineral of interest in this chapter; and the structure and site available for substitute have been outlined in the previous chapter. These substitution sites are also potential sites for diffusion. The previous section showed that the partitioning of the trace and minor elements in plagioclase can be affected by the melt composition due to charge balancing requirements. This study aims to investigate if these charge balance mechanisms relate to diffusive speeds of trace elements.

Diffusion in plagioclase has been studied previously with focus on the minor elements such as Mg, K and Sr. Magnesium diffusion in plagioclase has shown its use as both a geothermometer and geospeedometer (Costa et al., 2003; Faak et al., 2013; Faak et al., 2014; Van Orman et al., 2014). New studies suggest that the rare earth element partitioning between plagioclase and clinopyroxene could be robust geothermometer as their diffusion rate in plagioclase is very slow and unlikely to be reset (Cherniak, 2003; Sun and Liang, 2017). Both these new tools depend on our understanding of the diffusion rates of these trace elements and in turn their substitution mechanisms.

Diffusion can play an important role in the redistribution of trace elements at high temperatures. This can be an important variable to consider when these trace elements are used for calculating age or formation conditions. Sr has been the focus of many diffusion in plagioclase studies (Cherniak and Watson, 1994; Giletti and Casserly, 1994) as it is highly compatible and Sr is used as a Rb-Sr geochronometer (Cherniak and Watson, 1994). Other relevant isotopic systems for geochronometry are U-Th-Pb, K-Ar and Nd-Sm.

The experimental techniques used here are both a mineral bucket method, championed by Spandler and O'Neill (2009) and a solid buffer method such as those presented by Jollands et al. (2014) and others. As the diffusion in plagioclase is very slow, experiments were run for over 1 month to ensure the profiles were measurable by LA-ICP-MS. Both of these experiments were done with gem quality plagioclase; labradorite (An_{58}-An_{68}) and anorthite (An_{95}).

Figure 42: Two polished anorthite rhombohedral prisms (left) and a single large, gem quality labradorite (right), unpolished. Scale are 1mm increments.

The anorthite crystals were gifted to me by Naotaka Tomioka of the Institute of the Study of the Earth's Interior, Misasa, Japan; from his personal collection. They were collected from Miyake-jima in Japan and are An_{95} in composition. These samples are completely transparent. The eruptions from this volcano are basaltic and include olivine and anorthite (Murakami et al., 1992).

The labradorite were obtained from the Gem and Mineral sale in Canberra and were chosen for their clarity and size. The compositions of these plagioclase range from An_{58}-An_{68} between samples. These labradorite are assumed to be volcanic in origin with no low grade metamorphism.

The solid buffer experiments were created from the simple system CASN (CaO-Al_2O_3-SiO_2-Na_2O) and synthesised phases (mixtures of corundum, mullite, tridymite hibonite, and gehlenite) to fix the activity of the major components. These experiments were doped with Y, Ba, La, Pr and Eu in the form of synthetic plagioclase. These represent activity controlled, simple experiments that can be used to understand diffusion in the more natural bucket experiments.

The bucket experiments were doped with Sc, Nb, Ba, Hf, Th, U, and REEs. The "natural" type melt that was based on USGS standard compositions two basaltic compositions (BIR, BF) and an andesitic composition (AGV) and will be the host for the diffusants. The plagioclase of labradorite composition (An_{58}-An_{68}) was fashioned into a bucket and the "natural" type melt was held within the bucket allowing diffusion around a circular shape. This allows the diffusion profiles to be measured in a number of crystal orientation allowing for the investigation of orientation effects on diffusion. These compositions are

more realistic to nature and allow for very complicated but more realistic types of diffusion

The aim is to compare the change in diffusion rate between plagioclase of different compositions as well as diffusion from different mediums.

4.1.1 Calculating Diffusion

Diffusion is described by the coefficient D (m^2/s), and can be solved by the following equation which assumes planar diffusion in a semi-infinite medium (Crank, 1975):

Equation 57:
Planar diffusion in a semi-infinite medium

$$C_x = (C_i - C_o) * \mathrm{ERFC}\left(\frac{x}{2\sqrt{Dt}}\right) + C_o$$

Where x is the distance from the diffusive interface in meters, C is the concentration; before diffusion (C_o), at the interface (C_i), and at any point within the crystal (C_x) and t is the time of diffusion in seconds. ERFC is an error function.

The squared difference between the predicted concentration at any given distance (C_x) and the measured concentration is minimised (least squared regression) to solve for D, C_i and C_o.

The sum of the squared difference between the measured and calculated values is minimised for the calculated fit. This value is divided by the number of measure point in the profile to give a standard error for the fit.

Arrhenius Relationships and Activation Energies

There is a linear relationship with the rate of diffusion and temperature. This relationship relates to a pre-exponential factor ($\log D_0$) and the activation energy (aE):

Equation 58:
Calculating activation energies from an Arrhenius relationship

$$\log D = \log D_0 + \frac{aE}{[2.3RK]})$$

Where R is the gas constant ($8.3145*10^{-3}$ kJ/K/mol) and K is temperature in Kelvin.

These relationships allow for the examination of how diffusion rates change with temperature and allude to the closure temperatures of the trace elements in minerals; i.e. the temperature at which the trace elements cease to diffuse at a measurable rate.

4.2 Experimental Method

4.2.1 Diffusion from simple buffers

Synthetic crystals in the Na_2O, CaO, SiO_2, Al_2O_3 (CASN) system (Figure 43) were used to buffer these simple system diffusion experiments. Plagioclase of both An_{95} and An_{70} composition doped with the diffusants; Y, Ba, La, Pr and Eu oxide powders were synthesised. These synthetic plagioclase were formed in the piston cylinder apparatus at 10kbar and 1250°C to minimise the loss of Na_2O. The results of these experiments were fine-grained plagioclase crystals along with some additional phases such as hibonite and corundum. These other phases were in such small quantities that they should have little effect to the buffer assemblage.

The buffer minerals were made by grinding the pure CaO-Al_2O_3-SiO_2 in an agate mortar under acetone for 30 minutes. The powders were then pressed into a ½" pellet and decarbonated in a box furnace at 900°C. The pellets were then hung in the 1 atm gas mixing furnace for 48h at 1400°C to allow for the buffer phases to form. The pellets were then grinded once again under acetone until a fine powder is produced and mixed by weight with twice as much synthetic plagioclase than each of the two buffer components.

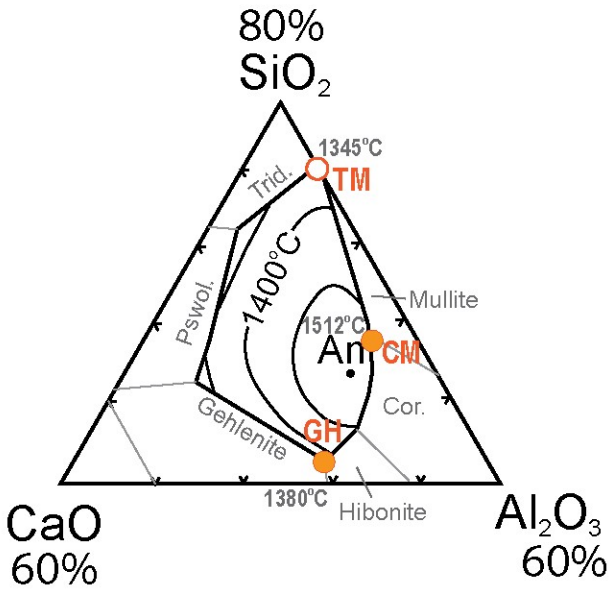

Figure 43: Buffer assemblies in simple system diffusion. High silica activity, TM; tridymite + mulllite (melted) CM; corundum + mulllite, low silica activity, GH; gehlenite + hibonite. TM solid buffers decomposed at the experimental temperature.

The high SiO_2 activity buffer consists of the synthetic plagioclase + tridymite + mullite (TM) while the low SiO_2 buffer consists of synthetic plagioclase + hibonite + gehlenite

(GH) and the moderate SiO_2 buffer consists of plagioclase + corundum + mullite (CM) (Figure 43).

Natural plagioclase of An_{67} and An_{95} were cut in to rhombehdrons and polished down to a 1/4µm grit until the surface had a mirror-like reflectance. The well mixed buffer compositions were then pasted onto a face of the plagioclase crystals with polyethylene oxide. Only two crystal of each composition were used; one with a buffer on one face and the other with different buffers on opposite faces. The diffusion rate of elements in plagioclase is so slow that it was extremely unlikely that the diffusion from each buffered face will interact.

The crystals were then wrapped in Pt wire and hung from a chandelier in the hot spot of the 1 atmosphere gas mixing furnace. The temperature was controlled using a type B thermocouple external to the furnace tube and was measured using a second type B thermocouple inside the alumina rod from which the chandelier is suspended.

One of the criticism of this powder-source technique is that there is non-homogenous contact of the diffusant with the crystal surface. It has been suggested that when diffusion profiles are measured as an average of an area (such as measurement with LA-ICP-MS), this removes these "point" contact effects (Watson and Dohmen, 2010).

4.2.2 Diffusion from melt

For the melt experiments, the gem quality labradorite crystals were cut into rectangular prisms with 3mm hole drilled on one face to create a crucible.

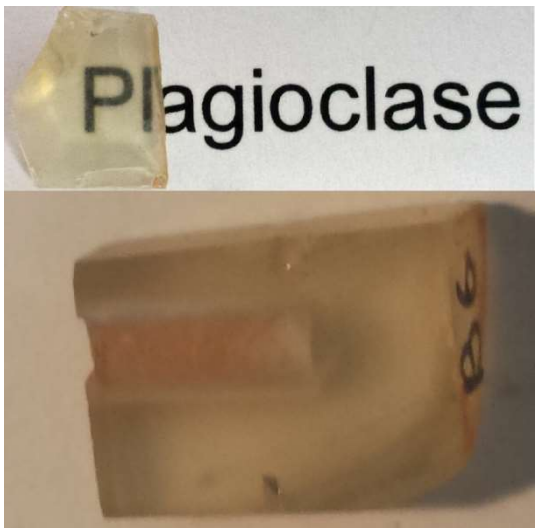

Figure 44: Top; translucent, gem quality labradorite crystal, bottom; labradorite fashioned into a crucible and filled with the oxide powders that will become a melt at the run temperature.

The melt compositions for these experiments were based on natural, USGS standards for basalt (BIR and BCR) and andesite (AGV) (Table 15). The starting compositions were created by mixing dried, pure oxide powders. The major and trace element oxides were weighed and ground in acetone for at least 45 minutes. When the powder was completely free of acetone, it was pressed into pellets. The pellets were then de-carbonated by heating in a box furnace; ramped over an hour to 900ºC and held overnight.

Chips of the plagioclase buckets (76-104μm) were then mixed with the melt, and hung on a platinum loop with polyethylene oxide. These experiments were run at 1195°C and an atmosphere of QFM (95% CO_2 + 5% CO) for 24 hours to ensure equilibrium. The resulting melt was analysed and a new starting mix was created and the method was repeated until no growth or dissolution of the plagioclase was observed.

Table 15: The major elements of the "natural" compositions based on USGS standards. For full analysis including trace elements are included in Appendix 3 in Table 53 (pg. 261). Total trace elements are assumed from the total measured oxides subtracted from 100.

USGS standard	**BIR**	**AGV**	**AGV**	**BCR**	**BCR**
Label	***BIR66***	***AGV58***	***AGV66***	***BF60***	***BF68***
An #	***66***	***58***	***66***	***60***	***68***
Major Elements (wt. %)					
Na_2O	2.52	4.08	4.03	3.52	2.80
MgO	7.77	1.59	1.52	3.08	3.10
Al_2O_3	14.16	15.73	16.37	15.69	14.42
SiO_2	49.93	58.90	60.37	50.69	46.59
K_2O	0.23	2.05	2.22	1.32	1.12
CaO	12.24	6.60	6.83	8.20	8.23
FeO	8.60	5.36	5.49	9.68	6.65
MnO	0.20	0.04	bdl	0.18	0.20
TiO_2	1.50	0.96	1.14	0.97	0.92
Total	97.16	95.27	97.96	93.67	84.33
Trace Elements	2.84	4.73	2.04	6.33	15.67

These equilibrium melt compositions were then packed inside the plagioclase crucibles and a sliver of plagioclase was used as a lid. The assembly was secured together with platinum wire and the charges were hung from a chandelier in the hot spot of a 1 atmosphere gas mixing furnace.

4.2.3 Run conditions

Three approximately 1 month long diffusion experiments were run. With very long experiments such as these there were some pauses to the experiment, however this should

have minimal effect on the diffusion coefficient. The temperature of all the experiments was logged by computer, so an exact calculation of seconds at temperature is possible.

The final run time of all experiments is summarised in Table 16. Details of pauses in each experiment are discussed in the following sections.

Table 16: Final run time for diffusion experiments.

Diffusion experiment	Plagioclase compositions	Melt	Temperature	Seconds	Hours	days
Simple System	An67, An96	CM & GH & TM	1290°C	2,490,880	691.91	28.8
Basaltic and Andesitic Melts	An58, An66	AGV & BIR	1190°C	2,799,269	777.57	32.4
Basaltic Melt	An60, An68	BF	1190°C	3,011,047	836.4	34.9

All experiments had a plagioclase of roughly An_{67} in composition. This will allow for comparison between the same plagioclase composition at 2 temperatures and between 5 diffusant compositions.

Simple system diffusion

The buffer assemblies were pasted on the polished faces of the An_{67} and An_{95} natural, gem quality plagioclase crystal (Figure 42). The crystals were hung in a wire cage for 692 hours at 1290°C and an atmosphere of QFM, (94% CO_2 +6% CO).

After 125 hours, there was a power outage which quenched the experiment. The experiment was at room temperature for a few days before being re-started. As diffusion rate is highly dependent on temperature, it can be assumed that this very short amount of time at low temperature would not affect the final diffusion rate.

At the end of the experiment, the experimental charges were quenched by dropping into a beaker of water.

It is important to note that sodium is highly volatile in at high temperatures and 1 atm pressure. This could cause a change in the sodium content over the length of the experiment.

The buffer-plagioclase interface was imaged using back-scattered electron imaging to visually determine if there was dissolution or re-growth (Figure 45).

Most of the experiments experienced a small amount of melting in the buffer assemblage. Anorthite-I (TM) and Labradorite-II (GH) experience high amounts of dissolution at the interface. These two experiments are omitted from all results.

After the experiment was completed, the buffers were removed from the crystals by using a spatula to gently push the buffer from the polished surface. In the case of anorthite-I, the buffer was welded onto the crystal surface and was unable to be retrieved.

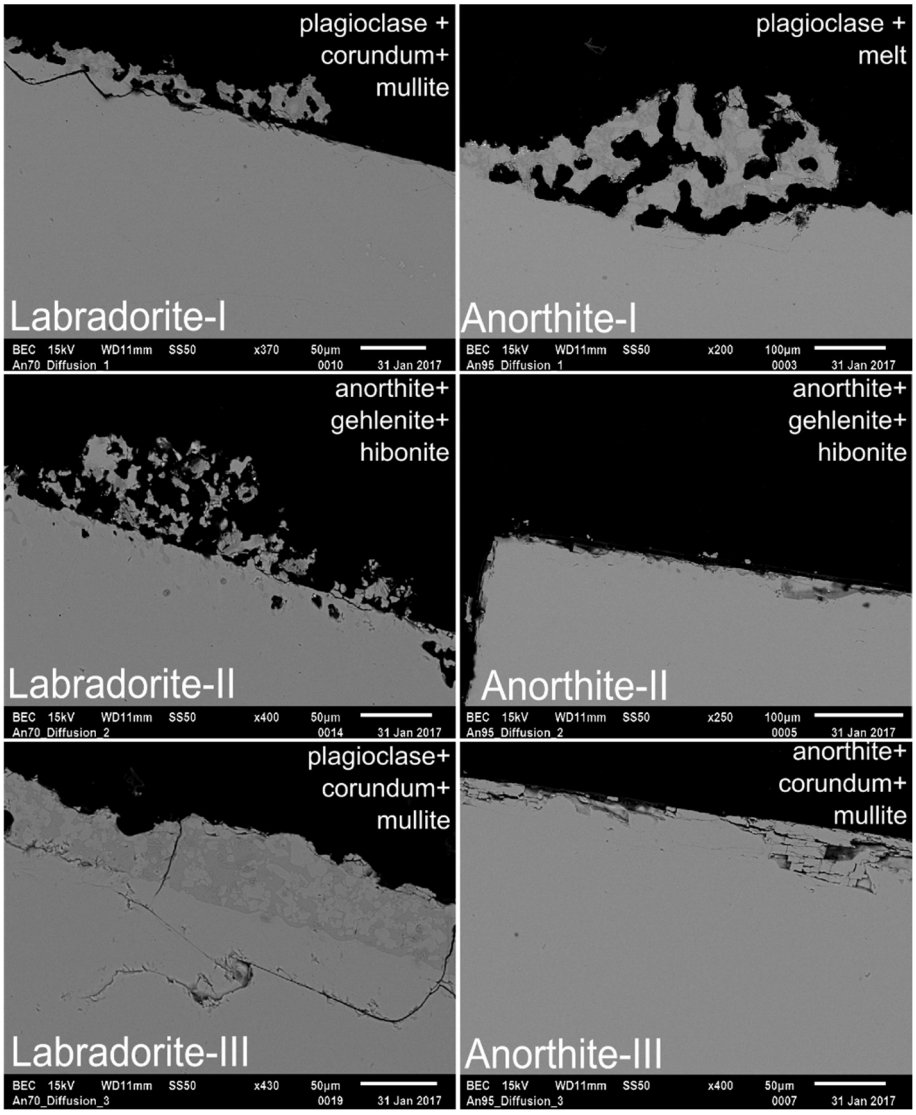

Figure 45: Edges of simple system diffusion experiments. Labradorite-II and Anorthite-I have significant dissolution so are not included in the results.

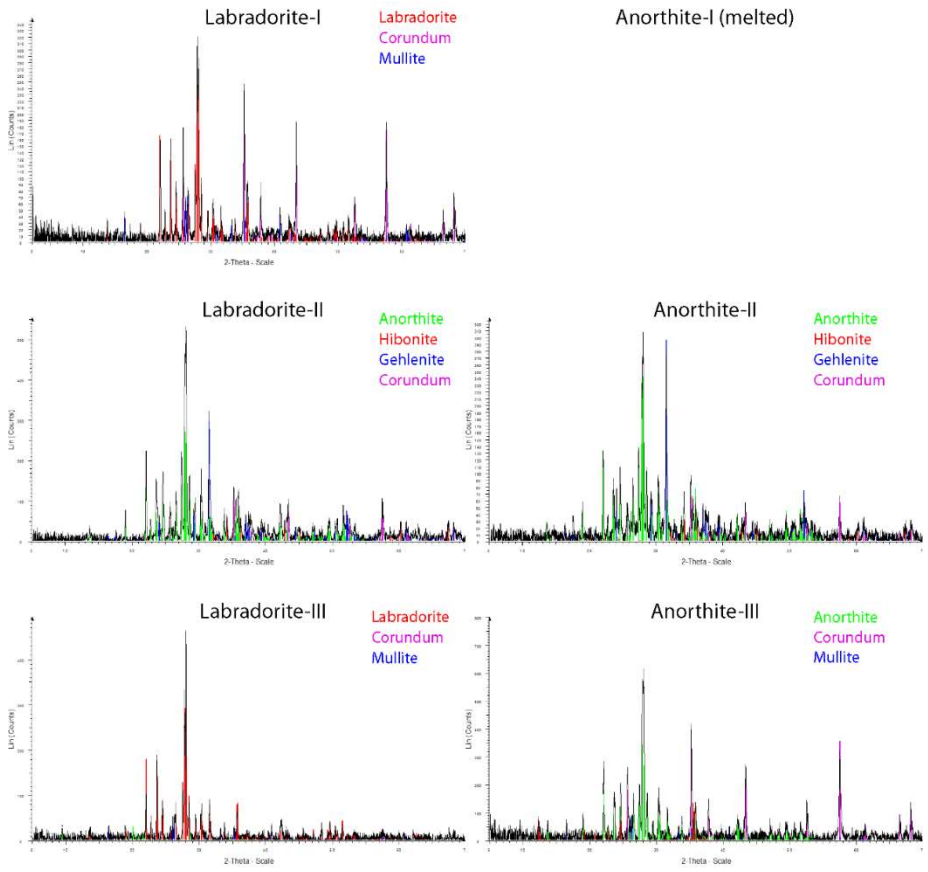

Figure 46: Buffer assemblages measured by XRD

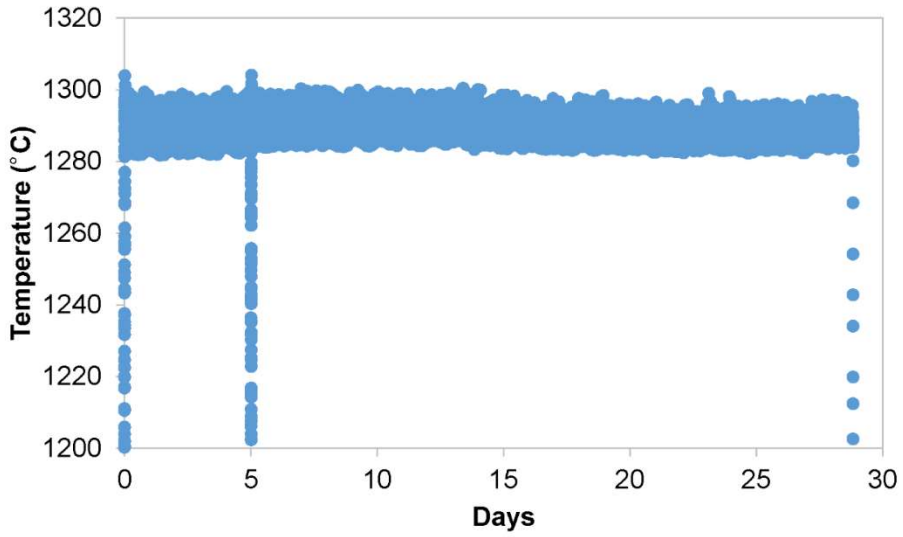

Figure 47: Temperature log for simple system diffusion

The buffer assemblages were then ground in acetone and an X-ray powder diffractometer was used to determine the crystalline buffer assemblages. The main peaks are shown in Figure 46 and the full assemblage noted in Table 17.

Table 17: Phases in buffer assemblages in each experiment. Experiments with strike-through text represent high levels of dissolution.

System	Experiment	Main Phases	Possible Phases
CASN	Labradorite-I	Labradorite, Corundum, Mullite	
	Labradorite-II	Anorthite, Gehlenite, Hibonite, Melt	Corundum
	Labradorite-III	Labradorite, Corundum, Mullite, Melt	Pyrophyllite
CAS	Anorthite-I	Labradorite + melt	
	Anorthite-II	Anorthite, Gehlenite, Hibonite	Corundum
	Anorthite-III	Anorthite, Corundum, Mullite	Antigorite

Changing plagioclase composition

The buffers for the labradorite experiments gained sodium, in comparison to the calculated starting mix. The buffer for the anorthite experiments had no measurable (by qualitative EDS) sodium at the end of the experiment. This suggests that the there was some sodium loss in this system. Also, measurements from the EPMA show some changes in CaO through the plagioclase (Figure 48).

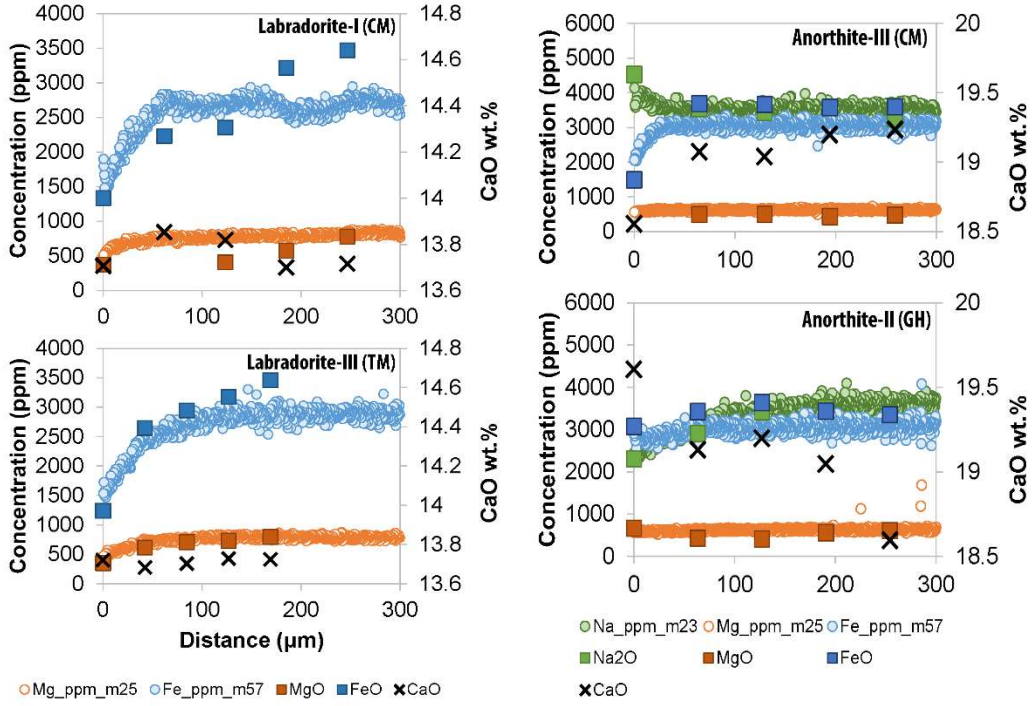

Figure 48: The change of minor and major elements in plagioclase toward the diffusive contact. Anorthite number change <2 units between core and edge.

This change is not visible in the raw counts for calcium on the LA-ICP-MS due to signal noise and makes very little difference when the profile is normalised to Si^{29} rather than Ca^{43}. Even though there has been some sodium and calcium changes in the plagioclase, the minor element diffusion as measured by EPMA and LA-ICP-MS are very similar. This confirms that the change in calcium does not affect the profiles measured by LA-ICP-MS.

It is possible, however, that the changes in CaO affects the diffusion rates of the trace elements themselves (Costa et al., 2003). The most significant diffusion of CaO occurs in experiment An_{70}-II (Gehlenite + hibonite buffer) which changes from an anorthite number of An_{69} in the crystal to An_{75} at the rim due to dissolution, so this experiment is not included in the results. It is well known that higher anorthite numbers allow for slower diffusion for all elements (Cherniak, 2010) so this could cause slower than expected profiles measured from this experiment. The other simple system experiments vary by an anorthite number of <2 between the core and the rim, which will have less of an effect.

Diffusion from basaltic melt BF: Experiment I

The first experiment run was An_{60} and An_{68} plagioclase with their equilibrium basaltic melt (BF). This composition is loosely based on the BCR2g USGS standard. These experiments are named as a combination of their equilibrium melt and anorthite composition; BF60 and BF68.

The gasses were set to fO_2= -8.5 by mixing 95% CO_2 and 5% CO, then the experiment was ramped up from 600ºC to 900ºC at 6ºC/min and held for 6 hours to ensure proper oxidation of all of the iron and other multi-valent elements. Then, due to a computing error, the furnace was ramped to 1178ºC and held for 10.61 hrs, after which it was ramped at 6ºC/min to the target temperature of 1190ºC.

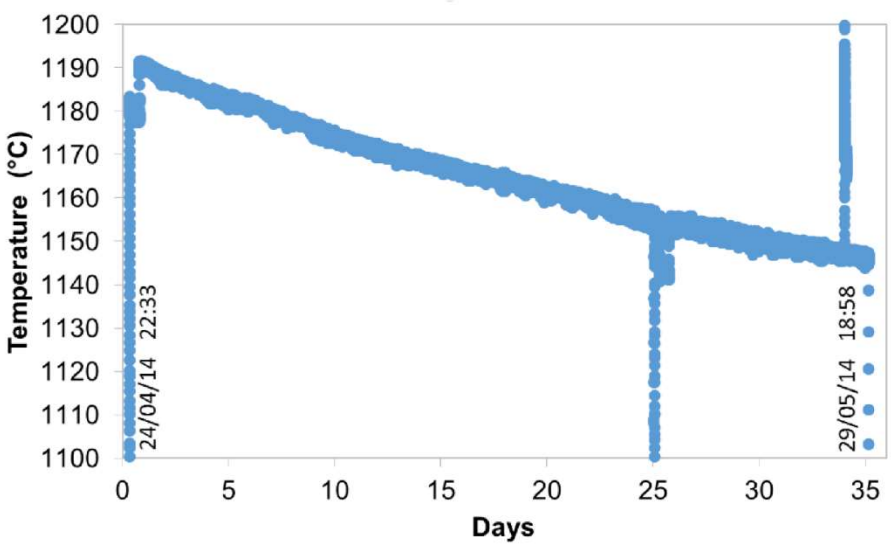

Figure 49: Temperature log for diffusion 1 experiment. Spikes (both positive and negative) are due to movement in the connection between the computer and the thermocouple.

The internal type-b thermocouple recorded a reduction in temperature over the length of the experiment which was most likely due to contamination of the thermocouple wires (Figure 49).

After 35 days, the gases ran out unexpectedly. The experiment was ceased by ramping down to 900ºC (to avoid the plagioclase buckets shattering from sudden temperature shock) then dropping the charges out of the furnace, into an empty beaker. This slow cooling allowed the melt to crystalize, which caused the interface to be obscured. The result of this experiment was a plagioclase crystal with a well of crystallised melt. The crystals in the melt consist of plagioclase, clinopyroxene and a melt (Figure 50).

The total time for this experiment at temperatures greater than 1180°C is 3,011,047 seconds.

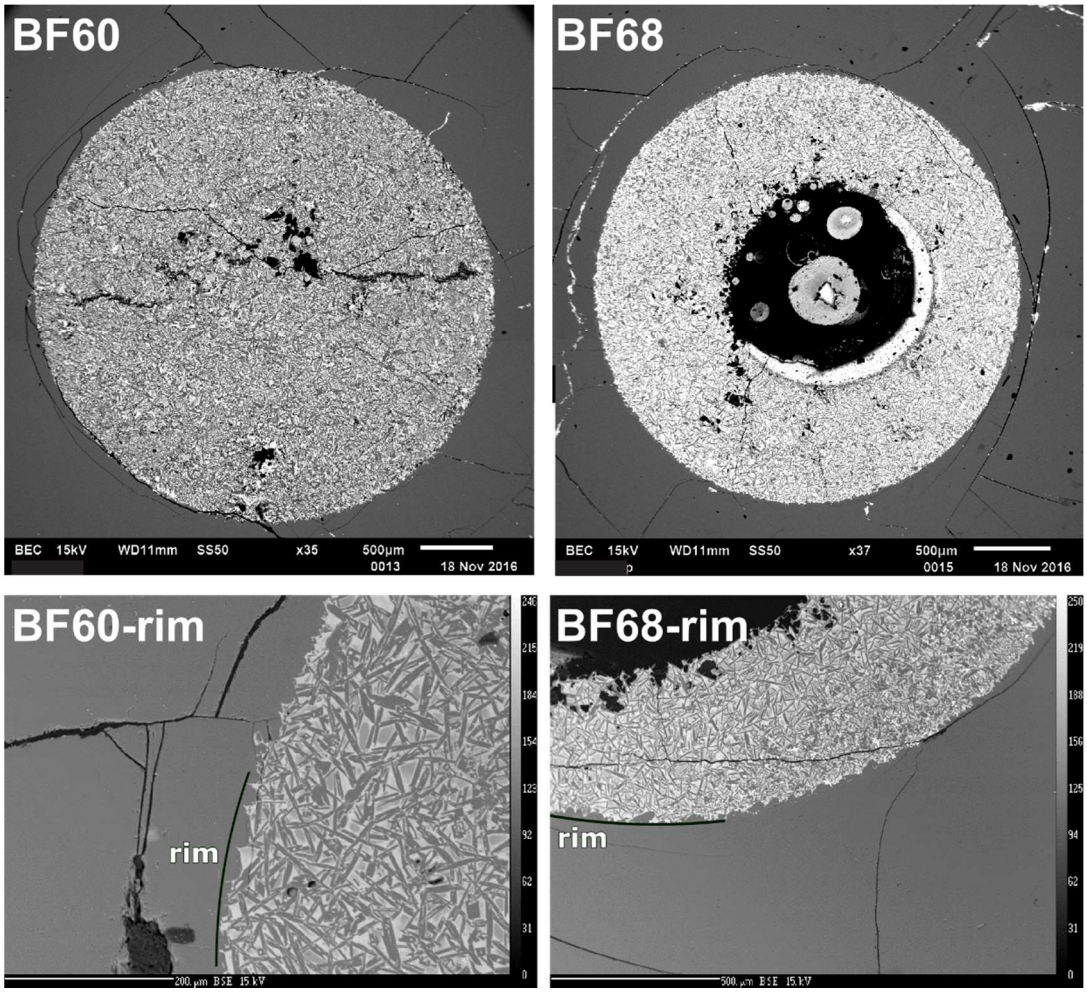

Figure 50: Experiment I – BF60 and BF68. Melt pool crystallised into plagioclase, clinopyroxene and melt. Growth of plagioclase assumed, so rim is regarded as where the melt penetrates deepest (drawn example) Rim of plagioclase growth on BF60, approximately 18µm. Rim of plagioclase growth on BF68, ~33µm.

Diffusion from basaltic (BIR) and andesitic (AGV) type melts: Experiment II and III

The second set of experiments consisted of plagioclase of composition An_{58} and An_{66} at 1190°C and QFM for 34 days. The composition of the melt in these experiments are based on the USGS standards BIR-1; Icelandic basalt and AGV-2; Oregon Andesite. The

following experiments are named for their melt compositions and anorthite content of the plagioclase bucket; AGV58, AGV66, BIR58, BIR66.

Once again, due to the length of this experiment there were a number of un-expected condition changes, all of which should have a negligible effect on the diffusion. The second experiment started with 4 different buckets (AGV58, AGV66, BIR58, and BIR66) however within the first hour, the thermocouple broke causing the experiment to be aborted. Removing the crystals from the furnace caused visible cracks in the crystal. The crystal were put back in the furnace for 24 hours and then slowly cooled and removed once again in an attempt to see if the cracks would heal; they did not. The experiment was duplicated and it was decided that all 8 crystals (4 old, 4 new) could be placed in the furnace together.

Unfortunately, after 6 days the power failed at the university, causing the experiment to quench, however no visible cracks formed. These 8 crystals were re-started and ran again for 28 days at 1190°C and QFM.

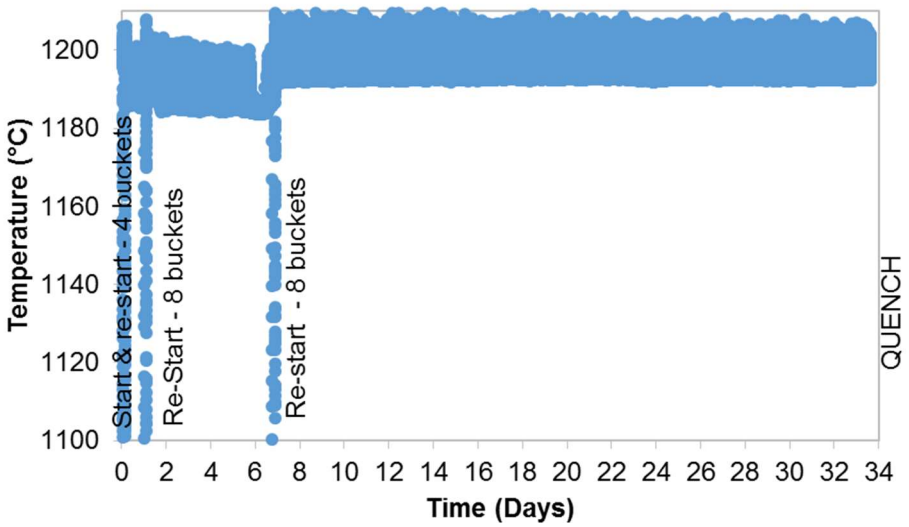

Figure 51: Diffusion experiment II and III. Cumulative experimental time at experimental temperature.

The final run time for these experiments is given by recording all the time the experiment was at a temperature great than 1185°C. The first 4 buckets had a total run time of 797.94 hours or 33.25 days, while the second set of 4 buckets were at temperature for 777.57 hours or 32.40 days.

At the end of these experiments, the experimental charges were dropped from the furnace into water to ensure the melt quenched.

The first set of buckets (Experiment II) had many cracks that allowed the melt to infiltrate and makes obtaining a smooth diffusion profile almost impossible. The buckets from the second set (experiment III) had cracks that are not filled with melt and most likely formed during the quench.

Experiment BIR58 experienced high amounts of dissolution (Figure 52) and is omitted from any further results.

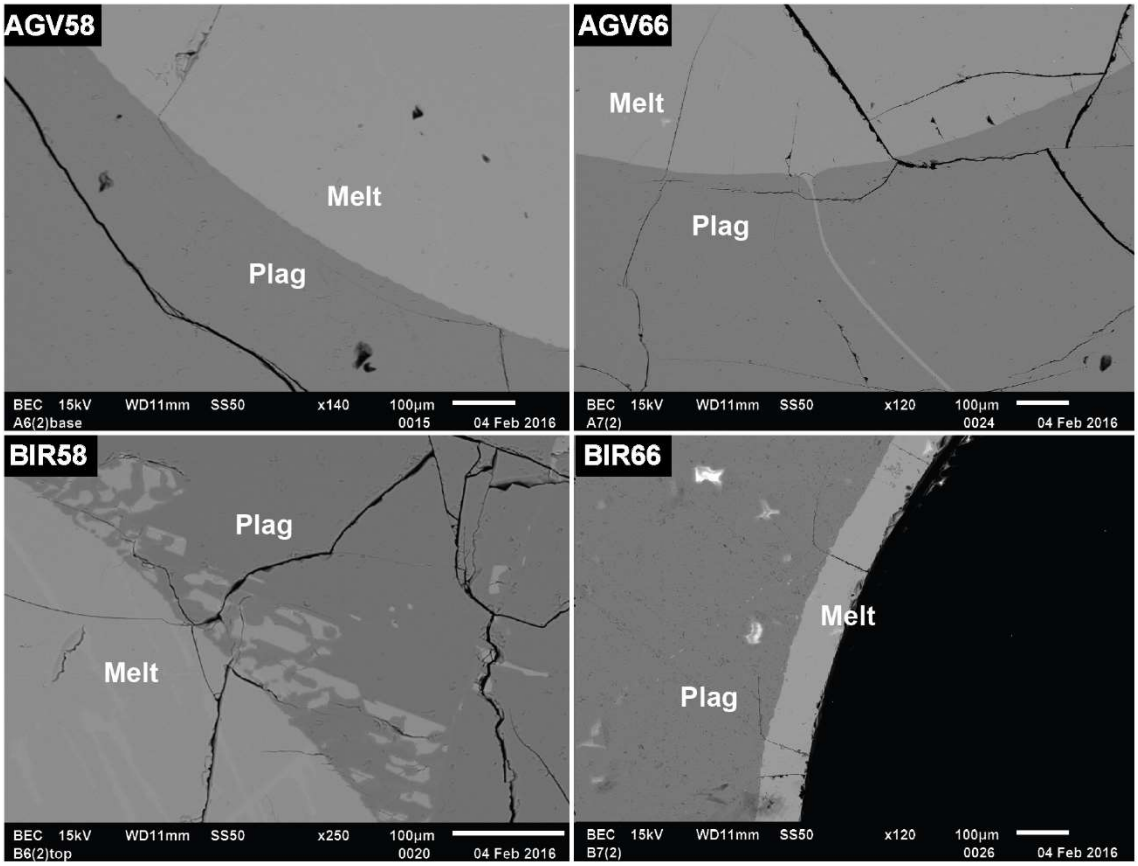

Figure 52: Backscattered electron image (BSEI) of quenched diffusion experiment III. Sample BIR58 has experienced significant dissolution and is not used to gather diffusion data.

4.3 Analytical Method

4.3.1 LA-ICP-MS

Trace elements were collected by laser ablation ICP-MS. This system is comprised of an ANU HelEX laser ablation cell and a sampling cell using a pulsed 193 nm ArF Excimer laser feeding an Agilent 7700S ICP-MS. Laser conditions set to ~80 mJ fluence and 5 Hz repetition rate. The laser was masked to create a rectangle shape (7 x 92 µm) which moved at either 0.5 µm/s or 1 µm/s.

For the diffusion profiles, trace element concentrations were determined by running a laser trace from deep within the plagioclase and moving toward the melt. This direction

is chosen due to the residence time of some elements on the detector. Therefore the analysis will be more accurate if run from low concentration to high concentration. Although some elements diffuse out of the crystal (i.e. the concentration at the interface is less than the original plagioclase composition), the concentration in the melt is much higher than in the plagioclase so the plagioclase to melt direction is still the ideal choice.

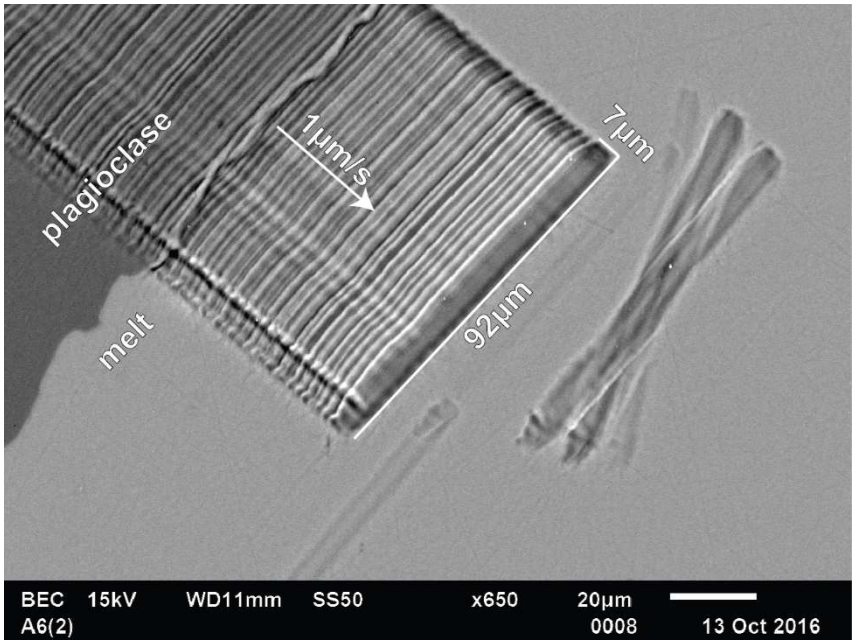

Figure 53: laser traverse through a plagioclase/melt experiment (AGV58)

The laser traces are checked to be parallel with the diffusive contact to ensure analysis of essentially a one dimensional (planar) diffusion profile. The diffusion paths are photographed and the samples are re-polished and the process is repeated. The counts were calibrated using NIST610 (Jochum et al., 2011) as the primary reference material and NIST612 as a secondary standard to check data quality. The internal standard was calcium, as it shows no diffusion in the raw count data, often has equal counts in the melt as in the crystal and has similar ablation properties to the rare earth elements (Jackson, 2008).

As the slit is 7 µm wide there is some uncertainty of the interface position. This problem will be less important for the long diffusion profiles, but could affect the diffusivity value for the shorter profiles.

4.3.2 Location of the interface

Manganese was used to determine the location of the interface. Mn diffuses out in all samples therefore there are very low concentrations at the interface and very high concentration in the melt (Figure 54). This rules out the possibility that these profiles are

false profiles caused by melt-filled micro cracks, as this would cause an increase in Mn near the interface, not a decrease. This is undeniably a change in the chemistry of the crystal.

Visible melt filled cracks are observed in some areas but these are avoided.

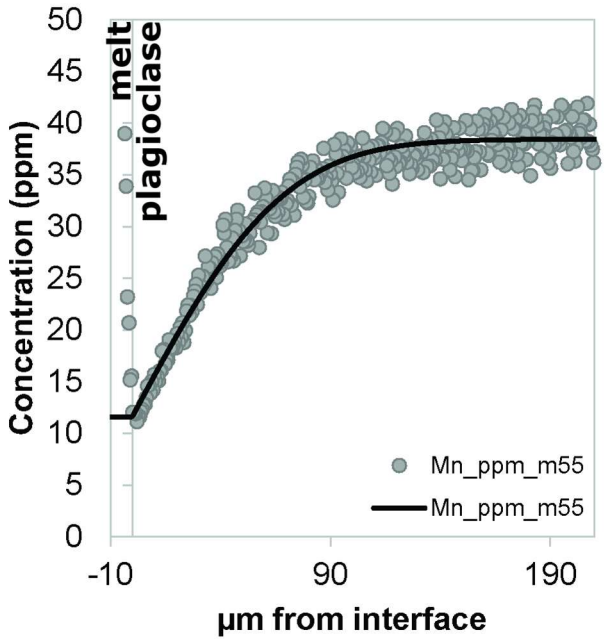

Figure 54: Interface determined by manganese. Points are measured data, line is calculated diffusion profile, fit to the data. Sharp increase in manganese indicated is interface from plagioclase to melt.

4.3.3 NanoSIMS

The CAMECA NanoSIMS 50L ion probe at the Centre for Microscopy, Characterisation and Analysis at the University of Western Australia was used to check the shorter diffusion profiles. Only samples AGV and BIR were analysed by this method.

Analysis were collected in two ways, using the stage control (for longer analysis) and the beam control (for shorter analysis) (Figure 55). Both were using an O- primary ion beam with a beam current of 50pA. The stage control was set up as 200 points with 1µm spacing and a 4 seconds per point analysis time. The first cycle was a presputter to remove surface contamination. Unfortunately, the stage movements were not precise and this method gave poor results.

The beam control was set up with 2 seconds pre point analysis time with 1 cycle of presputter and 2 acquisition cycles. This method gave very good results.

Routine 1 consisted of ^{9}Be, ^{24}Mg, ^{28}Si, ^{55}Mn, ^{88}Sr, ^{138}Ba, ^{153}Eu. Routine 2 was run with; ^{28}Si, ^{39}K, ^{56}Fe, ^{69}Ga, ^{139}La, ^{153}Eu and ^{165}Ho.

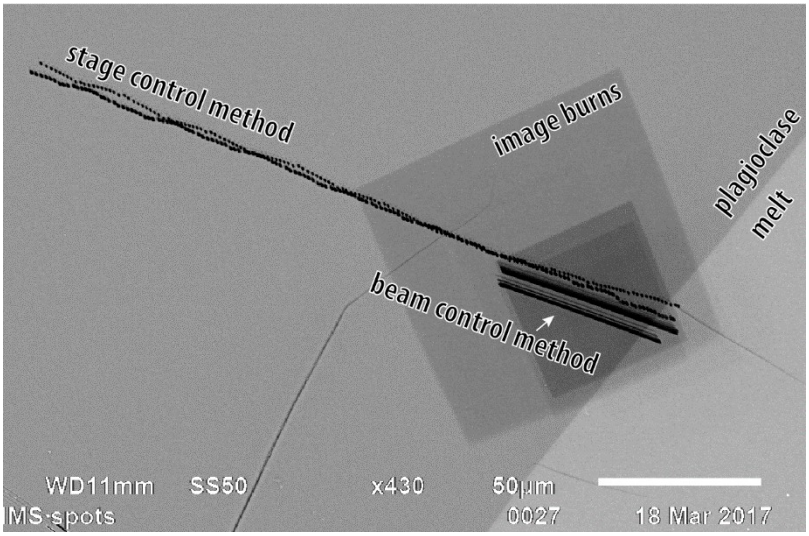

Figure 55: Back-scattered electron image from sample AGV66 after nanoSIMS analysis.

As no standards were measured, the data are qualitative; however diffusion coefficients can still be obtained. The counts were normalised to semi quantitative ppm values by the formula (Longerich et al., 1996) where the melt acts as a quasi-standard:

Equation 59: Normalising counts to semi-quantitative elemental concentrations

$$C_x^{sample} = \frac{R_x^{sample}}{\frac{R_x^{melt}}{C_x^{melt}} * \left(\frac{R_{Si}^{sample}}{R_{Si}^{melt}} * \frac{C_{Si}^{melt}}{C_{Si}^{sample}} \right)}$$

Where C_x is the concentration of the element of interest (x), R is the count rate of the given element and C is the concentration of the element by LA-ICP-MS. As no reference standards were measured by the nanoSIMS, these values are only semi quantitative and cannot be checked for precision.

The standard error is calculated as in the LA-ICP-MS data. The profiles are considered "unresolvable" if the calculated profile is longer than the measured distance or the error is larger than 10% of the concentration difference.

Using the nanoSIMS also allows a detailed examination of the interface interactions. Diffusion of major elements in melts is thought to be very fast (Guo and Zhang, 2016) but the trace elements in these melts show extremely short diffusion profiles (Figure 56). These profiles are shown both when analysing from melt to crystal and reversed. It is uncertain if this feature is an analytical artefact or evidence of changes in the melt composition as the interface is approached.

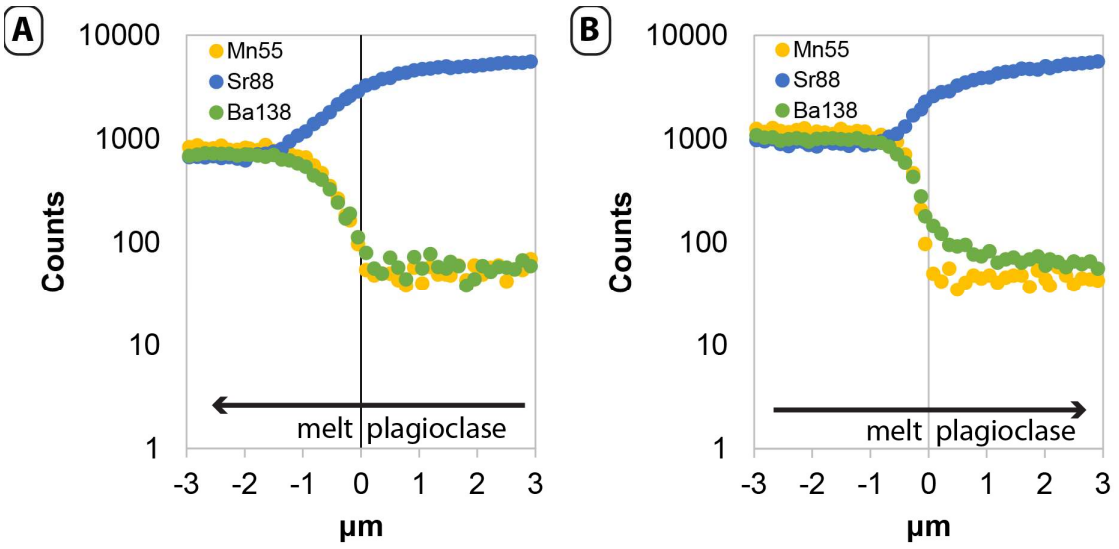

Figure 56: An in depth examination of the interface interactions of Ba, Sr and Mn between AGV66 and melt. Measured by nanoSIMS A) traverse from plagioclase into the melt B) a traverse from melt into the plagioclase.

If there are changes in the melt composition as the interface is approached, this may cause local equilibrium at the crystal interface, changing the partition coefficients.

4.3.4 Uncertainties

Diffusion in plagioclase is slow and this causes the diffusion profiles of many of the trace elements to be very short. The width of the LA-ICP-MS slit is approximately 7µm which means any diffusion coefficient that is less than log D = -17 will be smaller than the analysis window and have the potential to be false profiles caused by the mixing between melt and plagioclase signals. For the "natural" system experiments, these extremely short profiles were checked on the nanoSIMS and all are in very good agreement (Figure 60), however the nanoSIMS data was not standardised and therefore qualitative.

It has been found previously that crystal orientation can have an effect on diffusion rate, Cherniak and Watson (1994) found that the diffusion rate of strontium can differ by 0.7 log units between the (001) and (010) orientations. The experiments presented here are not orientated, but as we can take measurements at different orientations around the melt pool, we will be measuring an average diffusion rate of an entire plagioclase in all orientations. Because of changes in counting times and choice of isotopes in different analytical routines, the number of profiles is not consistent between elements or experiments. The summary of the number of analysis used to obtain the average and standard deviations are included in Appendix 3 in Table 56 and Table 57 (pg. 263).

Most of the experiments show minor deviations from perfectly straight interface. This could be caused by the initial crafting of the crucible or caused by disequilibrium within the first few hours of the experiment. In the case of experiment I (BF60 and BF68), the large growth rims may have occurred during the slow cooling at the end of the experiment or due to disequilibrium at the beginning. As the interface is determined by the first measurement of melt, growth of plagioclase around the rim will affect the diffusion profile less than dissolution into the plagioclase. During dissolution, the melt infiltrates the diffusion profile and the apparent diffusion profile becomes much shorter than realistic. These problems with the accuracy of the interface do not affect the calculated diffusivity significantly, however will affect the calculated equilibrium partition coefficient at the interface.

The experiments with obvious dissolution have been omitted from this study, while the samples with small growth rims are still included.

Table 18: Growth/dissolution rims on each experiment. Measured from BSEI images.

Experiment	Sample	Growth rim
I	BF60	18 µm
I	BF68	33 µm
III	AGV58	7 µm
III	AGV66	-
III	BIR66	8 µm

Any samples that have measurable diffusion profiles greater than the width of the laser slit, and/or greater than the irregularity of the interface should be considered indicative while all others should be treated with caution.

4.4 Results

Diffusion profiles were measured of both the “in” direction (high concentration at the interface and low in the crystal) and the “out” direction, where the interface concentration is less than the background concentration in the crystal.

Generally it is assumed that elements will diffuse through a gradient of chemical potential from high concentrations to low concentrations, however, some elements such as Mn, diffusion “out” even though the concentration in the melt (0.2 wt. % MnO) is greater than that in the plagioclase (50 ppm). This is due to the very low compatibility of these elements.

4.4.1 Partitioning and experimental equilibrium.

The diffusion from melt experiments are unique in their ability to give equilibrium partition coefficient along with diffusivities.

The interface between the melt and crystal represents equilibrium partitioning. The partition coefficients for the diffusion experiments were calculated by dividing the calculated interface concentration of the diffusion profile with the melt concentration. This will allow us to determine if the diffusion is real and if the plagioclase was in equilibrium. For a table of these calculated partition coefficients, refer to Appendix 3; Table 55 (pg.262).

To test the equilibrium partition coefficients, plagioclase crystals were synthesised from BIR66 melt by cooling the melt from 1209°C at 6°C/h to 1133°C and allowing the crystals to grow for four days. The plagioclase grown from the AGV melts were too small to analyse precisely for the partition coefficients. For these melts the partition coefficients were predicted from the equations outlined in the previous chapter. The divalent and monovalent cations were calculated by the linear relationship with the anorthite content or melt components. The rare earth elements were calculated by the stoichiometric equation outlined in the previous chapter (Equation 53).

Elements such as Fe and Mn were not tested thoroughly in the previous chapter. Furthermore, the effect of fO_2 on Eu and Ce has not yet been addressed. Therefore, these elements do not have predicted partitioning values.

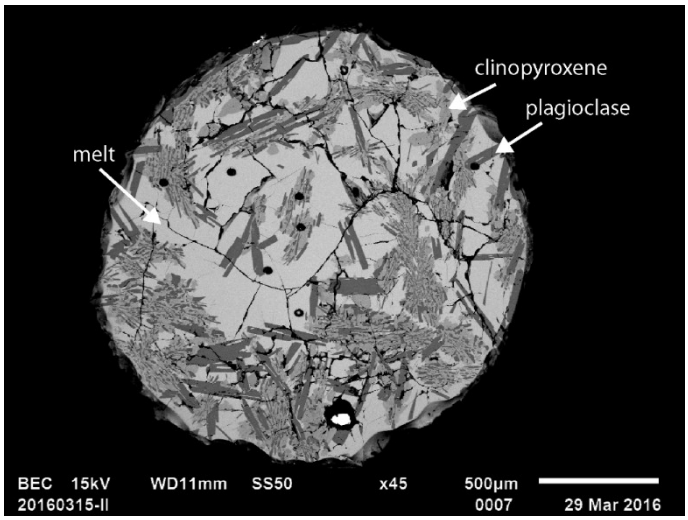

Figure 57: Experimental charge 20160315 – BIR66, a partitioning experiment, where plagioclase and clinopyroxene were grown from the same composition used in the BIR66 diffusion experiment.

Although this experiment was run, 60°C cooler than the diffusion experiment, the partition coefficients should change minimally. As this experiment was run on Pt loops at high temperature, there is a high likelihood that there was some monovalent cation loss due to volatility and Fe loss due to alloying with the Pt wire.

This experiment proves that the diffusing melt was in equilibrium with the plagioclase crucible as the plagioclase that were grown from the melt have an almost identical composition (Appendix 3; Table 54). The synthesised plagioclase has a composition of $An_{66.92}$ while the plagioclase crucibles were of composition $An_{66.27}$.

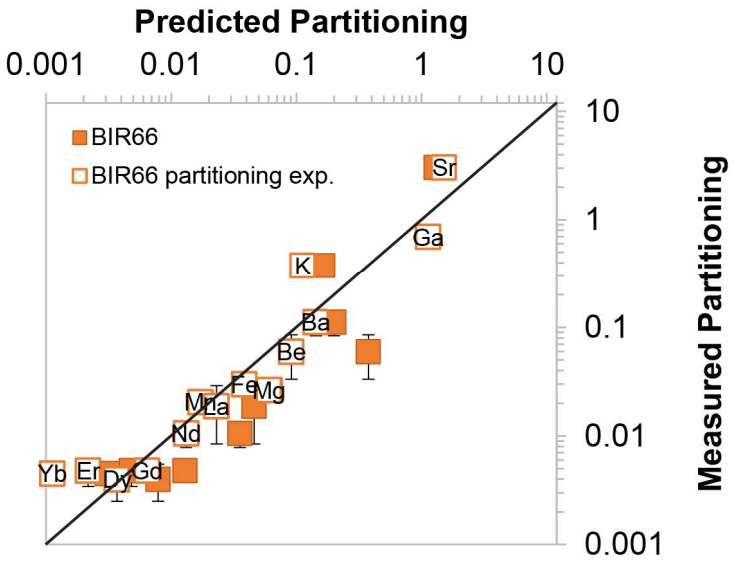

Figure 58: Partition coefficients from predicted from equations in the previous chapter vs those measured by LA-ICP-MS. Closed symbols are the partition coefficients of the diffusion experiments, i.e.; the interface concentration over the melt concentration. Open symbols are partitioning experiment; BIR66 and is 60°C cooler than the diffusion experiment.

The experiment BIR66 is in equilibrium as the interface concentrations from the diffusion experiment and the partition coefficients measured in the partitioning experiment (Figure 58) are almost identical. The predicted partitioning values from the previous chapters are more variable but close to measured values. Be is predicted to have much higher partitioning than measured in these experiments, which is an indication that the model for Be partitioning may not be precise when dealing in "natural" systems.

Comparing the predicted values for this experiment, the rare earth elements are overestimated by the predictive models. When comparing these predicted values to the diffusion partition coefficients for all other experiments, the same trends are observed; most of the REE are overestimated by the predictions by 2-3 times.

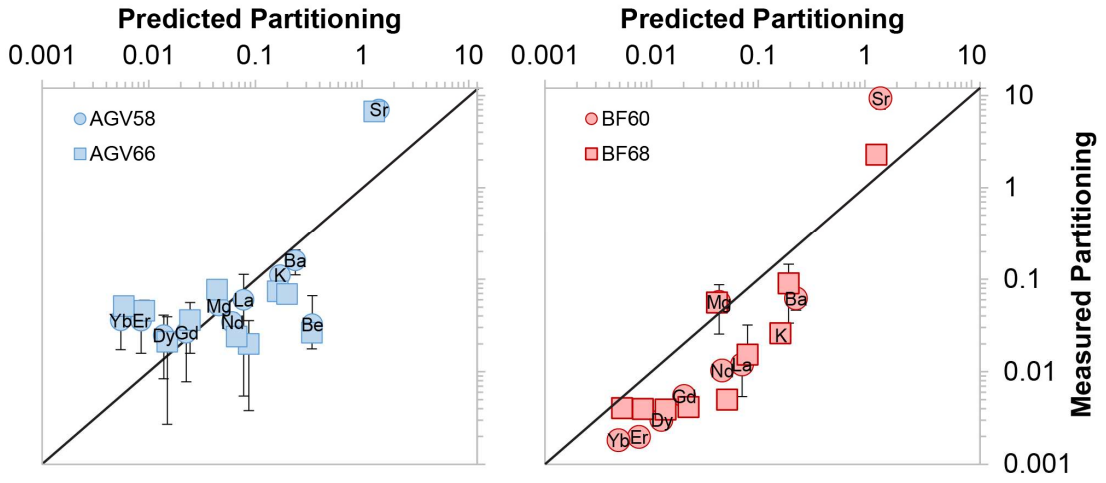

Figure 59: Comparing the measured interface partition coefficients from the diffusion experiments with the calculated partition coefficients, predicted from the equations outlined in the previous chapters.

The partitioning of strontium is always higher than predicted (Figure 59). As the diffusion direction of this elements is "out" and error in the placement of the interface will cause the measured partition coefficient to be higher than predicted. Additionally, when measuring diffusion profiles with the nanoSIMS, there seemed to be a diffusion profile measurable in the quenched melt (Figure 56). This may indicate that diffusion rate through the melt may also add to the error between the interface concentration and predicted partitioning using the equations in the previous chapter.

It can be confidently assumed that these experiments are in equilibrium with their paired melt. The differences between the predicted and measured interface values are due to errors in the prediction or errors in the measured interface concentration rather than disequilibrium with the melt. This is confirmed by comparing plagioclase crystals growth from the BIR66 melt, which are in very good agreement with the interface concentrations from the diffusion experiment.

4.4.2 A Comparison of Diffusivities of All Elements

Three samples were measured by both nanoSIMS and LA-ICP-MS and the data are in very good agreement (Figure 60). Many of these analysis have diffusion profiles less than 10µm, and although the laser ablation slit is ~7 µm, the slow movement speeds allows for these diffusion profiles to be resolved precisely by the LA-ICP-MS system. This is partly due to the precision and consistency of the interface location in all experiments, which is unique to this study.

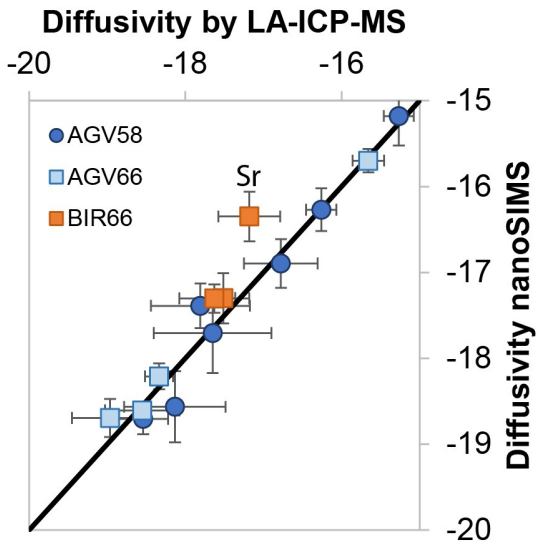

Figure 60: Comparison between the diffusivities calculated by nanoSIMS and LA-ICP-MS

There are two main groupings of diffusive speeds, the fast diffusers; Mg, K, Mn, Fe and the slow diffusers; Be, Ga, Sr, Ba, REE (Figure 61). The slow diffusing elements have a larger range of diffusion coefficients due to the analytical uncertainty in measuring the small profiles with the LA-ICP-MS system. Some elements such as Mg, and REE have two distinguishable diffusion mechanisms.

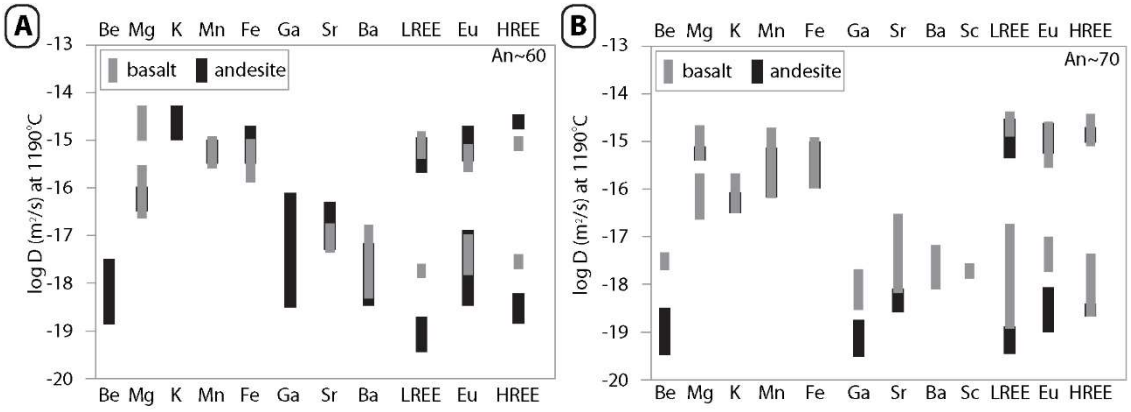

Figure 61: Comparing diffusivities of all elements at 1190°C in A) An~60 and B) An~70.

These combination of experiments allows for the effect of melt composition and crystal composition on diffusivity to be compared for a number of elements. There are four experimental pairs with the same (or at least very similar) crystal composition but variable melt composition. The pairs; An66 with AGV66 and BIR66, An~60 with AGV58 and BF60 for the "natural" systems and An70 buffered by corundum + mullite and tridymite + mullite, An95 with gehlenite + hibonite and corundum + mullite.

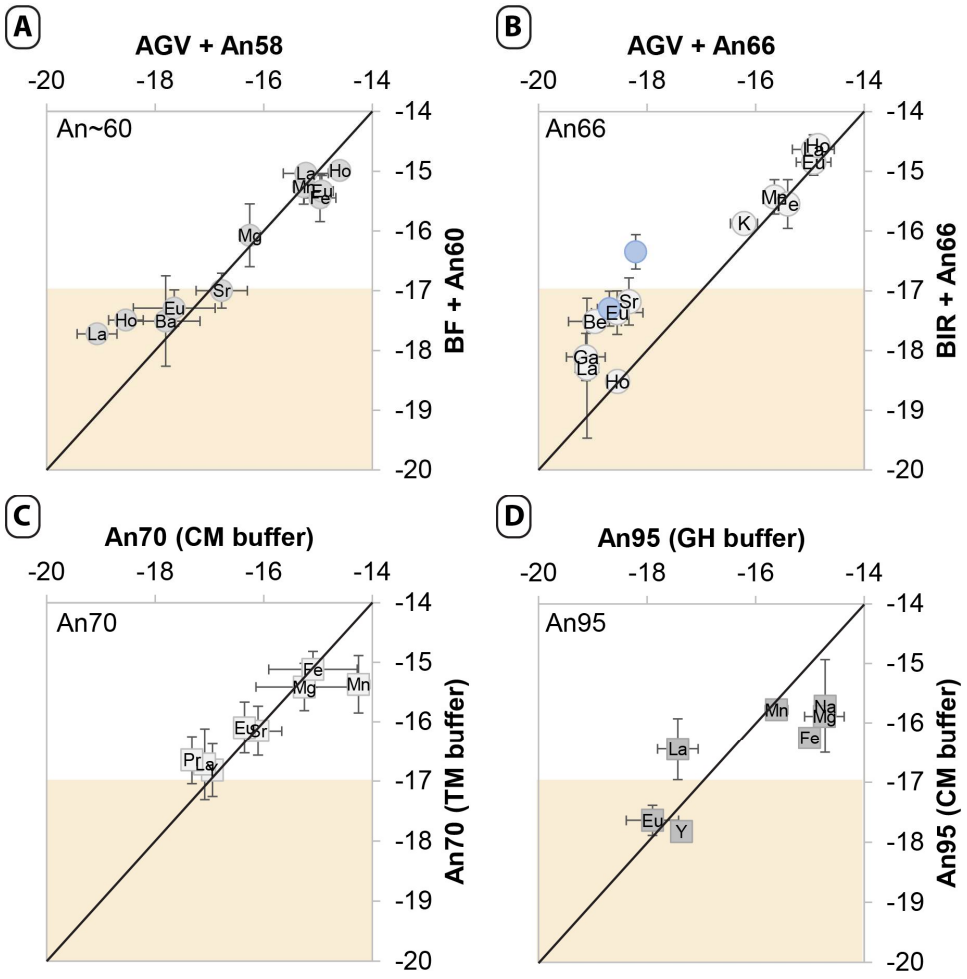

Figure 62: Diffusivities measurable diffusion profiles in all experiments, Yellow shaded area represents diffusion profiles that are less than the laser slit width (i.e. 10μm). If no error bars visible, only one measurement taken. A) Diffusivities in An58 at 1190°C. B) Diffusivities in An66 and An68 at 1190°C, C) Diffusivities in An67 at 1290°C, D) Diffusivities in An95 at 1290°C

The variations in melt composition have little effect on most elements. In An_{66}, Be, Sr, Eu and Ga diffuse an order of magnitude faster from the basaltic type melts (BIR) than the andesitic melt. This trend is not observed with comparing An_{58} with comparing BF and AGV. The simple system diffusion experiments are a more accurate comparison for varying melt compositions as the major element activities are fixed.

The simple system experiments vary mostly in silica activity; the tridymite + mullite (TM) buffer has the highest silica activity (1) and gehlenite + hibonite (GH) buffer has the lowest silica activity. Comparing the buffered experiments with An70 plagioclase, there is no significant difference for most elements. Mn is the only element that shows a significant variation, diffusing an order of magnitude faster in the lower silica activity buffer. Comparing An95 plagioclase, the variation in the rare earth element diffusivities is not constant for the heavy and light REE. This suggests that the variations in this comparison may be due to a factor other than just buffer activity.

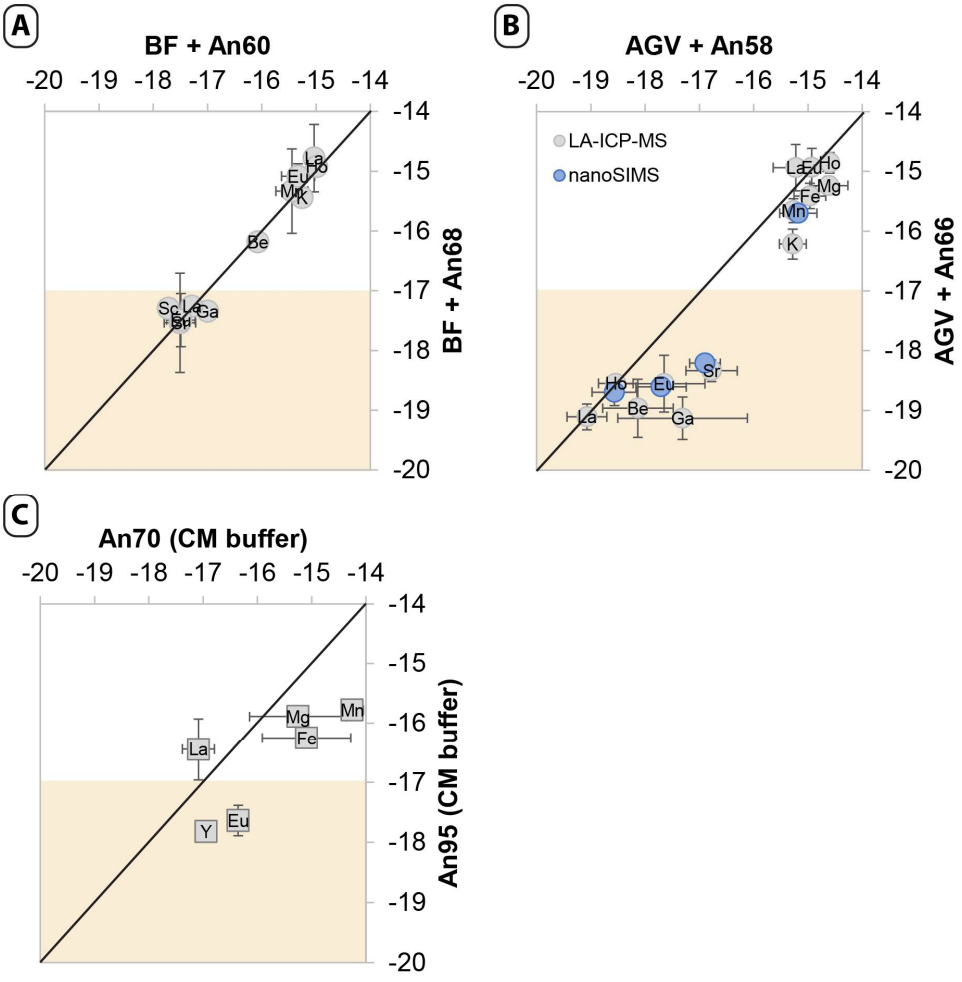

Figure 63: A) Diffusivities in An60 and An68 at 1190°C from a basaltic melt B) Diffusivities in An58 and An66 at 1190°C from an andesitic melt C) Diffusivities in An67 and An95 from a corundum + mullite buffer at 1290°C

There are also 3 experimental pairs with similar diffusant compositions and different plagioclase compositions. Generally, plagioclase with higher anorthite content have slower diffusion rates.

To understand the mechanisms of diffusion in plagioclase we must compare the effect of temperature, plagioclase composition and changes in diffusant composition on the diffusivities of each element.

4.4.3 Potassium diffusion

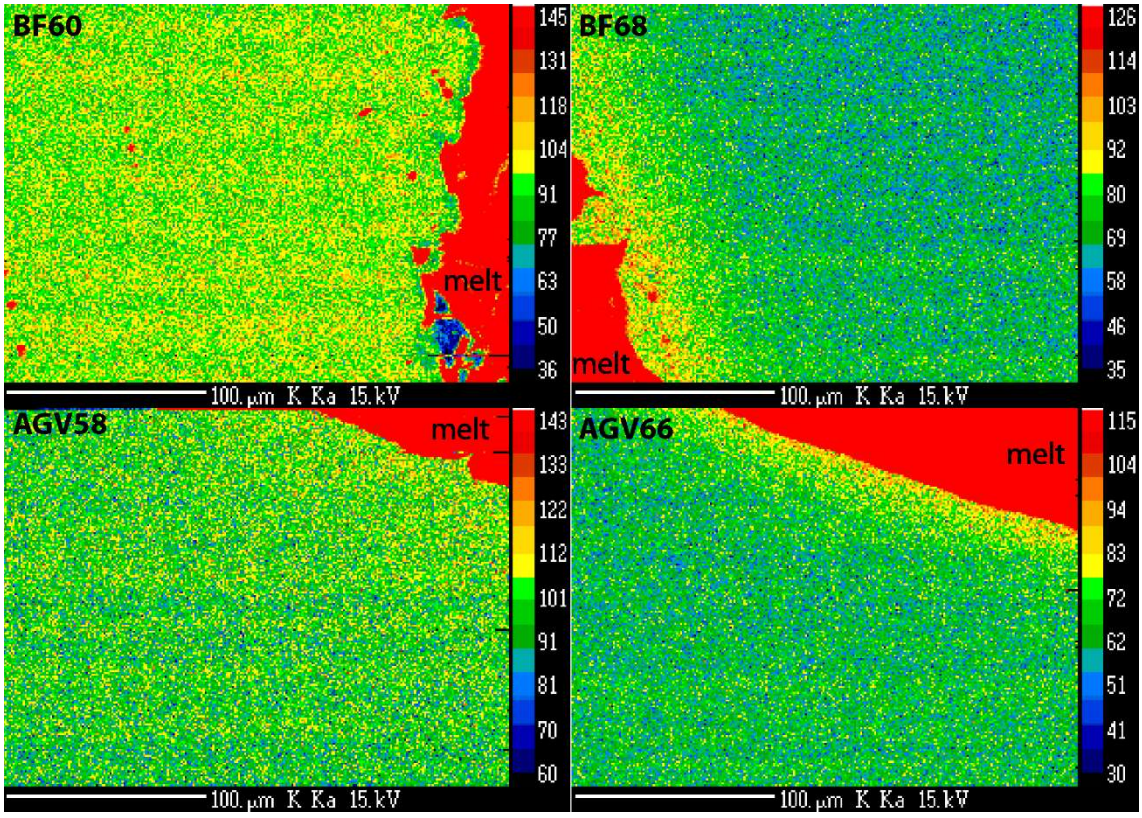

Figure 64: diffusion of potassium as mapped by EPMA, horizontal lines are a digital artefact.

In sample BIR66, K diffuses "out" from the plagioclase into the melt, while in all other experiments, the diffusion occurs from the melt into the plagioclase. This diffusion "out" occurs at the same rate as diffusion "in" all the other experiments with the exception of AGV58. This sample allow diffusion to occur an order of magnitude faster than the more anorthitic plagioclase with comparable melt (AGV66). This is due to the higher albite content.

Giletti and Shanahan (1997) found that potassium diffuses 20 times slower in labradorite than albite; which is due to the simple substitution of sodium for potassium. Potassium should freely substitute into the plagioclase as an orthoclase feldspar ($KAlSi_3O_8$) component.

K exchange in albite:

Equation 60
substituion of potassium in albite

$$NaAlSi_3O_8 + \frac{1}{2}K_2O = KAlSi_3O_8 + \frac{1}{2}Na_2O$$

The labradorite composition tested in this study ranged from An_{66}-An_{68} while Giletti and Shanahan (1997) studied An_{63}. If it is assumed that the change in diffusion rate is linear with anorthite content of the plagioclase, the difference between the labradorite studied by Giletti and Shanahan (1997) and the labradorite studied here would differ by $\Delta \log D_0 = 0.2$ and $\Delta aE = 2$ kJ / mol. This is within error of the calculated activation energy and pre-exponential factor so labradorite of compositions An_{63}-An_{68} can be treated as the same composition.

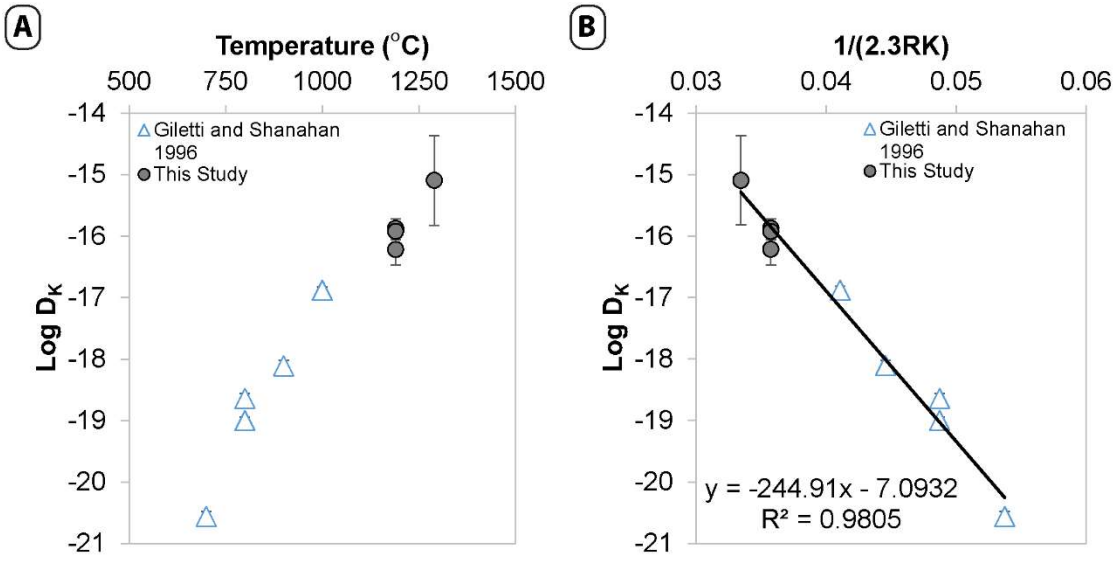

Figure 65: Arrhenius plot K diffusion in labradorite; open symbols – Labradorite ($An_{62.6}$) from (Giletti and Shanahan, 1997). Closed symbols; this study A) Diffusive rate of potassium increasing with temperature B) Arrhenius relationship calculating the activation energy (aE = 245 kJ / mol) and pre-exponential factor (log D_0 = -7.09 m^2 / s) .

Combining the data obtained in this study and the data published by Giletti and Shanahan (1997) an Arrhenius relationship for labradorite plagioclase can be defined. The relationship found by Giletti and Shanahan (1997) was $\log D_0 = -5.5 \pm 3.8$ m^2 / s and an activation energy of $aE = 278 \pm 82$ kJ / mol. Including this study, this diffusion rate gets a bit faster at log D_0 = -7.09 and an activation energy of aE=245 kJ / mol.

4.4.4 Divalent cation diffusion

Strontium Diffusion

The diffusion of strontium is very slow and therefore the profiles are very short. The LA-ICP-MS data for the "natural" melt diffusion experiments was confirmed by nanoSIMS (Appendix 3; Figure 121(pg. 263)) and the results are within error (Figure 60).

Strontium is assumed to partition onto the M site of plagioclase, and requires no charge balancing.

Equation 61
substituion of strontium in anorthite

$$CaAl_2Si_2O_8 + SrO = SrAl_2Si_2O_8 + CaO$$

Although anorthite has more calcium site available for diffusive exchange than albite, anorthite has a slower rate of diffusion for strontium than albite.

Cherniak and Watson (1994) found that the diffusion rate of strontium can differ by 0.7 log units between the (001) and (010) orientations. In this study, the largest deviation in Log D_{sr} is experiment AGV58, with a standard deviation of 0.5 log units (from 13 analysis). As the melt well is circular, it should be expected that the diffusion rate will change around the circumference of the melt pool, however the standard deviation of the diffusion coefficients is very low for most experiments. As the deviation is small, it suggests that the orientation of the crystal has very little effect on the diffusion of strontium.

The partition coefficient for strontium, is up to an order of magnitude higher than expected. As the diffusion direction is "out" (i.e. higher concentrations in the plagioclase than at the interface), this could indicate that we have not analysed the full profile.

Comparing BF60 and BF68, there is no significant difference between the diffusion rate of Sr into plagioclase of composition An_{60} and An_{68}. Although there is a significant variation in the strontium diffusion rate between experiments BIR66 and AGV66, which is measured by both nanoSIMS and LA-ICP-MS, this difference is not observed in the simple system experiments (Figure 62B,C). As such, AGV66 is considered an outlier.

Comparing this study with previous studies on the diffusion in labradorite, this AGV66 experiment is clearly anomalous (Figure 66). The interface between the plagioclase and melt is one of the best of all the experiments.

Determining the Arrhenius relationship between the data presented in this study (with AGV66 omitted) we obtain an activation energy of aE = 427 kJ /mol and a pre-exponential factor of log D_0 = -1.97 m^2 / s however you must keep in mind that this study is only 2 temperature points at extremely high temperatures compared to natural samples.

The closest composition of labradorite (An_{67}) was studied by Cherniak and Watson, (1994). These two experimental series cover different temperature ranges so can be combined to give a more accurate relationship between temperature and An_{67} (Figure 66). Cherniak and Watson (1994) concluded that Sr diffuses in An_{67} at a pre-exponential factor

of log D_0 = -7.03 ± 0.37 with an activation energy of aE = 268 ± 8 kJ / mol. With the inclusion of the hotter temperatures studied here this shifts to slower rates of log D_0 = -7.76 and an activation energy of aE = 254 kJ / mol.

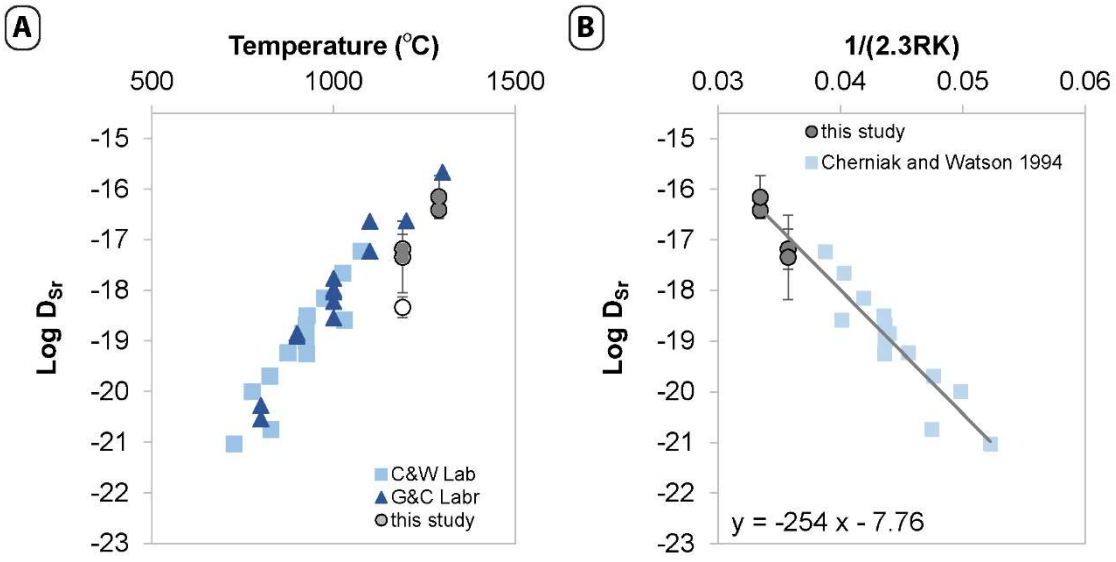

Figure 66: The Arrhenius relationship between the partitioning of strontium in labradorite (An_{61}-An_{68}) and temperature. squares; An_{67} Cherniak and Watson (1994), triangles; An_{63} Giletti and Casserly (1994), grey circles; This study An_{66}-An_{68}. Sample AGV66 (open circle) is considered an outlier.

This can be compared to Giletti and Casserly (1994) who studied a range of plagioclase compositions (Figure 66). Giletti and Casserly (1994) find a pre-exponential factor of Log D_0 = -5.8 and an activation energy of aE = 298 kJ / mol.

Barium Diffusion

Ba was measurable in all labradorite experiments even though the profiles are extremely short (Appendix 3; Figure 121(pg. 263)). Ba diffusion is not effected by melt composition.

There is an Arrhenius relationship between the diffusion of Ba in labradorite (~An_{67}) and temperature.

The diffusion of barium in labradorite (An_{67}) was investigated by Cherniak (2002) and the results are in good agreement with those discovered here, with the exception of the simple system diffusion experiment. Cherniak (2002) found that diffusion of barium along the (001) axis had a diffusion rate of log D_0 = -6.6 ± 0.84 and an activation energy of 323 ± 20 kJ / mol while the (010) has log D_0 = -5.98 ± 0.99 with an activation energy of aE = 341 ± 23 kJ / mol.

Combining the data presented here and the data from both orientations of labradorite given in Cherniak (2002) the relationship is changed to $aE = 376$ and a pre-exponential factor of $\log D_0 = -4.29$

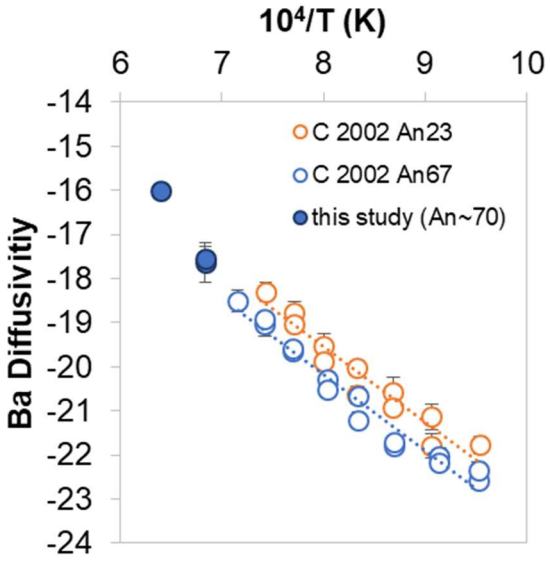

Figure 67: Arrhenius relationship of Ba in labradorite plagioclase (An_{66}-An_{68} in blue, An_{23} in orange) Open symbols represent published data from Cherniak (2002). Diffusivity is logD (m/s^2)

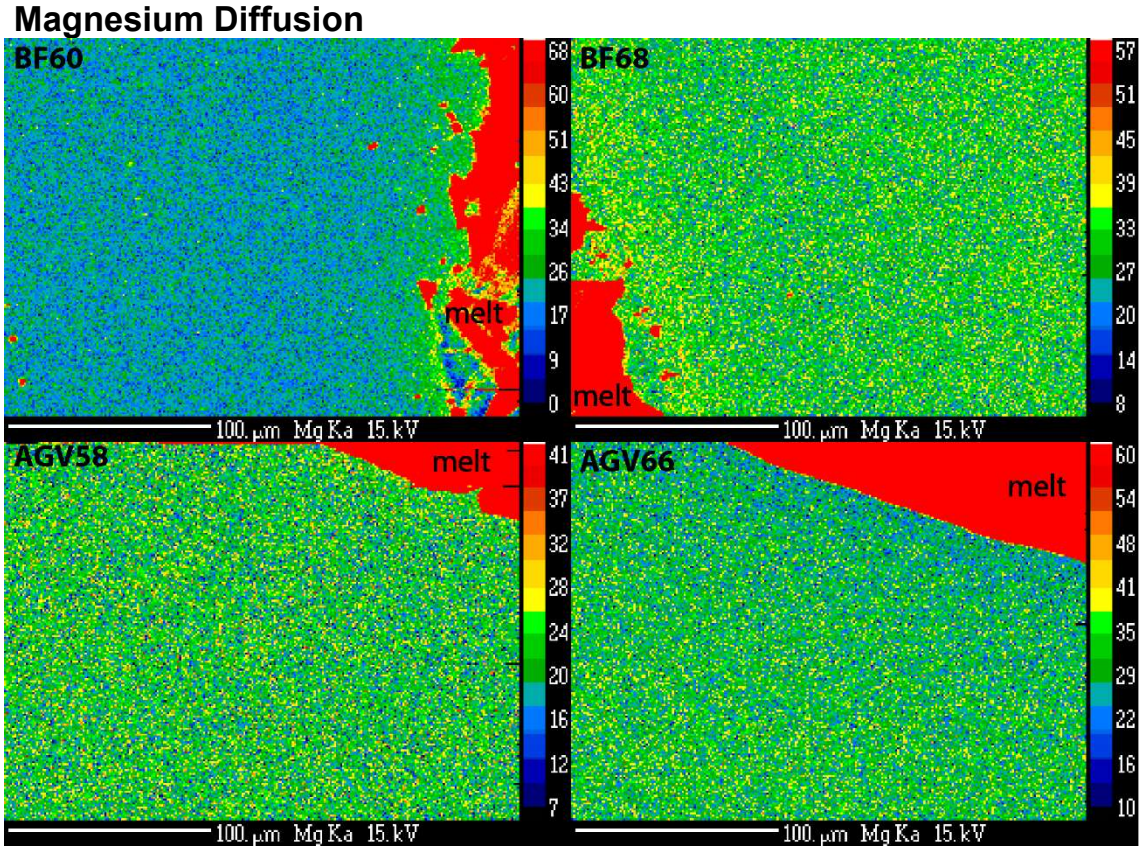

Figure 68: diffusion of Mg as mapped by EPMA in 4 samples. Diffusion directions are: BF60, diffusion in. BF68, diffusion in and out. AGV58, diffusion in and out. AGV66 diffusion out.

Magnesium was of high enough concentrations in the plagioclase that the diffusive change could be visually mapped. Both diffusion into the plagioclase from the melt (Figure 68, BF60) and diffusion from the plagioclase out into the melt (Figure 68, AGV66) are visible in these experiments.

In samples BF60 and BIR66, Mg diffuses into the crystals with diffusivities of -16.1±0.5 and -16.4±0.3 respectively. Sample AGV66 diffuses out of the plagioclase at a faster rate, with a diffusivity of -15.2±0.2 (Appendix 3; Table 57, pg.264).

Samples BF68 and AGV58 have two complimentary diffusion profiles visible. The Mg diffuses both "in" (slower) and "out" (faster) of the plagioclase. This diffusion behaviour is witnessed in all the measured Mg isotopes; Mg^{24}, Mg^{25} and Mg^{26}. This behaviour is not exhibited by either Fe or Mn, which also can be divalent cations, but are larger cations at 0.92 and 0.96 Å respectively compared to Mg^{2+} at 0.89 Å in VIII fold co-ordination.

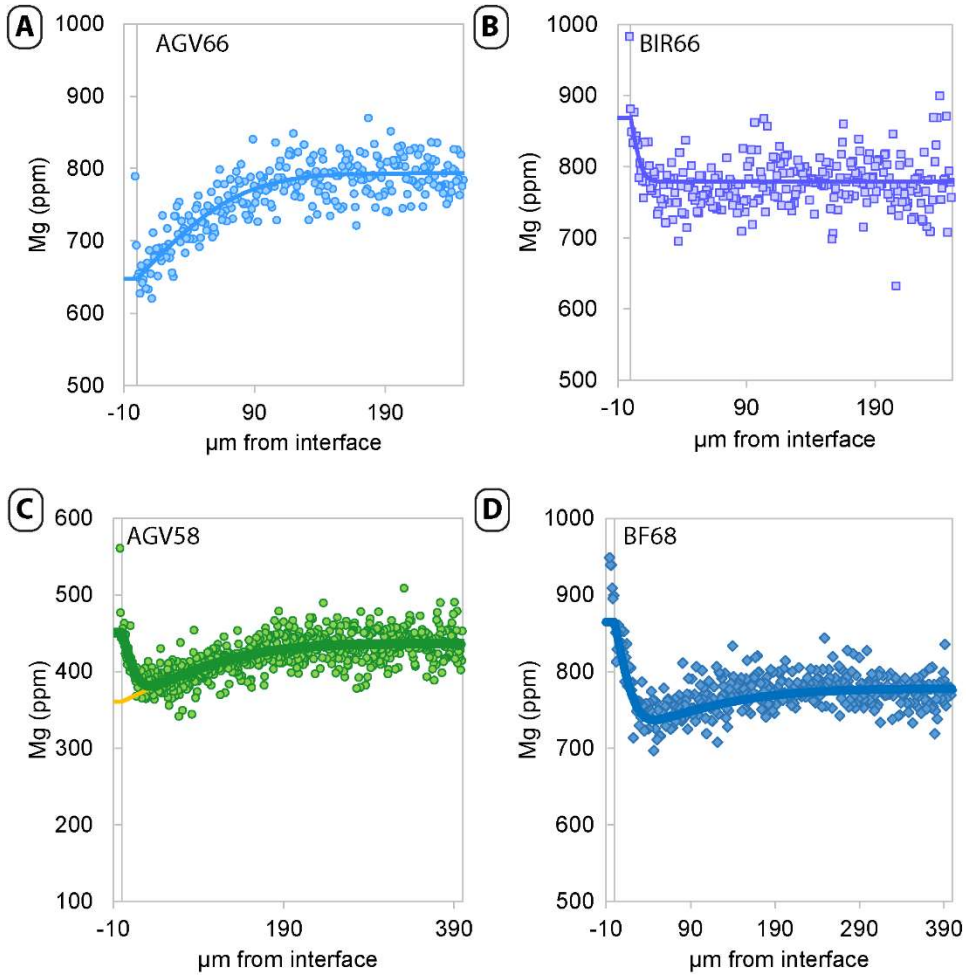

Figure 69: Diffusion of Mg between plagioclase and "natural" melts at 1190°C measured with LA-ICP-MS A) An66 with andesitic AGV melt B) An66 with basaltic BIR melt C) An58 with andesitic AGV melt D) An68 with basaltic BF melt. Both C and D display both diffusion "in" and "out" of two competing diffusion mechanisms.

Miller et al. (2006) investigated the partitioning of the divalent cations into anorthite and found that Mg can exist both on the large cation site as; $MgAl_2Si_2O_8$ and on the tetrahedral site as; $CaMgSi_3O_8$.

The simplified substitution of Mg into anorthite is given by the following exchanges:

Mg on the T site:

Equation 62
substitution of Mg on the tetrahedral site of anorthite

$$CaAl_2Si_2O_8 + MgO + SiO_2 = CaMgSi_3O_8 + Al_2O_3$$

Mg on the M site:

Equation 63
substitution of Mg into the large cation site in anorthite

$$CaAl_2Si_2O_8 + MgO = MgAl_2Si_2O_8 + CaO$$

The actual substitution will be complicated by the albitic component. The Mg on the T site exchange will be favoured by systems with high silica activity as the Mg exchange is tied with a Si. The Mg on the M site, is not dependent on silica activity so should not be affected by melt changes. It is likely that these to mechanisms generally overprint each other. It is generally assumed that elements that substitute onto the large cation site diffuse faster than those in the tetrahedral site. In the previous chapter it was concluded that Mg is most likely to partition onto the tetrahedral site in plagioclase as the partitioning is effected strongly by the silica activity of the melt.

The effective partition coefficient of these diffusion "out" profiles are calculated by projecting the diffusion profile to the interface. The effective partition coefficient is 80% of the actual partition coefficient; which suggests this fast diffusion is the more dominant mechanism for partitioning. As the tetrahedral coordinated Mg is known to be the dominant form in plagioclase, this suggests the fast diffusion is tetrahedral Mg.

Faak et al. (2013) found that the experiments buffered for silica are 0.75-1 order of magnitude faster than unbuffered experiments (Figure 70). It was observed that high silica activities allows for a higher proportion of silica vacancies in the form $\square Si_4O_8$ which likely contributes to the diffusion rate.

They conclude with giving a descriptor of the diffusion rate in plagioclase that depends on the activity of silica in the form:

$$D_{Mg}^{Pl} = 1.25 * 10^{-4} * \exp\left[-\frac{320{,}924}{RT}\right] * (\alpha SiO_2)^{2.6}$$

Which gives the log D_0 = -3.90 and an activation energy of 320 kJ / mol.

The additional SiO_2 would also allow an increase in the diffusion of the tetrahedral site Mg.

The diffusivities of Mg in the buffered "simple system" experiments are variable, with one experiment showing gradually faster diffusion toward one end of the crystal. This brings up a possible uncertainty of these diffusion profiles.

If the plagioclase crystal is not cut directly perpendicular to the diffusive interface, the diffusion profiles can be artificially lengthened. The profiles cannot be shortened by this method. Therefore, where there is a large standard deviation in the diffusivities, the shorter profiles represent more robust data than the longer profiles.

These buffered diffusion experiments are not useful in determining the diffusion mechanisms in Mg.

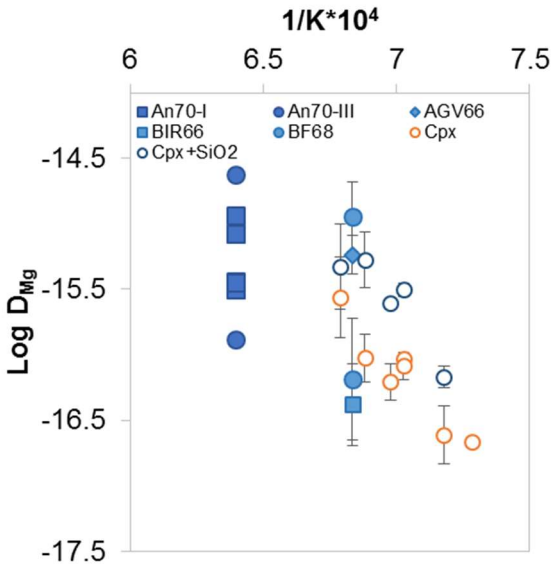

Figure 70: Diffusion of Mg in labradorite in both published work by Faak et al. (2013); open symbols, and this study; filled symbols

Beryllium diffusion

Beryllium was doped into only samples AGV66, AGV58 and BIR66. These experiments allow for the comparison of melt composition. As the plagioclase compositions are very similar and the experiments with beryllium are carried out at only 1 temperature, no other variables can be compared confidently.

The Be profiles are very short; <5µm for AGV experiments and <10µm for the BIR66 experiment (Appendix 3; Figure 121(pg. 263)). These samples were measured by both nanoSIMS and LA-ICP-MS and results are within error.

The partition coefficients are within an order of magnitude of the predicted partitioning values, with the nanoSIMS partition coefficients more precise than those calculated by LA-ICP-MS.

Beryllium exists as a divalent cation and is very small; 0.27 Å in IV-coordination. Rather than the large cation site "M", the beryllium is diffusing on the tetrahedral site replacing Al^{3+}. This would require a charge balancing in the form:

Equation 64
beryllium substitution for aluminium onto the tetrahedral site of anorthite

$$CaAl_2Si_2O_8 + BeO + SiO_2 = CaBeSi_3O_8 + Al_2O_3$$

$$Al^{3+} + Al^{3+} \rightarrow Be^{2+} + Si^{4+}$$

Incorporating beryllium on the tetrahedral site for aluminium causes the beryllium partitioning to increase as the aluminium activity of the melt decreases and/or the activity of silica in the melt increases.

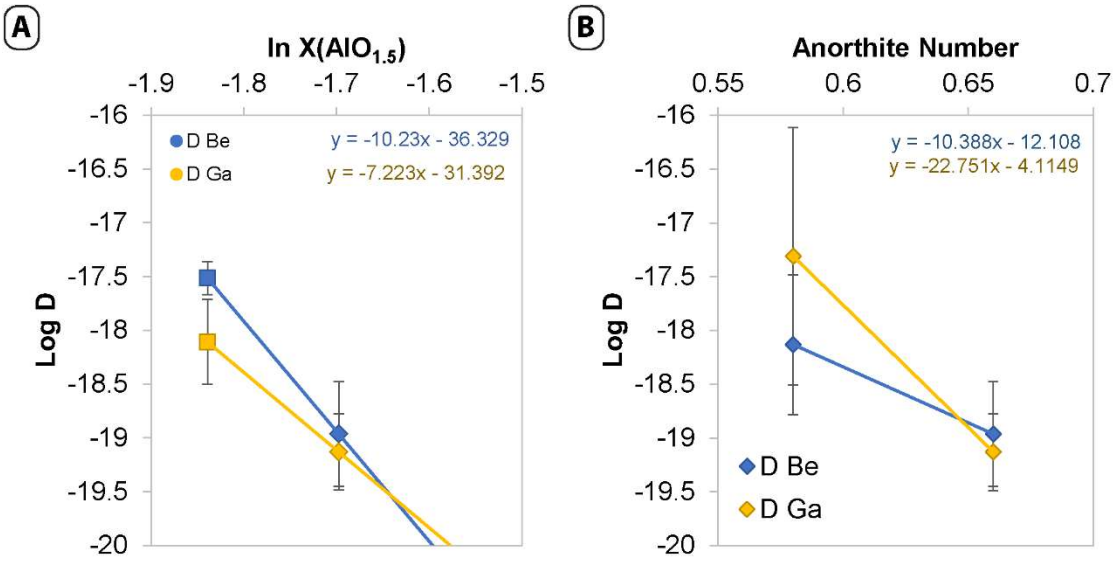

Figure 71: Diffusion rate of Be and Ga at 1190°C A) in An_{66} as a function of melt alumina content B) from the same melt composition as a function of anorthite content.

The diffusivity of beryllium is within error when comparing the two AGV experiments with different plagioclase compositions (Figure 63B). Conversely, when comparing similar plagioclase compositions and different melt compositions; there is an order of magnitude difference (Figure 62B). The samples with the andesitic melt have diffusivities

of -19.0 ± 0.5, while the basaltic melt diffuses faster ($logD_{Be}$ = -17.5 ± 0.2) (Appendix 3; Table 57, pg.264).

It is difficult to determine the activity of the components in a natural system. It is usually assumed that the increase in molar proportion indicates an increase in activity of that component. The proportion of aluminium and silica both increase when moving from basaltic (BIR) to andesitic (AGV) compositions while the diffusion rate decreases (Figure 71).

Beryllium diffusion was only measured at one temperature and this element has not been investigated as a diffusant in plagioclase previously and as such, no Arrhenius relationship can be calculated.

Manganese and Iron diffusion

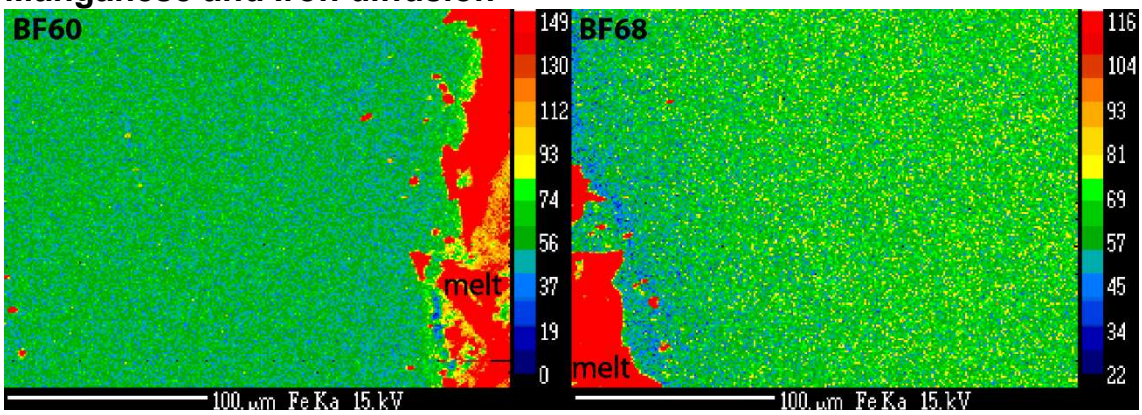

Figure 72: Diffusion of Fe as mapped by EPMA

Iron is a minor component in most plagioclase and occurs in these tested plagioclase at 0.40-0.46 wt. % FeO. Fe diffuses out of the plagioclase in all experiments. In the andesitic experiments, the change in concentration is only 300 ppm while in the basaltic experiments the change is in the range of 800 ppm. The change in concentration due to diffusion from the andesitic melt is too small to be resolved with EPMA.

Iron diffusion has been investigated in An_{66} at different oxygen fugacity by Behrens et al. (1990), however no data table was published. The Fe diffusivities at 1200°C are log D=-16.58 ± 0.19 at log αO_2 = -0.68 and log D = -15.28 ± 0.11 at log αO_2 = -10.59. Furthermore they discover a dependence of oxygen fugacity on the diffusion of Fe, of 1.5 log units in a change of 10 log units of αO_2 (Behrens et al., 1990; Cherniak, 2010). The Behrens et al. (1990) data point is within error of the data presented in this study.

Mn can exist as 2+, 3+, 4+, 5+, 6+ or 7+. Mn^{2+} would be the most compatible in plagioclase. Mn^{2+} is of similar size as Fe^{2+}; 0.96 and 0.92 Å respectively (assuming

divalent cation in VIII-fold co-ordination) and therefore these two elements are assumed to behave similarly. Mn is in much lower concentrations in plagioclase than Fe and can be measured precisely with LA-ICP-MS. As Mn diffuses out of the plagioclase in all experiments, though has high concentrations in the melt and buffers it was used as the indicator element for where the interface is placed.

Substitution of divalent cations on the "M" site is given by:

Equation 65
Divalent substituion in anorthite

$$CaAl_2Si_2O_8 + M^{2+}O = MAl_2Si_2O_8 + CaO$$

This equation shows that the substitution of divalent cations into the anorthite crystal structure is a straight substitution with no effect from the melt component.

There is very little orientation effect found with the diffusion of Mn with a standard deviation of ~0.2 log units for all experiments (Appendix 3; Table 57, pg.264) except for An_{67}-II(TM) which has the largest deviation of 0.5 log units. This is very robust data as between 11-28 profiles were collected for Mn in plagioclase diffusion from melt experiments.

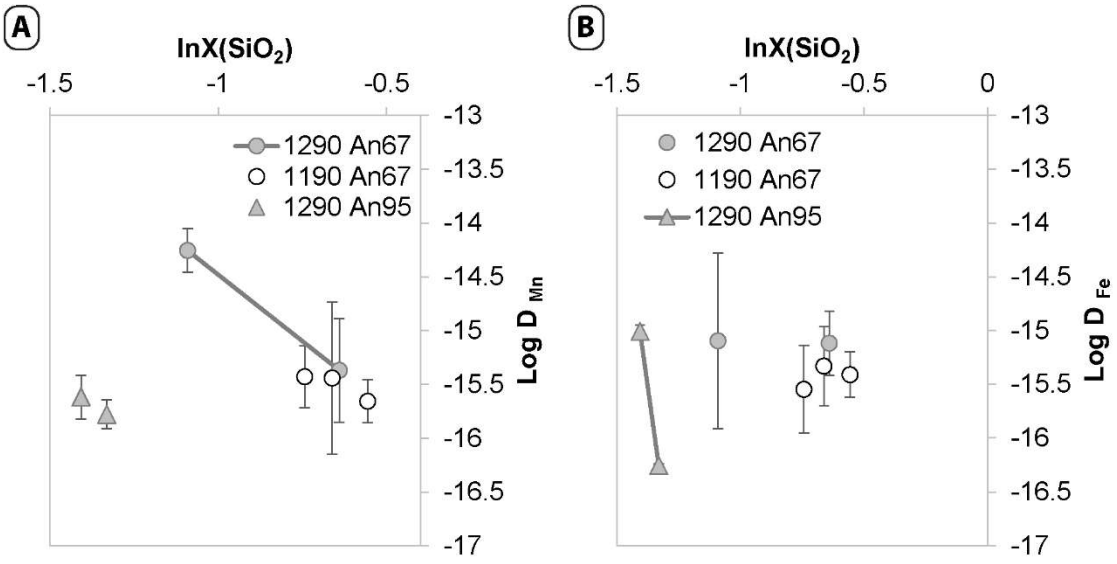

Figure 73: Diffusion as a function of the silica component of the melt, at 1290°C (grey symbols) and 1190°C (open symbols) in An_{66} (circles) and An_{95} (triangles) plagioclase. A) Diffusivity of Mn B) Diffusivities of Fe.

There is an apparent effect of melt composition on the diffusion of Mn in An_{67} at 1290°C. There is also an apparent effect of melt composition on the diffusion of Fe into An_{95} at 1290°C. This is not seen in An_{67}. As all other samples have diffusion rates within error of

one another; even when comparing An_{67} and An_{95}, it is likely that these are anomalous results (Figure 74).

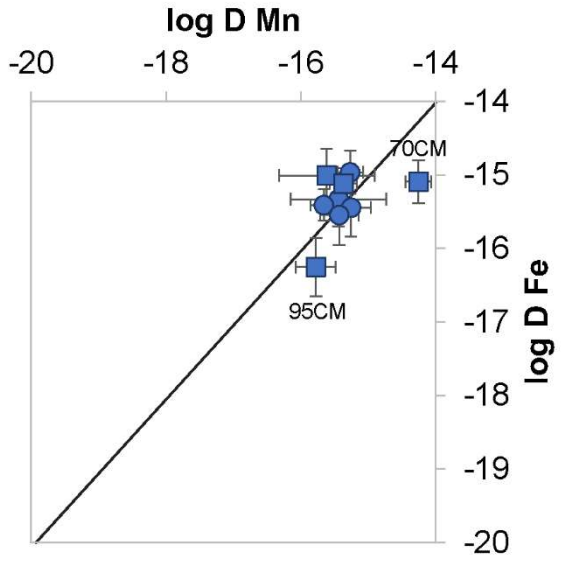

Figure 74: a comparison of the diffusivities of Mn and Fe at 1190°C (circles) and 1290°C (squares) and QFM.

Comparing divalent cation diffusivities

These multi-element diffusion experiments have the advantage of directly comparing the diffusivities of elements in each experiment. Strontium and barium both partition onto the large cation site of plagioclase while Be partitions onto the tetrahedral site. Mg is thought to prefer to partition onto the tetrahedral site however may have some input into the M-site.

Comparing the divalent cations in the M-site; Ba and Sr, the diffusivities of these two elements are identical at composition An_{68}. At composition An_{70} the diffusion of Ba is faster than Sr and as the calcium content of the plagioclase decreases, the diffusivity of Sr increases. In plagioclase with composition An_{58} Sr diffuses an order of magnitude faster than Ba (Figure 75A).

Beryllium partitions onto the tetrahedral site. Comparing the Sr and Be diffusivities, there are no discernible trends. This suggests different diffusion mechanisms for these two divalent cations (Figure 75d).

There are two observable diffusion mechanisms for Mg in plagioclase. Comparing the diffusivities of Mg and Sr (the latter of which diffuses only on the M-site), the contribution to the M-site diffusion in plagioclase can be assessed. The “slow” diffusion

of Mg, is consistently faster than strontium in all experiments (Figure 75C) by roughly an order of magnitude.

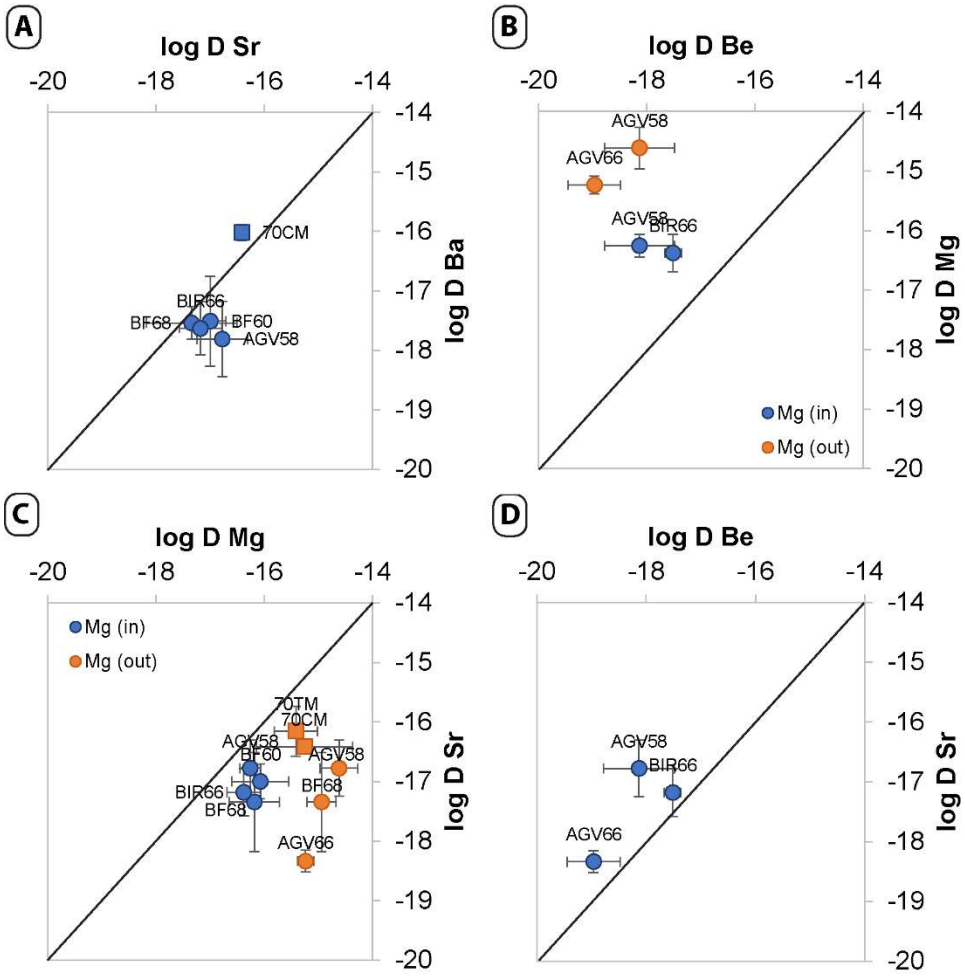

Figure 75: A comparison of the diffusivities of the divalent cations in all experiments (1190 and 1290°C). The black line represents identical diffusivities. Circles represent 1190°C and squares are 1290°C. A) comparing the diffusivities of VIII-fold coordinated divalent cations; Ba and Sr. B) comparing the diffusivities of Be and Mg. C) comparing the diffusivities of Mg and Sr. D) comparing the diffusivities of tetrahedral coordinated divalent cations (Be) and VIII-fold coordinated divalent cations (Sr).

As the relationship between the Mg slow diffusion and Sr is consistent, it is assumed this slow diffusion is the M-site diffusion mechanism for Mg. Additionally, the diffusion "in" and "out" of this diffusion mechanisms are comparable. The directionality of the diffusion profiles is dependent only on partition coefficients rather than diffusion mechanism.

There is a consistent ratio between the "fast" Mg diffusion and the diffusion of Be. This could suggest a relationship between these two diffusion mechanisms, however with only two data points, conclusions are not robust.

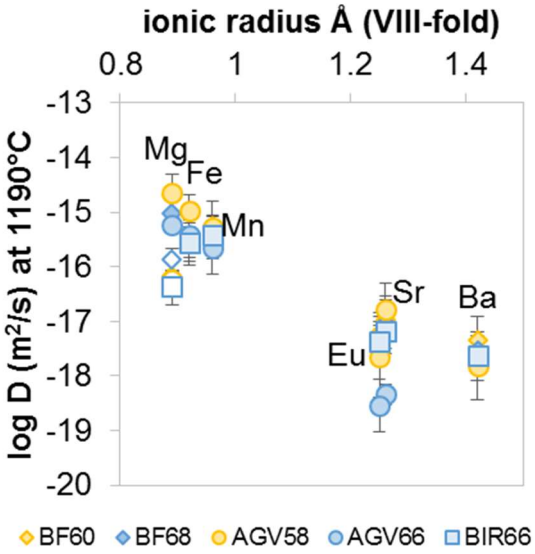

Figure 76: The comparison between diffusivities of divalent cations with their respective ionic radius in VIII-fold coordination. $An_{\sim 60}$ composition in yellow, and $An_{\sim 70}$ composition in blue. Open symbols are slow "in" diffusion of Mg. Fe, Mn and Eu diffusivities could be the sum of multiple valence cation diffusion, though the 2+ cations will be the most compatible.

4.4.5 Gallium Diffusion

Gallium was measurable as a diffusant in AGV58, AGV66 and BIR66. Gallium diffuses more than an order of magnitude faster from the basaltic melt (BIR66) than the andesitic melt (AGV66) into An_{67} plagioclase (Figure 62B), similar to Be.

Ga is a trivalent cation and most likely in IV-coordination as it is similar in size to Al (0.47 Å = Ga and 0.39 Å = Al) so will allow for straight substitution in the form:

Equation 66
gallium substitution into the tetrahedral site of plagioclase

$$CaAl_2Si_2O_8 + Ga_2O_3 = CaGa_2Si_2O_8 + Al_2O_3$$

$$NaAlSi_3O_8 + \frac{1}{2}Ga_2O_3 = NaGaSi_3O_8 + \frac{1}{2}Al_2O_3$$

This diffusion is very slow (Figure 62), and may represent the speed of the aluminium site diffusion. This diffusion was unable to be observed on the nanoSIMS.

Comparing tetrahedral site diffusion

As gallium partitions onto the tetrahedral site, it can compared with other tetrahedral coordinated trace elements such as Be and Mg. Due to their different charges, Be and Mg substitute onto the tetrahedral site via coupled substitution with silicon while Ga requires no charge balance.

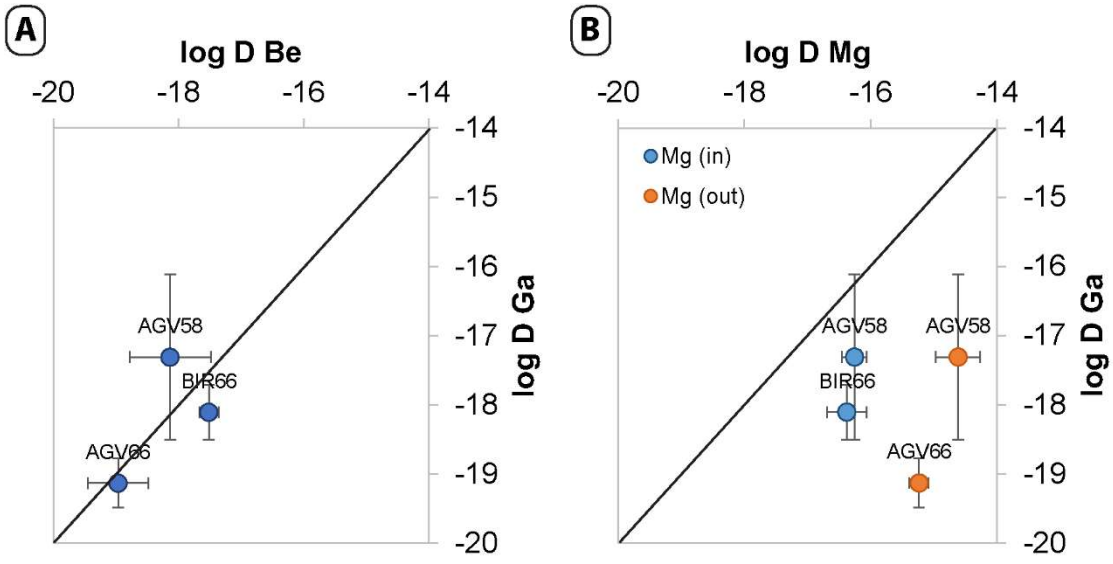

Figure 77: A comparison between the diffusivities of tetrahedral coordinated cations. A) A comparison between Be^{2+} and Ga^{3+} diffusivities B) A comparison between Mg^{2+} and Ga^{3+} diffusivities

The diffusivities of Be and Ga are comparable and near identical within error. These two elements have different charges, sizes (Be is 0.27Å and Ga is 0.47Å) and relationships with the melt activity. Their only common feature is their site preference. No such relationship is shown between Mg and Ga diffusivities.

4.4.6 Rare Earth Element Diffusion

Rare earth element diffusion profiles were measurable in all experiments. These elements diffuse very slowly and have diffusion profiles of less than 5µm which means the entire diffusion profile is made by one or two LA-ICP-MS points.

Diffusion of Ho was observed in experiment AGV58 on the nanoSIMS at a rate of $LogD_{Ho} = -18.71$ with a very small standard deviation (0.18) between the 4 analysis. This agrees well with the diffusion coefficients of Dy (-18.78 ± 0.25, n=4) and Er (-18.66 ± 0.36, n=2) measured by LA-ICP-MS. No rare earth element diffusion profiles were observed in the other experiments on the nanoSIMS. As the nanoSIMS agrees with the LA-ICP-MS data for sample AGV58 is assumed that the LA-ICP-MS data are precise for even very short profiles.

Diffusion of the rare earth elements is expected to be very slow as the incorporation of these trivalent cations would be charge balanced by an aluminium in the form:

Equation 67:
aluminium dependence on the substitution of REE

$$CaAl_2Si_2O_8 + \frac{1}{2}Ln_2O_3 + \frac{1}{2}Al_2O_3 = LnSiAl_3O_8 + CaO + SiO_2$$

$$NaAlSi_3O_8 + \frac{1}{2}Ln_2O_3 + Al_2O_3 = LnSiAl_3O_8 + \frac{1}{2}Na_2O + 2SiO_2$$

Additional to the very short diffusion profile, there is a very fast, low magnitude diffusion of the rare earth elements from the natural type melts (Figure 78). This type of diffusion is not observed in the simple system experiments due to the very low concentrations of trace elements.

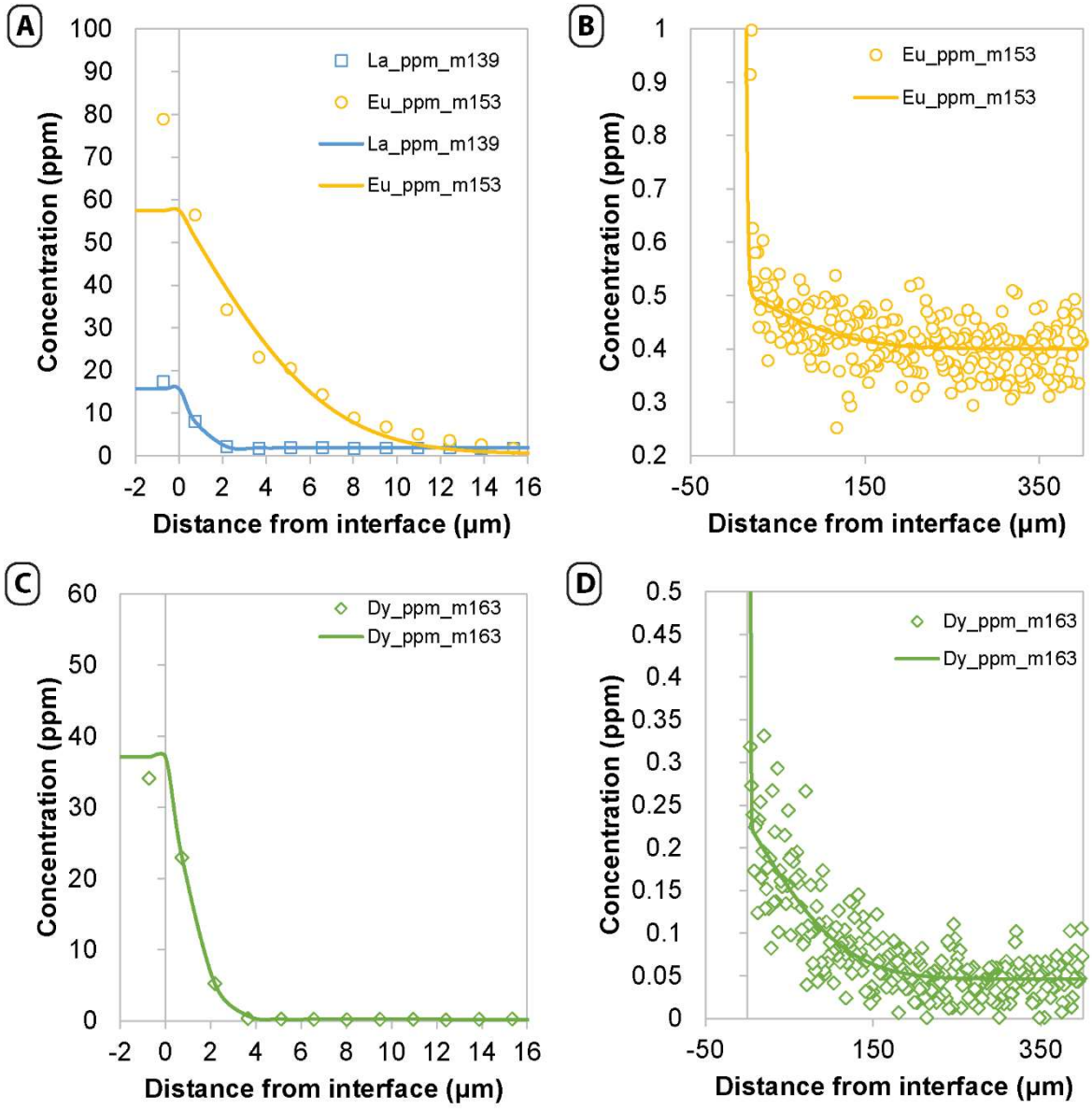

Figure 78: evidence of fast diffusion in the rare earth elements sample AGV58 A) slow diffusion profiles for Eu and La B) fast, low magnitude diffusion of Eu C) slow diffusion of Dy D) fast diffusion of Dy in the same profile.

These diffusion profile are 4 orders of magnitude faster than the normal diffusion rate (Figure 79). This suggests another mechanisms for diffusion possibly contributed by vacancy substitution in the form:

Equation 68
incorporation of rare earth elements with vacancy substitution

$$CaAl_2Si_2O_8 + \frac{2}{3}LnO_{1.5} = Ln_{\frac{2}{3}}\square Al_2Si_2O_8 + CaO$$

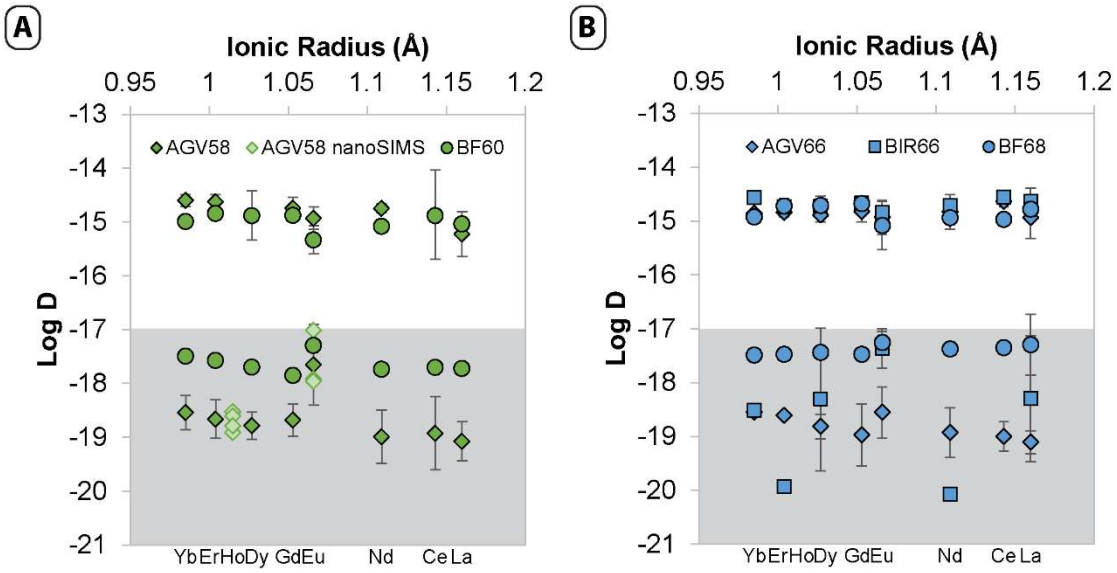

Figure 79: Diffusion of the rare earth elements in reference to their ionic radius in VIII-fold coordination. A) Diffusion in An60 B) Diffusion in An67

The diffusivities of the REE are not dependent on their respective ionic radius; and all the REE (except Eu^{2+}) diffuse at the same rate (Figure 79).

The data we've obtained from the LA-ICP-MS agrees well with data published in Cherniak (2003) (Figure 80).

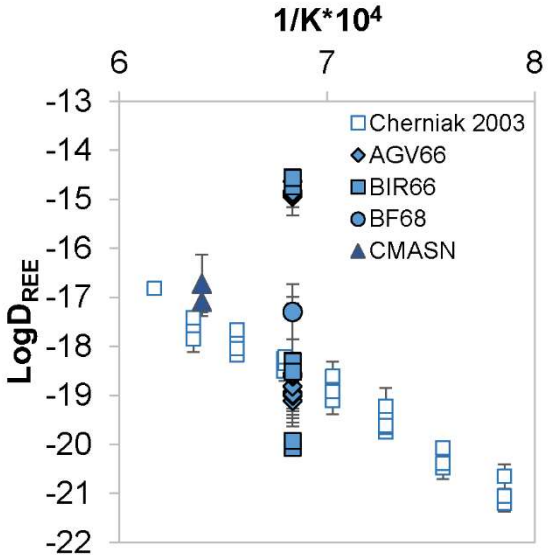

Figure 80: Rare earth element diffusion in labradorite, Published values of diffusion in An_{67} (Cherniak, 2003)

There is no fast diffusion observed in the simple system diffusion experiments. This is due to the much lower concentrations of rare earth elements in the diffusant. As the magnitude of this diffusion is very small, it is likely undistinguishable from the noise in the low rare earth elements counts.

Europium diffusion

Europium is by far the most compatible of the rare earth elements due to its ability to exist as either trivalent or divalent cations. The divalent cations are much more compatible in plagioclase, with Eu^{2+} assumed to partition onto the M site due its similar ionic radius to Sr (1.26Å and Eu^{2+} 1.25Å). Because of the high compatibility of Eu^{2+} the interface concentrations are very high.

The diffusivities are within error of the diffusivities of strontium. This is also evidence that diffusion "in" (Eu^{2+}) and diffusion "out" (Sr) occur by the same mechanisms.

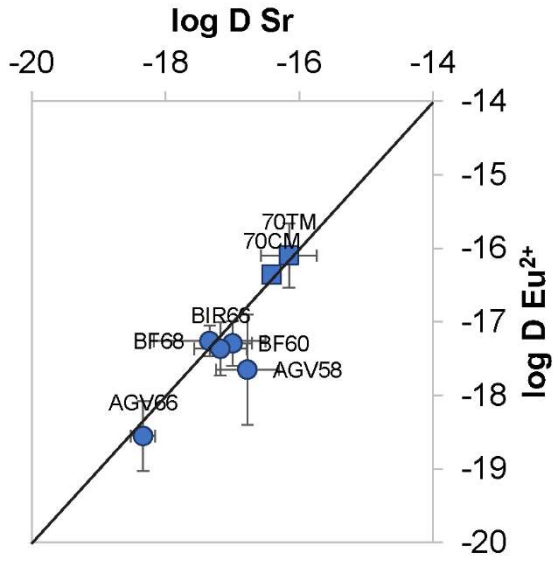

Figure 81: A comparison between the diffusivities of Eu^{2+} and Sr in all experiments. Circles represent 1190°C and squares are 1290°C

4.4.7 Fast diffusion mechanism

Both Mg and the REE show unusually fast diffusion mechanism in addition to their expected diffusion mechanism. These fast diffusion profiles are measured at almost an identical rate (with the exception of AGV58) (Figure 82) and is the fastest rate of diffusion in plagioclase.

This rate is not effected by ionic radius, melt composition or plagioclase composition (in the range An_{58}-An_{68})

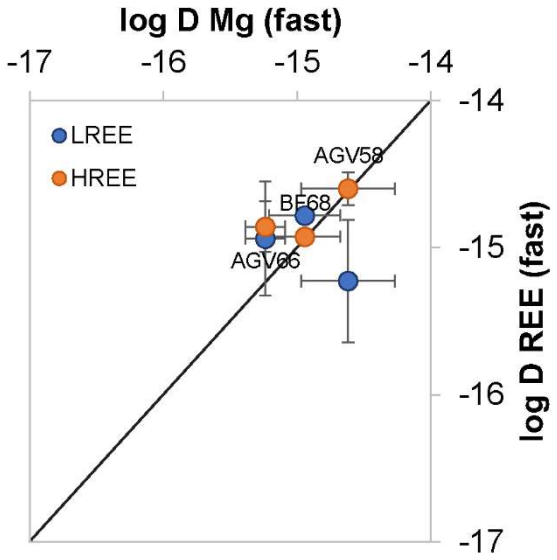

Figure 82: A comparison between the very fast diffusivities of both Mg and the rare earth elements (REE).

4.5 Discussion

Combining the data obtained in this study and published values for diffusion in labradorite, Arrhenius relationships were improved. Comparing the Arrhenius relationships for An~70 plagioclase, K and Sr (Cherniak and Watson, 1994; Giletti and Shanahan, 1997) have roughly parallel slopes as do; Ba, REE and Mg (Cherniak, 2002; Cherniak, 2003; Faak et al., 2013).

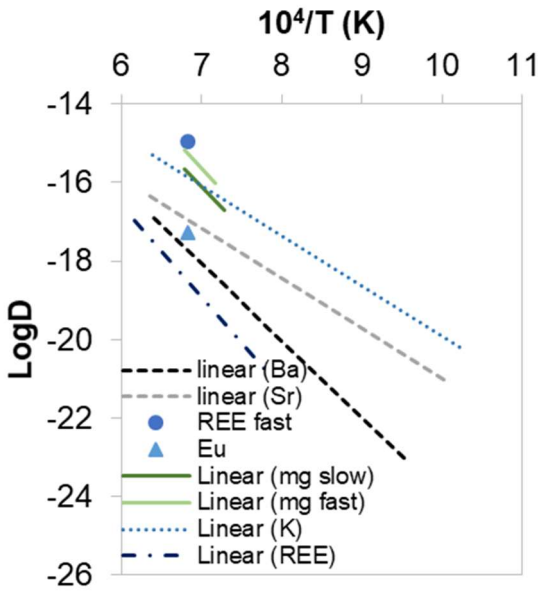

Figure 83: A comparison of the Arrhenius relationships of published diffusion data in An~70 plagioclase. (Cherniak, 2002; Cherniak, 2003; Cherniak and Watson, 1994; Faak et al., 2013; Giletti and Shanahan, 1997)

The relationship between the diffusivities of Ba and Sr change slightly with anorthite content of the plagioclase, suggesting there may be an effect of ionic radius on the diffusivities of the divalent cations in the M-site that changes with anorthite content. In simpler minerals such as forsterite, the ionic radius of the cations has no great effect on the diffusivity of the element, nor does the charge (Spandler and O'Neill, 2009).

Comparing literature data, the diffusivities of Ba and Sr change with anorthite content, with albite rich plagioclase diffusing significantly faster than anorthite rich plagioclase (Cherniak, 1996, 2002; Cherniak and Watson, 1994; Giletti and Casserly, 1994). Ba is affected by temperature much more than Sr (Figure 83). This suggests at high temperatures, Ba will diffuse faster than Sr, as discovered in An70 + corundum, mullite buffer at 1290 °C.

The data presented here suggests that the diffusion of the divalent cations in the M-site is affected by ionic radius (Figure 76). The smaller divalent cations are found to diffuse faster than the larger divalent cations.

Sr diffusivities in literature and this study are highly variable; attributed to crystal orientation effects (Cherniak, 2010). These experiments were not orientated but no other element shows a significant variation in the diffusion rate other than strontium. Cherniak (2010) notes that the only other element to show anisotropy is lead (Pb). The reason for this is still unknown. In these experiments, only sample AGV58 shows a significantly slower diffusion rate than any of the other experiments, and was only resolvable in three profiles.

The strontium partition coefficients are much higher than equilibrium concentrations in all experiments. All other extremely short diffusion profiles have partition coefficients close to equilibrium values which suggests it is not a problem with defining the placement of the interface.

When examining the melt Sr concentrations by nanoSIMS (Figure 56), the concentration changes gradually over 1-2µm. This may be an artefact of the analytical method or could represent local equilibrium of the melt immediately adjacent to the plagioclase crystal. This would cause the partition coefficients for these elements to be incorrect as the melt in the centre of the well is not in equilibrium with the crystal. Diffusion of major elements in melts is very fast (Guo and Zhang, 2016). Watson (1979) investigated the diffusion of calcium in melt and gives a result of approximately $\log D_{Ca}^{melt} = -6.2$ at 1 kbar and 1200 °C and assuming that strontium behaves the same way in a silicate melt, due to similar

charge and size, it should diffuse equally as fast. The diffusion of major elements is known to be very fast, however the diffusion of trace elements in melts is less well understood. To resolve this, the diffusion of trace elements in silicates melts could be investigates in a similar experimental set up as the Watson (1979) experiments. This would be an interesting study with applications for all mineral diffusion and partitioning. If trace elements diffuse slowly through melt, the "equilibrium melt" that is in contact with the growing face of the crystal might have a different composition than the "bulk melt" and therefore significantly impact partition coefficients.

Magnesium diffusion in plagioclase has previously been investigated by a number of authors (Costa et al., 2003; Faak et al., 2013; Faak et al., 2014; LaTourrette and Wasserburg, 1998; Van Orman et al., 2014).

Costa et al. (2003) show that the diffusion of trace elements, specifically Mg, can be tied to concentration gradients in the major elements. This is particularly relevant in the simple system experiments as some diffusive exchange of CaO was observed with the EPMA. The simple system experiments vary by an anorthite number of <2 between the core and the rim. Even though the results of trace element concentrations are not significantly changed when the internal standard for laser data is selected at Ca^{43} of Si^{29}, this change in major element concentration may have affected the diffusion profile itself. This assumption would need to be corrected by running additional experiments that are ensured to be in equilibrium and comparing the equilibrium diffusion with these experiments that cause changed in the plagioclase chemistry.

Here it was discovered that Mg partitions preferentially onto the tetrahedral site ($CaMgSi_3O_8$) however there may also be some contribution of the M-site ($MgAl_2Si_2O_8$). For Mg diffusion, there are two competing diffusion mechanisms.

In a few experiments, these two diffusion mechanisms work in direct competition with each other, with the fast mechanism diffusing out and the slow mechanism diffusing in. If the effective partition coefficient of the fast diffusion "out" is calculated, it is found to contribute approximately 80% of the equilibrium partition coefficient. As tetrahedral Mg is known to be the main contributor to Mg and plagioclase, it is assumed this fast diffusion represents tetrahedral Mg ($CaMgSi_3O_8$). These fast diffusivities also have a linear relationship with Be diffusivities, a known tetrahedral coordinated divalent cation. The fast diffusion mechanism was found to occur during high silica activity buffers in Faak et

al. (2013), however in the silica buffered experiments presented in this study there was no noticeable difference between the two.

Therefore, $CaMgSi_3O_8$ diffuses more quickly than $MgAl_2Si_2O_8$. If this assertion is true, it is the opposite of what would be assumed for these mechanisms. As $CaMgSi_3O_8$ requires a change balance exchange, it would assumedly diffuse much slower than $MgAl_2Si_2O_8$, which does not require a charge balance.

Mg does not have significant diffusional anisotropy (Faak et al., 2013; Van Orman et al., 2014), therefore the variation in diffusivities in the simple system experiments are likely due to the experiment being cut at an angle to the interface. The shorter diffusion profiles are effected less by this change in angle.

The fast diffusion mechanism is only observed within the natural type diffusion experiments. This is because of the extremely low magnitude of the compatibility of this type of diffusion. As the concentration gradient in the natural melts were much higher than the simple systems, this diffusion mechanisms was able to be distinguished from the background values.

The fast diffusion for both Mg and REE have very similar rates, suggesting that this is a common diffusion mechanism. Faak et al. (2013) found that the fast diffusion rates for Mg coincided with SiO_2 buffered experiments. We do not see the fast diffusion rates in our simple system buffered experiments, though the diffusion rates are highly variable.

Eu^{2+} is orders of magnitude faster than the trivalent REE. If Eu^{2+} diffusion occurs in plagioclase crystals, the europium anomalies would be exaggerated. With its very high compatibility, it could be used as an indicator of oxygen fugacity changes in the system.

Mn and Fe are assumedly diffusing as divalent cations. These cations diffuse at a rate similar to each other and do not change significantly within the tested temperature range.

4.6 Conclusions

Diffusion of all elements are very slow in plagioclase compared to other silicate minerals such as olivine (Jollands et al., 2016; Spandler and O'Neill, 2009).

There are at least three diffusion mechanisms displayed in these experiments.

<u>Diffusion mechanism one</u> – same valence straight substitution on M site:

$$NaAlSi_3O_8 + \frac{1}{2}M^{1+}{}_2O = MAlSi_3O_8 + \frac{1}{2}Na_2O$$

$$CaAl_2Si_2O_8 + M^{2+}O = MAl_2Si_2O_8 + CaO$$

Mg, Fe, Mn, Sr and Ba can all exist as divalent cations and substitute on the large cation site (M). These elements diffuse more slowly as the cation radius increases. K would also substitute on the large cation site (M) however would exchange for Na and is faster than Ba which has a similar size.

The second diffusion mechanism – substitution on tetrahedral site

$$CaAl_2Si_2O_8 + BeO + SiO_2 = CaBeSi_3O_8 + Al_2O_3$$

Divalent cations substituting onto the T site require charge balancing with silica, which means this substitution is dependent on silica activity. There is an inverse relationship between the speed of Be diffusion and the silica content in the melt. The diffusion rate for this mechanism is effected by ionic radius.

The third diffusion mechanism is charge balanced substitution on the M site:

$$CaAl_2Si_2O_8 + \frac{1}{2}REE_2O_3 + \frac{1}{2}Al_2O_3 = REESiAl_3O_8 + CaO + SiO_2$$

This substitution is dependent on alumina content of the melt. The diffusion of the REEs using this mechanism is very slow. Diffusion using this mechanism is independent of ionic radius.

The fourth mechanism is vacancy controlled diffusion:

Faak et al. (2013) states that high silica activities lead to the formation of vacancies by the following substitutions:

Equation 69
formation of vacancies in plagioclase

$$CaAl_2Si_2O_8 + 2SiO_2 = \square Si_4O_8 + CaO + Al_2O_3$$

$$NaAlSi_3O_8 + SiO_2 = \square Si_4O_8 + \frac{1}{2}Na_2O + \frac{1}{2}Al_2O_3$$

The rare earth elements could substitute on existing vacancies by:

$$CaAl_2Si_2O_8 + \frac{2}{3}LnO_{1.5} = Ln_{\frac{2}{3}}\square Al_2Si_2O_8 + CaO$$

This vacancy would contribute to the diffusion of all elements, however as the concentration of the REE are so low, the small contribution of this diffusion can be observed.

These large cation vacancies will allow for fast diffusion of any element on the M-site, however the contribution of this mechanism is very small.

4.7 Future work

This thesis has outlined two competing diffusion mechanisms for Mg. Although most Mg partitions into plagioclase in almost exclusively tetrahedral coordination, it is possible that Mg could diffuse in VIII-fold coordination. An alternative possibility is that one of the two diffusion mechanism is attributed to the large cation vacancy ($\square Si_4O_8$) which occurs naturally in plagioclase. As Mg has the potential as a geothermometer and geospeedometer (Faak et al., 2013; Faak et al., 2014) it is important to investigating these two diffusion mechanisms and how much they interact.

Another mystery is the seemingly unique diffusive anisotropy of Sr. An investigation of the diffusivity in orientated crystals and comparing if there is measurable anisotropy in different temperatures and plagioclase compositions would be important to properly define the Sr diffusivity. This has important implications in the Rb-Sr geochronometer.

Also, as mentioned previously, a study on the diffusivity of trace elements in silicate melts could have massive implication for all diffusion and partitioning studies. If diffusion is slow and the magma is stagnant, there is a possibility for a film of depleted melt to exist around the growing mineral, causing a vastly different partition coefficient.

CHAPTER 5. CLINOPYROXENE - MELT PARTITIONING

5.1 Introduction

The aim of this thesis is to examine the partitioning of the Rare Earth Elements (REEs) between plagioclase and clinopyroxene to create a tool for uncovering the formation conditions of gabbros and basalts. To fully understand the partitioning between plagioclase and clinopyroxene, we must first understand the major factors that affect the partitioning of trace elements into each phase from an equilibrium melt.

Pyroxenes are the most important group of rock-forming minerals that contain iron and magnesium (Deer et al., 1992). Pyroxenes have the general formula $[M2][M1]Si_2O_6$ where many elements can substitute into the M1 and M2 sites. Some end members of the pyroxene family include; enstatite ($Mg_2Si_2O_6$), diopside ($CaMgSi_2O_8$), jadeite ($NaAlSi_2O_6$) and hedenbergite ($CaFeSi_2O_6$). This chapter will focus on the high calcium, magnesian pyroxenes; near the diopside end-member.

Diopside contains two sites into which the trace elements are likely to partition, the M1 site which contains magnesium and the larger M2 site which contains calcium. The M1 site is VI-fold coordinated and the M2 site has VIII-fold coordination. It is generally believed that the M1 site is more "rigid" than the M2 site and less likely to take up cations of the wrong size (Wood and Blundy, 2014).

This chapter aims to investigate the trace element partitioning in clinopyroxene through two series of experiments. In the first series pure diopside was synthesised from melts of varying composition in the CaO-MgO-SiO_2 (CMS) system to determine if the activities of the major components of the melt effect partitioning. This section will also allow for thorough investigation of the partitioning site of these trace elements in diopside

The second series of experiments expands on the simple system to include Al_2O_3, Na_2O and Fe_2O_3 in the systems; CMAS, CMASN, CMASNF and natural like systems. This series of experiments gives a range of melt and crystal compositions, produced over a range of temperatures and pressures to determine what has the greatest influence on partitioning.

The most recent lattice strain models for the partitioning of trace elements in clinopyroxene (Dygert et al., 2014; Sun and Liang, 2012; Wood and Blundy, 1997) will be tested. Using the data presented in this thesis and other published experiments, a model for the best fit to the rare earth element partitioning into diopside will be created.

5.1.1 Models for the partitioning of rare earth elements in clinopyroxene

There are two lattice strain models for the partitioning of rare earth elements in high-Ca pyroxene. Both of these models assume partitioning only on the M2 site and assume that melt composition has a very little effect on partitioning in comparison to the crystal chemistry changes. The variables considered important in each of these models vary significantly.

The Sun and Liang (2012) model has crystal parameters including; mole fraction of Mg on the M2 site along with the tetrahedral (T) and octahedral coordinated (M1) aluminium. It also contains a parameter for the content of water in the melt. This data was modelled from 43 experiments over pressures of 1 atm – 4 GPa and temperatures of 1042-1470°C. This data was fit only to basaltic (<57 wt. % SiO_2) liquids.

Equation 70: Sun and Liang 2012. Lattice strain model for the rare earth element partitioning in clinopyroxene.

$$lnD_0 = -7.14 + \frac{7.19 * 10^4}{RT} + 4.37X_{Al}^{T} + 1.98X_{Mg}^{M2} - 0.91X_{H2O}^{melt}$$

$$r_0 = 1.066 - 0.104X_{Al}^{M1} - 0.212X_{Mg}^{M2}$$

$$E = [2.27r_0 - 2.00] * 10^3$$

Wood and Blundy (2014) is a summary of trace element partitioning for many common elements. The rare earth element partitioning in clinopyroxene is summarised from Wood and Blundy (1997) for anhydrous melts and Wood and Blundy (2002) for hydrous system. The anhydrous model is the focus as all experiments are assumed to be anhydrous.

Equation 71: Wood and Blundy, 2014. Lattice strain model for the rare earth element partitioning in clinopyroxene.

$$D_0^{3+} = \left\{ \frac{\left(\frac{Mg}{Mg + Fe}\right)_{melt}}{X_{Mg}^{M1}} \right\} * exp\left(\frac{88750 - 65.644T + 7050P - 770P^2}{RT}\right)$$

$$r_0^{3+} = 0.974 + 0.67X_{Ca}^{M2} - 0.051X_{Al}^{M1}$$

$$E_{M2}^{3+} = 318.6 + 6.9P - 0.036T$$

This equation also has crystal components including; the fraction of octahedrally (M1) coordinated Mg and Al, and the fraction of Ca in the M2 site. This equation also treats pressure and Mg number of the melt as variables.

The Mg# of the melt was calculated by the molar proportion of MgO divided by the sum of itself and the molar proportion of FeO.

This data are fit to 13 separate studies (1 unpublished) which are listed here:

Dunn (1987); Gaetani and Grove (1995); Gallahan and Nielsen (1992); Grutzeck et al. (1974); Hack et al. (1994); Hart and Dunn (1993); Hauri et al. (1994); Jones and Burnett (1987); McKay et al. (1994); McKay et al. (1986); Nicholls and Harris (1980); Watson et al. (1987).

These studies make up 454 individual rare earth element data points, over half of which (228) are from Gallahan and Nielsen (1992). These data are used to supplement the experimental results in this section to allow for more natural compositions to be investigated.

These two models have common variables. Both emphasise the importance of the crystal composition, however the only common term is the fraction of aluminium on the M1 site of the clinopyroxene.

This study covers 55 experiments. The pressures tested at 1atm, 5 kbar, 8kbar and 11 kbar. The temperature range in this series of experiments is 249°C between 1130 -1379 °C. The chemistry of the clinopyroxene ranges from Mg#53-100 i.e. diopside to augite. The advantage of this study is that all the rare earth elements are measured in each experiment which allows for a very accurate determination of what effects the partitioning of each of these elements

Adding in the Gallahan and Nielsen (1992) database give an additional 180 REE data points (omitting Y, Ce and Eu) from 110 experiments of more natural-like composition. This increases the temperature range to 329°C from 1050-1379°C.

5.2 The substitution of the rare earth elements in clinopyroxene

5.2.1 Introduction

It is assumed that the rare earth elements partition onto the M2 site of the clinopyroxene, paired with the substitution of aluminium on the tetrahedral site for charge balance.

Equation 72:
Substitution of rare earth elements on the M2 site in an aluminous system

$$\mathrm{CaMgSi_2O_{6_{px}}} + \mathrm{[REE]O_{1.5_{melt}}} + \mathrm{AlO_{1.5_{melt}}} = \mathrm{[REE]MgAlSiO_{6_{px}}} + \mathrm{CaO_{melt}} + \mathrm{SiO_{2_{melt}}}$$

It has been found that the rare earth elements are highly correlated with the content of tetrahedrally coordinated aluminium in the clinopyroxene (Hill et al., 2000; Lundstrom et al., 1998; Wood and Blundy, 2001).

In an aluminium free system, the rare earth elements are thought to partition onto the M2 site in the form:

Equation 73:
Substitution of rare earth elements on the **M2** site of clinopyroxene in aluminium free system (Wood and Blundy, 1997).

$$\mathrm{CaMgSi_2O_{6_{px}}} + \frac{2}{3}\mathrm{LnO_{1.5}}_{\mathrm{melt}} = \mathrm{Ln_{\frac{2}{3}}MgSi_2O_6}_{\mathrm{px}} + \mathrm{CaO_{melt}}$$

If this is the case, the partitioning of the rare earth elements should be inversely correlated with the calcium content of the melt.

As the M1 and M2 sites of clinopyroxene are of similar size, and the rare earth elements cover such a large range of ionic radius, it is possible that the rare earth elements could exist in both the M1 and M2 sites.

The stoichiometric control of the substitution of trivalent cations into the M1 site of diopside in an aluminium free system is:

Equation 74:
Substitution of rare earth elements on the **M1** site of clinopyroxene in aluminium free system.

$$\mathrm{CaMgSi_2O_{6_{px}}} + \frac{2}{3}\mathrm{LnO_{1.5}}_{\mathrm{melt}} = \mathrm{CaLn_{\frac{2}{3}}Si_2O_6}_{\mathrm{px}} + \mathrm{MgO_{melt}}$$

As such, the partitioning of the REEs should be inversely correlated with the Mg content of the melt.

The experiments presented in this chapter synthesise pure diopside from the simple system CaO-MgO-SiO_2. Working in such a simple system allows for the investigation of the site occupancy of the rare earth elements in diopside.

5.2.2 A summary of experimental method

The method is described in depth in the methods chapter (page 19).

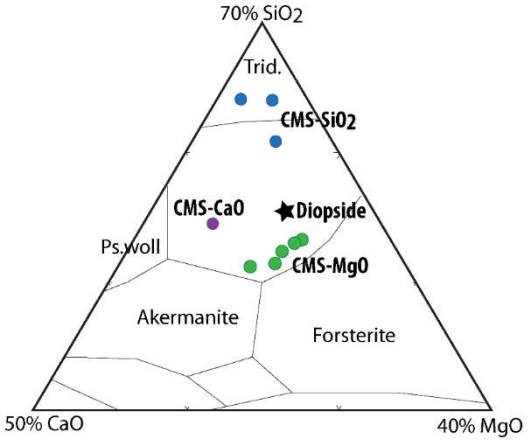

Figure 84: CMS-diagram with experimental diopside starting compositions (Levin et al., 1964), please note the change in scale. Melt compositions were measured by EPMA after completion of the experiment.

The original starting compositions had an unintentionally high concentration of trace elements (20 wt. % total trace). These concentrations were diluted by mixing small portions with new major element mixes, however this resulted in some variation in major element compositions (Figure 84).

5.2.3 Results

Clinopyroxene is notoriously difficult to synthesis in large, homogenous crystals. These crystals are homogenous with <2% variation in each of the major element components. The major element compositions of the diopside crystals (Table 19) are close to stoichiometric.

The Ca/Mg ratio in the crystals are not 1:1, with all crystals displaying more magnesium than calcium. This suggests a small component of $Mg_2Si_2O_6$ (enstatite) is included in these diopside. Although not end member diopside ($CaMgSi_2O_6$), the compositions are still classified in the diopside classification (45%-50% wollastonite component) (Deer et al., 1992). Although the major elements of the clinopyroxene are quite homogenous, the trace elements are zoned. The standard deviations from all the partition coefficients are included in all the models to ensure accuracy.

Table 19: Stoichiometry of Experimental Diopside (Aluminium Free)

Run	20140728	20140811	20140811	20140924	20140924
Sample	LS007	LS905	LS906	LS906	LS907
T2	1329	1349	1349	1370	1370
Category	CMS-CaO	CMS-SiO2	CMS-MgO	CMS-MgO	CMS-CaO
MgO	19.08	19.91	19.48	19.96	19.35
Al_2O_3	0.00	0.00	0.00	0.02	0.00
SiO_2	56.73	55.74	56.43	55.53	55.84
CaO	25.09	23.31	24.60	23.70	24.92
Total	100.90	98.96	100.51	99.21	100.11
Cations	6	6	6	6	6
Mg	1.01	1.07	1.04	1.07	1.04
Si	2.02	2.01	2.01	2.00	2.00
Ca	0.96	0.90	0.94	0.92	0.96
Total	3.98	3.99	3.99	4.00	4.00

Run	20140925	20140925	20150223	20150318	20150318
Sample	LS905	LS906	LS026	LS025	LS026
T2	1373	1373	1379	1366	1366
Category	CMS-SiO2	CMS-MgO	CMS-MgO	CMS-SiO2	CMS-MgO
MgO	19.80	19.96	21.12	20.97	20.84
Al_2O_3	0.00	0.02	0.01	0.02	0.01
SiO_2	55.28	55.46	55.88	56.02	56.12
CaO	23.72	23.75	22.99	22.98	22.93
Total	98.80	99.18	100.00	99.98	99.89
Cations	6	6	6	6	6
Mg	1.07	1.07	1.13	1.12	1.11
Si	2.00	2.00	2.00	2.00	2.01
Ca	0.92	0.92	0.88	0.88	0.88
Total	4.00	4.00	4.00	4.00	3.99

Henry's Law predicts that the partition coefficients do not change when the concentration of the element in the melt increases. The experiments with extremely high concentrations of trace elements had a depressed liquidus for diopside and these experiments crystallised at much cooler temperatures. Experiments with the same melt composition with a 200ppm difference in trace element concentration show identical partition coefficients, and therefore Henry's Law is obeyed. Adherence to Henry's Law has been observed previously up to 2 wt.% individual element doping concentration (Gallahan and Nielsen, 1992).

Rare earth element partitioning in diopside

The rare earth elements are mostly trivalent, with the exception of Eu and Ce. Their large cation size (Lu^{3+}; 0.977 Å, La^{3+}; 1.16 Å in VIII-fold coordination) and very similar chemical behaviour leads to the assumption that all the rare earth elements will partition onto the same site; the calcium containing M2 site (Blundy et al., 1996; Gaetani and Grove, 1995; Gallahan and Nielsen, 1992; Sun and Liang, 2012; Wood and Blundy, 2014). Without aluminium, the rare earth elements will partition into the M2 site of diopside by the exchange outlined in Equation 73 (Wood and Blundy, 2014).

This equation suggests that as the activity of CaO in the melt increases, the partitioning of rare earth elements into clinopyroxene will decrease. As the composition of the synthetic diopside crystals varies only slightly, the major variables in this series of experiments are temperature and melt composition.

If the partitioning of the rare earth elements is isolated to the M2 site, their partition coefficients against their ionic radius should define a simple parabola where the peak is the ideal radius for a trivalent cation in the M2 site of diopside.

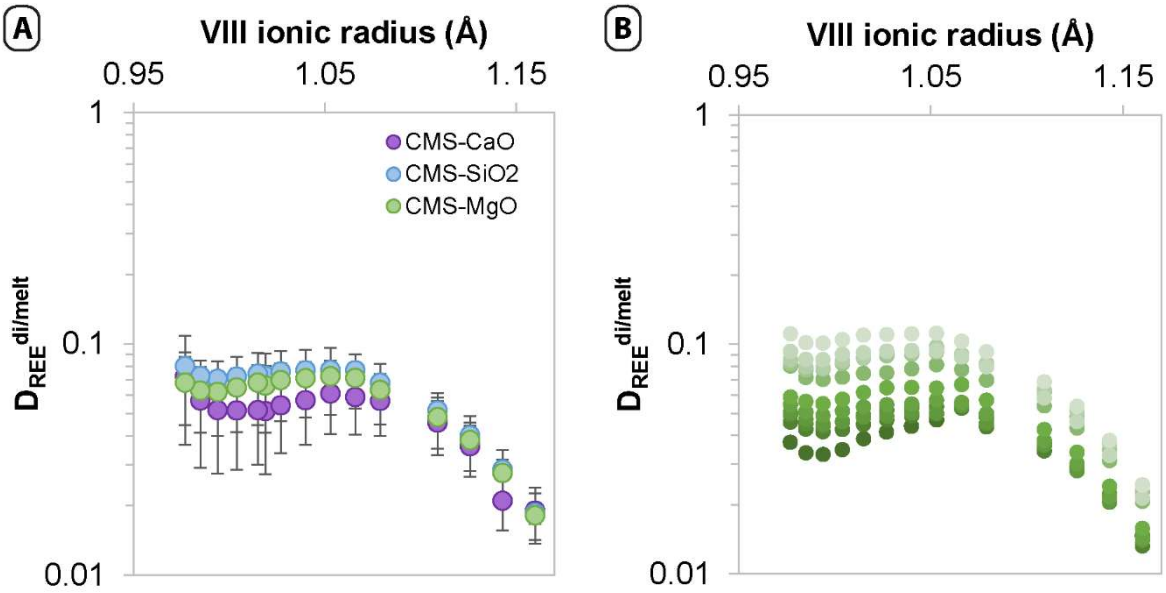

Figure 85: diopside melt partitioning in CMS system at 1 atm and 1370°C against ionic radius in VIII fold coordination. A) Diopside partitioning in three varying melt compositions at 1370°C with an atmosphere at QFM. Experiments are categorised by their most abundant component (i.e. CaO - purple, MgO-green or SiO_2-blue) Large errors are due to zoning in the crystal. B) Zoned clinopyroxene individual laser analysis against average melt. Each colour represents an individual laser spot in a single experiment, against the averaged equilibrium melt composition (CMS-MgO).

The patterns of rare earth element partitioning do not define simple parabolas (Figure 85), which suggests that this is more complex than simple partitioning onto the M2 site of the pyroxene. Even in the highly zoned crystals, the inflection of the heavy rare earth elements is consistent between each individual laser analysis and is not an effect of averaging zoned crystals.

It is possible that this inflection is caused by the addition of the heavy rare earth elements onto the M1 site, in addition to the M2 site. This phenomenon has been noted in nature (Olin and Wolff, 2010) however is attributed to high Fe contents which cannot be the solution in the simple CMS system.

The M1 site of diopside is much smaller and more “rigid” than the M2 site and is thought to reject the addition of the large rare earth elements. Sc is a very small (0.745 Å in VI-

fold coordination) trivalent cation and thought to partition exclusively onto the M1 site (Gallahan and Nielsen, 1992). For comparison, the smallest rare earth element; Lu is 13% larger at 0.861 Å in VI-fold coordination.

The measured partition coefficients are fit to 3 different models. 1) The lattice strain model with the assumption that all rare earth elements partition onto the M2 site 2) the double lattice strain model where the HREE that do not fit on the M2 parabola are fit onto the M1 site (Figure 86) 3) orthogonal polynomials in an attempt to describe the entire partitioning pattern as a single equation.

For the M2 + M1 lattice strain model, Sc and In were also fit to the M1 parabola, however, they were not included in the calculation of the error of the fit.

Table 20: Error associated with various fits to the partitioning of rare earth elements in clinopyroxene.

Based off	Equation	χ^2	χ^2_ν
Double lattice strain	M1+M2	0.75	0.0157
Orthogonal poly. (5 parameters)		3.42	0.0591
Single lattice strain	M2 only	13.81	0.1919
Orthogonal poly. (3 parameters)		16.24	1.8042

The double lattice strain, with both M1 and M2 components is by far the most accurate fit to the data. The orthogonal polynomial method is also very accurate but has difficulty in modelling the very sharp inflection in the heaviest rare earth elements. The orthogonal polynomial become less accurate as parameters are removed. The 3 parameter orthogonal polynomial is less accurate than the lattice strain model assuming all rare earth element partitioning on the M2 site.

Lattice Strain Model

The rare earth elements partition onto both the M1 and M2 sites in CMS diopside. Both these crystal sites will have an ideal radius (r_o), a rigidity coefficient (E) and a partition coefficient for an ideal cation (D_o). To determine what affects these components, each experiment was fit using a least squared regression to the lattice strain model.

One weakness of the lattice strain model is that it becomes difficult to precisely determine the lattice strain coefficients when only one limb of the parabola is defined. This is the case for the M1 site for trivalent cations. The parabola is defined only by Sc, and the remainder of the rare earth elements that do not fit the M2 site parabola (Figure 86).

Other trivalent cations that are small enough to possibly fit onto the M1 site include; In, Ga, Al and B. Aluminium is thought to prefer the tetrahedral site, and in cases such as the

calcium Tschermak's molecule ($CaAlAlSiO_6$), aluminium can exist in both the tetrahedral and M1 site (Hill et al., 2000; Okamura and Ghose, 1974). Ga behaves very similarly to aluminium and may also partition onto both the tetrahedral site and M1 sites. This means that only one limb of the parabola is defined using Sc and the HREE (and occasionally In when measured).

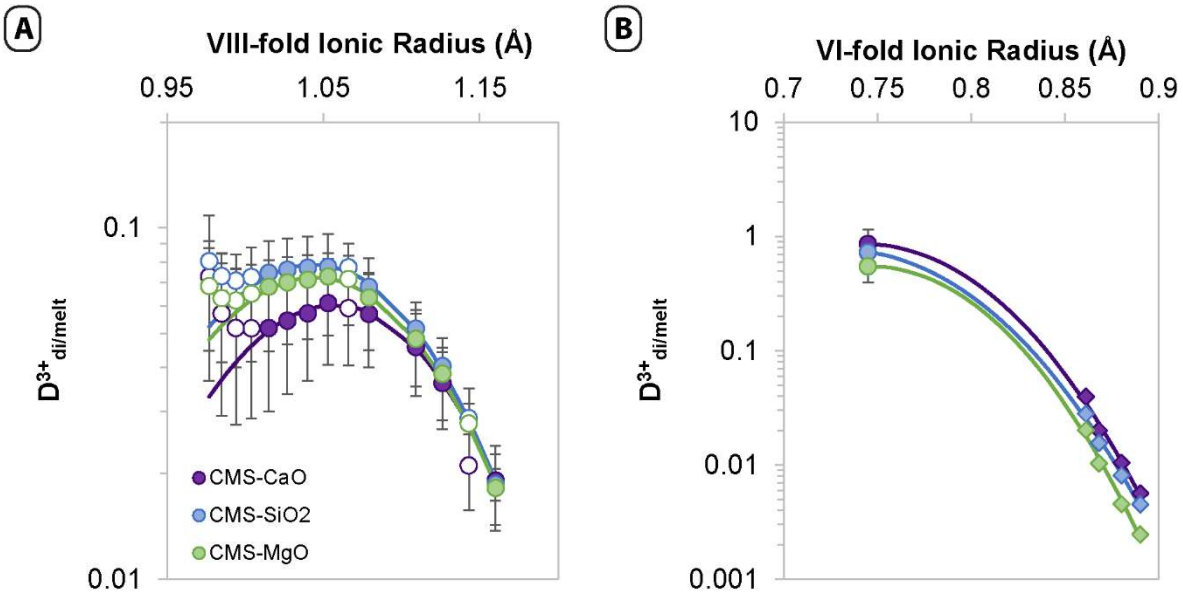

Figure 86: partitioning of trivalent cations into the M1 and M2 site of diopside. A) Rare earth elements into the VII-fold, M2 site of diopside, Open symbols were not included in the calculation of the lattice strain fit for the M2 site. b) Sc and HREE partitioning into the VI-fold, M1 site. Diamonds represent calculated partition coefficients from the difference between measured and calculated partitioning in the M2 site.

The data for r_0 and E for trivalent cation partitioning in both M1 and M2 are similar to those calculated by Olin and Wolff (2010). The D_0 values are much lower in this study as the partitioning for Sc is two orders of magnitude higher in Olin and Wolff (2010).

In both the M1 and M2 site partitioning, E and r_0 are highly positively correlated. This is very commonly observed (Sun and Liang, 2012) and is due to the relationship between E and r_o in the lattice strain model.

To determine what component has the strongest effect on D_0^{M2}, Gd will be used as a proxy, as it is one of the most compatible rare earth, and therefore will be similar to $D^{M2}{}_0^{3+}$. Similarly, Sc is the most compatible trivalent cation that is assumed to partition exclusively in the M1 site and will be used to determine what effects D_0^{M1}.

Table 21: Summary of lattice strain model parameters.

		M1 (IV-fold)			M2 (VIII-fold)			
		D_0^{M1}	E^{M1} (GPa)	R_0^{M1} (Å)	D_0^{M2}	E^{M2} (GPa)	R_0^{M2} (Å)	n
CMS-CaO	**average**	0.79	1380	0.76	0.05	340	1.06	2
	σ	0.16	79	0.001	0.014	3	0.002	
CMS-MgO	**average**	0.65	1588	0.76	0.07	322	1.05	3
	σ	0.06	77	0.001	0.012	14	0.001	
CMS-SiO_2	**average**	1.03	1499	0.76	0.10	292	1.04	3
	σ	0.50	262	0.009	0.044	38	0.003	

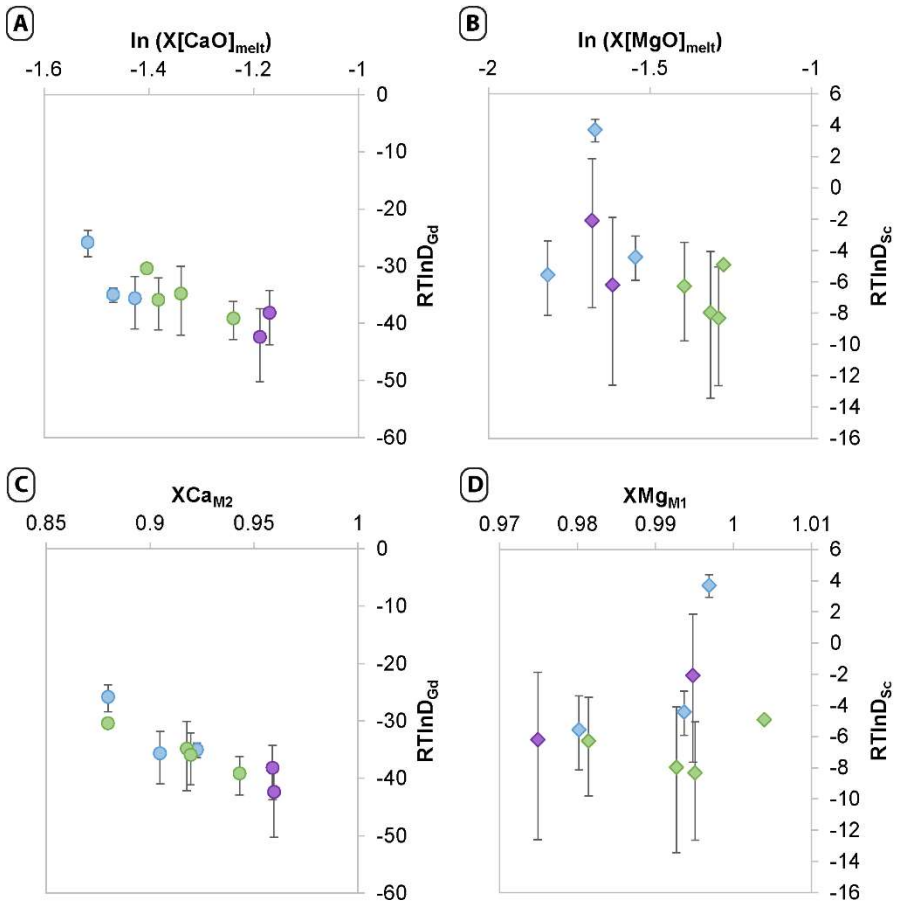

Figure 87: Partitioning of trivalent cations in clinopyroxene in the CMS system a) effect of the mole fraction of calcium in the melt on the partitioning of Gd into the M2 site of clinopyroxene. b) Effect of the mole fraction of magnesium on the partitioning of Sc on the M2 site of clinopyroxene. C) Correlation between Ca on the M2 site (APFU) and the partitioning of Gd. D) correlation between the Mg on the M1 site of clinopyroxene and the partitioning of Sc.

Partitioning of the REE into the M2 is governed by Equation 73. As the calcium activity of the melt increases, there will be a decrease in the partitioning of the rare earth elements on the M2 site and like-wise, an increase in the MgO activity of the melt will decrease the partitioning of rare earth elements (and scandium) on the M1 site (Equation 74).

A similar correlation should be made with the crystal chemistry of the pyroxene. An increase in the calcium content in the M2 site of the pyroxene would mean a decrease in the partitioning of the rare earth element on this site.

Unfortunately, the high error of the scandium partition coefficients makes conclusions difficult. There is a strong positive correlation between the X_{Mg}^{M1} and r_0^{M1} however, all the r_0^{M1} are within standard deviation of each other (Figure 87).

There is a strong correlation between the partitioning of Gd and partitioning of the divalent cations on the M2 site. The Ca content of the M2 site is negatively correlated with the partitioning of Gd which suggests it is partitioning onto this site (Equation 73). r_o^{M2} is strongly positively correlated with X_{Ca}^{M2}.

5.2.4 Conclusions

The rare earth elements in diopside partition onto both the M1 and M2 site of diopside. The partitioning of the rare earth elements on the M2 site is highly dependent on calcium, both in the melt and in the M2 site of the crystal.

This study is not conclusive in determining if melt composition can play a role in the partitioning of rare earth elements but rather that melt and diopside chemistry are intrinsically linked and it is difficult to change the major element components of the melt without changing the composition of the diopside. This is due to pyroxene family having a huge range of solid solutions within the general pyroxene formula.

Combining this study with the more complex systems in the next section will allow for a more in-depth analysis of what controls the partitioning of the all the trace elements in clinopyroxene.

5.3 High-Ca pyroxene/melt partitioning

5.3.1 Introduction

Clinopyroxene chemistry can be highly variable as there is partial or complete solid solution between many end members. In the previous section it was determined that even in the simple CMS system, diopside can have variations in crystal chemistry. Additional to the main end members of clinopyroxene, there are some variations in components that do not exist in pure form.

There is a component of clinopyroxene crystallised in SiO_2-saturated systems known as the Ca-eskolaite, which has a vacancy on the M2 site: $Ca_{0.5}\square_{0.5}AlSi_2O_6$ (Hill et al., 2011) to balance the substitution of aluminium on the M1 site. This causes non-stoichiometry in the clinopyroxene with only 3.5 cations per 6 oxygens.

Clinopyroxene can incorporate aluminium in its crystal structure in the form of a Calcium Tschermak's substitution ($CaAlAlSiO_6$) (Blundy et al., 1996; Gaetani and Grove, 1995; Hill et al., 2000; Lundstrom et al., 1998; Okamura and Ghose, 1974). This component has tetrahedral (IV-fold) and octahedrally (VI-fold) coordinated aluminium. The aluminium component of the diopside plays a vital role in the partitioning of trace elements into diopside (Gaetani and Grove, 1995; Wood and Blundy, 2014).

As the REEs are trivalent and substitute into a usually divalent M2-site (Gaetani and Grove, 1995), the charge must be balanced by the incorporation of an aluminium (Equation 72)(Blundy and Wood, 2003). The correlation between aluminium content in clinopyroxene on the partitioning of the REEs has been thoroughly studied (Blundy and Wood, 2003; Blundy et al., 1996; Francis and Minarik, 2008; Hill et al., 2000). Specifically the partitioning of the rare earth elements has been shown to increase with increasing proportion of tetrahedral coordinated aluminium (Gallahan and Nielsen, 1992; Wood and Blundy, 2014) which provides more evidence that this (Equation 75) is the main substitution mechanism for partitioning of rare earth elements in pyroxene.

In the previous section, it was discovered that the rare earth elements partition onto both the M2 and M1 sites. In an aluminium containing system these reactions would take the form of Equation 72 and Equation 75:

Equation 75:
Substitution of rare earth elements on the M1 site

$$\mathrm{CaMgSi_2O_{6_{px}}} + \mathrm{[REE]O_{1.5_{melt}}} + \mathrm{AlO_{1.5_{melt}}} = \mathrm{Ca[REE]AlSiO_{6_{px}}} + \mathrm{MgO_{melt}} + \mathrm{SiO_{2_{melt}}}$$

Both these substitutions will be affected by the tetrahedrally coordinated aluminium in an identical way. The difference between these two substitution mechanisms is that partitioning onto the M1 site replaces Mg, while partitioning onto the M2 site replaces Ca. Similarly, the REE in the M1 site will be affected by the Mg activity in the melt, while the M2 site will be effected by the Ca activity of the melt.

In this section the CMS series described in the previous section will be supplemented with additional experiments using CMAS, CMASN, CMASNF and natural like systems at 1atm, 5 kbar, 8kbar and 11 kbar. The temperature range in this series of experiments is 1379-1130°C. The chemistry of the clinopyroxene ranges from Mg#53-100; diopside to augite.

The aim of this study is to outline the main factors that influence the partitioning of each of the trace elements into clinopyroxene.

5.3.2 Method

The method is described in depth in the methods chapter (page 19). The run conditions are shown in Table 2 and Table 3.

This series is made up of CMS, CMAS, CMANS, CMASNF and "natural" compositions that synthesise clinopyroxene (and occasionally plagioclase) along with the equilibrium melt. This experimental series is made up of 57 experiments of the temperature range 1130-1379 °C, and pressures of 1atm, 5 kbar, 8 kbar and 11 kbar. The oxygen fugacity ranges from air, to QFM and the highly oxidising Pt-PtO_2. The Pt-PtO_2 buffer allows for the decomposition reaction of PtO_2 → $Pt+O_2$ which creates a highly oxidising environment in the capsule. This ensures that all iron is Fe^{3+}. The Mg# of the experiments range from 53-100 (Figure 88)

Additional to the experiments synthesised in this study, the published results of Gallahan and Nielsen (1992) are also included in some models to allow for more natural-like compositions to be assessed (Figure 88). These experiments were conducted at 1atm and a temperature range of 1180-1050°C. The partition coefficients of Sc, Y, La, Sm, Gd, Ho and Yb were measured. This experimental database is a good supplement for the data collected in this study. This study covers Mg# of 52-90. Gallahan and Nielsen (1992) conclude that the most important parameters in the partitioning of the rare earth elements and scandium into high-Ca pyroxene are temperature, pyroxene Ca content and Al content of the melt.

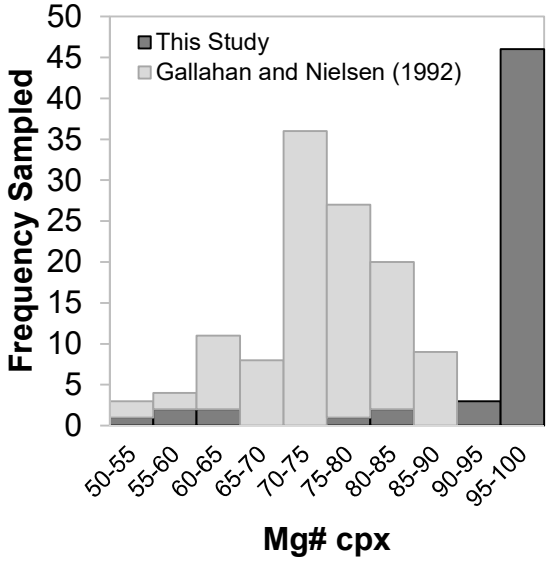

Figure 88: Frequency of clinopyroxene Mg# sampled in this study and the additional experiments of Gallahan and Nielsen (1992)

5.3.3 Results

Clinopyroxene Stoichiometry

There were 57 successful experiments in which clinopyroxene was synthesised. Of these, 7 contained augite, 37 diopside and 13 had more than 50 mol. % Ca in the clinopyroxene. One experiment measured 64% wollastonite component (D2488). Stoichiometric pyroxene with more than 50 mol. % Ca is impossible (Deer et al., 1992) therefore this overabundance of calcium may be indicative of the non-stoichiometric forms of pyroxene Ca-Tschermak's ($CaAlAlSiO_6$) and Ca-eskolaite $Ca_{0.5}\square_{0.5}AlSi_2O_6$.

The iron containing experiments were run in Pt capsule and buffered by PtO_2. As this is a one way reaction, PtO_2 decomposes to Pt and free oxygen; creating a very oxidising environment converting all Fe to Fe^{3+}. This allows for the partitioning of a single valance of iron to be investigated, and reduces the uncertainties in calculating Fe^{2+}/Fe^{3+} ratios which is notoriously difficult to do without synchrotron radiation or Mossbauer spectroscopy (Berry et al., 2010; Ottonello et al., 2001). To ensure that this one way reaction had not been completed, at the end of the experiment, the buffer layer at the base of the capsule was inspected under a reflected light microscope. The remaining PtO_2 is visibly different to the Pt walls of the capsule and the decomposed buffer. In some experiments, the buffer reaction had completed, with no visible PtO_2 after quench.

Clinopyroxene has very complex stoichiometry as it has multiple solid solution pathways. To determine the atoms per formula unit, the charge balanced method was used. Simply, the cations are normalised to 4.00, and the charge is calculated assuming all Fe is Fe^{2+}. A

stoichiometric pyroxene will have cations to the total of 12 positive charges, and therefore, any variation less than this is assumed to be the contribution of Fe^{3+}.

Table 22: Iron valence in clinopyroxene by buffer visibility and charge balancing methods.

Run no.	Composition	Fe^{2+}(M2)	Fe^{3+}(M1)	Fe^{2+}(M1)	Fe^{3+} %	Visible PtO2?
C5469	**Ab10-Fe5**	0.001	0.196	0.012	94%	No
C5442	**Ab10-Fe10**	0.001	0.363	0.013	96%	No
C5507	**Ab30-Fe10**	0.009	0.297	0.057	82%	Yes
C5430	**Ab50-Fe10**	0.003	0.350	0.032	91%	Yes
D2495	**Ab70-Fe10**	0.013	0.254	0.081	73%	Yes
D2488	**Ab10-Fe15**	0.000	0.450	0.000	100%	Yes

Assuming the experiments that have visible PtO_2 buffer remaining contain Fe entirely as Fe^{3+}, there is some miscalculation occurring. This assumption of stoichiometry for the calculation of Fe^{3+} is very imprecise for clinopyroxene (Canil and O'Neill, 1996). Although there may be some error associated with this method of stoichiometry calculation, it is used consistently throughout this chapter and also used to re-calculate the components of the Gallahan and Nielsen (1992) study. As all iron is Fe^{3+}, this fixes the Mg number of these experiments at 1.

A Summary of trace element partitioning in clinopyroxene

The partitioning of trace elements in clinopyroxene is complicated as the M1 and M2 sites are similar in size. The rare earth elements are the only set of homovalent cations that define both limbs of an Onuma parabola. The divalent cations are shared between the two sites, each with only one limb being defined. The monovalent cations partition only onto the M2 site, however are generally considered too large for this site (Figure 89). This makes the determination of the lattice strain parameters imprecise for most elements.

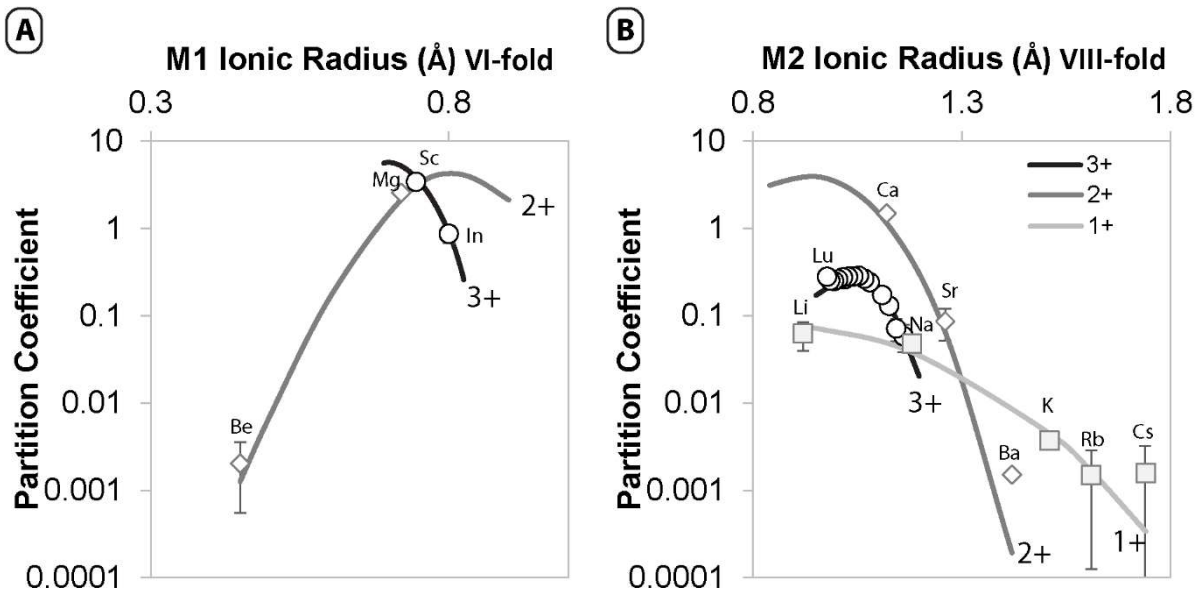

Figure 89: The partitioning of trace elements in composition Di2 at 1248°C and 1atm with schematic lattice strain models for a) M1 site and B) M2 site in clinopyroxene. Refer to Figure 7 for Di2 major element composition.

Monovalent cations

Wood and Blundy (2014) suggest that due to the small size of Li, it should fit into the M1 site however, Li exists in the M2 site in the end-member spodumene ($LiAlSi_2O_6$). Due to this end-member component, the monovalent cations are assumed to partition exclusively onto the M2 site of pyroxene.

The incorporation of the monovalent cation onto the M2 site requires a charge balance substitution with a trivalent cation (usually aluminium or ferric iron) onto the M1 site:

Equation 76:
The stoichiometric control for the substitution of monovalent cations on the M2 site of clinopyroxene.

$$CaMgSi_2O_{6_{px}} + \frac{1}{2}Na_2O_{melt} + \frac{1}{2}Al_2O_{3_{melt}} = NaAlSi_2O_{6_{px}} + CaO_{melt} + MgO_{melt}$$

This suggests that the monovalent cation partitioning in clinopyroxene will be controlled by the activity of aluminium in the melt.

Comparing the partitioning of lithium to the proportion of aluminium, calcium and magnesium in the melt, along with the aluminium in the M1 site of pyroxene; no strong trends emerge (Figure 90).

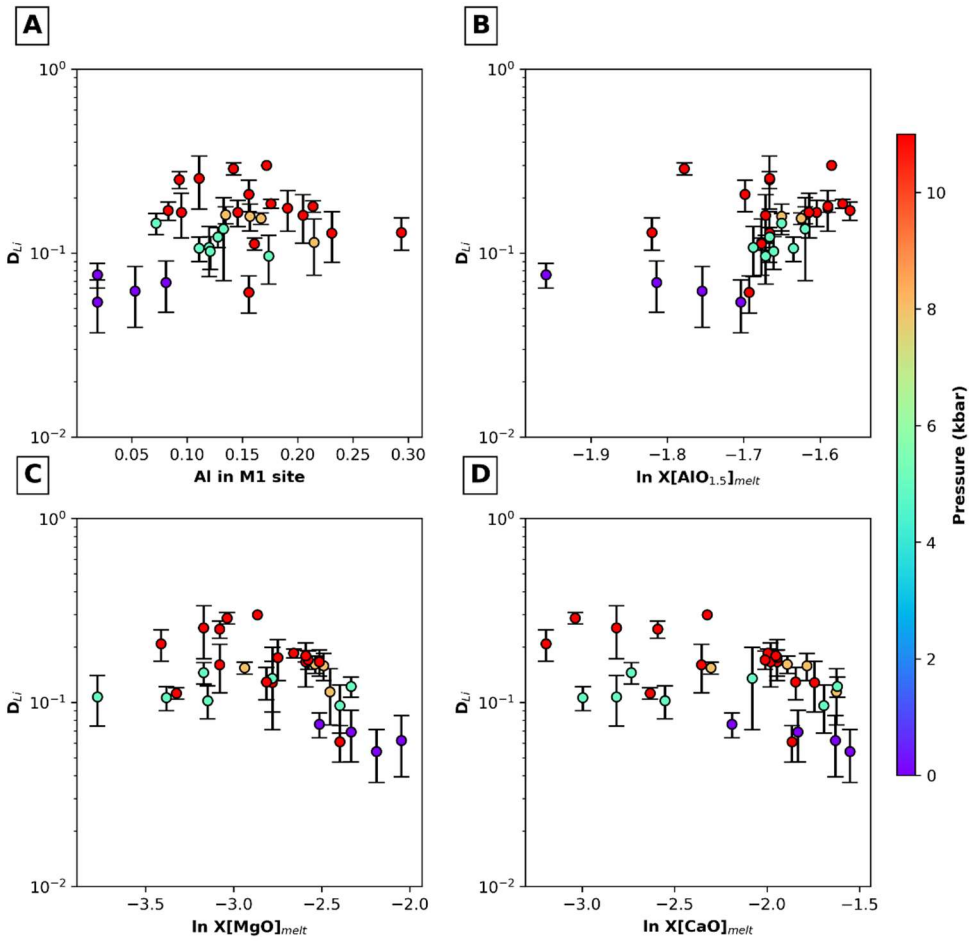

Figure 90: Controlling factors on the partitioning of lithium is pyroxene A) the effect of M1 site aluminium B) the natural log of the proportion of aluminium in the melt C) the natural log of the proportion of magnesium in the melt D) the natural log of the proportion of calcium in the melt

The partition coefficients for sodium and lithium are robust but the more incompatible monovalent cations have very high standard deviations. This causes difficulty in fitting the lattice strain model precisely. Cations that have standard deviations greater than 100% of the average partitioning value were removed but many analysis still had extremely high relative standard deviations. This is not due to detection limit problems in the LA-ICP-MS system; as most values are on the magnitude of a few ppm. These high standard deviations are most likely a results of the aluminium zonation noted previously; as aluminium is directly related to the partitioning of the monovalent cations (Equation 76).

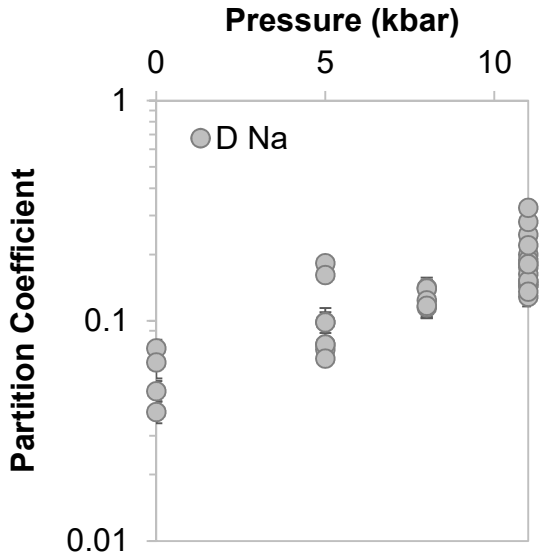

Figure 91: The relationship between the partitioning of sodium and pressure

Lithium and sodium have very similar compatibilities in clinopyroxene, with the ideal radius for monovalent cations (r_o^{1+}) likely to fit somewhere between these two cations.

Wood and Blundy (2014) have published a model for the partitioning of monovalent cations in clinopyroxene (Equation 77).

Equation 77
Wood and Blundy (2014) model for the partitioning of monovalent cations in clinopyroxene

$$D_{Na} = \exp\left(\frac{10367 + 2100P - 165P^2}{T} - 10.27 + 0.358P - 0.0184P^2\right)$$

$$E_{M2}^{1+} = \frac{1}{3}(318.6 + 6.9P - 0.036T)$$

$$r_o^{1+} = \left(0.974 + 0.067X_{Ca}^{M2} - 0.051X_{Al}^{M1}\right) + 0.12$$

Which is substituted into Equation 6.

This equation fits the data presented here very poorly (χ^2=36136 and χ^2_ν=516) but does emphasise the importance of pressure on the partitioning of monovalent cations in clinopyroxene. This relationship is also seen in this data (Figure 91).

Fitting the lattice strain model uniquely to all closed system experimental data (29 experiments and 83 data points), the average r_o^{1+} value is 1.02 ± 0.10 Å which varies linearly with aluminium content on the M1 site. The E^{1+} value varies by 55% with an average value of 28 GPa. The E^{1+} and r_o^{1+} values have a positive correlation. Using these observations, a new lattice strain model can be made:

Equation 78

$$D_{Na} = \exp\left(-2.62 + 0.63P + \frac{493}{T}\right)$$

$$E_{M2}^{1+} = 29.46$$

$$r_o^{1+} = 1.05 + 0.03 * X_{Al}^{M1}$$

Where P is in GPa, and the parameters are substituted into Equation 6. This equation fits the data with an error of χ^2=2487 and χ^2_ν=32.72.

Alternatively to the lattice strain model, the linear relationship between pressure and the partitioning of these cations were investigated.

Table 23: linear fit for the monovalent cations partitioning into clinopyroxene. Where P is in GPa.

	m	X	c	χ^2	No. points	χ^2_ν
lnD_{Li}	0.75	P	-2.53	133	28	5.11
lnD_{Na}	0.51	P	-2.24	777	28	29.9
lnD_{K}	-3.63	P	-0.51	131	10	16.3
lnD_{Rb}	0.61	P	-7.39	150	15	11.5
linear method			total	1190	81	16.31

Calculating the partitioning from the linear relationship with pressure gives a much more accurate prediction of the monovalent cations than the lattice strain model with an error of χ^2_ν=16.31.

Divalent cation partitioning

Diopside ($CaMgSi_2O_6$) has divalent cations in both the M1 and M2 sites. Calcium is generally thought to only occupy the M2 site, such as the case in diopside and hedenbergite ($CaFeSi_2O_6$). Similarly, the large divalent cations; Sr, Ba are thought to behave similarly to calcium. Magnesium can exist on both the M1 site, as in diopside; or occupy both the M1 and M2 sites such as enstatite ($Mg_2Si_2O_6$). Beryllium is a very small divalent cation and it thought to partition exclusively in the M1 site.

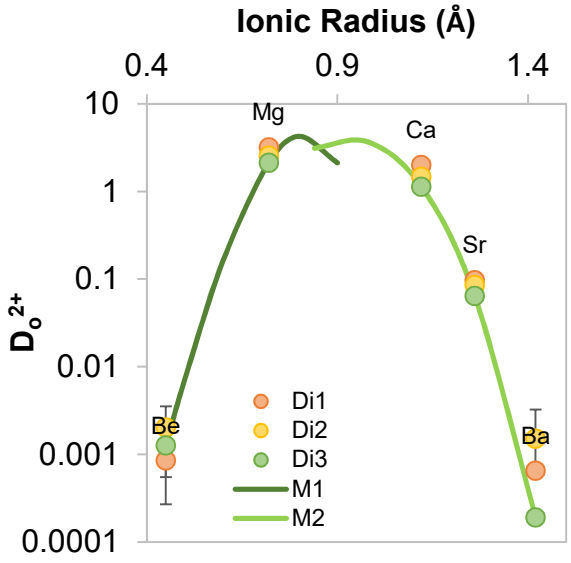

Figure 92: M1 and M2 site partitioning of the divalent cations in clinopyroxene from various melt compositions at 1248°C and 1 atm. Be and Mg assumed to partition entirely onto the M1 site (VI-fold coordinated) while Ca, Sr and Be assumed to partition exclusively on the M2 site (VIII-fold coordinated).

The Wood and Blundy (2014) model for the partitioning of divalent cations in clinopyroxene is calculated from a measured value of D_{Ca}. From this value, the lattice strain parameters listed below are used in Equation 6 to predict the partitioning of Sr and Ba.

Equation 79
Wood and Blundy (2014) model for the partitioning of monovalent cations in clinopyroxene

$$E_{M2}^{2+} = \frac{2}{3}(318.6 + 6.9P - 0.036T)$$

$$r_o^{2+} = \left(0.974 + 0.067X_{Ca}^{M2} - 0.051X_{Al}^{M1}\right) + 0.06$$

Using this equation, there is one outlier (experiment D2479) that increases the error substantially to $\chi 2v=3816$. When this single experiment is removed, the error decreases to $\chi^2_v=64$. There are no published lattice strain models to predict the partitioning of the divalent cations in the M1 site.

The ideal cation radius of the M1 and M2 sites for the divalent cations are very similar, therefore the lattice strain model is difficult to precisely define. Instead, the controlling factors for the partitioning of Be, as a representative divalent cation for the M1 site, and Sr, a representative cation for the M2 site can be examined.

The stoichiometric control for each of these exchanges requires no charge balance so should be highly correlated to the partitioning of the element it replaces (e.g. D_{Sr} would be correlated to D_{Ca} and D_{Be} with D_{Mg}):

Equation 80:
The stoichiometric control for the substitution of divalent cations on the M1 and M2 site of clinopyroxene.

$$CaMgSi_2O_{6_{pyroxene}} + BeO_{melt} = CaBeSi_2O_{6_{pyroxene}} + MgO_{melt}$$

$$CaMgSi_2O_{6_{pyroxene}} + SrO_{melt} = SrMgSi_2O_{6_{pyroxene}} + CaO_{melt}$$

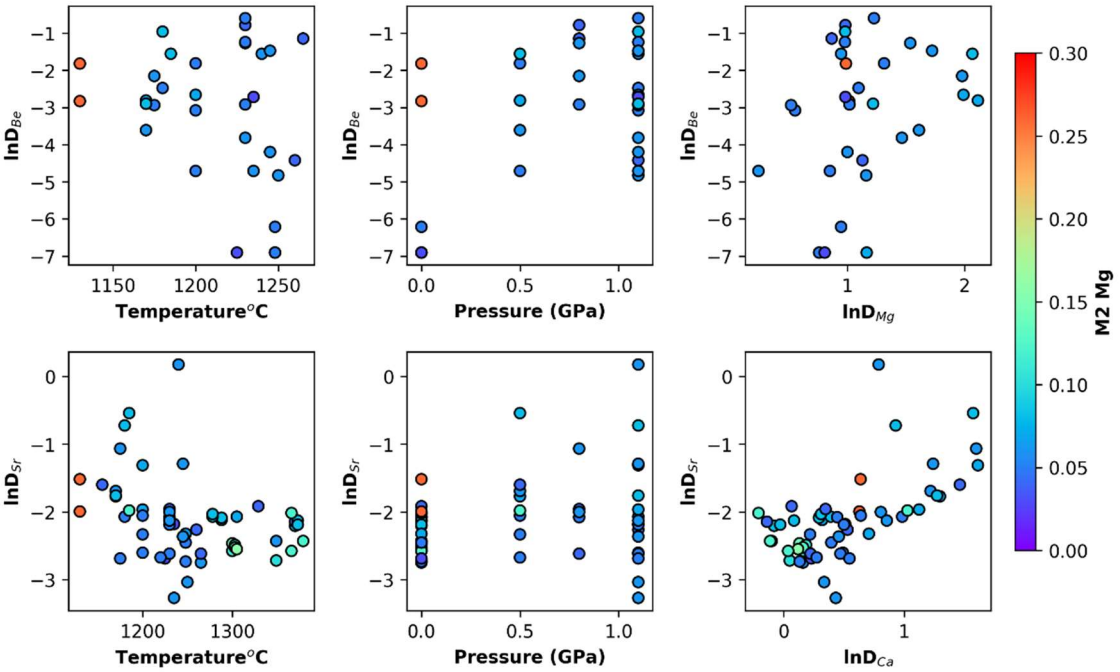

Figure 93: A comparison on the control factors on the divalent cation partitioning in clinopyroxene in the M1 and M2 sites. Be (top row) represents M1 divalent partitioning and Sr (bottom row) represents divalent partitioning in the M2 site. First column, temperature (°C). Second column, pressure (GPa). The right-most column compares the partitioning of the target cation with the partitioning of the element in which it replaces in diopside (i.e. Mg→Be and Ca→Sr). Colour scale is Mg on the M2 site.

The partitioning of beryllium is not strongly correlated with either the Mg content of the melt or the Mg content of the M1 site in clinopyroxene. Both the partitioning of Mg and Ca decrease with increasing temperature and have no strong dependence on pressure. As there are so few elements that define each parabola, it is difficult define the lattice strain parameters for each site precisely.

Table 24: Linear method for estimating the partition coefficients for the divalent cations in clinopyroxene in the M2 site

	m	X	c	chi^2	n	reduced chi^2
RTlnD$_{Sr}$	3.87	D$_{Ca}$	-35.26	1137	54	21.87
RTlnD$_{Ba}$	-10.13	D$_{Ca}$	-47.61	723	41	18.57
linear method			Large 2+	1861	95	20.45

Using the linear relationship between the partitioning of calcium and the partitioning of the other large divalent cations, the partitioning is modelled with an error of χ^2_ν=20.45 which is a significant improvement on the Wood and Blundy (2014) equation. Unfortunately the linear relationships cannot be used to predict the partitioning of elements not modelled; e.g. Ra, another large divalent cation. For this purpose the lattice strain model is superior.

Rare earth element partitioning

As discussed in the previous section, the rare earth elements partition into both the M1 and M2 sites of the clinopyroxene. This causes an increase in compatibility of the heaviest rare earth elements and an inflection in the partitioning curve. This inflection is visible in data from many of the experiments presented here (Figure 94). These models are fit to 660 individual REE points (omitting Ce, Eu and Y).

The most common way to express the rare earth element partitioning in clinopyroxene is to assume that all of the rare earth elements partition only onto the M2 site, as defined in Equation 72. Due to this assumption, the change in rigidity (E) and r_o^{M2} obtained in previous studies may be incorrect. This variation in the shape of the rare earth element partitioning pattern is actually due to the incorporation of the smaller REEs on the M1 site, causing higher compatibility of these elements and therefore a "flatter" partitioning pattern. If only a few of the rare earth elements were measured this will lead to incorrect determinations of the lattice strain parameters. It is extremely important to measure all the rare earth elements when fitting the lattice strain model to determine the intricacies of the pattern.

Sc, and In are measured in this series of experiments and help to constrain the M1 site contribution to the rare earth element partitioning pattern. The ideal radius for the partitioning of trivalent cations into the M1 site is that of Sc and for the M2 site is similar to that of Gd. Before trying to fit the lattice strain model to the data, we will investigate the major controls on the partitioning of these two elements in clinopyroxene. These will act as a proxy for the D_0 values without the added variables of r_o and E.

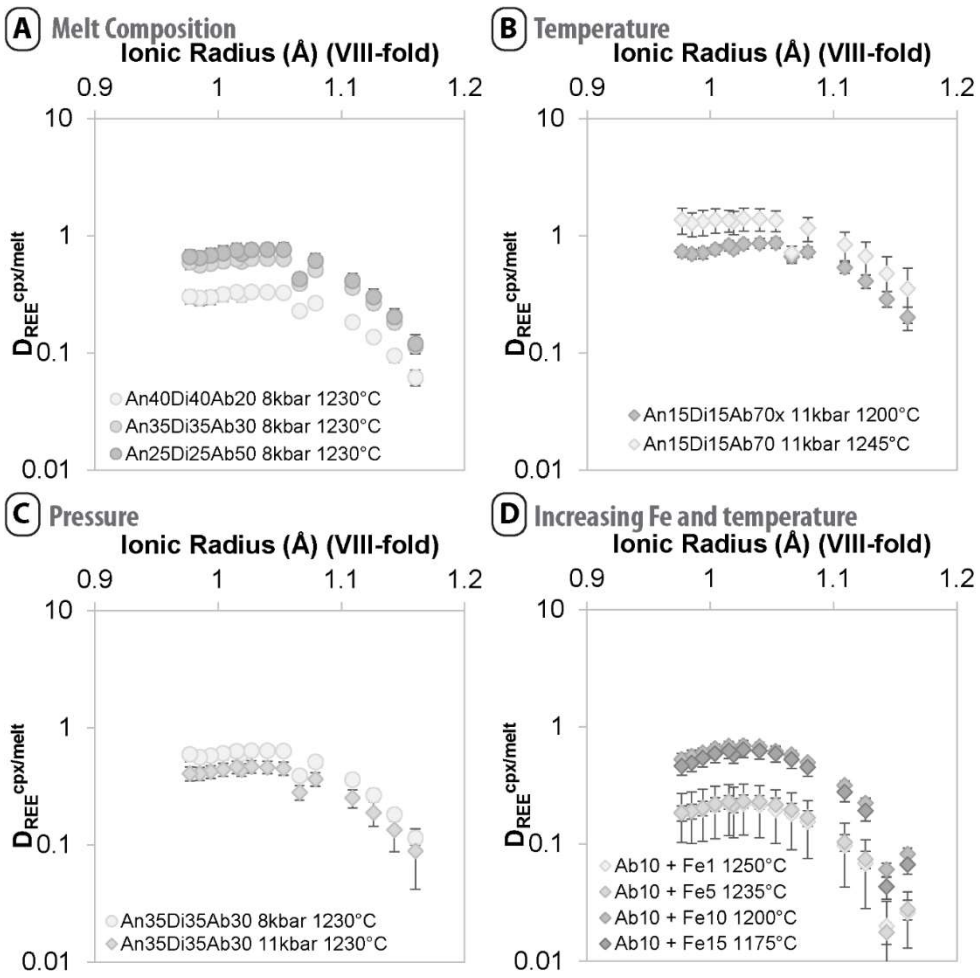

Figure 94: Comparison of similar experiments on the partitioning of the rare earth element between clinopyroxene and melt A) the effect of different melt compositions (an corresponding change in crystal compositions) at constant temperature and pressure B) change in temperature with the same melt composition and same pressure C) the effect of pressure with the same melt and same temperature D) increasing iron and decreasing crystallisation temperature at 11 kbar.

It is widely accepted that the aluminium is very important for the substitution of REE in clinopyroxene (Hill et al., 2000). Within each crystal there is zoning of aluminium and additionally the rare earth elements. To determine if the aluminium zonation is correlated with the rare earth element zonation the partitioning of aluminium and the partitioning of the trivalent cation of each individual crystal laser ablation spot were compared. The partition coefficients were calculated by the individual analysis over the average melt for the sample. There is a strong positive, linear correlation between the partitioning of aluminium and the partitioning of the trivalent cations. This suggests that there is an intrinsic correlation between the partitioning of trivalent cations in the M1 and M2 sites.

The partitioning of REE on the M2 site

By examining the two published high-Ca pyroxene REE partitioning models (Equation 70, Equation 71) the parameters that control partitioning are and combination of the following; $X_{Al}^{T}, X_{Al}^{M1}, X_{Mg,}^{M1}\ X_{Mg}^{M2}, X_{Ca}^{M2}$, Mg number of the melt, pressure and/or temperature

(Sun and Liang, 2012; Wood and Blundy, 2014). These variables were chosen due to their empirical relationships with the partitioning of the REE.

Using the stoichiometric substitution of the REE into the M2 site of clinopyroxene (Equation 72), the partitioning of the REE may be related to the X_{Al}^{T}, or X_{Ca}^{M2}.The data presented in this thesis covers a very small range calcium in the M2 site. The addition of the Gallahan and Nielsen (1992) data allows for a wider range of compositions to be assessed. Comparing a wider range of pyroxene values there is no correlation between the partitioning of calcium into the M2 site and the partitioning of the trivalent cations into this site (Figure 95).

As pyroxene is a very complex mineral, the calcium in the M2 site could represent a number of different substitutions rather than solely the charge balance of the trivalent cations. These other substitutions include the Ca-Tschermak's molecule and Ca-eskolaite.

Writing Equation 72 into the thermodynamic equilibrium equation (Equation 81), it's suggested that the partitioning of the rare earth elements partition onto the M2 site of will be related to the partitioning of calcium and the ratio of alumina to silica in the melt.

Equation 81:
The thermodynamic equilibrium constant for the substitution of REE in diopside

$$D_{REE}^{Di/melt} = \frac{X_{[REE]MgAlSiO_6}^{diopside}}{X_{[REE]O_{1.5}}^{melt}} = \exp\left(\frac{-\Delta G^0}{RT}\right) * \left(\frac{\gamma_{[REE]O_{1.5}}^{melt}}{\gamma_{[REE]MgAlSiO_6}^{diopside}}\right) * \left[\frac{\alpha AlO_{1.5melt}}{\alpha SiO_{2melt}}\right] * \left(\frac{\alpha CaMgSi_2O_{6Di}}{\alpha CaO_{melt}}\right)$$

Or

$$D_{REE}^{Di/melt} = \frac{X_{[REE]MgAlSi_{\ 6}}^{diopside}}{X_{[REE]O_{1.5}}^{melt}} = \exp\left(\frac{-\Delta G^0}{RT}\right) * \left(\frac{\gamma_{[REE]O_{1.5}}^{melt}}{\gamma_{[REE]MgAlSiO_6}^{diopside}}\right) * \left[\frac{\alpha AlO_{1.5melt}}{\alpha SiO_{2melt}}\right] * \left(D_{Ca}^{di/melt}\right)$$

There is a very strong correlation between the partitioning of the REE and the proportion of calcium in the melt (Figure 95) and similarly the partitioning of calcium between clinopyroxene and melt. There is also a strong dependence on the partitioning of the REE and temperature.

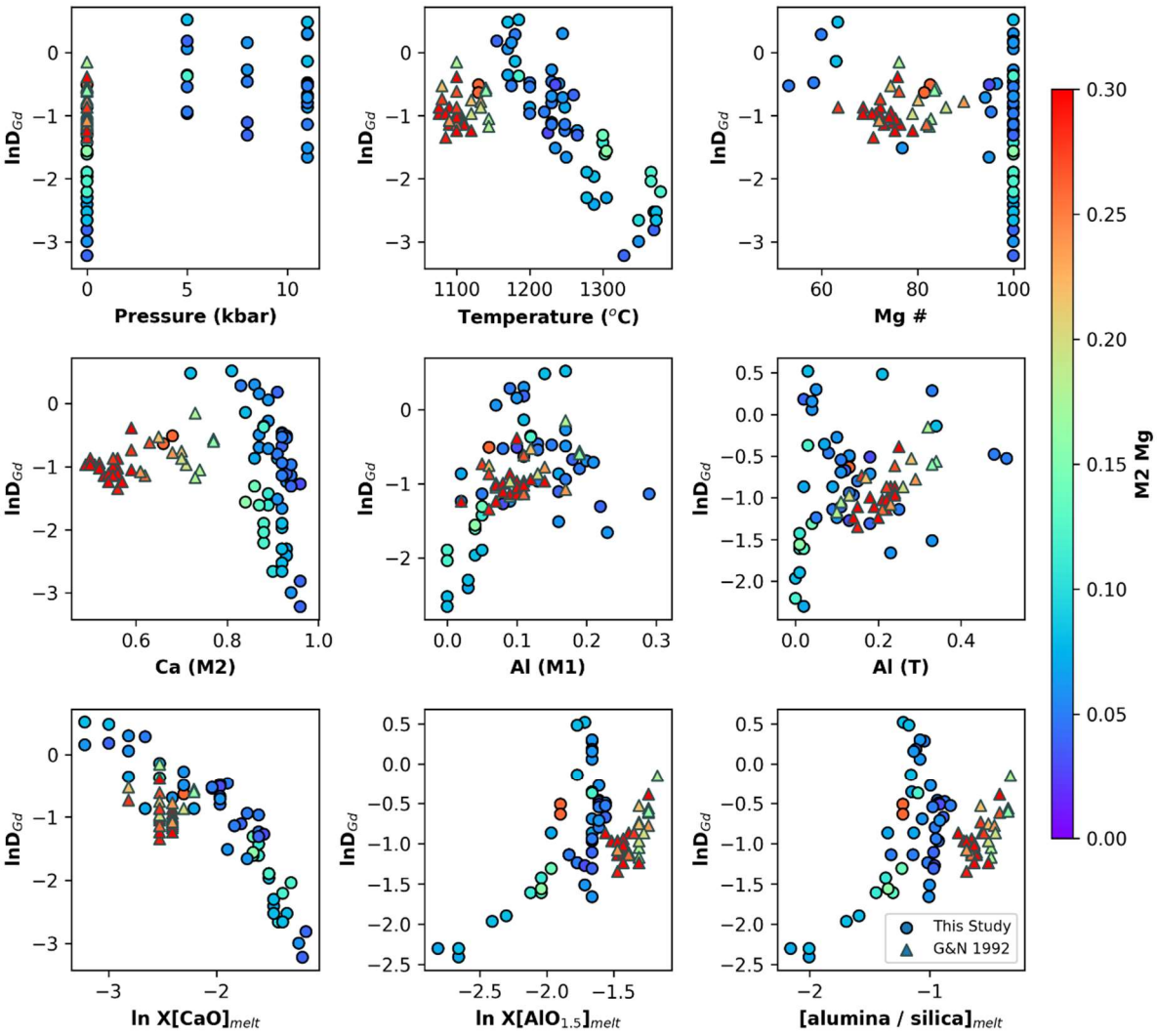

Figure 95: The natural log of the partitioning of Gd between clinopyroxene and melt against most tested variables. Circles represent this study, triangles represent Gallahan and Nielsen (1992). Middle row represent atoms per formula unit in the designated site. Bottom row represents the molar proportions of single cations components in the melt.

All other variables, included those outline in the previously published models ((Sun and Liang, 2012; Wood and Blundy, 2014)) show no strong correlation.

The partitioning of trivalent cations on the M1 site

The partitioning of the trivalent cations into the M1 site has not been extensively studied, however would behave similarly to the partitioning of the REE into the M2 site. The partitioning of the rare earth elements into the M1 site of the clinopyroxene has the same effect from melt composition as the partitioning of REE in the M2 site, however will be controlled by the partitioning of Mg rather than Ca. This is outlined in the thermodynamic equilibrium Equation 82:

Equation 82:
The thermodynamic equilibrium constant for the substitution of REE in diopside

$$D_{REE}^{Di/melt} = \frac{X_{[REE]MgAlSiO_6}^{diopside}}{X_{[REE]O_{1.5}}^{melt}} = \exp\left(\frac{-\Delta G^0}{RT}\right) * \left(\frac{\gamma_{[REE]O_{1.5}}^{melt}}{\gamma_{[REE]MgAlSiO_6}^{diopside}}\right) * \left[\frac{\alpha AlO_{1.5melt}}{\alpha SiO_{2melt}}\right] * \left(\frac{\alpha CaMgSi_2O_{6Di}}{\alpha MgO_{melt}}\right)$$

Or

$$D_{REE}^{Di/melt} = \frac{X_{[REE]MgAlS\ \ _6}^{diopside}}{X_{[REE]O_{1.5}}^{melt}} = \exp\left(\frac{-\Delta G^0}{RT}\right) * \left(\frac{\gamma_{[REE]O_{1.5}}^{melt}}{\gamma_{[REE]MgAlSiO_6}^{diopside}}\right) * \left[\frac{\alpha AlO_{1.5melt}}{\alpha SiO_{2melt}}\right] * \left(D_{\mathbf{Mg}}^{di/melt}\right)$$

Therefore, the partitioning of scandium can be assumed to be correlated to the ratio of alumina to silica in the melt, and the partitioning of magnesium between clinopyroxene and melt. Examining Figure 96, there are strong correlations with the partitioning of scandium with temperature and the proportion of magnesium in the melt (and similarly the partitioning of Mg between clinopyroxene and melt).

The crystal chemistry components show no strong relationship with the partitioning of scandium. Rather than the atoms per formula unit, the partitioning of the REE in the M1 site are more strongly correlated with the partitioning of the Mg in clinopyroxene.

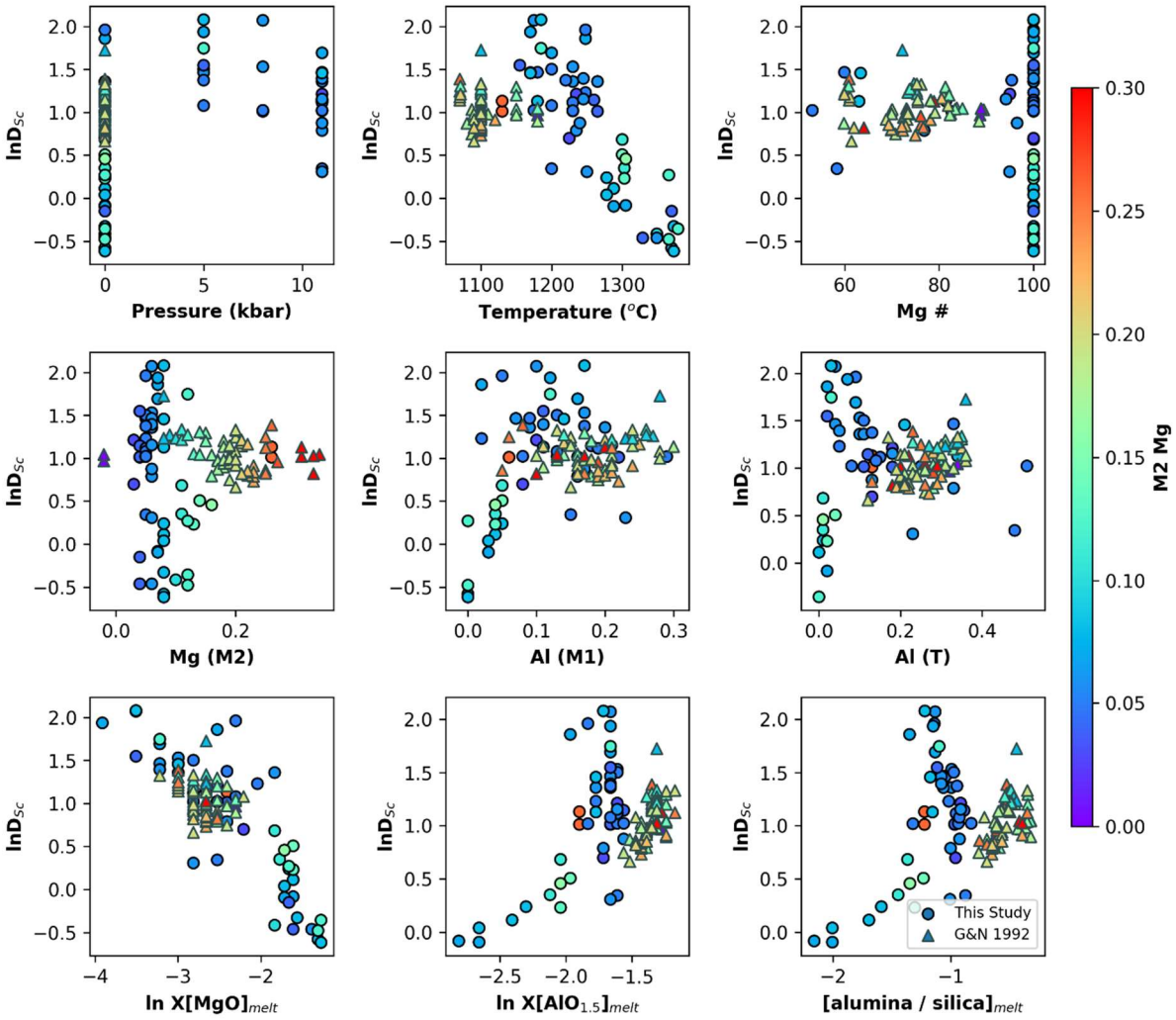

Figure 96: The natural log of the partitioning of Sc between clinopyroxene and melt against most tested variables. Circles represent this study, triangles represent Gallahan and Nielsen (1992). Middle row represent atoms per formula unit in the designated site. Bottom row represents the molar proportions of single cations components in the melt.

Lattice strain parameters for REE in pyroxene

The M1 site is difficult to define accurately with lattice strain parameters as only one limb of the parabola is defined, and additionally, many of the elements that define the parabola have interference with the M2 site. For the M1 site, the lattice strain model was fit in relation to Sc using Equation 6, therefore rather than D_o^{M1}, D_{Sc}^{M1} is calculated. The M2 site was fit to La, Pr, Nd, Sm, Gd, Tb, Dy and Ho, with the remainder from the heaviest four rare earth elements used to define the M1 parabola.

The lattice strain model was fit uniquely to each experiment and values for E^{M1}, r_o^{M1},D_{Sc}^{M1}, E^{M2}, r_o^{M2}, and D_0^{M2} were determined. This gives a very accurate fit with an error of χ^2_v=0.13.

The M1 parabola is poorly define, with the peak almost always centralised around Sc. Only one limb of this parabola is defined. The partition coefficients on this limb have

large uncertainties due to zoning and the uncertainties from the subtraction of the M2 model from the measured partitioning values. The M1 limb of the parabola is poorly defined which makes the lattice strain parameters for trivalent cations in the M1 highly variable.

r_o^{M2} only varies by about 0.7% (1.036 ± 0.008 Å) and there is a strong negative correlation between the X_{Al}^{M1} and a strong positive correlation between X_{Mg}^{M1}. E^{M2} varies 15% at 309 ± 46 GPa. There is no strong correlation between r_o^{M2} and E^{M2}.

A model to predict the rare earth element partitioning in clinopyroxene using melt components

There are two published models for predicting the rare earth element partitioning in clinopyroxene. Both equations assume partitioning of the rare earth elements entirely onto the M2 site of the clinopyroxene. Both these equations fit the experimental data poorly (Figure 97).

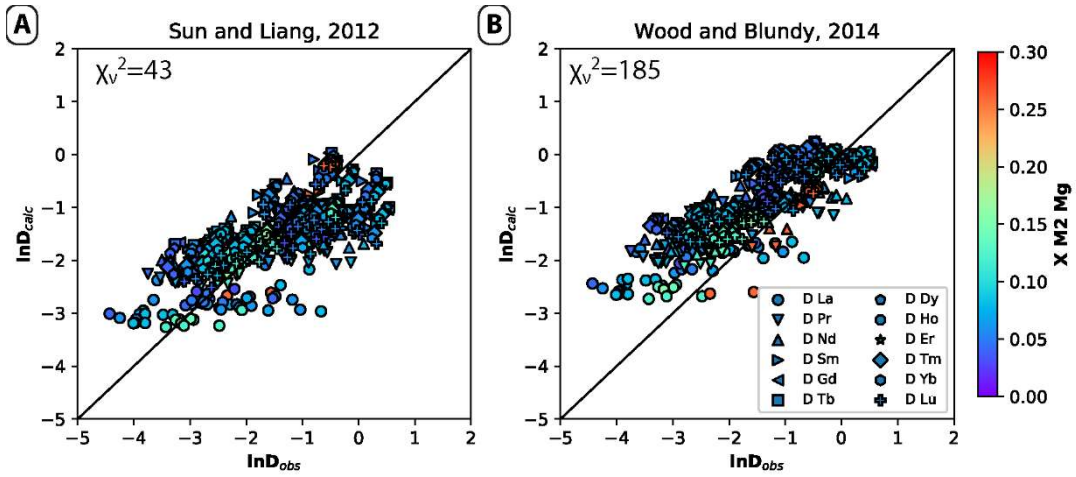

Figure 97: comparing commonly used partition models for the rare earth elements in clinopyroxene and the observed partitioning in this study. All rare earths are assumed to partition into the M2 site. A) The error between predicted values using the sun and Liang, 2012 model and observed values. A single experiment causes a large portion of the error. Starred value is with 1 less experiment than all other error fits. B) The error between predicted values using the Wood and Blundy, 2014 model and observed values.

As aluminium is one of the most common elements in the Earth's crust, it is can be assumed that most systems that synthesise diopside will contain some aluminium. The aluminium free experiments were omitted from these calculations. The substitution of REE into the M2 site of clinopyroxene will most likely take the form of Equation 81 and can be converted into a predictive equation by substituting the lattice strain model for the change in free energy of this equation to arrive at Equation 83.

Equation 83:
A stoichiometric control equation for the partitioning of REE in clinopyroxene

$$\ln D^{cpx/melt}_{REE} = \ln D_0^{3+} + \left(\frac{-910.17\,E}{T}\right) * \left[\frac{1}{2} r_0 * (r_i - r_0)^2 + \frac{1}{3} * (r_i - r_0)^3\right] + \ln\left(\frac{XAlO_{1.5melt}}{XSiO_{2melt}}\right) + \ln D_{Ca}^{\frac{cpx}{melt}}$$

Where

$\ln D_0^{3+} = -7.0(\pm 0.4) + \frac{1.00(\pm 0.06)}{T} * 10^4 + 0.032(\pm 0.004)P$

$r_0 = 1.05(\pm 0.003) - 0.2(\pm 0.02) * X_{Mg}^{M2}$ and

$E = 225(\pm 12)$.

Where pressure is in kbar.

This model fits both the aluminous data presented in this study, and those presented in Gallahan and Nielsen, 1992 (total 733 data points) with an error of χ_v^2=26.81 which is very accurate.

Reversing this equation to solve for temperature (as outlined in the previous chapter and Putirka (2003)) the result is fairly accurate. 37% of the 46 aluminous clinopyroxene + melt experiments conducted for this study are predicted within 50 °C and 70% are predicted within 100 °C.

There have been some indications that the mixing of the rare earth elements can be hindered by REE-SiO_2 relationships in the melt (Evans et al., 2008). Therefore, the same stoichiometric control with the addition of a $[X_{SiO2}]_{melt}$ term that represents $\left(\frac{\gamma^{melt}_{[REE]O_{1.5}}}{\gamma^{diopside}_{[REE]MgAlSiO_6}}\right)$ in the thermodynamic relationship is investigated. The inclusion of this term causes the uncertainty on the pressure variable to be higher than the value. Pressure was removed for this model:

Equation 84:
A stoichiometric control equation for the partitioning of REE in clinopyroxene, including a REE-SiO_2 interaction

$$\ln D^{cpx/melt}_{REE} = \ln D_0^{3+} + \left(\frac{-910.17\,E}{T}\right) * \left[\frac{1}{2} r_0 * (r_i - r_0)^2 + \frac{1}{3} * (r_i - r_0)^3\right] + \boldsymbol{\gamma_{REE}} + \ln\left(\frac{XAlO_{1.5melt}}{XSiO_{2melt}}\right) + \ln D_{Ca}^{\frac{cpx}{melt}}$$

Where

$\ln D_0^{3+} = -2.07(\pm 0.32) + \frac{0.52(\pm 0.04)}{T} * 10^4$

$\boldsymbol{\gamma_{REE}} = 2.54(\pm 0.09) * \ln(XSiO_{2\,melt})$

$r_0 = 1.036(\pm 0.002) - 0.08(\pm 0.02) * X_{Mg}^{M2}$ and

$E = 238(\pm 9)$.

Where pressure is in kbar.

This model fits both the data presented in this study (660 data points), and those presented in Gallahan and Nielsen (1992) (179 data points) with a reduced chi squared of 14.90.

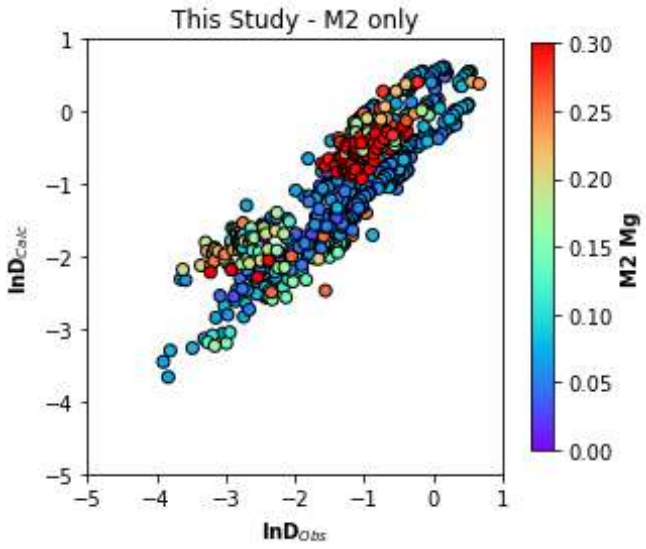

Figure 98: Comparison between observed and calculated partitioning of the rare earth elements in clinopyroxene using Equation 84. Fit to both the simple system data presented in this study (n=660) and the more natural-like compositions published by Gallahan and Nielsen (1992) (n=179).

An Orthogonal Polynomial

The higher partitioning than expected of the heavy rare earth elements is still visible in the new experiments. An orthogonal polynomial can be used to describe the entire rare earth element partitioning pattern with a singular equation.

The λ0 or magnitude of the rare earth element partitioning curve has a strong correlation with the natural log of the divalent melt components. The calcium proportion in the melt has the strongest correlation (r^2=0.8081), with a negative sense. λ1 and λ2 i.e. the slope and the curvature of the rare earth element partitioning pattern are strongly correlated with each other (r^2=0.7842), and weakly correlated with the natural log of the proportion of aluminium in the melt (λ1r^2=0.3427, λ2r^2=0.4007). λ3; or the inflection of the heavy rare earth elements is moderately negatively correlated with the atoms per formula unit of magnesium in the M1 site (r^2=0.4703)

Using both the data presented in this thesis and the data published by Gallahan and Nielsen (1992) we find the most accurate way to predict the rare earth element partitioning using the orthogonal polynomial is:

Equation 85:
An orthogonal polynomial for the partitioning of rare earth elements in clinopyroxene

$$\ln D_i^{cpx} = \lambda 0 + (ri - 1.05477) * \lambda 1 + (ri - 1.00533) * (ri - 1.12824) * \lambda 2 + (ri - 1.06055) * (ri - 1.14551989) * (ri - 0.9914122) * \lambda 3$$

$$\lambda 0 = -4.70(\pm 0.28) - 1.35(\pm 0.02) * \ln XCa + 894(\pm 449)/T$$

$$\lambda 1 = -8.93(\pm 0.69) - 1.47(\pm 0.36) * \ln XAl$$

$$\lambda 2 = -106(\pm 13) - 16(\pm 7) * \ln XAl$$

This equation fits this data as the Gallahan and Nielsen (1992) with a χ^2_v=15.44.

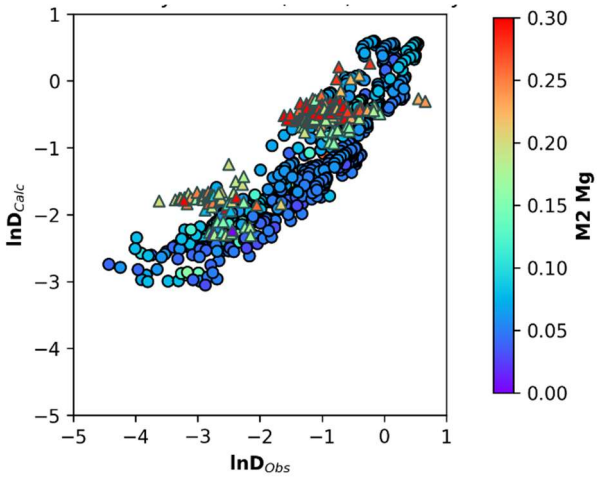

Figure 99: Comparison between observed and calculated partitioning of the rare earth elements in clinopyroxene using Equation 85. Fit to both the simple system data presented in this study (n=660): circles and the more natural-like compositions published by Gallahan and Nielsen (1992) (n=179): triangles.

It is more precise to predict the rare earth element partitioning in clinopyroxene using the lattice strain model than the orthogonal polynomial (Table 25).

Table 25: List of the goodness of fits of published models and discussed models fit to both these experiments and those from Gallahan and Nielsen (1992). This data are modelled to 165 experiments and 842 data points

Based off	Equation	In text reference	χ^2_v	n(par)
Lattice strain	M2 only+SiO_2-REE interaction	Equation 84	14.90	6
Orthogonal Polynomial	4 parameters	Equation 85	15.44	6
Lattice strain	M2 only	Equation 83	26.81	6
Wood and Blundy, 2014	minimised		39.87	10
Sun and Liang, 2012	minimised		64.55	9
Wood and Blundy, 2014	Published	Equation 71	145.8	10
Sun and Liang, 2012	Published	Equation 70	302.3	9

Rare earth element ratios

Due to the charge balance requirements for a trivalent rare earth to occupy a divalent crystal site, the partitioning is highly dependent on melt composition. The rare earth elements behave very similarly, and as such they will be affected equally by the melt change. If the ratio of the rare earth elements is taken, this will cancel out the effect of melt composition, leaving only formation conditions and crystal compositions as variables.

The rare earth element partitioning is divided by the partitioning of Gd as it is a middle rare earth element, and has an ionic radius (1.053 Å in VIII-fold) near the average of all the rare earth elements (1.056 Å) and therefore should represent the "average" partitioning of the rare earths. These REE partitioning ratios are given the notation $K_{REE/Gd}^{cpx/melt}$. The orthogonal polynomial form is used here due to its ability to model the inflection in the heavy rare earth elements. This inflection, caused by the contribution of HREE on the M1 site, is described by the λ3 term with more negative values representing a larger contribution of the M1 site. The λ3 term is strongly influenced by temperature; where higher temperatures allow for a larger inflection.

This suggests that the incorporation of REE into the M1 site is highly dependent on temperature while the partitioning into the M2 site is relatively insensitive to temperature.

Using the linear relationships outlined in Figure 100, a model for the rare earth element ratios was produced:

Equation 86:
An orthogonal polynomial model to describe the ratio of the REE partitioning when normalised to D_{Gd} for clinopyroxene

$$\lambda 0 = -0.288(\pm 0.004) - 0.0378(\pm 0.009) * \mathrm{P}$$

$$\lambda 1 = -5.27(\pm 0.07) - 11.8(\pm 0.7) * \mathrm{X}_{\mathrm{Al}}^{\mathrm{T}}$$

$$\lambda 2 = -38(\pm 7) + 6.2(\pm 1.1) * \lambda 1$$

$$\lambda 3 = -4095(\pm 640) + \frac{587(\pm 94) * 10^4}{\mathrm{T}}$$

Where P is in GPa and T is in kelvin. These parameters are substituted into the orthogonal polynomial Equation 23. This fits the data very well (χ^2=564 and χ^2_ν=0.87)

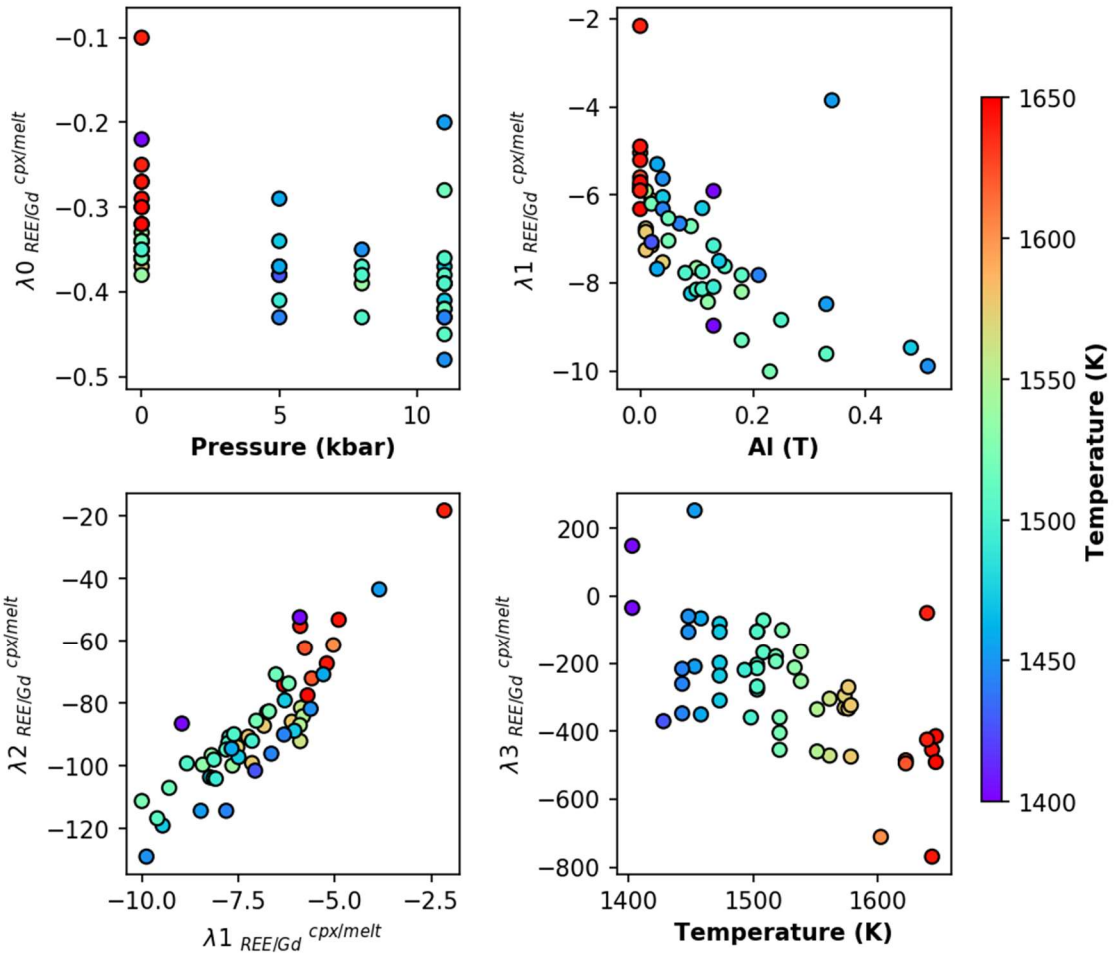

Figure 100: A) The relationship with the magnitude of the $K_{REE/Gd}$ and the pressure of the experiments B) The slope of the $K_{REE/Gd}$ pattern increases with increasing tetrahedrally coordinated aluminium in the crystal. C) The slope and the curvature of the $K_{REE/Gd}$ pattern are strongly correlated D) The sigmoidal shape is more pronounced in cooler temperatures.

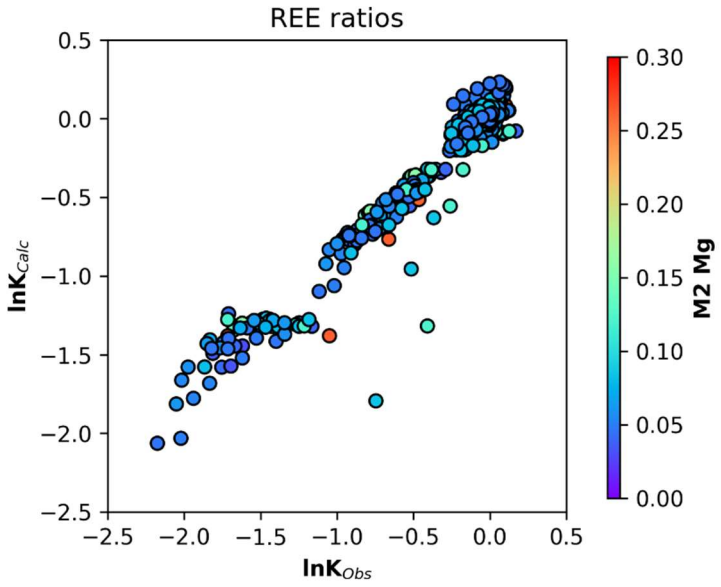

Figure 101: Comparison between the observed $\ln K_{REE/Gd}$ and those calculated using Equation 86

Reversing these relationships, the temperature can be predicted from the λ3 value, with 65% of the 55 experiments predicted within 50°C, and 87% predicted within 100°C.

5.3.4 Discussion

This experimental series consists of 57 experiments which focus on clinopyroxene with a magnesium number of 1. Most natural clinopyroxene has a magnesium number of less than 1 due to the incorporation of Fe^{2+}. Even though these experiments do not represent the majority of natural samples, it forms the basis of understanding how trace elements partition into clinopyroxene at a fundamental level. Once we understand the partitioning of trace elements in simple systems such as these, we can better understand the partitioning in complex systems.

In this study it was found that the trace element partitioning in clinopyroxene is difficult to constrain as there are two competing sites, with similar size. This causes most trace elements to be shared between both sites which makes the definition of the lattice strain parameters difficult.

Of the monovalent cations, Li and Na are of comparable compatibility, with the "ideal radius" (r_o^{1+}) situated between these two cations. It is assumed that all of the monovalent cation partition onto the M2 site, requiring a charge balance exchange of aluminium in the M1 site (Equation 76). The experimental clinopyroxene have inhomogeneous aluminium content which causes the monovalent cations to vary along with the aluminium. The partitioning values for Li and Na are robust. The most incompatible of the monovalent cations have extremely high standard deviations and it is difficult to draw meaningful conclusions from this partitioning data.

The divalent cations partition both onto the M1 and M2 sites. It is assumed that the larger cations (Ca, Sr and Ba) partition exclusively on the M2 site while Mg is shared between both sites and Be is exclusively on the M1 site. Practically, it is likely that there is some contribution of both sites in the partitioning of all the divalent cations in clinopyroxene as the lattice strain parabola overlap significantly (Figure 92). Due to this overlap, it is impossible to precisely define lattice strain parameters for the divalent cations in clinopyroxene. Additional divalent cations that may aid in the definition of the M1 parabola but were not investigated in this study include Zn, Ni and Co as described by Le Roux et al. (2011).

The rare earth element partitioning was investigated by combining both the data presented in this study and those published by Gallahan and Nielsen (1992) to include

clinopyroxene with magnesium number of <1, and therefore more natural compositions. The rare earth elements partition both onto the M1 and the M2 site in clinopyroxene. In these very simple systems, there is insignificant change in the calculated r_o^{3+M2} and E^{3+M2} for the rare earth elements. Previous studies that report changes in E and r_o^{3+} for the M2 partitioning of rare earth elements into diopside may have been influenced by this inflection in the heavy rare earths. This illustrates the importance of measuring all the rare earth elements. Many studies measure only a select few rare earth elements and extrapolate between them which causes vital information to be lost.

Additional to the heaviest REEs, Sc and In also partition onto the M1 site of clinopyroxene. This defines only the larger limb of the parabola which means the lattice strain parameters for the M1 site are difficult to precisely determine. This inflection in the heaviest rare earth elements is most pronounced with the partitioning of rare earth elements in the M2 site is low, such as in the aluminium free system.

The partitioning of the rare earth element onto the M2 site of clinopyroxene requires a charge balance in the form of an aluminium replacing a tetrahedrally coordinated Si cation (Equation 72). This exchange is dependent on the activities of aluminium, silica and calcium in the melt. Combining this study with the Gallahan and Nielsen (1992) study allows for more quasi-natural systems to be investigated. The stoichiometric control model (Equation 84) allows both data sets to be modelled the most accurately.

Using ratios between REE partition coefficients allows for the effect of melt to be cancelled out. This allows focus to be draw the crystal chemistry and formation conditions. Modelling the REE ratios with an orthogonal polynomial (Equation 86) allows for a very precise prediction. The magnitude of the pattern is effected by pressure while the curvature and slope are effect by the tetrahedrally coordinated aluminium. The HREE inflection is described by the λ3 term and is strongly correlated with temperature.

The experimental temperatures can be predicted very well using this λ3 term. This suggests that the incorporation of REE into the M1 site is strongly temperature dependant. Unfortunately, this also means that as the temperature drops, this M1 site contribution will become insignificant and we will lose the ability to use this term to be used as a thermometer.

Using only the partitioning of the REE into the M2 site of clinopyroxene in the stoichiometric equation (Equation 83), 37% of the 46 aluminous clinopyroxene + melt experiments conducted for this study are predicted within 50 °C and 70% are predicted

within 100 °C. This suggests that the partitioning of REE into the M2 site may have the potential as a geothermometer.

5.3.5 Conclusions

Clinopyroxene is a complex mineral to investigate as there is contribution from both sites (M1 & M2) in many of partition coefficients.

Generally, if the trace element substitution requires a charge balance then the partitioning of that element will be strongly influenced by melt composition. In the case of the REE, the effect of melt composition can be removed by examining the ratios of the REE partitioning to a common element; in this case Gd as $K_{REE/Gd}^{cpx/melt}$. These REE ratios, and therefore the partitioning of all REE on the M2 site of clinopyroxene, are most strongly correlated with pressure, temperature and tetrahedrally coordinated aluminium.

5.3.6 Future work

The effect of Fe^{2+}, water, and chromium should be tested to fully understand the partitioning of trace elements in clinopyroxene. Water is thought to be a significant variable in the partitioning of rare earth elements, by Wood and Blundy (2014), decreasing the partitioning of the rare earth elements with increasing water content. This however could be due to the intrinsic nature of water, decreasing the liquidus of the system, which reduces the formation temperature and therefore the partition coefficient. Therefore an experimental series could be run that isolates the effect of water on the partitioning of all elements in clinopyroxene.

Furthermore, natural clinopyroxene have magnesium numbers of less than one and also can incorporate significant amounts of chromium as a lattice forming element. These significant changes in crystal chemistry would change the partitioning and should be systematically investigated. Both Fe and Cr have multiple valence states, which further complicates the compatibilities and partitioning of these elements and in turn, any element that can partition into clinopyroxene and use these elements as a charge balance pair (similarly to the REE with aluminium).

CHAPTER 6. THE PARTITIONING OF TRACE ELEMENTS BETWEEN PLAGIOCLASE AND CLINOPYROXENE IN EXPERIMENTAL AND NATURAL SAMPLES

6.1 Experimental Partitioning Between Plagioclase and Clinopyroxene

6.1.1 Introduction

The previous chapters have outlined the major controls for the partitioning of trace elements between plagioclase /melt and clinopyroxene/melt. Contrary to popular belief, melt composition plays an important role in the partitioning of trace elements into these two minerals from a melt. This is especially true when the trace element requires a charge balance. Such as the case of the rare earth elements, which substitute primarily for calcium in both plagioclase and clinopyroxene.

In this section, rather than comparing mineral/melt partition coefficients, the partitioning between plagioclase and clinopyroxene will be compared. $D^{pl/cpx}$, in this section refers to the concentration of a trace element in plagioclase over the concentration of the same element in clinopyroxene.

The partitioning of trace elements is best described using balanced chemical equations. From these equations the charge balance requirements and the "stoichiometric control" for each substitution can be determined. When comparing the partitioning of trace elements between two solid phases, if the stoichiometric control for the partitioning of the trace elements are the same, the effect of melt composition will be cancelled out.

In natural samples, the melt is rarely preserved which makes mineral/melt partition coefficients very difficult to determine, therefore using mineral/mineral partition coefficients have more practical uses than traditional mineral/melt partition coefficients.

The partitioning of trace elements between solid phases is quickly gaining popularity as potential geothermometers. This is due to their assumedly high closer temperature (Sun and Liang, 2017) and the ease of measuring many trace elements by LA-ICP-MS.

Sun and Liang (2014) have designed a rare earth element between clinopyroxene and orthopyroxene thermometer using lattice strain fits to previously published experimental data. Additionally they created a rare earth element between plagioclase and clinopyroxene thermometer in Sun and Liang (2017) using the same clinopyroxene lattice strain model as in the previous study, and creating a new lattice strain model from

published experiments for plagioclase. This thermometer is made from separate clinopyroxene/melt and plagioclase/melt compositions and omits the potential effect of melt composition.

In this study, plagioclase and clinopyroxene were synthesised together in 34 separate experiments. Additionally, these experiments have been included in the plagioclase/melt and clinopyroxene/melt partitioning models. The mineral/melt partition coefficient models from the previous chapters will be combined and their precision in predicting the partitioning between plagioclase and clinopyroxene will be discussed.

Additionally, the Sun and Liang (2017) REE between plagioclase and clinopyroxene thermometer will be used to predict the experimental temperatures. A refined thermometer from the new, stoichiometric control equations will be created and the precision of these two thermometry methods compared.

All experiments in this chapter have been discussed thoroughly in the previous chapters. There were 34 successful experiments that synthesised diopside, plagioclase and melt (Table 3). The melt compositions include CMAS, CMASN, CMASNF and "natural" systems. The pressure ranges from 1 atm to 11 kbar, within a temperature range of between 1130-1265°C. The compositions of the minerals range between plagioclase of An_{97-24} and Mg# of clinopyroxene between 100 and 53.

6.1.2 Plagioclase/clinopyroxene partitioning

For an in-depth investigation of the plagioclase/melt and clinopyroxene/melt partition coefficients, please refer to the previous chapters.

Most trace elements are more compatible in clinopyroxene than plagioclase (Figure 102). Ba is the most compatible in plagioclase with respect to clinopyroxene. Hf is the most compatible in clinopyroxene with respect to plagioclase.

The large divalent cations are more compatible in plagioclase but Mg is far more compatible in clinopyroxene. Beryllium is close to unity.

To understand the preference in compatibility between each of the minerals, the mineral/melt partition coefficients must be compared.

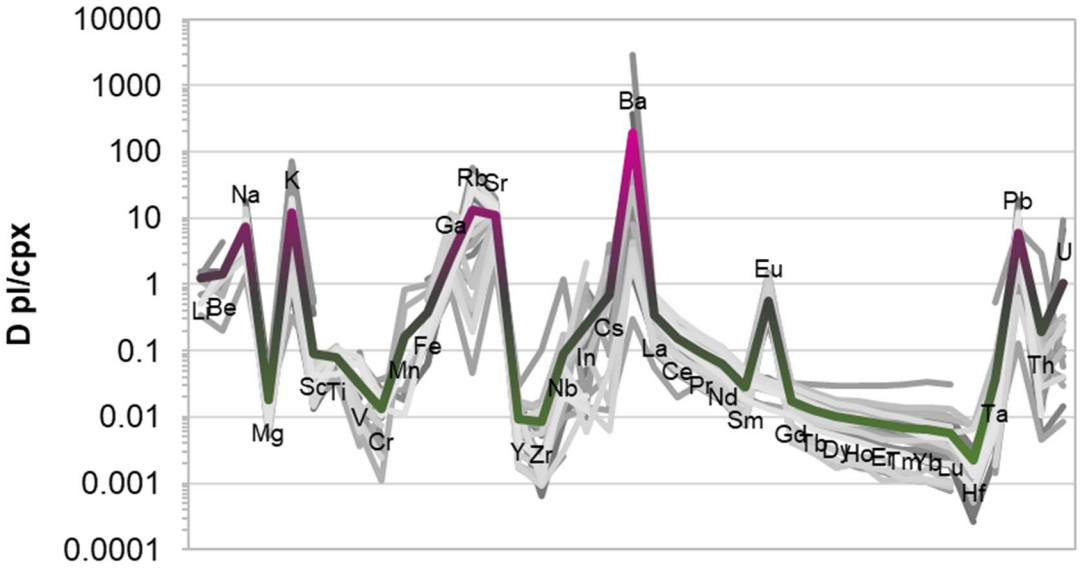

Figure 102: Partitioning of trace elements between plagioclase and clinopyroxene in all experiments. Bold line is average partition coefficient over all experiments. Green line represents elements that are more compatible in clinopyroxene (D<1), while pink represents more compatible in plagioclase (D>1).

Monovalent cations

The stoichiometric controls for the partitioning of monovalent cations in plagioclase and clinopyroxene are different;

Equation 87:
The stoichiometric control on the substitution of a monovalent cation into the large cation site of plagioclase

$$[\mathrm{Li}]\mathrm{O}_{0.5_{\mathrm{melt}}} + \mathrm{CaAl_2Si_2O}_{8_{\mathrm{pl}}} + \mathrm{SiO}_{1.5_{\mathrm{melt}}} = [\mathrm{Li}]\mathrm{AlSi_3O}_{8_{\mathrm{pl}}} + \mathrm{CaO}_{\ \mathrm{melt}} + \mathrm{AlO}_{1.5_{\mathrm{melt}}}$$

Equation 88:
The stoichiometric control for the substitution of monovalent cations on the M2 site of clinopyroxene.

$$[\mathrm{Li}]\mathrm{O}_{0.5_{\mathrm{melt}}} + \mathrm{CaMgSi_2O}_{6_{\mathrm{px}}} + \mathrm{AlO}_{1.5_{\mathrm{melt}}} = [\mathrm{Li}]\mathrm{AlSi_2O}_{6_{\mathrm{px}}} + \mathrm{CaO}_{\mathrm{melt}} + \mathrm{MgO}_{\mathrm{melt}}$$

In clinopyroxene, the reduction of charge from the Li substitution for Ca is balanced by an aluminium replacing Mg. In plagioclase, the charge is balanced by an extra silicon in place of an aluminium on the tetrahedral site.

As the stoichiometric control is not the same, the effect of melt composition will not be cancelled out when examining the partitioning between plagioclase and clinopyroxene, however, melt composition was found to play an insignificant role in the partitioning of monovalent cations in both phases.

The partitioning of the monovalent cations were fit most accurately by simple linear relationships.

Table 26: A combination of the linear fits in Table 11 and Table 23. Error is calculated from the misfit between measured pl/cpx partitioning and calculated partitioning.

Y	χ^2	No. points	χ^2_v
lnD_{Li}	439.2	28	18.30
lnD_{Na}	374.7	23	19.72
lnD_{K}	516.9	13	57.44
lnD_{Rb}	483.4	14	48.34
linear method	1814	78	23.26

The linear method gives very accurate predictions of the partitioning of lithium between plagioclase and clinopyroxene but gives poor predictions of the larger monovalent cations. The partitioning of potassium in particular should be treated with caution as the LA-ICP-MS has a very high background value for potassium (due to its similar weight to the carrier gas; argon). These high backgrounds lead to very poor sensitivity for potassium.

Divalent cations

The divalent cations are complicated as they partition into different sites in each mineral dependant on their size. The small cations; Be and Mg substitute into the tetrahedral site in plagioclase and into the M1 site of clinopyroxene. The large divalent cations; Ca, Sr and Ba partition into the VIII-fold coordinated site in both minerals (M2 site in clinopyroxene and the M-site of plagioclase). Therefore the small and large divalent cations must be considered separately.

The small divalent cations: Be and Mg

The substitution of the small divalent cations into plagioclase and clinopyroxene have different stoichiometric controls:

Equation 89:
The stoichiometric control on the substitution of a divalent cation into the tetradhedral site of plagioclase

$$CaAl_2Si_2O_{8_{plagioclase}} + BeO_{melt} + SiO_{2_{melt}} = CaBeSi_3O_{8_{plagioclase}} + Al_2O_{3_{melt}}$$

Equation 90:
The stoichiometric control for the substitution of divalent cations on the M1 site of clinopyroxene.

$$CaMgSi_2O_{6_{pyroxene}} + BeO_{melt} = CaBeSi_2O_{6_{pyroxene}} + MgO_{melt}$$

The substitution of the small divalent cations into plagioclase is controlled by the addition of silicon into anorthite and therefore is highly dependent on the activity of the melt components. The partitioning of the small divalent cations into clinopyroxene is a straight substitution of Be of Mg on the M1 site, with Mg being part of the ideal formula for clinopyroxene.

As the substitution of these small cations have different stoichiometric controls, the partitioning between plagioclase and clinopyroxene will be an extremely complex equation. Furthermore, as the effect of melt composition will not be cancelled out, the partitioning of these cations will not have useful application in natural samples.

The large divalent cations: Ca, Sr and Ba

The large divalent cations, have the same stoichiometric control between plagioclase and clinopyroxene, and therefore, the effect of melt composition will be cancelled out:

Equation 91:
The stoichiometric control on the substitution of a divalent cation into the large cation site of plagioclase

$$CaAl_2Si_2O_{8_{plagioclase}} + SrO_{melt} = SrAl_2Si_2O_{8_{Plagioclase}} + CaO_{melt}$$

Equation 92:
The stoichiometric control for the substitution of divalent cations on the M2 site of clinopyroxene.

$$CaMgSi_2O_{6_{pyroxene}} + SrO_{melt} = SrMgSi_2O_{6_{pyroxene}} + CaO_{melt}$$

The partitioning of the large divalent cations into plagioclase is controlled by the anorthite content of the plagioclase (Table 13).These linear relationships model the partitioning of the large divalent cations into the M-site of plagioclase with an error of χ^2_v=21.41. The partitioning of the large divalent cations into clinopyroxene is most correlated with the partitioning of calcium (Table 24).

These linear relationships model the partitioning of the large divalent cations into the M2-site of clinopyroxene with an error of χ^2_v=20.45.

In both minerals, the partitioning of the large divalent cations are controlled by the sample mechanism and are highly correlated to the partitioning of calcium between the mineral and the melt. Therefore the partitioning of the large divalent cations between plagioclase and clinopyroxene will be highly correlated with the partitioning of calcium between the two minerals (Table 27).

Table 27: A combination of the linear fits in Table 13 and Table 24. Error is calculated from the misfit between measured pl/cpx partitioning and calculated partitioning.

Y	m	X	c	χ^2	No. points	χ^2_v
$RTlnD_{Sr}$	7.14	lnD_{Ca}	36.47	606	31	20.92
$RTlnD_{Ba}$	2.69	lnD_{Ca}	5.29	348	10	43.60
linear method					41	25.83

Sr is above detection limit in both phases and therefore this relationship is better constrained and more precise than the relationship of Ba. The partitioning of both the large divalent cations are highly correlated with the partitioning of calcium between

plagioclase and clinopyroxene due to the shared stoichiometric control of these two substitutions.

The rare earth elements

The partitioning of rare earth elements into plagioclase is controlled by the substitution:

Equation 93
Stoichiometric control on the partitioning of rare earth elements into anorthite

$$[\mathrm{REE}]\mathrm{O}_{1.5_{\mathrm{melt}}} + \mathrm{CaAl_2Si_2O}_{8_{\mathrm{pl}}} + \mathrm{AlO}_{1.5_{\mathrm{melt}}} = [\mathrm{REE}]\mathrm{Al_3SiO}_{8_{\mathrm{pl}}} + \mathbf{CaO_{melt}} + \mathrm{SiO}_{2_{\mathrm{melt}}}$$

Where the substitution of the rare earth element (REE) is controlled by the availability of the Al in the melt to charge balance the trivalent cation. Also, the partitioning of the REE in plagioclase is highly correlated with the partitioning of calcium into plagioclase.

The partitioning of rare earth element into clinopyroxene can occur in both the M2 site (Ca site) and the M1 site (Mg site). This is controlled (in aluminous systems) by the two equations:

Equation 94:
Substitution of rare earth elements on the M2 site of diopside in an aluminous system

$$\mathrm{CaMgSi_2O}_{6_{\mathrm{px}}} + [\mathrm{REE}]\mathrm{O}_{1.5_{\mathrm{melt}}} + \mathrm{AlO}_{1.5_{\mathrm{melt}}} = [\mathrm{REE}]\mathrm{MgAlSiO}_{6_{\mathrm{px}}} + \mathbf{CaO_{melt}} + \mathrm{SiO}_{2_{\mathrm{melt}}}$$

Equation 95:
Substitution of rare earth elements on the M1 site of diopside in an aluminous system

$$\mathrm{CaMgSi_2O}_{6_{\mathrm{px}}} + [\mathrm{REE}]\mathrm{O}_{1.5_{\mathrm{melt}}} + \mathrm{AlO}_{1.5_{\mathrm{melt}}} = \mathrm{Ca}[\mathrm{REE}]\mathrm{AlSiO}_{6_{\mathrm{px}}} + \mathbf{MgO_{melt}} + \mathrm{SiO}_{2_{\mathrm{melt}}}$$

Where the M1 site only allows the smallest (and heaviest) of the rare earth elements to substitute. Following these stoichiometric controls, the partitioning of the rare earth elements in both sites is highly dependent on melt composition.

The partitioning of the REE on both sites have the same contribution from the melt, but the REE on the M1 site will be effected by the partitioning of Mg in clinopyroxene while the partitioning of the REE into the M2 will be affected by the partitioning of calcium.

Visually comparing the partitioning between plagioclase and clinopyroxene, it appears that the variables tested here do not change the partitioning of between the two minerals significantly. Comparing experiments conducted at the same temperature and pressure but vary melt composition (and likewise mineral composition), the slope of the rare earth

element pattern changes. The slope becomes steeper as the albite content of the melt increases (Figure 103A). With increasing pressure, the magnitude of the pattern increases (Figure 103C); along with the occasional display a HREE inflection. An increase in temperature may cause in increase in magnitude of the pattern however this change is within error.

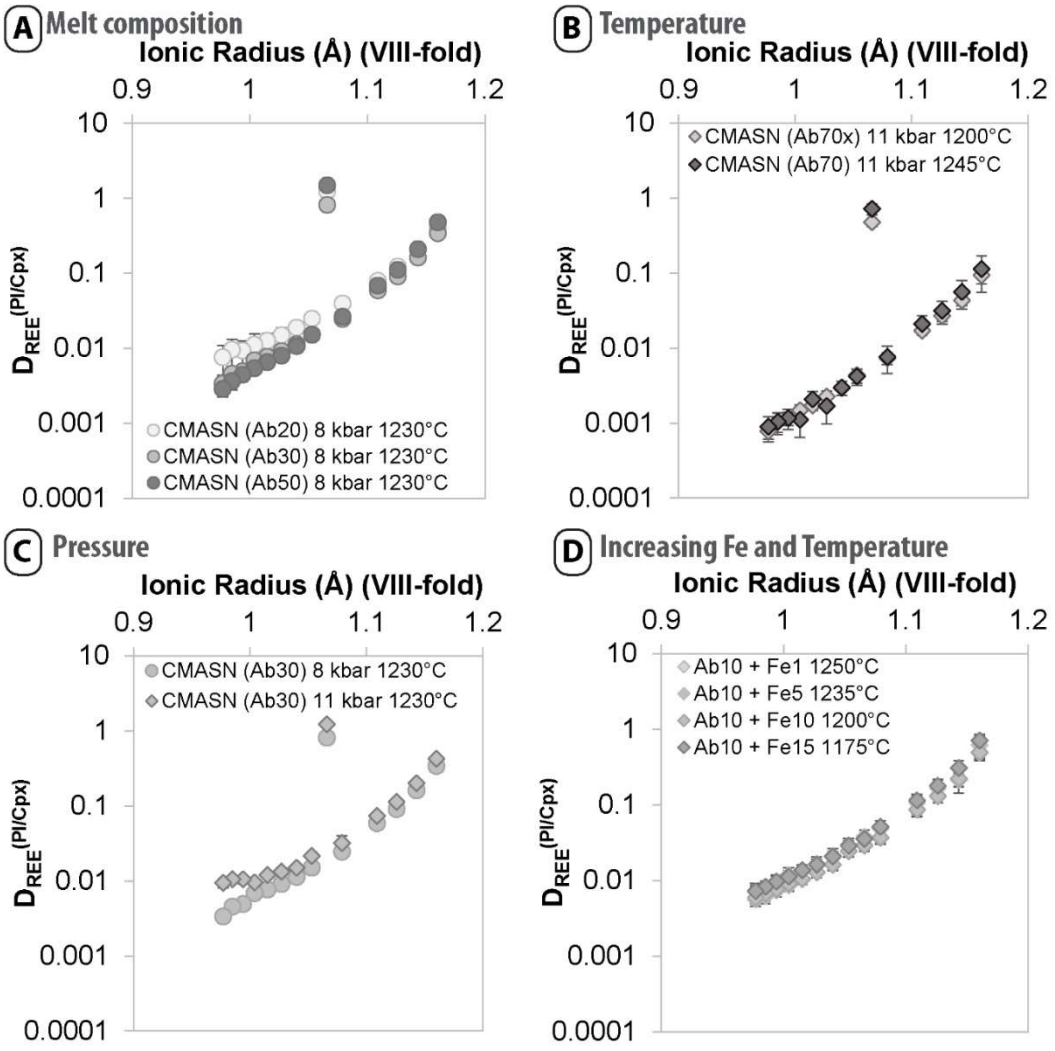

Figure 103: Comparison of plagioclase/clinopyroxene REE partitioning A) Various melt compositions at 8kbar and 1230°C, B) temperature dependence at 11 kbar and melt composition $An_{15}Di_{15}Ab_{70}$, C) Pressure effect on partitioning at 1230°C and melt composition $An_{35}Di_{35}Ab_{30}$, D) the addition of iron into composition $An_{45}Di_{45}Ab_{10}$ and subsequent change in crystallisation temperature on the partitioning between plagioclase and clinopyroxene.

Testing the validity of a REE in plagioclase thermometer

To create a geothermometer from these equations, the equation must be rearranged as outlined by Sun and Liang (2012) and Putirka (2008) to take the form:

Equation 96:
The basic equation for geothermometer

$$lnD = A + \frac{B - f(P)}{T}$$

$$B = (lnD - A) * T + f(P)$$

The lattice strain models and orthogonal polynomials can be rearranged into the form outlined in Equation 96 then temperature (in Kevin) is calculated from the slope of the relationship between similar cations (e.g. the rare earth elements).

The stoichiometric control equation (Equation 53) predicts the rare earth elements the most precisely of all the tested equations. Theoretically this equation could be used as a thermometer. Solving for temperature using these coefficients allows the experimental temperatures to be predicted within 50 °C for 14% of the samples and within 100°C for 40% of the samples. Although the stoichiometric control Equation 53 was much more accurate in predicting the rare earth elements than any other tested equation, it is an imprecise thermometer.

Removing the variable of melt completely, the REE ratios are modelled precisely (Equation 55). Solving for temperature using these coefficients allows the experimental temperatures to be predicted within 50 °C for 28% of the samples and within 100°C for 58% of the samples.

The Putirka (2008) major element plagioclase-liquid thermometer (equation 24a in that study) is quite precise, with 72% of the data predicted within 100 °C .

Therefore, the partitioning of the rare earth element in plagioclase is relatively insensitive to temperature.

A test of the Sun and Liang (2017) REE-in-plagioclase-clinopyroxene thermometer

The plagioclase/clinopyroxene geothermometer of Sun and Liang (2017) is based on a double lattice strain approach. This is the ratio of the lattice strain model of plagioclase/melt (Sun et al., 2017) and clinopyroxene/melt (Sun and Liang, 2012) in the form of Equation 20.

The Sun and Liang (2012) clinopyroxene lattice strain model was fit to partition coefficients in 43 basaltic type melt experiment that span a temperature range of 1042-1470°C and pressures from 1 atm to 4 GPa. The Mg# of these pyroxenes range from 54-100.

Equation 70:
Sun and Liang 2012. Lattice strain model for the rare earth element partitioning in clinopyroxene.

$$lnD_0 = -7.14 + \frac{7.19 * 10^4}{RT} + 4.37X_{Al}^{T} + 1.98X_{Mg}^{M2} - 0.91X_{H2O}^{melt}$$

$$r_0 = 1.066 - 0.104X_{Al}^{M1} - 0.212X_{Mg}^{M2}$$

$$E = [2.27r_0 - 2.00] * 10^3$$

The Sun et al. (2017) plagioclase lattice strain model was fit to 29 experiments from the published literature. The temperature range for this model is 1127-1410°C with pressures from 1 atm to 1.5 GPa. The anorthite number of these experiments ranges from 41-98.

Equation 24:
Sun et al. (2017) model for rare earth elements partitioning between plagioclase and basaltic melt

$$lnD_0^{3+} = 16.05(\pm 1.57) - \frac{19.45(\pm 1.78) + 1.17(\pm 0.14)P^2}{RT} * 10^4 - 5.17(\pm 0.37) * \left(X_{Ca}^{pl}\right)^2$$

$$r_0^{3+}(\text{Å}) = 1.179(\pm 0.027)$$

$$E^{3+}\ (GPa) = 196(\pm 51)$$

These experiments were chosen as they form from basaltic melts. Note that this thermometer was never tested on experimental melts that contained both plagioclase and clinopyroxene together. These mineral/melt models were formed from empirical relationships observed in these experiments, assuming little contribution of melt composition on the partitioning.

Using these equations to calculate the partitioning of the rare earth elements gives an extremely large error ($\chi^2_\nu = 8142$) (Figure 104b). The experimental temperatures were calculated using the thermometer included as supplementary material in Sun and Liang (2017). The calculated temperatures for the experiments using this trace element thermometer cover a range of 400°C between 945-1336°C. The true experimental temperatures only range between 1130-1265°C. Using only the experiments within the

calibration range (26), 38% were predicted within 50 °C and 62% were predicted within 100 °C.

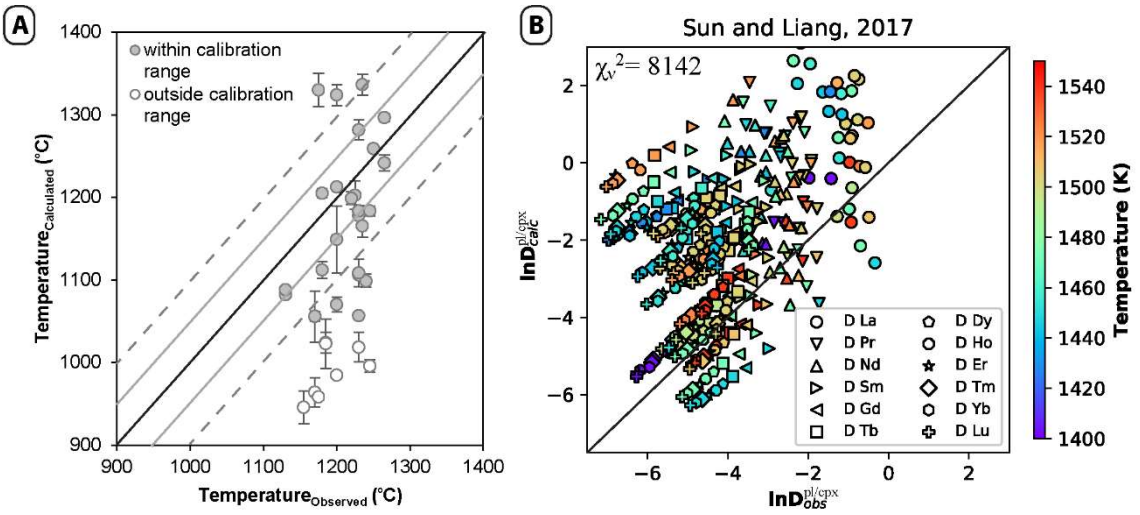

Figure 104: Test of the existing thermometer based on the partitioning between plagioclase and clinopyroxene (Sun and Liang, 2017) A) comparing temperatures of the experiments (observed) with the calculated temperatures using the rare earth element thermometer. Open symbols represent plagioclase outside the calibration range ($An_{<41}$). Black solid line represents perfect prediction, grey solid line represents Δ50°C from observed and broken line is Δ100°C of observed. B) comparing the rare earth element partitioning observed with the predicted rare earth elements from the (Sun and Liang, 2017) model. Black line represents a perfect prediction.

The plagioclase compositions that are outside the calibration range (i.e. An#<41) are on average 198 °C lower than the experimental temperature. Furthermore, there is a linear relationship between the temperature error and the anorthite number of the plagioclase.

This thesis has outlined that melt composition plays a key role in the partitioning of REE between both these phases and their equilibrium melt. As these lattice strain models are calculated on empirical relationships and the melt contribution is omitted, the REE thermometer will have propagated errors.

This thermometer is imprecise for these simple, synthetic systems.

Wood and Blundy 2014 lattice strain models

This equation is based on the Bindeman et al. (1998) and Bindeman and Davis (2000) studies of the Drake and Weill (1975) experiments. These experiments were grown from basaltic and andesitic melts between 1150-1343 °C. It has 89 individual rare earth element partitioning data points (omitting Y, Ce, and Eu) over 8 melt compositions.

Equation 26:
Wood and Blundy (2014) model for rare earth element partitioning between plagioclase and melt

$$D_{La} = exp * \left(\frac{-10.8(\pm 2.6) * X_{An} - 12.4(\pm 1.8)}{RT} \right)$$

$$r_0^{3+}(\text{Å}) = (1.258 - 0.057 * X_{An}) - 0.03$$

$$E^{3+}\ (GPa) = 210$$

Wood and Blundy (2014) is a summary of trace element partitioning for many common elements from Wood and Blundy (1997) for anhydrous melts.

Equation 71:
Wood and Blundy, 2014. Lattice strain model for the rare earth element partitioning.

$$D_0^{3+} = \left\{ \frac{\left(\frac{Mg}{Mg+Fe}\right)_{melt}}{X_{Mg}^{M1}} \right\} * exp\left(\frac{88750 - 65.644T + 7050P - 770P^2}{RT}\right)$$

$$r_0^{3+} = 0.974 + 0.67X_{Ca}^{M2} - 0.051X_{Al}^{M1}$$

$$E_{M2}^{3+} = 318.6 + 6.9P - 0.036T$$

This data are fit to 13 separate studies (1 unpublished) which are listed here:

Dunn (1987); Gaetani and Grove (1995); Gallahan and Nielsen (1992); Grutzeck et al. (1974); Hack et al. (1994); Hart and Dunn (1993); Hauri et al. (1994); Jones and Burnett (1987); McKay et al. (1994); McKay et al. (1986); Nicholls and Harris (1980); Watson et al. (1987)

These studies make up 454 individual rare earth element data points, over half of which (228) are from Gallahan and Nielsen (1992).

These two models are used in the double lattice strain model to predict the partitioning between plagioclase and clinopyroxene. The fit is very poor χ^2_ν=3596 (Figure 105) however is more precise than the Sun and Liang (2017) prediction.

The clinopyroxene/melt equation also contains a melt component in the Mg# of the melt. This melt component is not cancelled out in the plagioclase/clinopyroxene partitioning equation and therefore the use of this model for natural samples is limited.

A new lattice strain model

This thesis has outlined that the stoichiometric control and the melt components described within are an important consideration in the partitioning in both plagioclase and clinopyroxene. The lattice strain models that include a REE-SiO_2 interaction term (γ_{REE}) model the data with the most accuracy (Equation 53, Equation 84). These parameters do not have the same relationship in the plagioclase/melt and clinopyroxene/melt models, which is most likely a model error as this should be equal when plagioclase and

clinopyroxene grow from the same melt. Therefore, it is best to use the models that assume minimal REE-SiO_2 interaction (Equation 52, Equation 83). Therefore this component would be taken up into the $\ln D_0^{3+}$ value.

Each of these precise equations can be rearranged to solve for temperature.

Equation 52:
A stoichiometric control equation for the partitioning of REE in plagioclase, relative to lanthanum

$$\ln D^{\mathrm{pl/melt}}{}_{\mathrm{REE}} = \ln D_0^{3+} + \left(\frac{-910.17\ \mathrm{E}}{\mathrm{T}}\right) * \left[\frac{\mathrm{r}_0}{2}(\mathrm{r}_{La}^2 - \mathrm{r}_\mathrm{i}^2) + \frac{1}{3}(\mathrm{r}_\mathrm{i}^3 - \mathrm{r}_\mathrm{La}^3)\right] + \ln\left(\frac{\mathrm{XAlO}_{1.5\mathrm{melt}}}{\mathrm{XSiO}_{2\mathrm{melt}}}\right) + \ln D_{\mathrm{Ca}}^{\frac{\mathrm{pl}}{\mathrm{melt}}}$$

Where

$\ln D_0^{3+} = 1.38(\pm 0.32) - \frac{0.55(\pm 0.05)}{T} * 10^4$

$r_0 = 1.17(\pm 0.008) * (1 - 0.019(\pm 0.004) * X_{Ab})$ and

$E = 235(\pm 16)$.

This equation is modelled from 864 data points from 72 individual plagioclase/melt experiments. This equation predicts all plagioclase experiments with a $\chi^2_\nu = 34.25$. Solving for temperature using these coefficients allows the experimental temperatures to be predicted within 50 °C for 14% of the samples and within 100°C for 40% of the samples. This shows that that the partitioning of the rare earth elements in plagioclase is insensitive to temperature.

Equation 83:
A stoichiometric control equation for the partitioning of REE in clinopyroxene

$$\ln D^{\mathrm{cpx/melt}}{}_{\mathrm{REE}} = \ln D_0^{3+} + \left(\frac{-910.17\ \mathrm{E}}{\mathrm{T}}\right) * \left[\frac{1}{2}\mathrm{r}_0 * (\mathrm{r}_\mathrm{i} - \mathrm{r}_0)^2 + \frac{1}{3} * (\mathrm{r}_\mathrm{i} - \mathrm{r}_0)^3\right] + \ln\left(\frac{\mathrm{XAlO}_{1.5\mathrm{melt}}}{\mathrm{XSiO}_{2\mathrm{melt}}}\right) + \ln D_{\mathrm{Ca}}^{\frac{cpx}{\mathrm{melt}}}$$

Where

$\ln D_0^{3+} = -7.0(\pm 0.4) + \frac{1.00(\pm 0.06)}{T} * 10^4 + 0.032(\pm 0.004)P$

$r_0 = 1.05(\pm 0.003) - 0.2(\pm 0.02) * X_{Mg}^{M2}$ and

$E = 225(\pm 12)$.

Where pressure is in kbar.

This model fits both the aluminous data presented in this study, and those presented in Gallahan and Nielsen, 1992 (total of 733 data points) with a χ^2_ν= 26.81. Using this equation to predict the temperature in the 46 aluminous diopside experiments presented in this study, 40% were predicted within 50°C and 70% were predicted within 100°C.

As the melt components are the same in both equations, the effect of melt composition is cancelled out. The partitioning of calcium in each of the equations will convert into the partitioning of calcium between plagioclase and clinopyroxene:

Equation 97:
The stoichiometric equation for the partitioning of rare earth elements between plagioclase and clinopyroxene

$$\ln D^{\frac{pl}{cpx}}_{\mathrm{REE}} = \ln D_0^{3+} + \left(\frac{-910.17\ \mathrm{E}^{pl}}{\mathrm{T}}\right) * \left[\frac{{r_0}^{pl}}{2}(r_{La}^2 - r_i^2) + \frac{1}{3}(r_i^3 - r_{La}^3)\right] - \left(\frac{-910.17\ \mathrm{E}^{cpx}}{\mathrm{T}}\right) * \left[\frac{1}{2}{r_0}^{cpx} * (r_i - {r_0}^{cpx})^2 + \frac{1}{3} * (r_i - {r_0}^{cpx})^3\right] + \ln D^{\frac{pl}{cpx}}_{Ca}$$

$\ln D_0^{3+}$=$8.38(\pm 0.42) - \frac{1.55(\pm 0.11)}{T} * 10^4 - 0.032(\pm 0.004)P$

${r_0}^{cpx} = 1.05(\pm 0.003) - 0.2(\pm 0.02) * X_{Mg}^{M2}$

$E^{cpx} = 225(\pm 12)$.

${r_0}^{pl} = 1.17(\pm 0.008) * (1 - 0.019(\pm 0.004) * X_{Ab})$ and

$E^{pl} = 235(\pm 16)$.

The partitioning between plagioclase and clinopyroxene (31 experiments with 372 points) is modelled with a combination of these two equations with an error of χ^2_ν=32.95. This is the most accurate of the REE between plagioclase and clinopyroxene models tested.

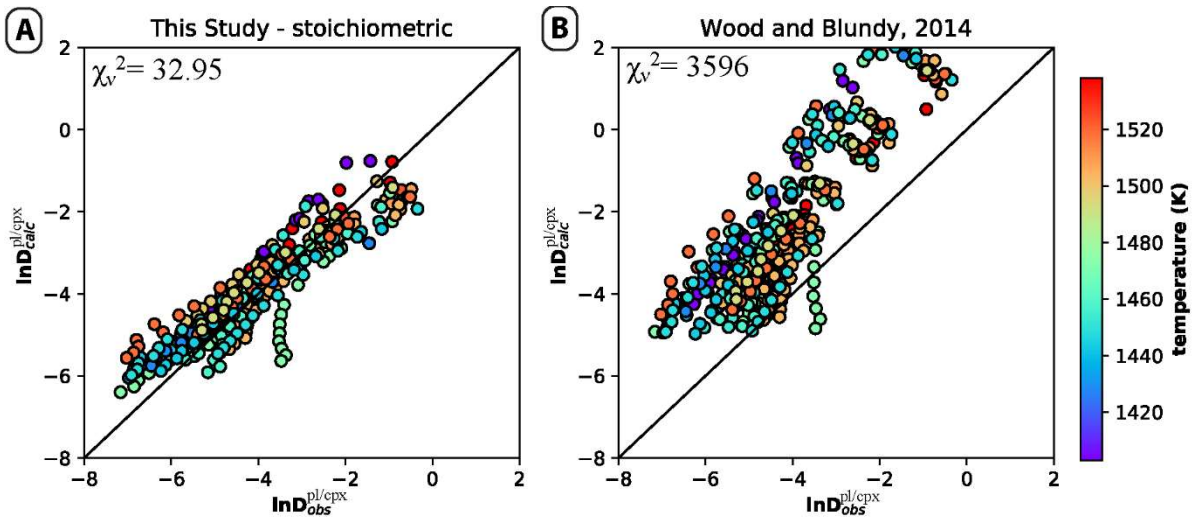

Figure 105: The error between predicted and observed partitioning of the REE between plagioclase and clinopyroxene. This study is a combination of Equation 52 and Equation 83 and fits the data with χ^2_v=32.95. The Wood and Blundy (2014) prediction combines Equation 26 and Equation 71 and fits the data with χ^2_v=3596. Solid lines represent a prefect prediction.

To test if the REE are a suitable thermometer, Equation 97 was rearranged to take the form B=T(lnD_{REE}-A); as shown in Equation 98. The slope of the linear relationship between B and lnD_{REE}-A (passing through the origin) solves the temperature.

Equation 98:
A REE between plagioclase and clinopyroxene thermometer from Equation 97

$$\left[\ln \mathrm{D}^{\frac{pl}{cpx}}{}_{\mathrm{REE}} - \left(8.38(\pm 0.42) - 0.032(\pm 0.004)P + \ln \mathrm{D}^{\frac{\mathrm{pl}}{\mathrm{cpx}}}_{\mathrm{Ca}}\right)\right] * \mathrm{T}$$

$$= -910.17\ \mathrm{E}^{pl} * \left[\frac{\mathrm{r_0}^{pl}}{2}(\mathrm{r}_{La}^2 - \mathrm{r_i^2}) + \frac{1}{3}(\mathrm{r_i^3} - \mathrm{r_{La}^3})\right] + 910.17\ \mathrm{E}^{cpx} *$$

$$* \left[\frac{1}{2}\mathrm{r_0}^{cpx} * (\mathrm{r_i} - \mathrm{r_0}^{cpx})^2 + \frac{1}{3} * (\mathrm{r_i} - \mathrm{r_0}^{cpx})^3\right] - 1.55(\pm 0.11) * 10^4$$

This equation predicts the experimental temperatures accurately, with 52% of the 31 experiments predicted within 50 °C and 90% predicted within 100 °C (Figure 106). This is much more accurate than the Sun and Liang (2017) thermometer, however the experimental range is only 135 °C. This thermometer will need to be tested at a wider range of temperatures to ensure it is correct.

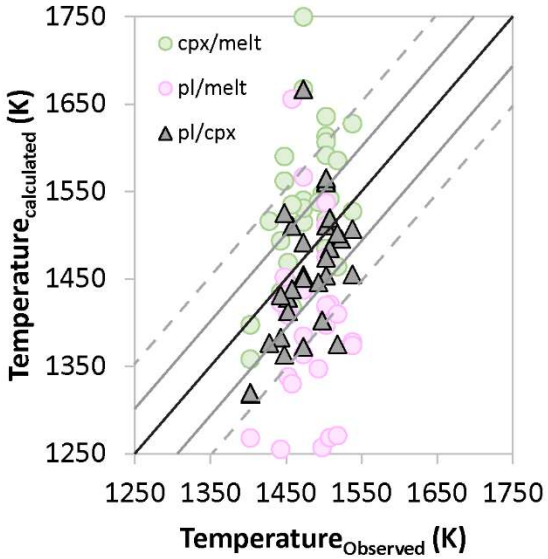

Figure 106: Comparison between the observed experimental temperatures with the temperatures calculated from Equation 98 for pl/cpx, Equation 52 for pl/melt and Equation 83 for cpx/melt. 52% of the 31 experiments predicted within 50 °C and 90% predicted within 100 °C. Experimental range 1130-1265 °C. Black solid line represents a perfect prediction, grey solid line represents Δ50°C from observed, and broken line represents Δ100°C.

REE ratios

Using the ratio of the partitioning of the rare earth elements to a common rare earth allows for the melt effects to be cancelled in the mineral/melt partitioning models. In the previous chapters, these rare earth element ratios ($K_{D_{REE}/D_{Gd}}$) where modelled for plagioclase/melt (Equation 55) and clinopyroxene/melt (Equation 86) using orthogonal polynomials. To compare the partitioning between plagioclase and clinopyroxene these models will need to be combined:

Equation 99:
The combined orthogonal polynomial for comparing partitioning between two mineral phases

$$\ln K^{\frac{pl}{cpx}}_{\frac{D_{REE}}{D_{Gd}}} = (\lambda 0^{pl} - \lambda 0^{cpx}) + (r_i^{3+} - 1.06) * (\lambda 1^{pl} - \lambda 1^{cpx}) + (r_i^{3+} - 1.01) * (r_i^{3+} - 1.13) * (\lambda 2^{pl} - \lambda 2^{cpx}) + (r_i^{3+} - 1.06) * (r_i^{3+} - 1.15) * (r_i^{3+} - 0.99) * (\lambda 3^{pl} - \lambda 3^{cpx})$$

Equation 100:
Orthogonal polynomial parameters for the $lnK^{pl/melt}_{D_{REE}/D_{Gd}}$

$$\lambda 0^{pl} = -0.20(\pm 0.01)$$

$$\lambda 1^{pl} = -9.96(\pm 2.8) - 2.49(\pm 0.73) * X_{An} + 4.19(\pm 0.36) * \frac{10^4}{T} - 0.21(\pm 0.02) * P$$

$$\lambda 2^{pl} = -35.19(\pm 2.07)$$

$$\lambda 3^{pl} = 154(\pm 37)$$

Equation 101:
Orthogonal polynomial parameters for the $lnK_{D_{REE}/D_{Gd}}^{cpx/melt}$

$$\lambda 0^{cpx} = -0.288(\pm 0.004) - 0.0378(\pm 0.009) * P$$

$$\lambda 1^{cpx} = -5.27(\pm 0.07) - 11.8(\pm 0.7) * X_{Al}^{T}$$

$$\lambda 2^{cpx} = -38(\pm 7) + 6.2(\pm 1.1) * \lambda 1$$

$$\lambda 3^{cpx} = -4095(\pm 640) + \frac{587(\pm 94) * 10^4}{T}$$

The slope of the combined rare earth element ratios is strongly controlled by the anorthite content of the plagioclase. Pressure controls the magnitude of the pattern and temperature contributes to the sinusoidal nature of the pattern and has a minor impact on the slope. The λ3 term in the clinopyroxene/melt model is an indicator of the contribution of the M1 site partitioning in the heaviest REE. This fits the experimental data with an error of $\chi^2\nu$=1.9 (Figure 107)

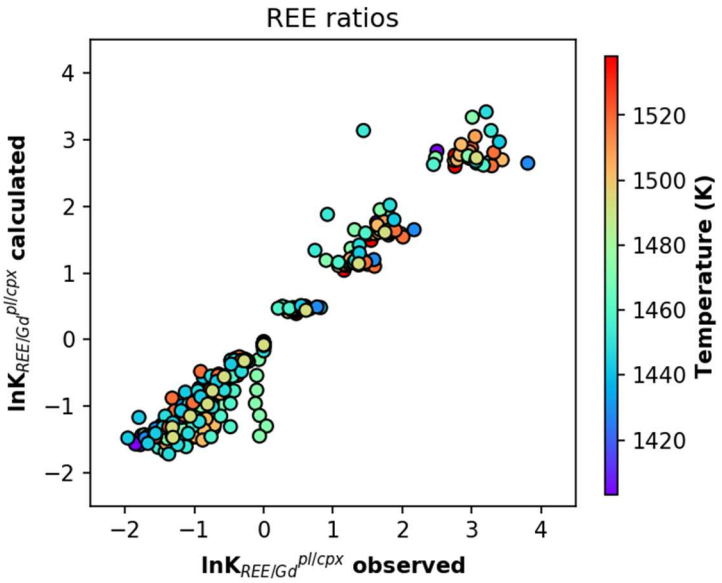

Figure 107: The comparison between with observed REE ratio ($lnK^{pl/cpx}_{REE/Gd}$) with the predicted ratio using Equation 100 and Equation 101 The error on this fit is χ^2_ν=1.9

This is the most accurate fit to the rare earth element partitioning, using only crystal chemistry, pressure and temperature. To test if the REE are a suitable thermometer, Equation 100 and Equation 101 were rearranged to take the form B=T(lnK-A) as outlined in the previous chapters. The slope of the linear relationship (passing through the origin) between B and lnK-A solves the temperature.

Of the 31 experiments that synthesised both plagioclase and clinopyroxene, 42% were predicted within 50 °C of the experimental temperature, and 55% were predicted within 100 °C. This is not an improvement from the Sun and Liang (2017) thermometer.

Although this equation is the most accurate of all the models, it does not prove to be an accurate thermometer. This suggests that the partitioning between these two minerals may not be sensitive to temperature.

6.1.3 Discussion

31 experiments successfully synthesised both plagioclase and clinopyroxene spanning a temperature range of only 1130-1265 °C and a pressure range between 1atm and 11 kbar. The minerals span a large compositional range; with anorthite numbers between 97-24, and clinopyroxene magnesium numbers between 100-53. Although the temperature range is small, the individual mineral/melt partition coefficients models were calibrated in a larger temperature range.

The plagioclase/melt partitioning data are fit to 7 individual plagioclase / experiments. These experiments range from 1130-1453 °C with anorthite numbers of An_{100-24}. The clinopyroxene/melt partitioning was examined over 55 experiments. These data cover a temperature range of 1130-1373 °C and magnesium numbers of 100-52. With the addition of Gallahan and Nielsen (1992) data for the rare earth elements, the temperature range is increased with a lower limit of 1050 °C.

The partitioning of monovalent cations between plagioclase and clinopyroxene are controlled by different stoichiometric mechanisms. Although the substitution of the monovalent cation occurs for calcium in both minerals, the charge balanced substitution is different. In clinopyroxene, the aluminium is likely to be incorporated onto the M1 site, replacing Mg, while in plagioclase, the additional charge is included as an additional silicon in tetrahedral coordination. As the stoichiometric control for these substitutions is different, the melt composition effect is not cancelled out when comparing the partitioning between the two solid phases. Fortunately, for the monovalent cations, melt composition plays a secondary role with the partitioning being strongly controlled by the anorthite content in plagioclase and pressure in clinopyroxene. Combining these two relationships the partitioning of the monovalent cations between plagioclase and clinopyroxene can be predicted very accurately (χ^2_ν=23.26).

The small divalent cations (Be and Mg) have different stoichiometric controls. The partitioning of the small cations into plagioclase occurs on the tetrahedral site, and is

affected strongly by melt composition. The partitioning of the small cations in clinopyroxene occurs in the M1 site. Mg is a major component of clinopyroxene, and is therefore highly compatible. Mg in the tetrahedral site in plagioclase is extremely incompatible. The main aim when looking at partitioning between two solid phases is to negate the effect of melt composition so that the partition coefficients can be used in natural systems where melt is rarely preserved. This is not the case for the small divalent cations.

The large divalent cations have the same stoichiometric control in both mineral phases. The partitioning of Ba and Sr are strongly correlated to the calcium content in both mineral phases and therefore, the partitioning of these two elements between plagioclase and clinopyroxene will be strongly correlated with the partitioning of calcium between these two phases. Using this relationship, linear relationships were fit to 31 experiments containing both plagioclase and clinopyroxene and $D_{Sr}^{pl/cpx}$ was modelled with an error of χ^2_v=20.92. D_{Ba} was above detection in only 10 experiments, which leads to a more imprecise model of χ^2_v=43.60.

The rare earth elements also share the same stoichiometric control in both plagioclase and clinopyroxene. These REE partitioning models are very robust as the REEs were the focus of this study. The plagioclase / melt lattice strain model was fit to 863 individual rare earth elements. Clinopyroxene / melt rare earth element partitioning was fit to 660 individual rare earth elements and an additional 179 individual rare earth elements from Gallahan and Nielsen (1992). The 31 plagioclase/clinopyroxene experiments give 372 individual rare earth element analysis that can be used to fit to analyse what effects the partitioning of REE between plagioclase and clinopyroxene.

Melt plays a very important role in the partitioning of the rare earth elements between both phases and their equilibrium melt. This is due the trivalent rare earth elements requiring a charge balance to substitute into the calcium site of both plagioclase (Equation 93) and clinopyroxene (Equation 94). As the stoichiometric control is the same between both minerals, the effect of melt composition will cancel out when comparing the partitioning between plagioclase and clinopyroxene. Using the two stoichiometric control equations, the partitioning between plagioclase and clinopyroxene can be predicted with an accuracy of χ^2_v=32.95.

The melt effect was removed in each of the mineral/melt partitioning models by normalised the partitioning of the REE to the partitioning of Gd (e.g. $D_{REE/Gd}^{pl/melt} = \frac{D_{REE}}{D_{Gd}}$).

These ratios were calculated in the previous chapters are and repeated here as Equation 100 and Equation 101. Comparing these ratios between plagioclase and clinopyroxene, the rare earth element can be predicted with the highest precision of any model (χ^2_ν=1.9).

The rare earth element partitioning between plagioclase and clinopyroxene has been used as a geothermometer by Sun and Liang (2017). Using the thermometry spreadsheet included as supplementary material to the published paper, the experimental temperatures were treated as unknowns and calculated from the partitioning of the rare earth elements between plagioclase and clinopyroxene. The results are very poor, with only 38% of experiments predicted within 50 °C and 62% predicted within 100 °C. Using these published partitioning equations to predict the partitioning of the trace elements (with known pressure and temperature) gives the worst fit of all models tested (χ^2_ν=8142).

The Sun and Liang (2012) clinopyroxene lattice strain model was to 43 basaltic type melt experiments that span a temperature range of 1042-1470°C and pressures from 1 atm to 4 GPa. The Mg# of these pyroxenes range from 54-100. The plagioclase lattice strain model was fit to 29 experiments from the published literature. The temperature range for this model is 1127-1410°C with pressures from 1 atm to 1.5 GPa. The anorthite number of these experiments ranges from An_{41-98}. This thermometer was not tested experimentally in systems where plagioclase and clinopyroxene are co-crystallised.

The Sun and Liang (2012) study is focussed on more natural compositions, which although is more representative of the natural world, may entangle and complicate the effects on the partitioning of trace elements. The data presented in this thesis are from simple, synthetic systems to help to thoroughly outline the basics of partitioning.

The previous chapters outlined that the partitioning of the REE in plagioclase is insensitive to temperature. However, the REE in clinopyroxene are sensitive to temperature. This suggests that any thermometer created from the partitioning between these two minerals will be dependant mostly on the partitioning in clinopyroxene.

Using the most robust predictive model, the REE ratios (Equation 100 and Equation 101) and following the Sun and Liang (2012) method to rearrange to create a thermometer, gives poor results. 36% were predicted within 50 °C of the experimental temperature, and 61% were predicted within 100 °C. This model is based on empirical relationships with only the crystal chemistry and the formation conditions, as the melt components should be entirely cancelled out. As this model makes a very poor thermometer, this suggests that the partitioning between these two minerals is relatively insensitive to temperature.

The stoichiometric control equation is the second most precise equation, and is constructed from the thermodynamic relationship of the partitioning equation rather than empirical relationships. This stoichiometric control equation (Equation 98) is the most accurate thermometer, with 52% of the 31 experiments predicted within 50 °C and 90% predicted within 100 °C.

This thermometer has been proven to be accurate for these simple, synthetic systems. Natural systems are much more complex and may include some un-tested variables. The next section will compare and contrast this thermometer in natural samples, evaluating its accuracy and outline the possible weaknesses.

6.2 A comparison between experimental and natural partitioning between plagioclase and clinopyroxene

6.2.1 Introduction

Plagioclase and clinopyroxene are some of the most common minerals in the Earth's crust. They occur together in a range of settings including volcanic and plutonic rocks. Some rocks such as gabbros rarely have assemblages that allow for thermometry calculations. If a precise thermometer can be established using these two ubiquitous minerals, it would have many different applications.

In the next section, the experimental results are compared to the REE partitioning between plagioclase and clinopyroxene from 20 natural rock samples from 6 locations. These locations are; Vanuatu, the Lesser Antilles (Dominica and St Vincent), New Caledonia, Alaska and Italy (Ivrea). The plagioclase ranges from An_{50}-An_{95} with paired clinopyroxene that has Mg# between 90-67. These compositions are well within the experimentally calibrated range.

The previous sections suggest the partitioning of the rare earth elements between plagioclase and clinopyroxene may have the potential to act as a thermometer. Although melt composition plays a significant role in the partitioning of the REE between each of these minerals and their equilibrium melt, as the stoichiometric control is the same, the effect of melt composition will be cancelled out. A REE-between plagioclase and clinopyroxene thermometer has already been suggested by Sun and Liang (2017). This thermometer was shown to be inaccurate when dealing with synthetic systems. This is due to the plagioclase/melt and clinopyroxene/melt REE partitioning models on which this thermometer is based, omit the substantial effect of melt composition. This allows for propagated errors and an inaccurate thermometer. Using thermodynamic theory and the "stoichiometric control" for the partitioning between each of the phases and their melt, a refined thermometer was created that was fairly accurate for the simple synthetic systems (Equation 98).

For the thermometry to be accurate, the plagioclase and clinopyroxene must be in equilibrium. Diffusion of elements is an important variable to consider when dealing with long-lived hot rocks such as gabbros. Diffusion may allow for the trace or minor elements to re-equilibrate while the rock is sub-solidus and therefore the temperature recorded will not be the original magmatic temperature. Faak et al. (2013) showed that magnesium can diffuse relatively quickly from clinopyroxene into plagioclase, which indicates that the "closure temperature" i.e. the temperature at which it no longer exchanges, is much lower

than the REE. As the REE diffusion so slow in both plagioclase (this study) and clinopyroxene (Van Orman et al., 2001), they should retain temperatures close to their original magmatic temperatures.

It has been shown in the previous chapters that plagioclase has an affinity for the LREEs while in clinopyroxene the middle REEs are the most compatible. This may cause issues in the natural samples if the concentrations of the HREEs in plagioclase and the LREEs in clinopyroxene are near or below the detection limit, as the complete $D^{REE}_{(Pl/cpx)}$ profile will not be accurately measured.

Volcanic and plutonic rocks have been investigated in this chapter. Theoretically, these two rock types will have very different formation and cooling histories. The volcanic systems generally cool quickly, from high temperatures and at lower pressures while the plutonic rocks often have long cooling times at moderate temperatures and pressures. If partition coefficients are dependent on formation histories, these two rock types should show the largest variance. Volcanic rocks also have the benefit of potentially quenching the equilibrium melt along with the minerals which will allow for additional plagioclase/melt and clinopyroxene/melt partition coefficients to be calculated. These samples will have temperatures estimated by clinopyroxene-liquid thermometers (Putirka, 2003).

A few of the samples include an additional mineral; orthopyroxene. This allows for temperatures to be calculated from both a major element thermometer (Brey and Köhler, 1990) and an additional trace element thermometer (Liang et al., 2013).

There have been many published studies that measure partition coefficients in natural samples. I have used the following three studies to add to the collection of natural partition coefficient values and as additional tests for these new thermometers.

Two lavas from the 1955 eruption of Kilauea volcano, Hawai'i were sampled and analysed by Norman et al. (2005). These lavas consist of a crystalline matrix with phenocrysts of the same minerals; plagioclase, pyroxene and olivine. Sample 2 contains both high-Ca and low-Ca pyroxene, while sample 8 contains only High-Ca type pyroxene. The samples are of very similar composition, with an average plagioclase compositions of An_{65} and clinopyroxene with Mg# (MgO/(MgO+FeO)) of 66 and 70 for samples 2 and 8 respectively. These samples are thought to have formed at between 1127-1147°C (Norman et al., 2005) based on plagioclase compositions and the Helz and Thornber

(1987) thermometer. These samples were also used in the published Sun and Liang (2017) study to test the validity of the REE between plagioclase and clinopyroxene thermometer.

Cumulate gabbro samples were taken from the Bushveld complex, Bellevue Core and published in Tanner et al. (2014). These samples are gabbros, taken at roughly 50m intervals down the core, through multiple layers of the intrusion. There are 12 samples that contain plagioclase, clinopyroxene pairs. The plagioclase increases from An_{53} to An_{76} downhole. Similarly the Mg# of the clinopyroxene increases from 64 to 84 downhole. The Bushveld complex is thought to have been emplaced at 1200-1300°C (Cawthorn and Walraven, 1998).

Mid-ocean ridge gabbros (MORG) from the International Ocean Drilling Program (IODP) were recovered from hole 1256D and the results published in Koepke et al. (2011). These results were collected on expedition 312 to the Cocos plate, eastern equatorial Pacific. This database has 6 samples that contain plagioclase, clinopyroxene pairs. The plagioclase compositions range from An_{62} to An_{79} with the corresponding clinopyroxene of Mg# 62 to 85. The calculated equilibrium temperatures for these samples range from 976-1005 °C from the "QUILF" 2-pyroxene thermometer developed by Andersen et al. (1993).

6.2.2 Sample Descriptions

The locations were chosen due to the occurrence of plagioclase and clinopyroxene together. The samples were picked with preference to homogenous plagioclase and clinopyroxene grains with no obvious zoning or dissolution. Samples that were heavily altered or deformed where avoided.

All samples were measured by LA-ICP-MS and the collection of the entire rare earth element suite was prioritised. The counting times and spot sizes were changed to allow for these elements to be above detection limit where possible (for full analytical method see methods section on page 29).

One sample from each location was also examined for trace element diffusion profiles. The elements investigated include Na^{23}, Mg^{25}, Mn^{55}, Fe^{57}, Sr^{88}, Y^{89}, La^{139} and Eu^{153}. No diffusion profiles where found.

Vanuatu Volcanics

The Vanuatu samples were collected from Tanna island by Mike Jollands. This island has an active volcano known as Mount Yasur which has small, sporadic and violent eruptions (Strombolian-type).

Three samples were chosen for analysis and a summary of the stoichiometry of the plagioclase and the clinopyroxene from each sample is included in Appendix 4; Table 64 and Table 65 on page 270.

WS5 was collected from the White Sands location of Vanuatu. In hand specimen it is black with many vesicles that exhibit flow banding and has visible clasts up to 3mm. Much of the rock is made up of glass with very few phenocrysts of plagioclase (An48) and clinopyroxene (Mg#73). There is very little chemical variation in this sample (Figure 108).

TUK6 was collected from Tukasmera. The hand specimen is grey/black with visible plagioclase phenocrysts up to 5mm long and randomly oriented. In the finer scale the ground mass is made up of glass, fragmented plagioclase (An56), clinopyroxene (Mg#77) and olivine with phenocrysts of these same minerals. There is minimal chemical variation in the crystals (Figure 108).

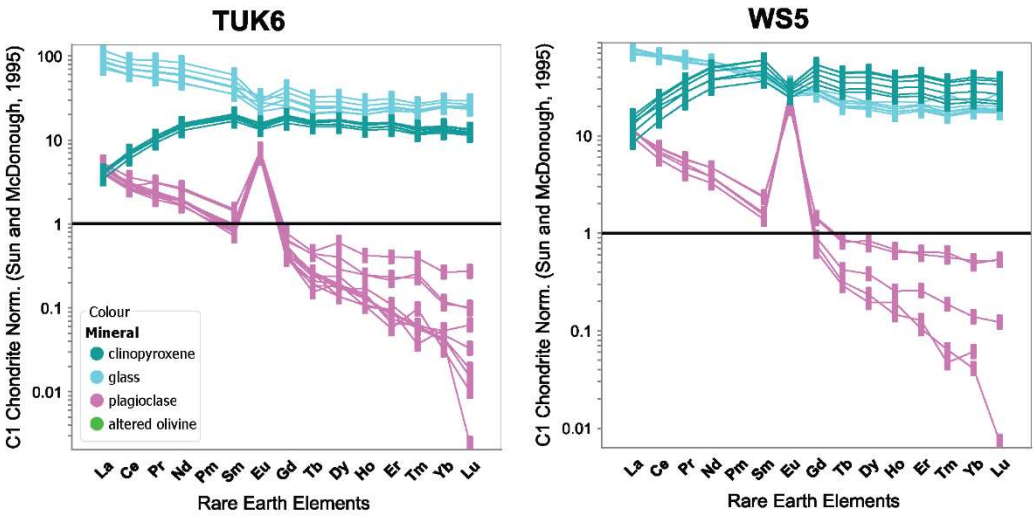

Figure 108: REE patterns C1 Chondrite Normalised (McDonough and Sun, 1995).

Temperature and pressures were calculated using jadeite crystallization and jadeite-diopside + hedenbergite exchange equilibria, of Putirka (2003). WS5 formed at much higher temperatures than TUK6 which formed at pressure of 2.9 and 1 kbar, respectively (Table 28).

The eruptions from Mount Yasur were studied in depth by Firth et al. (2014). Using the Putirka (2008) mineral-liquid thermobarometers, the plagioclase from the White Sands tephra sequence give a temperature range of 1078-1095 °C. Clinopyroxene-liquid pairs yield temperatures of between 1048-1079 °C and pressures between 2.4-4.9 kbar (Firth et al. 2014).

Table 28: Calculated temperatures and pressures from cpx-liquid composition (Putirka, 2003)

	thermometer		minerals	WS5	TUK6
				P (kbar)	P (kbar)
	Putirka et al (2003)		cpx/liquid	2.9	1
				T (C)	T (C)
	Putirka et al (2003)		cpx/liquid	1030	727.1
Equation (13)	Putirka RiMG '08	T(C)	liquid only	1044.4	994.9
Equation (14)	Putirka RiMG '08	T(C)	liquid only	1051.3	943.0
Equation (15)	Putirka RiMG '08	T(C)	liquid only	1060.8	928.5
Equation (16)	Putirka RiMG '08	T(C)	liquid only	1060.2	788.1
Helz and Thornber '87	Mg-thermometer	T(C)	liquid only	1052.2	1014.4
Helz and Thornber '87	Ca-thermometer	T(C)	liquid only	1041.2	1003.2
	Beattie (1993)	T(C)	Ol/Liquid	1080.1	735.1
Beattie (1993)	w/ Herz corr	T(C)	Ol/Liquid	1082.6	742.6
Putirka et al. 2007	Their Eqn. 4	Eqn 22 in RiMG T(C)	Ol/Liquid	1053.6	627.5
Putirka et al.	Their Eqn. (2)	Eqn. 21 in RiMG T(C)	Ol/Liquid	983.5	493.9
	Sisson & Grove	(1992) Eqn. 2 T(C)	Ol/Liquid	954.7	497.9

New Caledonian Gabbros

New Caledonia is made up of many massifs. The samples mentioned in this report have been collected from the Massif du Sud; specifically, Montagne des Sources. These samples were collected and studied in depth in the PhD thesis Pirard (2010) and published in brevity in Pirard et al. (2013). In this study, it is calculated that these rocks formed at 2-4 kbar. The temperature of the gabbronorites was calculated from the Ca in two pyroxene thermometer (Brey and Köhler, 1990) at 1050 ± 81 °C. The Ca between olivine and clinopyroxene thermometer (Köhler and Brey, 1990) gives 1256 ± 90 °C.

Two gabbronorites from the New Caledonian samples were chosen for this study. These samples were both collected from the Casse-Cou Mt track of Spring Mountain (Pirard et al., 2013). They were chosen based on their equilibrium textures in had minimal chemical zoning.

MDS37 is a gabbronorite with cumulate texture, collected from New Caledonia on (S 22º8’6” E 166º36’20”) (Pirard et al., 2013). This sample is made up of primarily clinopyroxene, orthopyroxene and plagioclase but also contains olivine. The plagioclase in this sample is An_{92} and the clinopyroxene has a Mg# of 90.

MDS41 is an olivine gabbro with cumulate texture. The clinopyroxene in this sample has exsolved into two pyroxene compositions. These exsolution lamella are parallel and very narrow, this causes the analyses to have a high standard deviation due to the random

sampling of the two pyroxene compositions. See Appendix 4; Table 60 for a summary of the mineral compositions. The plagioclase is of An_{94}.

The heavy REEs are have very low absolute values in plagioclase. MDS37 had Tm detectable in 3 of 8 analysis with 0.60 ± 0.06 ppb. Dy is consistently detectable at 6.2 ± 1.3 ppb. MDS41 had the Lu detectable in 3 of 8 analysis at 0.83 ± 0.39 ppb. Er is consistently detectable at 3.0 ± 0.9 ppb.

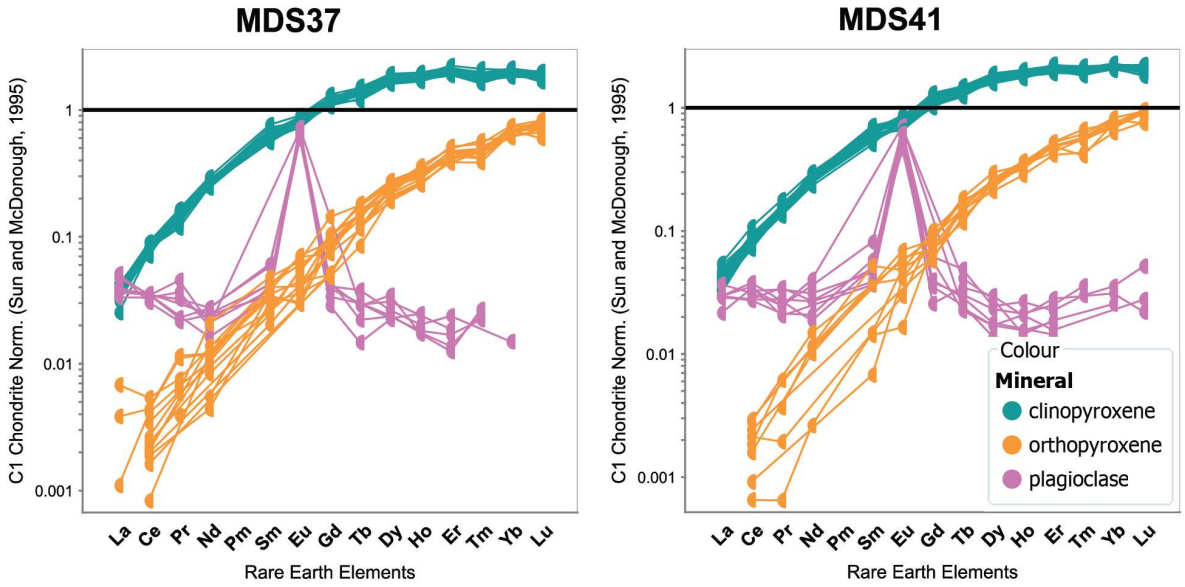

Figure 109: Chondrite normalised (McDonough and Sun, 1995) REE patterns for all phases in New Caledonian samples

Alaskan Gabbros

The Alaskan samples were collected by a team from the ANU and one sample was chosen due to the occurrence of plagioclase and clinopyroxene that were unzoned.

These samples are known as “Alaskan-Type” gabbros, which are cumulates originating from the differentiation of basalt (Himmelberg et al., 1986). However, this island specifically differs from the general Alaskan-type as they contain plagioclase (Himmelberg et al., 1986). The plagioclase of this sample has an An# of 92 and clinopyroxene with a Mg# of 80.

The heavy REEs have very low absolute values in plagioclase. Er was detectable in 7 of 8 analysis at 2.7 ± 0.7 ppb. All heavier REEs are below detection limit.

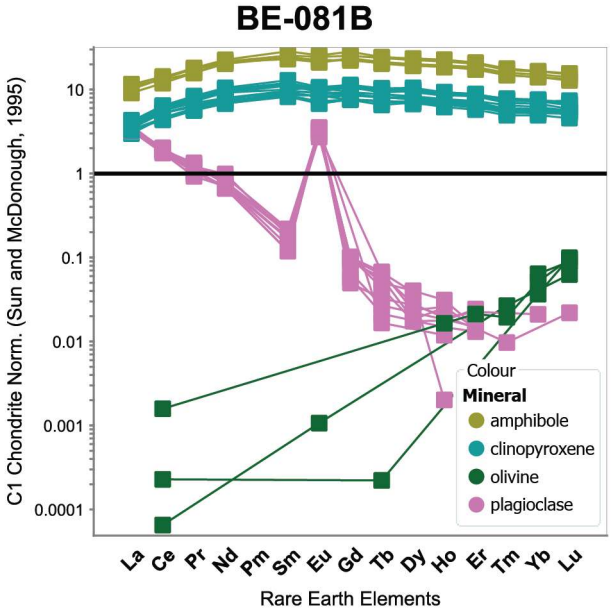

Figure 110: Chondrite normalised (McDonough and Sun, 1995) REE patterns for all phases in Alaskan sample

Ivrea-Verbano Gabbros

The Ivrea-Verbano Zone is located in northern Italy in the Southern Alps. The Ivrea Suite is an exposed section of the lower crust (Ewing et al., 2015). Estimates of the peak metamorphic conditions are described in Redler et al. (2012) as ~3.6-6.5 kbar at ~650ºC to ~10-12 kbar.

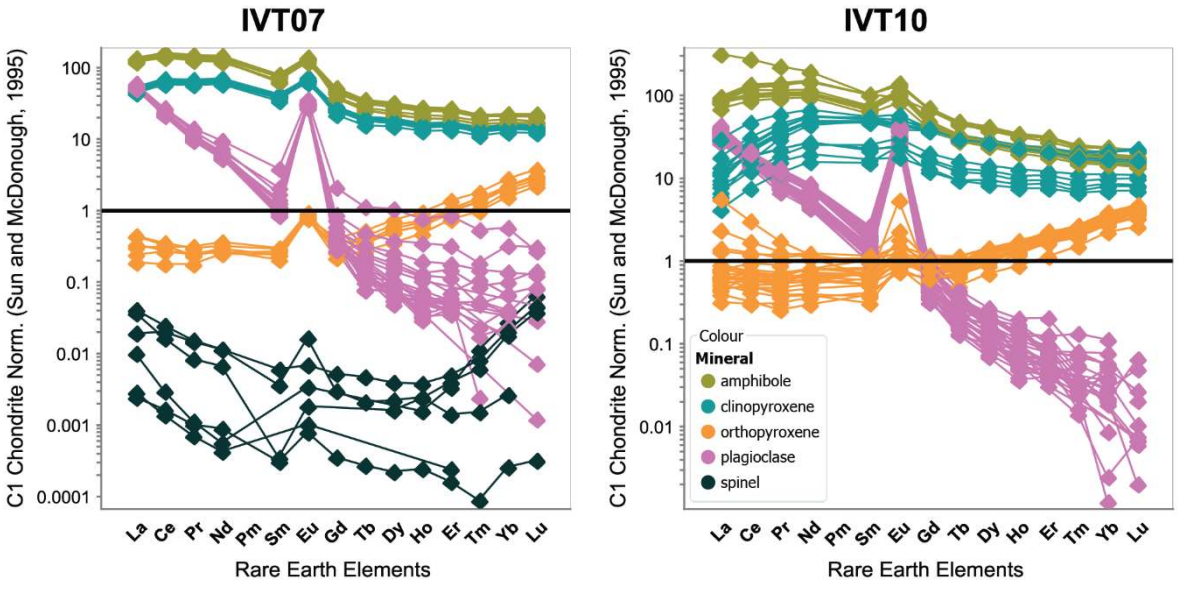

Figure 111: Chondrite normalised (McDonough and Sun, 1995) REE patterns for all phases in Ivrea samples

Both samples are coarse grained containing plagioclase (An_{69-76}), clinopyroxene (Mg# 71), orthopyroxene and amphibole. IVT07 also contains some spinel (Figure 111).

The Lesser Antilles

The Lesser Antilles are an active island arc in the Caribbean Sea, with the arc extending 750 km with islands spaced at 15-125 km intervals.

Dominica was studied by Howe et al. (2015) and are estimated to form at temperatures ranging from 750-1000°C and pressures of 1.1-2.3 kbar. The recent study by (Ziberna et al., 2017) suggests these samples formed at higher pressure; 2-4 kbar.

Stamper et al. (2014) studied samples from Grenada; the southern-most island in the chain. The conclusions from this study suggest that the cumulate rocks were formed at a narrow pressure range of between 2-5 kbar. The high water content of the rocks, (7 wt. % H_2O) causes the plagioclase crystallization to be suppressed.

The study presented herein investigates the trace elements in plagioclase and clinopyroxene from two islands in the Lesser Antilles, Dominica and St. Vincent.

St Vincent

The island of St. Vincent in north of Grenada in the island chain. The samples are cumulate xenoliths, found *ex-situ* as blocks on Soufriere volcano. The samples have been studied previously in Tollan et al. (2011), with focus on the major elements and stable isotope variations. The data presented in this thesis is a new study focussed on the trace element analysis of all phases.

Temperatures for these samples are calculated at 980-1020ºC from plagioclase + hornblende mineral pairs, however the plagioclase compositions are out of the calibration range and therefore many indicate inaccurate temperatures (Tollan et al., 2011). For these thermometers, a pressure of 5 kbar was estimated.

Samples V4, VS14 and VS2a were analysed with spots taken from adjacent plagioclase and clinopyroxene. The partition coefficients for this sample were calculated as adjacent spots and averaged. The rare earth elements are above detection in both the clinopyroxene and plagioclase for most of the samples. Sample VS4 shows some variation in the plagioclase (Figure 112). These samples have plagioclase compositions between An_{92-95} and Mg# 70 for clinopyroxene.

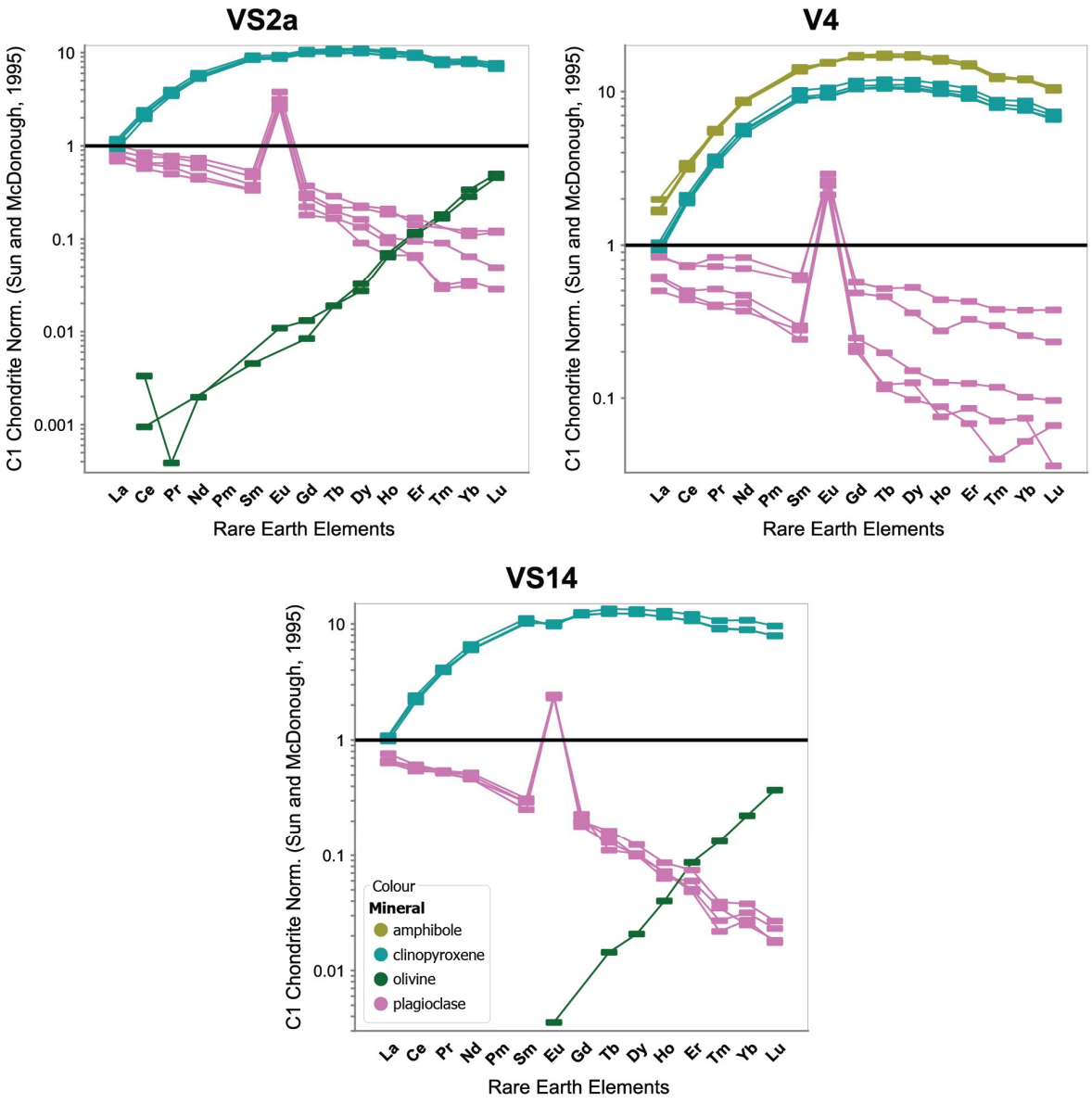

Figure 112: Chondrite normalised (McDonough and Sun, 1995) REE patterns for all phases in St Vincent samples

Dominica

Dominica is located three islands north of St. Vincent. Samples DC90-DC104 were collected from the same area near Petite Savanne, in the south east of the island. Samples DC47 and DC66 were collected along the river near St. Joseph, approximately 15km to the north-west. In total, there were 10 samples analysed for trace elements.

These samples were recently used in a new geobarometry calculation by Ziberna et al. (2017) (Table 29). This gives very accurate pressure estimates using clinopyroxene + olivine + plagioclase + spinel major element mineral chemistry and thermodynamic exchanges. The data presented here is new work on the trace element analysis of all phases in these samples. The major element analysis was carried out by (Ziberna et al.,

2017). All trace element concentrations that were determined in this study and have not been published previously.

Table 29: Barometry of Dominca samples from Ziberna et al. (2017) using plagioclase + clinopyroxene + olivine + spinel major element chemistry.

Sample	Pressure (kbar)	σ
DC90	3.58	0.91
DC93a	2.67	1.35
DC91	1.94	1.09
DC93b	2.81	1.55

The estimated temperature of formation from the Ziberna et al. (2017) ranges from 870-1000 °C however the temperature estimates are much less precise than those for pressure. The Ca-between two pyroxene thermometer agrees with this temperature range giving approximately 896 °C (Ziberna et al., 2017).

The concentration of the heavy rare earth elements in plagioclase is very low (7 ppb ± 4 ppb) but still above detection limit. The chondrite normalised rare earth element patterns show that the trace element concentrations are homogenous for most minerals. Sample DC94 shows the most variation in trace elements of all the samples (Figure 113).

Table 30: Mineral chemistry of clinopyroxene and plagioclase from Dominica, Lesser Antilles

Sample	DC47	DC66	DC90	DC93	DC94	DC96	DC98	DC100	DC102	DC104
Mg#	66.6	70.2	76.9	77.4	76.4	75.9	76.1	75.2	76.4	76.5
An	80.0	86.0	93.5	90.4	94.2	87.6	90.6	90.9	91.2	92.9

Samples DC47 and DC66 were collected from a different location on the island and show a different mineral assemblage (Figure 113). These two samples contain orthopyroxene as well as the minerals common in all samples; plagioclase and clinopyroxene. These samples also have higher concentrations of the REE in all phases and lower Mg# and An# for the clinopyroxene and plagioclase (Table 30). Samples DC90-DC104 have olivine rather than orthopyroxene, which is completely altered in some samples. These samples also have higher Mg# and An#.

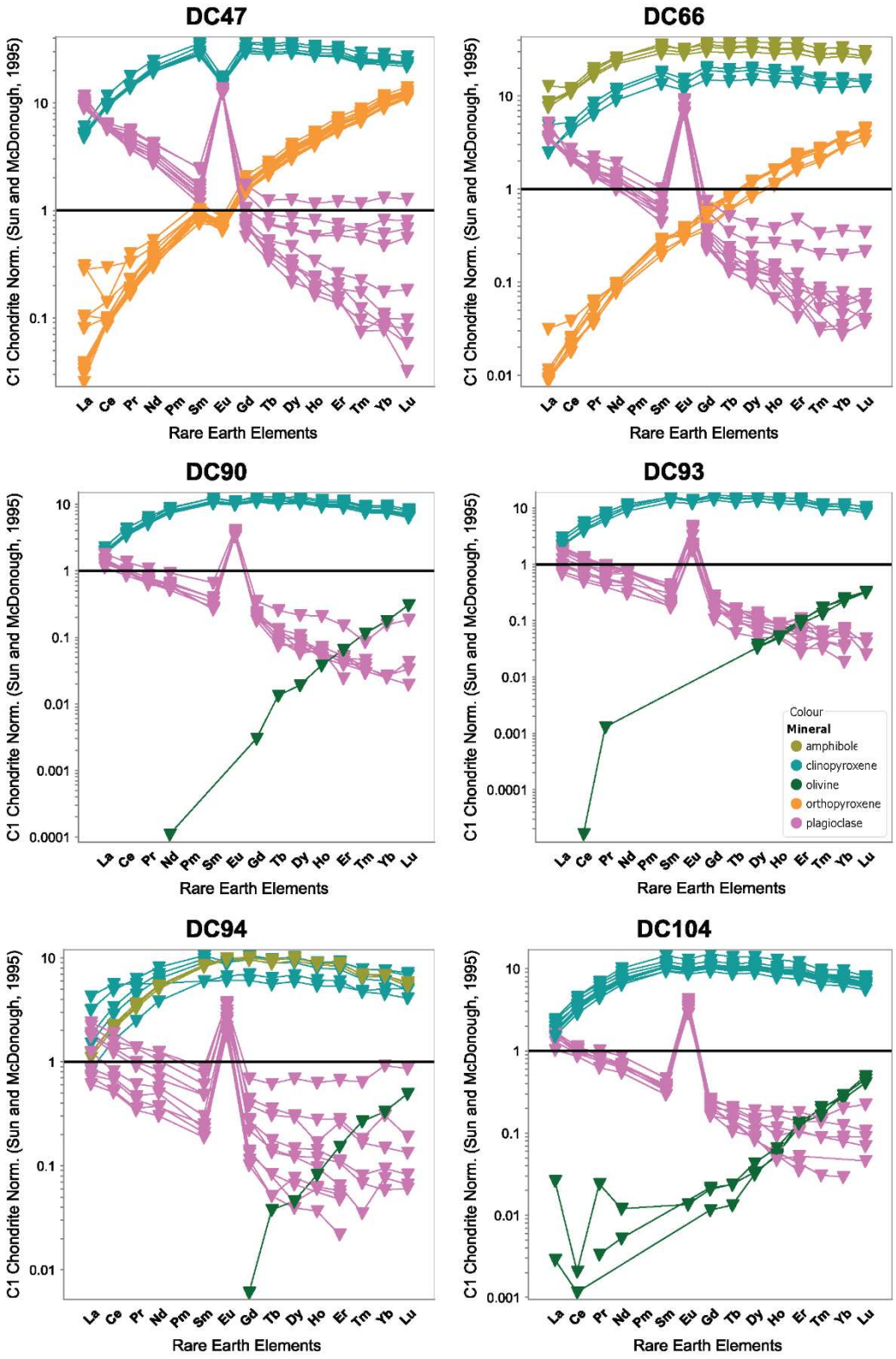

Figure 113: Chondrite normalised (McDonough and Sun, 1995) REE patterns for all phases in Dominca samples; DC47, DC66, DC90, DC93, DC94 and DC104. DC47 and DC66 were collected from a different location on Dominica than DC90-DC104. DC90 and DC93 were used in the (Ziberna et al., 2017) barometry study.

6.2.3 Mineral Chemistry

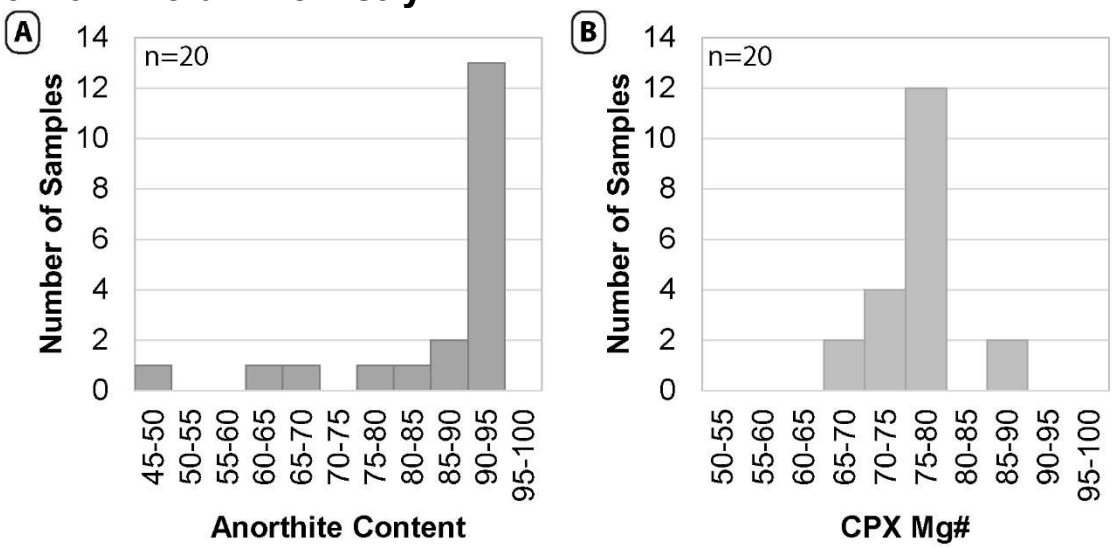

Figure 114: Mineral Chemistries A) Anorthite number and frequency of samples B) Magnesium number in clinopyroxene and frequency of samples.

The chemistry of the rocks is varied, with most samples containing An_{91-95} plagioclase and Mg# 75-78 clinopyroxene (Figure 114). All the minerals in the natural samples have chemistries comparable to those synthesised experimentally.

6.2.4 Partitioning Results

Although the focus of this research was on the partitioning of the rare earth elements, the partitioning of many elements was investigated. Some additional elements were measured in the natural samples that were not doped in the experimental samples. These elements are mostly transition metals including Co, Ni, Cu, Zn, Mo, Cd and W. Also, Ge, As, Sn and Sb are measured in the natural samples.

Zn is a divalent cation with an ionic radius of 0.6Å in tetrahedral coordination, of very similar size to Mg (0.57Å). The behaviour of Zn was not investigated experimentally, however, the comparison of the compatibilities between Sr and Mg suggests that Zn may behave similarly to Mg as it is much more compatible in clinopyroxene than plagioclase.

The average Cu partitioning between plagioclase and clinopyroxene is near unity. Cu can exist in 1+, 2+ or 3+ valence. Cu^{2+} is a small cation (0.57Å in IV-fold coordination) with no ionic radius listed for coordination's higher than VI-fold (Shannon, 1976). If Cu was existing as Cu^{2+}, it would behave similarly to Mg. As the partitioning is near unity, it is possible that Cu^{1+} is being incorporated preferentially into plagioclase, however this would suggest that Cu^{1+} is VIII-fold coordinated.

More experimental work needs to be carried out to determine where these elements are partitioning into these two phases.

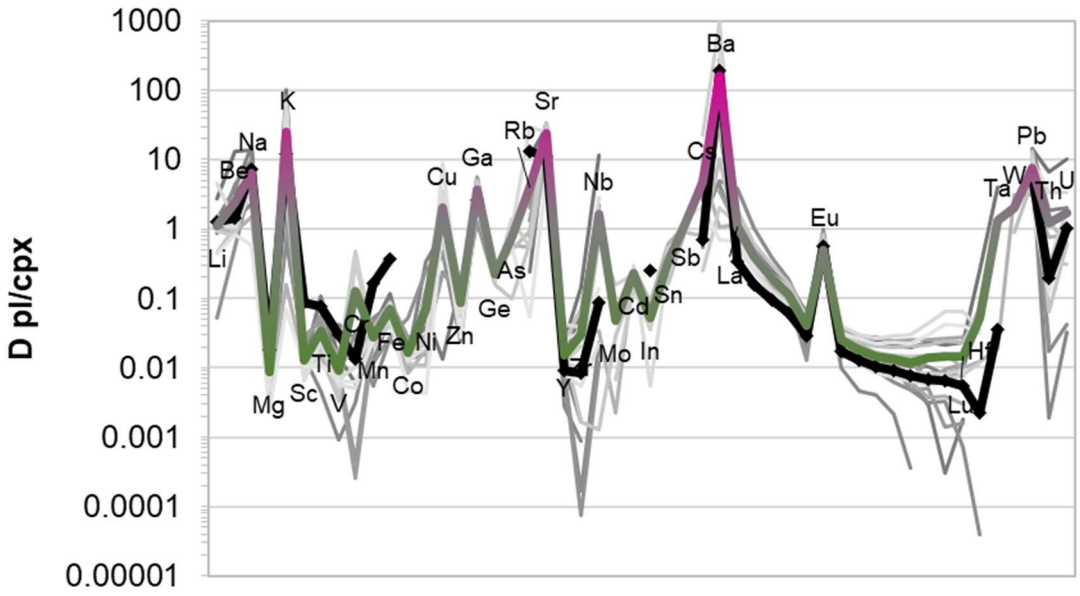

Figure 115: The partitioning of trace elements between plagioclase and clinopyroxene in experimental and natural samples. Green+pink line is natural samples, black line is experimental average. Grey lines are individual location averages. Green line represents elements that are more compatible in clinopyroxene, while pink represents more compatible in plagioclase.

Rare earth elements

The partitioning of the rare earth elements between plagioclase and clinopyroxene is very similar between all natural samples. As these natural samples cover a wide range of geological settings and include both volcanic and plutonic rocks, it can be assumed that these samples have a wide range of formation conditions.

The synthetic experiments have a very small temperature range (135°C) but reflect a broad range of pl/cpx REE partitioning values (Figure 116). The natural samples span a much smaller range of REE pl/cpx partition values but are distinctly different from the experimental partitioning values. These differences can be quantified by modelling the partitioning with orthogonal polynomials (O'Neill, 2016).

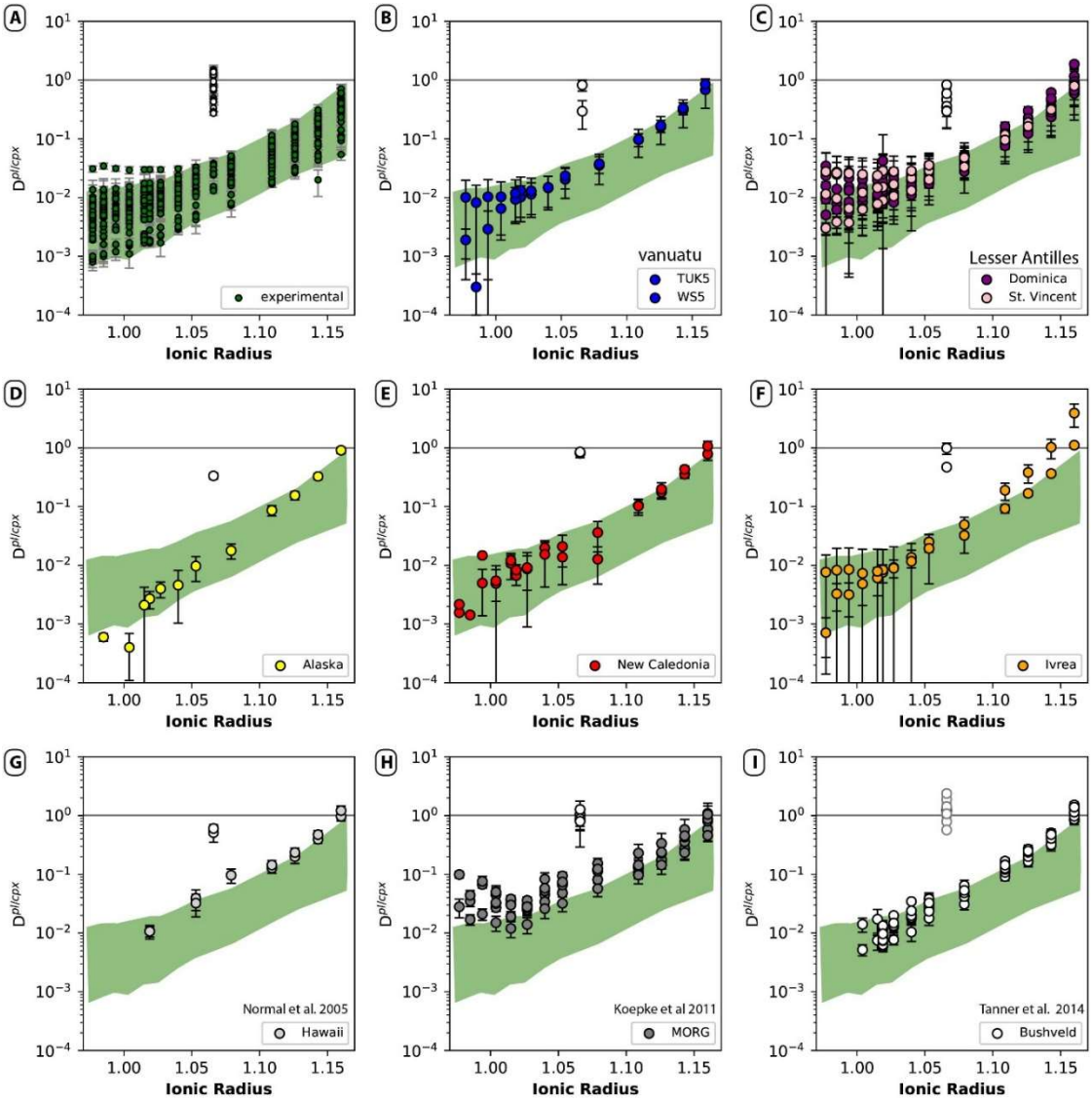

Figure 116: The partitioning between plagioclase and clinopyroxene. Green field represents experimental results, outlined in (A). B) Vanuatu volcanic samples, C) Lesser Antilles gabbros from Dominica and St. Vincent, D) Alaskan gabbro E) New Caledonian gabbro F) Ivrea, Italy gabbros G) Hawai'i' basalt H) Mid-ocean ridge basalt from the Pacific plate I) Cumulate gabbros from the Bushveld Complex, Greenland.

The heavy rare earth elements are commonly below detection limit in many of the natural plagioclase. Also, these heavy rare earth elements are small enough to substitute into the M1 site of clinopyroxene, which would lead to a change in the stoichiometric control. Due to these two reasons, the orthogonal polynomial values were calculated using the REE from La-Dy omitting Ce and Eu (7 elements).

The relationship between the slope and magnitude of the rare earth element partitioning pattern is different between the experimental and natural samples (Figure 117). The experimental samples do not vary significantly in the slope of the pattern and the magnitude is strongly related to the partitioning of Ca between plagioclase and clinopyroxene.

The most accurate thermometer from the partitioning of the REE between plagioclase and clinopyroxene is the stoichiometric control equation (Equation 97).

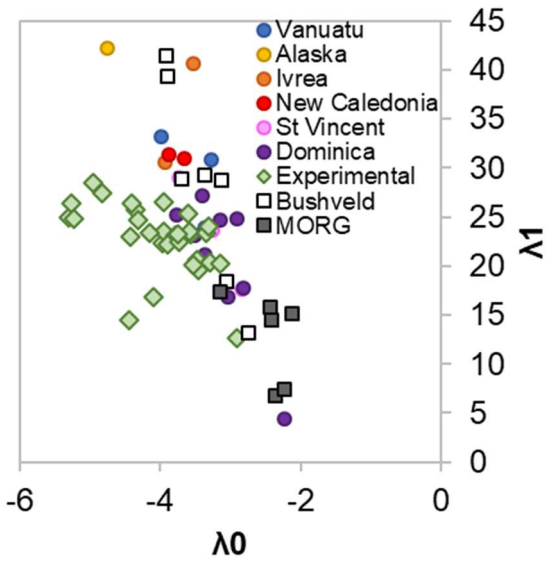

Figure 117: The relationship between the magnitude (λ0) and the slope (λ1) of the rare earth element partitioning pattern between plagioclase and clinopyroxene.

6.2.5 Thermometry comparison

Of the collected samples, there are three locations (each which contain two samples) that contain the minerals plagioclase, clinopyroxene and orthopyroxene. This allows for the temperatures to be calculated from the widely used Brey and Köhler (1990) thermometer that compares the calcium content between clinopyroxene and orthopyroxene. Additionally Liang et al. (2013) published a REE between clinopyroxene and orthopyroxene thermometer and Sun and Liang (2017) published a REE between plagioclase and clinopyroxene thermometer which can also be compared.

The two pyroxene thermometer outlined in Table 31, is based on Brey and Köhler (1990) and incorporated in a spreadsheet in the supplementary material of Putirka (2008). The pressure and temperature of the New Caledonian gabbros is calculated to be ~1060ºC and 4 kbar which is in good agreement with the published results for this sample (Pirard et al., 2013). The equilibrium test (K_D) should be 1.09 ±0.14 for equilibrium to be confirmed, this suggests that the Ivrea samples are far from equilibrium and the calculated temperatures and pressures should be disregarded (Table 31). Most samples are out of calculated equilibrium with the exception of Dominica sample DC47. The pressures calculated for the Dominca samples using this method are far from that calculated by Luca Ziberna.

Table 31: temperature and pressure calculations from two pyroxene thermo-barometer (Putirka, 2008)

	P				T (°C)				
	Av.	**stdev**	**min**	**max**	**Av.**	**stdev**	**min**	**max**	(K_D should be 1.09±.14)
MDS37	4.9	1.3	4.0	6.9	1056	25	1034	1084	0.81
MDS41	4.9	1.3	3.9	6.7	1046	21	1026	1072	0.88
DC47	9.7	3.1	6.7	12.4	947	17	927	968	0.95
DC66	12.4	5.8	6.9	17.4	892	26	861	924	0.69
IVT07	16.4	7.5	9.0	22.9	945	41	896	996	0.62
IVT10	-24.4	31.9	-58.1	2.9	1301	334	948	1753	0.54

The mineral/melt thermometers from Putirka (2008) were found to be accurate in predicting the experimental temperatures. The temperatures for the volcanic rocks were calculated using this method.

The REE between solid phases thermometers of Liang et al. (2013) and Sun and Liang (2017) are modelled on experimental data of separate mineral/melt partitioning data and combined. The combined equation is rearranged into the formula B=(lnD-A)*T where the temperature is calculated from the slope (passing through the origin) of this relationship.

Only the New Caledonian samples are within the calibration range of the cpx/opx REE thermometer (Figure 118). The clinopyroxene and orthopyroxene of sample IVT10 are significantly out of equilibrium. With calculated temperatures for all cpx/opx thermometers retrieving unrealistically low temperatures (300-800 °C). This thermometer was calibrated from minerals with the Mg# > 54 for clinopyroxene and >70 for orthopyroxene (Liang et al., 2013). Samples from Dominica (DC47 and DC66) and Ivrea (IVT10 and IVT07) are out of the calibration range of the REE between clinopyroxene and orthopyroxene thermometer. The orthopyroxene of these samples range from Mg# 57-66.

The REE-between plagioclase and clinopyroxene thermometer is not modelling the pl/cpx partitioning data accurately, as the linear relationship does not pass through all of the rare earth elements (Figure 118C, D). Even when the heavy rare earth elements are excluded from the fit, the line does not pass through the REE points. This suggests that there are variables not being accounted for the parameterisation. As the slope forced through the origin and do not pass through the majority of the rare earth element points, the temperature calculated using this pl/cpx REE thermometer cannot be accurate.

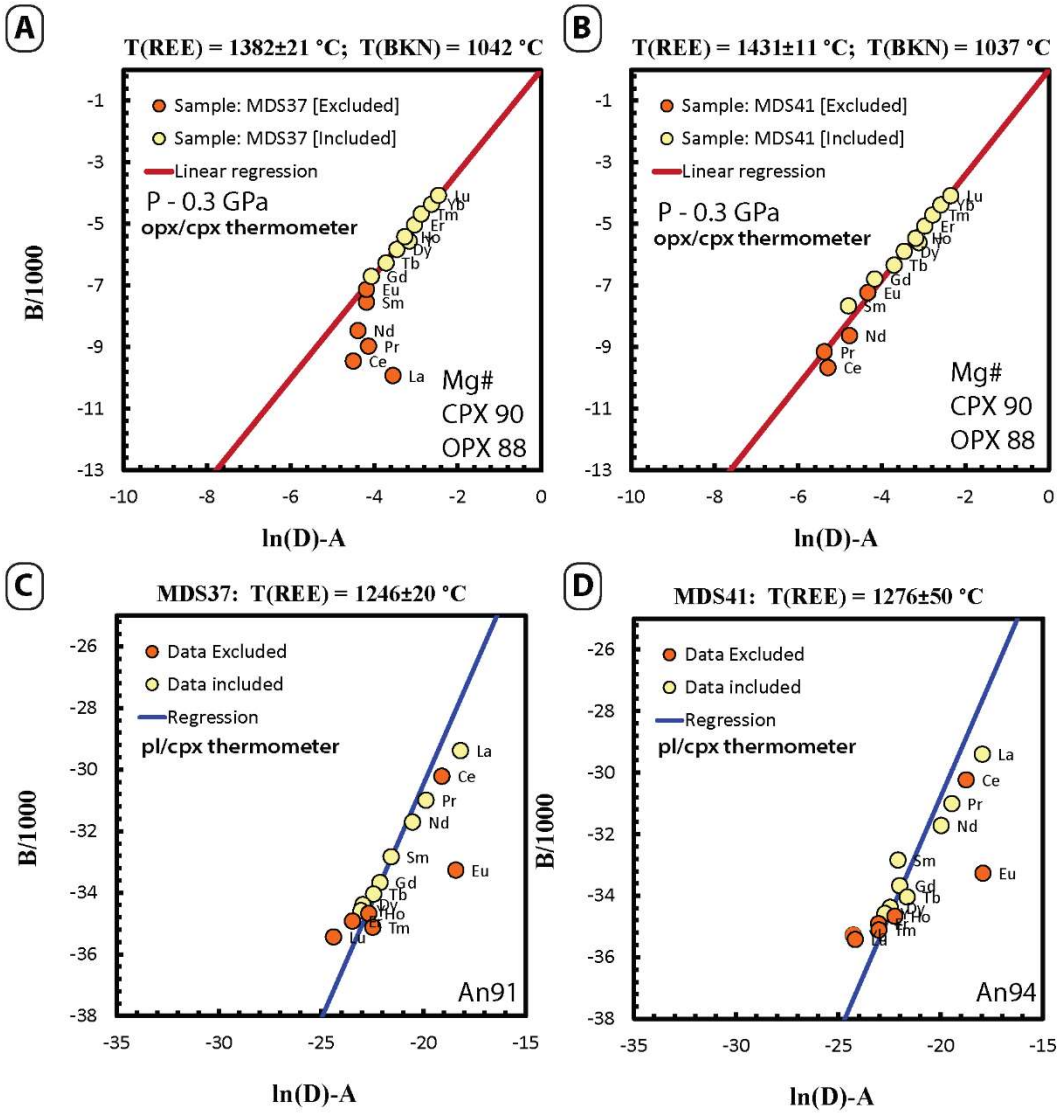

Figure 118: Comparing the REE between two pyroxene thermometer (Liang et al., 2013) and the REE between plagioclase and clinopyroxene thermometer (Sun and Liang, 2017) in the New Caledonian samples MDS37 and MDS41. A) Opx/cpx thermometer for MDS37, B) Opx/cpx thermometer for MDS41, C) pl/cpx thermometer for MDS37 and D) pl/cpx thermometer for MDS41.

The traditional Ca between pyroxene thermometer Brey and Köhler (1990) gives temperatures of approximately 1040 °C for both samples. The temperatures calculated from the orthopyroxene/clinopyroxene (Liang et al., 2013) and plagioclase/clinopyroxene rare earth element thermometers (Sun and Liang, 2017) for the New Caledonian samples are significantly different. The opx/cpx thermometers give temperatures of approximately 1400-1420 °C while the pl/cpx thermometers give ~1250 °C (Figure 120A).

The differences in these trace elements and major element thermometers (Figure 119B) are often attributed to higher closure temperatures of the trace elements, while the major elements continue to re-equilibrate and record lower, sub-solidus temperatures (Dygert and Liang, 2015; Liang, 2014; Sun and Liang, 2017). As the diffusion of the REE in all

phases is very slow, these two thermometers are not likely to be recording different temperatures.

Table 32: Comparison of various geothermometers. Bold and italicised integers represent calculated temperatures out of calibration range or out of calculated equilibrium

			Calculated Temperature (°C)					
		Type	REE pl/cpx	REE pl/cpx	REE opx/cpx	Ca. opx/cpx	cpx/ liquid	
			This study					
Sample	Location	P (kbar)	Stoich. control	Liang et al. 2017	Liang et al. 2012	Brey and Kohler 1990	Putirka et al. 2003	Published T
BE-081B	Alaska	3	1070	1242				
DC100	Dominica, Lesser Antilles	3	1216	1271				
DC102		3	1243	1298				
DC104		3	1194	1277				
DC47		3	1241	1209	***1278***	908		
DC66		3	1180	1233	***1144***	***812***		
DC90		3.54	1304	1317				870
DC93		2.64	1139	1239				980
DC94		3	1266	1312				
DC96		3	1270	1244				
DC98		3	1173	1260				
IVT07	Ivrea, Italy	5	1197	1161	***1065***	***735***		
IVT10		5	1157	1217				
MDS37	New Caledonia	3	1170	1246	1382	***1042***		1166-1346
MDS41		3	1211	1276	1431	***1037***		1166-1346
TUK6	Vanuatu	1	1274	1130			727	
WS5		1	1217	1049			1030	
VS14	St. Vincent, Lesser Antilles	5	1146	1368				980-1020
VS2a		5	1213	1303				980-1020
VS4		5	1280	1393				980-1020

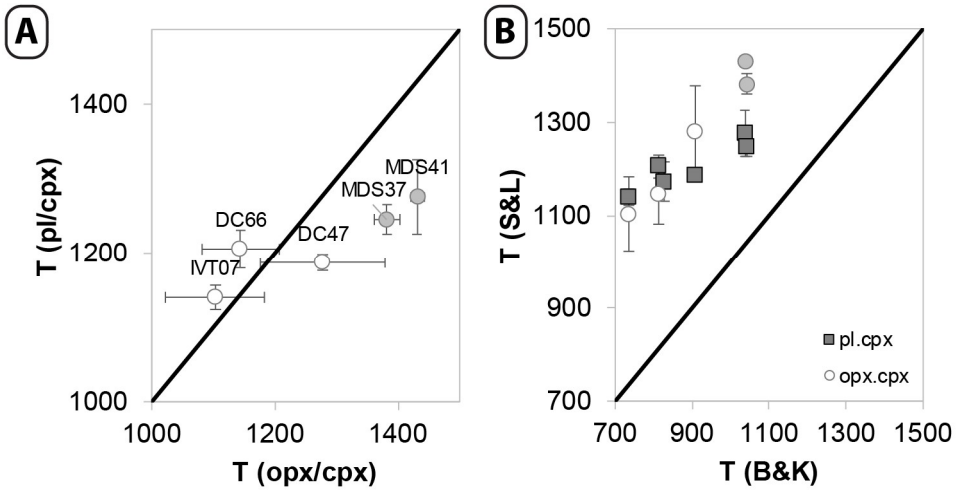

Figure 119: A comparison between thermometry methods. A) comparing the temperature (°C) as given from the REE partitioning between plagioclase and clinopyroxene (pl/cpx) (Sun and Liang, 2017) and the REE partitioning between orthopyroxene and clinopyroxene (opx/cpx) (Liang et al., 2013). Open symbols represent orthopyroxene outside the calibration range B) Comparing clinopyroxene/orthopyroxene calcium thermometry (Brey and Köhler, 1990) with the REE between plagioclase and clinopyroxene (Sun and Liang, 2017) and the REE partitioning between orthopyroxene and clinopyroxene (Liang et al., 2013). Open symbols represent orthopyroxene outside the calibration range. DC samples from Dominica, Lesser Antilles. IVT samples from Ivrea, Italy. MDS samples from New Caledonia.

The comparison of all these thermometry methods and the published temperatures on these samples and/or areas is included in Table 32. The temperatures do not agree between any tested thermometers.

The stoichiometric control thermometer was very accurate for the experimental samples, though the experimental temperature range was small. For the natural samples, all but two of the temperatures obtained from the stoichiometric control thermometer are suspiciously within the experimental range (1130-1265 °C).

Similarly to the Sun and Liang (2017) equation displayed in Figure 118, the relationship between lnD-A and the B is not completely linear and therefore there is some uncertainty in the slope; i.e. temperature, calculation (Figure 120). As these two components do not define a linear trend, particularly in the natural samples, this suggests that there is an effect on the partitioning between plagioclase and clinopyroxene that was not observed in the simple synthetic experiments.

Although this thermometer predicted the experimental temperatures very well, this equation seems to be too simple to be a precise thermometer in complex, natural systems.

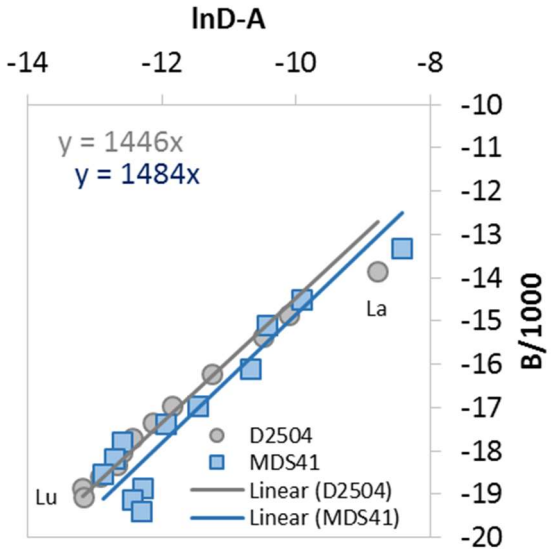

Figure 120: The calculation of temperature using Equation 97 for a natural and experimental sample. The linear relationship between lnD-A and B where the slope is equal to the temperature. As such the Y intercept of the linear relationship must be set at zero. A natural gabbro from New Caledonia is shown by blue squares T calculated is 1484 K. Experiment D2504 at 5 kbar, 1493 K with composition Ab10-Fe1 in grey circles. T calculated for the experimental sample is 1446 K.

The thermometer will remain inaccurate until the partitioning between plagioclase and clinopyroxene can be modelled precisely enough to create a linear relationship. It is also possible that the partitioning of the rare earth elements between plagioclase and

clinopyroxene are not sensitive enough to temperature to ever make an accurate thermometer.

6.2.6 Discussion

It is generally believed that the partitioning of trace elements in minerals is dependant mainly on the crystal chemistry and formation conditions, however melt plays a significant role. When comparing the partitioning of an element between two solid phases (minerals) the melt effect should cancel out if the stoichiometric control is the same. This is beneficial as the equilibrium melt is rarely preserved in natural samples.

The rare earth elements in plagioclase and into the M2 site of clinopyroxene have the same stoichiometric control and therefore can be compared without considering melt composition.

In the case of the REE between plagioclase and clinopyroxene thermometer published by Sun and Liang (2017), melt components were not considered in the individual mineral/melt partitioning models and then these two models are combined in the double lattice strain model, the errors are propagated into the temperature calculations. Therefore, the temperature calculated by this thermometer is very different to temperatures calculated by other methods.

The difference between the temperatures calculated by this method and other thermometers such as Brey and Köhler (1990) are attributed to the plagioclase-clinopyroxene REE thermometer having high closure temperatures due to the very slow rates of diffusion of these elements.

It has been confirmed in this study that the diffusion of REE in plagioclase is very slow. The lack of diffusion profiles in the minerals; as examined by LA-ICP-MS could indicate either of two possibilities; either the trace element compositions represent the original equilibrium compositions, or, the system is completely re-equilibrated.

The REE partitioning between clinopyroxene and orthopyroxene can also be useful for thermometry (Liang et al., 2013) but generally gives much hotter temperatures than the plagioclase-clinopyroxene thermometer. As the REE diffusion in all three phases is fairly slow, the difference in these calculated temperatures should not be due to differences in closure temperatures.

The contrast between the experimental and natural partitioning is stark. The mineral chemistry in these natural samples are well within the experimentally calibrated range for

the new REE between plagioclase and clinopyroxene thermometer. The experimental range spans 1130-1265 °C between 1 atm and 11 kbar which is within the realm of possibility for natural samples, however the natural samples are likely to be formed in a much larger temperature range.

The experiments were modelled very precisely and the thermometry for the simple synthetic systems was very accurate. However, this equation does not directly translate into the natural, complex systems. The REE-partitioning between plagioclase and clinopyroxene does not define a simple, linear relationship (Figure 120). This suggests there is some variable that is not well parametrised in the synthetic experiments; such as the effect of water, divalent iron or chromium.

The effect of water in on the partitioning of trace elements in plagioclase and clinopyroxene has not been experimentally tested in this study. Water in clinopyroxene/melt systems decrease the partitioning of the REE (Wood and Blundy, 2014). The addition of water also significantly decreases the solidus temperature for plagioclase. Sun and Liang (2017) suggest that the contribution of water to the partitioning between plagioclase and clinopyroxene is small in comparison to the effect of temperature.

Iron was added to the system in entirely 3+ valence. Divalent iron will be much more compatible in both plagioclase and clinopyroxene and should be investigated. Similarly, diopside can occur in nature with a significant proportion of chromium. Although chromium was measured as a minor component in these experiments, chromium as a major lattice forming element has not been investigated. These changes in mineral chemistry may have in impact on the partitioning of trace elements between these two minerals.

The effect of melt composition has been modelled precisely for simple synthetic systems, but the system will become much more complicated in natural systems. All of the rare earth elements should be measured in all phases where possible so we can begin to collate a database on the partition coefficients between minerals and their equilibrium phases.

6.2.7 Conclusions

Thermometers can be created from almost any element exchange in minerals, however if the original partitioning model is not well constrained, these temperatures will be inherently false.

The Sun and Liang (2017) thermometer of REE partitioning between plagioclase and clinopyroxene has been proven to be imprecise in synthetic systems. As the effect of melt composition is neglected in the mineral/melt partitioning models, and these models are then combined to create the mineral/mineral thermometer, there will be significant propagated errors. In the synthetic experiments, temperature can be calculated using an equation based on the stoichiometric control, however due to some un-tested variables, this equation does not directly translate to natural systems.

As previously outlined, the partitioning of the REE in plagioclase is insensitive to temperature, so this thermometer is relying almost entirely on the partitioning of REE in clinopyroxene for the thermometry. The geothermometer would be much more accurate if the partitioning in both phases were highly sensitive to temperature.

CHAPTER 7. SUMMARY

The partition coefficients for a multitude of elements were examined between plagioclase, clinopyroxene and melt, however, the rare earth elements have become the focus of this study. As there are 14 of these elements that are of a comparable size and similar chemical activity they define an easily interpretable pattern.

When considering the partitioning of trace elements into minerals there are a few key considerations:

1) The size and charge of the substituting cation

2) The site in which the trace element is substituting

3) The stoichiometric control for this substitution

In aliovalent substitution the stoichiometric control requires input from the melt. This is most prevalent when considering the thermodynamic equilibrium of such an exchange. An example is the partitioning of the REE into plagioclase;

Equation 102:
substitution to REE in anorthite

$$[REE]O_{1.5_{melt}} + CaAl_2Si_2O_{8_{pl}} + AlO_{1.5_{melt}} = [REE]Al_3SiO_{8_{pl}} + CaO_{\ melt} + SiO_{2_{melt}}$$

Equation 103:
The thermodynamic equilibrium constant for the substitution of REE in anorthite

$$D_{REE}^{An/melt} = \frac{X_{[REE]Al_3Si_{\ 8}}^{plagioclase}}{X_{[REE]O_{1.5}}^{melt}} = \exp\left(\frac{-\Delta G^0}{RT}\right) * \left(\frac{\gamma_{[REE]O_{1.5}}^{melt}}{\gamma_{[REE]Al_3Si_{\ 8}}^{plagioclase}}\right) * \left[\frac{\alpha AlO_{1.5_{melt}}}{\alpha SiO_{2_{melt}}}\right] * \left(\frac{\alpha CaAl_2Si_2O_{8_{An}}}{\alpha CaO_{melt}}\right)$$

This equation outlines that the partitioning of the REE in anorthite $\left(\frac{X_{[REE]Al_3Si_{\ 8}}^{plagioclase}}{X_{[REE]O_{1.5}}^{melt}}\right)$ is dependent on the activity of the trace element in the melt $\left(\frac{\gamma_{[REE]O_{1.5}}^{melt}}{\gamma_{[REE]Al_3Si_{\ 8}}^{plagioclase}}\right)$, the stoichiometric control $\left(\left[\frac{\alpha AlO_{1.5_{melt}}}{\alpha SiO_{2_{melt}}}\right] * \left(\frac{\alpha Ca_{\ 2}Si_2O_{8_{An}}}{\alpha CaO_{melt}}\right)\right)$ and the change in free energy of the equation $\left(\exp\left(\frac{-\Delta G^0}{RT}\right)\right)$. The latter parameter can be represented by the lattice strain model (Brice, 1975).

The partitioning of the REE in pure anorthite showed that melt composition can change the partition coefficient significantly; D_{La}=0.45-0.06. As the minerals synthesised were all anorthite (>An_{95}) at the same temperature, this change in partition coefficient can be attributed to melt composition alone.

Comparing the partitioning of plagioclase of more sodic composition, the trend continues, with melt composition playing a significant role in the partitioning of the REE. Consequently, the most precise model for predicting these rare earth element partition coefficients contains the mole proportion of the major constituents of the melt. The models that use only the mineral chemistries fit the data poorly (Sun et al., 2017; Wood and Blundy, 2014). Using this stoichiometric control model the temperature was solved however gives poor results which suggests the partitioning of the REE in plagioclase is relatively insensitive to temperature. This has been previously noted by Drake and Weill (1975).

The rare earth elements in clinopyroxene were found to partition preferentially into the VIII-fold coordinated M2 site, however, the smallest and heaviest of the REE also partition onto the VI-fold coordinated M1 site, along with Sc. The lattice strain model for the partitioning of REE into the M2 site in clinopyroxene should be fit to the REE omitting the heaviest 4 REE, due to the interference with M1 site partitioning. This partitioning behaviour has been seen in nature and attributed to high Fe contents, however this cannot be the case in this experimental series (Olin and Wolff, 2010).

Examining plagioclase and clinopyroxene individually has allowed for greater understanding of these two very common minerals. These mineral/melt relationship can be translated into solid phase partitioning from a shared equilibrium melt. 31 experiments in this series synthesised both plagioclase and clinopyroxene so these relationships can be directly examined.

When comparing partition coefficients in solid phases, if the trace elements have the same stoichiometric control for both minerals, the effect of melt composition will be cancelled out. This is advantageous because in natural samples, the equilibrium melt is rarely preserved.

The stoichiometric control equation for the partitioning of the REE between plagioclase and clinopyroxene is the most accurate of all the models tested (Sun and Liang, 2017; Wood and Blundy, 2014). Rearranging this equation to solve for temperature gives precise results.

Using this geothermometer on natural samples, gives ambiguous results. The resulting temperatures are within the very small experimental range (1130-1265°C), however it is likely that the wide range of natural samples tested cover a much large temperature range. Therefore it is suggested that this thermometer does not work in natural systems.

As the partitioning of REE in plagioclase is insensitive to temperature, the thermometer is related mostly on the composition of the clinopyroxene. For a more accurate thermometer, the partitioning of trace elements in both minerals should be sensitive to temperature, therefore the application of any plagioclase-clinopyroxene REE thermometer is limited.

7.1 Future directions

This study is a comprehensive look into the partitioning of trace elements between plagioclase, clinopyroxene and melt. More variables and elements were examined than have been presented in this thesis. The oxygen fugacity of the experiments were changed between air, QFM and IW in the 1 atm. furnaces and between Pt-PtO_2 buffer and no buffer in the pressurized experiments. This data could be used to examine the multi-valent trace element partitioning such as Fe, V, Eu^{2+}, Ce^{4+}, Th and U into and between these two minerals.

The effect of water has not been tested in this study. Conducting experiments in hydrous conditions will cause the solidus of the minerals to be depressed, and allow the experiments to be conducted at lower temperatures. Furthermore, water in the melt has been shown to be an important variable in the partitioning of clinopyroxene, decreasing the partitioning of the REE (Wood and Blundy, 2014). The effect of water of the partitioning of trace elements into plagioclase has not been investigated previously.

Moving away from the simple-system experiments toward more natural-like compositions will allow the mechanisms learned in the simple systems to be tested and combined in the complex natural systems.

Appendix 1. PRECISION OF LA-ICP-MS

Table 33: List of measured isotopes of BCR2g compared with published values.

		BCR2g						
		Measured				GeoRem Reference		
Mass	Element	Average	Stdev	RSD	n	Value	Uncertainty	%Diff
7	Li	9.84	0.907	9%	130	9	2	9%
9	Be	2.19	0.216	10%	95	2.3	0.8	-5%
11	B	18.6	3.15	17%	6			
23	Na	24807	956	4%	228	23962	-	4%
24	Mg	19558	397	2%	126	21467	-	-9%
25	Mg	19491	596	3%	120	21467	-	-9%
27	Al	75048	2350	3%	228	70913	-	6%
28	Si	281265	7160	3%	17	254270	-	11%
29	Si	274764	8760	3%	213	254270	-	8%
31	P	1597	18	1%	10	1615	-	-1%
39	K	16592	735	4%	246	14900	-	11%
43	Ca	50344	1450	3%	22	50429	-	0%
44	Ca	51001	518	1%	42	50429	-	1%
45	Sc	34.4	1.68	5%	246	33	4	4%
47	Ti	13156	124	1%	18	14100	-	-7%
49	Ti	13112	207	2%	57	14100	-	-7%
51	V	442	12	3%	122	425	36	4%
52	Cr	16.7	1.15	7%	38	17	4	-2%
53	Cr	15.5	0.983	6%	82	17	4	-9%
55	Mn	1573	48.8	3%	75	1550	140	1%
56	Fe	103083	1290	1%	6	96385	-	7%
57	Fe	82692	6570	8%	171	96385	-	-14%
59	Co	38.1	0.765	2%	67	38	4	0%
60	Ni	14.4	1.9	13%	8	13	4	11%
61	Ni	15.1	1.85	12%	57	13	4	16%
63	Cu	18.3	1.15	6%	67	21	10	-13%
65	Cu	19.8	0.504	3%	8	21	10	-6%
64	Zn	163	3.65	2%	6	125	10	30%
66	Zn	161	7.64	5%	65	125	10	29%
69	Ga	51.7	11.7	23%	46	23	2	125%
71	Ga	23.1	0.77	3%	82	23	2	0%
72	Ge	3.89	0.284	7%	71	1.5	0.2	159%
75	As	2.71	0.147	5%	6			
85	Rb	51.6	2.07	4%	126	47	1	10%
88	Sr	340	5.27	2%	246	342	8	-1%
89	Y	31.8	0.908	3%	222	35	6	-9%
90	Zr	173	5.04	3%	108	184	30	-6%
93	Nb	12	0.336	3%	232	12.5	2	-4%
111	Cd	0.246	0.0461	19%	6	0.2	-	23%
115	In	0.109	0.0178	16%	61	0.11	0.04	-1%
121	Sb	0.508	0.0277	5%	6	0.35	0.16	45%
133	Cs	1.22	0.071	6%	93	1.16	0.14	5%
137	Ba	691	13.1	2%	210	683	14	1%
138	Ba	678	10.7	2%	15	683	14	-1%
139	La	24.5	0.59	2%	252	24.7	0.6	-1%
140	Ce	52.4	1.09	2%	246	53.3	1	-2%
141	Pr	6.52	0.169	3%	246	6.7	0.8	-3%
146	Nd	27.6	0.755	3%	246	28.9	-	-5%
147	Sm	6.33	0.266	4%	246	6.59	0.14	-4%
153	Eu	1.91	0.0779	4%	252	1.97	0.04	-3%
157	Gd	6.28	0.293	5%	246	6.71	0.14	-6%
159	Tb	0.937	0.0485	5%	246	1.02	0.16	-8%
163	Dy	5.99	0.255	4%	246	6.44	0.12	-7%
165	Ho	1.19	0.0594	5%	246	1.27	0.16	-6%
166	Er	3.43	0.158	5%	246	3.7	0.08	-7%
169	Tm	0.47	0.0326	7%	246	0.51	0.08	-8%
172	Yb	3.15	0.163	5%	246	3.39	0.06	-7%
175	Lu	0.455	0.0302	7%	246	0.503	0.01	-9%
178	Hf	4.61	0.23	5%	226	4.84	0.56	-5%
181	Ta	0.697	0.0398	6%	105	0.78	0.12	-11%
205	Tl	0.25	0.0174	7%	6	0.3	0.2	-17%
208	Pb	11.3	0.39	3%	126	11	2	3%
209	Bi	0.0717	0.00545	8%	6	0.05	0.02	43%
232	Th	5.67	0.202	4%	205	5.9	0.6	-4%
238	U	1.72	0.126	7%	205	1.69	0.24	2%

Table 34: List of measured isotopes of NIST612 compared with published values.

		NIST612						
		Measured				Jochum et al. 2011		
Mass	Element	**Average**	stdev	RSD	*n*	Value	Uncertainty	% Diff
7	Li	**41.1**	1.19	3%	*128*	40.2	1.3	2%
9	Be	**40.2**	1.16	3%	*89*	37.5	1.5	7%
11	B	**52.7**	4.64	9%	*6*	34.3	1.7	54%
23	Na	**102119**	1840	2%	*232*	101635		0%
24	Mg	**58**	2.85	5%	*113*	68	5.1	-15%
25	Mg	**57**	3.42	6%	*131*	68	5.1	-16%
27	Al	**10833**	163	2%	*232*	10744		1%
28	Si	**340711**	3870	1%	*19*	337024		1%
29	Si	**339480**	5330	2%	*221*	337024		1%
31	P	**55**	8.12	15%	*14*	46.6	6.9	18%
39	K	**59**	33.2	56%	*244*	62.3	2.4	-6%
43	Ca	**84679**	1080	1%	*26*	85049		0%
44	Ca	**85453**	677	1%	*45*	85049		0%
45	Sc	**42.6**	7.31	17%	*260*	39.9	2.5	7%
47	Ti	**42**	1.68	4%	*22*	44	2.3	-4%
49	Ti	**40**	0.639	2%	*57*	44	2.3	-9%
51	V	**39.1**	0.415	1%	*120*	38	1.1	3%
52	Cr	**36.7**	0.856	2%	*47*	36.4	1.5	1%
53	Cr	**36.3**	0.865	2%	*67*	36.4	1.5	0%
55	Mn	**39**	0.35	1%	*79*	38.7	0.9	0%
56	Fe	**48**	2.25	5%	*6*	51	2	-6%
57	Fe	**125**	62.4	50%	*181*	51	2	145%
59	Co	**35.4**	0.3	1%	*71*	35.5	1	0%
60	Ni	**38.7**	0.389	1%	*8*	38.8	0.2	0%
61	Ni	**43.9**	2.83	6%	*57*	38.8	0.2	13%
63	Cu	**39.5**	1.2	3%	*71*	37.8	1.5	5%
64	Cu	**37.5**	0.389	1%	*12*	39.1	1.7	-4%
65	Zn	**37.6**	0.458	1%	*6*	37.8	1.5	-1%
66	Zn	**39.3**	2.59	7%	*65*	39.1	1.7	1%
69	Ga	**36.9**	0.687	2%	*49*	36.9	1.5	0%
71	Ga	**36.8**	0.438	1%	*73*	36.9	1.5	0%
72	Ge	**40.9**	0.66	2%	*71*	36.1	3.8	13%
75	As	**36**	0.579	2%	*6*	35.7	5.5	1%
85	Rb	**32.1**	0.456	1%	*120*	31.4	0.4	2%
88	Sr	**79.3**	1.09	1%	*260*	78.4	0.2	1%
89	Y	**38.7**	0.683	2%	*220*	38.3	1.4	1%
90	Zr	**38.4**	0.631	2%	*102*	37.9	1.2	1%
93	Nb	**38.8**	0.575	1%	*242*	38.9	2.1	0%
111	Cd	**27.8**	0.904	3%	*6*	28.1	1.1	-1%
115	In	**37.2**	0.567	2%	*55*	38.9	2.1	-4%
121	Sb	**33.9**	0.345	1%	*6*	34.7	1.8	-2%
133	Cs	**42.3**	0.647	2%	*87*	42.7	1.8	-1%
137	Ba	**39.8**	0.952	2%	*239*	39.3	0.9	1%
139	La	**36.3**	0.62	2%	*266*	36	0.7	1%
140	Ce	**38.6**	0.579	2%	*260*	38.4	0.7	0%
141	Pr	**37.9**	0.664	2%	*260*	37.9	1	0%
146	Nd	**35.6**	0.604	2%	*260*	35.5	0.7	0%
147	Sm	**37.9**	0.727	2%	*260*	37.7	0.8	0%
153	Eu	**35.9**	0.511	1%	*266*	35.6	0.8	1%
157	Gd	**38.2**	0.824	2%	*260*	37.3	0.9	2%
159	Tb	**36.9**	0.951	3%	*260*	37.6	1.1	-2%
163	Dy	**35.9**	0.719	2%	*260*	35.5	0.7	1%
165	Ho	**37.9**	0.989	3%	*260*	38.3	0.8	-1%
166	Er	**38.6**	0.834	2%	*260*	38	0.9	2%
169	Tm	**36.8**	0.992	3%	*260*	37.38	0.08	-1%
172	Yb	**38.6**	0.762	2%	*260*	39.2	0.9	-2%
175	Lu	**36.6**	0.894	2%	*260*	37	0.9	-1%
178	Hf	**37.4**	0.89	2%	*236*	36.7	1.2	2%
181	Ta	**73.9**	136	184%	*99*	37.6	1.9	97%
205	Tl	**14.5**	0.59	4%	*6*	14.9	0.5	-3%
208	Pb	**38.8**	0.772	2%	*120*	38.57	0.2	1%
209	Bi	**33.9**	0.431	1%	*6*	30.2	2.3	12%
232	Th	**37.9**	0.779	2%	*215*	37.79	0.08	0%
238	U	**37.6**	0.86	2%	*215*	38.8	1.2	-3%

Appendix 2. MAJOR AND TRACE ELEMENT SUMMARY FOR ALL PARTITIONING EXPERIMENTS

The following section includes many data tables of the averages and standard deviations measured in each phase in each experiment. The tables are separated into chemical system. Which are:

CMS - CaO-MgO-SiO_2

This series of experiments has 3 major element variations and 3 different concentrations of total trace element doping. The experiments are named for the major element oxide that they are most enriched in compared to the other two major element variations. Experiments labelled LS00* (where * is a number between 5 and 7) have total trace elements of ~20 wt. % oxide (5,000-10,000 ppm each element). Those labelled LS90* have ~9 wt. % total trace oxides (1,000-2,000 ppm each element). LS20* labels are doped with 1% total trace oxides at 400-800 ppm per element.

CAS – CaO-Al_2O_3-SiO_2

This series of experiments includes 5 major element variations which are given the label; CAS30, CAS37, CAS45, CAS52 and CAS64 which are named for their SiO_2 wt. % oxide component in the melt. Repetitions of these major element compositions are completed with various concentrations of trace elements. Compositions coded LS00* (where star is a number 2, 2.5, 3, 3.5 or 4) have extremely high trace element doping with a total of 8 wt. % O of trace (~4000 ppm per element). Compositions LS90* has a total of 3 wt. % O traces doped in the melt (~1300 ppm per element). Compositions LS02* have 1 wt. % O (~500 ppm per element), and compositions LS01* are <1 wt. % O (~70 ppm per element). The trace elements in this experimental series include; Sc, Fe, Sr, Nb, Ba, REE, Hf, Th, and U

CMAS - CaO-MgO- Al_2O_3-SiO_2

There are two categories in this system, anorthite + melt experiment and clinopyroxene + melt experiments. The anorthite + melt experiments are named composition 2b-*-1a (where * is a number between 4 and 7) and are based from Miller et al. (2006). These experiments are relabelled CMAS* where the number (*) refers to the wt. % MgO in the melt. These experiments are doped with <1% total trace elements at approximately 600 ppm per element.

The clinopyroxene + melt experiments have similar ratios of CaO-MgO-SiO_2 but increase the Al_2O_3. With

There is an additional composition LS031 which was made from mixing 50% stoichiometric diopside and 50% stoichiometric anorthite.

CMASN - CaO-MgO- Al_2O_3-SiO_2-Na_2O

This category has two sections. The first are experiments based off Dohmen and Blundy (2014) and are chosen from isotherms in the diopside and plagioclase space in the anorthite + albite + diopside ternary (Figure 7). There are 3 experiments in the diopside space (labelled Di*) and 5 in the plagioclase space (labelled Plag*). These experiments are doped at a total trace elements of 1 wt. % oxide at about 300 ppm per element.

The second series consist of mixing together a 50:50 stoichiometric anorthite + diopside mix with a pure albite mix. These experiments are named with reference to their position in the anorthite + albite + diopside ternary (i.e. $An_{25}Di_{25}Ab_{50}$ or shortened to Ab_{50}). The first series of these experiments were only doped in the anorthite diopside mix so reduce the amount of trace elements toward more albite rich compositions. A repeat series with higher trace elements was run with the a signature of "x" at the end of the run name (e.g. $An_{15}Di_{15}Ab_{70}$x)

CMASNF - CaO-MgO- Al_2O_3-SiO_2-Na_2O-Fe_2O_3

This experimental series adds 1, 5 or 10 wt. % Fe_2O_3 to the series mentioned above. All these experiments are doped at approximately 1 wt. % oxide total trace.

And, "natural like"

These compositions are based on the USGS standards BIR-1, an Icelandic basalt and the experiment of Aigner-Torres et al. (2007) composition ALV-3352-7.

Table 35: CaO-MgO-SiO2 system experiments. Experimental conditions, average and standard deviations (stdev) of the major elements in each phase and trace elements up to mass 137; Ba

Run	comp.	type	T1	T2	fO2	P	time	System	Na2O	MgO	Al2O3	SiO2	CaO	Total	major (count)	Na_ppm	Mg_ppm	Al_ppm	Si_ppm	K_ppm	Sc_ppm	Fe_ppm	Sr_ppm	Nb_ppm	Ba_ppm
20140728	LS006	olivine	1389	1329	air	1 atm	153	CMS		35.9		48.8	13	98.2	2		4040000	1.46	2740000	67.4	1390		13.1	8.43	
20140728	LS006	olivine_stdev	1389	1329	air	1 atm	153	CMS		23.4		11.7	17	5.22			119000	4.14	103000	93.4	56.7		1.1	2.02	
20140728	LS006	melt	1389	1329	air	1 atm	153	CMS		11.9		38.8	21.6	72.8	2	113	77700	121	196000	17.1	2110		11800	11800	12200
20140728	LS006	melt_stdev	1389	1329	air	1 atm	153	CMS		1.56		2.81	2.49	3.6		1.96	582	2.1	638	4.87	24.2		128	125	86.5
20140728	LS007	diopside	1389	1329	air	1 atm	153	CMS		19.1		56.7	25.1	101	3	53.9	105000	22.3	260000	2.44	1230		1640	11.2	9.01
20140728	LS007	diopside_stdev	1389	1329	air	1 atm	153	CMS		0.469		1.25	0.539	2.16		7.78	1950	3.81	4550	4.39	469		28.2	9.95	9.33
20140728	LS007	melt	1389	1329	air	1 atm	153	CMS		11		41	23.5	75.9	3	196	64000	160	199000	39.6	1960		11200	12800	11500
20140728	LS007	melt_stdev	1389	1329	air	1 atm	153	CMS		0.125		0.215	0.132	0.527		5.76	663	4.24	2090	3.75	25.8		156	354	123
20140811	LS905	diopside	1392	1349	air	1 atm	165	CMS		19.9		55.7	23.3	99.1	5	41.4	108000	153	258000	0.875	99		210	6.32	1.96
20140811	LS905	diopside_stdev	1392	1349	air	1 atm	165	CMS		0.606		1.15	0.518	2.13		5.76	3360	31.2	4670	3.03	15.9		24.9	6.16	4.68
20140811	LS905	melt	1392	1349	air	1 atm	165	CMS		10.8	0.79	58.1	22.2	92.3	5	581	59200	4310	272000	240	150		3190	2920	3130
20140811	LS905	melt_stdev	1392	1349	air	1 atm	165	CMS		0.25	0.0235	1.41	0.357	2.01		11	1540	157	9430	24	10.3		22.2	74.9	21.1
20140811	LS906	diopside	1392	1349	air	1 atm	165	CMS		19.5		56.4	24.6	101	3	36.6	114000	196	275000	2.56	92.8		291	2.78	0.955
20140811	LS906	diopside_stdev	1392	1349	air	1 atm	165	CMS		0.2		0.439	0.286	0.569		8.16	3910	37.1	7650	4.96	21.2		57.1	0.898	0.216
20140811	LS906	olivine	1392	1349	air	1 atm	165	CMS		53.6		41.8	1.58	97.1	3		353000	7.11	240000		11.6		0.394	0.253	
20140811	LS906	olivine_stdev	1392	1349	air	1 atm	165	CMS		2.54		1.64	0.177	4			49700	1.13	33000		1.32		0.0584	0.144	
20140811	LS906	melt	1392	1349	air	1 atm	165	CMS		16.7	0.67	45.6	27.2	90.4	2	89.7	96500	4090	224000	7.83	148		3320	3210	3480
20140811	LS906	melt_stdev	1392	1349	air	1 atm	165	CMS		0.403	0.0283	1.29	0.714	2.47		1.06	1490	78.7	3820	7.14	2.08		53.9	40.8	40.8
20140924	LS906	diopside	1397	1370	air	1 atm	153	CMS		20	0.018	55.5	23.7	99.2	7	24.5	24700	197	267000	0.756	81.5	209	262	3.61	1.33
20140924	LS906	diopside_stdev	1397	1370	air	1 atm	153	CMS		0.557	0.0477	1.4	0.866	2.53		6.36	842	52.9	4880	2.27	26.8	11.5	26.2	2.72	1.13
20140924	LS906	olivine	1397	1370	air	1 atm	153	CMS		53.7		40.6	1.33	95.7	2		75200	6.29	231000	0.989	12.4	184	0.907	0.767	0.667
20140924	LS906	olivine_stdev	1397	1370	air	1 atm	153	CMS		1.2		0.901	0.0416	2.14			7480	3.58	23000	2.97	0.693	26.2	1.91	1.96	2
20140924	LS906	melt	1397	1370	air	1 atm	153	CMS		18.9	0.577	48.5	25.7	93.8	3	75.9	23700	2920	238000	12.6	146	1090	2380	2200	2370
20140924	LS906	melt_stdev	1397	1370	air	1 atm	153	CMS		0.757	0.0285	1.82	1.05	3.6		6.28	212	48.3	3730	5.07	2.9	39.6	36.8	44.4	28.8
20140924	LS907	diopside	1397	1370	air	1 atm	153	CMS		19.4		55.8	24.9	100	3	29.1	23500	138	263000		88.9	251	203	1.87	0.967
20140924	LS907	diopside_stdev	1397	1370	air	1 atm	153	CMS		0.208		0.539	0.286	1.01		5.33	272	49	3280		29.7	17.6	7.12	0.859	0.686
20140924	LS907	melt	1397	1370	air	1 atm	153	CMS		12.4	0.495	49.1	28.6	90.6	5	106	15600	2400	242000	25.1	104	940	1730	1740	1940
20140924	LS907	melt_stdev	1397	1370	air	1 atm	153	CMS		0.843	0.0418	3.22	1.87	5.95		4.59	239	27.1	1580	3.67	1.86	14.2	11.6	21.9	12.9
20140925	LS905	diopside	1393	1373	QFM (-6.59)	1 atm	161	CMS		19.8		55.3	23.7	98.8	3	3.7	25000	65	263000	0.667	74.1	182	190	0.907	0.392
20140925	LS905	diopside_stdev	1393	1373	QFM (-6.59)	1 atm	161	CMS		0.424		0.913	0.387	1.7		8.78	409	7.14	2880	2.31	7.56	15.9	4.71	0.137	0.0552
20140925	LS905	melt	1393	1373	QFM (-6.59)	1 atm	161	CMS		14.5	0.371	55.9	21.8	92.5	2	48.1	18000	1870	272000	46.8	102	240	1600	1310	1410
20140925	LS905	melt_stdev	1393	1373	QFM (-6.59)	1 atm	161	CMS		0.297	0.0671	0.621	0.189	1.04		2.17	271	25.6	6720	2.62	1.49	10.7	21.9	23.2	24.5
20140925	LS906	diopside	1393	1373	QFM (-6.59)	1 atm	161	CMS		20	0.0152	55.5	23.7	99.2	7	14.9	25700	109	267000		67.9	166	210	1.69	0.689
20140925	LS906	diopside_stdev	1393	1373	QFM (-6.59)	1 atm	161	CMS		0.387	0.0401	0.714	0.306	1.23		9.83	1080	10.4	7380		18.3	11.7	27.2	0.779	0.212
20140925	LS906	olivine	1393	1373	QFM (-6.59)	1 atm	161	CMS		56.1	0.0582	42.4	1.29	99.9	2		81000	4.84	241000	2	12.4	163	0.236	0.0992	0.0024
20140925	LS906	olivine_melt	1393	1373	QFM (-6.59)	1 atm	161	CMS		0.259	0.0823	0.174	0.0573	0.293			2950	0.633	10800	4.47	0.526	21.8	0.0109	0.0746	0.00537
20140925	LS906	melt	1393	1373	QFM (-6.59)	1 atm	161	CMS		19.3	0.468	48.8	24.5	93.1	4	12.4	24500	2210	240000	3.5	125	222	1870	1640	1770

Run	comp.	type	T1	T2	fO2	P	time	System	Na2O	MgO	Al2O3	SiO2	CaO	Total	major (count)	Na_ppm	Mg_ppm	Al_ppm	Si_ppm	K_ppm	Sc_ppm	Fe_ppm	Sr_ppm	Nb_ppm	Ba_ppm
20140925	LS906	melt_stdev	1393	1373	QFM (-6.59)	1 atm	161	CMS		0.211	0.0475	0.457	0.241	0.941		8.53	99.1	15.2	1210	7	1.62	5.38	19.7	16.1	4.65
20150223	LS026	olivine	1399	1376	air	1 atm	165	CMS		56.9		41.8	1.33	100	5		371000	1.61	254000		18.3	46.7	0.125	0.0977	
20150223	LS026	olivine_stdev	1399	1376	air	1 atm	165	CMS		0.12		0.2	0.25				90300	0.29	60200		5.6	15	0.0532	0.0712	
20150223	LS026	diopside	1399	1376	air	1 atm	165	CMS		21.1	0.01	55.9	23	100	5	33.2	111000	91	263000		89.2	201	123	3.38	0.507
20150223	LS026	diopside_stdev	1399	1376	air	1 atm	165	CMS		0.72	0.03	0.33	0.91			3.7	1700	11.2	2070		7.33	10	8.08	0.919	0.287
20150223	LS026	melt	1399	1376	air	1 atm	165	CMS		21.1	0.23	52.9	25.7	100	5	561	107000	942	237000	39.5	128	544	1400	1410	1540
20150223	LS026	melt_stdev	1399	1376	air	1 atm	165	CMS		0.04	0.16	0.62	0.7			5.48	1240	13.5	3310	6.51	1.14	29.3	16.5	20.1	23.4
20150318	LS025	diopside	1400	1366	air	1 atm	41	CMS	0.02	21	0.0183	56	23	100	6	79.9	108000	56.1	268000		107	369	79.3	5.82	3.06
20150318	LS025	diopside_stdev	1400	1366	air	1 atm	41	CMS	0.0443	0.372	0.0354	0.354	0.529			7.26	1070	8.25	2630		5.65	6.97	5.45	4.24	4.54
20150318	LS025	melt	1400	1366	air	1 atm	41	CMS	0.255	13.6	0.318	63.6	22.1	100	4	2280	67800	949	298000	421	81.5	620	1040	917	996
20150318	LS025	melt_stdev	1400	1366	air	1 atm	41	CMS	0.173	0.365	0.19	0.264	0.494			4.73	436	14	1860	4.51	0.436	19.3	4.58	19	4.58
20150318	LS026	diopside	1400	1366	air	1 atm	41	CMS	0.104	20.8	0.0113	56.1	22.9	100	8	71.4	105000	187	253000		78	297	221	115	128
20150318	LS026	diopside_stdev	1400	1366	air	1 atm	41	CMS	0.0761	0.278	0.028	0.233	0.478			19.3	8430	171	14700		15.4	73.5	162	160	177
20150318	LS026	olivine	1400	1366	air	1 atm	41	CMS	0.0375	56.8		41.8	1.34	100	4	bdl	280000	19.5	195000		16.4	106	0.67	0.61	1.16
20150318	LS026	olivine_stdev	1400	1366	air	1 atm	41	CMS	0.0386	0.395		0.205	0.187												
20150318	LS026	melt	1400	1366	air	1 atm	41	CMS	0.07	20.4	0.295	50.9	28.3	100	4	318	105000	1470	243000	11.2	126	874	1650	1660	1790
20150318	LS026	melt_stdev	1400	1366	air	1 atm	41	CMS	0.0804	0.373	0.147	0.225	0.209			3.04	472	25.3	1280	0.283	2.69	14.4	8.74	25.7	7.04

Table 36: CaO-MgO-SiO_2 system experiments. Average and standard deviations (stdev) of the trace elements from mass 139 (La) to mass 238 (U)

Run	comp.	type	La_ppm	Ce_ppm	Pr_ppm	Nd_ppm	Sm_ppm	Eu_ppm	Gd_ppm	Tb_ppm	Dy_ppm	Y_ppm	Ho_ppm	Er_ppm	Tm_ppm	Yb_ppm	Lu_ppm	Hf_ppm	Th_ppm	U_ppm	trace (count)
20140728	LS006	olivine	0.281	1.08	3.05	5.01	22.2	44.2	36.3	69.2	111		176	271	390	562	772	39	0.00963		8
20140728	LS006	olivine_stdev	0.136	0.16	0.177	0.7	2.37	1.86	1.98	3.4	4.83		7.46	10.1	16.1	25.4	37.6	7.61	0.0272		
20140728	LS006	melt	10800	12100	11500	10000	10600	12200	6010	6220	6070		6180	6150	6090	6200	6030	11900	5740	4000	6
20140728	LS006	melt_stdev	92.2	126	79.7	92.4	108	161	59.3	98.7	76.3		82.1	88.2	85.6	81.7	88.7	184	84.4	52.5	
20140728	LS007	diopside	127	158	270	307	389	452	246	238	226		229	203	196	229	266	154	1.63	1.93	11
20140728	LS007	diopside_stdev	55.8	65.2	119	138	173	198	110	104	96.9		97.2	84.4	80.5	92.2	108	133	4.9	4.94	
20140728	LS007	melt	10700	12600	11400	10200	10300	11600	5930	6240	6020		6520	5790	5850	6110	5890	12500	5900	5830	7
20140728	LS007	melt_stdev	130	183	135	120	142	139	91.7	78.9	82		113	86.8	98.5	109	104	468	179	617	
20140811	LS905	diopside	48.1	69.2	101	112	145	173	95.2	89.7	92.1		91.8	90.1	86.5	95.4	98.4	108	1.04	1.3	12
20140811	LS905	diopside_stdev	21.5	27.2	37.6	41	49.4	55.7	31.1	28.8	29.4		30.2	29.8	29	31.7	31.9	66.1	2.37	4.01	
20140811	LS905	melt	2400	2820	2590	2290	2300	2540	1340	1270	1340		1350	1360	1320	1390	1270	3090	1440	578	7
20140811	LS905	melt_stdev	16.9	42.3	25.1	28	37.8	41.1	20.6	19.6	20.2		31.5	32.9	27.8	27.2	34.5	183	49.2	224	
20140811	LS906	diopside	37.1	50.2	82.1	92.9	119	143	75.9	70.8	72		70.4	67.6	62.6	66.3	72.2	30.4	0.141	0.0198	11
20140811	LS906	diopside_stdev	7.35	9.51	17.5	20.1	27.3	32.4	18.4	16.4	17		16.5	15.7	14.1	14.5	15.9	29.4	0.048	0.0139	
20140811	LS906	olivine	0.004	0.0542	0.117	0.188	0.707	1.47	1.14	2.04	3.36		5.3	7.75	10.9	15.8	21.1	0.767		0.0001	6
20140811	LS906	olivine_stdev	0.0044	0.0159	0.012	0.0515	0.109	0.113	0.0761	0.149	0.19		0.415	0.58	0.843	1.44	1.99	0.167		0.000245	
20140811	LS906	melt	2590	3060	2800	2490	2460	2760	1380	1330	1400		1410	1400	1340	1380	1320	3070	1520	494	6
20140811	LS906	melt_stdev	33.5	52.8	36.6	23.5	27.4	30.6	20.7	14.3	19.6		17.3	24.4	19.6	23.6	19.1	66.1	24.8	50	
20140924	LS906	diopside	40.1	52.2	85	94.7	120	143	77.3	72.7	73.7	1.1	72.7	69.4	64.4	68.6	73.9	51.1	0.44	0.257	9
20140924	LS906	diopside_stdev	17.6	19.9	33.8	37.5	47.5	56.6	32	30.7	31.9	0.479	32.3	31.3	29.6	31.4	34.4	62.8	0.654	0.692	
20140924	LS906	olivine	0.518	0.578	0.593	0.617	0.994	1.51	1.09	1.77	2.8	0.065	4.11	5.96	8.07	11.4	15.3	1.06	0.259	0.0489	9
20140924	LS906	olivine_stdev	1.53	1.66	1.54	1.42	1.47	1.53	0.805	0.788	0.714	0.0155	0.817	0.76	0.718	0.857	0.817	1.56	0.777	0.147	
20140924	LS906	melt	1780	2020	1930	1720	1720	1910	987	954	986	15.3	1000	987	947	983	950	2140	1040	171	4
20140924	LS906	melt_stdev	30.3	23.9	25.7	23.7	30.4	27.9	17.9	14.7	20.3	0.382	17.1	15.7	18.9	15.3	15	45.7	21.2	2.58	
20140924	LS907	diopside	27.1	36.9	57.8	63.8	78.7	92.5	48.5	43.6	43.6	0.635	42	41	39.8	45	53.7	32.9	0.121	0.115	12
20140924	LS907	diopside_stdev	6.89	9.41	15.1	17.6	23.3	29	16.2	15.6	16.6	0.296	17.7	18.3	18.7	22	26.5	41.2	0.25	0.373	
20140924	LS907	melt	1420	1750	1600	1390	1380	1570	794	763	801	12.4	809	793	768	790	741	1640	813	211	4
20140924	LS907	melt_stdev	10.2	15.8	7.68	5.74	6.34	7.87	4.69	7.93	8.76	0.311	8.83	8.49	9.36	8.76	12.3	19.3	8.25	10.2	
20140925	LS905	diopside	20.5	38.1	49.1	55.9	73.8	93.2	48.5	46	47.9	0.696	47.1	45.7	42.5	47.4	47.9	7.1	0.0327	0.0371	12
20140925	LS905	diopside_stdev	2.11	3.83	4.7	5.51	6.59	7.34	4.34	3.93	4.1	0.0715	3.99	3.84	3.38	4.17	4.32	1.72	0.0134	0.0116	
20140925	LS905	melt	1100	1330	1220	1080	1090	1210	626	597	630	9.53	632	631	602	651	596	1280	620	1140	4
20140925	LS905	melt_stdev	13.5	15.2	13.7	14.4	18.5	16.9	11.3	8.87	7.63	0.188	10.2	11.9	12.4	10.6	7.44	20.1	7.27	20.6	
20140925	LS906	diopside	24	43.6	55.9	62.8	82.2	103	53.9	50.5	51.9	0.748	50.9	48.5	44.4	46.4	48.6	7.76	0.11	0.159	11
20140925	LS906	diopside_stdev	5.88	11.2	14.7	16.9	24.1	27	17.4	16.4	17.4	0.28	17.6	17.4	15.7	15.9	16.8	5.31	0.164	0.33	
20140925	LS906	olivine	0.0183	0.0324	0.0754	0.121	0.426	0.84	0.764	1.35	2.27	0.0518	3.69	5.64	8.05	11.5	16.3	0.648	0.0008	0.00596	5
20140925	LS906	olivine_melt	0.0045	0.0124	0.005	0.0293	0.0396	0.017	0.074	0.0347	0.141	0.0167	0.108	0.248	0.511	0.857	1.63	0.241	0.00179	0.00386	
20140925	LS906	melt	1320	1570	1450	1300	1300	1440	742	709	742	11.3	748	749	716	738	712	1600	769	1320	4
20140925	LS906	melt_stdev	12	8.96	12.4	11	6.29	14.8	5.07	0.957	7.5	0.0757	5.32	7.33	7.48	5.2	4.27	19.4	8.02	9.18	

Run	comp.	type	La_ppm	Ce_ppm	Pr_ppm	Nd_ppm	Sm_ppm	Eu_ppm	Gd_ppm	Tb_ppm	Dy_ppm	Y_ppm	Ho_ppm	Er_ppm	Tm_ppm	Yb_ppm	Lu_ppm	Hf_ppm	Th_ppm	U_ppm	trace (count)
20150223	LS026	olivine	0.0151	0.0273	0.0527	0.098	0.368	0.672	0.476	1.15	1.92	0.0535	3.03	4.73	6.97	10.8	15.6	0.407		0.00595	3
20150223	LS026	olivine_stdev	0.0062	0.017	0.0397	0.0636	0.227	0.562	0.372	0.913	1.57	0.0615	2.48	4.25	6.14	9.63	14.1	0.209		0.00233	
20150223	LS026	diopside	39.3	47.1	76.5	84.4	110	133	69	69.3	68.4	1.12	67.8	67.5	63.4	66.6	70.4	84.7	0.244	0.047	3
20150223	LS026	diopside_stdev	2.15	3.1	5.76	8.52	11.3	14.4	9.08	9.34	9.01	0.138	9.76	10.5	10.2	11.3	12.1	51.3	0.0137	0.0118	
20150223	LS026	melt	1220	1390	1260	1100	1130	1270	630	640	634	10.7	642	656	637	644	618	1380	694	1030	4
20150223	LS026	melt_stdev	16.4	17.6	17	14.6	10.6	20	7.74	12.1	14.5	0.345	12	13.4	9.97	10.7	10.4	21.7	12.5	32.5	
20150318	LS025	diopside	35	47.5	69.4	75.3	92.6	113	60.4	59.5	59.2	1.6	60.5	60.4	57.9	62.1	55.2	74.2	1.28	1.83	7
20150318	LS025	diopside_stdev	10.1	12.6	16.6	16.8	18.1	20.6	10.3	10.1	9.95	0.207	10.3	10.2	9.81	11.1	9.32	31.5	1.83	2.51	
20150318	LS025	melt	784	894	852	734	706	803	402	403	404	11.5	413	418	404	413	323	812	420	417	3
20150318	LS025	melt_stdev	12.7	14.7	12.3	14.5	10.7	9.62	4.24	5.21	8.06	0.187	8.36	9.56	7.2	7.27	7.07	22.2	9.66	6.19	
20150318	LS026	diopside	118	130	144	136	153	180	92.1	92.5	90.8	1.9	92.3	92.2	90.1	94.6	93.4	148	58.2	39.4	6
20150318	LS026	diopside_stdev	136	149	139	120	119	133	66.1	66.7	65.8	1.48	67.3	68.3	67.2	69	64.8	165	79.8	55.7	
20150318	LS026	olivine	0.38	0.38	0.47	0.47	0.95	1.5	1.23	2.01	3.14	0.091	5.04	7.54	10.4	14.9	21.3	1.5	0.2	0.22	1
20150318	LS026	olivine_stdev																			
20150318	LS026	melt	1410	1620	1490	1290	1310	1480	733	739	728	15.2	739	749	737	762	714	1660	812	619	4
20150318	LS026	melt_stdev	11.3	3.1	6.14	9.5	11.9	12.1	8.24	10.5	9.33	0.244	11.3	8.52	12.5	9.64	9.64	43.6	15.9	23	

Table 37: CaO-Al_2O_3-SiO_2 system experiments. Experimental conditions, average and standard deviations (stdev) of the major elements in each phase

Run	Label	type	T1	T2	fO2	P	time	comp.	System	Na2O	MgO	Al2O3	SiO2	K2O	CaO	TiO2	MnO	FeO	P2O5	Total	major (count)
20140416	CAS45	plagioclase	1520	1453	air	1 atm	156 h	LS003	CAS	0.05		35.5	42.6	0.01	20.4			0.02	0.53	99.1	4
20140416	CAS45	plagioclase_stdev	1520	1453	air	1 atm	156 h	LS003	CAS	0.03		0.32	0.88	0.01	0.12			0.01	0.05	1.11	
20140416	CAS45	melt	1520	1453	air	1 atm	156 h	LS003	CAS	0.08		24.4	41.1	0.02	25.9	0.02		0.24	0.67	92.4	4
20140416	CAS45	melt_stdev	1520	1453	air	1 atm	156 h	LS003	CAS	0.03		0.3	0.78		0.18	0.01		0.02	0.05	0.98	
20140416	CAS64	plagioclase	1520	1453	air	1 atm	156 h	LS004	CAS	0.35		34.5	45.7	0.02	19.2			0.02	0.5	100	3
20140416	CAS64	plagioclase_stdev	1520	1453	air	1 atm	156 h	LS004	CAS	0.01		0.07	0.06		0.06			0.03	0.01	0.05	
20140416	CAS64	melt	1520	1453	air	1 atm	156 h	LS004	CAS	0.47		23.4	53.1	0.15	14.1	0.03		0.26	0.38	91.8	4
20140416	CAS64	melt_stdev	1520	1453	air	1 atm	156 h	LS004	CAS	0.04		0.39	0.59	0.01	0.09	0.01		0.02	0.05	0.98	
20140428	CAS30	plagioclase	1520	1399	air	1 atm	168 h	LS002	CAS			36.4	42.8	0.02	20.4		0.01		0.55	100	4
20140428	CAS30	plagioclase_stdev	1520	1399	air	1 atm	168 h	LS002	CAS	0.05		0.42	0.54	0.01	0.08		0.01		0.05	0.87	
20140428	CAS30	melt	1520	1399	air	1 atm	168 h	LS002	CAS	0.05		32.5	30.6	0.02	26.2	0.02		0.12	0.75	90.3	4
20140428	CAS30	melt_stdev	1520	1399	air	1 atm	168 h	LS002	CAS	0.04		0.42	0.74	0.01	0.17	0.01		0.02	0.06	1.03	
20140428	CAS45	plagioclase	1520	1399	air	1 atm	168 h	LS003	CAS	0.01		36.5	44	0.01	20.5	0.01		0.01	0.56	102	3
20140428	CAS45	plagioclase_stdev	1520	1399	air	1 atm	168 h	LS003	CAS	0.03		0.13	0.02	0.01	0.09	0.01		0.01	0.06	0.24	
20140428	CAS45	melt	1520	1399	air	1 atm	168 h	LS003	CAS	0.04		20.8	40.7	0.01	27.7	0.03		0.11	0.73	90.1	4
20140428	CAS45	melt_stdev	1520	1399	air	1 atm	168 h	LS003	CAS	0.03		0.13	0.02	0.01	0.09	0.01		0.01	0.06	0.24	
20140428	CAS64	plagioclase	1520	1399	air	1 atm	168 h	LS004	CAS	0.21		34.3	46.7	0.02	18.9	0.01		0.03	0.51	101	3
20140428	CAS64	plagioclase_stdev	1520	1399	air	1 atm	168 h	LS004	CAS	0.07		0.36	0.51	0.01	0.31	0.01		0.02	0.07	0.59	
20140428	CAS64	melt	1520	1399	air	1 atm	168 h	LS004	CAS	0.2		20.2	54.9	0.2	12.8	0.1		0.19	0.37	89	5
20140428	CAS64	melt_stdev	1520	1399	air	1 atm	168 h	LS004	CAS	0.04		0.28	0.5	0.01	0.07	0.02		0.01	0.03	0.51	
20140804	CAS30	plagioclase	1521	1408	air	1 atm	140 h	LS902	CAS	bdl	0.103	37.1	42.5	bdl	20.3	0.13	bdl	bdl		100	4
20140804	CAS30	plagioclase_stdev	1521	1408	air	1 atm	140 h	LS902	CAS		0.0153	0.488	0.795		0.293					1.39	
20140804	CAS30	melt	1521	1408	air	1 atm	140 h	LS902	CAS	0.06	0.14	35.7	32.5	bdl	28.4	0.095	bdl	0.445		97.4	2
20140804	CAS30	melt_stdev	1521	1408	air	1 atm	140 h	LS902	CAS		0.0283	0.219	0.0849		0.184	0.00707		0.163		0.163	
20140804	CAS45	plagioclase	1521	1408	air	1 atm	140 h	LS903	CAS	0.103	0.1	36.2	43.2	0.04	19.9	bdl	0.11	0.15		99.5	5
20140804	CAS45	plagioclase_stdev	1521	1408	air	1 atm	140 h	LS903	CAS	0.0252		0.328	0.213		0.16					0.63	
20140804	CAS45	melt	1521	1408	air	1 atm	140 h	LS903	CAS	0.06	0.11	22.5	44.7	0.04	30.2	0.13	bdl	0.38		98	2
20140804	CAS45	melt_stdev	1521	1408	air	1 atm	140 h	LS903	CAS	0.0141	0.0141	0.0283			0.099			0.141		0.0919	
20140804	CAS64	plagioclase	1521	1408	air	1 atm	140 h	LS904	CAS	0.28	0.1	34.5	46.6	bdl	18.8	bdl	0.11	0.156		100	5
20140804	CAS64	plagioclase_stdev	1521	1408	air	1 atm	140 h	LS904	CAS	0.03	1.7E-17	0.529	0.298		0.191			0.0358		0.789	
20140804	CAS64	melt	1521	1408	air	1 atm	140 h	LS904	CAS	0.345	0.16	20.6	59.9	0.18	12.2	0.15	bdl	1.19		94.7	2
20140804	CAS64	melt_stdev	1521	1408	air	1 atm	140 h	LS904	CAS	0.00707	0.0283	0.0707	0.297	0.0566	0.0424	0.0283		0.191		0.226	
20141014	CAS30	plagioclase	1517	1407	QFM (-6.21)	1 atm	141 h	LS902	CAS	bdl	bdl	38.3	42.5		20.4			bdl		101	7
20141014	CAS30	plagioclase_stdev	1517	1407	QFM (-6.21)	1 atm	141 h	LS902	CAS			0.148	0.16		0.0721					0.295	
20141014	CAS30	melt	1517	1407	QFM (-6.21)	1 atm	141 h	LS902	CAS	bdl	bdl	37	32.7		29			bdl		98.7	6
20141014	CAS30	melt_stdev	1517	1407	QFM (-6.21)	1 atm	141 h	LS902	CAS			0.193	0.104		0.2					0.265	
20141014	CAS45	plagioclase	1517	1407	QFM (-6.21)	1 atm	141 h	LS903	CAS	0.038	bdl	38.2	42.7		20.3			bdl		101	7
20141014	CAS45	plagioclase_stdev	1517	1407	QFM (-6.21)	1 atm	141 h	LS903	CAS	0.00849		0.204	0.317		0.111					0.404	
20141014	CAS45	melt	1517	1407	QFM (-6.21)	1 atm	141 h	LS903	CAS	0.0371	bdl	22.9	44.6		30.7			bdl		98.2	6
20141014	CAS45	melt_stdev	1517	1407	QFM (-6.21)	1 atm	141 h	LS903	CAS	0.00962		0.0746	0.275		0.112					0.333	
20150112	CAS30	plagioclase	1530	1412	air	1 atm	144 h	LS012	CAS	bdl	bdl	38.3	42.5		20.4			bdl		101	7
20150112	CAS30	plagioclase_stdev	1530	1412	air	1 atm	144 h	LS012	CAS			0.226	0.171		0.129					0.279	
20150112	CAS30	melt	1530	1412	air	1 atm	144 h	LS012	CAS	0.0413	bdl	37.4	33.4		29.8			0.165		101	6
20150112	CAS30	melt_stdev	1530	1412	air	1 atm	144 h	LS012	CAS	0.0108		0.177	0.202		0.106			0.0555		0.243	
20150112	CAS45	plagioclase	1530	1412	air	1 atm	144 h	LS013	CAS	0.0595	bdl	37.9	42.7		20.3			bdl		101	7
20150112	CAS45	plagioclase_stdev	1530	1412	air	1 atm	144 h	LS013	CAS	0.00826		0.34	0.335		0.0811					0.559	
20150112	CAS45	melt	1530	1412	air	1 atm	144 h	LS013	CAS	0.0456	0.0678	22.7	47.1		31.3			0.166		101	6
20150112	CAS45	melt_stdev	1530	1412	air	1 atm	144 h	LS013	CAS	0.0114	0.00354	0.147	0.257		0.0982			0.0119		0.402	
20150112	CAS64	plagioclase	1530	1412	air	1 atm	144 h	LS014	CAS	0.318	bdl	34.6	46.5		18.5			bdl		99.9	7
20150112	CAS64	plagioclase_stdev	1530	1412	air	1 atm	144 h	LS014	CAS	0.0155		0.183	0.343		0.129					0.187	
20150112	CAS64	melt	1530	1412	air	1 atm	144 h	LS014	CAS	0.499	0.0482	21.4	65.6		13			0.2		101	6
20150112	CAS64	melt_stdev	1530	1412	air	1 atm	144 h	LS014	CAS	0.0139		0.205	0.297		0.197			0.0345		0.574	
20150128	CAS45	plagioclase	1520	1414	air	1 atm	144 h	LS023	CAS			36.1	42.8		21.5					100	7
20150128	CAS45	plagioclase_stdev	1520	1414	air	1 atm	144 h	LS023	CAS			0.553	0.347		0.288					0.729	
20150128	CAS45	melt	1520	1414	air	1 atm	144 h	LS023	CAS			22.3	45.4		32.1					99.9	5
20150128	CAS45	melt_stdev	1520	1414	air	1 atm	144 h	LS023	CAS			0.12	0.143		0.201					0.245	
20150128	CAS64	plagioclase	1520	1414	air	1 atm	144 h	LS024**	CAS			34.1	47.3		18.4					99.9	10
20150128	CAS64	plagioclase_stdev	1520	1414	air	1 atm	144 h	LS024**	CAS			0.378	0.38		0.0997					0.536	
20150128	CAS64	melt	1520	1414	air	1 atm	144 h	LS024**	CAS			21.4	64.2		12.6					98.2	5
20150128	CAS64	melt_stdev	1520	1414	air	1 atm	144 h	LS024**	CAS			0.088	0.188		0.0338					0.242	

Run	Label	type	T1	T2	fO2	P	time	comp.	System	Na2O	MgO	Al2O3	SiO2	K2O	CaO	TiO2	MnO	FeO	P2O5	Total major (count)	
20150223	CAS30	plagioclase	1513	1403	IW (-9.71)	1 atm	148 h	LS022	CAS	bdl	bdl	38.5	43.1		20.1			bdl		102	6
20150223	CAS30	plagioclase_stdev	1513	1403	IW (-9.71)	1 atm	148 h	LS022	CAS			0.0737	0.29		0.134					0.251	
20150223	CAS30	melt	1513	1403	IW (-9.71)	1 atm	148 h	LS022	CAS	0.0335	0.0704	37.1	33.2		29.8			bdl		100	6
20150223	CAS30	melt_stdev	1513	1403	IW (-9.71)	1 atm	148 h	LS022	CAS	0.00424	0.0131	0.201	0.0788		0.112					0.189	
20150223	CAS45	plagioclase	1513	1403	IW (-9.71)	1 atm	148 h	LS023	CAS	bdl	bdl	38.3	43.6		20			bdl		102	7
20150223	CAS45	plagioclase_stdev	1513	1403	IW (-9.71)	1 atm	148 h	LS023	CAS			0.165	0.207		0.114					0.222	
20150223	CAS45	melt	1513	1403	IW (-9.71)	1 atm	148 h	LS023	CAS	0.0971	0.0709	22.8	47.1		30.4			bdl		100	6
20150223	CAS45	melt_stdev	1513	1403	IW (-9.71)	1 atm	148 h	LS023	CAS		0.0147	0.186	0.277		0.175					0.421	
20150428	CAS37	plagioclase	1520	1400	air	1 atm	141 h	LS022.1	CAS	0.0988	bdl	37.4	43		20.5			bdl		101	8
20150428	CAS37	plagioclase_stdev	1520	1400	air	1 atm	141 h	LS022.1	CAS	0.0251		0.442	0.145		0.125					0.498	
20150428	CAS37	melt	1520	1400	air	1 atm	141 h	LS022.1	CAS	0.26	0.193	28.6	37.3		30.9		0.157			97.4	4
20150428	CAS37	melt_stdev	1520	1400	air	1 atm	141 h	LS022.1	CAS	0.0148	0.0155	0.191	0.323		0.13		0.0154			0.21	
20150428	CAS37	plagioclase	1520	1400	air	1 atm	141 h	LS902.5	CAS	0.102	bdl	37.1	43		20.4			bdl		101	8
20150428	CAS37	plagioclase_stdev	1520	1400	air	1 atm	141 h	LS902.5	CAS	0.0211		0.83	0.173		0.0867					0.734	
20150428	CAS37	melt	1520	1400	air	1 atm	141 h	LS902.5	CAS	0.292	0.0494	28.8	36.5		29.9		0.134			95.6	4
20150428	CAS37	melt_stdev	1520	1400	air	1 atm	141 h	LS902.5	CAS	0.0337		0.548	0.0925		0.213		0.0118			0.504	
20150428	CAS52	plagioclase	1520	1400	air	1 atm	141 h	LS903.5	CAS	0.691	bdl	35.8	44.8		19.2			bdl		100	8
20150428	CAS52	plagioclase_stdev	1520	1400	air	1 atm	141 h	LS903.5	CAS	0.112		0.576	0.288		0.188					0.479	
20150428	CAS52	melt	1520	1400	air	1 atm	141 h	LS903.5	CAS	1.23	0.0463	21.1	51.4		22.3		0.124			96.1	4
20150428	CAS52	melt_stdev	1520	1400	air	1 atm	141 h	LS903.5	CAS	0.0144		0.333	0.219		0.0701		0.026			0.524	
20150428	CAS30	plagioclase	1520	1400	air	1 atm	141 h	LS902	CAS	bdl	bdl	37.4	42.8		20.5			bdl		101	8
20150428	CAS30	plagioclase_stdev	1520	1400	air	1 atm	141 h	LS902	CAS			0.359	0.353		0.104					0.505	
20150428	CAS30	melt	1520	1400	air	1 atm	141 h	LS902	CAS	0.274	bdl	36.5	31.3		28		0.114			96.1	5
20150428	CAS30	melt_stdev	1520	1400	air	1 atm	141 h	LS902	CAS	0.0271		0.444	0.191		0.0859		0.0161			0.569	
20150616	CAS30	plagioclase	1520	1385	IW (-9.71)	1 atm	62 h	LS902	CAS	bdl	bdl	37.5	42.5		20.5			bdl		100	8
20150616	CAS30	plagioclase_stdev	1520	1385	IW (-9.71)	1 atm	62 h	LS902	CAS			0.609	0.201		0.103					0.581	
20150616	CAS30	melt	1520	1385	IW (-9.71)	1 atm	62 h	LS902	CAS	bdl	0.0437	36.8	31.1		28.9			bdl		96.8	4
20150616	CAS30	melt_stdev	1520	1385	IW (-9.71)	1 atm	62 h	LS902	CAS			0.363	0.395		0.0781					0.658	
20150616	CAS37	plagioclase	1520	1385	IW (-9.71)	1 atm	62 h	LS902.5	CAS	bdl	bdl	37.7	42.5		20.4			bdl		101	8
20150616	CAS37	plagioclase_stdev	1520	1385	IW (-9.71)	1 atm	62 h	LS902.5	CAS			0.6	0.172		0.127					0.546	
20150616	CAS37	melt	1520	1385	IW (-9.71)	1 atm	62 h	LS902.5	CAS	bdl	0.0458	28.6	36.6		30.7			bdl		95.9	4
20150616	CAS37	melt_stdev	1520	1385	IW (-9.71)	1 atm	62 h	LS902.5	CAS			0.765	0.333		0.0804					0.425	
20150616	CAS45	plagioclase	1520	1385	IW (-9.71)	1 atm	62 h	LS903	CAS	bdl	bdl	37.5	42.8		20.3			bdl		101	8
20150616	CAS45	plagioclase_stdev	1520	1385	IW (-9.71)	1 atm	62 h	LS903	CAS			0.483	0.237		0.11					0.562	
20150616	CAS45	melt	1520	1385	IW (-9.71)	1 atm	62 h	LS903	CAS	bdl	bdl	21.6	44		30.7			bdl		96.2	4
20150616	CAS45	melt_stdev	1520	1385	IW (-9.71)	1 atm	62 h	LS903	CAS			0.281	0.228		0.111					0.367	
20150616	CAS64	plagioclase	1520	1385	IW (-9.71)	1 atm	62 h	LS904	CAS	0.173	bdl	35	45.9		19.2			bdl		100	8
20150616	CAS64	plagioclase_stdev	1520	1385	IW (-9.71)	1 atm	62 h	LS904	CAS	0.0161		0.599	0.155		0.0583					0.698	
20150616	CAS64	melt	1520	1385	IW (-9.71)	1 atm	62 h	LS904	CAS	0.283	0.0434	20	62.6		12			bdl		94.9	4
20150616	CAS64	melt_stdev	1520	1385	IW (-9.71)	1 atm	62 h	LS904	CAS	0.0164	0.00337	0.166	0.0928		0.0724					0.283	
c4791	CAS30	plagioclase	1520	1400	none	10 kbar	48 h	LS012	CAS			36.3	42.1		21.8					100	13
c4791	CAS30	plagioclase_stdev	1520	1400	none	10 kbar	48 h	LS012	CAS			0.302	0.147		0.109					0.268	
c4791	CAS30	melt	1520	1400	none	10 kbar	48 h	LS012	CAS	0.101	0.101	32.1	36.1		31.9					100	4
c4791	CAS30	melt_stdev	1520	1400	none	10 kbar	48 h	LS012	CAS	0.0143	0.0143	0.0715	0.0742		0.108					0.228	
c4828	CAS64	plagioclase	1520	1400	none	10 kbar	48 h	LS024	CAS	0.202	bdl	35.1	46.4		18.6			bdl		100	7
c4828	CAS64	plagioclase_stdev	1520	1400	none	10 kbar	48 h	LS024	CAS	0.0286		0.361	0.675		0.237					0.382	
c4828	CAS64	melt	1520	1400	none	10 kbar	48 h	LS024	CAS	0.173	0.315	25.7	58.9		14.5			bdl		99.5	6
c4828	CAS64	melt_stdev	1520	1400	none	10 kbar	48 h	LS024	CAS	0.0102	0.096	0.274	0.318		0.164					0.407	
c4856	CAS45	plagioclase	1520	1400	none	10 kbar	48 h	LS023	CAS	0.132	bdl	37.1	43.1		20.2			bdl		101	8
c4856	CAS45	plagioclase_stdev	1520	1400	none	10 kbar	48 h	LS023	CAS	0.025		0.48	0.178		0.151					0.638	
c4856	CAS45	melt	1520	1400	none	10 kbar	48 h	LS023	CAS	0.176	1.81	26.3	43.8		27.1			bdl		99.2	4
c4856	CAS45	melt_stdev	1520	1400	none	10 kbar	48 h	LS023	CAS	0.0181	0.0262	0.606	0.584		0.154					0.423	
c4874	CAS37	plagioclase	1520	1400	none	10 kbar	48 h	LS022.1	CAS	0.0493	bdl	38.2	42.5		20.2			bdl		101	7
c4874	CAS37	plagioclase_stdev	1520	1400	none	10 kbar	48 h	LS022.1	CAS	0.00777		0.184	0.216		0.103					0.333	
c4874	CAS37	melt	1520	1400	none	10 kbar	48 h	LS022.1	CAS	0.25	0.541	31.8	38.2		29.4			bdl		100	6
c4874	CAS37	melt_stdev	1520	1400	none	10 kbar	48 h	LS022.1	CAS	0.0181	0.0255	0.188	0.185		0.235					0.383	
c4970	CAS52	plagioclase	1520	1400	none	10 kbar	48 h	LS903.5	CAS			35.9	45.1		19					100	8
c4970	CAS52	plagioclase_stdev	1520	1400	none	10 kbar	48 h	LS903.5	CAS			0.176	0.276		0.232					0.683	
c4970	CAS52	melt	1520	1400	none	10 kbar	48 h	LS903.5	CAS		4.63	24.6	49.7		21.1					100	5
c4970	CAS52	melt_stdev	1520	1400	none	10 kbar	48 h	LS903.5	CAS		0.0783	0.285	0.325		0.226					0.915	

Table 38: CaO-Al_2O_3-SiO_2 system experiments. Average and standard deviations (stdev) of the trace elements from mass 7 (Li) to mass 138 (Ba)

Run	Label	type	Li_ppm	Be_ppm	Na_ppm	Mg_ppm	Al_ppm	Si_ppm	K_ppm	Sc_ppm	Fe_ppm	V_ppm	Cr_ppm	Ga_ppm	Rb_ppm	Sr_ppm	Zr_ppm	Nb_ppm	In_ppm	Cs_ppm	Ba_ppm
20140416	CAS45	plagioclase								13.5						486		4.66			712
20140416	CAS45	plagioclase_stdev								0.422						13.7		4.46			119
20140416	CAS45	melt								850						525		4460			4350
20140416	CAS45	melt_stdev								10.1						5.16		10.7			28.5
20140416	CAS64	plagioclase								11.8						582		4.96			466
20140416	CAS64	plagioclase_stdev								0.347						3.71		0.481			27
20140416	CAS64	melt								933						615		5120			4920
20140416	CAS64	melt_stdev								4.73						1.71		60			39.5
20140428	CAS30	plagioclase								11.6						562		11.6			1110
20140428	CAS30	plagioclase_stdev								0.82						11.7		1.3			67.9
20140428	CAS30	melt			144					1000						545		5640			5310
20140428	CAS30	melt_stdev			8.06					8.98						7.14		49.9			70.5
20140428	CAS45	plagioclase			217					15.9						507		3.08			855
20140428	CAS45	plagioclase_stdev			38.6					1.03						14.4		0.656			112
20140428	CAS45	melt			202					1110						526		5930			5290
20140428	CAS45	melt_stdev			5.24					11.4						9.89		66.2			104
20140428	CAS64	plagioclase			1510					14.6						596		11.2			511
20140428	CAS64	plagioclase_stdev			188					1.26						12.6		5.73			24
20140428	CAS64	melt			1740					1220						627		6890			6310
20140428	CAS64	melt_stdev			44.8					11.7						6.18		96.4			75.4
20140804	CAS30	plagioclase			4.32	17.3			16.8	6.74						375		29.8			376
20140804	CAS30	plagioclase_stdev			13	7.49			22.9	1.96						15.1		18.7			31.1
20140804	CAS30	melt			223	507			42.2	159						377		1700			1580
20140804	CAS30	melt_stdev			4.68	9.61			22	3.01						1.89		19.5			12.9
20140804	CAS45	plagioclase			403	11.5			39.5	3.55						360		0.943			245
20140804	CAS45	plagioclase_stdev			89.1	3.48			22.5	0.642						15		0.2			37.7
20140804	CAS45	melt			329	386			39.8	159						391		1640			1510
20140804	CAS45	melt_stdev			12.2	13			9.7	1.98						2.13		20.6			13.3
20140804	CAS64	plagioclase			1940	17.9			84.5	3.41						249		1.67			117
20140804	CAS64	plagioclase_stdev			119	3.56			17.5	0.906						7.17		0.287			6.4
20140804	CAS64	melt			3010	300			1700	186						290		1970			1840
20140804	CAS64	melt_stdev			40.6	14.2			95.8	3.27						2.98		45.9			17.4
20141014	CAS30	plagioclase			bdl	5.62	222000	236000	bdl	2.9	101					368		3.43			270
20141014	CAS30	plagioclase_stdev				0.89	2680	3970		0.243	18.9					4.69		0.422			9.21
20141014	CAS30	melt			57.5	403	223000	186000	bdl	156	185					411		1780			1660
20141014	CAS30	melt_stdev			0.707	4.79	4030	4260		2.24	28					8.15		31.7			13.9
20141014	CAS45	plagioclase			85.1	19.1	215000	234000	22.5	3.51	95.5					361		0.91			237

Run	Label	type	Li_ppm	Be_ppm	Na_ppm	Mg_ppm	Al_ppm	Si_ppm	K_ppm	Sc_ppm	Fe_ppm	V_ppm	Cr_ppm	Ga_ppm	Rb_ppm	Sr_ppm	Zr_ppm	Nb_ppm	In_ppm	Cs_ppm	Ba_ppm
20141014	CAS45	plagioclase_stdev			17.8	2.97	2040	3440	6.36	0.229	16.7					14.4		0.244			29.4
20141014	CAS45	melt			67.9	484	134000	238000	12.3	156	161					431		1750			1630
20141014	CAS45	melt_stdev			13.2	7.14	1060	5860		2.49	17.3					6.82		34.3			18.2
20150112	CAS30	plagioclase			58.3	7.93	213000	246000	bdl	1.83	177					74.6		bdl			1.86
20150112	CAS30	plagioclase_stdev				1.86	1750	3560		0.125	24.2					1.42					0.252
20150112	CAS30	melt			149	638	215000	192000	53	1.74	1390					85.3		2.43			13.8
20150112	CAS30	melt_stdev			7	26.4	1920	4280	0.566	0.0899	324					0.952		0.584			0.992
20150112	CAS45	plagioclase			369	27.6	212000	243000	bdl	1.65	195					73.1		bdl			1.83
20150112	CAS45	plagioclase_stdev			55.6	9.56	2850	3630		0.126	27.4					1.96					0.347
20150112	CAS45	melt			265	663	129000	257000	10.3	2.11	1280					90.9		1.84			15.4
20150112	CAS45	melt_stdev			7.19	4.36	838	2970	0.557	0.17	25.3					0.869		0.0829			0.661
20150112	CAS64	plagioclase			2620	21.4	198000	266000	30.3	1.73	232					46.3		bdl			1.28
20150112	CAS64	plagioclase_stdev			124	2.73	2970	5610	8.72	0.124	38.3					2.39					0.336
20150112	CAS64	melt			4130	315	123000	348000	820	2.64	1430					57.4		2.07			23.2
20150112	CAS64	melt_stdev			55.5	4.85	1940	5260	14.2	0.0999	112					1.3		0.816			1.36
20150128	CAS45	plagioclase			433	17.3	224000	253000		4.4	249					121		0.343			97.9
20150128	CAS45	plagioclase_stdev			67.5	3.85	3510	5550		0.232	14.4					3.68		0.05			7.1
20150128	CAS45	melt			293	396	134000	257000		122	876					139		634			579
20150128	CAS45	melt_stdev			3.19	5.59	1880	3220		1.16	11.1					2.26		8.82			5.92
20150128	CAS64	plagioclase			2740	34	233000	317000	42.8	7.08	296					120		17			74.3
20150128	CAS64	plagioclase_stdev			78.1	6.7	3900	5430	10.7	2.44	37					2.45		14.1			13
20150128	CAS64	melt			5880	549	209000	586000	989	261	1440					198		1420			1290
20150128	CAS64	melt_stdev			57.1	13.9	2570	7790	39.9	5.23	108					3.16		28.2			10.3
20150223	CAS30	plagioclase			bdl	13.5	207000	239000	bdl	5.26	139					114		0.939			95.3
20150223	CAS30	plagioclase_stdev				9.48	2380	2970		1.33	19.2					1.75		0.851			8.83
20150223	CAS30	melt			69.8	764	215000	198000	bdl	110	192					130		64.5			579
20150223	CAS30	melt_stdev			13.8	4.98	2700	1380		1.22	26.6					1.11		0.966			9.21
20150223	CAS45	plagioclase			116	18.4	204000	237000	45	4.78	148					104		0.347			68.5
20150223	CAS45	plagioclase_stdev			16	6.81	3790	5380		0.416	24.4					2.29		0.211			4.81
20150223	CAS45	melt			106	643	132000	257000	16	116	229					133		375			537
20150223	CAS45	melt_stdev			9.02	78.2	717	1980		1.38	12.7					1.31		104			7.46
20150428	CAS37	plagioclase			851	24.9	210000	242000	bdl	6.13	259					106		4.17			76.7
20150428	CAS37	plagioclase_stdev			258	4.97	4000	3860		0.327	17.7					3.4		2.71			5.39
20150428	CAS37	melt			2450	1510	156000	204000	16.4	109	1410					122		620			558
20150428	CAS37	melt_stdev			36.4	23.3	1460	3150	10.4	1.76	36.6					2.45		3.92			8.76
20150428	CAS37	plagioclase			826	7.88	212000	245000	21.9	6.27	239					368		1.93			276
20150428	CAS37	plagioclase_stdev			169	2.28	1690	4450		0.385	23					5.75		1.21			11.5
20150428	CAS37	melt			2580	518	159000	205000	14.7	168	1100					406		1860			1780
20150428	CAS37	melt_stdev			59.6	14.6	2140	4430	3.1	2.57	37.7					6.73		26.3			15.2

Run	Label	type	Li_ppm	Be_ppm	Na_ppm	Mg_ppm	Al_ppm	Si_ppm	K_ppm	Sc_ppm	Fe_ppm	V_ppm	Cr_ppm	Ga_ppm	Rb_ppm	Sr_ppm	Zr_ppm	Nb_ppm	In_ppm	Cs_ppm	Ba_ppm
20150428	CAS52	plagioclase			6050	14.9	205000	251000	35.7	6.18	246					300		1.21			184
20150428	CAS52	plagioclase_stdev			796	2.33	2690	7170	5.71	0.515	26.6					9.07		0.0771			17.5
20150428	CAS52	melt			10500	458	120000	273000	111	175	1150					361		1910			1810
20150428	CAS52	melt_stdev			199	4.49	1480	4770	3.53	2.08	22.6					2.78		22.6			17
20150428	CAS30	plagioclase			274	4.16	216000	240000	11.6	5.55	201					375		6.69			275
20150428	CAS30	plagioclase_stdev			241	1.01	2260	3930		0.334	14.4					11.2		3.13			26.8
20150428	CAS30	melt			2590	406	209000	184000	13.6	147	1050					394		1710			1610
20150428	CAS30	melt_stdev			63.1	7.78	1330	4460	4.87	3.3	50.1					2.81		29.6			17.2
20150616	CAS30	plagioclase	0.065	0.73	8.67	13.8	214000	253000	bdl	8.45		0.437	0.416	2.84	0.153	367	0.621	21.8	0.0103	0.026	275
20150616	CAS30	plagioclase_stdev	0.0636	0.846	0.562	10.8	2750	4380		4.2		0.25	0.236	0.542	0.0972	5.33	1.15	41.5	0.0136	0.0247	29.2
20150616	CAS30	melt	0.328	40.3	36.8	544	208000	193000	5.23	167		10.3	11.9	30.1	2.88	397	45.7	1750	0.0188	0.049	1680
20150616	CAS30	melt_stdev	0.284	7.63	2.28	12.8	640	2600	3.44	1.65		4.48	4.54	2.48	0.0854	5	1.1	47.5	0.0211	0.0304	6.55
20150616	CAS37	plagioclase	bdl	0.654	46.1	11.3	214000	254000	3.5	6.83		0.0896	0.766	1.28	0.075	356	0.206	1.52	0.009	0.026	249
20150616	CAS37	plagioclase_stdev		0.153	23.4	1.93	1200	4720	2.12	0.369		0.024	0.473	0.135	0.052	3.14	0.0996	0.461		0.0194	34.1
20150616	CAS37	melt	0.248	44	71.8	607	155000	214000	176	193		7.56	6.5	35.5	3.81	406	135	1680	0.014	0.029	1870
20150616	CAS37	melt_stdev	0.154	18.9	35.9	26.8	2040	2170	143	5.53		1.89	1.14	4.72	0.323	3.44	2.82	147	0.00693	0.0154	44
20150616	CAS45	plagioclase	0.275	2.61	79.9	27.1	211000	253000	6.33	7.11		0.0698	0.637	0.45	0.075	355	0.005	0.345	0.003	0.035	213
20150616	CAS45	plagioclase_stdev	0.148	0.425	18.6	2.91	2130	9090	7.77	0.172		0.0324	0.351	0.134	0.0354	6.2	0.00744	0.126		0.0217	20.3
20150616	CAS45	melt	0.53	34.8	68.6	534	120000	248000	11.1	172		3.9	5.68	28.2	3.3	424	66.4	986	0.0255	0.0233	1690
20150616	CAS45	melt_stdev	0.139	3.25	2.58	13	1020	1780	5.34	1.7		0.956	1.6	7.66	0.354	2.5	1.33	50.6	0.0177	0.0154	13
20150616	CAS64	plagioclase	1.44	2.86	1640	30.4	201000	273000	80.3	7.41		0.192	0.65	1.56	0.152	252	0.291	3.68	0.022	0.0326	123
20150616	CAS64	plagioclase_stdev	0.254	0.503	86.9	3.93	1410	3390	11.3	1.24		0.0528	0.551	0.532	0.165	8.17	0.583	5.91	0.0297	0.032	8.74
20150616	CAS64	melt	3.82	39	2460	450	113000	344000	1700	218		4.27	2.68	18.9	9.22	308	104	1400	0.002	0.479	2160
20150616	CAS64	melt_stdev	0.246	5	19.6	6.42	1120	3500	14.3	6.25		0.636	0.954	1.28	0.468	4.62	2.11	71.1		0.0229	24.1
c4791	CAS30	plagioclase			486	11.3	233000	259000		2.04	131					82.8					1.97
c4791	CAS30	plagioclase_stdev			80.6	3.41	7510	5870		0.184	21.8					1.81					0.277
c4791	CAS30	melt			3160	942	197000	213000	97.5	1.79	198					91.9		0.101			12
c4791	CAS30	melt_stdev			74.7	57.5	3080	5720	7.5	0.22	22.4					0.934		0.0268			0.478
c4828	CAS64	plagioclase	2.04	0.288	1730	69	196000	272000	24	5.93		0.175	bdl	0.852	bdl	88.4	0.015	0.564	bdl	bdl	45.1
c4828	CAS64	plagioclase_stdev	0.438	0.137	75.1	22	2500	5340		0.419				0.274		2.8		0.144			5.57
c4828	CAS64	melt	4.84	1.76	1540	1700	148000	319000	124	108		0.488	bdl	4.11	1.36	111	45.5	177	bdl	bdl	546
c4828	CAS64	melt_stdev	0.231	0.345	28.1	353	435	365	9.74	3.14		0.0922		0.0796	0.111	1.25	2.08	18.3			22.7
c4856	CAS45	plagioclase			1170	301	205000	242000	38	4.03	101					111		0.413			77.2
c4856	CAS45	plagioclase_stdev			103	59	2160	3410	24	0.468	30.8					5.41		0.608			13.6
c4856	CAS45	melt			1480	11800	140000	227000	104	84.9	146					128		262			410
c4856	CAS45	melt_stdev			24.3	2440	2150	2980	11.6	1.73	17.6					2.75		14.2			11.2
c4874	CAS37	plagioclase			403	41.4	221000	245000	bdl	4.66	143					108		0.272			84.9
c4874	CAS37	plagioclase_stdev			147	10.6	4090	5720		0.347	15.9					3.1		0.0879			12.1

Run	Label	type	Li_ppm	Be_ppm	Na_ppm	Mg_ppm	Al_ppm	Si_ppm	K_ppm	Sc_ppm	Fe_ppm	V_ppm	Cr_ppm	Ga_ppm	Rb_ppm	Sr_ppm	Zr_ppm	Nb_ppm	In_ppm	Cs_ppm	Ba_ppm
c4874	CAS37	melt			2220	3860	189000	211000	93.2	85.4	226					129		223			431
c4874	CAS37	melt_stdev			78.1	124	1530	2940	4.37	1.04	15					2.14		11.7			6.88
c4970	CAS52	plagioclase	0.407	0.014	1770	575	201000	255000	77.7	6.28		0.053	0.373	0.424	0.103	285	0.002	0.629	0.0035	0.0155	153
c4970	CAS52	plagioclase_stdev	0.237	0.0152	105	226	2880	3950	20	0.473		0.0391	0.373	0.14	0.119	5.99		0.15	0.00212	0.00551	17.3
c4970	CAS52	melt	0.983	0.127	1150	32900	138000	264000	335	106		0.312	0.853	8.91	3.17	339	76.7	326	0.005	0.0608	1130
c4970	CAS52	melt_stdev	0.147	0.0434	14	717	1470	1800	8.23	1.08		0.0706	0.402	0.55	0.235	3.38	4.46	6.21		0.0197	26.8

Table 39: CaO-Al_2O_3-SiO_2 system experiments. Average and standard deviations (stdev) of the trace elements from mass 139 (La) to mass 238 (U)

Run	Label	type	La_ppm	Ce_ppm	Pr_ppm	Nd_ppm	Sm_ppm	Eu_ppm	Gd_ppm	Tb_ppm	Dy_ppm	Y_ppm	Ho_ppm	Er_ppm	Tm_ppm	Yb_ppm	Lu_ppm	Hf_ppm	Ta_ppm	Pb_ppm	Th_ppm	U_ppm	trace (count)
20140416	CAS45	plagioclase	129	96.6	96.9	77	59.5	69.4	98.2	70.3	59.9		48.8	39.1	30.9	26.2	23.1	5.62			1.24	0.0398	8
20140416	CAS45	plagioclase_stdev	24.9	19.2	17.5	13.5	10.9	11.1	17.3	13	10.7		9	6.97	5.51	4.85	4	2.69			1.38	0.0332	
20140416	CAS45	melt	1880	1990	2060	1810	1950	2050	4180	3910	4090		3990	4000	3900	3950	3990	3930			1920	16.9	3
20140416	CAS45	melt_stdev	11.5	13	11.9	16.5	21.2	23	61.7	60	69.2		55.8	60.6	67	55.8	88.7	82.1			21	0.262	
20140416	CAS64	plagioclase	216	211	194	160	130	190	235	176	152		129	98.6	82.3	68.4	57.9	4.34			1.28	0.019	9
20140416	CAS64	plagioclase_stdev	13.4	11.7	8.92	6.77	4.39	5.87	8.26	7.59	7.07		6.29	5.18	4.59	3.48	3.03	0.538			0.236		
20140416	CAS64	melt	2080	2560	2400	2080	2150	2350	4710	4480	4660		4660	4290	4530	4570	4480	4490			2210	8.57	4
20140416	CAS64	melt_stdev	15.5	15.8	3.59	9.57	16.6	6.75	22.1	11.4	10.1		20.3	14.9	21.9	33.5	16.7	30.6			12.5	0.977	
20140428	CAS30	plagioclase	585	445	469	375	275	330	512	394	339		291	241	188	167	138	13.1			7.55	0.0499	9
20140428	CAS30	plagioclase_stdev	34.1	30.9	30.8	23.5	17.9	26.2	41.1	35.9	34.5		30.9	27.8	22.8	23.1	19.2	1.6			1.12	0.0236	
20140428	CAS30	melt	2170	2450	2500	2200	2130	2460	4950	4800	4920		4930	4900	4750	5040	4840	4760			2510	156	4
20140428	CAS30	melt_stdev	26	100	27.7	23.1	22.4	24.7	59.7	38	55		40.5	31.7	31.8	36.1	36.3	33			13.3	175	
20140428	CAS45	plagioclase	128	94.4	94.1	73.6	55.2	64.9	90.1	63.4	54.2		43.8	35.2	27.5	23.2	20.9	4.95			0.524	0.0366	10
20140428	CAS45	plagioclase_stdev	32.3	24.4	23.4	18.1	13.7	16.7	23.9	16.9	14.7		12.3	10.2	7.76	6.25	5.61	1.02			0.231	0.0444	
20140428	CAS45	melt	2420	2620	2660	2330	2520	2680	5470	5150	5410		5300	5290	5190	5270	5290	5240			2560	53.5	4
20140428	CAS45	melt_stdev	15.7	35.6	16.6	13.6	26.5	9.81	52.4	40.4	40.5		38.4	31.2	50.1	15.2	36.3	30.2			21.2	1.62	
20140428	CAS64	plagioclase	231	221	203	167	135	204	246	183	158		135	104	86	71.7	61.2	7.57			2.51	0.389	8
20140428	CAS64	plagioclase_stdev	14.4	12.4	12.1	11.6	10.6	8.72	17.6	17.3	15.4		13.5	11.8	9.82	8.67	7.89	3.11			1.8	0.661	
20140428	CAS64	melt	2660	3290	3100	2710	2820	3090	6170	5900	6190		6160	5760	6080	6170	5970	5980			2950	16.2	4
20140428	CAS64	melt_stdev	18.2	25.9	44.3	26.4	20.4	28.3	45.5	65	71.4		48.6	47.2	48.6	75.5	58.3	58.5			37.9	2.1	
20140804	CAS30	plagioclase	249	207	206	171	136	150	257	207	184		160	141	115	105	92.4	27.1			17.5	3.83	9
20140804	CAS30	plagioclase_stdev	23.9	26.2	25.9	25.4	24.9	24.8	51.2	46.8	45.5		43.4	39.9	34.5	35	31.8	16.1			10.4	2.88	
20140804	CAS30	melt	550	681	635	570	584	679	1310	1300	1350		1330	1360	1320	1380	1350	1410			724	267	4
20140804	CAS30	melt_stdev	2.77	3.07	3.7	2.66	4.14	5.44	9.68	18.3	16.1		16.5	21.7	16.5	18.7	21	22.7			8.85	16.1	
20140804	CAS45	plagioclase	37.1	28.4	27.2	21.5	15.1	19.8	26.1	19	16		13.4	11.1	8.56	7.35	6.48	1.7			0.171	0.00108	12
20140804	CAS45	plagioclase_stdev	6.06	4.92	4.38	3.5	2.67	3.04	4.58	3.25	2.86		2.4	2.09	1.64	1.45	1.24	0.364			0.0814	0.00375	
20140804	CAS45	melt	666	758	734	660	667	766	1510	1450	1510		1510	1530	1470	1500	1480	1480			732	105	5
20140804	CAS45	melt_stdev	7.41	6.04	8.63	10.5	5.56	10.3	20.5	23.2	23.8		21.4	21.6	24.8	27.3	22	21.1			12.6	1.98	
20140804	CAS64	plagioclase	68.2	63.8	58.7	49.9	40	62.9	77.7	59.3	52.4		44.7	37.7	28.9	24.5	21.1	1.37			0.491	0.008	11
20140804	CAS64	plagioclase_stdev	5.05	5.04	4.65	4.77	3.66	5.67	7.02	5.32	4.65		3.78	3.64	2.65	2.14	2.14	0.166			0.0488	0.0189	
20140804	CAS64	melt	762	887	833	744	759	851	1720	1670	1760		1730	1760	1700	1750	1730	1710			852	134	5
20140804	CAS64	melt_stdev	8.67	6.47	8.34	9.34	12.4	5.72	16.7	12.1	16.6		16.5	22.5	18.6	18.3	14.2	21.9			7.44	87.1	
20141014	CAS30	plagioclase	151	145	125	102	80.2	214	146	115	102	0.565	86.3	74.4	58.1	54.8	42.7	4			2.1	0.681	12
20141014	CAS30	plagioclase_stdev	11.6	13.3	13.3	11.8	10.4	29.6	20.4	17.4	16.7	0.16	14.6	13.2	10.9	11.7	8.23	0.475			0.248	0.251	
20141014	CAS30	melt	619	764	725	632	637	701	1420	1380	1430	9.35	1420	1450	1390	1450	1410	1460			742	918	4
20141014	CAS30	melt_stdev	6.55	8.45	8.46	9.98	5.2	7.59	25.6	30	21.9	0.192	31.3	21.6	34.7	29	30.1	20.8			16.9	13.1	
20141014	CAS45	plagioclase	32.8	29.8	24.2	19.3	13.9	103	23.4	17.2	14.5	1.95	11.8	9.7	7.66	6.95	5.89	1.49			0.124	0.0566	11

Run	Label	type	La_ppm	Ce_ppm	Pr_ppm	Nd_ppm	Sm_ppm	Eu_ppm	Gd_ppm	Tb_ppm	Dy_ppm	Y_ppm	Ho_ppm	Er_ppm	Tm_ppm	Yb_ppm	Lu_ppm	Hf_ppm	Ta_ppm	Pb_ppm	Th_ppm	U_ppm	trace (count)
20141014	CAS45	plagioclase_stdev	6.02	5.47	4.41	3.68	2.66	9.37	4.06	3.23	2.6	0.448	2.29	2.01	1.56	1.55	1.11	0.341			0.0461	0.0167	
20141014	CAS45	melt	687	827	775	677	683	740	1510	1450	1510	251	1480	1520	1460	1520	1470	1480			738	1070	4
20141014	CAS45	melt_stdev	11.4	14.6	15.1	11.3	11.7	14	29	32	33.9	3.76	28.3	29.9	28.9	39.6	31.7	38.1			20.4	136	
20150112	CAS30	plagioclase	14.9	2.54	0.0959	9.95	7.39	7.61	5.83	0.00645	0.068	0.995	0.00113	bdl	bdl	0.001	0.00105	bdl			0.0012	0.0036	12
20150112	CAS30	plagioclase_stdev	1.1	0.281	0.0143	0.687	0.64	0.82	0.528	0.00544		0.131	0.000757				0.0012						
20150112	CAS30	melt	69.9	31.7	0.714	72.9	72.4	72	73.6	0.15	0.264	21.7	0.158	0.237	0.122	0.342	0.148	1.63			0.607	3.92	6
20150112	CAS30	melt_stdev	1.14	16.9	0.036	1.47	1.61	1.08	1.21	0.0153	0.0451	0.215	0.0285	0.0549	0.0162	0.0394	0.0195	0.0572			0.0253	2.2	
20150112	CAS45	plagioclase	2.72	0.616	0.0335	1.68	1.2	1.42	0.904	0.0081	bdl	1.35	0.034	bdl	0.03	bdl	0.015	bdl			bdl	0.046	12
20150112	CAS45	plagioclase_stdev	0.524	0.225	0.011	0.464	0.385	0.297	0.419	0.0093		0.752											
20150112	CAS45	melt	71.1	57.9	1.43	70.3	69.7	70.7	74.1	0.919	1.04	183	1.02	1.16	0.883	1.04	0.883	1.65			0.882	2.09	6
20150112	CAS45	melt_stdev	0.356	1.2	0.0706	0.79	0.903	0.426	1.03	0.0408	0.0674	1.3	0.0535	0.0909	0.0391	0.0692	0.019	0.0816			0.0476	0.0684	
20150112	CAS64	plagioclase	7.21	1.89	0.0547	5.47	4.28	6.09	3.65	0.012	bdl	0.566	0.0012	0.001	bdl	bdl	bdl	bdl			bdl	bdl	12
20150112	CAS64	plagioclase_stdev	0.788	0.396	0.0199	0.743	0.587	0.861	0.538	0.00714		0.111											
20150112	CAS64	melt	85.1	54.2	0.9	85	86.5	84.4	91.4	0.175	0.495	24.5	0.197	0.393	0.156	0.43	0.148	1.92			1.52	1.48	6
20150112	CAS64	melt_stdev	2.12	14.7	0.0566	2.61	2.88	2.38	3.33	0.0233	0.0991	1.12	0.0199	0.0523	0.0167	0.0513	0.00841	0.139			0.0638	0.794	
20150128	CAS45	plagioclase	13.1	10.4	9.59	7.55	5.57	6.86	9.17	6.74	5.67	0.0456	4.65	3.67	2.99	2.59	2.33	0.544			0.0487	0.015	11
20150128	CAS45	plagioclase_stdev	1.27	1.15	1	0.711	0.887	0.766	1.15	0.875	0.738	0.0203	0.613	0.551	0.346	0.364	0.246	0.083			0.0167		
20150128	CAS45	melt	263	319	287	251	273	289	591	559	583	7.63	573	568	564	572	577	570			279	22.5	6
20150128	CAS45	melt_stdev	4.24	4.6	2.6	4.04	3.64	4.98	9.91	7.82	6.09	0.218	6.61	8.84	8.63	9.65	9	9.15			4.73	0.619	
20150128	CAS64	plagioclase	37.3	42	36	30.3	26.9	42.4	50.6	40.3	38	0.408	34	28.2	26.2	24.5	22.7	13.7			6.49	2.48	12
20150128	CAS64	plagioclase_stdev	5.05	6.66	5.76	4.41	5.06	5.88	10.7	10.2	10.9	0.15	10.9	10.1	11.2	11.6	11.5	11.9			5.73	2.79	
20150128	CAS64	melt	537	726	620	539	579	620	1270	1220	1280	16.9	1290	1210	1280	1290	1270	1260			623	200	6
20150128	CAS64	melt_stdev	9.01	18.3	9.87	8.14	7.54	5.54	19.3	13.6	16	0.367	14.4	14.3	15.4	9.63	13.5	17.2			7.61	60.7	
20150223	CAS30	plagioclase	55	52.6	45.3	36.4	27.6	103	51.6	40.1	34.1	0.229	30.1	25.5	20.4	21.5	15.9	4.63			2.42	3.33	12
20150223	CAS30	plagioclase_stdev	5.93	6.08	5.67	5.53	4.67	11	9.48	8.77	8.28	0.0807	8.21	7.99	6.91	8.58	7.12	6.89			3.4	6.23	
20150223	CAS30	melt	229	274	268	237	234	212	546	524	535	4.67	540	538	523	549	539	529			277	530	6
20150223	CAS30	melt_stdev	2.25	2.02	3.2	1.67	2.91	3	6.55	7.14	5.09	0.127	3.67	7.25	4.52	5.85	6.81	6.23			3.91	5.68	
20150223	CAS45	plagioclase	10.2	9.02	7.34	5.95	4.59	80.7	7.76	5.5	4.57	0.00767	3.94	3.08	2.48	2.5	1.93	0.462			0.118	0.189	11
20150223	CAS45	plagioclase_stdev	2.21	1.91	1.52	1.4	1.03	2.11	1.67	1.26	1.07	0.00929	0.876	0.679	0.489	0.478	0.288	0.144			0.103	0.262	
20150223	CAS45	melt	250	283	270	242	259	224	571	535	554	5.27	549	546	538	544	549	544			265	522	6
20150223	CAS45	melt_stdev	1.45	2.09	2	2.52	3.22	1.78	7.06	3.7	3.66	0.168	2.83	5.35	5.11	2.81	5.88	4.27			2.7	14.2	
20150428	CAS37	plagioclase	27.6	22.9	21.3	17.7	13.4	14.8	22	16.4	13.9	0.124	12	10.1	8.22	7.52	6.4	2.54			1.29	0.228	10
20150428	CAS37	plagioclase_stdev	4.18	3.85	3.4	2.87	2.23	2.41	4.02	2.99	2.62	0.047	2.47	2.3	2.05	2.32	1.88	1.45			0.906	0.212	
20150428	CAS37	melt	242	295	271	243	255	275	522	504	518	6.25	507	499	498	508	507	507			259	22.4	6
20150428	CAS37	melt_stdev	1.4	1.38	3.06	1.93	1.46	3.09	2.76	2.85	3.19	0.174	2.31	4.39	5.58	2.8	5.49	3.52			2.23	0.537	
20150428	CAS37	plagioclase	74.6	55.4	56.9	44.3	31.6	35.1	52.7	38.2	31.5	0.199	25.9	21.1	15.5	13.3	10.9	2.33			0.678	0.0293	12
20150428	CAS37	plagioclase_stdev	6.17	6.21	5.51	4.62	3.43	4.89	6.02	4.91	4.15	0.0477	3.78	3.28	2.52	2.17	1.74	0.948			0.468	0.0146	
20150428	CAS37	melt	712	831	812	716	720	841	1560	1510	1550	11.6	1550	1560	1500	1570	1500	1530			801	20.9	6
20150428	CAS37	melt_stdev	10.6	9.79	13.1	12.9	9.54	12.5	19.5	17.9	22.7	0.3	20.4	19.2	17.3	24.3	18.7	15			9.63	0.4	

Run	Label	type	La_ppm	Ce_ppm	Pr_ppm	Nd_ppm	Sm_ppm	Eu_ppm	Gd_ppm	Tb_ppm	Dy_ppm	Y_ppm	Ho_ppm	Er_ppm	Tm_ppm	Yb_ppm	Lu_ppm	Hf_ppm	Ta_ppm	Pb_ppm	Th_ppm	U_ppm	trace (count)
20150428	CAS52	plagioclase	38.9	33.7	30.5	24.6	17.7	27.3	31.2	22.7	18.8	0.126	15.7	13	9.81	8.43	7.21	1.23			0.158	0.021	11
20150428	CAS52	plagioclase_stdev	3.54	3.34	2.96	2.49	2.09	2.09	3.54	2.68	2.36	0.044	1.81	1.42	1.1	1.03	0.848	0.146			0.0602		
20150428	CAS52	melt	766	956	860	758	757	883	1690	1610	1650	15	1640	1690	1590	1660	1620	1610			828	12.5	6
20150428	CAS52	melt_stdev	4.85	11.2	9.2	7.47	9.45	7.05	19.8	24	17.7	0.292	22.5	17.8	17.8	25.5	27.8	22.4			11.8	0.385	
20150428	CAS30	plagioclase	163	129	131	106	80	93	141	108	93.8	0.562	79.9	67.8	52.1	45.8	38.6	5.68			3.52	0.16	12
20150428	CAS30	plagioclase_stdev	18.9	16.7	18.5	16.7	14.5	21.8	27.9	23.7	23	0.163	19.9	18.1	15	13.4	11.9	2.03			1.22	0.335	
20150428	CAS30	melt	596	695	692	609	617	719	1340	1290	1330	9.26	1320	1350	1280	1350	1310	1340			711	18.2	6
20150428	CAS30	melt_stdev	11.3	9.52	14	12.7	9.87	18.4	29.2	31.1	29.3	0.422	26.2	28.3	31.6	30.6	30.7	42.7			16.2	1.05	
20150616	CAS30	plagioclase	147	142	120	97.8	77.1	276	141	111	98.2	1.05	85.4	75.4	61.8	63.6	49.3	20.2	0.0478	0.075	10.3	17	7
20150616	CAS30	plagioclase_stdev	16.7	18.1	16.5	15.2	14.7	29.5	31.6	30.8	31.9	0.39	30.2	31.3	31.4	31.8	32.4	37.2	0.0768	0.0503	18.8	34.5	
20150616	CAS30	melt	634	756	725	643	660	644	1470	1440	1490	17.6	1470	1510	1450	1520	1480	1510	2.3	0.0255	773	1480	4
20150616	CAS30	melt_stdev	5.91	6.45	5.42	6.32	4.21	2.87	17.3	14.5	16.6	0.195	15.7	22.4	15.9	12.2	20.5	32.5	0.137	0.0276	10.2	45.7	
20150616	CAS37	plagioclase	78.6	73.1	59.6	47.6	35.9	236	61.3	46.5	39.6	0.358	33.3	27.5	21.2	19.8	15.3	2.61	0.0011	0.03	0.73	0.505	7
20150616	CAS37	plagioclase_stdev	4.95	4.31	3.3	2.84	2.59	6.71	3.53	2.75	2.31	0.0486	2.21	2.07	1.35	1.94	1.12	0.533		0.0198	0.248	0.287	
20150616	CAS37	melt	792	927	878	779	796	724	1770	1740	1800	18.7	1790	1820	1770	1830	1780	1790	3.56	0.065	910	1760	4
20150616	CAS37	melt_stdev	25.3	27.7	26.1	19.5	24.6	19.5	49.8	49.5	53.3	0.447	56.6	57.1	51.4	61.5	56.7	70.1	0.165	0.0679	26.1	202	
20150616	CAS45	plagioclase	22.7	20.9	16.8	13.5	9.38	204	15.7	11.3	9.26	0.0547	7.61	6.28	4.98	4.85	3.99	1.03	0.0039	0.027	0.108	0.147	4
20150616	CAS45	plagioclase_stdev	2.91	2.72	2.2	2.2	1.32	4.33	2.39	1.69	1.22	0.0181	1.06	0.897	0.448	0.344	0.24	0.08		0.002	0.0807	0.189	
20150616	CAS45	melt	738	852	809	726	735	693	1640	1590	1640	16	1620	1650	1590	1660	1600	1580	2.35	0.042	810	1580	6
20150616	CAS45	melt_stdev	5.74	4.61	5.57	2.61	7.33	3.98	12.4	11.7	15.4	0.185	8.96	19	15.7	17.1	18.8	13.3	0.085	0.0312	6.65	37.4	
20150616	CAS64	plagioclase	68.1	69.7	60.4	51.1	42.3	346	79.2	61	54.3	0.588	46.9	39.8	31.1	33.6	23.7	5.12	0.0281	0.032	2.44	4.43	7
20150616	CAS64	plagioclase_stdev	7.13	7.19	6.32	5.88	4.42	18.9	8.36	7.53	6.94	0.103	7.19	6.83	6.22	6.17	6.62	8.24	0.0381	0.0275	4.47	8.01	
20150616	CAS64	melt	873	1030	965	863	890	629	2010	1930	2050	26.9	2040	2100	2010	2080	2030	2000	3.47	0.02	1030	1850	4
20150616	CAS64	melt_stdev	23.6	21	21.6	17.3	22	8.27	46.4	45.6	42.7	0.629	41.5	50.5	49.5	42.6	49.1	25.4	0.122	0.0278	18.9	237	
c4791	CAS30	plagioclase	7.82			4.89	3.77	19.2	2.88			0.427											12
c4791	CAS30	plagioclase_stdev	0.347			0.449	0.427	0.544	0.325			0.0703											
c4791	CAS30	melt	67.4			68.6	67.3	60.9	67.7			16.7											6
c4791	CAS30	melt_stdev	4.84			5.87	5.79	3.45	5.8			1.37											
c4828	CAS64	plagioclase	18.6	20	17.2	14.5	12.6	101	22.1	17.4	15.4	0.14	13.5	10.6	9	8.49	6.51	0.335	bdl	0.134	0.143	0.185	7
c4828	CAS64	plagioclase_stdev	2.68	2.66	2.29	2	1.22	8.03	2.8	2.18	2.07	0.0161	1.63	1.33	1.13	1.17	0.679	0.089		0.0411	0.042	0.0408	
c4828	CAS64	melt	232	283	263	228	241	212	511	489	510	5.76	511	473	498	504	495	485	0.763	0.465	245	529	4
c4828	CAS64	melt_stdev	8.02	10.4	9.23	9.04	8.88	3.63	15.7	15.6	18.6	0.319	13.8	12.7	14.7	18.8	15.9	17.9	0.0386	0.0733	8.08	19.3	
c4856	CAS45	plagioclase	8.13	7.19	6.04	4.7	3.77	54.6	6.61	4.83	4.12	0.006	3.52	2.87	2.32	2.29	1.95	0.702			0.366	0.82	11
c4856	CAS45	plagioclase_stdev	1.41	1.24	1.03	0.72	0.44	3.07	1.05	0.818	0.76		0.855	0.824	0.695	0.736	0.777	0.955			0.6	1.09	
c4856	CAS45	melt	188	202	198	175	191	188	411	387	405	7.85	396	397	390	393	399	396			192	395	6
c4856	CAS45	melt_stdev	5.54	5.37	6.06	5.25	3.78	2.84	12.7	12.2	12.5	3.38	10.3	12.4	9.92	9.96	11.2	10.9			4.69	9.53	
c4874	CAS37	plagioclase	23.4	20.6	18	14.7	11.3	57.9	18.5	13.7	12	0.0789	9.95	7.93	6.34	5.49	4.57	0.522			0.181	0.0981	12
c4874	CAS37	plagioclase_stdev	1.71	1.53	1.12	1.06	0.952	2.4	1.45	1.09	1.09	0.0465	1.04	0.822	0.761	0.856	0.586	0.157			0.0505	0.057	

Run	Label	type	La_ppm	Ce_ppm	Pr_ppm	Nd_ppm	Sm_ppm	Eu_ppm	Gd_ppm	Tb_ppm	Dy_ppm	Y_ppm	Ho_ppm	Er_ppm	Tm_ppm	Yb_ppm	Lu_ppm	Hf_ppm	Ta_ppm	Pb_ppm	Th_ppm	U_ppm	trace (count)
c4874	CAS37	melt	191	211	208	181	195	190	402	384	402	3.77	390	387	380	390	389	396			199	406	6
c4874	CAS37	melt_stdev	4.34	4.19	3.94	3.15	4.03	1.4	8.72	7.04	9.01	0.25	8.27	9.63	6.79	8.09	11	30.8			9.97	19.1	
c4970	CAS52	plagioclase	21.6	21.4	18.3	15.2	11.5	207	20.9	16.2	13.9	0.0716	11.8	9.98	7.76	7.91	5.82	0.644	bdl	0.0912	0.102	0.15	7
c4970	CAS52	plagioclase_stdev	2.24	2.02	1.73	1.52	1.3	5.92	1.52	1.4	1.26	0.0173	1.04	1.03	0.679	0.728	0.522	0.131		0.0421	0.0359	0.0509	
c4970	CAS52	melt	468	539	508	452	455	501	1010	972	1010	23.4	998	1020	973	1010	974	923	1.41	0.19	478	1020	4
c4970	CAS52	melt_stdev	2.25	4.94	3.15	5.07	6.01	3.23	7.41	11.3	9.11	1.87	5.26	3.3	5.12	6.88	4.32	5.19	0.123	0.0664	5.68	10.1	

Table 40: CaO-MgO-Al_2O_3-SiO_2 system experiments. Experimental conditions, average and standard deviations (stdev) of the major elements in each phase

Run	comp.	type	T1	T2	fO2	P	time	Label	System	Na2O	MgO	Al2O3	SiO2	CaO	FeO	Total	major (count)
20140604	LS008	diopside	1350	1304	air	1 atm	154		CMAS		20	0.533	52.9	23.6		97.2	
20140604	LS008	diopside_stdev	1350	1304	air	1 atm	154		CMAS		0.235	0.127	0.847	0.282		1.07	
20140604	LS008	melt	1350	1304	air	1 atm	154		CMAS		10.9	3.94	43.1	17.6		75.6	
20140604	LS008	melt_stdev	1350	1304	air	1 atm	154		CMAS		0.158	0.0479	0.642	0.131		0.688	
20140701	LS008	diopside	1351	1288	air	1atm	155		CMAS		18.6	0.666	53.5	23.1		96.2	5
20140701	LS008	diopside_stdev	1351	1288	air	1atm	155		CMAS		0.138	0.0709	0.478	0.262		0.906	
20140701	LS008	melt	1351	1288	air	1atm	155		CMAS		9.49	4.47	40	16.8		71.5	3
20140701	LS008	melt_stdev	1351	1288	air	1atm	155		CMAS		0.218	0.0781	0.593	0.235		1.24	
20140701	LS009	diopside	1351	1288	air	1atm	155		CMAS		19.2	0.923	54.9	23.7		99.2	3
20140701	LS009	diopside_stdev	1351	1288	air	1atm	155		CMAS		0.238	0.0153	0.636	0.455		1.18	
20140701	LS009	melt	1351	1288	air	1atm	155		CMAS		11.1	6.72	41.4	17.7		77.4	3
20140701	LS009	melt_stdev	1351	1288	air	1atm	155		CMAS		0.107	0.0929	0.114	0.14		0.162	
20140718	LS008	diopside	1352	1278	air	1 atm	150		CMAS		19.4	0.656	55.2	23.5		99.1	7
20140718	LS008	diopside_stdev	1352	1278	air	1 atm	150		CMAS		0.292	0.126	0.539	0.26		0.875	
20140718	LS008	melt	1352	1278	air	1 atm	150		CMAS		8.58	4.53	37.6	15.9		67.3	4
20140718	LS008	melt_stdev	1352	1278	air	1 atm	150		CMAS		0.217	0.11	0.505	0.341		1.1	
20140718	LS009	diopside	1352	1278	air	1 atm	150		CMAS		18.9	1.42	54.3	23.4		98.3	1
20140718	LS009	diopside_stdev	1352	1278	air	1 atm	150		CMAS								
20140718	LS009	melt	1352	1278	air	1 atm	150		CMAS		10.6	7.32	40.9	17.1		76.6	1
20140718	LS009	melt_stdev	1352	1278	air	1 atm	150		CMAS								
20140828	LS909	diopside	1351	1300	air	1 atm	154		CMAS		19.7	1.52	55.4	23.2		100	9
20140828	LS909	diopside_stdev	1351	1300	air	1 atm	154		CMAS		0.195	0.227	0.703	0.47		1.06	
20140828	LS909	melt	1351	1300	air	1 atm	154		CMAS		11.4	11.7	54.1	19.7		97.3	3
20140828	LS909	melt_stdev	1351	1300	air	1 atm	154		CMAS		0.106	0.187	0.471	0.124		0.543	
20140828	LS910	diopside	1351	1300	air	1 atm	154		CMAS		20.6	1.96	55	22.5		100	9
20140828	LS910	diopside_stdev	1351	1300	air	1 atm	154		CMAS		0.203	0.199	0.222	0.199			
20140828	LS910	melt	1351	1300	air	1 atm	154		CMAS		14.6	12.7	52.9	19.8		100	6
20140828	LS910	melt_stdev	1351	1300	air	1 atm	154		CMAS		0.133	0.161	0.157	0.144			
20141111	LS909	diopside	1350	1303	air	1 atm	164		CMAS		19.9	1.3	55	22.9		99.2	8
20141111	LS909	diopside_stdev	1350	1303	air	1 atm	164		CMAS		0.285	0.264	0.944	0.582		1.75	
20141111	LS909	melt	1350	1303	air	1 atm	164		CMAS		11.7	10.9	52.6	19.1		94.3	8
20141111	LS909	melt_stdev	1350	1303	air	1 atm	164		CMAS		0.147	0.119	0.803	0.359		1.36	
20141111	LS910	diopside	1350	1303	air	1 atm	164		CMAS		20.2	1.31	54.6	22.4		98.5	9
20141111	LS910	diopside_stdev	1350	1303	air	1 atm	164		CMAS		0.515	0.268	0.863	0.319		1.49	
20141111	LS910	melt	1350	1303	air	1 atm	164		CMAS		13.9	11.6	50.8	19		95.4	5
20141111	LS910	melt_stdev	1350	1303	air	1 atm	164		CMAS		0.352	0.309	1.33	0.674		2.64	
20150306	LS029	diopside	1353	1305	air	1 atm	62		CMAS	0.045	20.9	1.27	55.7	22.1		100	8
20150306	LS029	diopside_stdev	1353	1305	air	1 atm	62		CMAS	0.0655	0.342	0.401	0.434	0.351			
20150306	LS029	melt	1353	1305	air	1 atm	62		CMAS	0.113	13.5	12	54.8	19.6		100	4
20150306	LS029	melt_stdev	1353	1305	air	1 atm	62		CMAS	0.0741	0.156	0.229	0.563	0.426			
20150402	LS031	plagioclase	1301	1265	air	1 atm	58 h		CMAS	0.265	0.627	35.2	44.5	19.8		100	11
20150402	LS031	plagioclase_stdev	1301	1265	air	1 atm	58 h		CMAS	0.0193	0.052	0.544	0.621	0.0818		0.975	
20150402	LS031	diopside	1301	1265	air	1 atm	58 h		CMAS	0.0409	18.2	4.67	53.1	24.4	0.0303	100	6
20150402	LS031	diopside_stdev	1301	1265	air	1 atm	58 h		CMAS	0.0117	0.148	0.394	0.508	0.171		0.72	
20150402	LS031	melt	1301	1265	air	1 atm	58 h		CMAS	0.244	11.6	16.2	51.3	20.8	0.036	100	4
20150402	LS031	melt_stdev	1301	1265	air	1 atm	58 h		CMAS	0.0131	0.117	0.17	0.262	0.0429	0.000901	0.475	

Run	comp.	type	T1	T2	fO2	P	time	Label	System	Na2O	MgO	Al2O3	SiO2	CaO	FeO	Total	major (count)
20151113	2b-4-1a	plagioclase	1412	1332	air	1 atm	76	CMAS8	CMAS	0.13	0.274	36.7	43	19.8	bdl	100	6
20151113	2b-4-1a	plagioclase_stdev	1412	1332	air	1 atm	76	CMAS8	CMAS	0.0236	0.0188	0.519	1.04	0.107		1.51	
20151113	2b-4-1a	melt	1412	1332	air	1 atm	76	CMAS8	CMAS	0.116	8.16	18.7	46.5	25.6	0.128	99.2	6
20151113	2b-4-1a	melt_stdev	1412	1332	air	1 atm	76	CMAS8	CMAS	0.0103	0.095	0.0983	0.184	0.209	0.0225	0.479	
20151113	2b-5-1a	plagioclase	1412	1332	air	1 atm	76	CMAS10	CMAS	0.132	0.278	36.4	42.8	19.8	bdl	99.4	5
20151113	2b-5-1a	plagioclase_stdev	1412	1332	air	1 atm	76	CMAS10	CMAS	0.00599	0.024	0.279	0.407	0.151		0.815	
20151113	2b-5-1a	melt	1412	1332	air	1 atm	76	CMAS10	CMAS	0.123	9.88	19.5	46.1	23.6	0.141	99.3	6
20151113	2b-5-1a	melt_stdev	1412	1332	air	1 atm	76	CMAS10	CMAS	0.0109	0.0345	0.054	0.207	0.117	0.0243	0.317	
20151113	2b-6-1a	plagioclase	1412	1332	air	1 atm	76	CMAS12	CMAS	0.143	0.31	36.7	42.9	19.7	bdl	99.8	6
20151113	2b-6-1a	plagioclase_stdev	1412	1332	air	1 atm	76	CMAS12	CMAS	0.0105	0.0208	0.441	0.646	0.319		1.35	
20151113	2b-6-1a	melt	1412	1332	air	1 atm	76	CMAS12	CMAS	0.152	13.8	22	45.5	18.3	0.108	99.8	6
20151113	2b-6-1a	melt_stdev	1412	1332	air	1 atm	76	CMAS12	CMAS	0.00967	0.0999	0.115	0.207	0.0886	0.0181	0.199	
20151113	2b-7-1a	plagioclase	1412	1332	air	1 atm	76	CMAS14	CMAS	0.142	0.281	36.7	42.9	19.8	bdl	99.8	6
20151113	2b-7-1a	plagioclase_stdev	1412	1332	air	1 atm	76	CMAS14	CMAS	0.0121	0.0249	0.69	0.615	0.35		1.65	
20151113	2b-7-1a	melt	1412	1332	air	1 atm	76	CMAS14	CMAS	0.126	11.7	20.1	45.6	21.2	0.137	98.9	6
20151113	2b-7-1a	melt_stdev	1412	1332	air	1 atm	76	CMAS14	CMAS	0.00933	0.0497	0.0734	0.14	0.168	0.0385	0.345	

Table 41: CaO-MgO-Al_2O_3-SiO_2 system experiments. Trace element analysis of experimental phases from mass 7 (Li) to mass 139 (Ba)

Run	comp.	type	Li_ppm	Be_ppm	Na_ppm	Mg_ppm	Al_ppm	Si_ppm	K_ppm	Ca_ppm	Sc_ppm	Fe_ppm	V_ppm	Cr_ppm	Ga_ppm	Rb_ppm	Sr_ppm	Zr_ppm	Nb_ppm	In_ppm	Cs_ppm	Ba_ppm
20140604	LS008	diopside			99.1	107000	2950	262000	1.01		1670						1500		11.2			4.52
20140604	LS008	diopside_stdev			8.92	1810	434	3030	2.27		300						52		3.91			1.15
20140604	LS008	melt			301	61100	22800	211000	32.4		1810						11900		12100			12100
20140604	LS008	melt_stdev			3.44	370	128	1760	8.7		10.5						69.5		57.4			43.2
20140701	LS008	diopside			107	102000	3490	246000	3.84		1610						1600		10.2			4.76
20140701	LS008	diopside_stdev			9.13	2530	343	6460	4.54		262						107		3.05			2.61
20140701	LS008	melt			331	55900	25600	192000	39.6		1770						13400		14000			14000
20140701	LS008	melt_stdev			4.79	248	231	930	11.2		11.7						74.6		68.5			105
20140701	LS009	diopside			88.8	107000	6520	258000	4.76		1920						1210		11.5			2.56
20140701	LS009	diopside_stdev			8.19	2080	1330	7600	5.6		421						55.9		3.34			0.41
20140701	LS009	melt			424	65700	39600	204000	59.1		1720						9760		10200			10200
20140701	LS009	melt_stdev			3.67	524	221	2220	9.74		10.9						84.1		84.7			65.3
20140718	LS008	diopside			116	106000	4030	256000	6.65		1750						1720		11.2			4.17
20140718	LS008	diopside_stdev			14.6	925	573	2310	7.31		261						146		3.8			0.313
20140718	LS008	melt			325	51100	26000	186000	53.1		1680						13600		14300			14600
20140718	LS008	melt_stdev			7.34	550	227	2240	6.38		17.8						189		136			129
20140718	LS009	diopside			96.2	106000	7790	251000	3.3		1990						1350		55.9			65.6
20140718	LS009	diopside_stdev			7.35	1630	170	2620	4.67		67.9						92.6		60.9			88.3
20140718	LS009	melt			424	61400	40900	200000	68		1570						10400		10900			10700
20140718	LS009	melt_stdev			6.18	709	510	2300	9.47		22.6						88.4		85.5			118
20140828	LS909	diopside			73	25400	8310	269000	0.473		158	280					117		10.2			0.258
20140828	LS909	diopside_stdev			9.76	666	1060	5980	1.57		21.4	15.1					6.45		4.4			0.241
20140828	LS909	melt			767	14900	66400	271000	211		79.9	448					1550		1660			1710
20140828	LS909	melt_stdev			10.2	118	191	1420	10.1		0.73	18.1					9.54		7.27			9.54
20140828	LS910	diopside			50.4	25000	9620	266000			158	358					95.8		3.41			0.115
20140828	LS910	diopside_stdev			4.54	465	996	4780			24.5	10.8					2.74		1.6			0.0604
20140828	LS910	melt			613	17200	67300	256000	126		95	593					1130		1160			1200
20140828	LS910	melt_stdev			12.9	369	465	4420	4.93		1.74	22.4					12.9		6.95			15.2
20141111	LS909	diopside			62	108000	6760	262000	bdl		122	226					119		5.21			0.636
20141111	LS909	diopside_stdev			7.41	1730	1480	3810	bdl		25	7.95					4.58		3.95			1.46
20141111	LS909	melt			790	66600	60600	261000	191		85.9	626					1430		1550			1580
20141111	LS909	melt_stdev			14.5	971	679	4160	3.64		2.18	24.9					18		21			19.8
20141111	LS910	diopside			50.7	109000	6240	257000	bdl		124	251					87.1		1.96			0.134
20141111	LS910	diopside_stdev			4.29	2630	1500	3680	bdl		22.2	12					6.37		0.319			0.0451
20141111	LS910	melt			629	78300	64300	252000	124		99	518					1090		1100			1140
20141111	LS910	melt_stdev			11.7	918	587	4470	3.66		1.8	17.8					11.9		14.4			18.3

Run	comp.	type	Li_ppm	Be_ppm	Na_ppm	Mg_ppm	Al_ppm	Si_ppm	K_ppm	Ca_ppm	Sc_ppm	Fe_ppm	V_ppm	Cr_ppm	Ga_ppm	Rb_ppm	Sr_ppm	Zr_ppm	Nb_ppm	In_ppm	Cs_ppm	Ba_ppm
20150306	LS029	diopside			72.4	103000	6870	252000	bdl		123	241					47.3		1.42			0.033
20150306	LS029	diopside_stdev			4.27	1070	610	1450	bdl		13.2	13.4					0.825		0.504			bdl
20150306	LS029	melt			956	71700	63300	268000	144		77.7	358					606		540			551
20150306	LS029	melt_stdev			31.3	800	762	3420	13		1.08	18.2					7.68		2.72			13.5
20150402	LS031	plagioclase			2250	3930	202000	248000	50.6		4.81	215					582		0.697			104
20150402	LS031	plagioclase_stdev			128	200	1320	3330	7.46		0.454	14.3					28.7		1.23			11.3
20150402	LS031	diopside			122	104000	23800	255000			201	335					39		6.01			0.28
20150402	LS031	diopside_stdev			10.6	5050	3300	6470			43.4	17.8					2.86		2.59			0.167
20150402	LS031	melt			2130	64900	88900	259000	317		51.8	401					608		904			894
20150402	LS031	melt_stdev			32.1	1050	1330	2070	11.7		1.22	11.9					8.75		27.3			31.4
20151113	2b-4-1a	plagioclase	0.998	0.923	1160	2100	201000	253000	69.6	141000	3.06		0.107	bdl	75.2	bdl	803	0.0223	0.339	0.0894	bdl	101
20151113	2b-4-1a	plagioclase_stdev	0.12	0.18	134	55	1990	4180	6.63	1120	0.191				4.49		30.9	0.0268	0.369	0.0318		13
20151113	2b-4-1a	melt	6.23	16.4	1000	50100	107000	269000	167	182000	65.1		41.2	bdl	161	1.36	799	69.4	641	2.34	bdl	659
20151113	2b-4-1a	melt_stdev	0.486	0.437	11.7	321	733	1290	3.41	543	0.718		0.773		3.27	0.111	4.44	1.08	5.27	0.0971		6.23
20151113	2b-5-1a	plagioclase	1.26	0.612	1120	2020	205000	255000	72.9	143000	2.86		0.062	bdl	65.3	bdl	887	0.036	0.264	0.0887	bdl	122
20151113	2b-5-1a	plagioclase_stdev	0.169	0.191	68.8	41.5	1190	3630	11.4	1340	0.147		0.0636		1.25		24.3	0.0509	0.0645	0.0255		12
20151113	2b-5-1a	melt	5.82	15.4	1060	60100	110000	263000	164	168000	66		38.6	bdl	143	1.35	812	67.4	661	2.33	bdl	661
20151113	2b-5-1a	melt_stdev	0.157	0.914	16.5	611	687	3110	5.19	719	0.643		0.57		1.73	0.112	6.42	0.841	5.88	0.0415		3.15
20151113	2b-6-1a	plagioclase	1.02	0.473	1130	2230	202000	250000	75.5	140000	2.62		0.0922	bdl	76.5	bdl	1260	0.0877	0.262	0.074	bdl	137
20151113	2b-6-1a	plagioclase_stdev	0.183	0.13	72.3	62.5	1590	4300	5.84	1290	0.15		0.0168		2.69		36.1	0.0729	0.0531	0.0178		9.04
20151113	2b-6-1a	melt	7.07	15	1370	83900	124000	265000	270	131000	61.6		38	bdl	175	1.33	947	67.7	623	2.28	bdl	620
20151113	2b-6-1a	melt_stdev	0.219	0.433	7.78	416	622	1300	5.76	859	0.863		0.821		2.65	0.131	4.09	1	4.79	0.0909		4.35
20151113	2b-7-1a	plagioclase	1.14	0.729	980	1960	201000	249000	55.2	141000	2.45		0.264	bdl	54.9	bdl	982	0.005	0.202	0.0582	bdl	116
20151113	2b-7-1a	plagioclase_stdev	0.251	0.301	164	79.1	2390	4090	11.2	1610	0.205		0.0568		3.25		24.3		0.0631	0.0103		9.16
20151113	2b-7-1a	melt	6.19	16.5	1110	71200	114000	261000	175	151000	75.9		92.8	bdl	172	1.35	861	62.4	638	2.03	bdl	656
20151113	2b-7-1a	melt_stdev	0.168	0.909	6.06	706	684	1830	6.81	945	0.971		4.4		21.5	0.054	5.4	1.18	2.72	0.0904		5.9

Table 42: CaO-MgO-Al_2O_3-SiO_2 system experiments. Trace element analysis of experimental phases from mass 139 (La) to mass 238(U)

Run	comp.	type	La_ppm	Ce_ppm	Pr_ppm	Nd_ppm	Sm_ppm	Eu_ppm	Gd_ppm	Tb_ppm	Dy_ppm	Y_ppm	Ho_ppm	Er_ppm	Tm_ppm	Yb_ppm	Lu_ppm	Hf_ppm	Ta_ppm	Pb_ppm	Th_ppm	U_ppm	trace (count)
20140604	LS008	diopside	225	318	547	638	864	1030	566	516	531		529	530	477	474	509	481			4.03	0.654	11
20140604	LS008	diopside_stdev	41.8	53.8	95.6	113	151	178	102	90.6	92.8		94.5	93.1	84.1	85.7	93.5	221			1.83	0.289	
20140604	LS008	melt	10300	11600	11500	9850	10000	11500	5750	5510	5560		6080	6130	5910	5610	5690	11000			5380	3490	6
20140604	LS008	melt_stdev	38.8	61	50	31.9	60.3	49.4	26.3	36.1	20.6		42.7	53.9	25.8	36.6	28.9	84.3			22.4	13.4	
20140701	LS008	diopside	240	331	574	668	905	1050	575	524	539		538	544	481	484	517	520			4.7	0.767	11
20140701	LS008	diopside_stdev	35.9	45.1	79	91.7	116	139	76.9	69.2	69.2		71.8	72.3	64.6	66.7	75.4	191			1.64	0.925	
20140701	LS008	melt	11900	13400	13300	11600	11800	13300	6730	6500	6560		6910	6970	6860	6430	6570	12900			6340	4360	6
20140701	LS008	melt_stdev	74.2	93.4	33.9	78.7	80.2	91.8	38.4	36.8	43		41.6	48.3	44.2	45	51.7	91.3			27.9	74.1	
20140701	LS009	diopside	264	378	628	733	1020	1240	642	635	641		657	605	537	544	542	702			7.63	0.312	10
20140701	LS009	diopside_stdev	48.7	62.3	100	119	158	193	104	101	105		114	111	104	111	114	348			3.35	0.113	
20140701	LS009	melt	8530	10000	9410	8320	8650	9410	4710	4630	4830		5150	5120	4830	4950	4730	9480			4680	4390	6
20140701	LS009	melt_stdev	35	36.2	38.7	79.2	43.7	53.2	25	39.4	31.7		28.4	45.1	40.4	36	21.8	41.4			25.9	30.1	
20140718	LS008	diopside	270	376	656	758	1010	1200	651	599	612		598	606	544	533	572	609			5.56	0.595	11
20140718	LS008	diopside_stdev	46.1	58.6	103	117	149	178	96.2	87.7	86.5		86.2	88.8	79.2	78.8	82.7	223			2.14	0.247	
20140718	LS008	melt	12100	13700	13500	11700	11900	13400	6770	6550	6570		6950	7070	6880	6500	6640	12800			6430	4650	6
20140718	LS008	melt_stdev	102	168	120	139	111	167	59.4	59.4	70.8		84.7	76.1	70.6	53.3	88.9	94.8			71.9	92.7	
20140718	LS009	diopside	330	498	771	886	1210	1460	748	747	763		769	725	659	653	659	862			23.4	24.1	2
20140718	LS009	diopside_stdev	37.2	62.2	34.6	26.9	3.54	7.78	6.36	14.8	13.4		9.19	14.1	8.49	11.3	12	91.9			18.5	33.4	
20140718	LS009	melt	9030	10700	9830	8660	8930	9770	4840	4770	4960		5260	5260	4920	5050	4790	9630			4860	4420	6
20140718	LS009	melt_stdev	72.3	122	77.7	99.1	80.2	81	47.5	55.3	49.6		59.9	58	55.9	68.3	55	122			54.7	101	
20140828	LS909	diopside	65.7	99.5	156	177	235	291	155	148	153	0.509	152	147	136	139	141	284			5.08	0.184	11
20140828	LS909	diopside_stdev	14.5	20.9	32.8	37.2	49.1	59.9	32.1	31.3	31.6	0.104	31.2	30.7	28.4	29.6	29.4	64.9			1.82	0.126	
20140828	LS909	melt	1240	1480	1360	1180	1150	1320	638	608	636	2.26	645	644	623	651	603	1370			723	420	4
20140828	LS909	melt_stdev	5.32	2.5	5.69	6.5	5.1	10.5	5.68	3.11	6.08	0.147	3.77	1.89	1.89	4.11	4.27	4.57			7.79	27.2	
20140828	LS910	diopside	41.7	70	111	128	184	233	123	122	126	0.358	124	118	110	109	107	176			2.63	0.0411	12
20140828	LS910	diopside_stdev	5.51	7.86	13.9	16.5	24.2	28.9	16.4	16.1	16.2	0.067	16	15.5	14.5	14.8	15	65.9			0.824	0.013	
20140828	LS910	melt	829	1020	934	803	822	943	455	436	459	1.4	461	451	444	455	429	963			489	441	4
20140828	LS910	melt_stdev	6.03	10.9	13.4	10.2	5.68	7.72	6.38	4.22	2.82	0.0379	5.1	6.18	4.77	3.65	4.48	8.06			4.19	6.55	
20141111	LS909	diopside	47.6	76.1	118	133	182	229	121	117	122	0.444	120	114	106	108	107	184			2.73	0.481	12
20141111	LS909	diopside_stdev	11.7	16.8	25.4	27.7	35.3	43.4	23.8	22.4	23.7	0.0973	23.6	21.7	20.9	22.2	22.6	99.5			1.93	1.42	
20141111	LS909	melt	1150	1370	1260	1090	1100	1240	612	581	616	2.45	619	616	596	619	583	1320			680	372	6
20141111	LS909	melt_stdev	10.2	19.9	16.5	14.5	17.9	14.1	7.71	6.07	5.26	0.0656	5.68	9.46	7.6	8.27	7.03	26.6			6.5	53	
20141111	LS910	diopside	30.8	51	83.3	96.5	139	176	93	91.8	95.3	0.263	92.9	88.1	79.5	79.6	76.2	86.6			1.22	0.0225	12
20141111	LS910	diopside_stdev	4.73	7.13	10.9	11.9	16.2	21.2	11.5	12	12.8	0.065	13.1	13.9	13.6	14.4	14.8	34.1			0.487	0.0111	
20141111	LS910	melt	806	979	903	789	813	923	455	436	459	1.45	458	459	443	459	433	965			485	345	6
20141111	LS910	melt_stdev	7.26	13.9	9.67	7.14	10.1	8.1	5.1	4.74	6.07	0.0544	5.37	5.76	4.73	4.99	7.3	12.2			4.54	8.39	
20150306	LS029	diopside	18.1	29	46	55.4	78.1	96.8	50.6	51	51	0.514	54.6	51.4	47.1	47.7	47.1	71.2			0.836	0.0266	4

Run	comp.	type	La_ppm	Ce_ppm	Pr_ppm	Nd_ppm	Sm_ppm	Eu_ppm	Gd_ppm	Tb_ppm	Dy_ppm	Y_ppm	Ho_ppm	Er_ppm	Tm_ppm	Yb_ppm	Lu_ppm	Hf_ppm	Ta_ppm	Pb_ppm	Th_ppm	U_ppm	trace (count)
20150306	LS029	diopside_stdev	2.14	2.64	4.25	5.08	5.92	8.37	4.65	4.26	4.42	0.0635	4.99	4.73	4.4	4.52	4.99	19.7			0.235	0.00856	
20150306	LS029	melt	430	518	471	423	434	483	237	232	236	2.87	254	250	241	247	235	482			243	266	3
20150306	LS029	melt_stdev	6.52	10.6	7.7	7.39	4.38	5.75	5.07	2.86	1.99	0.137	3.42	3.87	2.25	4.71	2.64	4.59			1.51	3.88	
20150402	LS031	plagioclase	13	9.77	10.2	7.64	5.46	6.6	3.06	2.35	1.92	0.0402	1.66	1.36	1.07	0.894	0.765	0.476			0.307	0.592	11
20150402	LS031	plagioclase_stdev	1.86	1.68	1.63	1.21	0.936	1.29	0.723	0.606	0.608	0.025	0.542	0.622	0.443	0.538	0.442	0.621			0.447	0.866	
20150402	LS031	diopside	32.7	52	86.6	96.2	136	173	122	121	125	4.08	122	116	107	108	94.7	268			4.29	0.088	12
20150402	LS031	diopside_stdev	6.78	9.4	14.3	14.3	20.1	23.1	17.7	16.2	16.2	0.734	17.4	16.3	14.5	14.8	12.6	49.6			1.48	0.0631	
20150402	LS031	melt	636	721	681	576	564	629	418	404	413	12.7	412	414	406	429	366	609			389	477	6
20150402	LS031	melt_stdev	19.6	23.3	18.2	15.4	17.2	16.3	14.9	10.1	10.3	0.796	11	11.2	9.97	14	9.42	16.1			15.3	29.5	
20151113	2b-4-1a	plagioclase	20.1	15	15.1	11.7	8.03	10.1	6.85	4.86	4.1	0.0416	3.41	2.64	2.09	1.78	1.53	0.361	bdl	bdl	0.101	0.027	8
20151113	2b-4-1a	plagioclase_stdev	3.46	2.56	2.48	1.72	1.42	1.71	1.25	0.728	0.622	0.0126	0.607	0.516	0.396	0.367	0.324	0.209			0.124	0.0311	
20151113	2b-4-1a	melt	589	668	654	569	579	661	654	627	647	8.06	652	653	629	652	610	589	1.2	0.363	289	17.2	5
20151113	2b-4-1a	melt_stdev	5.85	3.81	4.91	4.56	3.06	6.48	5.5	3.56	4.85	0.156	7.08	6.42	5.41	6.7	4.01	6.43	0.0445	0.0403	2.89	2.35	
20151113	2b-5-1a	plagioclase	28.8	22	21.2	16.9	11.5	14.1	9.46	7.08	5.55	0.0522	4.73	3.87	2.86	2.45	1.99	0.313	bdl	0.806	0.0378	bdl	5
20151113	2b-5-1a	plagioclase_stdev	3.36	2.34	2.2	1.62	1.21	1.33	0.868	0.648	0.703	0.00898	0.458	0.499	0.28	0.266	0.128	0.1		0.305	0.00971		
20151113	2b-5-1a	melt	586	682	649	574	585	665	656	634	653	7.74	651	651	626	651	622	590	1.01	0.856	286	14.1	5
20151113	2b-5-1a	melt_stdev	6.21	3.65	2.64	3.49	3.95	4.67	2.65	3.06	3	0.155	3.86	5.61	3.9	3.65	4.82	3.32	0.0506	0.343	1.52	0.451	
20151113	2b-6-1a	plagioclase	43.3	33.8	32.4	25.8	18	21.1	15.6	10.8	9.04	0.0767	7.39	5.85	4.39	3.58	2.93	0.3	bdl	bdl	0.0696	bdl	9
20151113	2b-6-1a	plagioclase_stdev	3.86	2.91	2.91	1.9	0.818	1.45	0.976	0.756	0.736	0.00847	0.529	0.524	0.377	0.349	0.209	0.0841			0.0382		
20151113	2b-6-1a	melt	567	659	626	552	556	634	636	593	618	7.25	621	616	599	614	579	551	0.962	0.39	264	9.73	5
20151113	2b-6-1a	melt_stdev	3.34	3.72	3.04	4.82	3.62	1.99	4.25	3.18	4.19	0.156	4.82	4.38	3.35	4.49	4.76	6.83	0.0186		3.31	0.262	
20151113	2b-7-1a	plagioclase	31.8	24.8	23.3	18.6	13.1	15.5	11.1	7.86	6.34	0.0559	5.51	4.26	3.19	2.55	2.21	0.211	bdl	bdl	0.0598	bdl	7
20151113	2b-7-1a	plagioclase_stdev	6.49	4.96	4.69	3.83	2.47	2.75	2.27	1.63	1.23	0.0126	1.13	1.04	0.681	0.547	0.467	0.0884			0.0453		
20151113	2b-7-1a	melt	594	689	642	577	586	662	670	636	655	7.35	666	659	621	650	624	587	0.93	0.35	281	11.5	5
20151113	2b-7-1a	melt_stdev	7.28	7.3	6.93	6.46	7.37	8.29	9.83	6.68	8.36	0.186	7.07	9.21	9.71	6.64	8.94	6.25	0.106	0.01	3.12	1.22	

Table 43: CaO-MgO-Al_2O_3-SiO2-Na_2O system experiments. Experimental conditions, average and standard deviations (stdev) of the major elements in each phase

Run	comp.	type	T1	T2	fO2	P	time	System	Na2O	MgO	Al2O3	SiO2	CaO	FeO	Total	major (count)
20160928	Plag 1	plagioclase	1347	1248	air	1 atm	49 h	CMASN	1.67	0.472	33.6	47.3	17.6	0.0346	101	6
20160928	Plag 1	plagioclase_stdev	1347	1248	air	1 atm	49 h	CMASN	0.0606	0.0362	0.314	0.407	0.137		0.738	
20160928	Plag 1	melt	1347	1248	air	1 atm	49 h	CMASN	1.89	9.58	16.3	52	20.3		100	5
20160928	Plag 1	melt_stdev	1347	1248	air	1 atm	49 h	CMASN	0.105	0.219	0.177	0.224	0.326			
20160928	Plag 2	plagioclase	1347	1248	air	1 atm	49 h	CMASN	3.12	0.307	31.7	51	14.9	0.0295	101	6
20160928	Plag 2	plagioclase_stdev	1347	1248	air	1 atm	49 h	CMASN	0.183	0.02	0.293	0.343	0.121		0.686	
20160928	Plag 2	melt	1347	1248	air	1 atm	49 h	CMASN	4.13	6.9	18	55	16	0.0485	100	6
20160928	Plag 2	melt_stdev	1347	1248	air	1 atm	49 h	CMASN	0.0635	0.0371	0.0924	0.364	0.0365	0.00737	0.354	
20160928	Di1	diopside	1347	1248	air	1 atm	49 h	CMASN	0.275	19.8	1.01	55.8	24.1	0.0312	101	6
20160928	Di1	diopside_stdev	1347	1248	air	1 atm	49 h	CMASN	0.0314	0.083	0.137	0.251	0.178	0.000566	0.293	
20160928	Di1	melt	1347	1248	air	1 atm	49 h	CMASN	7.11	6.16	13.5	61.5	11.9	0.0573	100	6
20160928	Di1	melt_stdev	1347	1248	air	1 atm	49 h	CMASN	0.118	0.0623	0.086	0.415	0.0625	0.0126	0.429	
20161008	Plag3	plagioclase	1347	1248	air	1 atm	49 h	CMASN	3.64		30.5	52.4	13.5		100	
20161008	Plag3	plagioclase_stdev	1347	1248	air	1 atm	49 h	CMASN	0.113		0.231	0.394	0.176			
20161008	Plag3	melt	1347	1248	air	1 atm	49 h	CMASN	5.1	5.48	18.6	57.6	13.3		100	
20161008	Plag3	melt_stdev	1347	1248	air	1 atm	49 h	CMASN	0.0974	0.218	0.175	0.26	0.273			
20161008	Plag4	plagioclase	1347	1248	air	1 atm	49 h	CMASN	4.74		29	54.9	11.4		100	
20161008	Plag4	plagioclase_stdev	1347	1248	air	1 atm	49 h	CMASN	0.17		0.0808	0.175	0.282			
20161008	Plag4	melt	1347	1248	air	1 atm	49 h	CMASN	7.55	3.14	20.1	61.3	7.9		100	
20161008	Plag4	melt_stdev	1347	1248	air	1 atm	49 h	CMASN	0.137	0.142	0.181	0.15	0.0443			
20161008	Di2	diopside	1347	1248	air	1 atm	49 h	CMASN	0.207	19.3	1.76	54.5	24.5	0.0349	100	6
20161008	Di2	diopside_stdev	1347	1248	air	1 atm	49 h	CMASN	0.0223	0.113	0.224	0.261	0.202	0.00509	0.175	
20161008	Di2	melt	1347	1248	air	1 atm	49 h	CMASN	4.32	7.16	15.2	55.6	16.5	0.0512	98.9	5
20161008	Di2	melt_stdev	1347	1248	air	1 atm	49 h	CMASN	0.00547	0.0721	0.204	0.529	0.0607	0.00542	0.691	
20161008	Di3	diopside	1347	1248	air	1 atm	49 h	CMASN	0.101	18.6	3.31	53.4	24.6	0.0426	100	6
20161008	Di3	diopside_stdev	1347	1248	air	1 atm	49 h	CMASN	0.0158	0.0821	0.268	0.622	0.184	0.00841	0.428	
20161008	Di3	melt	1347	1248	air	1 atm	49 h	CMASN	1.55	8.18	16.8	50.6	21.5	0.0541	98.7	6
20161008	Di3	melt_stdev	1347	1248	air	1 atm	49 h	CMASN	0.017	0.058	0.18	0.713	0.082	0.0108	0.767	
20161025	Plag1	plagioclase	1329	1225	QFM (-7.95)	1 atm	47 h	CMASN	1.41	0.477	33.6	46.2	18		99.7	6
20161025	Plag1	plagioclase_stdev	1329	1225	QFM (-7.95)	1 atm	47 h	CMASN	0.227	0.132	0.589	1.07	0.423		1.13	
20161025	Plag1	diopside	1329	1225	QFM (-7.95)	1 atm	47 h	CMASN	0.142	17.8	4.94	52.4	25		100	5
20161025	Plag1	diopside_stdev	1329	1225	QFM (-7.95)	1 atm	47 h	CMASN	0.0145	0.246	0.564	0.261	0.265		0.291	
20161025	Plag1	melt	1329	1225	QFM (-7.95)	1 atm	47 h	CMASN	2.28	7.23	16.1	51	19.9		96.5	
20161025	Plag1	melt_stdev	1329	1225	QFM (-7.95)	1 atm	47 h	CMASN	0.0758	0.256	0.523	0.854	0.281		1.96	
20161025	Plag2	plagioclase	1329	1225	QFM (-7.95)	1 atm	47 h	CMASN	3.38	0.336	31.4	50.2	14.9		100	6
20161025	Plag2	plagioclase_stdev	1329	1225	QFM (-7.95)	1 atm	47 h	CMASN	0.128	0.0297	0.344	0.558	0.214		0.542	
20161025	Plag2	melt	1329	1225	QFM (-7.95)	1 atm	47 h	CMASN	4.05	7.16	17.7	55.4	16		100	
20161025	Plag2	melt_stdev	1329	1225	QFM (-7.95)	1 atm	47 h	CMASN	0.0483	0.0379	0.0722	0.507	0.058		0.537	
20161025	Plag3	plagioclase	1329	1225	QFM (-7.95)	1 atm	47 h	CMASN	4.14	0.258	30.7	52.2	13.5	0.0349	101	6
20161025	Plag3	plagioclase_stdev	1329	1225	QFM (-7.95)	1 atm	47 h	CMASN	0.0774	0.0219	0.221	0.51	0.183	0.00509	0.368	
20161025	Plag3	melt	1329	1225	QFM (-7.95)	1 atm	47 h	CMASN	5.29	5.86	18.6	57.4	13.5	0.0512	101	6
20161025	Plag3	melt_stdev	1329	1225	QFM (-7.95)	1 atm	47 h	CMASN	0.062	0.0624	0.165	0.407	0.0747	0.00542	0.23	
c5075	An45Di45Ab10	plagioclase	1350	1250	none	8 kbar	48 h	CMASN	2.07	0.376	33.6	49.1	16.4	bdl	102	3
c5075	An45Di45Ab10	plagioclase_stdev	1350	1250	none	8 kbar	48 h	CMASN	0.111	0.145	0.471	0.393	0.203		0.624	
c5075	An45Di45Ab10	diopside	1350	1250	none	8 kbar	48 h	CMASN	0.265	16.2	8.7	51.5	24.4	bdl	101	3
c5075	An45Di45Ab10	diopside_stdev	1350	1250	none	8 kbar	48 h	CMASN	0.0214	1.03	2.9	1.32	0.326		0.708	
c5075	An45Di45Ab10	melt	1350	1250	none	8 kbar	48 h	CMASN	1.94	5.02	17	53.2	20	bdl	97.2	3
c5075	An45Di45Ab10	melt_stdev	1350	1250	none	8 kbar	48 h	CMASN	0.00971	0.0896	0.166	0.195	0.0575		0.324	
c5083	An45Di45Ab10	plagioclase	1350	1265	none	8 kbar	48 h	CMASN	2.13	0.349	31.6	48.4	16		98.5	8
c5083	An45Di45Ab10	plagioclase_stdev	1350	1265	none	8 kbar	48 h	CMASN	0.0666	0.0301	0.363	0.437	0.21		0.675	
c5083	An45Di45Ab10	diopside	1350	1265	none	8 kbar	48 h	CMASN	0.249	15.3	9.27	50	24.1		98.9	8
c5083	An45Di45Ab10	diopside_stdev	1350	1265	none	8 kbar	48 h	CMASN	0.0199	0.413	1.14	0.636	0.0856		0.674	
c5083	An45Di45Ab10	melt	1350	1265	none	8 kbar	48 h	CMASN	1.76	6.1	16.7	52.4	19.3		96.3	7
c5083	An45Di45Ab10	melt_stdev	1350	1265	none	8 kbar	48 h	CMASN	0.0426	0.0665	0.171	0.211	0.107		0.397	
c5094	An40Di40Ab20	plagioclase	1330	1230	none	8 kbar	48 h	CMASN	3.19	0.243	31.3	50.4	14.4		99.6	4
c5094	An40Di40Ab20	plagioclase_stdev	1330	1230	none	8 kbar	48 h	CMASN	0.0753	0.0232	0.263	0.349	0.0779		0.439	
c5094	An40Di40Ab20	diopside	1330	1230	none	8 kbar	48 h	CMASN	0.412	16.6	6.33	52.8	24.2		100	4
c5094	An40Di40Ab20	diopside_stdev	1330	1230	none	8 kbar	48 h	CMASN	0.0472	0.671	1.29	0.883	0.209		0.441	
c5094	An40Di40Ab20	melt	1330	1230	none	8 kbar	48 h	CMASN	2.93	6.11	17.8	55.1	17.1		99	3
c5094	An40Di40Ab20	melt_stdev	1330	1230	none	8 kbar	48 h	CMASN	0.0181	0.114	0.112	0.464	0.0313		0.672	
c5121	An35Di35Ab30	plagioclase	1330	1230	none	8 kbar	48 h	CMASN	4.05	0.23	30.2	52.3	13.1		100	4
c5121	An35Di35Ab30	plagioclase_stdev	1330	1230	none	8 kbar	48 h	CMASN	0.152	0.0233	0.303	0.823	0.27		0.918	
c5121	An35Di35Ab30	diopside	1330	1230	none	8 kbar	48 h	CMASN	0.461	17.1	5.21	53.7	24.1		101	5
c5121	An35Di35Ab30	diopside_stdev	1330	1230	none	8 kbar	48 h	CMASN	0.072	0.808	1.57	1.31	0.126		0.773	
c5121	An35Di35Ab30	melt	1330	1230	none	8 kbar	48 h	CMASN	3.71	5.85	18.5	55.7	15.5		99.2	5
c5121	An35Di35Ab30	melt_stdev	1330	1230	none	8 kbar	48 h	CMASN	0.0601	0.171	0.132	0.283	0.0295		0.355	
C5473	An15Di15Ab70x	plagioclase	1300	1200	none	11 kbar	48 h	CMASN	8.21	0.0755	24.3	61.2	5.64	bdl	99.4	

Run	comp.	type	T1	T2	fO2	P	time	System	Na2O	MgO	Al2O3	SiO2	CaO	FeO	Total	major (count)
C5473	An15Di15Ab70x	plagioclase_stdev	1300	1200	none	11 kbar	48 h	CMASN	0.529	0.0234	1.04	1.07	1.1		0.825	
C5473	An15Di15Ab70x	diopside	1300	1200	none	11 kbar	48 h	CMASN	1.36	17.3	4.57	55.3	21.9		100	
C5473	An15Di15Ab70x	diopside_stdev	1300	1200	none	11 kbar	48 h	CMASN	0.0948	0.392	0.661	0.53	0.384		0.618	
C5473	An15Di15Ab70x	melt	1300	1200	none	11 kbar	48 h	CMASN	8.83	2.55	17.8	68.3	4.36	bdl	102	
C5473	An15Di15Ab70x	melt_stdev	1300	1200	none	11 kbar	48 h	CMASN	0.056	0.0418	0.139	0.565	0.163		0.518	
C5480	An25Di25Ab50x	plagioclase	1300	1200	none	11 kbar	48 h	CMASN	6.4	0.135	26.5	58.3	8.84	bdl	100	
C5480	An25Di25Ab50x	plagioclase_stdev	1300	1200	none	11 kbar	48 h	CMASN	0.362	0.0186	0.654	1.18	0.616		1.04	
C5480	An25Di25Ab50x	diopside	1300	1200	none	11 kbar	48 h	CMASN	0.931	17.3	6.01	53.9	22.8	bdl	101	
C5480	An25Di25Ab50x	diopside_stdev	1300	1200	none	11 kbar	48 h	CMASN	0.0707	0.223	0.435	0.493	0.304		0.713	
C5480	An25Di25Ab50x	melt	1300	1200	none	11 kbar	48 h	CMASN	6.43	2.62	17.4	65	7.4	bdl	98.8	
C5480	An25Di25Ab50x	melt_stdev	1300	1200	none	11 kbar	48 h	CMASN	2.55	0.198	0.29	1.41	0.276		1.55	
d2061	An25Di25Ab50	plagioclase	1330	1230	none	8 kbar	48 h	CMASN	5.92	0.131	28.4	59.2	9.35		103	5
d2061	An25Di25Ab50	plagioclase_stdev	1330	1230	none	8 kbar	48 h	CMASN	0.173	0.0165	0.126	0.564	0.182		0.618	
d2061	An25Di25Ab50	diopside	1330	1230	none	8 kbar	48 h	CMASN	0.724	16.7	6.31	53	23.1		99.9	5
d2061	An25Di25Ab50	diopside_stdev	1330	1230	none	8 kbar	48 h	CMASN	0.0655	0.484	0.747	0.585	0.658		0.66	
d2061	An25Di25Ab50	melt	1330	1230	none	8 kbar	48 h	CMASN	6.28	3.95	18.4	59.3	10.3		98.2	6
d2061	An25Di25Ab50	melt_stdev	1330	1230	none	8 kbar	48 h	CMASN	0.023	0.0684	0.0931	0.289	0.0351		0.352	
D2067	An35Di35Ab30	plagioclase	1330	1230	none	5 kbar	48 h	CMASN	3.31		31.3	51.5	13.9		100	8
D2067	An35Di35Ab30	plagioclase_stdev	1330	1230	none	5 kbar	48 h	CMASN	0.23		0.33	0.23	0.25			
D2067	An35Di35Ab30	melt	1330	1230	none	5 kbar	48 h	CMASN	3.34	7.32	17.8	55.4	16.2		100	4
D2067	An35Di35Ab30	melt_stdev	1330	1230	none	5 kbar	48 h	CMASN	0.19	0.16	0.44	0.89	0.66			
d2074	An15Di15Ab70	plagioclase	1300	1200	none	8 kbar	48 h	CMASN	7.32	0.0925	24.5	60	6.84		98.8	6
d2074	An15Di15Ab70	plagioclase_stdev	1300	1200	none	8 kbar	48 h	CMASN	0.0886	0.0126	0.258	0.581	0.121		0.836	
d2074	An15Di15Ab70	melt	1300	1200	none	8 kbar	48 h	CMASN	7.87	2.82	19.1	63	6.87		99.7	6
d2074	An15Di15Ab70	melt_stdev	1300	1200	none	8 kbar	48 h	CMASN	0.0728	0.094	0.127	0.79	0.0818		0.906	
d2075	An35Di35Ab30	diopside	1360	1260	none	11 kbar	48 h	CMASN	0.665	16.1	6.99	52.6	24		100	4
d2075	An35Di35Ab30	diopside_stdev	1360	1260	none	11 kbar	48 h	CMASN	0.0354	1.6	1.39	1.44	1.93			
d2075	An35Di35Ab30	melt	1360	1260	none	11 kbar	48 h	CMASN	4.49	5.2	19.6	56.6	14.1		100	3
d2075	An35Di35Ab30	melt_stdev	1360	1260	none	11 kbar	48 h	CMASN	0.145	0.135	0.159	0.366	0.359			
d2076	An35Di35Ab30	plagioclase	1300	1200	none	5 kbar	48 h	CMASN	4.2	0.247	29.4	53.3	12.6		99.8	6
d2076	An35Di35Ab30	plagioclase_stdev	1300	1200	none	5 kbar	48 h	CMASN	0.189	0.0486	0.427	0.496	0.332		0.209	
d2076	An35Di35Ab30	diopside	1300	1200	none	5 kbar	48 h	CMASN	0.388	17	5.77	52.5	24.1		99.8	6
d2076	An35Di35Ab30	diopside_stdev	1300	1200	none	5 kbar	48 h	CMASN	0.0699	0.643	1.27	1.13	0.185		0.73	
d2076	An35Di35Ab30	melt	1300	1200	none	5 kbar	48 h	CMASN	4.97	4.51	18.2	57.1	12.7		97.5	6
d2076	An35Di35Ab30	melt_stdev	1300	1200	none	5 kbar	48 h	CMASN	0.0275	0.0544	0.174	0.445	0.0496		0.615	
d2079	An35Di35Ab30	plagioclase	1330	1230	none	11 kbar	48 h	CMASN	4.38	0.15	30.5	54.2	12.4		102	6
d2079	An35Di35Ab30	plagioclase_stdev	1330	1230	none	11 kbar	48 h	CMASN	0.0974	0.0211	0.33	0.529	0.184		0.611	
d2079	An35Di35Ab30	diopside	1330	1230	none	11 kbar	48 h	CMASN	0.662	16.2	8.17	51.9	23.7		101	6
d2079	An35Di35Ab30	diopside_stdev	1330	1230	none	11 kbar	48 h	CMASN	0.02	0.404	1.23	0.631	0.148		0.531	
d2079	An35Di35Ab30	melt	1330	1230	none	11 kbar	48 h	CMASN	4.05	4.65	18.7	55.5	14.4		97.3	6
d2079	An35Di35Ab30	melt_stdev	1330	1230	none	11 kbar	48 h	CMASN	0.0341	0.0563	0.137	0.19	0.0679		0.221	
d2087	An25Di25Ab50	plagioclase	1270	1170	none	5 kbar	48 h	CMASN	6.07		27.4	57.2	9.35		100	7
d2087	An25Di25Ab50	diopside	1270	1170	none	5 kbar	48 h	CMASN	0.78	17.9	4.58	54.2	23		100	7
d2087	An25Di25Ab50	diopside_stdev	1270	1170	none	5 kbar	48 h	CMASN	0.0608	0.502	0.902	0.64	0.505			
d2087	An25Di25Ab50	melt	1270	1170	none	5 kbar	48 h	CMASN	7.9	1.69	17.6	66.6	6.28		100	5
d2087	An25Di25Ab50	melt_stdev	1270	1170	none	5 kbar	48 h	CMASN	0.588	0.337	0.473	0.984	0.088			
d2088	An35Di35Ab30	plagioclase	1330	1230	none	11 kbar	48 h	CMASN	6.22	0.146	27.8	59.5	9.01		103	6
d2088	An35Di35Ab30	plagioclase_stdev	1330	1230	none	11 kbar	48 h	CMASN	0.115	0.0275	0.329	0.447	0.276		0.734	
d2088	An35Di35Ab30	diopside	1330	1230	none	11 kbar	48 h	CMASN	1.01	16.1	7.46	53.2	22.9		101	6
d2088	An35Di35Ab30	diopside_stdev	1330	1230	none	11 kbar	48 h	CMASN	0.0893	0.65	1.79	1.08	0.329		0.544	
d2088	An35Di35Ab30	melt	1330	1230	none	11 kbar	48 h	CMASN	6.63	3.41	17.6	60.8	9.72		98.1	6
d2088	An35Di35Ab30	melt_stdev	1330	1230	none	11 kbar	48 h	CMASN	0.0736	0.141	0.149	0.188	0.103		0.401	
d2091	An45Di45Ab10	plagioclase	1300	1200	none	5 kbar	48 h	CMASN	1.67	0.323	33.6	47.3	17.2		100	6
d2091	An45Di45Ab10	plagioclase_stdev	1300	1200	none	5 kbar	48 h	CMASN	0.0907	0.0418	0.151	0.499	0.149		0.596	
d2091	An45Di45Ab10	diopside	1300	1200	none	5 kbar	48 h	CMASN	0.171	17.1	6.2	51.7	24.4		99.7	6
d2091	An45Di45Ab10	diopside_stdev	1300	1200	none	5 kbar	48 h	CMASN	0.0272	0.625	0.648	0.756	0.335		1.43	
d2091	An45Di45Ab10	melt	1300	1200	none	5 kbar	48 h	CMASN	1.73	6.9	17	51.4	19.6		96.6	6
d2091	An45Di45Ab10	melt_stdev	1300	1200	none	5 kbar	48 h	CMASN	0.0315	0.0641	0.0949	0.461	0.0719		0.476	
d2092	An45Di45Ab10	plagioclase	1330	1230	none	11 kbar	48 h	CMASN	2.62	0.339	30.4	51	15		99.4	6
d2092	An45Di45Ab10	plagioclase_stdev	1330	1230	none	11 kbar	48 h	CMASN	0.052	0.0308	0.367	0.335	0.126		0.701	
d2092	An45Di45Ab10	diopside	1330	1230	none	11 kbar	48 h	CMASN	0.364	14.1	12.8	48.6	23.9		99.8	6
d2092	An45Di45Ab10	diopside_stdev	1330	1230	none	11 kbar	48 h	CMASN	0.0272	0.201	0.586	0.69	0.106		0.543	
d2092	An45Di45Ab10	melt	1330	1230	none	11 kbar	48 h	CMASN	1.29	4.09	13.9	60.3	14.9		94.5	7
d2092	An45Di45Ab10	melt_stdev	1330	1230	none	11 kbar	48 h	CMASN	0.287	1.07	2.94	5.42	2.78		1.72	
d2097	An15Di15Ab70	plagioclase	1270	1170	none	5 kbar	48 h	CMASN	7.35	0.135	24.2	58.6	6.78		97.1	6
d2097	An15Di15Ab70	plagioclase_stdev	1270	1170	none	5 kbar	48 h	CMASN	0.059	0.0237	0.279	0.704	0.169		0.724	
d2097	An15Di15Ab70	diopside	1270	1170	none	5 kbar	48 h	CMASN	0.593	17.3	2.39	51.1	21.7		93.2	3
d2097	An15Di15Ab70	diopside_stdev	1270	1170	none	5 kbar	48 h	CMASN	0.064	0.519	0.54	1.15	0.14		1.26	
d2097	An15Di15Ab70	melt	1270	1170	none	5 kbar	48 h	CMASN	7.97	3	17.3	59.2	6.42		93.9	6
d2097	An15Di15Ab70	melt_stdev	1270	1170	none	5 kbar	48 h	CMASN	0.0359	0.166	0.268	0.788	0.142		0.731	
d2098	An15Di15Ab70	plagioclase	1330	1230	none	11 kbar	48 h	CMASN	8.5		24	62.2	5.3		100	9
d2098	An15Di15Ab70	plagioclase_stdev	1330	1230	none	11 kbar	48 h	CMASN	0.467		0.749	1.06	0.79			

Run	comp.	type	T1	T2	fO2	P	time	System	Na2O	MgO	Al2O3	SiO2	CaO	FeO	Total	major (count)
d2098	An15Di15Ab70	diopside	1330	1230	none	11 kbar	48 h	CMASN	1.33	17.1	5.03	54.7	21.9		100	4
d2098	An15Di15Ab70	diopside_stdev	1330	1230	none	11 kbar	48 h	CMASN	0.0834	0.678	0.892	0.49	0.691			
d2098	An15Di15Ab70	melt	1330	1230	none	11 kbar	48 h	CMASN	8.18	1.96	17.7	67.9	4.29		100	5
d2098	An15Di15Ab70	melt_stdev	1330	1230	none	11 kbar	48 h	CMASN	0.156	0.274	0.401	1.02	0.454			
d2262	An15Di15Ab70	plagioclase	1345	1245	none	11 kbar	48 h	CMASN	8.71	0.0912	25.7	65.4	5.75		106	8
d2262	An15Di15Ab70	plagioclase_stdev	1345	1245	none	11 kbar	48 h	CMASN	0.0999	0.0201	0.0833	0.759	0.0845		0.766	
d2262	An15Di15Ab70	diopside	1345	1245	none	11 kbar	48 h	CMASN	1.21	18	3.78	55.2	22.7		101	5
d2262	An15Di15Ab70	diopside_stdev	1345	1245	none	11 kbar	48 h	CMASN	0.084	0.32	0.163	0.218	0.116		0.39	
d2262	An15Di15Ab70	melt	1345	1245	none	11 kbar	48 h	CMASN	8.89	3.36	18.9	66.3	6.55		104	6
d2262	An15Di15Ab70	melt_stdev	1345	1245	none	11 kbar	48 h	CMASN	0.0641	0.061	0.127	0.497	0.0239		0.476	
d2267	An15Di15Ab70	plagioclase	1255	1155	none	5 kbar	48 h	CMASN	7.59	0.145	25.3	62.7	6.62		102	7
d2267	An15Di15Ab70	plagioclase_stdev	1255	1155	none	5 kbar	48 h	CMASN	0.181	0.0346	0.574	1.05	0.332		1.72	
d2267	An15Di15Ab70	diopside	1255	1155	none	5 kbar	48 h	CMASN	0.652	17.3	2.97	54.9	23.5		99.4	5
d2267	An15Di15Ab70	diopside_stdev	1255	1155	none	5 kbar	48 h	CMASN	0.113	0.351	0.721	0.249	0.376		0.345	
d2267	An15Di15Ab70	melt	1255	1155	none	5 kbar	48 h	CMASN	8.34	2.66	19.4	68.4	5.44		104	7
d2267	An15Di15Ab70	melt_stdev	1255	1155	none	5 kbar	48 h	CMASN	0.123	0.111	0.208	0.296	0.0878		0.488	
D2275	An25Di25Ab50	plagioclase	1285	1185	none	5 kbar	48 h	CMASN	6		27.4	57.1	9.48		100	4
D2275	An25Di25Ab50	plagioclase_stdev	1285	1185	none	5 kbar	48 h	CMASN	0.118		0.119	0.193	0.147			
D2275	An25Di25Ab50	diopside	1285	1185	none	5 kbar	48 h	CMASN		18.7	3.47	55	22.9		100	4
D2275	An25Di25Ab50	diopside_stdev	1285	1185	none	5 kbar	48 h	CMASN		0.347	0.667	0.349	0.485			
D2275	An25Di25Ab50	melt	1285	1185	none	5 kbar	48 h	CMASN	6.91	3.26	18.1	63.6	8.2		100	4
D2275	An25Di25Ab50	melt_stdev	1285	1185	none	5 kbar	48 h	CMASN	0.114	0.192	0.0589	0.424	0.25			
D2293	An15Di15Ab70x	plagioclase	1275	1285	none	8 kbar	48 h	CMASN	7.98	0.113	24.6	61.8	6.4	bdl	101	
D2293	An15Di15Ab70x	plagioclase_stdev	1275	1285	none	8 kbar	48 h	CMASN	0.214	0.0235	0.308	0.456	0.372		0.29	
D2293	An15Di15Ab70x	diopside	1275	1285	none	8 kbar	48 h	CMASN	1.02	18	3.45	54.8	22.6	bdl	99.9	
D2293	An15Di15Ab70x	diopside_stdev	1275	1285	none	8 kbar	48 h	CMASN	0.127	0.444	0.506	0.671	0.411		0.987	
D2293	An15Di15Ab70x	melt	1275	1285	none	8 kbar	48 h	CMASN	8.71	2.63	18.5	68.7	4.58	bdl	103	
D2293	An15Di15Ab70x	melt_stdev	1275	1285	none	8 kbar	48 h	CMASN	0.0476	0.133	0.216	0.611	0.333		0.595	
D2479	An25Di25Ab50x	plagioclase	1235	1185	none	5 kbar	48 h	CMASN	5.35	0.268	28.1	56.8	10.5	bdl		
D2479	An25Di25Ab50x	plagioclase_stdev	1235	1185	none	5 kbar	48 h	CMASN	0.064	0.152	0.447	0.421	0.144			
D2479	An25Di25Ab50x	diopside	1235	1185	none	5 kbar	48 h	CMASN	0.701	17.1	4.29	54.9	23.1	bdl		
D2479	An25Di25Ab50x	diopside_stdev	1235	1185	none	5 kbar	48 h	CMASN	0.309	1.08	1.28	0.708	1.52			
D2479	An25Di25Ab50x	melt	1235	1185	none	5 kbar	48 h	CMASN	5.45	4.3	18.7	63.9	9.91	bdl		
D2479	An25Di25Ab50x	melt_stdev	1235	1185	none	5 kbar	48 h	CMASN	0.0409	0.428	0.192	1.31	0.725			

Table 44: CaO-MgO-Al_2O_3-SiO_2-Na_2O system experiments. Trace element analysis of experimental phases from mass 7 (Li) to mass 139 (Ba)

Run	comp.	type	Li_ppm	Be_ppm	B_ppm	Na_ppm	Mg_ppm	P_ppm	K_ppm	Ca_ppm	Sc_ppm	Mn_ppm	Fe_ppm	Ti_ppm	V_ppm	Cr_ppm	Ga_ppm	Rb_ppm	Sr_ppm	Zr_ppm	Nb_ppm	In_ppm	Cs_ppm	Ba_ppm
20160928	Plag 1	plagioclase	29.1	45.3			2970		99.4	121000	1.56				0.474	5.4	268	4.13	392	0.215	0.193	6.75	0.178	69
20160928	Plag 1	plagioclase_stdev	0.812	0.983			124		11.8	439	0.0591				0.11	0.271	5.59	0.251	10.2	0.0905	0.0711	0.362	0.0757	4.74
20160928	Plag 1	melt	216	246			52100		542	145000	26.7				258	225	234	195	322	252	264	216	207	276
20160928	Plag 1	melt_stdev	6.41	5.71			2070		25.2	1240	0.447				4.28	6.39	9.63	5.53	2.83	3.26	3.89	7.14	4.6	4
20160928	Plag 2	plagioclase	47.1	46.5		27900	2310		83.8		2.58	1.7	201	6.58	0.603	6.88	275	4.22	438	0.431	0.238	8.95	0.28	76.7
20160928	Plag 2	plagioclase_stdev	1.63	3.96		1570	59.8		4.35		0.241	bdl	10.3	1.8	0.234	0.759	19.3	0.334	21.7	0.465	0.179	0.394	0.17	7.7
20160928	Plag 2	melt	306	265		35600	42900		741		28.7	3.94	479	121	287	191	259	256	314	269	285	262	251	286
20160928	Plag 2	melt_stdev	7.21	7.54		546	456		27.8		0.938	0.871	35.1	9.21	4.08	77.5	4.09	4.77	4.41	2.92	4.26	2.28	20.7	4.67
20160928	Di1	diopside	25.9	0.284			108000		bdl	167000	59.1				11.5	980	37	0.325	49.3	58.8	5.89	214	0.287	0.24
20160928	Di1	diopside_stdev	3.98	0.195			1240		bdl	427	4.78				1.22	315	2.42	0.18	1.3	5.46	2.34	13	0.317	0.273
20160928	Di1	melt	340	331			33700		853	83600	9.23				332	6.23	344	306	505	318	334	176	289	366
20160928	Di1	melt_stdev	1.85	1.83			162		11.7	608	0.129				2.09	0.866	3.68	3.46	3.3	1.3	1.44	1.31	6.32	1.04
20161008	Plag3	plagioclase	41.6	43.8		32400	1580		81.2		3.24	bdl	213	9.1	0.47	9.23	253	3.25	459	0.16	0.18	8.17	bdl	89.7
20161008	Plag3	plagioclase_stdev	3.32	3.73		3740	91.5		16.7		0.308	bdl	17.7	1.04	0.192	0.885	25.5	0.254	11.2	bdl	0.144	1.16	bdl	2.79
20161008	Plag3	melt	280	263		46800	33400		695		29.7	4.7	532	131	284	278	260	253	305	264	274	252	264	281
20161008	Plag3	melt_stdev	5.89	6.43		462	449		14.3		0.853	0.739	25.6	6.31	1.53	5.16	4.32	2.74	2.67	2.46	5.45	3.11	4.51	6.18
20161008	Plag4	plagioclase	42.6	36.9		43100	896		78		3.52	bdl	185	11.3	2.14	11.1	268	3.47	552	1.27	1.32	11.8	1.78	94.8
20161008	Plag4	plagioclase_stdev	4.46	6.71		4050	177		13		0.548	bdl	23	1.4	1.72	0.666	30.8	2.07	24	1.5	1.47	2.57	1.54	6.39
20161008	Plag4	melt	254	258		66100	16600		699		29.2	2.53	455	124	272	248	253	246	257	261	260	236	257	269
20161008	Plag4	melt_stdev	5.93	10.2		949	660		16.1		1.07	0.525	15.9	9.62	7.35	18.3	9.24	4.98	5.03	11.5	10.9	9.47	4.29	5.13
20161008	Di2	diopside	21.9	0.68			105000		3	172000	36.6				8.68	368	52.1	0.46	44.2	50.6	2.6	173	0.471	0.557
20161008	Di2	diopside_stdev	7.93	0.497			1310		bdl	618	4.86				1.72	114	11.9	0.421	2.74	24.5	1.18	38.1	0.483	0.626
20161008	Di2	melt	351	333			40700		812	115000	10.7				329	9.73	342	309	513	301	336	199	298	366
20161008	Di2	melt_stdev	3.58	2.93			178		9.31	365	0.112				1.16	0.526	3.1	3.62	3.33	3.33	1.97	1.94	9.47	3.55
20161008	Di3	diopside	24.7	0.462			102000		bdl	169000	54.7				9.09	987	68.1	0.145	37.2	71.7	5.46	193	bdl	0.078
20161008	Di3	diopside_stdev	7.71	0.15			733		bdl	515	1.26				0.372	57.3	4.06	0.0183	1.02	4.25	0.77	11.4	bdl	0.00624
20161008	Di3	melt	358	363			47900		837	151000	7.7				360	5.01	354	308	573	290	376	188	243	406
20161008	Di3	melt_stdev	2.17	6.4			180		9.59	696	0.15				2.92	1.31	2.25	6.63	3.56	1.36	1.06	1.7	33.8	2.5
20161025	Plag1	plagioclase	65.8	47			3040		109		40.2				4.5	3.33	116	4.51	381	0.0908	0.0768	0.192	0.112	60.1
20161025	Plag1	plagioclase_stdev	3.18	5.52			259		23.9		0.507				0.195	0.21	27.6	0.508	10.1	0.0173	0.00526	0.0858	0.0359	8.26
20161025	Plag1	diopside	33.4	0.815			99800		5.95		110				365	1120	36.3	0.218	34.2	142	9.08	3.62	bdl	0.33
20161025	Plag1	diopside_stdev	10.7	0.375			636		4.6		6.86				58.5	269	1.34	0.0587	2.4	3.18	0.24	1.83	bdl	bdl
20161025	Plag1	melt	617	573			44500		1460		54.7				291	4.44	98.3	544	507	464	594	2.65	523	632
20161025	Plag1	melt_stdev	6.44	54.7			1010		114		2.43				29.4	4.11	54.6	58.9	21.6	54.8	79.9	2.55	75	63.2
20161025	Plag2	plagioclase	47.2	52.1			2330		89.3	104000	1.62				6.52	3.9	93.4	3.87	418	0.182	0.194	0.204	0.116	77.7
20161025	Plag2	plagioclase_stdev	1.55	1.7			86.5		4.48	289	0.0557				0.309	0.113	35.6	0.24	10.3	0.0312	0.11	0.179	0.0555	4.62
20161025	Plag2	melt	286	257			39800		667	110000	27.6				253	153	51.1	242	296	269	283	0.319	254	280
20161025	Plag2	melt_stdev	4.31	2.67			296		28.1	390	0.591				8.43	25	22	5.89	1.56	4.8	5.05	0.234	5.11	2.54

Run	comp.	type	Li_ppm	Be_ppm	B_ppm	Na_ppm	Mg_ppm	P_ppm	K_ppm	Ca_ppm	Sc_ppm	Mn_ppm	Fe_ppm	Ti_ppm	V_ppm	Cr_ppm	Ga_ppm	Rb_ppm	Sr_ppm	Zr_ppm	Nb_ppm	In_ppm	Cs_ppm	Ba_ppm
20161025	Plag3	plagioclase	46.7	46.5		35800	1790		101		3.96	bdl	55.9	7.91	6.42	13.7	117	3.78	447	0.133	0.164	0.154	bdl	76.2
20161025	Plag3	plagioclase_stdev	1.87	6.18		1370	135		20.6		0.26	bdl	21.2	3	0.853	4.38	41.7	0.489	11.2	0.0404	0.0497	bdl	bdl	5.75
20161025	Plag3	melt	300	274		45100	34500		789		33	1.27	48	132	260	127	28.4	265	296	279	295	0.053	268	278
20161025	Plag3	melt_stdev	10.4	8.47		981	691		35.4		1.11	0.413	5.7	7.86	7.58	5.22	4.58	6.89	2.55	4.86	5.25	bdl	7.15	6.12
c5075	An45Di45Ab10	plagioclase	162	134		18200	2830		174		5.17				7.88	bdl	24.9	30	454	13.6	12.4	0.137	13.7	101
c5075	An45Di45Ab10	plagioclase_stdev	16.1	30.7		1200	402		20.2		0.209				1.3		8.4	14.9	48.5	14	11.4	0.0318	11.4	18.6
c5075	An45Di45Ab10	diopside	59.8	20.9		3340	81700		56		69.5				777	1420	21.6	7.73	64.8	200	18.6	0.597	20.1	12.5
c5075	An45Di45Ab10	diopside_stdev	45.3	30.1		2550	7600				5.65				134	499	1.95	12.9	61.6	11	14.7	0.138		21.2
c5075	An45Di45Ab10	melt	821	845		16000	29800		1100		21.8				140	28.8	22.9	939	577	1160	887	0.0473	880	893
c5075	An45Di45Ab10	melt_stdev	12.3	10.9		361	455		24.8		0.604				1.67	3.76	0.932	23.3	4.97	9.54	7.54	0.0105	22.6	12.3
c5083	An45Di45Ab10	plagioclase	143	96.5	13.2	18500	2560	38.6	124	113000	3.14	bdl	6.5		3.62	4.3	8.31	15.4	394	1.06	0.825	0.0884	1.25	74.2
c5083	An45Di45Ab10	plagioclase_stdev	10.9	12.6	2.26	1600	327	6.06	18.5	1100	1.23				1.23	3.62	5.19	2.24	24.1	1.19	0.837	0.115	1.19	10
c5083	An45Di45Ab10	diopside	76.4	6.37	16.6	2160	83800	38.6	13.3	168000	61.2	1.8	5.5		349	439	4.38	2.52	36.7	169	8.97	0.787	2.08	3.97
c5083	An45Di45Ab10	diopside_stdev	25.9	6.39	1.42	712	2890	5.11	11.1	1500	10.2	0.377	2.69		79	154	3.19	3.42	15.7	24	3.75	0.743	3.5	5.01
c5083	An45Di45Ab10	melt	673	634	52.2	14900	35200	202	702	138000	22.3	5.69	8.65		102	28.2	25.6	662	503	862	584	0.221	607	645
c5083	An45Di45Ab10	melt_stdev	13.1	50.8	4.28	444	1070	24.3	39.5	1210	1.68	0.474	2.05		5.32	2.65	11.5	77.9	14.8	97.8	77.4	0.201	82.1	62.1
c5094	An40Di40Ab20	plagioclase	86.4	79.6	10.7	28800	2140	33.5	112	98700	4.02	bdl	bdl		1.59	1.92	4.91	13.3	363	0.716	0.384	0.035	0.95	71.1
c5094	An40Di40Ab20	plagioclase_stdev	3.37	4.26		1370	856	5.19	11.8	1380	1.02				0.757	0.941	3.36	1.73	8.27	0.726	0.548	0.00566	1.28	7.69
c5094	An40Di40Ab20	diopside	67.7	9.45	13.2	5170	91600	28.9	11.7	168000	113	0.41	bdl		158	130	2.3	4.7	52.1	136	4.71	0.041	4.11	7.31
c5094	An40Di40Ab20	diopside_stdev	11	8.56	2.22	2770	6520	3.18	11.4	1080	8.35				20.1	16.3	1.58	5.03	29.5	32.4	3.18	0.0257	5	7.93
c5094	An40Di40Ab20	melt	429	438	29	25200	34300	46.1	488	121000	40.8	bdl	4.8		32.4	11.3	12.4	461	368	655	279	0.0265	436	447
c5094	An40Di40Ab20	melt_stdev	14.1	28	3.53	1110	1120	6.85	41.8	1310	2.92				3.7	1.47	3.9	52	7.51	104	20.9	0.00743	79.7	34.5
c5121	An35Di35Ab30	plagioclase	35.5	51.7		24700	1080		51.6	69000	1.5				1.79	bdl	4.93	6.46	252	0.42	0.347	0.125	0.302	55.4
c5121	An35Di35Ab30	plagioclase_stdev	2.15	10.2		1820	42.8		7.77	261	0.116				0.315	bdl	0.639	1.24	15.2	0.342	0.267	0.12	0.212	11.8
c5121	An35Di35Ab30	diopside	53.5	23.4		6340	87700		43	164000	49.3				296	356	1.86	22.6	52.8	199	25.2	0.0343	27.1	20.9
c5121	An35Di35Ab30	diopside_stdev	17.1	32.2		3520	4580		36.6	991	8.29				60.7	80.6	1.39	39	28.8	76.3	39.1	0.0162	48.1	30.6
c5121	An35Di35Ab30	melt	180	170		21400	22900		191	75900	14.2				62	24.4	11	167	181	277	148	0.051	153	170
c5121	An35Di35Ab30	melt_stdev	3.56	20.1		412	421		11.6	586	0.757				3.52	4.17	2.65	19.6	6.98	25.2	17.4	0.0317	19.6	21.7
C5473	An15Di15Ab70x	plagioclase	105	50.8		60400	527		210		2.81	bdl	22	6.14	6.58	bdl	83.3	13.4	501	0.31	0.16	bdl	0.448	144
C5473	An15Di15Ab70x	plagioclase_stdev	17	5.31		11000	74.8		42		0.364	bdl	bdl	2.69	1.46	bdl	21.9	3.86	19	0.0608	0.0592	bdl	0.226	35.1
C5473	An15Di15Ab70x	diopside	149	54.8		13900	97000		93.8		156	3.06	148	168	1170	1530	107	31.3	68.1	294	60.7	91.8	30.7	23.3
C5473	An15Di15Ab70x	diopside_stdev	28.5	33.3		2660	3080		70.5		12.6	0.913	43.2	19.6	501	774	58.6	38.9	12	51.1	35.9	62.3	37.6	28
C5473	An15Di15Ab70x	melt	732	788		73400	13200		1170		29.1	1.92	82.7	226	96.3	11.7	218	768	253	1170	785	27.5	768	598
C5473	An15Di15Ab70x	melt_stdev	25.8	20.3		3190	313		72.1		2.32	0.935	33.9	10.6	30.7	3.37	125	42.5	6.49	500	49.6	21	45	13.6
C5480	An25Di25Ab50x	plagioclase	129	73.6		53300	1150		187		3.02	bdl	32	6.53	10.2	4.3	95.5	19.5	485	12.9	7.57	0.598	8.72	120
C5480	An25Di25Ab50x	plagioclase_stdev	5.71	4.82		2380	46.5		16.1		0.14	bdl	bdl	1.46	0.438	bdl	49.5	1.16	13	0.133	0.0617	0.137	0.116	6.78
C5480	An25Di25Ab50x	diopside	85	bdl		7180	97400		bdl		99.8	2	86.5	65.1	872	1150	44.7	1.33	46.9	124	6.33	39.6	2.15	3.2
C5480	An25Di25Ab50x	diopside_stdev	5.51	bdl		407	1620		bdl		4.54	0.176	16.4	5.37	86.9	162	27.2	1.99	2.34	12	1.71	41	2.89	bdl
C5480	An25Di25Ab50x	melt	758	735		60900	14600		1200		18.4	1.78	22.3	163	82.5	18.2	90.9	820	334	862	779	6.49	794	669
C5480	An25Di25Ab50x	melt_stdev	23.8	99.1		2970	577		116		0.78	0.46	8.54	29.1	5.99	6.4	70.7	103	10.4	185	141	5.32	104	78.7

Run	comp.	type	Li_ppm	Be_ppm	B_ppm	Na_ppm	Mg_ppm	P_ppm	K_ppm	Ca_ppm	Sc_ppm	Mn_ppm	Fe_ppm	Ti_ppm	V_ppm	Cr_ppm	Ga_ppm	Rb_ppm	Sr_ppm	Zr_ppm	Nb_ppm	In_ppm	Cs_ppm	Ba_ppm
d2061	An25Di25Ab50	plagioclase	36.8	37.3	11.3	50400	858	32.6	48.3	67400	2.71	bdl	bdl		1.55	bdl	54.5	4.57	262	0.215	0.0783	0.402	0.116	58.9
d2061	An25Di25Ab50	plagioclase_stdev	1.53	4.49	1.27	2630	39.2	1.5	5.76	1120	0.558				0.307		16.7	0.562	11.7	0.118	0.027	0.52	0.0462	12.5
d2061	An25Di25Ab50	diopside	29.5	1.71	15	5340	93300	28.2	7.67	165000	63.6	0.675	bdl		373	405	19.3	1.15	21.6	89.1	2.33	0.554	1.31	1.22
d2061	An25Di25Ab50	diopside_stdev	2.1	1	2.54	583	2040	3	2.15	843	4.97	0.0915			89.5	113	8.24	1.61	1.12	18.2	1.45	0.371	1.53	1.22
d2061	An25Di25Ab50	melt	192	150	53.3	47900	20100	37.7	225	64300	13.8	bdl	bdl		18.8	8.69	15.6	157	160	318	112	0.124	142	153
d2061	An25Di25Ab50	melt_stdev	3.06	15.5	9.15	1070	426	3.9	12.1	789	0.617				4.37	1.36	11.8	15.4	3.27	35.7	21.7	0.122	18.8	15.8
D2067	An35Di35Ab30	plagioclase	48.1	43.1		29600	1910		54.1	98700	3.94				2.33	bdl	18.5	6.12	301	0.362	0.234	bdl	0.297	51.1
D2067	An35Di35Ab30	plagioclase_stdev	6.62	1.04		921	80.5		6.13	1010	0.213				0.367		7.07	0.344	0.943	0.361	0.192		0.28	7.58
D2067	An35Di35Ab30	melt	254	228		28500	39700		271	115000	24				23.5	11.5	17.2	232	255	385	165	bdl	223	233
D2067	An35Di35Ab30	melt_stdev	5.57	6.57		411	689		6.3	1460	0.522				6.82	1.57	1.17	4.35	3.23	4.47	14.5		1.17	3.47
d2074	An15Di15Ab70	plagioclase	22.9	18.2		62100	710		43.3		2.73	bdl	24	10.6	2.06	3.2	46.8	3.27	181	0.182	bdl	bdl	0.18	43.1
d2074	An15Di15Ab70	plagioclase_stdev	0.927	2.33		5020	78.1		11.1		0.229	bdl	bdl	0.606	0.56	0.566	12.4	0.528	5.47	0.104	bdl	bdl	0.0424	6.1
d2074	An15Di15Ab70	melt	118	106		68100	16300		199		11.7	0.967	21	107	34.5	13.8	53.7	108	109	298	79.1	bdl	96.9	105
d2074	An15Di15Ab70	melt_stdev	3.69	2.68		1200	360		8.2		0.265	0.309	bdl	2.49	1.05	3.23	1.8	2.23	2.02	2.95	3.92	bdl	1.96	4.09
d2075	An35Di35Ab30	diopside	45.3	2.74		5730	94200		11.6	172000	67.8				115	204	1.12	0.877	26.6	96.2	1.71	0.131	1.64	1.16
d2075	An35Di35Ab30	diopside_stdev	2.09	1.22		278	1300		2.33	1050	4.78				15.7	12.3	1.02	1.49	2.03	13.4	0.742	0.182	1.96	1.74
d2075	An35Di35Ab30	melt	245	226		36100	30400		264	102000	21.6				14.9	10	13.5	220	255	385	120	0.201	207	224
d2075	An35Di35Ab30	melt_stdev	8.44	5.99		707	294		4.21	1060	0.569				2.05	0.882	1.05	3.71	4.39	6.89	8.13	0.129	6.66	5.22
d2076	An35Di35Ab30	plagioclase	66.9	57.3		36900	1500		61.5		2.41	0.87	64	2.5	1.53	3.8	82.9	5.22	343	0.245	0.249	0.69	bdl	77.2
d2076	An35Di35Ab30	plagioclase_stdev	2.69	6.79		3040	154		3.54		0.361	bdl	bdl	0.424	0.283	bdl	10	0.255	13.5	0.0778	0.157	bdl	bdl	12.6
d2076	An35Di35Ab30	diopside	53.4	47.5		5130	99700		48.2		82.8	1.06	65.2	63.3	414	363	30.9	19.7	33.5	160	19	0.707	35.3	27.5
d2076	An35Di35Ab30	diopside_stdev	25.3	20.6		2680	2040		19.5		12.6	0.263	5.4	7.06	152	116	16.6	25.8	16.1	13.7	18.9	0.655	29.2	25.1
d2076	An35Di35Ab30	melt	394	292		44200	26800		428		18.4	1.18	43.8	88.3	20.8	10.3	7.79	331	262	497	210	bdl	292	307
d2076	An35Di35Ab30	melt_stdev	3.21	17.9		667	456		15.7		0.526	0.351	12.7	5.06	2.71	1.34	1.24	8.68	3.32	18.4	10.8	bdl	15.4	9.04
d2079	An35Di35Ab30	plagioclase	58.6	68.2	7.65	37600	1110	31.7	66.9	88700	1.68	0.275	0.55	bdl	1.37	0.33	9.24	8.81	337	1.3	0.816	0.145	1.01	58.5
d2079	An35Di35Ab30	plagioclase_stdev	2.37	9	0.495	1130	65.3	0.566	7.67	1520	0.574	0.0495	3.32	bdl	0.231		3.14	0.829	16.1	1.19	0.664	0.109	0.747	11.8
d2079	An35Di35Ab30	diopside	51.9	9.89	11.5	5680	88800	32.3	7.09	166000	56.2	0.616	0.713	bdl	221	298	4.84	7.34	33	104	7.09	0.295	7.79	7.32
d2079	An35Di35Ab30	diopside_stdev	12.6	14.7	1.97	1730	3920	4.35	20.7	5320	4.69	0.104	2.41	bdl	74.1	68.3	4.26	15.3	13.6	19	11.2	0.244	15.4	14.6
d2079	An35Di35Ab30	melt	297	281	20.8	34700	26000	32.8	330	101000	18.4	0.673	2.43	bdl	31.2	15.4	10.5	277	293	459	207	0.227	259	282
d2079	An35Di35Ab30	melt_stdev	18.2	23.7	1.57	2050	2240	5.12	13.2	4540	1.71	0.271	4.78	bdl	5.89	2.74	2.03	11.6	19.6	49.2	20.1	0.413	21.5	15.3
d2087	An25Di25Ab50	plagioclase	70.9	bdl		60200	1490		73		3.08	bdl	32	9.7	3.93	bdl	64.5	11.2	286	6	2.78	0.22	4.97	77.4
d2087	An25Di25Ab50	diopside	42.3	22.3		6440	95200		23		71.4	1.39	74.7	105	271	239	27.6	9.05	24.3	222	15	5.77	25.1	21.8
d2087	An25Di25Ab50	diopside_stdev	12.9	bdl		2660	5220		18.4		5.52	0.177	5.03	3.76	30.3	123	5.46	15.1	4.27	6.51	7.24	2.32	bdl	bdl
d2087	An25Di25Ab50	melt	396	371		71900	11500		522		10.3	1	29.8	149	13.3	7.2	42.2	404	143	782	227	2.33	377	313
d2087	An25Di25Ab50	melt_stdev	8.85	10.8		663	309		13.1		0.813	0.24	10.6	9.27	3.13	1.2	40	4.85	3.02	21.2	49.7	2.14	7.68	5.58
d2088	An35Di35Ab30	plagioclase	53.6	48.5		58300	1030		77.5		3.51	bdl	25.5	10.9	0.65	bdl	6.91	9.05	266	2.23	0.825	bdl	1.45	69.1
d2088	An35Di35Ab30	plagioclase_stdev	1.84	1.06		1340	175		3.54		0.12	bdl	0.707	0.919	0.0707	bdl	3.25	0.0707	12.9	0.0707	0.0495	bdl	0.389	4.95
d2088	An35Di35Ab30	diopside	43.6	5.6		8490	90600		17.3		56.9	1.13	69.5	92.2	130	214	3.84	7.4	23.2	126	5.06	0.336	6.25	4.6
d2088	An35Di35Ab30	diopside_stdev	12.8	bdl		806	2050		bdl		1.06	bdl	2.12	27.2	43.7	70	1.7	bdl	1.48	5.16	2.61	0.218	bdl	bdl
d2088	An35Di35Ab30	melt	272	259		57700	20900		361		14.6	1.21	36	137	22.6	9.83	21.8	262	194	545	203	0.246	249	242
d2088	An35Di35Ab30	melt_stdev	4.55	6.39		1540	482		18.3		0.376	0.525	7.94	6.78	4.32	0.894	11.9	7.46	5.06	17.7	12.6	0.0387	4.25	6.48

Run	comp.	type	Li_ppm	Be_ppm	B_ppm	Na_ppm	Mg_ppm	P_ppm	K_ppm	Ca_ppm	Sc_ppm	Mn_ppm	Fe_ppm	Ti_ppm	V_ppm	Cr_ppm	Ga_ppm	Rb_ppm	Sr_ppm	Zr_ppm	Nb_ppm	In_ppm	Cs_ppm	Ba_ppm
d2091	An45Di45Ab10	plagioclase	93.4	96.5		15200	2410		94.6	122000	2.79				5.19	2.6	37.3	10.3	434	0.328	0.214	0.0307	0.362	72.4
d2091	An45Di45Ab10	plagioclase_stdev	4.55	9.23		627	121		8.56	958	0.166				0.33	bdl	2.52	0.916	23	0.163	0.211	0.00945	0.339	8.06
d2091	An45Di45Ab10	diopside	66.5	4		1510	95600		bdl	175000	63				588	702	12.2	0.374	38.5	184	4.29	0.182	0.144	0.993
d2091	An45Di45Ab10	diopside_stdev	8.31	1.47		226	2310			917	9.13				59.5	421	2.22	0.149	7.35	28.7	1.08	0.0813	0.111	1.29
d2091	An45Di45Ab10	melt	546	443		14600	40800		499	136000	21.5				198	40.3	38.9	459	397	716	451	0.13	433	455
d2091	An45Di45Ab10	melt_stdev	7.5	3.99		154	436		6.44	841	0.183				1.85	1.24	1.94	4.51	1.7	10.2	5.36	0.0566	6.99	3.02
d2092	An45Di45Ab10	plagioclase	156	158	bdl	21600	2180	bdl	514	109000	2.67	bdl	bdl		3.21	bdl	12.7	25.9	532	2.62	1.72	0.146	2.5	117
d2092	An45Di45Ab10	plagioclase_stdev	10.1	19.9	bdl	1380	198	bdl	35.9	3040	1.13	bdl	bdl		0.247	bdl	1.08	3.82	17.6	3.28	2.16	bdl	3.02	11.9
d2092	An45Di45Ab10	diopside	76.5	6.92	12.2	2990	84400	37.2	52.3	173000	53.5	1.29	4.55		454	538	10.6	3.18	36.8	185	9.82	1.96	4.5	4.07
d2092	An45Di45Ab10	diopside_stdev	14.3	8.4	1.45	356	3020	1.49	64.7	1560	5.87	0.164	0.212		106	205	5.8	9.33	11.6	16.8	8.29	1.37	12.1	10.1
d2092	An45Di45Ab10	melt	595	552	42.2	13700	31700	85.1	1850	131000	19.3	2.49	6.95		55.1	18.4	26.5	578	506	901	510	0.425	535	580
d2092	An45Di45Ab10	melt_stdev	41.9	73.3	5.33	1220	2900	10.2	247	6590	1.66	0.311	2.47		11.4	7.84	9.08	86	38.3	129	73.4	0.239	84.3	77.6
d2097	An15Di15Ab70	plagioclase	19.7	16.7		53700	764		36		2.34	bdl	39	7.33	4.54	2.6	70.7	2.46	184	bdl	bdl	bdl	0.26	46.1
d2097	An15Di15Ab70	plagioclase_stdev	2.25	1.25		3070	74.8				0.217	bdl	bdl	1.5	1.22	bdl	15.6	0.504	3.83	bdl	bdl	bdl	bdl	4.43
d2097	An15Di15Ab70	diopside	18.2	3.5		5760	97200		9.1		52.1	0.52	65	86.4	128	128	7.28	2.75	16.2	108	2.42	bdl	2.37	3.05
d2097	An15Di15Ab70	diopside_stdev	2.4	bdl		1160	354		bdl		0.141	bdl	2.83	2.62	22	6.22	1.7	2.9	1.85	2.33	1.39	bdl	2.45	bdl
d2097	An15Di15Ab70	melt	125	130		63800	19400		183		12.1	0.86	37.7	122	39	10.3	47.1	115	88.1	375	82.5	0.226	120	110
d2097	An15Di15Ab70	melt_stdev	2.31	14.9		1890	612		4.03		0.482	bdl	8.02	11.7	9.7	1.94	19.3	4.22	3.66	36.3	12.2	0.0884	7.11	4.27
d2098	An15Di15Ab70	plagioclase	29.2	18.9		64000	653		44.3	38200	3.09	5.31	1.79				87.4	4.52	149	1.2	0.733	17.9	0.936	42.4
d2098	An15Di15Ab70	plagioclase_stdev	3.07	1.96		3970	77.4		7.48	538	0.208	0.867	0.333				13.7	1.34	5.18	1.39	0.812	49.7	1.18	9.28
d2098	An15Di15Ab70	diopside	124	95.5		159000	65500		169	169000	34.5	236	157				220	55.1	302	376	45.7	12.6	41.4	144
d2098	An15Di15Ab70	diopside_stdev	12	11.3		5660	13400		16.3	11500	5.87	32.4	59.6				5.66	4.17	29	300	9.19	7.16	3.82	10.4
d2098	An15Di15Ab70	melt	192	195		69700	10700		276	30800	9.13	16.5	4.48				37.7	198	76.4	573	146	0.817	196	155
d2098	An15Di15Ab70	melt_stdev	21.4	61.5		4800	1220		42.4	603	0.871	9.63	1.5				28.7	47.1	4.14	191	61.7	0.58	60.2	34.8
d2262	An15Di15Ab70	plagioclase	26.8	22.2		75100	605		71		3.17	bdl	25.7	14.1	1.8	3.8	39.7	6.17	160	0.261	0.31	bdl	0.25	58.6
d2262	An15Di15Ab70	plagioclase_stdev	0.944	4.43		5300	24.5		21.3		0.44	bdl	6.51	1.27	0.661	1.13	9.68	0.673	6.62	0.02	0.169	bdl	0.0638	14.3
d2262	An15Di15Ab70	diopside	34.6	29.1		15000	100000		35.6		45.9	1.13	59.8	158	185	152	14.4	14.7	26.3	139	237	10.9	15.9	13.6
d2262	An15Di15Ab70	diopside_stdev	11.1	32.7		5460	1400		29.8		10.4	0.586	4.32	30	115	59.5	8.02	18.9	6.04	30.4	113	12.1	21	13.1
d2262	An15Di15Ab70	melt	137	127		69800	17900		228		11.4	1.32	20	159	27.7	8.58	27.4	159	95.7	105	386	93	137	142
d2262	An15Di15Ab70	melt_stdev	2.52	9.86		1160	449		5.31		0.641	0.544	4.24	11.6	1.13	3.17	8.4	7	1.86	7.21	19.2	6.09	11.6	12.6
d2267	An15Di15Ab70	plagioclase	24.4	19.8		61800	796		31.5		2.79	1.9	36.5	14.4	7.63	3	102	2.61	198	0.273	0.134	0.33	0.32	54.7
d2267	An15Di15Ab70	plagioclase_stdev	1.23	3.93		1850	190		8.02		0.257	bdl	16.3	3.55	2.47	bdl	5.42	0.407	6.04	0.0351	0.0509		0.0283	12.8
d2267	An15Di15Ab70	diopside	17.1	bdl		4480	97500		17		56.9	2.89	108	142	513	395	19.7	0.46	16.9	163	2.06	1.76	bdl	bdl
d2267	An15Di15Ab70	diopside_stdev	2.42	bdl		353	361		bdl		7.64	1.06	12.2	20.8	277	70.7	11.8	0.0707	0.64	42.6	0.863	1.43	bdl	bdl
d2267	An15Di15Ab70	melt	162	129		76200	15000		251		12.1	1.34	43.3	174	42.4	4.18	81.4	130	83.5	483	103	0.267	124	111
d2267	An15Di15Ab70	melt_stdev	8.32	15.1		4420	520		13.9		1.04	0.598	24.8	15.8	22.1	0.856	25	10.1	3.36	53.6	15.6	0.243	12.6	8.47
D2275	An25Di25Ab50	plagioclase	53.9	40.7		52900	1300		50.3		3.76	bdl	30.5	10.6	3.38	5.3	63.7	4.55	274	1.56	0.393	0.76	0.865	75.1
D2275	An25Di25Ab50	plagioclase_stdev	1.9	8.84		2710	217		11.8		0.584	bdl	19.1	2.03	1.14	bdl	10.5	1.09	16.7	0.0141	0.237	0.17	0.417	6.19
D2275	An25Di25Ab50	diopside	34.2	bdl		4060	93800		bdl		69.4	0.905	75.7	95.4	257	485	5.4	0.54	21.4	271	5.28	0.354	0.33	1.01
D2275	An25Di25Ab50	diopside_stdev	6.87	bdl		281	1630		bdl		3.97	0.474	7.64	22.4	42.6	38.2	5.63	0.288	0.512	70	2.58	0.342	bdl	bdl
D2275	An25Di25Ab50	melt	334	234		60100	18700		376		12.1	1.19	43.2	116	29.1	5.04	17.9	255	156	645	202	0.762	228	242

Run	comp.	type	Li_ppm	Be_ppm	B_ppm	Na_ppm	Mg_ppm	P_ppm	K_ppm	Ca_ppm	Sc_ppm	Mn_ppm	Fe_ppm	Ti_ppm	V_ppm	Cr_ppm	Ga_ppm	Rb_ppm	Sr_ppm	Zr_ppm	Nb_ppm	In_ppm	Cs_ppm	Ba_ppm
D2275	An25Di25Ab50	melt_stdev	6.05	15		1820	407		13.1		0.721	0.386	9.36	8.31	1.84	1.85	3.15	11.8	1.35	73.8	14.2	0.363	11.7	8.26
D2293	An15Di15Ab70x	plagioclase	115	71.6			918		205		3.09		52.5		21.2	3.25	302	19.4	648	2.88	3.94	350	4.88	219
D2293	An15Di15Ab70x	plagioclase_stdev	2.9	1.41			107		9.05		0.354		10.6		1.66	0.778	8.49	5.65	24	3.71	5.31	bdl	6.39	10.2
D2293	An15Di15Ab70x	diopside	377	276			97400		523		201		287		1810	1210	184	308	175	427	310	80.1	301	226
D2293	An15Di15Ab70x	diopside_stdev																						
D2293	An15Di15Ab70x	melt	694	687			16200		1180		31.3		86.7		224	14.7	259	686	295	718	667	21.6	677	559
D2293	An15Di15Ab70x	melt_stdev	13.3	12.8			253		19.4		0.705		14.4		10.6	3.92	21.2	12.4	5.91	44.7	36.5	4.97	13.7	6.56
D2479	An25Di25Ab50x	plagioclase	81.2	70.8		48200	1410		128		3.28	bdl	32.5	7.88	11	bdl	188	13.7	575	2.74	3.46	0.73	3.73	131
D2479	An25Di25Ab50x	plagioclase_stdev	7.66	14.9		6660	152		22		0.209	bdl	1.39	1.11	0.794	bdl	139	0.39	38.4	0.446	0.237	0.751	0.933	18.9
D2479	An25Di25Ab50x	diopside	89.7	33.5		10500	99700		51.9		120	3.45	90.5	50.2	1010	1800	83.7	38.6	91.3	118	35.8	69.5	39.7	36.3
D2479	An25Di25Ab50x	diopside_stdev																						
D2479	An25Di25Ab50x	melt	416	328		49100	26000		570		31	1.54	32.1	84.6	164	62.9	93.6	339	324	383	305	6.64	322	314
D2479	An25Di25Ab50x	melt_stdev	6.89	8.8		1000	491		21.8		1.65	0.615	7.51	3.81	18.4	14.7	25.4	8.64	3.67	8.85	5.48	5.68	10.6	4.75

Table 45: CaO-MgO-Al_2O_3-SiO_2-Na_2O system experiments. Trace element analysis of experimental phases from mass 139 (La) to mass 238 (U)

Run	comp.	type	La_ppm	Ce_ppm	Pr_ppm	Nd_ppm	Sm_ppm	Eu_ppm	Gd_ppm	Tb_ppm	Dy_ppm	Y_ppm	Ho_ppm	Er_ppm	Tm_ppm	Yb_ppm	Lu_ppm	Hf_ppm	Ta_ppm	Pb_ppm	Th_ppm	U_ppm	trace (count)
20160928	Plag 1	plagioclase	8.13	5.81	5.38	4.25	2.81	3.24	2.26	1.54	1.25	1.16	1.01	0.805	0.63	0.545	0.474	0.171	0.176	15.5	0.059	0.122	5
20160928	Plag 1	plagioclase_stdev	0.231	0.268	0.184	0.143	0.229	0.154	0.224	0.0608	0.12	0.0954	0.0607	0.086	0.0919	0.106	0.0852	0.0874	0.109	0.688	0.0387	0.0846	
20160928	Plag 1	melt	204	234	218	199	196	222	222	210	215	239	217	219	207	218	206	234	231	205	118	243	5
20160928	Plag 1	melt_stdev	2.72	4.43	4.55	5.74	2.86	3.04	2.96	2.49	3.24	3.33	2.94	2.76	3.29	4.06	4.45	6.78	5.83	14.6	1.44	13.4	
20160928	Plag 2	plagioclase	11.6	8.17	7.24	5.28	3.59	4.49	2.73	1.92	1.58	1.41	1.18	1.06	0.724	0.653	0.577	0.25	0.253	14.6	0.156	0.38	4
20160928	Plag 2	plagioclase_stdev	0.661	0.566	0.413	0.37	0.322	0.318	0.284	0.215	0.294	0.1	0.0744	0.28	0.148	0.203	0.128	0.127	0.194	1.84	bdl	bdl	
20160928	Plag 2	melt	213	251	231	210	208	238	230	218	227	250	227	225	222	225	216	246	246	108	122	260	5
20160928	Plag 2	melt_stdev	3.25	2.42	3.2	4.55	3.94	3.21	5.38	3.9	4.55	4.57	1.79	3.96	2.88	3.85	4.03	6.27	1.48	37.3	2.42	7.01	
20160928	Di1	diopside	26.7	35	55.1	62.6	80.3	95.8	104	96	96.6	98.5	95	93.1	86.8	91.9	98	89.1	10.5	1	1.5	0.246	4
20160928	Di1	diopside_stdev	5.49	6.4	8.9	9.52	11.1	13	14	12.7	12.6	12.9	12.5	12.7	11.2	11.4	11.2	3.35	3.11	0.0258	0.588	0.286	
20160928	Di1	melt	263	302	269	233	223	250	249	238	246	268	247	253	241	249	231	262	307	80.4	151	316	4
20160928	Di1	melt_stdev	0.785	0.943	1.98	1.92	0.31	0.64	1.1	1.1	1.63	0.746	0.618	1.12	1.65	1.16	1.03	1.13	1.62	5.42	1.2	1.53	
20161008	Plag3	plagioclase	13.3	9.45	8.22	6.41	3.92	5.35	2.79	1.94	1.4	1.32	1.13	0.88	0.662	0.548	0.445	0.13	0.133	19	bdl	bdl	5
20161008	Plag3	plagioclase_stdev	1.07	1.19	0.523	0.54	0.512	0.65	0.401	0.286	0.143	0.24	0.137	0.154	0.0652	0.157	0.0913	bdl	0.0859	1.18	bdl	bdl	
20161008	Plag3	melt	210	241	227	206	204	235	228	216	228	244	223	223	221	226	212	237	245	244	119	250	5
20161008	Plag3	melt_stdev	1.88	2.37	1.05	1.69	3.83	2.75	4.58	2.42	3.78	2.71	2.33	2.7	2.13	2.76	1.5	1.14	2.65	3.43	1.53	2.41	
20161008	Plag4	plagioclase	22.3	16.2	13.7	11.1	6.56	8.91	5.37	3.61	3.13	2.79	2.35	1.84	1.5	1.59	1.01	0.89	1.05	20.2	0.86	1.64	3
20161008	Plag4	plagioclase_stdev	0.875	1.11	1.57	0.361	0.783	0.992	0.941	0.811	0.897	0.9	1.05	0.769	0.622	1	0.55	0.973	0.976	2.02	bdl	1.25	
20161008	Plag4	melt	198	241	214	198	196	226	216	209	211	234	217	219	209	216	208	247	236	192	115	257	6
20161008	Plag4	melt_stdev	7.68	6.05	10.8	8.53	7.45	8.66	9.35	10.6	4.89	11	8.05	9.86	12.2	9.61	8.09	9.19	6.02	14.8	3.81	7.94	
20161008	Di2	diopside	15.7	21.7	35.8	42.3	56.1	68.6	73.7	68.1	69.4	70.7	68.2	65.8	61.5	63.7	66.4	88.5	6.27	1.33	1.12	0.442	4
20161008	Di2	diopside_stdev	3.82	4.91	8.9	10.8	13.4	17.3	18.7	16.9	17.6	17.7	16.9	16.5	15.2	16.4	16.5	39.6	4.12	0.196	0.4	0.538	
20161008	Di2	melt	269	305	275	244	231	259	258	241	249	270	249	253	245	252	237	249	295	144	148	316	5
20161008	Di2	melt_stdev	1.69	1.73	2.62	1.76	2.01	1.65	1.52	1.7	2.84	1.53	1.3	2.32	1.12	1.34	1.4	4.13	3.55	29.4	0.635	2.32	
20161008	Di3	diopside	19.5	25.9	42	49.6	64.1	78.9	84.8	78.9	79.3	82.9	77.8	75.6	69.6	73	76.4	128	11.9	0.735	2.79	0.0433	5
20161008	Di3	diopside_stdev	1.99	2.17	3.99	4.59	5.85	7.18	7.59	7.2	7.31	7.26	7.06	6.63	5.96	6.6	6.2	5.19	0.879	0.0794	0.373	0.00495	
20161008	Di3	melt	279	320	282	251	237	269	263	249	256	285	254	260	249	260	247	240	320	43.7	162	337	5
20161008	Di3	melt_stdev	0.876	2.01	1.78	2.33	1.85	2.18	1.6	1.75	2.6	3.16	2.06	1.88	2.26	2.41	2.23	2.77	4.11	12.3	1.56	4.41	
20161025	Plag1	plagioclase	7.39	6.17	5	3.79	2.46	29.2	2.22	1.42	1.24	0.998	0.952	0.73	0.55	0.512	0.393	0.0757	0.0638	1.77			5
20161025	Plag1	plagioclase_stdev	0.662	0.436	0.421	0.248	0.197	1	0.243	0.113	0.169	0.074	0.111	0.0621	0.0467	0.0712	0.0352	0.0348	0.0255	0.516			
20161025	Plag1	diopside	26.5	45.9	62.1	72.3	97.5	107	125	122	123	127	122	119	108	113	112	241	26.4	0.0935	3.9	2.44	2
20161025	Plag1	diopside_stdev	1.28	2.66	3.16	2.4	4.67	7.64	4.45	2.76	0.495	1.56	0.707	0.0707	1.06	2.9	3.46	0.141	1.03	0.0728	0.502	0.58	
20161025	Plag1	melt	471	518	478	421	397	427	440	421	431	483	439	451	432	445	416	381	498	13.5	267	572	5
20161025	Plag1	melt_stdev	53	53.4	53.7	42.2	39.9	40.2	42.1	38.2	41.8	46	42.4	44.5	40.4	45.4	40.3	38	69.4	7.98	35.3	72.2	
20161025	Plag2	plagioclase	10.8	9.03	6.96	5.38	3.01	46.8	2.69	1.72	1.44	1.2	1.1	0.907	0.606	0.516	0.46	0.184	0.133	1.21	0.039	0.0745	3
20161025	Plag2	plagioclase_stdev	0.176	0.132	0.245	0.322	0.0379	1.5	0.155	0.106	0.132	0.0935	0.0249	0.0153	0.0425	0.0197	0.0414	0.0632	0.0424	0.235	0.0242	0.0813	
20161025	Plag2	melt	216	250	237	214	208	224	236	226	225	249	230	234	218	227	217	241	246	2.47	124	260	5
20161025	Plag2	melt_stdev	1.86	3.41	2.35	3.88	2.03	1.84	2.9	3.09	2.14	3.68	1.48	2.42	1.48	2.21	2.05	4.95	2.25	0.42	2.22	5.19	

Run	comp.	type	La_ppm	Ce_ppm	Pr_ppm	Nd_ppm	Sm_ppm	Eu_ppm	Gd_ppm	Tb_ppm	Dy_ppm	Y_ppm	Ho_ppm	Er_ppm	Tm_ppm	Yb_ppm	Lu_ppm	Hf_ppm	Ta_ppm	Pb_ppm	Th_ppm	U_ppm	trace (count)
20161025	Plag3	plagioclase	11.9	9.43	7.59	5.71	3.38	56.6	2.7	1.72	1.44	1.17	1.12	0.781	0.633	0.501	0.47	bdl	0.0874	0.603	bdl	bdl	7
20161025	Plag3	plagioclase_stdev	0.735	0.453	0.433	0.542	0.231	1.94	0.17	0.16	0.185	0.0509	0.107	0.121	0.0879	0.217	0.103	bdl	0.0324	0.178	bdl	bdl	
20161025	Plag3	melt	217	245	242	212	213	229	236	224	233	257	231	235	232	237	228	244	257	2.25	125	276	5
20161025	Plag3	melt_stdev	2.35	4.48	4.86	5.67	2.65	2.73	3.39	3.82	1.94	3.08	3.45	1.97	3.92	3.37	3.24	4.84	3.6	0.149	2.89	6.07	
c5075	An45Di45Ab10	plagioclase	19.1	19.7	17.3	14.3	11.2	73.2	11.3	9.68	9.33	9.4	9.42	8.78	8.77	8.75	8.06	6.95	10	7.27	7.65	11.9	3
c5075	An45Di45Ab10	plagioclase_stdev	10.2	11.3	10.7	9.35	8.08	15.2	9.07	8.17	8.08	8.62	8.52	8.13	8.59	8.4	8.53	7.5	9.87	1.74	4.31	11.1	
c5075	An45Di45Ab10	diopside	30.7	51.9	67.7	78.9	112	122	151	148	154	143	154	148	136	136	129	210	36.3	1.37	8.19	11.9	3
c5075	An45Di45Ab10	diopside_stdev	11.6	13.3	11.5	9.79	7.97	19	6.18	6.99	4.83	5.05	5.52	4.99	5.17	6.33	5.98	8.75	12.4	1.16	6.2	12	
c5075	An45Di45Ab10	melt	758	842	766	660	630	648	684	645	667	678	675	680	664	692	650	570	774	49.6	393	834	4
c5075	An45Di45Ab10	melt_stdev	7.48	6.22	9.22	8.73	7.63	7.72	9.5	8.09	7.91	5.46	8.11	11	11.1	8.45	8.7	9.23	12.8	1.2	4.32	6.81	
c5083	An45Di45Ab10	plagioclase	9.09	8.87	6.85	5.32	3.63	65.2	3.18	2.38	2.18	1.75	1.78	1.51	1.29	1.26	1.1	0.578	0.585	2.98	0.207	0.634	16
c5083	An45Di45Ab10	plagioclase_stdev	0.985	1.13	0.96	0.807	0.723	4.13	0.716	0.529	0.696	0.523	0.578	0.623	0.579	0.586	0.573	0.607	0.537	0.541	0.166	0.53	
c5083	An45Di45Ab10	diopside	24.1	45	57.2	67.9	97.4	97.5	133	130	134	127	135	133	123	121	115	183	23.1	0.544	4.32	5.79	16
c5083	An45Di45Ab10	diopside_stdev	4.02	5.78	6.71	6.97	9.21	9.59	11.3	11.1	11.4	10.9	11.5	11.5	10.9	10.7	10.5	20.7	6.99	0.333	1.87	2.79	
c5083	An45Di45Ab10	melt	522	603	536	468	456	489	500	472	486	489	491	506	493	500	474	466	531	34.3	275	585	21
c5083	An45Di45Ab10	melt_stdev	64.3	67.6	60.9	50	45.6	39.1	50.8	47.5	48.5	49.5	49.9	52.4	49.4	51.6	50.7	43.7	71.8	4.14	37.5	78.8	
c5094	An40Di40Ab20	plagioclase	9.14	8.09	6.49	4.83	3.46	100	2.92	2.14	1.75	1.52	1.47	1.26	0.985	1.02	0.784	0.373	0.383	0.786	0.02	0.099	7
c5094	An40Di40Ab20	plagioclase_stdev	0.788	0.685	0.637	0.619	0.533	4.5	0.446	0.348	0.447	0.406	0.372	0.512	0.324	0.384	0.327	0.341	0.446	0.198	0.0113	0.0537	
c5094	An40Di40Ab20	diopside	22.7	38.6	52.7	61.3	87.4	80.7	118	114	118	111	117	113	106	107	103	137	12.4	0.308	3.87	6.71	7
c5094	An40Di40Ab20	diopside_stdev	2.74	2.73	2.95	3.22	5.76	7.83	7.8	7.49	8.44	9.31	8.89	10	9.78	10.4	9.45	32.3	7.15	0.199	1.95	4.49	
c5094	An40Di40Ab20	melt	370	410	387	336	329	354	361	347	356	357	356	358	356	365	341	312	362	8.63	186	406	10
c5094	An40Di40Ab20	melt_stdev	34.6	37.9	34.8	30.1	28.6	15.1	31	29.9	32.2	33.4	32.4	33.5	35.2	36.6	34.2	42.6	62.9	0.549	20	38	
c5121	An35Di35Ab30	plagioclase	7.26	6.46	4.78	3.7	2.35	62.5	1.85	1.39	1.14	0.945	0.957	0.814	0.634	0.625	0.468	0.19	0.246	1.24	0.159	0.426	10
c5121	An35Di35Ab30	plagioclase_stdev	1.48	1.3	0.91	0.597	0.414	8.63	0.328	0.265	0.257	0.233	0.236	0.223	0.194	0.205	0.169	0.18	0.188	0.133	0.0754	0.361	
c5121	An35Di35Ab30	diopside	40.2	63.3	74.7	83.6	113	99.8	149	144	146	139	148	144	132	136	133	181	34.2	1.32	13.1	27.1	4
c5121	An35Di35Ab30	diopside_stdev	31.9	37.3	33.2	29.1	28.7	23.8	30.5	29.5	30.3	31.5	30.8	31.7	31.2	32	32.2	39.7	41.7	1.52	20.7	42.9	
c5121	An35Di35Ab30	melt	137	161	147	130	131	151	148	141	143	145	147	149	142	147	140	147	138	13.5	69.4	145	7
c5121	An35Di35Ab30	melt_stdev	17.8	20.2	18	15.6	14.7	14	16	14.6	14.9	14.7	15.2	14.8	15.3	15.8	14.7	10.6	14.5	0.663	7.8	18.6	
C5473	An15Di15Ab70x	plagioclase	12.3	9.29	7.37	5.38	3.04	148	2.35	1.49	1.21	0.833	0.895	0.728	0.537	0.486	0.349	0.18	0.141	4.22	bdl	bdl	5
C5473	An15Di15Ab70x	plagioclase_stdev	0.589	0.517	0.551	0.245	0.453	2.56	0.445	0.0522	0.216	0.0818	0.0874	0.119	0.0965	0.129	0.0626	bdl	0.0724	0.515	bdl	bdl	
C5473	An15Di15Ab70x	diopside	129	209	270	309	404	303	531	498	528	480	511	479	450	451	440	311	94.1	5.49	24.6	36.6	4
C5473	An15Di15Ab70x	diopside_stdev	28.9	31.9	35.5	33.1	38.4	37.6	54.9	45.1	46.2	40.9	50.8	40.6	41.3	42.1	45.7	60.5	25	6.72	17.8	33.4	
C5473	An15Di15Ab70x	melt	647	723	659	579	555	458	613	578	622	625	620	628	633	647	603	665	775	81.4	363	732	4
C5473	An15Di15Ab70x	melt_stdev	17.2	11.3	17	9.42	16.2	11.1	9.57	12	12.1	11.7	13.9	27.7	32.7	17.1	14.3	15.9	62.2	45	25.1	58.1	
C5480	An25Di25Ab50x	plagioclase	17	16.7	13.2	10.5	8.34	114	7.92	7.2	7.13	6.78	7.22	6.9	6.56	7.2	6.4	12.4	9.36	7.78	8.19	0.243	4
C5480	An25Di25Ab50x	plagioclase_stdev	0.725	0.471	0.403	0.404	0.031	3.21	0.277	0.136	0.142	0.0704	0.0384	0.0719	0.0635	0.0794	0.0374	bdl	0.053	0.726	bdl	bdl	
C5480	An25Di25Ab50x	diopside	42.8	79.9	107	128	183	161	239	232	238	225	242	235	210	208	206	165	17.8	1.14	2.84	4.14	4
C5480	An25Di25Ab50x	diopside_stdev	6.69	10.3	12	13.5	17	11.9	24.4	23.9	25.3	25.9	27.8	32.8	22	24.1	25.9	12.4	5	0.368	0.919	2.14	
C5480	An25Di25Ab50x	melt	635	729	650	562	537	487	569	542	564	571	577	581	563	584	549	568	719	53	342	723	4
C5480	An25Di25Ab50x	melt_stdev	81	88.8	77.9	70.6	62.4	45.7	66.3	68.1	69.9	69.1	69.3	89.5	69.3	74.9	73.8	129	155	10	70.7	140	

Run	comp.	type	La_ppm	Ce_ppm	Pr_ppm	Nd_ppm	Sm_ppm	Eu_ppm	Gd_ppm	Tb_ppm	Dy_ppm	Y_ppm	Ho_ppm	Er_ppm	Tm_ppm	Yb_ppm	Lu_ppm	Hf_ppm	Ta_ppm	Pb_ppm	Th_ppm	U_ppm	trace (count)
d2061	An25Di25Ab50	plagioclase	7.12	5.88	4.34	3.25	1.87	84.5	1.53	1.01	0.784	0.621	0.641	0.497	0.381	0.308	0.233	0.0696	0.0666	1.32	0.0968	0.062	11
d2061	An25Di25Ab50	plagioclase_stdev	0.814	0.572	0.387	0.377	0.209	7.09	0.145	0.0941	0.0985	0.0692	0.0947	0.0602	0.0573	0.0627	0.0471	0.0437	0.0342	0.309	0.106	0.025	
d2061	An25Di25Ab50	diopside	14.9	28.1	39.3	47.5	70.9	56.9	100	94.1	97.9	90.8	97.8	91.8	85.9	84.8	81.1	65.2	6.13	0.34	1.14	2.11	11
d2061	An25Di25Ab50	diopside_stdev	1.99	3.14	3.91	4.18	6.07	4.36	9.68	8.4	8.74	8.52	9.52	9.32	8.5	8.43	7.54	12.2	3.02	0.127	0.589	1.46	
d2061	An25Di25Ab50	melt	125	139	131	115	116	133	132	124	129	129	130	129	127	131	123	127	129	8.21	59.9	135	12
d2061	An25Di25Ab50	melt_stdev	16.4	19.2	16.8	14.9	14.2	9.59	14.7	13.5	14.7	14.5	14.2	14.6	14.5	14.3	14	12.7	15.6	1.09	2.62	6.63	
D2067	An35Di35Ab30	plagioclase	6.9	6.03	4.74	3.71	2.4	89.7	2	1.4	1.21	0.934	0.965	0.768	0.585	0.557	0.457	0.16	0.194	0.595	0.0775	0.239	6
D2067	An35Di35Ab30	plagioclase_stdev	0.406	0.226	0.233	0.259	0.223	1.24	0.103	0.157	0.196	0.221	0.206	0.182	0.147	0.146	0.173	0.194	0.206	0.0909	0.108	0.236	
D2067	An35Di35Ab30	melt	192	218	205	183	186	211	206	196	202	200	202	206	195	205	194	207	197	5.48	96.1	207	6
D2067	An35Di35Ab30	melt_stdev	1.38	2.77	2.45	1.07	1.16	1.83	2.61	1.58	1.95	2.44	1.72	2.77	1.7	2.07	1.47	2.74	2.06	0.744	0.886	1.99	
d2074	An15Di15Ab70	plagioclase	4.03	3.22	2.35	1.65	0.995	59.5	0.67	0.476	0.307	0.258	0.301	0.192	0.147	0.148	0.102	bdl	0.046	0.62	bdl	bdl	4
d2074	An15Di15Ab70	plagioclase_stdev	0.159	0.231	0.196	0.231	0.108	1.61	0.092	0.0457	0.0713	0.0489	0.0262	0.0688	0.0184	0.0264	0.0206	bdl	0.0177	0.0852	bdl	bdl	
d2074	An15Di15Ab70	melt	76.9	92.3	84.2	76.8	77.4	88.2	85.1	84.8	84.8	86.1	87	84.9	81.3	84.3	82	96.1	88.3	6.78	41.1	88.2	5
d2074	An15Di15Ab70	melt_stdev	1.36	1.98	2.28	2.72	2.64	2.04	1.97	1.17	3.2	1.96	0.968	2.58	1.66	1.48	1.81	6.4	2.23	0.731	1.24	1.05	
d2075	An35Di35Ab30	diopside	15.2	28.2	39.5	47.6	71.2	60.9	98.1	96	99.4	93.9	101	97.2	88.9	89.5	85.8	89.6	7.91	0.389	1.31	2.2	6
d2075	An35Di35Ab30	diopside_stdev	1.31	1.96	2.85	3.7	5.24	3.64	8.06	6.64	6.93	6.83	7.26	6.99	6.39	6.25	5.9	14.4	2.7	0.183	0.553	1.07	
d2075	An35Di35Ab30	melt	182	206	193	171	173	203	191	182	186	186	191	191	184	192	182	183	184	5.2	91.9	196	6
d2075	An35Di35Ab30	melt_stdev	2.74	3.67	2.8	2.54	1.93	3.11	2.27	2.45	2.06	3.32	2.42	2.41	2.93	2.98	2.7	4.27	4.46	0.483	2.02	4.62	
d2076	An35Di35Ab30	plagioclase	9.68	8.45	6.18	4.63	2.94	118	2.05	1.55	1.18	0.845	1.13	1.03	0.777	0.85	0.33	0.14	0.148	2.3	bdl	bdl	2
d2076	An35Di35Ab30	plagioclase_stdev	0.82	0.0636	0.0141	0.247	0.0212	1.34	0.163	0.099	0.113	0.0495	0.342	0.382	0.387	0.636	bdl	bdl	bdl	0.375	bdl	bdl	
d2076	An35Di35Ab30	diopside	33.9	55.4	69	77.1	103	78.6	139	131	133	125	134	130	119	119	116	143	27.8	0.655	9.1	20.1	5
d2076	An35Di35Ab30	diopside_stdev	20.8	26	24.3	21.8	18.5	14.1	20.5	18.7	17.5	17.6	18.2	18.9	19.3	22.3	21.3	22.8	16.7	0.739	10.3	24	
d2076	An35Di35Ab30	melt	237	276	256	221	216	246	239	226	230	232	235	241	234	240	223	252	251	7.91	122	262	5
d2076	An35Di35Ab30	melt_stdev	10.6	12	11.3	10.7	8.02	5.38	11.2	8.84	10	9.89	9.97	8.69	9.61	10.4	8.68	9.62	10.3	0.477	5.92	11.6	
d2079	An35Di35Ab30	plagioclase	9.29	8.6	6.63	5.26	3.68	95.8	2.88	2.18	1.77	1.54	1.62	1.33	1.13	1.19	0.924						12
d2079	An35Di35Ab30	plagioclase_stdev	1.03	1.2	0.912	0.803	0.73	7.48	0.654	0.613	0.62	0.513	0.494	0.528	0.53	0.627	0.543						
d2079	An35Di35Ab30	diopside	20.1	34.8	45.2	53	76.9	67.1	105	103	106	100	108	102	95.6	94.7	90.5						13
d2079	An35Di35Ab30	diopside_stdev	10.6	11.8	10.3	8.81	9.02	8.85	10.6	9.61	9.89	9.51	9.87	9.65	9.25	9.59	9.47						
d2079	An35Di35Ab30	melt	226	259	240	212	211	239	235	223	227	229	235	233	227	234	223						13
d2079	An35Di35Ab30	melt_stdev	17.7	18.4	16.4	14.9	14.3	12.8	17.2	17.5	18.4	18.6	18.1	19.5	17.2	18.6	19.4						
d2087	An25Di25Ab50	plagioclase	8.69	7.56	5.66	4.72	3.13	99.7	3.04	2.39	2.44	2.15	2.16	1.98	1.77	1.8	1.97	1.61	2.81	1.57	1.04	3.91	1
d2087	An25Di25Ab50	diopside	38.5	65.4	86	100	133	94.9	176	169	165	161	166	155	140	146	140	115	31.4	0.848	7.02	10.2	3
d2087	An25Di25Ab50	diopside_stdev	6.72	5.17	2.43	2.93	4.61	2.93	7.4	10.4	7.36	8.41	8.49	7.23	5.8	5.05	4.04	15.9	7.23	1.03	5.44	11.8	
d2087	An25Di25Ab50	melt	282	310	285	247	238	194	252	247	248	271	260	263	256	269	241	216	339	13.5	163	336	6
d2087	An25Di25Ab50	melt_stdev	9.82	6.74	8.27	6.38	8.92	2.01	10.8	8.76	4.46	8	11.3	8.6	12.1	10.3	5.94	11	6.85	12.5	7.12	16.2	
d2088	An35Di35Ab30	plagioclase	7.57	6.54	5.12	4	2.54	79.6	2.31	1.54	1.43	1.25	1.32	0.96	1	1.01	0.855	0.63	1.02	1.26	0.315	1.42	2
d2088	An35Di35Ab30	plagioclase_stdev	0.368	0.629	0.219	0.163	0.594	3.68	0.184	0.106	0.0495	0.106	0.00707	0.0849	0.0566	0.0212	0.0495	0.0707	0.332	0.184	0.0495	0.516	
d2088	An35Di35Ab30	diopside	17.8	32.8	44.9	54.3	78.9	65	107	102	106	101	109	101	95.5	94.8	91	84.4	12.7	0.286	2.25	4.4	2
d2088	An35Di35Ab30	diopside_stdev	1.45	0.0707	1.84	3.89	6.93	2.33	10.8	7.71	12.2	11.8	10.3	5.66	10.5	9.19	11.4	1.7	1.58	0.246	0.757	3.28	
d2088	An35Di35Ab30	melt	207	238	223	196	194	199	213	200	204	205	211	210	207	210	198	207	235	8.73	112	245	6
d2088	An35Di35Ab30	melt_stdev	3.13	4.27	3.52	2.35	3.85	3.97	3.37	3.65	4.06	4.67	3.89	5.01	3.91	3.75	2.98	4.16	5.6	0.679	1.6	3.72	

Run	comp.	type	La_ppm	Ce_ppm	Pr_ppm	Nd_ppm	Sm_ppm	Eu_ppm	Gd_ppm	Tb_ppm	Dy_ppm	Y_ppm	Ho_ppm	Er_ppm	Tm_ppm	Yb_ppm	Lu_ppm	Hf_ppm	Ta_ppm	Pb_ppm	Th_ppm	U_ppm	trace (count)
d2091	An45Di45Ab10	plagioclase	9.47	8.45	6.75	5.09	3.43	56.3	2.74	1.9	1.62	1.32	1.33	1.04	0.802	0.722	0.577	0.0932	0.15	8.87	0.0645	0.235	6
d2091	An45Di45Ab10	plagioclase_stdev	0.539	0.444	0.352	0.18	0.333	3.61	0.229	0.127	0.181	0.0448	0.0997	0.126	0.0815	0.0721	0.108	0.103	0.116	0.65	0.0375	0.258	
d2091	An45Di45Ab10	diopside	25.1	47.3	63.9	75.6	105	115	140	134	137	128	135	130	120	121	118	177	13.4	1.51	1.75	2.27	6
d2091	An45Di45Ab10	diopside_stdev	4.01	6.89	9.02	10.3	12.3	14.3	15.8	13.6	14.5	13.2	13.9	13.2	13.2	14	14.3	22.6	3.33	0.37	0.268	0.329	
d2091	An45Di45Ab10	melt	369	423	392	341	337	373	370	351	358	361	364	368	358	371	348	330	390	70.8	195	418	6
d2091	An45Di45Ab10	melt_stdev	4.45	4.7	3.72	3.32	3.74	3.7	3.55	3.68	2.97	4.06	3.07	4.77	4.18	4.88	3.51	5.11	5.3	1.17	2	6.71	
d2092	An45Di45Ab10	plagioclase	13.7	12.2	9.85	7.86	5.04	117	4.53	3.19	2.58	2.38	2.52	2.14	1.84	1.78	1.66	1.22	1.65	3.59	0.617	1.88	3
d2092	An45Di45Ab10	plagioclase_stdev	2.12	1.63	1.6	1.91	0.9	8.22	1.5	1.09	0.792	1.41	1.03	0.845	0.835	0.918	0.738	0.697	1.34	0.292	0.45	2.21	
d2092	An45Di45Ab10	diopside	24.3	44.1	58.6	68.9	100	98.6	139	135	143	136	144	140	130	129	122	164	23.7	0.569	5.6	9.43	17
d2092	An45Di45Ab10	diopside_stdev	6.74	8.27	7.1	6.26	6.69	6.97	7.76	7.31	7.98	7.49	7.93	7.68	7.1	7.51	7.23	10.1	9.13	0.431	6.3	12.9	
d2092	An45Di45Ab10	melt	474	529	483	416	400	438	434	406	418	422	424	427	421	433	414	390	484	33.8	243	522	16
d2092	An45Di45Ab10	melt_stdev	68.2	74.9	67.5	57.8	51.8	50.7	56.8	51.3	53.6	54.8	54.6	54.7	55.4	56.3	55.1	51.1	72.5	3.77	43.5	94.7	
d2097	An15Di15Ab70	plagioclase	4.57	3.27	2.64	2.1	1.56	69.3	0.917	0.552	0.365	0.196	0.273	0.242	0.125	0.165	0.104	bdl	0.056	1.36	bdl	bdl	3
d2097	An15Di15Ab70	plagioclase_stdev	0.437	0.225	0.393	0.622	0.335	1	0.612	0.269	0.0919	0.00778	0.0212	0.0445	0.0219	0.00707	0.0134	bdl	bdl	0.226	bdl	bdl	
d2097	An15Di15Ab70	diopside	23.6	44.2	55.3	67	92.7	56.1	124	119	118	113	113	98	102	103	99.2	45.1	6.97	0.455	1.73	3	2
d2097	An15Di15Ab70	diopside_stdev	3.46	4.49	4.19	4.03	6.08	2.83	5.37	5.87	5.09	4.88	5.8	5.59	6.22	3.68	3.68	0.919	2.17	0.346	1.04	2.33	
d2097	An15Di15Ab70	melt	103	125	110	99.9	104	94.9	116	111	116	117	114	109	112	115	108	143	106	4.88	52.3	110	3
d2097	An15Di15Ab70	melt_stdev	7.13	7.79	7.78	5.16	5.6	3.92	8.31	6.57	8.93	9.18	7.86	7.52	10.3	8.47	8.66	25.3	5.35	0.993	3.97	9.46	
d2098	An15Di15Ab70	plagioclase	3.86	3.25	2.48	1.76	1.15	50.5	0.88	0.623	0.48	0.449	0.473	0.382	0.311	0.305	0.257	0.344	0.495	2.29	0.204	0.784	8
d2098	An15Di15Ab70	plagioclase_stdev	0.485	0.623	0.56	0.463	0.383	2.07	0.218	0.268	0.227	0.258	0.281	0.227	0.223	0.218	0.196	0.304	0.517	0.794	0.21	0.838	
d2098	An15Di15Ab70	diopside	57.9	78.4	95.8	94.6	114	178	144	128	130	125	133	145	115	130	119	150	68.3	10.5	19.5	49.2	2
d2098	An15Di15Ab70	diopside_stdev	14.9	25.2	39.7	42.3	53.2	22.1	78.6	65.3	71.5	62.6	76.8	95	63.2	78.4	72.5	135	44.3	0.0919	10.8	5.87	
d2098	An15Di15Ab70	melt	157	179	164	139	134	113	146	135	147	147	148	153	146	153	144	173	168	7.19	80.8	165	4
d2098	An15Di15Ab70	melt_stdev	53.2	64.4	54.5	45.5	41	21.7	43.1	44.3	45.4	45	47.6	42.6	43.5	49.9	45.7	85.8	59.3	3.51	30.1	58.5	
d2262	An15Di15Ab70	plagioclase	4.04	3.21	2.33	1.72	0.848	54.6	0.61	0.412	0.249	0.296	0.165	0.159	0.066	0.134	0.116	bdl	bdl	0.97	bdl	bdl	5
d2262	An15Di15Ab70	plagioclase_stdev	0.623	0.437	0.367	0.251	0.283	5.46	0.0927	0.0251	0.0912	0.0621	0.0596	0.0311	bdl	0.0318	0.0328	bdl	bdl	0.145	bdl	bdl	
d2262	An15Di15Ab70	diopside	36	57.3	74	82.5	111	76.3	145	139	147	143	148	136	0.692	128	130	81.2	21.5	0.728	9.08	17.7	5
d2262	An15Di15Ab70	diopside_stdev	17.5	22.2	22.2	21	23.8	10.6	27.1	28	30.2	28.8	32.7	30.9	0.504	28.6	30.6	22.2	25.9	0.441	12.4	24.4	
d2262	An15Di15Ab70	melt	102	120	111	98.2	95.7	108	108	99.5	105	106	108	103	0.186	101	94.6	93.5	92.6	8.75	43.4	96.9	5
d2262	An15Di15Ab70	melt_stdev	10.2	9.52	11.2	9.63	8.24	6.2	7.24	8.27	8.68	7.28	9.39	10.2	0.0426	7.51	7.47	4.06	6.82	0.496	2.69	4.97	
d2267	An15Di15Ab70	plagioclase	5.06	3.61	2.62	1.76	1.08	77.5	0.665	0.485	0.387	0.308	0.263	0.205	0.163	0.118	0.0993	bdl	0.0585	2.98	bdl	0.126	4
d2267	An15Di15Ab70	plagioclase_stdev	0.866	0.543	0.355	0.499	0.28	6.08	0.146	0.0267	0.109	0.0543	0.0246	0.059	0.0319	0.0197	0.0168	bdl	0.0403	0.478	bdl	bdl	
d2267	An15Di15Ab70	diopside	21.6	40.4	57.8	69.2	96.5	56.1	128	123	123	109	121	128	103	109	106	61.2	6.58	0.278	0.74	1.03	3
d2267	An15Di15Ab70	diopside_stdev	0.153	2.9	0.777	1.4	2.17	1.59	1.34	2.72	7.19	1.07	3.86	8.22	12.3	5.59	3.36	20.3	2.68	0.0936	0.125	0.274	
d2267	An15Di15Ab70	melt	99.9	113	106	93.9	94.6	88.4	107	101	103	106	106	110	105	106	103	113	111	8.82	51.3	113	7
d2267	An15Di15Ab70	melt_stdev	11	11.2	12.1	8.77	7.5	5.59	9.69	9.52	9.8	9.57	9.51	12.5	14	9.84	11	23.5	13.9	6.47	6.52	10.8	
D2275	An25Di25Ab50	plagioclase	7.47	5.93	4.64	3.31	1.59	75.1	1.69	1.01	0.873	0.633	0.747	0.563	0.493	0.533	0.397	0.36	0.53	2.59	0.161	0.465	3
D2275	An25Di25Ab50	plagioclase_stdev	1.18	0.825	0.931	0.985	0.316	10.2	0.271	0.0153	0.102	0.11	0.0902	0.0513	0.0341	0.203	0.0654	0.17	0.0424	0.509	0.0481	0.0919	
D2275	An25Di25Ab50	diopside	24.3	44.5	60.6	70	99.4	79.4	131	126	129	120	127	123	112	114	115	174	15.9	1.47	2.09	1.83	3
D2275	An25Di25Ab50	diopside_stdev	1.71	3.7	4.04	6.52	6.27	4.29	8.78	10.3	8.9	8	9.95	11.3	11.3	9.36	11.6	62.2	7.1	2.25	0.263	0.14	
D2275	An25Di25Ab50	melt	194	214	202	174	171	182	189	180	184	186	187	186	180	187	175	171	193	13.8	91.2	198	5

Run	comp.	type	La_ppm	Ce_ppm	Pr_ppm	Nd_ppm	Sm_ppm	Eu_ppm	Gd_ppm	Tb_ppm	Dy_ppm	Y_ppm	Ho_ppm	Er_ppm	Tm_ppm	Yb_ppm	Lu_ppm	Hf_ppm	Ta_ppm	Pb_ppm	Th_ppm	U_ppm	trace (count)
D2275	An25Di25Ab50	melt_stdev	9.02	9.67	8.75	9	5.72	5.18	9.09	8.91	9.3	9.68	9.54	8.97	8.53	10.2	8.46	25.8	21.6	1.1	9.31	17.2	
D2293	An15Di15Ab70x	plagioclase	19.4	16.7	12.2	9.47	5.99	180	4.53	3.34	3.05	2.91	2.66	2	2.05	2	1.85	1.88	3.02	17.6	1.97	8.3	
D2293	An15Di15Ab70x	plagioclase_stdev	4.5	5.54	4.55	3.73	2.85	6.43	2.36	2.21	2.05	2.53	2.32	1.84	2.05	1.98	2.05	2.3	4.07	3.94	bdl	bdl	2
D2293	An15Di15Ab70x	diopside	311	419	434	450	543	470	684	647	675	626	657	620	595	616	594	381	268	63.1	125	254	1
D2293	An15Di15Ab70x	diopside_stdev																					
D2293	An15Di15Ab70x	melt	579	682	607	526	517	467	568	545	588	584	585	574	572	586	561	539	602	119	287	614	6
D2293	An15Di15Ab70x	melt_stdev	9.7	16.3	10.6	11.7	11.4	7.04	12.6	9.16	9.36	11.3	14.8	14.4	12.9	16.9	13.1	60.4	47.3	13.1	19.5	38.2	
D2479	An25Di25Ab50x	plagioclase	16.7	14.8	11.4	8.86	5.78	135	5.22	3.89	3.24	3.42	3.25	3.02	2.42	2.73	2.05	1.56	2.48	8.37	0.857	2.59	2
D2479	An25Di25Ab50x	plagioclase_stdev	2.85	1.71	1.35	0.863	0.0139	14.8	0.418	0.0975	0.766	0.738	0.0557	0.738	0.473	0.0418	0.362	0.111	0.752	2.34	0.32	0.571	
D2479	An25Di25Ab50x	diopside	65.6	99.4	121	138	182	175	239	229	232	218	228	223	206	201	200	134	39.3	7.73	17.2	36.2	1
D2479	An25Di25Ab50x	diopside_stdev																					
D2479	An25Di25Ab50x	melt	263	313	287	259	258	275	294	275	287	285	288	290	279	290	274	314	295	38.3	137	290	5
D2479	An25Di25Ab50x	melt_stdev	2.95	8.06	4.31	2.93	1.4	4.4	2.11	3.7	3.27	2.36	3.21	6.98	8.48	4.12	2.4	48.2	5.58	8.32	1.4	8.16	

Table 46: CaO-MgO-Al_2O_3-SiO_2-Na_2O-Fe_2O_3 system experiments. Experimental conditions and major element average and standard deviation (stdev)

Run	comp.	type	T1	T2	fO2	P	time	System	Na2O	MgO	Al2O3	SiO2	CaO	FeO	Total	major (count)
C5430	Ab50-Fe10	plagioclase	1280	1180	none	11 kbar	48 h	CMASNF	6.06	0.155	26	56.9	9.79	2.14	101	8
C5430	Ab50-Fe10	plagioclase_stdev	1280	1180	none	11 kbar	48 h	CMASNF	0.204	0.138	0.671	0.872	0.399	0.329	0.794	
C5430	Ab50-Fe10	diopside	1280	1180	none	11 kbar	48 h	CMASNF	1.54	10.4	9.65	44.7	20.8	12.3	99.4	8
C5430	Ab50-Fe10	diopside_stdev	1280	1180	none	11 kbar	48 h	CMASNF	0.115	0.569	0.888	0.989	0.335	0.789	0.448	
C5430	Ab50-Fe10	melt	1280	1180	none	11 kbar	48 h	CMASNF	6.26	3.42	17.9	60.3	7.78	5.49	101	6
C5430	Ab50-Fe10	melt_stdev	1280	1180	none	11 kbar	48 h	CMASNF	0.0573	0.0311	0.133	0.366	0.0396	0.188	0.477	
C5442	Ab10-Fe10	plagioclase	1300	1200	none	11 kbar	48 h	CMASNF	2.48	0.191	31.5	49.2	15.9	1.75	101	8
C5442	Ab10-Fe10	plagioclase_stdev	1300	1200	none	11 kbar	48 h	CMASNF	0.13	0.0147	0.332	0.551	0.208	0.0531	0.493	
C5442	Ab10-Fe10	diopside	1300	1200	none	11 kbar	48 h	CMASNF	0.416	9.48	14.2	40.6	22.9	12	99.7	8
C5442	Ab10-Fe10	diopside_stdev	1300	1200	none	11 kbar	48 h	CMASNF	0.0354	0.559	1	0.887	0.0687	0.506	0.313	
C5442	Ab10-Fe10	melt	1300	1200	none	11 kbar	48 h	CMASNF	2.08	5.67	17.8	50.3	14	6.99	96.8	6
C5442	Ab10-Fe10	melt_stdev	1300	1200	none	11 kbar	48 h	CMASNF	0.019	0.0569	0.134	0.156	0.0583	0.0353	0.169	
C5443	Ab10-Fe1	plagioclase	1350	1250	none	11 kbar	48 h	CMASNF	2.66	0.293	31.6	50	15.6	0.295	101	8
C5443	Ab10-Fe1	plagioclase_stdev	1350	1250	none	11 kbar	48 h	CMASNF	0.113	0.0211	0.342	0.415	0.252	0.0148	0.606	
C5443	Ab10-Fe1	diopside	1350	1250	none	11 kbar	48 h	CMASNF	0.402	14.7	11	49.5	23.9	1.4	101	8
C5443	Ab10-Fe1	diopside_stdev	1350	1250	none	11 kbar	48 h	CMASNF	0.0464	0.861	1.94	1.02	0.18	0.175	0.316	
C5443	Ab10-Fe1	melt	1350	1250	none	11 kbar	48 h	CMASNF	2.21	4.32	16.8	54.8	17.1	1.03	96.2	6
C5443	Ab10-Fe1	melt_stdev	1350	1250	none	11 kbar	48 h	CMASNF	0.0536	0.0555	0.185	0.308	0.105	0.0124	0.561	
C5469	Ab10-Fe5	plagioclase	1335	1235	none	11 kbar	48 h	CMASNF	1.86	0.309	31.9	47.3	16.6	1.49	99.5	
C5469	Ab10-Fe5	plagioclase_stdev	1335	1235	none	11 kbar	48 h	CMASNF	0.216	0.0199	0.483	0.699	0.349	0.0642	0.344	
C5469	Ab10-Fe5	diopside	1335	1235	none	11 kbar	48 h	CMASNF	0.33	12.7	11.2	45.5	23.2	6.82	99.8	
C5469	Ab10-Fe5	diopside_stdev	1335	1235	none	11 kbar	48 h	CMASNF	0.0109	0.601	1.02	1.28	0.139	0.4	0.83	
C5469	Ab10-Fe5	melt	1335	1235	none	11 kbar	48 h	CMASNF	2.29	6.37	16.3	51.2	15.1	4.79	96	
C5469	Ab10-Fe5	melt_stdev	1335	1235	none	11 kbar	48 h	CMASNF	0.056	0.039	0.0756	0.278	0.0992	0.058	0.383	
C5470	Ab70-Fe1	plagioclase	1335	1235	none	11 kbar	48 h	CMASNF	7.29	0.0679	25.4	59.7	7.22	0.389	100	
C5470	Ab70-Fe1	plagioclase_stdev	1335	1235	none	11 kbar	48 h	CMASNF	0.185	0.015	0.242	0.699	0.28	0.0256	0.559	
C5470	Ab70-Fe1	melt	1335	1235	none	11 kbar	48 h	CMASNF	7.8	2.84	19.8	64.5	6.28	1.07	102	
C5470	Ab70-Fe1	melt_stdev	1335	1235	none	11 kbar	48 h	CMASNF	0.05	0.0481	0.0846	0.48	0.0317	0.0243	0.496	
C5485	Ab50-Fe1	plagioclase	1340	1240	none	11 kbar	48 h	CMASNF	6.01	0.114	27.3	55.9	9.33	0.201	98.9	
C5485	Ab50-Fe1	plagioclase_stdev	1340	1240	none	11 kbar	48 h	CMASNF	0.0844	0.0141	0.223	0.477	0.136	0.00431	0.571	
C5485	Ab50-Fe1	diopside	1340	1240	none	11 kbar	48 h	CMASNF	0.936	15.8	7.04	51.2	22.2	1.02	98.2	
C5485	Ab50-Fe1	diopside_stdev	1340	1240	none	11 kbar	48 h	CMASNF	0.151	1.35	2.32	1.73	0.116	0.151	0.775	
C5485	Ab50-Fe1	melt	1340	1240	none	11 kbar	48 h	CMASNF	6.17	4.2	19.2	58.1	10.1	0.59	98.4	
C5485	Ab50-Fe1	melt_stdev	1340	1240	none	11 kbar	48 h	CMASNF	0.0244	0.0448	0.198	0.163	0.0547	0.0126	0.507	
C5505	Ab30-Fe1	plagioclase	1335	1235	none	11 kbar	48 h	CMASNF	4.08	0.192	30.1	52.4	12.9	0.368	100	
C5505	Ab30-Fe1	plagioclase_stdev	1335	1235	none	11 kbar	48 h	CMASNF	0.147	0.0323	0.298	0.32	0.147	0.0118	0.592	
C5505	Ab30-Fe1	diopside	1335	1235	none	11 kbar	48 h	CMASNF	0.568	16	6.2	48.9	23.2	1.51	96.4	
C5505	Ab30-Fe1	diopside_stdev	1335	1235	none	11 kbar	48 h	CMASNF	0.0558	0.621	1.66	1.35	0.243	0.246	2.45	
C5505	Ab30-Fe1	melt	1335	1235	none	11 kbar	48 h	CMASNF	4.4	5.47	18.3	54.2	13.9	1.1	97.3	
C5505	Ab30-Fe1	melt_stdev	1335	1235	none	11 kbar	48 h	CMASNF	0.0741	0.0886	0.198	0.376	0.13	0.0339	0.624	
C5507	Ab30-Fe10	plagioclase	1280	1180	none	11 kbar	48 h	CMASNF	4.05	0.637	28.1	53.3	12.9	2.68	100	
C5507	Ab30-Fe10	plagioclase_stdev	1280	1180	none	11 kbar	48 h	CMASNF	0.605	0.956	2.43	1.58	1.23	1.08		
C5507	Ab30-Fe10	diopside	1280	1180	none	11 kbar	48 h	CMASNF	0.967	11.7	9.11	45.9	22	11.3	101	
C5507	Ab30-Fe10	diopside_stdev	1280	1180	none	11 kbar	48 h	CMASNF								
C5507	Ab30-Fe10	diopside rim	1280	1180	none	11 kbar	48 h	CMASNF	0.911	9.95	11.1	42.8	21.6	13.2	99.6	
C5507	Ab30-Fe10	diopside rim_stdev	1280	1180	none	11 kbar	48 h	CMASNF								
C5507	Ab30-Fe10	melt	1280	1180	none	11 kbar	48 h	CMASNF	3.69	4.5	16.6	60.7	8.09	5.97	100	
C5507	Ab30-Fe10	melt_stdev	1280	1180	none	11 kbar	48 h	CMASNF	0.108	0.0998	0.137	0.635	0.301	0.132		

Run	comp.	type	T1	T2	fO2	P	time	System	Na2O	MgO	Al2O3	SiO2	CaO	FeO	Total	major (count)
D2488	Ab10-Fe15	plagioclase	1275	1175	none	11 kbar	48 h	CMASNF	2.57	0.138	31	48.7	15.2	1.78	99.5	
D2488	Ab10-Fe15	plagioclase_stdev	1275	1175	none	11 kbar	48 h	CMASNF	0.123	0.0128	0.134	0.58	0.186	0.0535	0.566	
D2488	Ab10-Fe15	diopside	1275	1175	none	11 kbar	48 h	CMASNF	0.448	8.88	13	38.6	22.2	13.9	97.1	
D2488	Ab10-Fe15	diopside_stdev	1275	1175	none	11 kbar	48 h	CMASNF	0.0361	0.672	1	1.22	0.0662	0.872	0.578	
D2488	Ab10-Fe15	melt	1275	1175	none	11 kbar	48 h	CMASNF	2.03	5.25	18.3	49.8	12.9	6.95	95.2	
D2488	Ab10-Fe15	melt_stdev	1275	1175	none	11 kbar	48 h	CMASNF	0.0277	0.0542	0.133	0.285	0.0721	0.0728	0.362	
D2489	Ab30-Fe1	plagioclase	1345	1245	none	11 kbar	48 h	CMASNF	4.06	0.186	29.2	51.7	12.6	0.296	98.1	
D2489	Ab30-Fe1	plagioclase_stdev	1345	1245	none	11 kbar	48 h	CMASNF	0.105	0.0222	0.11	0.541	0.141	0.0615	0.66	
D2489	Ab30-Fe1	diopside	1345	1245	none	11 kbar	48 h	CMASNF	0.711	14.5	9.01	49.4	22.5	1.6	97.7	
D2489	Ab30-Fe1	diopside_stdev	1345	1245	none	11 kbar	48 h	CMASNF	0.0652	0.711	1.33	1.02	0.255	0.171	0.692	
D2489	Ab30-Fe1	melt	1345	1245	none	11 kbar	48 h	CMASNF	3.93	5.39	18.6	53.9	14.2	1.01	97	
D2489	Ab30-Fe1	melt_stdev	1345	1245	none	11 kbar	48 h	CMASNF	0.203	0.0857	0.13	0.332	0.148	0.0528	0.705	
D2495	Ab70-Fe10	plagioclase	1270	1170	none	11 kbar	48 h	CMASNF	7.44	0.0697	23.3	59.9	6.83	2.32	99.8	
D2495	Ab70-Fe10	plagioclase_stdev	1270	1170	none	11 kbar	48 h	CMASNF	0.286	0.00764	0.411	0.657	0.44	0.0783	0.103	
D2495	Ab70-Fe10	diopside	1270	1170	none	11 kbar	48 h	CMASNF	2.57	10.8	8	47.9	18	11.1	98.4	
D2495	Ab70-Fe10	diopside_stdev	1270	1170	none	11 kbar	48 h	CMASNF	1.06	2.65	3.21	1.72	2.53	2.04	1.3	
D2495	Ab70-Fe10	melt	1270	1170	none	11 kbar	48 h	CMASNF	7.86	3.63	16.2	62.4	5.04	6.08	101	
D2495	Ab70-Fe10	melt_stdev	1270	1170	none	11 kbar	48 h	CMASNF	0.142	0.0988	0.186	0.648	0.15	0.18	0.507	
D2504	Ab10-Fe1	plagioclase	1320	1220	none	5 kbar	48 h	CMASNF	1.88	0.528	32	47.6	16.5	0.365	98.9	
D2504	Ab10-Fe1	plagioclase_stdev	1320	1220	none	5 kbar	48 h	CMASNF	0.206	0.419	0.732	0.704	0.352	0.0742	0.841	
D2504	Ab10-Fe1	diopside	1320	1220	none	5 kbar	48 h	CMASNF	0.354	15.2	7.01	50.6	23.4	1.31	97.9	
D2504	Ab10-Fe1	diopside_stdev	1320	1220	none	5 kbar	48 h	CMASNF	0.23	1.38	2.29	1.56	0.85	0.211	1.2	
D2504	Ab10-Fe1	melt	1320	1220	none	5 kbar	48 h	CMASNF	2.18	6.36	16.5	50.6	17.8	1.08	94.6	
D2504	Ab10-Fe1	melt_stdev	1320	1220	none	5 kbar	48 h	CMASNF	0.106	0.428	0.279	0.34	0.294	0.0872	1.04	

Table 47: CaO-MgO-Al_2O_3-SiO_2-Na_2O-Fe_2O_3 system experiments. Trace element average and standard deviation (stdev) between mass 7 (Li) and mass 138 (Ba)

Run	comp.	type	Li_ppm	Be_ppm	Na_ppm	Mg_ppm	Si_ppm	K_ppm	Sc_ppm	Mn_ppm	Fe_ppm	Ti_ppm	V_ppm	Cr_ppm	Ga_ppm	Rb_ppm	Sr_ppm	Zr_ppm	Nb_ppm	In_ppm	Cs_ppm	Ba_ppm
C5430	Ab50-Fe10	plagioclase	53.9	41.4		750	294000	157	49.5		2200		1.82	2.81	192	6.5	463	4.09	1.98	4.35	1.45	82.4
C5430	Ab50-Fe10	plagioclase_stdev	4.31	2.82		154	10400	23.4	2.2		187		1.08	0.751	11.3	1.16	62.2	3.48	1.31	1.35	1.4	16.5
C5430	Ab50-Fe10	diopside	83.7	26.4		66400	263000	17.2	117		15800		11.9	176	225	3.99	44.1	454	18	357	3.42	4.92
C5430	Ab50-Fe10	diopside_stdev	5.19	5.64		2360	5240	6.05	11.8		541		4.09	10.9	11.2	3.14	3.81	60.8	8.87	34.6	2.87	3.01
C5430	Ab50-Fe10	melt	287	253		18400	283000	879	62.2		5300		264	177	207	249	288	744	265	161	249	264
C5430	Ab50-Fe10	melt_stdev	3.23	2		126	4920	18.7	1.02		125		4.25	5.55	2.97	3.81	2.5	9.33	6.31	3.22	5.56	4.18
C5442	Ab10-Fe10	plagioclase	87.6	75		1320	275000	251	42.6		2480		0.458	1.57	222	9.08	567	0.107	0.165	2.99	0.257	66.8
C5442	Ab10-Fe10	plagioclase_stdev	2.79	2.95		30.8	5410	14.3	0.733		88.5		0.117	0.219	4.31	0.331	27.5	0.0504	0.0761	0.21	0.143	10.8
C5442	Ab10-Fe10	diopside	63	17.4		57300	227000	10.6	72.1		14700		4.87	353	225	0.191	39.1	96.2	7.15	204	bdl	0.0233
C5442	Ab10-Fe10	diopside_stdev	10.2	3.02		588	1440	0.772	5.66		316		0.743	14	11.2	0.0518	3.22	14.5	1.46	18	bdl	0.0426
C5442	Ab10-Fe10	melt	379	377		32900	267000	1240	51.1		8140		402	131	250	362	531	327	405	203	370	435
C5442	Ab10-Fe10	melt_stdev	3.71	7.11		492	2540	12.2	0.988		107		4.33	1.2	4.86	5.81	4.41	6.01	3.65	2.6	1.49	4.92
C5443	Ab10-Fe1	plagioclase	147	88		1940	272000	796	44.8		845		0.443	2.06	273	13.8	463	0.14	0.212	4.59	0.445	84.6
C5443	Ab10-Fe1	plagioclase_stdev	3.81	10.7		61.4	3760	85.7	2.7		22.4		0.107	bdl	6.81	0.799	15.4	0.0805	0.159	0.169	0.0584	3.6
C5443	Ab10-Fe1	diopside	86.6	5.76		82700	246000	11	83.2		2420		5.6	435	184	0.321	35.1	85.2	6.35	216	0.295	0.554
C5443	Ab10-Fe1	diopside_stdev	26.5	2.11		2080	3840	3.99	2.23		103		1.52	36.3	13.8	0.291	3.6	12.7	2.03	26.7	0.48	0.537
C5443	Ab10-Fe1	melt	677	759		25900	289000	5620	61		1700		883	134	332	818	726	716	889	353	790	911
C5443	Ab10-Fe1	melt_stdev	7.31	8.26		302	3780	75.7	1.34		16.6		14.4	1.57	3.27	14.8	8.57	17	18.8	4.59	16.8	16.9
C5469	Ab10-Fe5	plagioclase	104	64.2		2190	278000	220	1.94		11500		0.391	bdl	268	9.65	477	0.111	0.133	5.05	0.268	81.7
C5469	Ab10-Fe5	plagioclase_stdev	13.1	17.9		99.7	9510	50.2	0.11		518		0.094	bdl	19.9	2.07	78.7	0.024	0.0499	0.592	0.11	24.1
C5469	Ab10-Fe5	diopside	39.9	6.63		49300	158000	3.3	29.2		32200		4.04	137	120	0.166	24.2	68.5	4.04	158	bdl	0.26
C5469	Ab10-Fe5	diopside_stdev	8.92	1.75		3400	4880	bdl	1.92		3000		0.21	28	13.7	0.0781	3.32	8.02	1.6	5.74	bdl	bdl
C5469	Ab10-Fe5	melt	650	711		38700	291000	2040	13.3		38100		843	372	317	755	643	591	856	310	786	833
C5469	Ab10-Fe5	melt_stdev	12.8	61.1		1240	6470	162	0.525		582		108	7.88	10.2	86.9	27.3	65.5	115	13.3	110	86.8
C5470	Ab70-Fe1	plagioclase	44.7	35.6		507	313000	127	2.78		2860		0.423	1.71	220	5.66	508	0.166	0.112	5.66	0.112	91.3
C5470	Ab70-Fe1	plagioclase_stdev	1.8	1.56		18.5	8730	12.1	0.218		124		0.109	0.275	11.9	0.341	13.9	0.0472	0.0314	0.425	0.0291	19.6
C5470	Ab70-Fe1	melt	219	210		14200	292000	588	23.3		6940		220	216	210	187	261	228	211	194	191	206
C5470	Ab70-Fe1	melt_stdev	2.32	12.5		852	4200	13	1.12		291		11.8	11.7	6.26	4.36	4.17	17.8	10.2	10.4	6.79	6.17
C5485	Ab50-Fe1	plagioclase	45.5	39.3	48400	776	288000	159	2.7	0.76	1350	6.1	0.324	4.85	200	5.81	389	bdl	0.068	3.18	0.19	64.9
C5485	Ab50-Fe1	plagioclase_stdev	2.25	3.66	1860	18.5	8030	16.7	0.325	bdl	58.2	1.14	0.11	0.495	7.96	0.589	8.38	bdl	0.0311	0.2	0.02	17.8
C5485	Ab50-Fe1	diopside																				
C5485	Ab50-Fe1	diopside_stdev																				
C5485	Ab50-Fe1	melt	264	251	51300	22800	294000	816	19.7	18.9	4590	127	268	239	240	228	315	346	268	203	241	271
C5485	Ab50-Fe1	melt_stdev	11	23.8	1420	1980	5980	26.7	1.83	0.657	168	15	34.6	21	14.5	11.9	16.2	47.9	37.4	11.2	27.3	17
C5505	Ab30-Fe1	plagioclase	56.7	52.9	36500	1570	301000	186	2.63	1.2	2960	6.3	0.422	4.33	251	7.21	437	0.58	0.294	5.1	0.37	77.1
C5505	Ab30-Fe1	plagioclase_stdev	2.77	13.8	3010	137	16300	32.6	0.256	bdl	115	0.913	0.39	0.987	17.5	1.5	47.1	bdl	0.292	0.354	0.31	16.3
C5505	Ab30-Fe1	diopside	54.2	18.6	5210	90400	247000	35.9	67.6	22.5	11300	71.6	13	116	115	7.32	38.9	82.3	9.51	263	8.26	17.8
C5505	Ab30-Fe1	diopside_stdev	14.7	17	2260	1600	11900	48.3	3.43	1.68	1180	9.74	15.4	21.4	23.3	16	11.5	13.9	15	18.2	17.1	20.9
C5505	Ab30-Fe1	melt	327	281	37700	33800	298000	953	20.1	22.7	8560	115	295	273	262	276	344	265	298	205	278	307

Run	comp.	type	Li_ppm	Be_ppm	Na_ppm	Mg_ppm	Si_ppm	K_ppm	Sc_ppm	Mn_ppm	Fe_ppm	Ti_ppm	V_ppm	Cr_ppm	Ga_ppm	Rb_ppm	Sr_ppm	Zr_ppm	Nb_ppm	In_ppm	Cs_ppm	Ba_ppm
C5505	Ab30-Fe1	melt_stdev	2.86	3.49	655	534	6820	6	0.578	1.03	142	6.86	5.65	9.42	17.7	3.82	4.33	7.73	6.02	11.9	5.99	6.49
C5507	Ab30-Fe10	plagioclase	92.6	44.7	34500	1150	295000	206	3.37	4.13	15900	4.8	2.25	5.88	213	8.65	411	0.742	2.18	2.51	2.43	63
C5507	Ab30-Fe10	plagioclase_stdev	7.25	9.37	3740	85.3	19600	14.8	0.362	0.768	877	0.827	1.79	0.64	15.5	2.39	16.5	0.568	0.935	0.409	1.54	5.05
C5507	Ab30-Fe10	diopside	85.1	17.5	9060	64600	241000	12.2	56.6	142	101000	68.4	6.8	141	205	1.13	38	95	6.37	223	3.02	2.93
C5507	Ab30-Fe10	diopside_stdev	11.1	4.15	415	3530	3860	bdl	7.6	12.8	1610	14.5	2.39	18.2	12.5	1.4	6.37	21.6	2.63	42.6		
C5507	Ab30-Fe10	diopside rim	280	225	25500	67300	322000	651	38.2	163	89400	113	225	255	260	189	212	269	229	181	195	217
C5507	Ab30-Fe10	diopside rim_stdev	8.17	41	1990	3960	12500	112	5.32	4.72	4220	2.06	54.1	20.6	7.01	39.4	19.7	37.4	60.1	28.6	41.1	45.2
C5507	Ab30-Fe10	melt	546	556	46400	23900	296000	1970	11.7	135	43700	149	646	292	269	586	416	476	625	132	585	608
C5507	Ab30-Fe10	melt_stdev	19.1	35.2	1870	1500	10400	85.1	0.599	21.8	2150	3.37	38.8	18.4	17.9	40	22.3	20.5	41.1	57.9	24.6	43.1
D2488	Ab10-Fe15	plagioclase	90	84.3		1040	274000	202	1.79		12500		0.364	bdl	196	7.25	641	0.071	0.106	2.19	0.125	59.5
D2488	Ab10-Fe15	plagioclase_stdev	5.27	5.66		48.5	5890	13	0.157		591		0.0434	bdl	3.43	0.382	25.9	bdl	0.0151	0.149	bdl	12.7
D2488	Ab10-Fe15	diopside	64.7	20.7		52300	210000	bdl	31.4		103000		3.72	144	184	0.173	38.8	68.8	3.08	166	bdl	bdl
D2488	Ab10-Fe15	diopside_stdev	7.36	3.64		3140	3570	bdl	3.49		5420		0.387	23.3	13.7	0.0372	3.97	9.02	1.03	9.38	bdl	bdl
D2488	Ab10-Fe15	melt	381	390		31100	275000	1130	11.3		53300		415	154	232	378	569	321	405	189	383	453
D2488	Ab10-Fe15	melt_stdev	4.42	5.13		211	2690	15.6	0.413		564		3.1	1.62	3.86	3.88	2.75	1.86	3.71	2.61	5.39	3.42
D2489	Ab30-Fe1	plagioclase	47.2	47	35800	1220	291000	145	2.84	bdl	2350	5.16	0.29	2.2	223	6.4	391	bdl	0.0963	3.45	0.237	55.4
D2489	Ab30-Fe1	plagioclase_stdev	2.26	3.83	1330	19.9	5100	9.95	0.442	bdl	23.9	0.713	0.0959	bdl	10.5	0.422	14.2	bdl	0.019	0.252	0.108	13.7
D2489	Ab30-Fe1	diopside	47.1	3.56	5420	88300	248000	bdl	64	18.2	11300	47.6	3.72	111	129	0.24	31.8	51.4	1.68	216	0.16	0.615
D2489	Ab30-Fe1	diopside_stdev	3.3	bdl	328	3600	8420	bdl	4.15	0.888	1060	10.8	0.828	10.8	17.8	0.0794	1.19	5.85	0.589	6.21	bdl	0.0354
D2489	Ab30-Fe1	melt	263	238	34400	32400	290000	677	20.2	19	7820	101	237	224	244	220	338	195	215	240	183	226
D2489	Ab30-Fe1	melt_stdev	2.61	5.15	381	703	6540	10.5	0.594	0.723	133	6.27	3.96	4.86	1.98	2.94	3.4	4.23	2.08	3.28	2.96	4.73
D2495	Ab70-Fe10	plagioclase	50.2	28.6	58000	463	301000	168	2.8	2.04	15700	7.08	0.713	2.95	193	6.46	470	0.303	0.185	5.85	0.254	107
D2495	Ab70-Fe10	plagioclase_stdev	3.41	3.46	3880	11.2	11800	19.9	0.194	0.355	721	1.91	0.128	0.354	9.6	1.11	45.5	0.0651	0.0643	0.387	0.155	4.11
D2495	Ab70-Fe10	diopside	96.3	16.7	15600	62800	216000	8.7	113	183	82800	82.6	11.6	219	147	0.735	34.4	144	9.04	458	0.17	bdl
D2495	Ab70-Fe10	diopside_stdev	5.85	1.61	814	1790	8770	bdl	5.13	8.1	2870	11	0.782	7.57	9.24	0.117	0.915	12	1.86	32.2	bdl	bdl
D2495	Ab70-Fe10	melt	335	303	70500	18600	306000	906	26.3	119	47000	84.6	333	199	222	310	200	297	313	237	315	284
D2495	Ab70-Fe10	melt_stdev	13	28	2840	604	10200	25.6	2.68	8.1	1710	6.41	24.1	18.3	8.97	17.7	13	13.5	19.3	6.89	26.3	23.5
D2504	Ab10-Fe1	plagioclase	68.9	70.8	15000	2160	263000	433	2.56	1.07	2780	5.13	0.403	4.8	276	5.78	464	0.14	0.12	5.49	0.177	64.5
D2504	Ab10-Fe1	plagioclase_stdev	5.35	7.4	1430	214	14600	37.2	0.239	bdl	230	0.833	0.135	bdl	19.2	0.956	44.4	bdl	0.024	1.15	0.0513	11.6
D2504	Ab10-Fe1	diopside	45.6	bdl	1610	90900	245000	bdl	61.7	17.8	11100	114	5.85	453	134	0.215	30.1	106	6.4	263	bdl	bdl
D2504	Ab10-Fe1	diopside_stdev	13.4	bdl	39	1390	3430	bdl	14	1.61	985	9.9	0.217	36.2	11.7	0.0354	2.79	9.96	2.94	17	bdl	bdl
D2504	Ab10-Fe1	melt	476	406	17200	40900	265000	2990	15.6	32.8	8440	205	441	208	282	401	436	351	442	253	402	458
D2504	Ab10-Fe1	melt_stdev	7.4	4.04	164	195	5540	32.6	0.46	0.77	61.4	5.45	5.86	1.96	7.3	6.99	5.8	2.91	5.98	6.07	4.87	9.57

Table 48: CaO-MgO-Al_2O_3-SiO_2-Na_2O-Fe_2O_3 system experiments. Trace element average and standard deviation (stdev) between mass 139 (La) and mass 238 (U)

Run	comp.	type	La_ppm	Ce_ppm	Pr_ppm	Nd_ppm	Sm_ppm	Eu_ppm	Gd_ppm	Tb_ppm	Dy_ppm	Y_ppm	Ho_ppm	Er_ppm	Tm_ppm	Yb_ppm	Lu_ppm	Hf_ppm	Ta_ppm	Pb_ppm	Th_ppm	U_ppm	trace (count)
C5430	Ab50-Fe10	plagioclase	15.3	4.71	9.96	7.67	4.85	4.73	3.97	3.02	2.59	2.2	2.25	1.93	1.71	1.8	1.39	1.17	1.34	25.8	0.699	1.71	5
C5430	Ab50-Fe10	plagioclase_stdev	3	1.17	1.6	1.25	1.17	1.08	0.893	0.91	0.875	0.754	0.921	0.848	0.961	1.19	0.935	1.21	1.22	4.18	0.772	0.976	
C5430	Ab50-Fe10	diopside	46.5	30.9	119	147	207	258	279	277	287	291	284	273	249	237	218	228	37.5	7.21	7.27	2.99	4
C5430	Ab50-Fe10	diopside_stdev	8.44	4.43	16	18.8	22.5	26.1	28.6	26	25.5	25.4	24.1	22.3	19	18.2	18.4	30.4	12.2	2.24	2.38	2.49	
C5430	Ab50-Fe10	melt	207	239	208	186	174	193	195	182	188	208	187	191	187	191	183	216	226	241	116	243	6
C5430	Ab50-Fe10	melt_stdev	3.44	4.96	2.72	3.47	1.75	3.14	2.82	1.62	1.55	2.46	3.24	3.48	1.68	3.27	2.22	3.14	3.91	4.6	2.15	4.03	
C5442	Ab10-Fe10	plagioclase	12.1	4.64	8.3	6.67	4.05	3.95	3.55	2.37	1.97	1.9	1.59	1.38	1.04	0.888	0.713	0.101	0.128	34.5	0.0475	0.107	5
C5442	Ab10-Fe10	plagioclase_stdev	0.519	0.165	0.383	0.344	0.124	0.197	0.166	0.0851	0.142	0.0904	0.0535	0.135	0.0377	0.118	0.0382	0.0428	0.0415	1.89	0.0219	0.087	
C5442	Ab10-Fe10	diopside	24.4	20.8	63.9	77.5	109	137	146	147	153	161	151	151	136	133	121	156	21.2	3.45	4.28	0.0115	6
C5442	Ab10-Fe10	diopside_stdev	3.86	4.37	11.4	13.2	17.4	21.6	22	21.6	22.5	24.5	22.3	23.1	21.1	20.8	19.2	15.4	4.68	0.57	0.799	0.00495	
C5442	Ab10-Fe10	melt	298	346	286	246	220	237	236	217	222	256	221	232	227	237	231	261	342	384	180	391	6
C5442	Ab10-Fe10	melt_stdev	3	3.04	1.76	2.55	2.99	2.11	3.67	4.29	2.78	3.24	3.62	3.79	3.98	4.1	4.18	3.54	4.14	6.77	2	4.19	
C5443	Ab10-Fe1	plagioclase	8.48	3.29	5.95	4.76	2.95	3.07	2.68	1.81	1.51	1.4	1.22	1	0.779	0.66	0.553	0.137	0.169	30.6	0.0453	0.078	4
C5443	Ab10-Fe1	plagioclase_stdev	0.582	0.242	0.443	0.334	0.168	0.132	0.147	0.158	0.0892	0.114	0.0654	0.0993	0.0856	0.104	0.0609	0.0685	0.0749	1.71	0.0441	0.0453	
C5443	Ab10-Fe1	diopside	17.4	15.4	45.1	55.7	80.9	103	111	112	119	127	118	116	106	106	99.2	142	18	2.84	3.01	0.296	7
C5443	Ab10-Fe1	diopside_stdev	3.51	2.89	8.15	9.6	13.3	14.9	16.2	15.8	15.9	17.9	16.4	15.7	15	14.8	14.1	15.5	4.91	0.907	0.728	0.444	
C5443	Ab10-Fe1	melt	670	772	664	577	524	571	570	524	540	609	539	548	535	563	532	540	748	874	396	849	6
C5443	Ab10-Fe1	melt_stdev	9.71	12.1	9.73	10.2	7.26	7.32	8.34	7.64	9.05	9.55	8.16	10	10.1	9.86	8.78	10.4	17.9	11.3	10	14.9	
C5469	Ab10-Fe5	plagioclase	10.1	2.7	6.78	5.12	3.32	3.23	2.69	1.94	1.57	1.6	1.27	1.11	0.835	0.617	0.56	bdl	0.0877	27.6	bdl	bdl	6
C5469	Ab10-Fe5	plagioclase_stdev	2.55	0.79	1.47	1.11	0.725	0.498	0.409	0.35	0.251	0.278	0.164	0.216	0.119	0.0656	0.126	bdl	0.0258	7.62	bdl	bdl	
C5469	Ab10-Fe5	diopside	16.5	12.2	40.8	48	68.4	85.9	92.2	91.3	94.6	101	95.1	93.7	85.9	84.3	78.7	112	12.3	2.1	2.52	0.018	5
C5469	Ab10-Fe5	diopside_stdev	3.94	2.68	8.48	9.48	11.6	14.3	14.9	14.5	14.6	16	15.1	14.7	13.3	13.5	11.9	14.5	4.24	0.57	0.639	bdl	
C5469	Ab10-Fe5	melt	594	691	552	465	409	442	427	401	408	472	415	428	425	444	429	442	705	764	371	812	6
C5469	Ab10-Fe5	melt_stdev	64	76.6	54.9	44.9	36.2	37.3	37.3	32.9	33	38.2	35	36.8	37	39.6	38.7	42.1	94.7	48.4	50.3	112	
C5470	Ab70-Fe1	plagioclase	13.4	3.09	8.1	6.15	3.66	3.42	2.76	1.86	1.43	1.17	1.13	0.849	0.591	0.421	0.375	0.147	0.0932	22.4	bdl	bdl	5
C5470	Ab70-Fe1	plagioclase_stdev	0.765	0.178	0.411	0.254	0.139	0.0945	0.254	0.0951	0.132	0.144	0.054	0.0799	0.0232	0.0781	0.03	0.0194	0.0277	0.719	bdl	bdl	
C5470	Ab70-Fe1	melt	169	194	182	164	164	187	186	176	185	201	186	184	174	185	176	188	195	186	92.4	197	7
C5470	Ab70-Fe1	melt_stdev	9.97	13.9	9.99	9.72	10.5	12.4	12	12.1	11.1	13.8	10.6	11.6	11.9	12.3	11.4	12.2	12.1	7.96	6.33	9.17	
C5485	Ab50-Fe1	plagioclase	7.22	1.97	4.64	3.77	2.23	2.28	1.89	1.22	0.987	0.844	0.812	0.546	0.475	0.313	0.313	bdl	0.078	20.1	bdl	bdl	3
C5485	Ab50-Fe1	plagioclase_stdev	0.927	0.346	0.485	0.297	0.18	0.03	0.104	0.0984	0.104	0.0307	0.0859	0.0323	0.0399	0.0321	0.0645	bdl	0.0099	1.56	bdl	bdl	
C5485	Ab50-Fe1	diopside																					
C5485	Ab50-Fe1	diopside_stdev																					
C5485	Ab50-Fe1	melt	205	248	219	195	188	216	204	195	199	217	201	203	197	201	189	205	228	235	113	249	5
C5485	Ab50-Fe1	melt_stdev	24.2	31.2	24.4	19.9	18.4	20.5	22.3	19.2	20.5	23.6	21.2	22.1	22	21.1	21.1	26.5	33.9	13.4	18.5	38.4	
C5505	Ab30-Fe1	plagioclase	9.23	2.24	6	4.59	2.99	2.96	2.56	1.55	1.31	1.26	1.17	1.02	0.658	0.595	0.515	0.51	0.307	23.6	0.35	0.92	4
C5505	Ab30-Fe1	plagioclase_stdev	2.35	0.58	1.41	0.925	0.565	0.579	0.382	0.275	0.273	0.328	0.284	0.477	0.217	0.336	0.296	bdl	0.392	6.73	bdl	bdl	
C5505	Ab30-Fe1	diopside	23.8	16.8	55.9	67.8	97.6	122	129	124	129	137	127	126	115	113	108	132	14.9	9.07	3.9	11.3	6
C5505	Ab30-Fe1	diopside_stdev	9.06	11.7	10.7	9.42	8.42	11.3	10.5	10.1	9.98	9.44	9.49	9.32	9.57	9.76	8.97	19.4	12.7	14.9	5.45	17.8	
C5505	Ab30-Fe1	melt	217	258	227	205	201	226	216	204	210	235	210	218	209	212	202	222	250	289	123	268	6

Run	comp.	type	La_ppm	Ce_ppm	Pr_ppm	Nd_ppm	Sm_ppm	Eu_ppm	Gd_ppm	Tb_ppm	Dy_ppm	Y_ppm	Ho_ppm	Er_ppm	Tm_ppm	Yb_ppm	Lu_ppm	Hf_ppm	Ta_ppm	Pb_ppm	Th_ppm	U_ppm	trace (count)
C5505	Ab30-Fe1	melt_stdev	3.6	3.75	3.5	1.86	3.69	2.84	2.42	2.15	2.63	2.88	2.24	3.88	2.83	3.14	3.63	5.82	7.66	15.7	2.17	4.52	
C5507	Ab30-Fe10	plagioclase	10.1	4.05	7.18	5.86	3.75	4.04	3.38	2.23	1.75	1.76	1.5	1.27	1.09	1.04	0.927	0.603	1.11	29.9	0.503	2.02	6
C5507	Ab30-Fe10	plagioclase_stdev	0.812	1.72	0.987	0.336	0.334	0.401	0.557	0.363	0.449	0.193	0.215	0.283	0.428	0.382	0.255	0.54	0.823	4.2	0.29	1.77	
C5507	Ab30-Fe10	diopside	26.8	18.2	68.8	84.6	118	154	162	157	163	169	162	155	144	138	128	149	17.7	5.29	3.83	1.35	3
C5507	Ab30-Fe10	diopside_stdev	4.36	4.01	9.9	12.6	13.6	17.9	18.5	17.2	15.3	16.7	14.7	15.6	13	12.9	14	33.1	5.67	2.85	0.63	1.82	
C5507	Ab30-Fe10	diopside rim	191	207	227	222	226	269	268	247	253	274	252	249	239	230	225	265	230	238	113	242	3
C5507	Ab30-Fe10	diopside rim_stdev	35.9	46.3	26.3	17.7	5.73	10.8	7.73	6.26	7.23	7.42	6.75	7.21	11	2.14	9.93	20.1	64.6	60.5	30.5	75.1	
C5507	Ab30-Fe10	melt	435	522	411	347	290	309	291	261	259	302	264	268	270	277	270	346	534	636	263	590	4
C5507	Ab30-Fe10	melt_stdev	25.6	39.3	24.6	20.2	16.9	18.1	15.6	16.8	19.8	21.1	20.7	23.7	26.9	29.7	26.6	16.1	25.7	46.4	12.5	39.7	
D2488	Ab10-Fe15	plagioclase	14.2	4.59	9.69	7.54	4.89	4.26	3.67	2.62	2.13	1.95	1.79	1.45	1.14	0.94	0.75	bdl	0.0817	39.2	0.026	bdl	6
D2488	Ab10-Fe15	plagioclase_stdev	1.41	0.367	0.854	0.45	0.497	0.195	0.181	0.172	0.176	0.221	0.133	0.169	0.115	0.051	0.0631	bdl	0.0179	1.91	bdl	bdl	
D2488	Ab10-Fe15	diopside	20	14.9	54.6	66.2	95.3	120	128	126	132	138	131	128	118	113	104	115	9.93	3.6	2.41	0.0091	6
D2488	Ab10-Fe15	diopside_stdev	3.44	3.23	9.9	11.6	15.9	19.1	19.1	18.3	19.5	21.3	19.5	20.5	19.1	18.2	17	12.2	3.88	0.329	0.665	bdl	
D2488	Ab10-Fe15	melt	301	347	284	239	211	228	219	203	206	241	210	219	218	230	224	255	342	400	182	393	6
D2488	Ab10-Fe15	melt_stdev	2.2	3.13	2.48	1.47	1.57	2.15	2.41	1.45	1.47	2.69	1.65	1.71	1.84	1.5	1.67	2.69	3.45	4.28	1.57	2.58	
D2489	Ab30-Fe1	plagioclase	7.33	1.82	4.98	4	2.47	2.51	1.96	1.38	1.05	1.01	0.929	0.703	0.566	0.45	0.351	0.13	0.0613	19.7	bdl	bdl	5
D2489	Ab30-Fe1	plagioclase_stdev	0.847	0.221	0.522	0.53	0.311	0.15	0.263	0.0808	0.082	0.106	0.0501	0.0936	0.0436	0.0485	0.025	bdl	0.0251	1.25	bdl	bdl	
D2489	Ab30-Fe1	diopside	12.2	8.14	34.3	42.4	63.9	84.5	90.1	87.8	93.6	96	92.7	89.2	81.6	81.2	76.7	91.8	4.98	2.1	0.958	0.11	4
D2489	Ab30-Fe1	diopside_stdev	1.7	0.803	4.1	4.88	6.61	9.17	9.27	9.36	9.62	9.68	9.52	8.38	8.1	7.66	6.7	7.3	2.16	0.166	0.356	0.13	
D2489	Ab30-Fe1	melt	256	180	211	190	170	168	191	184	173	179	178	181	173	181	171	188	201	227	101	214	5
D2489	Ab30-Fe1	melt_stdev	3.28	2.15	3.83	3.76	1.75	3.39	2.38	3.04	3.09	2.19	2.71	3.08	2.82	2.97	2.81	2.75	4.11	3.33	2.45	4.15	
D2495	Ab70-Fe10	plagioclase	18.6	5.14	11.7	8.81	5.47	5.15	4.31	2.58	2.16	1.8	1.7	1.21	0.979	0.723	0.59	0.175	0.14	29.9	0.063	bdl	4
D2495	Ab70-Fe10	plagioclase_stdev	1.33	0.375	0.782	0.875	0.252	0.231	0.372	0.134	0.453	0.219	0.122	0.13	0.0622	0.234	0.0541	0.0212	0.0629	2.9	bdl	bdl	
D2495	Ab70-Fe10	diopside	59.4	41.5	170	212	305	393	414	395	411	418	406	381	348	331	301	206	25	4.27	5.82	0.116	4
D2495	Ab70-Fe10	diopside_stdev	5.68	3.56	14.8	17.3	25.7	30	30.3	27.5	26.8	25.9	26.4	18.2	20.6	17.7	12.3	18.3	6.03	0.642	1.88	bdl	
D2495	Ab70-Fe10	melt	237	291	261	233	228	261	256	241	249	274	252	252	248	251	239	236	260	307	133	299	5
D2495	Ab70-Fe10	melt_stdev	24.1	31.3	22	16.5	11.7	13.4	11.3	9.26	7.83	14.9	10.7	9.72	9.59	14	12.3	25.6	15.6	32.5	9.12	21	
D2504	Ab10-Fe1	plagioclase	8.13	3.12	5.46	4.53	2.89	2.75	2.13	1.55	1.2	1.19	1.01	0.89	0.637	0.493	0.477	0.23	0.145	26.2	bdl	0.073	3
D2504	Ab10-Fe1	plagioclase_stdev	1.26	0.453	0.676	0.471	0.346	0.35	0.275	0.24	0.195	0.118	0.113	0.09	0.141	0.104	0.105	bdl	0.0361	3.88	bdl	bdl	
D2504	Ab10-Fe1	diopside	20.2	17.3	50.8	61.6	84.7	109	115	110	114	119	114	108	98.6	99.3	94.8	175	19.6	2.12	2.95	bdl	3
D2504	Ab10-Fe1	diopside_stdev	1.09	1.05	1.88	2.48	3.23	6.09	6.22	4.85	5.2	5.03	6.19	5.85	5	7.02	4.8	22.1	6.32	0.337	1.01	bdl	
D2504	Ab10-Fe1	melt	319	374	327	288	269	305	293	276	287	320	291	290	284	298	280	277	368	427	192	416	5
D2504	Ab10-Fe1	melt_stdev	2.47	3.23	2.7	4.84	2.48	2.66	2.6	1.05	4.02	3.06	2.47	1.81	2.22	3.33	2.89	0.612	4.36	7.5	2.45	6.09	

Table 49: Natural-like system experiments. Experimental conditions and major element analysis with average and standard deviation (stdev)

Run	comp.	type	T1	T2	fO2	P	time	System	Na2O	MgO	Al2O3	SiO2	CaO	TiO2	FeO	Total	major (count)
20160304	ALV-3352-7	plagioclase	1245	1190	QFM	1 atm	59 h	natural	2.86		31.6	51.1	14.5			100	7
20160304	ALV-3352-7	plagioclase_stdev	1245	1190	QFM	1 atm	59 h	natural	0.118		0.294	0.349	0.319				
20160304	ALV-3352-7	melt	1245	1190	QFM	1 atm	59 h	natural	2.74	9.09	15.5	55	12.7	1.64	4.06	100	5
20160304	ALV-3352-7	melt_stdev	1245	1190	QFM	1 atm	59 h	natural	0.194	0.0851	0.314	0.496	0.148	0.179	0.214		
20160315	BIR64	plagioclase	1245	1130	QFM	1 atm	86 h	natural	3.81	0.31	29	51	12.6		0.635	97.4	3
20160315	BIR64	plagioclase_stdev	1245	1130	QFM	1 atm	86 h	natural	0.195	0.0588	0.896	0.779	0.8		0.13	2.01	
20160315	BIR64	diopside	1245	1130	QFM	1 atm	86 h	natural	0.36	18	4.23	49.1	16.7		6.72	95.1	3
20160315	BIR64	diopside_stdev	1245	1130	QFM	1 atm	86 h	natural	0.226	0.456	0.575	0.628	0.695		0.663	0.88	
20160315	BIR64	melt	1245	1130	QFM	1 atm	86 h	natural	3.11	5.98	12.4	49.9	8.81		9.82	90	4
20160315	BIR64	melt_stdev	1245	1130	QFM	1 atm	86 h	natural	0.0152	0.0486	0.0719	0.38	0.0669		0.0731	0.482	
20160315	BIR70	plagioclase	1245	1130	QFM	1 atm	86 h	natural	3.36	0.285	28.7	47.9	12.3		0.516	93.1	3
20160315	BIR70	plagioclase_stdev	1245	1130	QFM	1 atm	86 h	natural	0.223	0.042	0.477	0.592	0.498		0.0688	0.821	
20160315	BIR70	diopside	1245	1130	QFM	1 atm	86 h	natural	0.299	16.7	4.98	47.3	15.6		6.76	91.6	3
20160315	BIR70	diopside_stdev	1245	1130	QFM	1 atm	86 h	natural	0.0627	0.407	0.772	1.1	0.884		0.68	2.09	
20160315	BIR70	melt	1245	1130	QFM	1 atm	86 h	natural	2.8	5.72	11.6	46.5	8.35		9.14	84.1	3
20160315	BIR70	melt_stdev	1245	1130	QFM	1 atm	86 h	natural	0.0526	0.101	0.128	0.403	0.131		0.301	0.488	

Table 50: Natural-like system experiments. Trace element analysis with average and standard deviation (stdev) from mass 7 (Li) to mass 138 (Ba)

Run	comp.	type	Li_ppm	Be_ppm	Na_ppm	Mg_ppm	Si_ppm	K_ppm	Sc_ppm	Mn_ppm	Fe_ppm	Ti_ppm	V_ppm	Cr_ppm	Ga_ppm	Rb_ppm	Sr_ppm	Zr_ppm	Nb_ppm	In_ppm	Cs_ppm	Ba_ppm
20160304	ALV-3352-7	plagioclase	83.4	52.9	24400	1960	272000	252	3.35	22.9	2360	303	4.73	8	355	5.76	621	0.46	0.058	0.276	bdl	113
20160304	ALV-3352-7	plagioclase_stdev	12.1	6.83	2970	77.3	20100	34.7	0.467	2.23	498	28	0.503	1.27	36.9	0.931	32.5	bdl	bdl	0.158	bdl	25.3
20160304	ALV-3352-7	melt	442	400	23300	53300	301000	1540	40.4	1030	33200	8920	391	363	308	344	411	366	430	1.62	309	509
20160304	ALV-3352-7	melt_stdev	7.5	13.9	544	1290	10100	44	0.37	32.6	1110	146	7.44	11.6	19.1	9.32	6.37	4.85	7.13	0.738	6.54	9.37
20160315	BIR64	plagioclase	bdl	237	29400	2010	266000	564	3.35	34.3	3230	371	0.28	bdl	1130	bdl	192	bdl	0.345	bdl	bdl	426
20160315	BIR64	plagioclase_stdev	bdl	9.9	2190	2.83	7070	4.95	0.247	3.54	127	27.6	bdl	bdl	94.8	bdl	2.69	bdl	0.0636	bdl	bdl	24
20160315	BIR64	diopside	bdl	349	5950	90900	256000	665	213	1540	50900	7190	14.8	91.4	516	2.24	25.1	18.7	350	bdl	0.613	306
20160315	BIR64	diopside_stdev	bdl	261	3280	5710	25500	540	24.9	183	8540	1160	1.05	25.8	110	0.768	13.3	5.44	283	bdl	0.275	264
20160315	BIR64	melt	5.1	2160	25400	33800	268000	4380	77.3	1690	73000	14900	9.41	4.76	1100	7.98	115	61.5	2230	0.071	2.64	2070
20160315	BIR64	melt_stdev	bdl	39	1760	1100	16000	319	1.84	88.7	4400	299	0.51	0.847	77.3	0.754	2.23	1.63	58.8	bdl	0.295	32.4
20160315	BIR70	plagioclase	2.8	186	26900	1900	261000	326	2.91	42.3	3230	313	bdl	bdl	1240	bdl	167	bdl	0.4	bdl	0.17	303
20160315	BIR70	plagioclase_stdev	bdl	6.16	655	58.2	4570	23.9	0.506	2.66	54.5	7.02	bdl	bdl	33.7	bdl	4.07	bdl	0.195	bdl	bdl	33.3
20160315	BIR70	diopside	1.82	120	3140	86900	235000	76.7	222	2070	51600	6180	10.3	117	486	1.42	15.1	13.1	87.3	bdl	0.0955	73.6
20160315	BIR70	diopside_stdev	bdl	34.2	1200	4130	3540	45.6	20.4	128	2580	235	0.509	50.1	27.4	0.146	7.37	1.52	24.4	bdl	0.0361	41.4
20160315	BIR70	melt	2.92	2040	23400	31500	255000	2910	71.5	2470	80500	14400	6.58	4.26	1100	7.33	111	57.6	2260	bdl	1.8	2110
20160315	BIR70	melt_stdev	0.785	18.6	589	453	6360	86.2	1.63	36.3	2010	103	0.431	1.55	32	0.507	1.82	1.14	21.1	bdl	0.169	31.3

Table 51: Natural-like system experiments. Trace element analysis with average and standard deviation (stdev) from mass 139 (La) to mass 238 (U)

Run	comp.	type	La_ppm	Ce_ppm	Pr_ppm	Nd_ppm	Sm_ppm	Eu_ppm	Gd_ppm	Tb_ppm	Dy_ppm	Y_ppm	Ho_ppm	Er_ppm	Tm_ppm	Yb_ppm	Lu_ppm	Hf_ppm	Ta_ppm	Pb_ppm	Th_ppm	U_ppm	trace (count)
20160304	ALV-3352-7	plagioclase	14.3	12.8	9.73	7.49	4.95	57	3.84	2.98	2.48	2.01	1.78	1.5	1.09	0.9	0.713	0.47	0.185	bdl	bdl	bdl	5
20160304	ALV-3352-7	plagioclase_stdev	2.33	1.78	1.01	0.569	0.637	2.59	0.519	0.285	0.216	0.0779	0.0559	0.15	0.0659	0.352	0.133	bdl	bdl	bdl	bdl	bdl	
20160304	ALV-3352-7	melt	304	359	330	295	300	312	337	322	329	364	335	341	333	332	320	370	357	0.26	173	368	5
20160304	ALV-3352-7	melt_stdev	6.63	6.1	5.54	2.94	4.32	9.8	8.11	4.55	4.84	6.2	4.51	3.82	4.22	4.53	5.58	7.9	4.57	bdl	2.09	6.12	
20160315	BIR64	plagioclase	25.1	20.5	16	12.4	7.35	125	10.7	7.88	5.78	0.0785	4.83	3.86	2.76	2.48	1.81	0.3	bdl	bdl	bdl	0.17	2
20160315	BIR64	plagioclase_stdev	0.919	1.63	1.71	1.13	1.34	1.84	1.91	0.658	0.728	0.00778	0.467	0.141	0.163	0.191	0.00707	bdl	bdl	bdl	bdl	bdl	
20160315	BIR64	diopside	181	242	276	288	366	378	935	938	993	8.53	1000	999	962	954	941	739	1.17	bdl	158	315	6
20160315	BIR64	diopside_stdev	95.4	100	82.3	61.6	41.6	45	61.7	58	57.4	0.567	58.6	64.8	69.2	76.4	74.3	123	0.676	bdl	114	266	
20160315	BIR64	melt	859	948	889	763	735	748	1560	1480	1520	13.7	1530	1540	1530	1560	1550	1630	6.37	bdl	968	2020	5
20160315	BIR64	melt_stdev	14.5	12.9	12.3	14.5	9.8	12.6	17	20.8	19.9	0.177	20.7	19.5	17.5	26.4	25.9	11.8	0.263	bdl	14.3	67.7	
20160315	BIR70	plagioclase	19.1	16.2	12.5	9.57	5.96	89.1	9.21	6.2	5.24	0.0417	3.87	3.1	2.12	1.6	1.44	0.17	bdl	bdl	0.12	bdl	4
20160315	BIR70	plagioclase_stdev	1.78	1.03	0.975	0.635	0.59	1.02	0.335	0.389	0.314	0.0095	0.247	0.211	0.114	0.14	0.12	0.0183	bdl	bdl	bdl	bdl	
20160315	BIR70	diopside	79.4	131	172	202	285	307	764	770	830	7.6	829	820	769	775	761	656	0.517	0.065	44	67.9	3
20160315	BIR70	diopside_stdev	7.95	6.56	5.3	2.76	1.91	2.82	13.1	12.1	10.2	0.329	15.8	15.6	17.2	17.6	16	68.7	0.0577	bdl	9.99	24.5	
20160315	BIR70	melt	826	912	844	725	684	717	1430	1370	1410	13.1	1400	1420	1370	1420	1410	1520	6.09	bdl	934	2000	5
20160315	BIR70	melt_stdev	7.63	11.3	9.34	7.37	11.2	6.5	13.4	13.9	16.9	0.227	20.6	14	15.5	17.1	15.4	28.4	0.243	bdl	9.02	23.6	

Appendix 3. **DIFFUSION**

Table 52: Major and trace elements of experimental plagioclase crucibles

Run	**BF60**		**BF68**		**BIR66**		**AGV58**		**AGV66**	
	Average	σ	Average	σ	Average	σ	Average	σ	Average	σ
					Major Elements (wt%)					
Na_2O	4.19	0.04	3.42	0.09	3.63	0.04	4.44	0.03	3.59	0.03
MgO	0.06	0.03	0.11	0.02	0.11	0.02	0.06	0.01	0.10	0.02
Al_2O_3	29.61	0.31	31.35	0.19	30.79	0.21	29.61	0.17	31.42	0.12
SiO_2	51.56	0.54	50.32	0.52	52.09	0.25	53.81	0.22	51.79	0.26
K_2O	0.25	0.01	0.14	0.01	0.13	0.02	0.25	0.02	0.13	0.01
CaO	11.95	0.07	13.52	0.11	13.21	0.13	11.55	0.09	13.30	0.10
FeO	0.40	0.02	0.46	0.01	0.42	0.02	0.40	0.02	0.42	0.02
MnO	0.01	0.01	0.00	0.01	bdl		bdl		bdl	
TiO_2	0.13	0.14	0.05	0.01	0.04	0.01	0.06	0.01	0.04	0.01
Total	98.24		99.45		100.42	0.35	100.18	0.31	100.80	0.21
					Cations based on 8 Oxygens					
Na	0.38		0.30		0.32		0.39		0.31	
Mg	0.00		0.01		0.01		0.00		0.01	
Al	1.62		1.70		1.64		1.58		1.67	
Si	2.39		2.31		2.36		2.43		2.34	
K	0.01		0.01		0.01		0.01		0.01	
Ca	0.59		0.67		0.64		0.56		0.64	
Fe	0.02		0.02		0.02		0.02		0.02	
Total	5.01		5.01		5.00		4.99		5.00	
					Mol % Ca/(Ca+Na+K)					
An#	**60.26**		**68.02**		**66.27**		**58.05**		**66.65**	
					Trace Elements (ppm)					
Li	9.52	0.23	5.57	0.40	2.97	0.10	4.30	0.50	3.01	0.14
Be	0.15		0.01		bdl		0.12	0.07	0.08	0.00
B	10.30	1.49	9.88	1.35	12.98	1.26	17.73	0.86	15.72	1.05
Sc	1.76	0.13	1.87	0.09	3.86	0.12	4.77	0.09	4.49	0.10
Mn	40.88	0.95	47.69	0.68	48.09	0.91	44.61	11.38	47.64	0.38
Ga	21.18	0.50	21.37	0.35	19.78	0.31	21.84	0.45	19.98	0.36
Rb	0.70	0.06	0.14	0.02	0.13	0.01	0.73	0.33	0.13	0.03
Sr	991.50	7.47	599.33	4.72	664.05	6.37	971.83	4.75	672.63	5.64
Y	0.20	0.02	0.23	0.02	0.22	0.01	0.20	0.00	0.22	0.01
Ba	92.66	2.33	71.06	1.66	67.88	1.73	92.45	1.32	67.33	1.42
La	1.94	0.04	0.44	0.03	0.45	0.01	1.87	0.08	0.44	0.01
Ce	3.00	0.04	0.85	0.03	0.82	0.02	2.93	0.06	0.81	0.03
Pr	0.29	0.01	0.10	0.01	0.10	0.01	0.29	0.01	0.10	0.01
Nd	1.01	0.10	0.47	0.05	0.48	0.04	1.07	0.03	0.47	0.03
Sm	0.13	0.03	0.06	0.02	0.10	0.01	0.14	0.01	0.10	0.01
Eu	0.41	0.01	0.24	0.02	0.24	0.01	0.42	0.01	0.23	0.01
Gd	0.08	0.03	0.06	0.01	0.08	0.02	0.14	0.01	0.07	0.02
Tb	0.01	0.00	0.01	0.00	0.01	0.00	0.01	0.00	0.01	0.00
Dy	0.03	0.01	0.04	0.01	0.05	0.01	0.05	0.01	0.05	0.01
Ho	0.01	0.00	0.01	0.00	0.01	0.00	0.01	0.00	0.01	0.00
Er	0.02	0.00	0.02	0.00	0.02	0.00	0.02	0.00	0.02	0.00
Tm	0.00		0.00	0.00	0.00	0.00	0.00	0.00	0.00	0.00
Yb	bdl		0.01	0.00	0.02		bdl		0.02	0.00
Lu	0.00		0.00		bdl		bdl		0.00	
Pb	0.31	0.02	0.21	0.03	0.19	0.02	0.40	0.24	0.19	0.01

Table 53: Major and trace elements in the final melt

Label	**BF60**		**BF68**		**BIR66**		**AGV58**		**AGV66**	
Melt	BF	σ	BF	σ	BIR	σ	AGV	σ	AGV	σ
Major Elements (wt%)										
Na2O	3.52		2.80		2.52	0.05	4.08	0.07	4.03	0.05
MgO	3.08		3.10		7.77	0.17	1.59	0.06	1.52	0.03
Al2O3	15.69		14.42		14.16	0.19	15.73	0.14	16.37	0.13
SiO2	50.69		46.59		49.93	0.26	58.90	1.04	60.37	0.56
K2O	1.32		1.12		0.23	0.06	2.05	0.06	2.22	0.04
CaO	8.20		8.23		12.24	0.07	6.60	0.30	6.83	0.07
FeO	9.68		6.65		8.60	0.19	5.36	0.36	5.49	0.06
MnO	0.18		0.20		0.20	0.02	0.04		bdl	
TiO2	0.97		0.92		1.50	0.03	0.96	0.04	1.14	0.03
Total	93.33		84.03		97.16	0.44	95.27	1.76	97.96	0.47
Trace Elements (ppm)										
Be	0	0	0	0	1084	8	1114	8	1013	4
P	840	314	1216	94	211	2	1928	95	1621	23
Sc					102	1	96	1	92	0
Ga	143	19	332	29	1096	10	1040	31	868	11
Sr	74	11	206	12	140	0	93	2	73	0
Y	23	11	21	3	8	0	2	0	2	0
Nb					1050	4	972	6	946	4
Ba	3505	453	8670	782	1097	5	957	9	915	7
La	939	403	3662	270	418	2	394	2	391	4
Ce	1049	468	4218	340	480	2	442	2	440	4
Pr	1017	461	4108	392	454	2	426	1	426	4
Nd	869	390	3464	396	408	3	379	2	379	3
Sm	877	402	3449	466	408	3	386	3	385	4
Eu	1370	183	4078	438	467	3	431	16	434	2
Gd	2066	959	8026	1251	918	6	879	3	873	6
Tb	1970	932	7620	1097	883	6	849	4	843	7
Dy	1984	925	7945	1117	923	7	885	6	879	7
Ho	1999	943	8125	1092	907	6	877	5	877	6
Er	2027	953	8255	1035	921	8	895	5	886	5
Tm	2063	973	7873	908	880	6	861	5	853	7
Yb	2039	953	8408	859	902	8	883	5	876	6
Lu	2116	997	7919	772	892	6	881	6	872	6
Th	1213	559	3722	586						
U	2420	1096	7509	825						

Table 54: Comparison of the stoichiometry of plagioclase crucible with plagioclase grown from the diffusing melt. .

T	**BIR66 1190°C**	**BIR66 1133°C**
Type	**Plagioclase Crucible**	**Grown plagioclase**
Na_2O	3.63	3.36
MgO	0.11	0.28
Al_2O_3	30.79	28.71
SiO_2	52.09	47.90
K_2O	0.13	
CaO	13.21	12.29
FeO	0.42	0.52
Total	100.39	93.06
Cations	8	8
Na	0.32	0.32
Mg	0.01	0.02
Al	1.64	1.66
Si	2.36	2.35
K	0.01	0.00
Ca	0.64	0.64
Fe	0.02	0.02
Total	5.00	5.01
X An	66.27	66.92

Table 55: Partition coefficients between plagioclase and natural melts

	BIR66 D pl/melt			BIR66 D pl/melt 1133		AGV58 D pl/melt			AGV66 D pl/melt			BF60 D pl/melt			BF68 D pl/melt		
	average	σ	**pred.**	**BIR66 exp.**	σ	average	σ	**pred.**	average	σ	**pred.**	average	σ	**pred.**	average	σ	**pred.**
Be	0.059	0.026	**0.21**	**0.091**	0.003	0.032	0.034	**0.15**	0.026	0.009	**0.15**			**0.14**			**0.14**
Mg	0.026	0.004	**0.067**	**0.060**	0.002	0.051	0.003	**0.051**	0.077	0.002	**0.049**	0.056	0.031	**0.048**	0.056	0.006	**0.046**
K	0.375	0.078	**0.16**	**0.112**	0.009	0.110	0.004	**0.16**	0.074	0.007	**0.16**			**0.16**	0.026	0.001	**0.16**
Mn	0.021	0.002		**0.017**	0.001	0.072	0.017		0.097	0.014		0.042	0.019		0.034	0.004	
Fe	0.030	0.003		**0.040**	0.001	0.057	0.003		0.064	0.005		0.059	0.025		0.063	0.011	
Ga	0.693	0.006		**1.13**	0.05	0.048	0.038		0.074	0.029							
Sr	3.03	0.46	**1.28**	**1.50**	0.04	7.00	1.73	**1.40**	6.68	0.94	**1.28**	9.23	2.13	**1.37**	2.27	0.27	**1.27**
Ba	0.112	0.028	**0.19**	**0.143**	0.016	0.160	0.048	**0.22**	0.069	0.001	**0.19**	0.062	0.015	**0.22**	0.090	0.056	**0.19**
La	0.019	0.010	**0.038**	**0.023**	0.002	0.059	0.054	**0.052**	0.020	0.016	**0.056**	0.012	0.006	**0.054**	0.015	0.017	**0.059**
Ce	0.011	0.000		**0.018**	0.001	0.091	0.051		0.029	0.014		0.014			0.006		
Nd	0.011	0.003	**0.020**	**0.013**	0.001	0.034	0.009	**0.028**	0.024	0.005	**0.030**	0.010		**0.030**	**0.005**		**0.032**
Eu	0.073	0.045		**0.124**	0.002	0.164	0.107		0.052	0.062		0.126	0.036		0.130	0.050	
Gd	0.005	0.000	**0.008**	**0.0064**	0.0002	0.026	0.018	**0.012**	0.036	0.020	**0.012**	0.005		**0.012**	0.004		**0.013**
Dy	0.004	0.001	**0.005**	**0.0037**	0.0002	0.025	0.016	**0.007**	0.021	0.018	**0.008**	0.003		**0.008**	0.004		**0.008**
Er	0.005	0.001	**0.003**	**0.0022**	0.0001	0.036	0.020	**0.005**	0.045	0.014	**0.005**	0.002		**0.005**	0.004		**0.005**
Yb	0.005	0.000	**0.002**	**0.0011**	0.0001	0.036	0.018	**0.003**	0.051	0.014	**0.003**	0.002		**0.003**	0.004		**0.003**

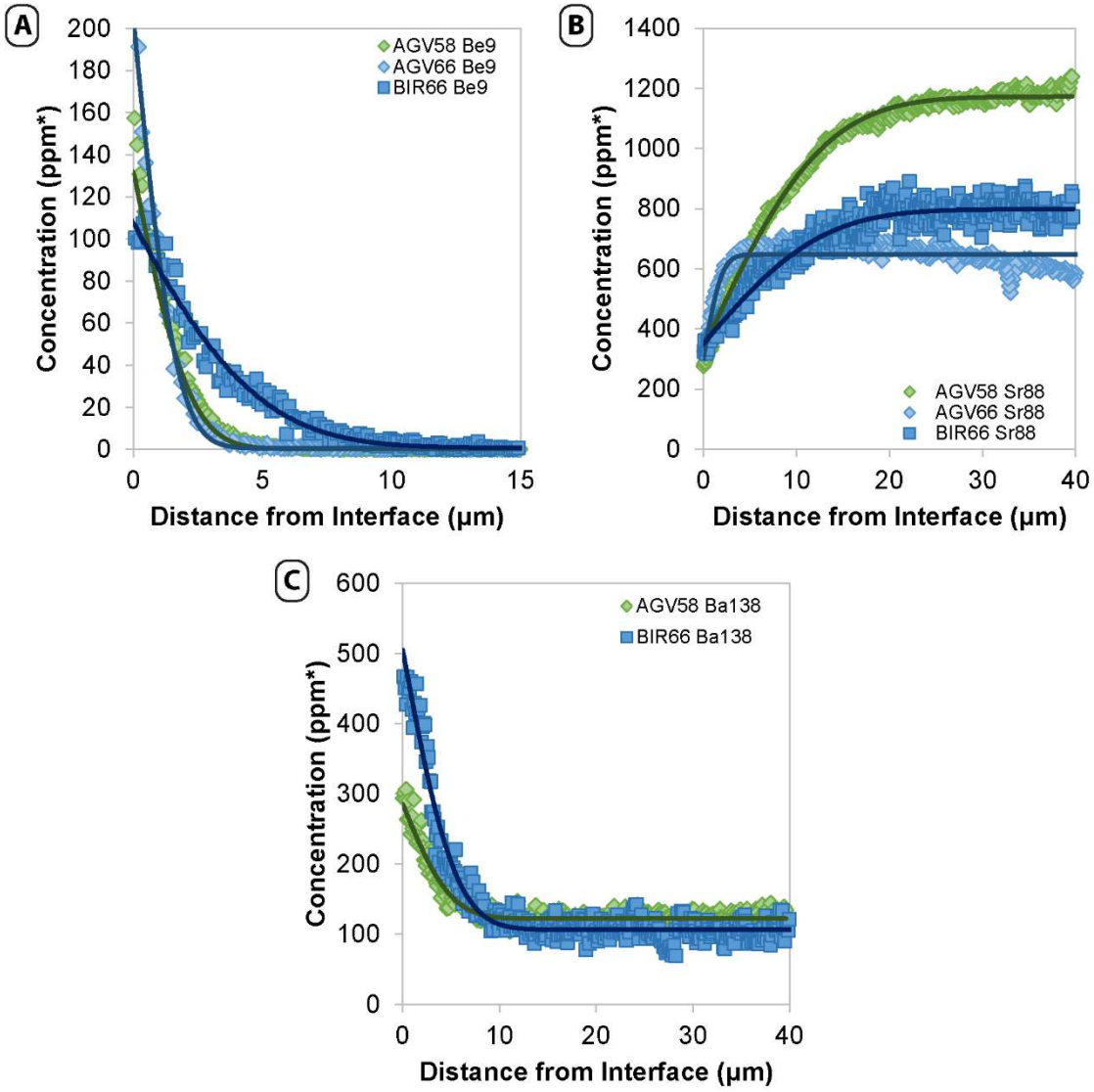

Figure 121: examples of nanoSIMS diffusion profiles of the very slow diffusing elements A) Be, B) Sr and C) Ba

Table 56: summary of diffusion coefficients in An_{67} and An_{95} at 1290°C. Grey shading indicated diffusion "out"

	An67-I CM			An67-III TM			An95-II GH			An95-III CM		
	average	σ	n	average	σ	n	Average	σ	n	Average	σ	n
Na							-14.72	0.09	4	-15.72	0.78	2
Mg	-15.26	0.89	2	-15.41	0.40	6	-14.74	0.37	2	-15.89		1
Si							-14.31	0.10	2			
K				-15.09	0.73	3	-14.20		1			
Mn	-14.26	0.20	2	-15.37	0.48	4	-15.62	0.20	4	-15.78	0.13	2
Fe	-15.10	0.82	3	-15.12	0.30	6	-15.01	0.06	2	-16.25	0.02	2
Sr	-16.10	0.43	2	-16.15	0.42	5						
Y	-16.95	0.15	3	-16.82	0.44	3	-17.37	0.16	2	-17.82		1
Ba	-16.02	0.13	2									
La	-17.09	0.29	3	-16.72	0.59	2	-17.44	0.37	4	-16.45	0.51	2
Pr	-17.32		1	-16.65	0.40	4	-18.37		1			
Eu	-16.35	0.12	4	-16.10	0.43	6	-17.90	0.48	4	-17.64	0.25	2

Table 57: Diffusive coefficients at 1190°C for all natural melt diffusion experiments. Grey coloured boxes indicates diffusion out of the plagioclase

Element	BF60			BF68			AGV58			AGV66			BIR66			Analytical
	Log D	σ	n	Log D	σ	n	Log D	σ	n	Log D	σ	n	Log D	σ	n	Method
Be							-18.13	0.65	4	-18.96	0.49	3	-17.51	0.15	6	LA-ICP-MS
Be										-14.64						LA-ICP-MS
Be							**-18.57**	**0.41**	**9**	**-18.69**	**0.22**	**5**	**-17.3**	**0.29**	**11**	**nanoSIMS**
Mg out	-14.68		1	-15.01	0.25	6	-14.62	0.35	14	-15.24	0.15	10				LA-ICP-MS
Mg in	-16.17	0.29	12	-15.88	0.21	7	-16.26	0.19	14				-16.38	0.31	11	LA-ICP-MS
Mg in							**-16.27**	**0.25**	**3**				**-16.72**		**1**	**nanoSIMS**
K				-15.83	0.22	12	-15.28	0.25	12	-16.28	0.1	7	-15.72	0.24	8	LA-ICP-MS
Sc				-17.69	0.16	2										LA-ICP-MS
Mn	-15.25	0.19	11	-15.47	0.67	12	-15.27	0.19	20	-15.66	0.2	15	-15.43	0.29	12	LA-ICP-MS
Mn							**-15.18**	**0.34**	**3**	**-15.7**	**0.14**	**2**				**nanoSIMS**
Fe	-15.42	0.4	10	-15.41	0.49	13	-14.97	0.29	13	-15.41	0.21	6	-15.55	0.41	9	LA-ICP-MS
Ga							-17.31	1.2	5	-19.13	0.36	3	-18.11	0.4	2	LA-ICP-MS
Sr	-16.96	0.43	13	-17.05	0.44	6	-16.78	0.47	13	-18.34	0.18	3	-17.18	0.4	7	LA-ICP-MS
Sr							**-16.9**	**0.28**	**7**	**-18.21**	**0.15**	**3**	**-16.35**	**0.29**	**4**	**nanoSIMS**
Ba	-17.34	0.42	10	-17.54	0.28	12	-17.81	0.63	8				-17.63	0.45	10	LA-ICP-MS
Ba							**-17.39**	**0.26**	**5**				**-17.3**	**0.17**	**3**	**nanoSIMS**
La	-17.72	0.1	2	-17.3	0.56	2	-19.07	0.37	6	-19.11	0.22	5	-18.3	1.17	8	LA-ICP-MS
La							**-18.08**		**1**							**nanoSIMS**
La	-15.04			-14.78			-15.23	0.42	4	-14.94	0.39	6	-14.63	0.24	4	LA-ICP-MS
Ce	-17.7			-17.35			-18.92	0.68	5	-19	0.27	3				LA-ICP-MS
Ce	-14.88			-14.97			-14.87	0.83	2	-14.64	0.1	3	-14.56		1	LA-ICP-MS
Nd	-17.73			-17.38			-18.99	0.5	2	-14.83	0.33	3	-20.07		1	LA-ICP-MS
Nd	-15.08			-14.94			-14.75	0.08	2	-18.93	0.46	3	-14.72	0.1	2	LA-ICP-MS
Eu (2+)	-17.22	0.38	17	-17.3	0.22	19	-17.65	0.75	26	-18.55	0.48	12	-17.37	0.36	14	LA-ICP-MS
Eu (2+)							**-17.71**	**0.46**	**7**	**-18.61**		**1**				**nanoSIMS**
Eu	-15.25	0.24	4	-15.1	0.44	6	-14.93	0.21	6	-14.93	0.32	10	-14.85	0.22	6	LA-ICP-MS
Gd	-17.85			-17.48			-18.68	0.3	2	-18.97	0.58	3				LA-ICP-MS
Gd	-14.88			-14.68			-14.74	0.2	2	-14.83	0.18	3	-14.67		1	LA-ICP-MS
Dy	-17.7			-17.44			-18.78	0.25	4	-18.82	0.23	4	-18.31	1.32	3	LA-ICP-MS
Dy	-14.88			-14.71			-14.88	0.46	3	-14.89	0.12	4	-14.72	0.18	4	LA-ICP-MS
Ho							**-18.71**	**0.18**	**4**							**nanoSIMS**
Er	-17.57			-17.48			-18.66	0.36	2	-18.61	0.04	2	-19.93		1	LA-ICP-MS
Er	-14.84			-14.72			-14.62	0.13	2	-14.84	0.08	2	-14.74	0.16	2	LA-ICP-MS
Yb	-17.49			-17.49			-18.54	0.32	2	-18.55	0.09	2	-18.52		1	LA-ICP-MS
Yb	-14.99			-14.92			-14.6	0.11	2	-14.86	0.17	2	-14.57	0.08	2	LA-ICP-MS

Appendix 4. NATURAL SAMPLES MAJOR AND TRACE ELEMENTS

Table 58: Average of Major and Trace Elements in Sample MDS37

	MDS37					
	OPX		cpx		Plag	
	Average	STDEV	average	stdev	average	stdev
SiO2	55.2	4.87	53.2	0.667	45.3	0.725
TiO2	0.0128	0.0225	0.0678	0.019	0.000497	0.0027
Al2O3	1.88	0.882	2.47	0.281	36.1	0.914
Cr2O3	0.435	0.109	0.818	0.0472	0.00157	0.00779
FeO	7.99	0.575	3.79	0.55	0.215	0.0566
MnO	0.213	0.0372	0.138	0.0171	0.000722	0.00451
MgO	31.9	3.63	18.6	1.4	0.0428	0.193
CaO	1.54	0.862	21.6	2.16	18.7	0.628
Na2O	0.0122	0.0211	0.16	0.025	0.957	0.188
K2O	0.00663	0.017	0.00121	0.00566	0.00822	0.0397
NiO	0.151	0.179	0.0424	0.0209		
Total	99.3	7.9	101	0.918	101	1.08
Trace Elements (ppm)						
Li	0.171	0.0822	0.833	0.0759	0.337	0.195
Be						
Al	8880	979	14200	869	174000	3130
K	4.72	2.84	6.44	4.41	8.84	6.38
Sc	36.1	2.87	69	2.34	1.64	0.82
Ti	202	15.6	363	25.6	20.5	7.94
V	118	9.95	235	6.75	1.84	0.436
Cr	3170	226	5290	162	1.38	0.897
Mn	1570	39.6	1150	23.9	27.4	44
Co	75.6	2.25	40.4	1.32	0.728	1.37
Ni	527	12.7	343	10.5	7.82	4.29
Cu	0.177	0.207	1.43	5.36	0.341	0.177
Zn	51.2	2.24	20.3	1.07	2.52	3.71
Ga	2.15	0.147	2.85	0.115	15.9	0.426
Ge	2.82	0.0946	2.81	0.127	0.653	0.18
Rb	0.018	0.00588	0.024	0.0118	0.049	
Sr	0.0969	0.117	1.66	0.17	41.2	0.751
Zr	0.0811	0.0265	0.4	0.0307		
Nb	0.00501	0.00158	0.0136	0.00271		
Cs			0.0029			
Ba			0.0327	0.00551	0.116	0.0564
La	0.00121	0.000791	0.00885	0.00102	0.00949	0.00159
Ce	0.0026	0.00329	0.0493	0.00335	0.0212	0.00244
Pr	0.00103	0.000972	0.0135	0.00118	0.00267	0.000724
Nd	0.00713	0.00776	0.12	0.00583	0.0123	0.00377
Sm	0.00682	0.00686	0.0937	0.00789	0.00339	0.00177
Eu	0.00326	0.00244	0.0451	0.00299	0.0382	0.00367
Gd	0.0191	0.0119	0.234	0.0128	0.00489	0.00267
Tb	0.00579	0.00266	0.0498	0.00316	0.000953	0.000267
Dy	0.0645	0.0224	0.43	0.0239	0.0062	0.00133
Y	0.533	0.119	2.64	0.108	0.0277	0.00415
Ho	0.0178	0.00445	0.0984	0.00424	0.00107	0.00017
Er	0.0733	0.014	0.32	0.0161	0.00274	0.000713
Tm	0.012	0.00181	0.0446	0.00284		
Yb	0.11	0.0109	0.319	0.013		
Lu	0.0188	0.0019	0.0462	0.00206		
Hf	0.00354	0.00292	0.0186	0.00325		
Ta			0.00003	1.41E-05		
Pb	0.0104	0.0127	0.00657	0.00544	0.0142	0.0141
Th			0.00052	0.000467		
U						
count	16		23		23	

Table 59: Average of Major and Trace Elements in Sample MDS41

	MDS41					
Mineral	OPX		cpx		Plag	
	Average	STDEV	average	stdev	average	stdev
SiO2	56.4	0.399	52.6	1.59	44.3	0.427
TiO2	0.00294	0.0135	0.059	0.0304	0.000368	0.00491
Al2O3	1.72	0.117	2.58	0.768	35	0.778
Cr2O3	0.483	0.0421	0.812	0.0913	0.00191	0.00834
FeO	7.72	0.133	3.73	0.72	0.265	0.289
MnO	0.207	0.0143	0.136	0.0222	0.00123	0.00682
MgO	33.3	0.908	18.3	1.86	0.122	0.651
CaO	1.23	0.287	21.6	2.69	19.5	0.793
Na2O			0.113	0.0663	0.691	0.161
Total	101	1	99.9	2.81	99.9	0.849
Trace Elements (ppm)						
Li	0.279	0.066	1.18	0.122	0.369	0.15
K	3.31	1.51	6.28	4.45	14.8	14.5
Sc	33.1	2.34	60.2	1.31	1.74	1.24
Ti	207	8.82	357	22.7	16.4	3.42
V	115	4.96	227	4.83	2.21	0.42
Cr	3120	94.3	5370	268	2.4	2.75
Mn	1460	56.4	1060	15	31.7	32
Co	73.1	1.25	38.9	1.01	1.08	1.41
Ni	500	24.7	326	5.79	9.02	6.09
Cu	0.551	0.24	1.28	0.76	0.294	0.211
Zn	51.7	0.853	20.5	0.877	2.54	1.3
Ga	1.92	0.159	2.59	0.0706	13.7	0.488
Ge	2.93	0.157	2.7	0.0944	0.731	0.305
Rb	0.0133	0.00741	0.0201	0.00964	0.0517	0.0257
Sr	0.0552	0.0834	1.25	0.239	29.4	2.62
Zr	0.0663	0.0111	0.37	0.0573		
Nb	0.00362	0.00178	0.00619	0.00115		
Ba	0.00144	0.00161	0.000717		0.204	0.0937
La			0.00948	0.00145	0.00743	0.00118
Ce	0.00117	0.00051	0.0518	0.00441	0.0184	0.00229
Pr	0.000288	0.00022	0.0139	0.00119	0.00245	0.000557
Nd	0.00462	0.00208	0.122	0.00784	0.0128	0.00311
Sm	0.00345	0.00258	0.0935	0.00816	0.00761	0.00222
Eu	0.00258	0.00091	0.0438	0.00321	0.0353	0.00505
Gd	0.0157	0.00292	0.227	0.0168	0.00855	0.00275
Tb	0.0055	0.00077	0.0499	0.00288	0.00115	0.000334
Dy	0.0607	0.00591	0.432	0.0233	0.00526	0.00142
Y	0.546	0.034	2.73	0.112	0.0284	0.00484
Ho	0.0187	0.0014	0.101	0.00427	0.00108	0.000238
Er	0.0771	0.00563	0.336	0.016	0.00308	0.000907
Tm	0.0136	0.0019	0.0488	0.00234	0.00081	0.000099
Yb	0.118	0.00919	0.349	0.0131	0.00493	0.000802
Lu	0.0219	0.00182	0.0511	0.00288	0.00083	0.000387
Hf	0.00272	0.00171	0.0197	0.00548		
Ta	0.0008		0.000201	0.000311		
Pb	0.0804	0.156	0.00714	0.00417	0.0115	0.018
Th			0.00002			
U			0.00011	1.41E-05		
count	10		24		22	

Table 60: Major element variations in Clinopyroxene in sample MDS41

Sample	MDS41 cpx				
Mineral	**clinopyroxene**				**Field**
Location	**Centre**		**rim**		**Analy.**
sample no.	**Average**	**σ**	**Average**	**σ**	
SiO2	53.25	0.60	53.28	0.30	52.88
TiO2	0.06	0.03	0.04	0.04	0.05
Al2O3	2.75	0.10	2.35	0.14	2.70
Cr2O3	0.84	0.06	0.82	0.07	1.16
FeO	4.18	0.79	3.44	0.22	4.35
MnO	0.14	0.01	0.14	0.02	0.08
MgO	19.72	2.44	18.15	0.75	18.94
CaO	19.91	3.59	22.58	1.25	18.94
Na2O	0.11	0.03	0.11	0.01	0.20
Total	100.95	0.26	100.91	0.65	99.30
Oxy Fact (6)	2.16	0.02	2.17	0.01	2.19
Si	1.91	0.01	1.92	0.01	1.93
Ti	0.00	0.00	0.00	0.00	0.00
Al	0.12	0.01	0.10	0.01	0.12
Cr	0.02	0.01	0.02	0.00	0.03
Fe	0.12	0.03	0.10	0.01	0.13
Mn	0.00	0.00	0.00	0.00	0.00
Mg	1.05	0.12	0.98	0.04	1.03
Ca	0.77	0.14	0.87	0.05	0.74
Na	0.01	0.00	0.01	0.00	0.01
Cation Total	4.02	0.01	4.02	0.00	4.00
Mol. % Mg	**93.67**	**1.90**	**94.68**	**1.13**	**88.80**
Jadeite	**0.96**	**0.13**	**0.87**	**0.09**	**1.83**
Aegirine	**4.30**	**1.71**	**4.36**	**1.04**	**0.23**

Table 61: Major element variations in Plagioclase in sample MDS41

	MDS41-6-2	MDS41-6-3	MDS41-12-1	MDS41-12-2	MDS41-5-3	MDS41-5-4
location	**PLAG**	**PLAG**	**PLAG**	**PLAG**	**PLAG**	**PLAG**
sample no.	**nose**	**centre**	**centre**	**rim**	**rim**	**rim**
SiO2	44.93	45.28	44.91	44.39	44.42	44.52
Al2O3	35.10	35.10	34.92	35.11	35.34	35.37
CaO	19.54	19.24	19.42	19.52	19.51	19.44
Na2O	0.71	0.86	0.78	0.64	0.66	0.72
K2O						
TiO2	0.00	0.00	0.00	0.00	0.00	0.00
FeO	0.24	0.24	0.20	0.21	0.29	0.25
MgO	0.00	0.08	0.00	0.00	0.04	0.00
Total	100.52	100.79	100.23	99.87	100.27	100.31
Oxy Fact (32)	11.08	11.05	11.11	11.15	11.12	11.11
Si	8.29	8.33	8.30	8.24	8.22	8.23
Al	7.63	7.60	7.61	7.68	7.71	7.71
Ca	3.86	3.79	3.85	3.88	3.87	3.85
Na	0.25	0.31	0.28	0.23	0.24	0.26
K	0.00	0.00	0.00	0.00	0.00	0.00
Cation Total	20.03	20.03	20.03	20.03	20.04	20.05
Mol. % An	**93.86**	**92.52**	**93.22**	**94.39**	**94.26**	**93.69**

Table 62: IVT07 Summary of major and trace elements

	IVT07							
	amphibole		cpx		Plag		OPX**	
	Average	STDEV	average	stdev	average	stdev	average	stdev
SiO2	37.7	1.43	48.9	0.651	49.3	1.85	51	0.35
TiO2	4.32	0.33	0.712	0.141	0.0379	0.123		
Al2O3	13.2	1.18	5.19	0.6	28.6	1.67	3.66	0.2
Cr2O3	0.011	0.00649	0.00593	0.00633				
FeO	14.7	0.698	9.17	0.296	0.877	2.01	23.8	0.35
MnO	0.133	0.0198	0.26	0.022				
MgO	9.37	0.735	12.4	0.449	0.2	0.627	19.9	0.39
CaO	12.1	1.13	21.3	0.229	13.6	1.34	0.62	0.2
Na2O	1.45	0.284	0.675	0.0564	3.36	0.329		
K2O	2.68	0.409			0.248	0.0878		
Total	95.7	1.77	98.7	0.488	96.2	2.24	99	0.49
Trace Elements (ppm)								
Li	1.06	0.514	9.91	2.75	0.522	0.505	2.13	0.993
Be	0.626	0.0587	0.421		0.229	0.00907	0.0093	0.00806
Na	12800	363	5850	345	28700	943	158	28.6
Mg	52600	1180	66600	1250	670	1000	109000	1480
Al	74600	1360	34700	1390	149000	2930	21200	1280
K	17800	289	139	144	1880	271	96.5	39.2
Ca	78000	1080	152000	2120	81700	2610	4560	689
Sc	141	20.2	176	14.1	1.85	0.998	48.9	10.5
Ti	21800	1410	5170	478	106	72.4	662	68.7
V	824	87.8	573	42	4.53	5.84	202	32
Cr	33.7	7.56	20.3	3.19	0.649	0.272	9.16	1.86
Mn	1120	30.3	2330	119	27.8	20.9	4450	84.6
Fe	96700	8370	71100	4480	1980	1970	147000	5490
Co	51.1	1.35	33.3	2.44	1.73	1.7	69.4	1.49
Ni	19.7	2.4	18.3	1.86	4.6	1.99	11.1	0.608
Cu	2.29	1.47	6.72	6.7	3.26	2.08	7.37	4.36
Zn	93.5	3.25	68.1	4.91	4.69	2.96	249	1.56
Ga	19.3	1.58	15.7	0.775	19.6	0.9	14	1.13
Ge	3.88	0.231	3.89	0.132	0.633	0.235	5.03	0.168
Rb	19.5	1.15	0.0812	0.0588	0.185	0.121	0.116	0.0422
Sr	201	16.1	28.7	5.37	802	20.7	1.45	0.618
Zr	274	26.3	307	32.6	0.023	0.0204	13	3.77
Nb	9.09	0.658	0.0834	0.0377	0.001		0.00544	0.00617
Cs	0.204	0.0407	0.0289		0.0154	0.0017	0.03	0.0165
Ba	1380	143	12.7		586	81.6	2.63	0.495
La	30.5	1.23	11.6	0.68	12.8	0.478	0.0778	0.0243
Ce	91.5	4.52	39.5	1.85	14.4	0.866	0.175	0.0376
Pr	12.8	0.686	5.95	0.251	0.999	0.1	0.0237	0.0045
Nd	60	4.33	30.2	1.41	2.78	0.428	0.134	0.02
Sm	10.5	1.05	5.91	0.294	0.191	0.0954	0.0383	0.00515
Eu	7.49	0.376	3.78	0.16	1.77	0.124	0.0476	0.00358
Gd	8.9	1.17	5.28	0.333	0.102	0.0766	0.0608	0.0139
Tb	1.11	0.147	0.689	0.043	0.00806	0.00816	0.0139	0.00303
Dy	6.8	1	4.49	0.289	0.0401	0.0528	0.135	0.0318
Y	33.4	4.46	22	1.44	0.184	0.226	1.05	0.223
Ho	1.31	0.18	0.854	0.0552	0.00675	0.00929	0.0369	0.00869
Er	3.75	0.519	2.58	0.161	0.0188	0.0297	0.163	0.034
Tm	0.484	0.0595	0.336	0.0229	0.00285	0.00374	0.0329	0.00729
Yb	3.26	0.383	2.39	0.144	0.0198	0.0267	0.338	0.0674
Lu	0.491	0.0568	0.354	0.0213	0.00271	0.00261	0.0703	0.0137
Hf	6.61	0.633	7.55	0.594			0.468	0.0989
Ta	0.399	0.0481	0.0115		0.0003			
Pb	1.59	0.113	0.238	0.0698	2.57	0.183	0.091	0.0703
Th	0.604	0.0423	0.227		0.0053		0.0082	0.00297
U	0.0888	0.0106	0.0481				0.00146	0.00161
count	8		17		22		6	

Table 63: IVT10 Summary of major and trace elements

	IVT10					
	OPX		cpx		Plag	
	Average	1σ	Average	1σ	Average	1σ
SiO2	45.2	4.33	49.6	0.99	48	1.81
TiO2	1.2	1.4	0.39	0.0916	0.00127	0.0124
Al2O3	10.1	4.9	2.78	0.668	29.9	1.28
Cr2O3	0.0084	0.00678	0.00749	0.00653		
FeO	14.5	2.75	9.14	0.499	0.466	0.836
MnO	0.178	0.031	0.244	0.0273	0.00257	0.0213
MgO	10.9	2.42	12.7	0.381	0.203	0.791
CaO	12.2	1.43	21.8	0.566	15	1.46
Na2O	0.808	0.483	0.384	0.0906	2.68	0.614
Total	95.7	1.16	97	1.19	96.4	1.44
Trace Elements (ppm)						
Li	1.29	0.348	1.07	0.542	0.928	0.419
Be	0.0264	0.0295	0.0822	0.041	0.352	0.0835
K	301	291	1340	949	935	513
Sc	42.6	5.25	132	40.4	2.39	0.0739
Ti	520	55.1	2200	936	67.5	46.5
V	212	32.8	453	106	18.9	48.8
Cr	7.14	0.982	12.2	4.88	0.319	0.0731
Mn	3580	238	2340	577	13	7.57
Co	50.3	3.12	49.5	3.6	0.524	0.68
Ni	4.66	0.281	8.2	1.94	1.06	0.681
Cu	2.58	1.97	4.67	2.48	2.12	2.42
Zn	222	12.8	190	24.9	4.59	3.6
Ga	10.2	1.15	13.1	1.91	29.1	0.819
Ge	4.64	0.259	4.6	0.233	0.79	0.193
Rb	0.217	0.105	0.576	0.384	0.466	0.391
Sr	23.8	48.4	39.6	51.2	894	43.2
Zr	11.7	4.59	184	126	0.0311	0.0342
Nb	0.0149	0.0131	0.253	0.12	0.00598	0.00822
Cs	0.037		0.11	0.0491	0.15	
Ba	13.7	16.1	70.6	41.5	344	45.3
La	0.601	0.4	2.39	1.02	9.32	0.496
Ce	1.27	0.624	12.3	4.46	12.6	0.321
Pr	0.165	0.0898	3	1.02	1.14	0.0403
Nd	0.765	0.503	20.1	6.5	3.81	0.101
Sm	0.188	0.151	6.43	2.01	0.316	0.0433
Eu	0.146	0.0932	2.33	0.504	2.3	0.106
Gd	0.243	0.143	6.73	2.06	0.168	0.0224
Tb	0.0426	0.0218	0.951	0.286	0.0129	0.00193
Dy	0.355	0.132	5.78	1.76	0.0529	0.00692
Y	2.48	0.748	27.4	7.68	0.208	0.0382
Ho	0.0962	0.0298	1.13	0.336	0.0069	0.00279
Er	0.358	0.08	3.06	0.887	0.0148	0.00733
Tm	0.0653	0.012	0.4	0.112	0.00127	0.000647
Yb	0.572	0.0846	2.58	0.729	0.00846	0.00342
Lu	0.108	0.0162	0.387	0.121	0.000277	0.000202
Hf	0.404	0.137	5.16	2.99	0.0002	0.000283
Ta	0.0015		0.0122	0.00595		
Pb	0.185	0.119	0.294	0.121	2.35	0.201
Th	0.0173	0.0147	0.159	0.142	0.0028	
U	0.00377	0.00215	0.0466	0.0455	0.002	
count	6		9		10	

Table 64: Vanuatu WS5 major and trace element results

	WS5					
	cpx		Glass		Plag	
	average	STDEV	average	STDEV	average	STDEV
SiO2	51.9	0.425	61.6	0.844	56.3	1.09
TiO2	0.5	0.104	0.831	0.0946	0.0733	0.0594
Al2O3	2	0.488	15.6	0.506	27.2	0.856
Cr2O3	0.075	0.122	0.0375	0.0619	0.0733	0.0884
FeO	11.7	0.977	6.74	0.585	0.747	0.223
MnO	0.5	0.113	0.138	0.0885	0.0267	0.0458
MgO	14.6	0.627	1.9	0.572	0.0867	0.0516
CaO	18.4	0.444	4.41	0.746	9.53	0.798
Na2O	0.342	0.0515	4.02	0.597	5.28	0.332
K2O	0.025	0.0622	4.08	0.63	0.687	0.196
P2O5			0.575	0.1	0.02	0.0414
Total(Oxide Mass%)	100		100		100	
Trace Elements (ppm)						
Li	5	0.567	23	7.2	6.88	1.44
Be	0.0983	0.0304	1.64	0.154	0.372	0.0733
Na	2570	124	33500	1010	40800	1880
Mg	79700	4410	9450	199	526	154
Al	9790	885	81600	3180	148000	3810
K	120	269	36900	1960	6210	431
Ca	145000	2320	29200	1060	71300	3630
Sc	145	26.2	14.7	0.802	1.61	0.212
Ti	3280	226	4950	120	335	49.5
V	357	31.3	151	2.57	3.31	1.66
Cr	1.07	1.18	3.83			
Mn	4620	594	1440	17.1	60.5	23.4
Fe	93400	9570	48000	1050	4910	795
Co	46.6	2.23	29.7	37.9	0.666	0.218
Ni	11	0.635	3.71	3.1	3.78	0.841
Cu	12.1	16.9	159	51.3	10.7	4.61
Zn	136	23.4	138	3.35	11.1	1.44
Ga	5.49	0.219	18.3	0.3	22.7	0.82
Ge	5.21	0.414	2.9	0.145	1.01	0.109
Rb	0.393	0.621	65.9	1.96	1.74	0.882
Sr	51.5	2.78	431	17.2	1710	57
Zr	27.2	5.29	142	11.8	1.78	1.95
Nb	0.0144	0.0128	2.06	0.218	0.0321	0.0204
Cs	0.0277		2.18	0.0565	0.073	
Ba	2.09	4.38	762	16.1	467	77.9
La	3.07	0.659	17.9	0.992	2.61	0.18
Ce	12.8	2.56	41.6	0.931	4.27	0.453
Pr	2.86	0.557	5.69	0.26	0.48	0.0663
Nd	19.3	3.63	25.9	1.15	1.88	0.297
Sm	7.37	1.41	6.17	0.385	0.277	0.0702
Eu	1.66	0.174	1.65	0.184	1.36	0.251
Gd	8.94	1.67	5.7	0.303	0.209	0.0737
Tb	1.33	0.254	0.807	0.0946	0.0199	0.0101
Dy	9.2	1.82	5.16	0.349	0.12	0.074
Y	47.8	9.28	29.3	1.87	0.628	0.427
Ho	1.8	0.353	1.05	0.118	0.0212	0.0141
Er	5.49	1.14	3.24	0.24	0.0567	0.042
Tm	0.727	0.159	0.476	0.0974	0.00751	0.00704
Yb	5.05	1.18	3.18	0.233	0.0415	0.0385
Lu	0.736	0.181	0.498	0.0951	0.0074	0.00692
Hf	1.36	0.263	4.06	0.379	0.0727	0.0452
Ta	0.0016	0.000675	0.127	0.0572		
Pb	0.262	0.144	21.7	0.778	3.79	0.377
Th	0.032	0.0231	2.97	0.191	0.0607	0.0378
U	0.0167	0.015	1.84	0.132	0.0337	0.0198
count	6		6		5	

Table 65: Vanuatu TUK6 major and trace element results

	TUK6					
	cpx		Glass		Plag	
	average	σ	average	σ	average	σ
SiO2	51.4	0.391	65.9	3.41	53	0.377
TiO2	0.4	0.0707	0.25	0.138		
Al2O3	2.68	0.205	19.5	3.15	29	0.386
Cr2O3	0.06	0.0548	0.0333	0.0816	0.05	0.0577
FeO	10.3	0.716	0.917	0.833	0.95	0.129
MnO	0.32	0.0837	0.05	0.0548		
MgO	16	0.192	0.05	0.0837	0.15	0.0577
CaO	18.5	0.537	1.98	2.52	12.3	0.618
Na2O	0.36	0.0548	5.45	0.85	4.03	0.171
K2O	0.02	0.0447	5.98	2.59	0.425	0.0957
P2O5			0.0333	0.0816	0.025	0.05
Total(Oxide Mass%)	100		100		100	
Trace Element (ppm)						
Li	4.73	0.748	1.94	0.676	13.1	1.84
Be	0.0185	0.0179	2.1	0.197	0.239	0.122
Na	2350	157	31800	1410	32400	1540
Mg	90400	1310	2570	1630	839	205
Al	13800	1080	78300	2840	151000	4430
K	40	40.8	49500	1720	4090	893
Ca	142000	2400	13000	1150	86300	5240
Sc	118	4.83	9.5	1.9	1.46	0.28
Ti	2590	165	3870	1030	274	90
V	281	19.5	38.2	28.4	4.15	4.26
Cr	268	320	1.6		1.62	
Mn	2600	167	730	267	55.4	20.3
Fe	74300	3450	28700	11300	7080	856
Co	52	1.57	5.72	3.34	1.07	0.311
Ni	98.3	8.06	2.9	1.72	3.85	0.485
Cu	16.1	10.4	221	37.9	20.1	22.5
Zn	73.6	6.64	103	28.6	10.8	4.24
Ga	6	0.465	16.7	0.904	23.4	0.524
Ge	4.25	0.136	2.37	0.284	1.03	0.0962
Rb	0.13	0.0693	77.3	14.7	1.48	2.19
Sr	38.3	1.94	176	75.1	1150	23.3
Zr	13.6	1.13	212	10.6	2.01	4.56
Nb	0.00652	0.00466	2.7	0.224	0.0749	0.0803
Cs	0.018		2.54	0.615	0.119	0.101
Ba	1.09	1.17	1050	356	209	45.1
La	0.936	0.0955	21.8	3.74	1.23	0.459
Ce	4.09	0.379	45.7	7.01	2.06	0.812
Pr	0.945	0.0928	6.44	1.2	0.254	0.108
Nd	6.58	0.654	29.1	5.92	1.08	0.492
Sm	2.74	0.274	6.83	1.35	0.172	0.0993
Eu	0.808	0.0711	1.59	0.242	0.427	0.167
Gd	3.56	0.391	6.64	1.34	0.137	0.0961
Tb	0.556	0.0573	0.95	0.163	0.0148	0.0136
Dy	3.92	0.429	6.57	1.04	0.0965	0.106
Y	20.4	2.1	39.3	5.72	0.491	0.627
Ho	0.778	0.079	1.32	0.188	0.0167	0.021
Er	2.38	0.25	4.22	0.506	0.0458	0.07
Tm	0.31	0.0351	0.598	0.0573	0.00719	0.0104
Yb	2.15	0.22	4.37	0.351	0.0461	0.0824
Lu	0.299	0.034	0.644	0.054	0.00705	0.013
Hf	0.755	0.0715	6.05	0.322	0.194	0.203
Ta	0.0013		0.141	0.0104	0.00515	0.00346
Pb	0.156	0.0832	28.5	2.09	2.26	0.802
Th	0.0128	0.00433	4.25	0.192	0.0861	0.121
U	0.00613	0.00295	2.44	0.184	0.0631	0.0727
	9		7		15	

Table 66: Alaska BE-081B major and trace element results

	BE-081B							
Mineral	cpx		Plag		amphibole		olivine	
	Average	1σ	Average	1σ	Average	1σ	Average	1σ
SiO2	50.9	0.726	44.9	0.419	46.3	1.17	37.9	0.41
Al2O3	3.93	0.872	35.3	0.179	12	0.552	0.005	0.00707
TiO2	0.514	0.142	0.052	0.1	0.4	0.151	0.05	0.0707
Cr2O3	0.09	0.0909	0.024	0.0537	0.02	0.0346	0.07	0.0849
FeO	6.76	0.451	0.382	0.0928	9.18	1.26	21.4	0.721
MnO	0.247	0.0431	0.056	0.0559	0.127	0.0153	0.55	0.184
MgO	15	0.709	0.012	0.0268	18.4	1.08	39.7	0.24
CaO	22.2	0.389	18.3	0.293	11.4	0.927	0.045	0.0636
Na2O	0.214	0.0806	0.868	0.107	1.75	0.121	0.025	0.0354
K2O	0.0157	0.0257			0.377	0.0814	0.01	
Total	100		100		100		100	
Trace Element (ppm)								
Li	6.52	3.24	6.38	5.58	2.63	1.77	3.27	0.45
Be	0.0591	0.0209	0.0803	0.0603	0.179	0.0474		
K	319	220	216	69.5	5250	258	102	209
Sc	153	11.1	2.23	0.12	197	15.4	5.73	3.85
Ti	3020	420	13.9	5.67	11600	1110	156	305
V	322	30.8	0.291	0.22	730	43.3	11.8	23.9
Cr	77.1	29.3	0.239	0.0327	105	40.1	0.716	1.13
Mn	1650	115	85.3	34.7	1180	40.6	3270	154
Co	36.5	2.92	0.485	0.413	65.8	3	213	15.4
Ni	36.6	5.4	0.577	0.286	87.2	4.96	241	16.7
Cu	3.3	6.09			8.63	5.68	61.4	122
Zn	38.9	3.24	3.91	1.76	68.5	3.85	172	6.18
Ga	6.34	0.737	19.4	0.728	15.3	0.881	0.333	0.678
Ge	3.58	0.211	0.72	0.19	3.6	0.125	3.44	0.199
Rb	0.468	0.273	0.614	0.549	2.28	0.471	0.407	0.484
Sr	60.4	19.3	1080	30.5	261	54.4	3.25	6.52
Y	10.6	1.52	0.0293	0.00845	26.7	2.3	0.3	0.654
Zr	11.2	1.79	0.01		23.6	4.54	0.45	0.771
Nb	0.0685	0.0537			1.89	0.474	0.099	
Cs	0.093	0.0409	0.3	0.282			0.074	
Ba	11.8	7.98	51.5	5.59	111	7.73	1.15	2.14
La	0.886	0.0915	0.805	0.0486	2.53	0.248	0.131	
Ce	3.53	0.374	1.15	0.0564	8.17	0.556	0.125	0.25
Pr	0.675	0.0781	0.105	0.0118	1.57	0.0989	0.079	
Nd	4.06	0.546	0.35	0.0502	9.77	0.378	0.579	
Sm	1.57	0.207	0.0279	0.00704	3.73	0.308	0.215	
Eu	0.541	0.0476	0.18	0.0154	1.29	0.111	0.036	0.0508
Gd	1.93	0.251	0.0188	0.00817	4.87	0.475	0.235	
Tb	0.321	0.0424	0.00163	0.000617	0.797	0.0663	0.0202	0.0285
Dy	2.17	0.291	0.00872	0.00233	5.16	0.464	0.263	
Ho	0.435	0.0596	0.00119	0.000314	1.1	0.102	0.0294	0.0402
Er	1.22	0.177	0.00271	0.00072	3.04	0.251	0.0822	0.111
Tm	0.162	0.0242	0.00024		0.397	0.0325	0.00721	0.0115
Yb	1.03	0.157			2.45	0.194	0.0391	0.0619
Lu	0.147	0.0225			0.349	0.0295	0.00601	0.00867
Hf	0.494	0.0485			1.1	0.112	0.053	
Ta	0.00569	0.00458			0.0988	0.0308	0.0024	
Pb	0.129	0.044	0.969	0.0798	0.881	0.194	0.0341	0.0404
Th	0.16	0.0408	0.0003		0.24	0.0421	0.0164	0.0224
U	0.0838	0.0155	0.0028		0.144	0.0184	0.00962	0.0127
count	10		10		5		5	

Table 67: St Vincent, Lesser Antilles major and trace element results

	VS2a		VS2a		VS14		VS14	
	pl	σ	cpx	σ	pl	σ	cpx	σ
SiO2	44.7		50.4		39.9		49.1	
TiO2	0.01		0.66		0.01		0.91	
Al2O3	35		3.69		31.4		5.08	
Cr2O3			0.03				0.09	
FeO	0.58		7.51		0.52		6.92	
MnO			0.2		0.02		0.16	
MgO	0.03		14.6		0.05		14.1	
CaO	19.1		22.4		19.6		22.7	
Na2O	0.89		0.24		0.67		0.26	
Total	100		99.7		92.2		99.3	
Li	1.03	0.226	1.31	0.0575	0.116	0.0275	0.808	0.0557
Mg	420	110	99100	1090	472	39.6	96700	1710
Si	229000	1040	241000	1790	231000	1460	232000	3580
P	28.9	1.98	17.7	0.756	29.5	2.87	17.2	0.57
K	81.7	38.2	0.99	0.58	53.9	5.39	1.4	
Sc	2.21	0.19	165	7.98	2.27	0.359	173	8.2
Ti	77	14.5	3640	29.6	84	11.5	5090	259
V	1.87	0.653	362	7.94	2.02	1.11	425	10.6
Mn	49.7	4.19	1550	48.3	35.7	1.76	1160	70.9
Fe	1930	105	25500	135	1840	33.8	24700	326
Co	0.311	0.057	33.6	0.272	0.35	0.0822	31.6	0.416
Cu	3.12	0.787	1.94	0.053	0.482	0.532	1.85	0.128
Cu	3.22	0.835	2.35	0.0852	0.309	0.388	2.26	0.0611
Sr	351	11.6	14	0.138	320	4.05	13.3	0.192
Y	0.198	0.0673	13.1	0.544	0.139	0.0184	15.6	1.27
Ba	7	0.912			6.94	0.33	0.0115	
La	0.215	0.034	0.259	0.0232	0.198	0.0166	0.249	0.0168
Ce	0.466	0.0744	1.38	0.101	0.443	0.0211	1.41	0.109
Pr	0.0668	0.0117	0.353	0.0178	0.0613	0.00142	0.377	0.0214
Nd	0.287	0.0654	2.63	0.134	0.274	0.0145	2.87	0.192
Sm	0.066	0.0151	1.33	0.0537	0.0523	0.00458	1.57	0.11
Eu	0.185	0.0343	0.517	0.0178	0.166	0.00458	0.564	0.00875
Gd	0.0593	0.0165	2.07	0.0807	0.049	0.00565	2.43	0.109
Tb	0.00822	0.002	0.387	0.0167	0.00602	0.000904	0.458	0.0291
Dy	0.0445	0.0156	2.65	0.123	0.0328	0.00237	3.11	0.2
Ho	0.00808	0.00396	0.549	0.03	0.0051	0.000388	0.655	0.0494
Er	0.0187	0.00803	1.54	0.0781	0.0113	0.00212	1.8	0.157
Tm	0.00132	0.000979	0.202	0.0106	0.000895	0.000195	0.239	0.0254
Yb	0.0127	0.00737	1.32	0.0618	0.006	0.00115	1.56	0.189
Lu	0.00209	0.00126	0.181	0.0108	0.000635	0.000115	0.21	0.0259

Table 68: Dominica, Lesser Antilles (DC47) major and trace element results

	cpx		opx		plag		magnetite	
	average	σ	average	σ	average	σ	average	stdev
SiO2	52.3		51.9	0.16	48.2	0.406	0.0593	0.0205
TiO2	0.41		0.277	0.16	0.00808		10.1	1.84
Al2O3	2.39		2.86	1.92	33.3	0.342	4.2	1.44
FeOtot	11.6		20.9	5.46	0.386	0.0134	79.7	3.58
MnO	0.395		0.576	0.243	0.0166	0.00396	0.388	0.00624
MgO	13		22.4	3.53	0.015	0.00911	1.84	0.691
CaO	20.1		1.43	0.356	16.1	0.285	0.0648	0.0659
Na2O	0.345		0.0266	0.0307	2.22	0.171	0.0317	0.0224
K2O					0.0334	0.000254		
P2O5	0.0207		0.00412	0.00156				
total	101		100	0.124	100	0.0516	96.5	0.544
Trace Elements (ppm)								
Li	6.5	0.359	6.99	0.75	3.04	0.368	1.66	0.976
Be	0.23	0.0441	0.043		0.455	0.0854	0.026	
B	6.28	0.128	7.31	0.51	6.82	0.43	12.7	3.15
P	36.5	1.97	67.4	46.4	79.2	10.4	36.5	23.4
K	55.5	82.1	2.93		331	9.52	4.3	
Sc	188	6.49	76.5	4.3	1.34	0.187	61	60.7
Ti	2090	302	1130	66.2	49.1	9.4	149000	144000
V	284	54.2	147	26.9	0.924	0.547	5960	995
Cr	3.07	0.821	2.11	0.265	1.08	0.197	55.8	28.5
Mn	3180	48.4	7740	447	76.7	28.3	3380	728
Co	44.6	1.2	119	6.83	0.636	0.73	161	8.08
Ni	7.85	0.598	16.1	0.886	0.23	0.139	31.2	6.92
Cu	2.14	0.768	1.92	0.123	2.75	1.37	18.4	20.4
Zn	80.4	4.41	359	20.5	5.32	2.59	385	105
Ga	5.68	0.704	5.76	0.696	28.3	0.3	22.2	9.91
Ge	4.57	0.13	7.65	0.645	0.73	0.0909	3.2	0.166
As	5.16	9.29	1.05	0.416	0.52	0.121	4.28	4.32
Rb	0.209	0.336	0.0237	0.00898	0.133	0.0294		
Sr	13.9	1.28	0.437	0.703	464	5.11	0.336	0.227
Y	38.6	3.52	6.8	0.829	0.366	0.0398	0.453	0.387
Zr	20.7	0.996	2.36	0.272	0.0355	0.00874	74.2	103
Nb	0.0154	0.00796	0.00244	0.00115	0.00002		21.5	31.9
Mo	0.0712	0.00697	0.168	0.0126	0.0021		1.22	0.643
Cd	0.403	0.0281	0.206	0.023	0.0613	0.0156	0.036	0.0161
In	0.208	0.0104	0.132	0.019			0.272	0.11
Sn	1.32	1.23	0.415	0.0299	0.171	0.02	4.64	2.02
Sb	0.116	0.0608	0.484				0.166	
Cs	0.0045	0.000283	0.0164					
Ba	1.39	2.69	0.0977	0.0461	37.7	1.35	0.0943	0.0793
La	1.24	0.101	0.02	0.0221	2.33	0.206	0.046	0.0492
Ce	5.99	0.596	0.0699	0.0344	3.72	0.134	0.0728	0.0966
Pr	1.39	0.138	0.0202	0.00633	0.417	0.0626	0.0142	0.0144
Nd	9.57	0.922	0.167	0.0294	1.56	0.245		
Sm	4.56	0.449	0.137	0.0155	0.247	0.0684	0.0297	0.0257
Eu	0.873	0.0603	0.0404	0.00362	0.732	0.027	0.00448	0.00351
Gd	6.47	0.617	0.334	0.0366	0.191	0.0737	0.0337	0.0146
Tb	1.13	0.108	0.0871	0.00769	0.0225	0.0104		
Dy	7.85	0.705	0.852	0.0795	0.133	0.0823		
Ho	1.63	0.144	0.247	0.0224	0.0246	0.0182		
Er	4.64	0.413	0.988	0.0917	0.0688	0.0578	0.0889	0.0916
Tm	0.619	0.0577	0.185	0.0158	0.00948	0.00912		
Yb	3.99	0.338	1.62	0.136	0.0621	0.068	0.24	0.342
Lu	0.583	0.045	0.297	0.0211	0.00941	0.0105		
Hf	1.11	0.18	0.112	0.0112			2.08	2.79
Ta	0.00238	0.000716					1.23	1.91
W	0.00146	0.00204					0.272	0.374
Pb	0.156	0.0519	0.0167	0.0102	2.07	0.0245		
Th	0.0293	0.00859	0.00477	0.00116	0.00195	0.000778	0.00528	0.00436
U	0.0109	0.00527	0.00219	0.000983	0.0068		0.0398	0.0551
	6		12		4		7	

Table 69: Dominica, Lesser Antilles (DC104) major and trace element results

	DC104					
	cpx		plag		Olivine	
	average	σ	average	σ	Average	σ
SiO2	50.9	0.633	44.8	0.306	38.2	
TiO2	0.651	0.123	0.0217	0.0084	0.00888	
Al2O3	3.97	0.552	35	0.325		
FeOtot	7.93	0.0838	0.477	0.0433	26.8	
MnO	0.223	0.000369	0.00565	0.00635	0.529	
MgO	14.4	0.446	0.0292	0.00398	36.1	
CaO	22	0.221	18.8	0.318	0.155	
Na2O	0.241	0.0179	0.798	0.173	0.00254	
K2O			0.00939	0.00691		
P2O5	0.0178	0.000959				
total	100	0.158	99.9	0.137	102	
Li	1.27	0.0541	1.08	0.295	3.31	0.0361
Be	0.059	0.0172	0.117	0.0201		
B	5.27	0.459	5.37	0.476	6.01	0.368
Na	1740	99.2	6070	246	15.3	0.846
Mg	78600	1680	340	85.6	230000	666
Al	22300	2130	194000	1360	104	8.34
Si	236000	2700	234000	2540	214000	987
P	30.7	1.71	51.8	8.21	49.6	6.47
K			90.9	9.42		
Ca	157000	518	134000	691	1200	17.2
Sc	125	14	1.19	0.0856	6.76	0.145
Ti	3510	314	54	3.2	62.6	0.404
V	378	26.2	1.52	0.615	5.98	0.178
Cr	8.69	3.95	1.06	0.0966	1.02	0.0839
Mn	1760	65.5	51.3	2.74	4840	47.3
Fe	62900	732	4370	150	244000	1950
Co	35.9	0.413	0.365	0.143	237	1.92
Ni	20.8	1.76	0.243	0.0676	150	2.4
Cu	1.2	0.0675	2.89	1.33	2.4	0.0545
Zn	33.3	1.48	1.95	0.241	209	2.05
Ga	7.04	0.524	23.8	0.708	0.102	0.00529
Ge	3.8	0.0999	0.799	0.166	4.41	0.17
As	0.91	0.572	0.538	0.136	0.941	0.306
Rb			0.033	0.0052		
Sr	16.6	1.02	393	6.43	0.0485	0.0276
Y	12.8	1.61	0.315	0.24	0.114	0.0194
Zr	10.1	1.28	0.0245	0.015	0.0181	0.00234
Nb	0.0082	0.00239	0.00007			
Mo	0.0375	0.00518			0.105	0.00808
Cd	0.159	0.0259			0.0487	0.0133
In	0.0899	0.00932			0.0156	0.000954
Sn	0.537	0.06	0.166	0.0233	0.286	0.0306
Sb	0.11		0.192		0.357	0.161
Cs						
Ba	0.0357	0.0397	9.44	0.509	0.093	
La	0.475	0.0804	0.345	0.0505	0.00344	0.0039
Ce	2.23	0.351	0.616	0.054	0.00099	0.000396
Pr	0.51	0.0729	0.075	0.0102	0.00127	0.00136
Nd	3.55	0.512	0.308	0.0417	0.00395	0.00219
Sm	1.61	0.22	0.0541	0.00761		
Eu	0.564	0.0696	0.199	0.0248	0.00076	
Gd	2.23	0.32	0.0417	0.00698	0.00357	0.0011
Tb	0.377	0.0515	0.00596	0.00139	0.00073	0.000217
Dy	2.62	0.343	0.03	0.00942	0.00883	0.00155
Ho	0.531	0.0731	0.00603	0.00302	0.00314	0.000403
Er	1.49	0.201	0.0151	0.00863	0.0203	0.00146
Tm	0.192	0.0229	0.00254	0.00137	0.00466	0.000553
Yb	1.21	0.158	0.0169	0.0103	0.0448	0.00272
Lu	0.166	0.0195	0.00264	0.0017	0.011	0.00105
Hf	0.573	0.0886				
Ta	0.00161	0.000701				
W						
Pb	0.0257	0.00216	0.255	0.011		
Th	0.00785	0.00179				
U	0.00166	0.000289	0.0051	0.00172		
	8		9		12	

REFERENCES

Aigner-Torres, M., Blundy, J., Ulmer, P. and Pettke, T. (2007) Laser Ablation ICPMS study of trace element partitioning between plagioclase and basaltic melts: an experimental approach. Contrib Mineral Petrol 153, 647-667.

Andersen, D.J., Lindsley, D.H. and Davidson, P.M. (1993) QUILF: A pascal program to assess equilibria among Fe-Mg-Mn-Ti oxides, pyroxenes, olivine, and quartz. Computers & Geosciences 19, 1333-1350.

Bédard, J.H. (1994) A Procedure for calculating the equilibrium distribution of trace elements among the minerals of cumulate rocks, and the concentration of trace elements in the coexisting liquids. Chemical Geology 118, 143-153.

Bédard, J.H. (2006) Trace element partitioning in plagioclase feldspar. Geochimica et Cosmochimica Acta 70, 3717-3742.

Bédard, J.H. (2014) Parameterizations of calcic clinopyroxene—Melt trace element partition coefficients. Geochemistry, Geophysics, Geosystems 15, 303-336.

Behrens, H., Johannes, W. and Schmalzried, H. (1990) On the mechanisms of cation diffusion processes in ternary feldspars. Physics and Chemistry of Minerals 17, 62-78.

Berman, R.G. and Brown, T.H. (1984) A thermodynamic model for multicomponent melts, with application to the system CaO-Al2O3-SiO2. Geochimica et Cosmochimica Acta 48, 661-678.

Berry, A.J., Yaxley, G.M., Woodland, A.B. and Foran, G.J. (2010) A XANES calibration for determining the oxidation state of iron in mantle garnet. Chemical Geology 278, 31-37.

Bezos, A. and Humler, E. (2005) The Fe3+/ΣFe ratios of MORB glasses and their implications for mantle melting.

Bindeman, I., Davis, A.M. and Drake, M.J. (1998) Ion Microprobe Study of Plagioclase-Basalt Partition Experiments at Natural Concentration Levels of Trace Elements. Geochimica et Cosmochimica Acta 62, 1175-1193.

Bindeman, I.N. and Davis, A.M. (2000) Trace element partitioning between plagioclase and melt: Investigation of dopant influence on partition behavior. Geochimica et Cosmochimica Acta 64, 2863-2878.

Blundy, J.D. (1997) Experimental study of a Kiglapait marginal rock and implications for trace element partitioning in layered intrusions. Chemical Geology 141, 73-92.

Blundy, J.D., Robinson, J.A.C. and Wood, B.J. (1998) Heavy REE are compatible in clinopyroxene on the spinel lherzolite solidus. Earth and Planetary Science Letters 160, 493-504.

Blundy, J.D. and Wood, B. (2003) Partitioning of trace elements between crystals and melts. Earth and Planetary Science Letters 210, 383-397.

Blundy, J.D. and Wood, B.J. (1991) Crystal-chemical controls on the partitioning of Sr and Ba between plagioclase feldspar, silicate melts, and hydrothermal solutions. Geochimica et Cosmochimica Acta 55, 193-209.

Blundy, J.D., Wood, B.J. and Davies, A. (1996) Thermodynamics of rare earth element partitioning between clinopyroxene and melt in the system CaO-MgO-Al2O3-SiO2. Geochimica et Cosmochimica Acta 60, 359-364.

Boyd, F.R. and England, J.L. (1960) Apparatus for phase-equilibrium measurements at pressures up to 50 kilobars and temperatures up to 1750°C. Journal of Geophysical Research 65, 741-748.

Brey, G.P. and Köhler, T. (1990) Geothermobarometry in Four-phase Lherzolites II. New Thermobarometers, and Practical Assessment of Existing Thermobarometers. Journal of Petrology 31, 1353-1378.

Brice, J.C. (1975) Some thermodynamic aspects of the growth of strained crystals. Journal of Crystal Growth 28, 249-253.

Canil, D. and O'Neill, H.S.C. (1996) Distribution of Ferric Iron in some Upper-Mantle Assemblages. Journal of Petrology 37, 609-635.

Cawthorn, R.G. and Walraven, F. (1998) Emplacement and Crystallization Time for the Bushveld Complex. Journal of Petrology 39, 1669-1687.

Cherniak, D.J. (1996) Strontium diffusion in sanidine and albite, and general comments on strontium diffusion in alkali feldspars. Geochimica et Cosmochimica Acta 60, 5037-5043.

Cherniak, D.J. (2002) Ba diffusion in feldspar. Geochimica et Cosmochimica Acta 66, 1641-1650.

Cherniak, D.J. (2003) REE diffusion in feldspar. Chemical Geology 193, 17.

Cherniak, D.J. (2010) Cation Diffusion in Feldspars. Reviews in mineralogy and geochemistry 72, 691-733.

Cherniak, D.J. and Watson, E.B. (1994) A study of strontium diffusion in plagioclase using Rutherford backscattering spectroscopy. Geochimica et Cosmochimica Acta 58, 5179-5190.

Ching-oh, S., Williams, R.J. and Shine-soon, S. (1974) Distribution coefficients of Eu and Sr for plagioclase-liquid and clinopyroxene-liquid equilibria in oceanic ridge basalt: an experimental study. Geochimica et Cosmochimica Acta 38, 1415-1433.

Colson, R.O., McKay, G.A. and Taylor, L.A. (1988) Temperature and composition dependencies of trace element partitioning: Olivine/melt and low-Ca pyroxene/melt. Geochimica et Cosmochimica Acta 52, 539-553.

Coogan, L.A. (2011) Preliminary experimental determination of the partitioning of lithium between plagioclase crystals of different anorthite contents. Lithos 125, 711-715.

Costa, F., Chakraborty, S. and Dohmen, R. (2003) Diffusion coupling between trace and major elements and a model for calculation of magma residence times using plagioclase. Geochimica et Cosmochimica Acta 67, 2189-2200.

Crank, J. (1975) The Mathematics of Diffusion. Oxford Universtiry Press, London, W.I.

Deer, W.A., Howie, R.A. and Zussman, J. (1992) An introduction to the Rock-Forming Minerals, Second Edition ed. Pearson Education Limited, Harlow.

Deer, W.A., Howie, R.A. and Zussman, J. (1997) Rock Forming Minerals: Single Chain Silicates, Second ed. The Geological Society, London.

Deer, W.A., Howie, R.A. and Zussman, J. (2001) Rock-Forming Minerals: Framework Silicates - Feldspars, second ed. The Geological Society, London.

Dohmen, R. and Blundy, J. (2014) A predictive thermodynamic model for element partitioning between plagioclase and melt as a function of pressure, temperature and composition. American Journal of Science 314, 1319-1372.

Drake, M.J. and Weill, D.F. (1975) Partition of Sr, Ba, Ca, Y, Eu2+, Eu3+, and other REE between plagioclase feldspar and magmatic liquid: an experimental study. Geochimica et Cosmochimica Acta 39, 689-712.

Dudas, M.J., Schmitt, R.A. and Harward, M.E. (1971) Trace element partitioning between volcanic plagioclase and dacitic pyroclastic matrix. Earth and Planetary Science Letters 11, 440-446.

Duffy, J.A. (1993) A review of optical basicity and its applications to oxidic systems. Geochimica et Cosmochimica Acta 57, 3961-3970.

Dunn, T. (1987) Partitioning of Hf, Lu, Ti, and Mn between olivine, clinopyroxene and basaltic liquid. Contrib Mineral Petrol 96, 476-484.

Dunn, T. and Sen, C. (1994) Mineral/matrix partition coefficients for orthopyroxene, plagioclase, and olivine in basaltic to andesitic systems: A combined analytical and experimental study. Geochimica et Cosmochimica Acta 58, 717-733.

Dupuy, C., Dostal, J., Liotard, J.M. and Leyreloup, A. (1980) Partitioning of trasition elements between clinopyroxene and garnet. Earth and Planetary Science Letters 48, 303-310.

Dygert, N. and Liang, Y. (2015) Temperatures and cooling rates recorded in REE in coexisting pyroxenes in ophiolitic and abyssal peridotites. Earth and Planetary Science Letters, 151-161.

Dygert, N., Liang, Y., Sun, C. and Hess, P. (2014) An experimental study of trace element partitioning between augite and Fe-rich basalts. Geochimica et Cosmochimica Acta 132, 170-186.

Evans, T.M., C. O'Neill, H.S. and Tuff, J. (2008) The influence of melt composition on the partitioning of REEs, Y, Sc, Zr and Al between forsterite and melt in the system CMAS. Geochimica et Cosmochimica Acta 72, 5708-5721.

Ewing, T., Rubatto, D., Beltrando, M. and Hermann, J. (2015) Constraints on the thermal evolution of the Adriatic margin during Jurassic continental break-up: U–Pb dating of rutile from the Ivrea–Verbano Zone, Italy. Contrib Mineral Petrol 169, 1-22.

Faak, K., Chakraborty, S. and Coogan, L.A. (2013) Mg in plagioclase: Experimental calibration of a new geothermometer and diffusion coefficients. Geochimica et Cosmochimica Acta 123, 195-217.

Faak, K., Coogan, L.A. and Chakraborty, S. (2014) A new Mg-in-plagioclase geospeedometer for the determination of cooling rates of mafic rocks. Geochimica et Cosmochimica Acta 140, 691-707.

Fehr, K.T. and Huber, A.L. (2001) Stability and phase relations of Ca[ZnSi3]O8, a new phase with feldspar structure in the system CaO-ZnO-SiO2. American Mineralogist 86, 21-28.

Firth, C.W., Handley, H.K., Cronin, S.J. and Turner, S.P. (2014) The eruptive history and chemical stratigraphy of a post-caldera, steady-state volcano: Yasur, Vanuatu. Bull Volcanol 76, 837.

Francis, D. and Minarik, W. (2008) Aluminum-dependent trace element partitioning in clinopyroxene. Contrib Mineral Petrol 156, 439-451.

Gaetani, G.A. and Grove, T.L. (1995) Partitioning of rare earth elements between clinopyroxene and silicate melt Crystal-chemical controls. Geochimica et Cosmochimica Acta 59, 1951-1962.

Gallahan, W.E. and Nielsen, R.L. (1992) The partitioning of Sc, Y, and the rare earth elements between high-Ca pyroxene and natural mafic to intermediate lavas at 1 atmosphere. Geochimica et Cosmochimica Acta 56, 2387-2404.

Giletti, B.J. and Casserly, J.E.D. (1994) Strontium diffusion kinetics in plagioclase feldspars. Geochimica et Cosmochimica Acta 58, 3785-3793.

Giletti, B.J. and Shanahan, T.M. (1997) Alkali diffusion in plagioclase feldspar. Chemical Geology 139, 3-20.

Ginibre, C., Worner, G. and Kronz, A. (2002) Minor- and trace-element zoning in plagioclase: Implications for magma chamber processes at Parinacota volcano, northern Chile. Contrib Mineral Petrol 143, 300-315.

Grutzeck, M., Kridelbaugh, S. and Weill, D. (1974) The distribution of Sr and REE between diopside and silicate liquid. Geophysical Research Letters 1, 273-275.

Guo, C. and Zhang, Y. (2016) Multicomponent diffusion in silicate melts: SiO2–TiO2–Al2O3–MgO–CaO–Na2O–K2O System. Geochimica et Cosmochimica Acta 195, 126-141.

Hack, P.J., Nielsen, R.L. and Johnston, A.D. (1994) Experimentally determined rare-earth element and Y partitioning behavior between clinopyroxene and basaltic liquids at pressures up to 20 kbar. Chemical Geology 117, 89-105.

Hart, S.R. and Dunn, T. (1993) Experimental cpx/melt partitioning of 24 trace elements. Contrib Mineral Petrol 113, 1-8.

Hauri, E.H., Wagner, T.P. and Grove, T.L. (1994) Experimental and natural partitioning of Th, U, Pb and other trace elements between garnet, clinopyroxene and basaltic melts. . Chemical Geology 117, 149-166.

Helz, R.T. and Thornber, C.R. (1987) Geothermometry of Kilauea Iki lava lake, Hawaii. Bull Volcanol 49, 651-668.

Hill, E., Blundy, J.D. and Wood, B.J. (2011) Clinopyroxene-melt trace element partitioning and the development of a predictive model for HFSE and Sc. Contrib Mineral Petrol 161, 423-438.

Hill, E., Wood, B.J. and Blundy, J.D. (2000) The effect of Ca-Tschermaks component on trace element partitioning between clinopyroxene and silicate melt. Lithos 53, 203-215.

Himmelberg, G.R., Loney, R.A. and Craig, J.T. (1986) Petrogenesis of the Ultramafic Complex at the Blashke Islands, Southeastern Alaska. U.S. Geologcial Survey Bulletin v. 1662.

Howe, T.M., Lindsay, J.M. and Shane, P. (2015) Evolution of young andesitic–dacitic magmatic systems beneath Dominica, Lesser Antilles. Journal of Volcanology and Geothermal Research 297, 69-88.

Ito, J. (1976) High temperature solvent growth of anorthite on the join CaAl2Si2O8-SiO2. Contrib Mineral Petrol 59, 187-194.

Jackson, S.E. (2008) Calibration Strategies for Elemental Analysis by LA-ICP-MS, in: Sylvester, P. (Ed.), Laser Ablation-ICP-MS in the Earth Sciences: Current Practices and Outstanding Issues. Mineralogical Association of Canada, Vancouver, B.C., pp. 169-188.

Jochum, K.P., Weis, U., Stoll, B., Kuzmin, D., Yang, Q., Raczek, I., Jacob, D.E., Stracke, A., Birbaum, K., Frick, D.A., Günther, D. and Enzweiler, J. (2011) Determination of Reference Values for NIST SRM 610–617 Glasses Following ISO Guidelines. Geostandards and Geoanalytical Research 35, 397-429.

Jollands, M., O'Neill, H.C. and Hermann, J. (2014) The importance of defining chemical potentials, substitution mechanisms and solubility in trace element diffusion studies: the case of Zr and Hf in olivine. Contrib Mineral Petrol 168, 1-19.

Jollands, M.C., Burnham, A.D., O'Neill, H.S.C., Hermann, J. and Qian, Q. (2016) Beryllium diffusion in olivine: A new tool to investigate timescales of magmatic processes. Earth and Planetary Science Letters 450, 71-82.

Jones, J.H. and Burnett, D.S. (1987) Experimental geochemistry of Pu and Sm and the thermodynamics of trace element partitioning. Geochimica et Cosmochimica Acta 51, 769-782.

Koepke, J., France, L., Müller, T., Faure, F., Goetze, N., Dziony, W. and Ildefonse, B. (2011) Gabbros from IODP Site 1256, equatorial Pacific: Insight into axial magma chamber processes at fast spreading ocean ridges. Geochemistry, Geophysics, Geosystems 12.

Köhler, T.P. and Brey, G.P. (1990) Calcium exchange between olivine and clinopyroxene calibrated as a geothermobarometer for natural peridotites from 2 to 60 kb with applications. Geochimica et Cosmochimica Acta 54, 2375-2388.

Krogh, R. (2000) The garnet–clinopyroxene Fe2+–Mg geothermometer: an updated calibration. Journal of Metamorphic Geology 18, 211-219.

LaTourrette, T. and Wasserburg, G.J. (1998) Mg diffusion in anorthite: implications for the formation of early solar system planetesimals. Earth and Planetary Science Letters 158, 91-108.

Le Roux, V., Dasgupta, R. and Lee, C.T.A. (2011) Mineralogical heterogeneities in the Earth's mantle: Constraints from Mn, Co, Ni and Zn partitioning during partial melting. Earth and Planetary Science Letters 307, 395-408.

Levin, E.M., Robbins, C.R. and McMurdie, H.F. (1964) Phase Diagrams for Ceramists. The American Ceramic Society, 4055 N, High St., Columbus, Ohio.

Liang, Y. (2014) Time scales of diffusive re-equilibration in bi-mineralic systems with and without a fluid or melt phase. Geochimica et Cosmochimica Acta 132, 274-287.

Liang, Y., Sun, C. and Yao, L. (2013) A REE-in-two-pyroxene thermometer for mafic and ultramafic rocks. Geochimica et Cosmochimica Acta 102, 246-260.

Libourel, G., Boivin, P. and Biggar, G.M. (1989) The univariant curve liquid = forsterite + anorthite + diopside in the system CMAS at 1 bar: solid solutions and melt structure. Contrib Mineral Petrol 102, 406-421.

Longerich, H.P., Jackson, S.E. and Gunther, D. (1996) Laser Ablation Inductively Coupled Plasma Mass Spectrometric Transient Signal Data Acquisition and Analyte Concentration Calculation. Journal of Analytical Atomic Spectrometry 11, 899-904.

Longhi, J. and Hays, J.F. (1979) Phase equilibria and solid solution along the join CaAl2Si2O8-SiO2. American Journal of Science 279, 876-890.

Longhi, J., Walker, D. and Hays, J.F. (1976) Fe and Mg in plagioclase, in: New York, P.P., Inc (Ed.), 7th Lunar Science Conference, Houston, Texas, pp. 1281-1300.

Lundstrom, C.C., Shaw, H.F., Ryerson, F.J., Williams, Q. and Gill, J. (1998) Crystal chemical control of clinopyroxene-melt partitioning in the Di-Ab-An system: implications for elemental fractionations in the depleted mantle. Geochimica et Cosmochimica Acta 62, 2849-2862.

May, T.W. and Wiedmeyer, R.H. (1998) A table of polyatomic interferences in ICP-MS. Atomic Spectroscopy 19.

McDonough, W.F. and Sun, S.s. (1995) The composition of the Earth. Chemical Geology 120, 223-253.

McKay, G., Le, L., Wagstaff, J. and Crozaz, G. (1994) Experimental partitioning of rare earth elements and strontium: Constraints on petrogenesis and redox conditions during crystallization of Antarctic angrite Lewis Cliff 86010. Geochimica et Cosmochimica Acta 58, 2911-2919.

McKay, G., Wagstaff, J. and Yang, S.R. (1986) Clinopyroxene REE distribution coefficients for shergottites: The REE content of the Shergotty melt. Geochimica et Cosmochimica Acta 50, 927-937.

Megaw, H.D., Kempster, C.J.E. and Radoslovich, E.W. (1962) The structure of anorthite, CaAl2Si2O8. II. Description and discussion. Acta Crystallographica 15, 1017-1035.

Miller, S.A., Asimow, P.D. and Burnett, D.S. (2006) Determination of melt influence on divalent element partitioning between anorthite and CMAS melts. Geochimica et Cosmochimica Acta 70, 4258-4274.

Mollo, S., Putirka, K., Iezzi, G., Del Gaudio, P. and Scarlato, P. (2011) Plagioclase–melt (dis)equilibrium due to cooling dynamics: Implications for thermometry, barometry and hygrometry. Lithos 125, 221-235.

Murakami, H., Kimata, M. and Shimoda, S. (1992) Solubility of CaMgSi3O8 and []Si4O8 endmembers in anorthite. Journal of Mineralogy and Petrology and Economic Geology 87, 491-509.

Namur, O., Charlier, B., Toplis, M. and Vander Auwera, J. (2012) Prediction of plagioclase-melt equilibria in anhydrous silicate melts at 1-atm. Contrib Mineral Petrol 163, 133-150.

Nicholls, I.A. and Harris, K.L. (1980) Experimental rare earth element partition coefficients for garnet, clinopyroxene and amphibole coexisting with andesitic and basaltic liquids. Geochimica et Cosmochimica Acta 44, 287-308.

Nielsen, R.L., Davidson, P.M. and Grove, T.L. (1988) Pyroxene-melt equilibria: an updated model. Contrib Mineral Petrol 100, 361-373.

Nielsen, R.L., Ustunisik, G., Weinsteiger, A.B., Tepley, F.J., Johnston, A.D. and Kent, A.J.R. (2017) Trace element partitioning between plagioclase and melt: An investigation of the impact of experimental and analytical procedures. Geochemistry, Geophysics, Geosystems 18, 3359-3384.

Norman, M., Garcia, M.O. and Pietruszka, A.J. (2005) Trace-element distribution coefficients for pyroxenes, plagioclase, and olivine in evolved tholeiites from the 1955 eruption of Kilauea Volcano, Hawaii, and petrogenesis of differentiated rift-zone lavas. The American Mineralogist 90.

O'Neill, H.S.C. and Eggins, S.M. (2002) The effect of melt composition on trace element partitioning: an experimental investigation of the activity coefficients of FeO, NiO, CoO, MoO2 and MoO3 in silicate melts. Chemical Geology 186, 151-181.

O'Neill, H.S.C. (2016) The Smoothness and Shapes of Chondrite-normalized Rare Earth Element Patterns in Basalts. Journal of Petrology 57, 1463-1508.

Okamura, P.F. and Ghose, S. (1974) Structure and Crystal Chemistry of Calcium Tschermak's Pyroxene, CaAlAlSiO6. American Mineralogist 59, 549-557.

Olin, P.H. and Wolff, J.A. (2010) Rare earth and high field strength element partitioning between iron-rich clinopyroxenes and felsic liquids. Contrib Mineral Petrol 160, 761-775.

Onuma, N., Higuchi, H., Wakita, H. and Nagasawa, H. (1968) Trace element partition between two pyroxenes and the host lava. Earth and Planetary Science Letters 5, 47-51.

Ottonello, G., Moretti, R., Marini, L. and Vetuschi Zuccolini, M. (2001) Oxidation state of iron in silicate glasses and melts: a thermochemical model. Chemical Geology 174, 157-179.

Paton, C., Hellstrom, J., Paul, B., Woodhead, J. and Hergt, J. (2011) Iolite: Freeware for the visualisation and processing of mass spectrometric data. Journal of Analytical Atomic Spectrometry 26, 2508-2518.

Peters, M.T., Shaffer, E.E., Burnett, D.S. and Kim, S.S. (1995) Magnesium and titanium partitioning between anorthite and Type B CAI liquid: Dependence on oxygen fugacity and liquid composition. Geochimica et Cosmochimica Acta 59, 2785-2796.

Pirard, C. (2010) Transfer of melts in the sub-arc mantle: Insights from high-pressure experiments and from the New Caledonia Ophiolite., Research School of Earth Sciences. The Australian National University.

Pirard, C., Hermann, J. and O'Neill, H.S.C. (2013) Petrology and Geochemistry of the Crust-Mantle Boundary in a Nascent Arc, Massif du Sud Ophiolite, New Caledonia, SW Pacific. Journal of Petrology 54, 1759-1792.

Pun, A., Papike, J.J. and Layne, G.D. (1997) Subsolidus REE partitioning between pyroxene and plagioclase in cumulate eucrites: An ion microprobe investigation. Geochimica et Cosmochimica Acta 61, 5089-5097.

Putirka, K. (2008) Thermometers and Barometers for Volcanic Systems. Reviews in Mineralogy and Geochemistry 69, 61-120.

Putirka, K.D. (2003) New clinopyroxene-liquid thermobarometers for mafic, evolved, and volatile-bearing lava compositions, with applications to lavas from Tibet and the Snake River Plain, Idaho. American Mineralogist 88, 1542.

Redler, C., Johnson, T.E., White, R.W. and Kunz, B.E. (2012) Phase equilibrium constraints on a deep crustal metamorphic field gradient: metapelitic rocks from the Ivrea Zone (NW Italy). Journal of Metamorphic Geology 30, 235-254.

Sclar, C.B. and Kastelic, R.L. (1979) Iron in Anorthite: An Experimental Study. Lunar and Planetary Institute.

Senderov, E.E., Vasiliev, N.S. and Yudin, E.I. (1982) The order-disorder transition in gallium analogue of albite, NaGaSi3O8. Physics and Chemistry of Minerals 8, 51-54.

Severs, M.J., Beard, J.S., Fedele, L., Hanchar, J.M., Mutchler, S.R. and Bodnar, R.J. (2009) Partitioning behavior of trace elements between dacitic melt and plagioclase, orthopyroxene, and clinopyroxene based on laser ablation ICPMS analysis of silicate melt inclusions. Geochimica et Cosmochimica Acta 73, 2123-2141.

Shannon, R.D. (1976) Revised Effective Ionic Radii and Systematic Studies of Interatomic Distances in Halides and Chalcogenides. Acta Crystallographica, 751-767.

Spandler, C., O'Neill, H.S. and Kamenetsky, V.S. (2007) Survival times of anomalous melt inclusions from element diffusion in olivine and chromite. Nature 447, 303-306.

Spandler, C. and O'Neill, H.S.C. (2009) Diffusion and partition coefficients of minor and trace elements in San Carlos olivine at 1,300°C with some geochemical implications. Contrib Mineral Petrol 159, 791-818.

Stamper, C.C., Blundy, J.D., Arculus, R.J. and Melekhova, E. (2014) Petrology of Plutonic Xenoliths and Volcanic Rocks from Grenada, Lesser Antilles. Journal of Petrology 55, 1353-1387.

Sugawara, T. (2000) Thermodynamic analysis of Fe and Mg partitioning between plagioclase and silicate liquid. Contrib Mineral Petrol 138, 101-113.

Sugawara, T. (2001) Ferric iron partitioning between plagioclase and silicate liquid: thermodynamics and petrological applications. Contrib Mineral Petrol 141, 659-686.

Sun, C., Graff, M. and Liang, Y. (2017) Trace element partitioning between plagioclase and silicate melt: The importance of temperature and plagioclase composition, with implications for terrestrial and lunar magmatism. Geochimica et Cosmochimica Acta 206, 273-295.

Sun, C. and Liang, Y. (2012) Distribution of REE between clinopyroxene and basaltic melt along a mantle adiabat: effects of major element composition, water, and temperature. Contrib Mineral Petrol 163, 807-823.

Sun, C. and Liang, Y. (2014) An assessment of subsolidus re-equilibration on REE distribution among mantle minerals olivine, orthopyroxene, clinopyroxene, and garnet in peridotites. Chemical Geology 372, 80-91.

Sun, C. and Liang, Y. (2017) A REE-in-plagioclase–clinopyroxene thermometer for crustal rocks. Contrib Mineral Petrol 172, 24.

Tanner, D., Mavrogenes, J.A., Arculus, R.J. and Jenner, F.E. (2014) Trace Element Stratigraphy of the Bellevue Core, Northern Bushveld: Multiple Magma Injections Obscured by Diffusive Processes. Journal of Petrology 55, 859-882.

Tepley, F.J., Lundstrom, C.C., McDonough, W.F. and Thompson, A. (2010) Trace element partitioning between high-An plagioclase and basaltic to basaltic andesite melt at 1 atmosphere pressure. Lithos 118, 82-94.

Tollan, P.M.E., Bindeman, I. and Blundy, J.D. (2011) Cumulate xenoliths from St. Vincent, Lesser Antilles Island Arc: a window into upper crustal differentiation of mantle-derived basalts. Contrib Mineral Petrol 163, 189-208.

Tsuchiyama, A. (1983) Crystallization kinetics in the system CaMgSi2O6-CaAl2Si2O8: the delay in nucleation of diopside and anorthite. American Mineralogist 68, 687-698.

Van Orman, J.A., Cherniak, D.J. and Kita, N.T. (2014) Magnesium diffusion in plagioclase: Dependence on composition, and implications for thermal resetting of the 26Al–26Mg early solar system chronometer. Earth and Planetary Science Letters 385, 79-88.

Van Orman, J.A., Grove, T.L. and Chimizu, N. (2001) Rare earth element diffusion in diopside: influence of temperature, pressure, and ionic radius , and an elastic model for diffusion in silicates. Contrib Mineral Petrol 141, 687-703.

Watson, E.B. (1979) Calcium diffusion in a simple silicate melt to 30 kbar. Geochimica et Cosmochimica Acta 43, 313-322.

Watson, E.B. and Baxter, E.F. (2007) Diffusion in solid-Earth systems. Earth and Planetary Science Letters 253, 307-327.

Watson, E.B. and Dohmen, R. (2010) Non-traditional and Emerging Methods for Characterizing Diffusion in Minerals and Mineral Aggregates. Reviews in Mineralogy and Geochemistry 72, 61-105.

Watson, E.B., Othman, D.B., Luck, J.-M. and Hofmann, A.W. (1987) Partitioning of U, Pb, Cs, Yb, Hf, Re and Os between chromian diopsidic pyroxene and haplobasaltic liquid. Chemical Geology 62, 191-208.

Williamson, B.J., Herrington, R.J. and Morris, A. (2016) Porphyry copper enrichment linked to excess aluminium in plagioclase. Nature Geosci 9, 237-241.

Winter, J.D. (2012) Principles of igneous and metamorphic petrology, 2nd ed. Pearson Education Inc.

Witt-Eickschen, G. and O'Neill, H.S.C. (2005) The effect of temperature on the equilibrium distribution of trace elements between clinopyroxene, orthopyroxene, olivine and spinel in upper mantle peridotite. Chemical Geology 221, 65-101.

Wood, B. and Blundy, J.D. (1997) A predictive model for rare earth element partitioning between clinopyroxene and anhydrous silicate melt. Contrib Mineral Petrol 129, 166-181.

Wood, B.J. and Blundy, J.D. (2001) The effect of cation charge on crystal-melt partitioning of trace elements. Earth and Planetary Science Letters 188, 59-71.

Wood, B.J. and Blundy, J.D. (2002) The effect of H2O on crystal-melt partitioning of trace elements. Geochimica et Cosmochimica Acta 66, 3647-3656.

Wood, B.J. and Blundy, J.D. (2014) 3.11 - Trace Element Partitioning: The Influences of Ionic Radius, Cation Charge, Pressure, and Temperature, in: Holland, H.D., Turekian, K.K. (Eds.), Treatise on Geochemistry (Second Edition). Elsevier, Oxford, pp. 421-448.

Ziberna, L., Green, E.C.R. and Blundy, J.D. (2017) Multiple-reaction geobarometry for olivine-bearing igneous rocks. American Mineralogist 102, 2349-2366.